TECHNISCHE UNIVERSITÄT DARMSTADT

ULB

Topochemical fluorination and defluorination in the context of fluoride-ion batteries and tuning of magnetic properties

Wissel, Kerstin

(2020)

DOI (TUprints): https://doi.org/10.25534/tuprints-00013383

Lizenz:

CC-BY-SA 4.0 International - Creative Commons, Attribution Share-alike

Publikationstyp: Ph.D. Thesis

Fachbereich: 11 Department of Materials and Earth Sciences

Quelle des Originals: https://tuprints.ulb.tu-darmstadt.de/13383

Topochemical fluorination and defluorination in the context of fluoride-ion batteries and tuning of magnetic properties

TECHNISCHE UNIVERSITÄT DARMSTADT

Vom Fachbereich Material-und Geowissenschaften

der Technischen Universität Darmstadt

zur Erlangung des akademischen Titels

Dr. rer.-nat.

genehmigte Dissertation von

Kerstin Wissel, M.Sc.

aus Hanau

1. Gutachter: Prof. Dr. Oliver Clemens

2. Gutachter: Prof. Dr. Peter R. Slater

Tag der Einreichung: 18.06.2020

Tag der Prüfung: 20.08.2020

Darmstadt 2020

D17

Please cite this document as:
URN: urn:nbn:de:tuda-tuprints-133834
URI: https://tuprints.ulb.tu-darmstadt.de/id/eprint/13383

This document is published by TUprints,
TU Darmstadt publication service
http://tuprints.ulb.tu.darmstadt.de/
tuprints@ulb.tu-darmstadt.de

This publication is licensed under a Creative
Commons Attribution-ShareAlike 4.0 International
License (CC BY-SA 4.0).
https://creativecommons.org/licenses/

Erklärung zur Dissertation

Hiermit versichere ich, die vorliegende Dissertation ohne Hilfe Dritter und nur mit den angegebenen Quellen und Hilfsmitteln angefertigt zu haben. Alle Stellen, die Quellen entnommen wurden, sind als solche kenntlich gemacht worden. Diese Arbeit hat in gleicher oder ähnlicher Form noch keiner Prüfungsbehörde vorgelegen.

Darmstadt, den

(Kerstin Wissel)

The presented dissertation summarises in large parts the scientific findings reported in the following peer-reviewed articles. The provided results have been to a great extent restructured, rewritten or modified and additions have been applied; however, parts of this work are excerpts from the original publications. Respective permissions have been granted by the publishers (see footnotes).

[1] **Wissel, K.**; Dasgupta, S.; Benes, A.; Schoch, R.; Bauer, M.; Witte, R.; Fortes, A. D.; Erdem, E.; Rohrer, J.; Clemens, O., Developing intercalation based anode materials for fluoride-ion batteries: topochemical reduction of $Sr_2TiO_3F_2$ via a hydride based defluorination process. *J. Mater. Chem. A* **2018,** *6* (44), 22013-22026. [a]

[2] **Wissel, K.**; Vogel, T.; Dasgupta, S.; Fortes, A. D.; Slater, P. R.; Clemens, O., Topochemical Fluorination of n = 2 Ruddlesden-Popper Type $Sr_3Ti_2O_7$ to $Sr_3Ti_2O_5F_4$ and Its Reductive Defluorination. *Inorg. Chem.* **2020,** *59* (2), 1153-1163. [b]

[3] **Wissel, K.**; Heldt, J.; Groszewicz, P. B.; Dasgupta, S.; Breitzke, H.; Donzelli, M.; Waidha, A. I.; Fortes, A. D.; Rohrer, J.; Slater, P. R.; Buntkowsky, G.; Clemens, O., Topochemical Fluorination of La_2NiO_{4+d}: Unprecedented Ordering of Oxide and Fluoride Ions in $La_2NiO_3F_2$. *Inorg. Chem.* **2018,** *57* (11), 6549-6560. [c]

[4] **Wissel, K.**; Malik, A. M.; Vasala, S.; Plana-Ruiz, S.; Kolb, U.; Slater, P. R.; da Silva, I.; Alff, L.; Rohrer, J.; Clemens, O., Topochemical reduction of $La_2NiO_3F_2$: the first Ni-based Ruddlesden-Popper n = 1 T'-type structure and the impact of reduction on magnetic ordering. *Chem. Mater.* **2020**, *32* (7), 3160-3179. [d]

[5] Vasala, S.; Jakob, A.; **Wissel, K.**; Waidha, A. I.; Alff, L.; Clemens, O., Reversible Tuning of Magnetization in a Ferromagnetic Ruddlesden–Popper-Type Manganite by electrochemical Fluoride-Ion Intercalation. *Adv. Electron. Mater.*, **2019**, *6* (2), 1900974. [e]

[a] Reproduced in part with permission from reference 1. Copyright 2018 The Royal Society of Chemistry.

[b] Reproduced in part with permission from reference 2. Copyright 2020 American Chemical Society.

[c] Reproduced in part with permission from reference 3. Copyright 2018 American Chemical Society.

[d] Reproduced in part with permission from reference 4. Copyright 2020 American Chemical Society.

[e] Reproduced in part with permission from reference 5. Copyright 2019 John Wiley and Sons.

Abstract

Within this work, it was demonstrated that topochemical modifications of the anion sublattices of Ruddlesden-Popper-type oxides $A_{n+1}B_nO_{3n+1}$ and derived metastable oxyfluorides $A_{n+1}B_nO_{3n+1-x}F_{2x}$ with $0 < x \leq 2$ have a significant influence on the crystal and electronic structures of the newly synthesised phases. This could be used to effectively tailor and reversibly tune magnetic properties.

Different non-oxidative, reductive or oxidative modification routes, leading to fluoride intercalation, exchange and/or deintercalation processes, were investigated. Such topochemical reactions have been also found to take place upon the electrochemical fluorination of Ruddlesden-Popper-type oxides in fluoride-ion batteries and have led to the development of intercalation-based cathode materials. For the development of novel intercalation-based electrodes, oxyfluorides, obtained via a prior non-oxidative topochemical fluorination of the respective oxides, were examined concerning their potential use as active anode or cathode materials. During charging, the use of the oxyfluoride as active anode material results in defluorination, whereas additional fluorination occurs when the oxyfluoride contains additional vacancies and is used as active cathode material. For both cases, the oxyfluoride represents the discharged state of the electrode material. These additional topochemical modifications of the parent oxyfluorides could be also achieved via chemical preparation approaches. For the chemical preparation of the anode material in the charged state, a reductive defluorination method based on sodium hydride was developed. The additional fluorination was performed using highly oxidising F_2 gas. The non-oxidatively fluorinated oxyfluorides $Sr_2TiO_3F_2$, $Sr_3Ti_2O_5F_4$ and $La_2NiO_3F_2$ were modified accordingly. A focus was set on the defluorination of these phases, since this is related to the development of intercalation-based anode materials, a field, which has been conceptionally unexplored prior to this work. However, the structural stability of the oxyfluorides within the electrode composites was found only for $Sr_3Ti_2O_5F_2$ and $La_2NiO_3F_2$, of which primarily $La_2NiO_3F_2$ showed redox activity. This Ni-based phase could be successfully electrochemically defluorinated as well as additionally fluorinated, showing its potential to serve as both, active anode and cathode material.

The resulting composition-induced alterations of the crystal structure and magnetic properties of the chemically and electrochemically obtained phases were analysed by a variety of characterisation techniques, including different diffraction and spectroscopy methods, DFT-based calculations and magnetic measurements. The chemically and electrochemically formed phases showed to be structurally related. Therefore, the structural and magnetic characteristics of the chemically prepared phases, which were analysed in-depth, could be transferred to the electrochemically synthesised phases. Magnetic properties, related to the presence or absence of unpaired electrons and the strength of exchange interactions, were found to be highly dependent on the structural modifications and transition metal cation oxidations states. Even though a generally detrimental effect of irreversible side reactions, resulting in the progressive decrease of the electronic conductivity of the carbon additive, was found to exist, the reversibility of the structural changes over extended cycling was observed. This was found to offer the possibility to switch reversibly between different magnetic states

of the charged and discharged phases. A detailed investigation of magnetoelectric switching due to reversible fluoride intercalation was performed on $La_{1.3}Sr_{1.7}Mn_2O_7$. A switching between a strongly and weakly ferromagnetic state could be achieved, resulting in high relative changes of the magnetisation with one of the highest reported magnetoelectric voltage couplings reported for tuneable magnetic systems.

Abstrakt

In der vorliegenden Arbeit wurde aufgezeigt, dass topochemische Modifikationen des Anionenteilgitters von Ruddlesden-Popper-artigen Oxiden $A_{n+1}B_nO_{3n+1}$ und davon abgeleiteten metastabilen Oxyfluoriden $A_{n+1}B_nO_{3n+1-x}F_{2x}$ mit $0 < x \leq 2$ einen erheblichen Einfluss auf die Kristall- sowie elektronische Struktur der neu hergestellten Phasen hat. Dies kann genutzt werden, um magnetische Eigenschaften effektiv anzupassen und reversible einzustellen.

Verschiedene nicht-oxidative, reduktive oder oxidative Modifikationsrouten, die zu Fluorideinlagerung, -austausch und/oder –auslagerung führen, wurden untersucht. Es wurde bereits in früheren Studien aufgezeigt, dass derartige topochemische Reaktionen auch durch die elektrochemische Fluorierung von Ruddlesden-Popper-artigen Oxiden in Fluoridionenbatterien hervorgerufen werden kann. Dies hat zur Entwicklung von interkalationsbasierten Kathodenmaterialien geführt. Für die Entwicklung neuartiger interkalationsbasierter Elektroden wurden Oxyfluoride, die über eine vorherige nicht-oxidative topochemische Fluorierung der entsprechenden Oxide gewonnen wurden, in Hinblick auf einen potentiellen Einsatz als aktives Anoden- oder Kathodenmaterial untersucht. Während des Ladens führt die Nutzung des Oxyfluorids als aktives Anodenmaterial zu einer Defluorierung, während eine zusätzliche Fluorierung beobachtet wird, wenn das Oxyfluorid weitere Leerstellen besitzt und als Kathodenmaterial eingesetzt wird. In beiden Fällen stellt das Oxyfluorid den entladenen Zustand des Elektrodenmaterials dar. Diese zusätzlichen topochemischen Modifikationen der Ausgangsoxyfluoride konnten zudem über chemische Synthesewege erzielt werden. Für die chemische Präparation des Anodenmaterials im geladenen Zustand wurde eine reduktive Defluorierungsmethode basierend auf Natriumhydrid entwickelt. Die zusätzliche Fluorierung wurde durchgeführt mithilfe von stark oxidierendem F_2-Gas. Die nicht-oxidativ fluorierten Oxyfluoride $Sr_2TiO_3F_2$, $Sr_3Ti_2O_5F_4$ und $La_2NiO_3F_2$ wurden entsprechend modifiziert. Ein Fokus wurde gesetzt auf die Defluorierung dieser Phasen, da dies mit der Entwicklung von interkalationsbasierten Anodenmaterialien verbunden ist, was zu Beginn dieser Arbeit ein konzeptionell unerforschtes Feld darstellte. Strukturelle Stabilität der Oxyfluoride in den Elektrodenkompositen konnte jedoch nur für $Sr_3Ti_2O_5F_2$ und $La_2NiO_3F_2$ bestätigt werden. Von diesen Phasen zeigte vor allem $La_2NiO_3F_2$ Redox-Aktivität. Diese Ni-basierte Phase konnte erfolgreich elektrochemisch defluoriert und zusätzlich fluoriert werden. Dies zeigt das Potential von $La_2NiO_3F_2$ auf, sowohl als aktives Anoden-, als auch Kathodenmaterial eingesetzt werden zu können.

Die resultierenden zusammensetzungsinduzierten Änderungen der Kristallstruktur und der magnetischen Eigenschaften der chemisch und elektrochemisch erzeugten Phasen wurde mittels einer Vielzahl an Charakterisierungsmethoden analysiert, die verschiedene Diffraktions- und Spektroskopiemethoden, DFT-basierte Berechnungen und magnetische Messungen umfassten. Die chemisch und elektrochemisch hergestellten Phasen zeigten eine strukturelle Ähnlichkeit. Daher konnten strukturelle und magnetische Charakteristika der chemisch hergestellten Phasen, die experimentell eingehender untersucht werden konnten, auf die elektrochemisch synthetisierten Phasen übertragen werden. Magnetische Eigenschaften, die auf die Präsenz oder das Fehlen von ungepaarten Elektronen und die Stärke der Austauschwechselwirkungen zurückgeführt werden konnten, zeigten eine starke

Abhängigkeit von strukturellen Modifikationen und von den Oxidationszuständen der Übergangsmetallkationen. Obwohl ein prinzipiell nachteiliger Effekt von irreversiblen Nebenreaktionen, die zu einer zunehmenden Abnahme der elektronischen Leitfähigkeit des Kohlenstoffadditivs führten, nachgewiesen werden konnte, konnte die Reversibilität der strukturellen Änderungen während andauerndem Zyklierens bestätigt werden. Dies eröffnete Möglichkeiten, zwischen verschiedenen magnetischen Zuständen der geladenen und entladenen Phasen reversible zu schalten. Eine detaillierte Untersuchung dieses magnetoelektrischen Schaltens aufgrund einer reversiblen Einlagerung von Fluoridionen wurde an $La_{1.3}Sr_{1.7}Mn_2O_7$ durchgeführt. Schalten zwischen einem stark und schwach ferromagnetischen Zustand konnte erzielt werden, was zu hohen relativen Änderungen der Magnetisierung mit einem der höchsten berichteten magnetoelektrischen Spannungskopplungen für schaltbare magnetische Systeme einherging.

Table of Contents

1 Introduction

The continued demand for new materials with interesting functional properties requires the development of innovative synthesis methods, which allow for the preparation of otherwise inaccessible materials. Based on the close relationship between the crystal structure, the composition and the properties of a material, a property engineering is possible, when structural and compositional changes can be evoked within a material in a targeted manner. With respect to this, topochemical modifications offer great potential. [6-13] In a topochemical reaction, the structural framework of the material is preserved, while the high mobility of at least one of the involved ionic species facilitate ion intercalation, exchange or deintercalation processes, often at comparatively low temperatures.

Compounds with Ruddlesden-Popper-type structure $A_{n+1}B_nO_{3n+1}$ ($n = \infty$, 1, 2 and 3) show a high affinity towards the alteration of the anion sublattice via such low-temperature reactions. [6-9] The structure can be described as stacking of building blocks of n ABO_3 units separated by one AO rock salt-type layer. Within the rock salt-type layers, interstitial anion vacancies are present, which can be filled with up to two additional anions per formula unit. [14-17] In particular, topochemical fluorination reactions offer wide-ranging possibilities to alter oxidation states and/or coordination environments of the transition metal cations of the formed metastable oxyfluorides in comparison to their precursor oxides. Depending on the fluorination reagents used, the fluorination process can be oxidative, non-oxidative, or even reductive. The oxidative fluorination proceeds via an intercalation of up to two fluoride ions into the interstitial anion sites, resulting in $A_{n+1}B_nO_{3n+1}F_x$ with $0 < x \leq 2$. The non-oxidative fluorination leads to the formation of $A_{n+1}B_nO_{3n+1-x}F_{2x}$ with $0 < x \leq 2$ and takes place via a coupled substitution and intercalation process, in which for each substituted oxide ion two fluoride ions are intercalated under the maintenance of the oxidation state. A substitution of oxide ions by fluoride ions without an additional intercalation of fluoride ions leads to a reductive fluorination, yielding $A_{n+1}B_nO_{3n+1-x}F_x$ with $0 < x \leq 3n+1$. Besides these chemical methods based on various fluorination reagents, electrochemical approaches for the oxidative fluorination of Ruddlesden-Popper oxides have been investigated recently. [18-20] These reactions are performed within all-solid state fluoride-ion batteries and the Ruddlesden-Popper-type oxides are used as active intercalation-based cathode materials. The oxide represents the discharged state of the cathode material and the oxidatively fluorinated phase corresponds to the charged state.

Changed magnetic properties have been found for the formed fluorinated phases in comparison to the precursor oxides after the topochemical fluorination. An alteration of the transition metal oxidation state, when using an oxidative or reductive fluorination route, leads to a change of the electronic structure of the compound, which determines the ordering between the magnetic moments of the transition metal cations via indirect exchange interactions. [8, 9, 21, 22] Additionally, the exchange interactions are affected by the intercalation of fluoride ions into the interstitial anion site upon fluorination. An increased anisotropy of the exchange interactions is often observed, as they have to be mediated via longer distances between adjacent perovskite-type layers and/or over a larger number of anions, potentially hampering a three-dimensional ordering of the magnetic moments. [23-25]

Based on these widely investigated topochemical modification methods, new synthesis routes combining consecutively performed topochemical reactions are promising for the preparation of new magnetic materials, opening up a largely unexplored research field. In this context, a sequence of a non-oxidative fluorination and an additional topochemical modification step via a reductive defluorination or an oxidative fluorination (referred to as post-fluorination within this work) approach may also lead to alterations of the oxidation state of Ruddlesden-Popper-type compounds. However, these approaches have not been widely pursued so far.

One focus of this work is set on the development of respective reductive defluorination methods of oxyfluorides $A_{n+1}B_nO_{3n+1-x}F_{2x}$ with $0 < x \leq 2$, which might be promising for the stabilisation of unusually low oxidation states of the transition metal cations. After the non-oxidative topochemical fluorination step, leading to the formation of the oxyfluorides, two reductive approaches were considered. The first approach is based on a chemical reduction using sodium hydride as reducing agent, which can be regarded as an analogy to known chemical deoxygenation routes of Ruddlesden-Popper oxides [11, 12]. For a successful defluorination of oxyfluorides, the metastability of the oxyfluorides has to be taken into account for the choice of reaction conditions, which makes a complex balancing of the reaction chemistry between the stability of the educts as well as the products and kinetic limitations necessary. Another approach for the preparation of defluorinated phases is based on electrochemical reactions within fluoride-ion batteries. Facilitated by the broad stability window of the used electrolyte $La_{0.9}Ba_{0.1}F_{2.9}$ [26], not only the oxidative fluorination of Ruddlesden-Popper oxides, but also the reductive defluorination of the obtained oxyfluorides should be possible. For the targeted reduction within a fluoride-ion battery, the oxyfluoride $A_{n+1}B_nO_{3n+1-x}F_{2x}$ is used as active anode material and represents its discharged state. Upon charging, fluoride deintercalation would occur. The potential of such electrochemical reductions of intercalation-based anode materials for the improvement the cycling stability and rate capability has not been investigated so far. The development of intercalation-based anodes would lead to a significant advancement of fluoride-ion batteries, if a structural reversibility can be observed within the anode material upon reversible charging and discharging. In particular, the combination of intercalation-based anode and cathode materials could drive the development forward due to expectably improved long-term stability as compared to so far established battery systems with conversion-based electrodes [27-29].

Possibilities to additional fluorinate non-oxidatively fluorinated oxyfluorides $A_{n+1}B_nO_{3n+1-x}F_{2x}$ in a post-fluorination step are explored in addition, based on approaches known for the oxidative fluorination of Ruddlesden-Popper-type oxides. For this, highly oxidative F_2 gas is used in a chemical approach. Moreover, the application of the oxyfluoride as active cathode material within fluoride-ion batteries for a possible electrochemical fluorination is examined.

The reductive defluorination and oxidative additional fluorination processes should have a considerable impact on the magnetic properties of the obtained phases, since their crystal and electronic structures should be changed significantly in comparison to their parent oxyfluoride phase. Furthermore, the potential reversibility of structural and compositional changes of the Ruddlesden-Popper-type phases upon repeated charging and discharging within a fluoride-ion battery may offer the possibility to switch reversibly between magnetic states of the charged and discharged phases. This approach of magnetisation tuning via electrochemical reactions has been demonstrated previously for various lithium-ion battery systems [30-33] and can be interesting for different applications like spin-based electronics, magnetic data storage or magnetic actuation. [34, 35, 31] Since the magnetic properties of Ruddlesden-Popper-type phases

are strongly dependent on the fluoride content and the corresponding oxidation state, a magnetic switching based on the reversible electrochemical fluorination and defluorination of such oxides and oxyfluorides in fluoride-ion batteries is also promising and is, therefore, investigated in addition.

Within the scope of this thesis, the feasibility of the discussed topochemical modification methods and their influence on crystal structure and magnetic properties is investigated for different material systems. Starting from the respective Ruddlesden-Popper-type oxide $A_{n+1}B_nO_{3n+1}$, the following systems with different orders n are examined: Sr_2TiO_4 (n = 1), $Sr_3Ti_2O_7$ (n = 2), La_2NiO_{4+d} (n =1) and $La_{1.3}Sr_{1.7}Mn_2O_7$ (n =2).

A major part of the presented scientific findings is focussed on the first three compounds, which were non-oxidatively fluorinated and subsequently subjected to an additional chemical or electrochemical topochemical defluorination step. Besides the investigation of structural and magnetic properties, the development of a detailed understanding of the reaction process is also required. The influence of electrochemical reactions onto the oxyfluorides cannot be decoupled from the understanding of the corresponding chemical reactions. In principle, it can be expected that, if a topochemical modification of the oxyfluorides via electrochemical defluorination and post-fluorination methods is possible, similar structural distortions in the electrode composites as compared to the chemically prepared phases can be found. The presence of the reduced or oxidised Ruddlesden-Popper-type phases in a matrix of the solid electrolyte and carbon additive in the electrode composites renders a detailed analysis of small structural differences difficult, which is related to the fact that fluoride is a weak scatterer in comparison to the heavier elements contained in the electrode composites. However, the chemical synthesis routes can be regarded as ways to prepare the charged states of the anode and cathode materials ex-situ and a transfer of the obtained understanding of the structure including approximate fluoride contents and magnetic properties to the electrochemically formed phases might be possible. The reversibility of the electrochemical reactions is demonstrated and the cycling performance of cells with different electrode materials is examined. Advantages and limitations of the electrochemical synthesis approach are discussed.

Furthermore, after the analysis of crystal structure and magnetic property changes, the potential of magnetic tuning due to chemical and/or (reversible) electrochemical modifications in comparison to the parent oxides and oxyfluorides is examined. A special focus is placed on the investigation of reversible magnetoelectric tuning of the Ruddlesden-Popper-type oxide $La_{1.3}Sr_{1.7}Mn_2O_7$ via reversible oxidative fluorination within fluoride-ion batteries.

For the clarification of the complex and interdependent aspects investigated, a comprise overview over the different fields targeted within this work is given in Figure 1-1.

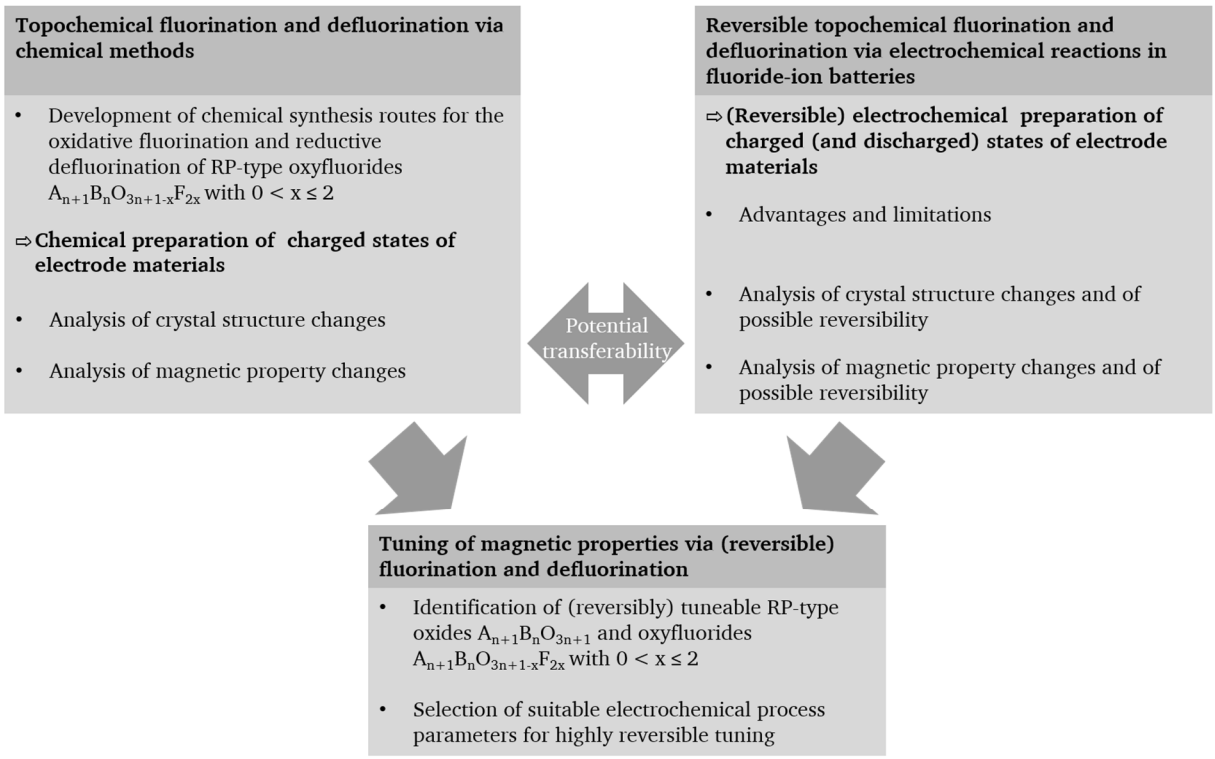

Figure 1-1: Overview over key aims of this work.

2 Fundamentals

This chapter provides a summary over fundamentals relevant for the understanding of the scientific findings reported in this work. The structure of Ruddlesden-Popper type compounds and the impact of low-temperature topochemical modifications on it are discussed. Furthermore, the arising changes of material properties, especially concerning magnetism, are considered. In addition, the working principles of the characterisation techniques used within this thesis and the experimental set-ups are presented. A strong focus is set on the basics of diffraction and the Rietveld method, which have been used as main characterisation tools for the determination of crystal structures of phases obtained via topochemical fluorination and defluorination reactions.

2.1 Ruddlesden-Popper compounds

Compounds with the perovskite-related Ruddlesden-Popper (RP) structure with the general formula $A_{n+1}B_nX_{3n+1}$ are known for a variety of properties including superconductivity [36-42] and a broad range of magnetic phenomena [43-48]. Due to the close relationship between the structure of a material and its property, a detailed understanding of the former is required to comprehend an arising property. Therefore, the crystal and electronic structure of RP-type compounds and their interplay are examined in the following. Moreover, correlations between structural considerations and magnetic properties are discussed.

2.1.1 Crystal structure

The crystal structure of the RP homologous series $A_{n+1}B_nX_{3n+1}$ can be described as a layered structure, in which n layers of ABX_3 perovskite-like units are separated by one AX rock salt-type layer. A and B are cations and X anions. A is an alkali, alkaline earth or rare earth metal cation and B is a transition metal cation. Oxide and fluoride ions are commonly found as anions. The crystal structures for $n = \infty$, 1, 2 and 3 are depicted in Figure 2-1. The $n = \infty$ member of the homologous series is equivalent to the perovskite structure. The $n = 1$ structure is also referred to as K_2NiF_4 or T structure. Lower-order members possess a tetragonal aristotype structure with space group *I4/mmm*. Independently on n, two formula units per unit cell are found. The 2-dimensional layered nature of RP compounds leads to a decrease in dimensionality as compared to the perovskite structure and anisotropic properties can be expected. [14-17]

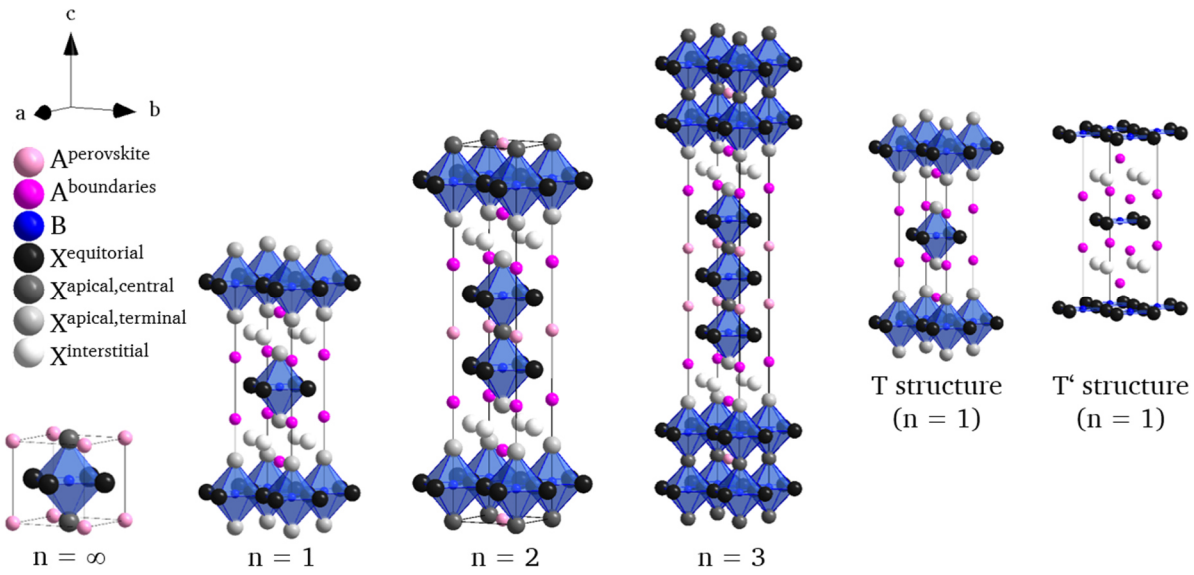

Figure 2-1: Crystal structures of the Ruddlesden-Popper series with n = ∞, 1, 2 and 3. The different A and B cation and X anion sites are denoted. In stoichiometric Ruddlesden-Popper-type compounds $A_{n+1}B_nX_{3n+1}$ with T structure, the interstitial anion site is not occupied. For comparison, the T' structure, in which the interstitial site is filled instead of the apical site, is shown.

Different crystallographic sites of the ions can be identified within the unit cell; for $n \geq 3$, due to the stacking of an increasing number of perovskite-type layers, different crystallographic sites exist for the B cation and $X^{equitorial}$ anion site. A general formula for RP compounds describing the relative occurrence of the sites as a function of n is given by

$$A_{n-1}^{perovskite} A_2^{boundaries} B_n X_{2n}^{equitorial} X_{n-1}^{apical,central} X_2^{apical,terminal}$$

For $n \geq 2$, two A cation sites can be distinguished. One cation $A^{perovskite}$ is located in the perovskite-type stack with a cuboctahedral anionic coordination with a coordination number of 12. The second cation $A^{boundaries}$ is found at the boundaries between the perovskite and rock salt building blocks and has a coordination number of 9; the coordination of the cation in a perfect rock salt structure should be 12, however, since the rock salt layer is less than one unit cell thick due the atomic displacements caused by the perovskite stacks, a lower coordination is observed. The two A sites can contain two different cations potentially resulting in different ordering scenarios. For example, for $Gd_2SrCo_2O_7$, an ordering of the larger Sr^{2+} cations at the position within the perovskite-type stacks and the smaller Gd^{3+} cations at the boundary has been reported. [49] The B cation is placed in the anionic octahedra of the perovskite blocks. Other coordinations than 6-fold, e.g. pyramidal or square-planar, are possible for the B cations, if vacancies are present. For octahedrally coordinated B cations, the octahedra are connected via corner-sharing to four octahedra (n = 1), five octahedra (n = 2), five or six octahedra ($n \geq 3$) or six octahedra (n = ∞). For the anions, three sites are found. All anions are coordinated by six cations; the sets of ions differ however. The anions $X^{equitorial}$ connect the octahedra within the *ab* plane. For $n \geq 2$, the octahedra of the perovskite-type stacks are linked together along the *c* axis by the anions $X^{apical,central}$. The anions $X^{apical,terminal}$ are located at the boundary between perovskite and rock salt buildings blocks and form the tips of the octahedra towards the rock salt layers. Moreover, within the rock salt layers, vacant interlayers are present. Per formula unit, these interstitial vacancies can be filled with up to two additional anions $X^{intersitial}$, e.g. with oxide ions in over-stoichiometric oxides or with fluoride ions in oxyfluorides. When the rock salt layer is filled completely, a CaF_2-type layer

with tetrahedrally coordinated anions is formed. The general formula can be modified to $A_{n+1}B_nX_{3n+1}X_x^{interstitial}$ with $0 < x \leq 2$. Hence, in total up to 3n+3 anions per $A_{n+1}B_n$ cationic unit may be present in a RP-type compounds. [14-17]

The interstitial vacancies play also an important role in the formation of the T' structure $A_{n+1}B_nX_{2n+2}$, in which the transition metal cations are square-planarly coordinated by anions and the interstitial site is filled by the remaining anions forming a CaF_2-type layer. [50] The T' structure can be described as stacking of alternating $A_{n-1}(B_nX_2^{equitorial})_n$ infinite layer structural blocks and $(A/X_2^{interstitial}/A)$ CaF_2-type layers. The differences between the T and T' structure for n = 1 is also illustrated in Figure 2-1. The transition from T to T' structure is related to the sizes of the A site cations. [51] For the T structure, the lattice mismatch between the perovskite and rock salt layers resulting in a compression of the Cu-O bonds increases when the A cation size decreases. If the cation is too small, the strain cannot be sustained and the T' structure becomes structurally more stable. [8] This can be exemplified on La_2CuO_4 [52, 53] (ionic radius of La^{3+}: 1.302 Å) [54], which exhibits the T structure, and Nd_2CuO_4 [50] (ionic radius of Nd^{3+}: 0.983 Å) [54], which has the T' structure.

2.1.2 Electronic structure

The valence, spin state and coordination of the non-bonding *d* orbitals of the transition metal cation have a significant influence on electronic properties. Therefore, the electronic structure of these cations in an interplay with the surrounding ligands needs to be considered in more detail. Especially, the non-degeneracy of the *d* orbital due to crystal field splitting and the Jahn-Teller effect are important. [17]

In RP-type compounds, the octahedral environment of the transition metal cations leads to a breaking of the degeneracy of the five *d* orbitals due to crystal field splitting. Electrostatic interactions between the electrons of the transition metal and the surrounding ligands result due the shape and directionality of their orbitals in two groups of orbitals separated by an energy Δ_{oct}: the lower energy t_{2g} orbitals including the d_{xy}, d_{xz} and d_{yz} orbitals and the higher energy e_g orbitals with the d_{z^2} and $d_{x^2-y^2}$ orbitals. The *d* orbitals and their splitting in an octahedral configuration are shown in Figure 2-2 and Figure 2-3, respectively. While the t_{2g} orbitals of an octahedrally coordinated transition metal point between the ligands, the e_g orbitals point directly towards the ligands, causing a higher repulsion between the negatively charged electrons of the e_g orbitals and the negatively charged ligands and consequently a higher energy. [17]

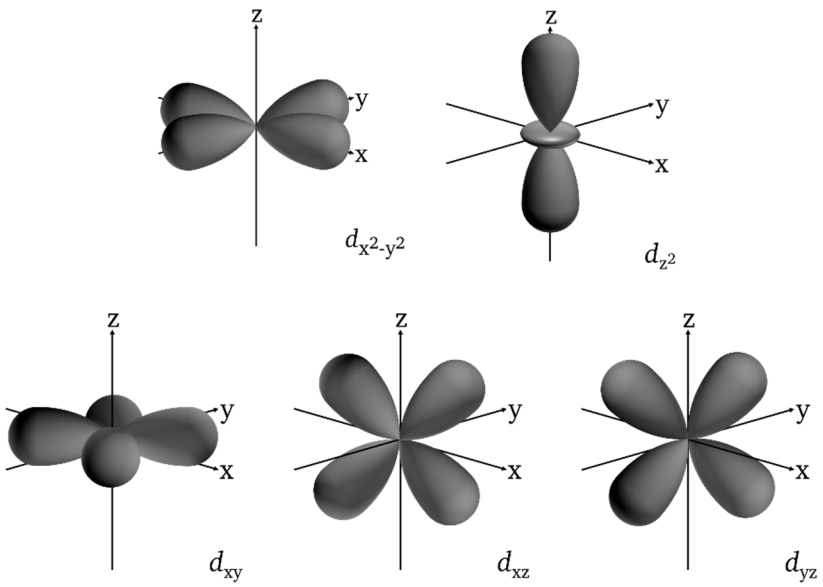

Figure 2-2: Form and directionality of the *d* orbitals.

According to Hund's rule, single electrons occupy different orbitals, before any orbital is occupied with two electrons with opposed spins, i.e. a maximisation of total spin number in accordance with Pauli's exclusion principle is preferred. For such a high-spin state, the energy difference Δ_{oct} has to be overcome to place an electron in an e_g orbital. On the other hand, due to the repulsive energy between electrons, the pairing of two electrons in one orbital leading to a low-spin state requires a pairing energy P. Therefore, it depends on the magnitude of Δ_{oct}, if a high-spin or low-spin behaviour is favoured. The splitting Δ_{oct} depends strongly on the ligands and the oxidation state of the metal. For weak-field ligands, a small splitting and high-spin configuration is observed, whereas for strong-field ligands, a large splitting and low-spin configuration is found. The ligand field splitting can be predicted using spectrochemical series. [17, 55]

For transition metal cations with d^4 high-spin, d^7 low-spin or d^9 electron configurations, the Jahn-Teller effect results in an additional breaking of the degeneracy of the t_{2g} and e_g orbitals. This leads to a distortion of the octahedron coordinating the cation. For these electron configurations, an odd number of electrons is found in the e_g orbitals. The distortion of the octahedra breaks the degeneracy of the d_{z^2} and $d_{x^2-y^2}$ orbitals, because the orbital, which is occupied by more electrons, experiences a stronger electrostatic repulsion. An elongation of the metal-ligand bonds in the direction of the stronger filled orbital, lowers the electrostatic repulsion and, consequently, an electronic stabilisation is achieved. If the d_{z^2} has more electrons, a lengthening along the *z* direction takes place, while the four bonds in the *xy* plane are elongated for a stronger occupied $d_{x^2-y^2}$ orbital. Even though the degeneracy of the t_{2g} orbitals can also be removed, the splitting is relatively small and can be neglected. The splitting of the orbitals of Jahn-Teller-active cations is given in Figure 2-3.

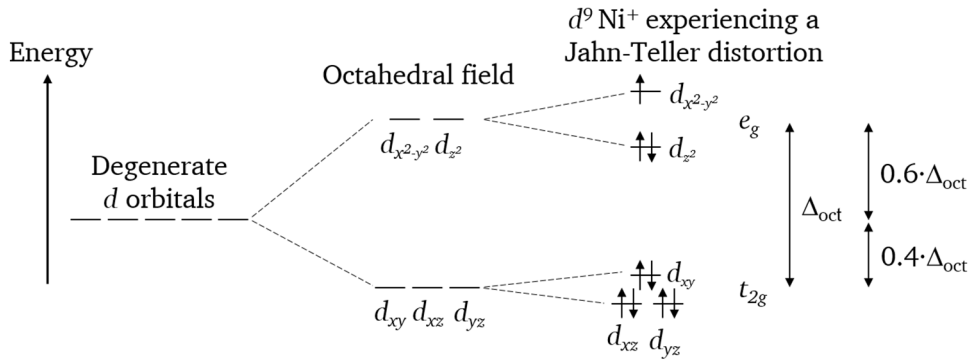

Figure 2-3: Energy level diagram of *d* orbitals in an octahedral field and of a d^9 Ni^+ additionally experiencing a Jahn-Teller distortion.

2.1.3 Magnetic properties

Ordering of magnetic moments in RP-type compounds is defined by the indirect exchange interaction (see section 2.3.2). The interactions can be ferromagnetic (i.e., parallel alignment of spins of neighbouring ions) or antiferromagnetic (i.e., antiparallel alignment of spins of neighbouring ions) depending on whether the dominating interaction is double exchange or superexchange. These interactions are, however, dependent on the crystal structure and electronic configuration of the transition metal cation, i.e., the degeneracy of orbitals and their occupations. The layered structure of RP-type compounds leads to highly anisotropic magnetic exchange interactions. [23-25] A decreased dimensionality (low n) corresponds to decreasing strengths of the magnetic interactions along the *c* direction via the rock salt layers. In particular for n = 1, quasi-two dimensional B-O-B networks are formed, which are separated by the non-magnetic rock salt layers. The in-plane (within the *ab*-plane of a perovskite-type layer) exchange interactions are mediated via B-X-B bonds, while exchange between perovskite-type building blocks (out-of-plane along the *c* axis) takes place via B-X-X-B (X being oxide or fluoride ions). For RP-type compounds with n ≥ 2, additionally, interactions between the n layers in one perovskite building have to be taken into account. The topochemical fluorination of a compound result in the introduction of additional anions into the interstitial site and further increases the distances between adjacent building blocks, reducing the strength of the exchange interactions significantly because they are mediated via longer distances and/or possibly via a larger number of anions (e.g. B-X-X-X-B). With respect to the type of anion, interactions via oxide ions are known to be stronger as compared to fluoride ions. [56]

2.2 Topochemical modifications

Topochemical modifications of perovskite and perovskite-related RP-type compounds allow for the synthesis of novel, often metastable phases that are inaccessible by conventional high-temperature reactions. In topochemical reactions, the principle structural framework of the compounds remains intact. The reaction proceeds due to a high mobility of at least one ionic species. If suitable reaction conditions are chosen, the nature of these reactions gives, therefore, in principle, the ability to control the oxidation state and the coordination environment of the transition metal. This is critical for the development of new materials with defined intrinsic properties.

The control of the transition metal oxidation state can be achieved via different approaches such as aliovalent substitution of cations in multinary phases containing more than one cation species or via manipulations of the anion sublattice. For the substitution of cations, typically thermodynamically driven reactions at high reaction temperatures are needed and are, therefore, not further considered here. For the manipulations of the anion sublattice, RP-type compounds show a vivid low-temperature reactivity with a wide range from anion intercalation, over anion exchange to extraction. [6-13] Furthermore, the different anion sites of RP-type compounds (see section 2.1.1) possess different distinct coordination environments, which results in a certain structural selectivity of the topochemically intercalated, exchanged or extracted anions because these processes have different effects on the stability of the phase depending on the anion site. [11] In this context, topochemical fluorination, deoxygenation and ion exchange reactions of RP-type oxides by chemical means are discussed. Additionally, electrochemical approaches within so-called fluoride-ion batteries are introduced.

2.2.1 Topochemical fluorination

Topochemical methods for the fluorination of oxide materials have been intensively studied due to the strong impact of fluoride incorporation on the crystal structure and electronic properties of materials. [6-9] In this respect, low-temperature fluorination methods using gaseous or solid-state reagents (e.g. F_2 or NF_3 gas, XeF_2, metal fluorides (CuF_2, AgF_2, AgF etc.), ammonium fluoride NH_4F, fluorinated polymers (polytetrafluoroethylene (PTFE), polyvinylidene difluoride (PVDF)) and electrochemical reactions can be used for the stabilisation of oxide and fluoride anions within one structure.[6, 8, 9, 57] Requirements for a successful low-temperature fluorination is the presence or in-situ formation of anion vacancies in the anion sublattice and/or the presence of additional interstitial vacancies that can be filled by anions leading to a relatively high anion mobility. In RP-type compounds, these conditions are fulfilled (see section 2.1.1) and a broad variety of structural modifications have been observed. Due to the topochemical nature of the fluorination reactions, group-subgroup relationships of the precursor oxide and the fluorinated compound can often be used to explain structural similarities, even though the anion sublattice may change considerably. [7]

Depending on the reaction method, the fluorination can be oxidative (intercalation of fluoride ions into vacant or interstitial sites, resulting in $A_{n+1}B_nO_{3n+1}F_x$ with $0 < x \leq 2$), non-oxidative (substitution of one oxide by one fluoride ion and an additional intercalation of one fluoride ion in interstitial site, leading to $A_{n+1}B_nO_{3n+1-x}F_{2x}$ with $0 < x \leq 2$, or even reductive (substitution of one oxide by one fluoride ion, yielding $A_{n+1}B_nO_{3n+1-x}F_x$ with $0 < x \leq 3n+1$). [6, 8, 9, 57] While simple insertion of fluoride into the interstitial site results in an increase of the transition metal oxidation state, the local coordination of the transition metal oxide stays mainly the same. In contrast, anion insertion and substitution leads to strong rearrangements of the anion lattice and a site selectivity can be expected due to different coordination of the different anion sites. [11] In this respect, in accordance with Pauling's second rule [58], substitutive fluoride is mostly found at apical anion sites, whereas oxide at the equatorial site is only rarely replaced. In principle, due to the presence of interstitial vacancies, $3n + 3$ anions can be stabilised in the RP structure, therefore, additional anion vacancies may still be present after fluorination. Furthermore, the combination of different fluorination methods can open vast possibilities for the adjustment of fluoride contents and transition metal oxidation states.

The strongest oxidisers F_2 and NF_3 gas and XeF_2 are difficult to handle and special equipment is required due to their toxicity and volatility. Additionally, a control of the level of

fluorination is only possible to a limited extent. Electrochemical fluorination routes are also highly oxidative. The fluoride content can be regulated through the choice of suitable capacity or potential cut-off conditions. The relatively simple set-up of a fluoride-ion battery, which can be utilised for such electrochemical fluorination reactions, and the operating principle are explained in section 2.2.3. Metal fluorides can be used also for oxidative fluorination reactions, even though their oxidising power is lower. As side product metal oxide is formed, which, if the metal fluoride is directly added to the reaction mixture, cannot be separated from the fluorinated phase; however, it is also possible to perform reactions keeping the metal fluoride separate from the oxide. While the fluoride content can be controlled through the amount of used metal fluoride in the first case, the control is difficult in the latter. NH_4F and fluorine-containing polymers favour substitution processes, which are non-oxidative or reductive depending on the surrounding atmosphere. The amount of NH_4F or polymer allows controlling the fluorination level in the fluorinated phase. When using NH_4F, strong degrees of decomposition are found. Typically, minor decomposition is observed and phase-pure sample can be obtained. [8]

The structural modifications observed after topochemical fluorination can be classified according to the anion ordering with preferred site occupations and/or by the type of fluorination method used resulting in an oxidative, non-oxidative or reductive fluorination. Two anion ordering types for RP type compounds can be distinguished: i) *fluoride insertion into interstitial sites only* and ii) *fluoride insertion into interstitial sites and/or substitution of terminal apical sites*. [59] The two types are examined in more detail below by means of several exemplarily compounds:

2.2.1.1 Fluoride insertion into interstitial sites only

The oxidative fluorination of $LaSrMnO_4$ using F_2 gas [21, 60], AgF_2 [20] or electrochemical fluorination [20] (see section 2.2.3) results in the formation of $LaSrMnO_4F_{2-x}$ ($x \sim 0.16 – 0.3$ depending on the fluorination method), in which the fluoride is only inserted into interstitial sites of the vacant rock salt layers. This is accompanied by a small contraction of the lattice parameter a and a large expansion of the lattice parameter c due to the fluoride insertion and the oxidation of Mn (Figure 2-4) compared to $LaSrMnO_4$ (space group: I4/mmm, $a = 3.786(1)$ Å, $c = 13.163(1)$ Å) [61]. When heating the fluorinated compound with appropriate amounts of the precursor oxide, the formation of a staged phase, in which only one of the two available rock salt layers of the unit cell is occupied by fluoride, is observed. Since only one rock salt layer is occupied, the expansion along the c axis is considerably smaller compared to the stronger fluorinated compound. Similar observations have been made for the fluorination of $La_{1.2}Sr_{1.8}Mn_2O_7$ to $La_{1.2}Sr_{1.8}Mn_2O_7F_2$ utilising F_2 gas [21], CuF_2 [22] or PVDF [62] (Figure 2-4).

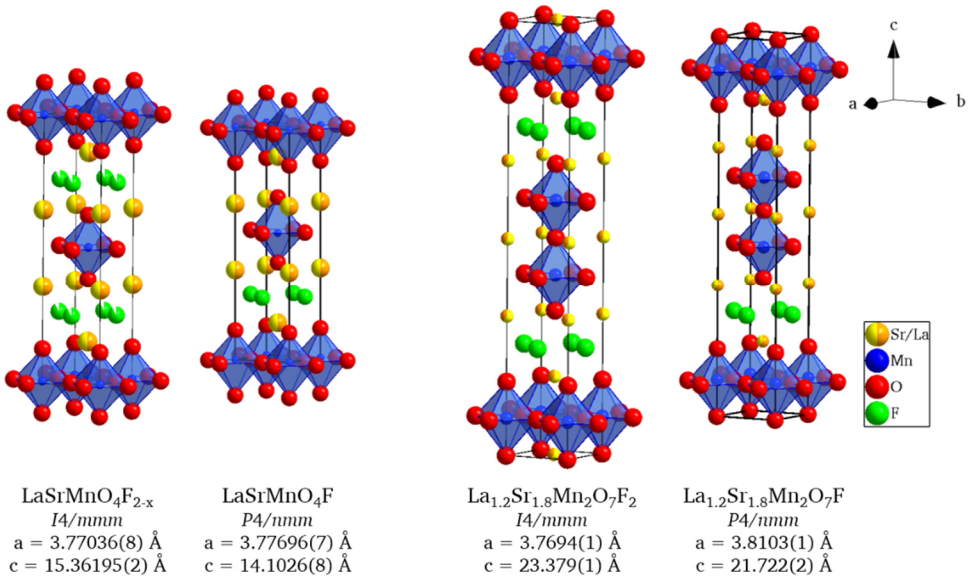

Figure 2-4: Crystal structures of $LaSrMnO_4F_{2-x}$ [20], $LaSrMnO_4F$ [60], $La_{1.2}Sr_{1.7}Mn_2O_7F_2$ [21] and $La_{1.2}Sr_{1.7}Mn_2O_7F$ [21].

An interesting fluorination behaviour has been found for the series $Ca_{2-x}Sr_xCuO_3$ with $0 \leq x \leq 2$. In particular, the end members Sr_2CuO_3 and Ca_2CuO_3 have been intensively studied in the context of superconductivity. The oxygen-deficient RP-type precursor oxides show a vacancy ordering leading to one-dimensional chains of corner-sharing CuO_4 sheets instead of CuO_6 octahedra. The stoichiometric incorporation of fluoride into the precursors result in the formation of $Ca_{2-x}Sr_xCuO_2F_2$, which conform to the T' structure for the whole series. However, while, when using non-oxidative PVDF and PTFE [63, 64] as fluorination reactants, the compounds can be obtained immediately, fluorination with oxidising F_2 gas [65, 66], XeF_2 [6], MF_2 (M = Cu, Zn, Ag, Ni) [67, 68] or NH_4F [66] leads to the insertion of additional fluoride δ into vacancies. The effects of the excess fluoride on the structure of $Sr_2CuO_2F_{2+\delta}$ and $Ca_2CuO_2F_{2+\delta}$ are discussed below. For $Sr_2CuO_2F_{2+\delta}$, the removal of the additional fluoride under reducing conditions using H_2/N_2 is needed to obtain the T' structure. [69] The structural changes are demonstrated on Sr_2CuO_3 and $Sr_2CuO_2F_2$ (Figure 2-5). The formation of 2-dimensional CuO_2 layers from quasi-1-dimensional CuO_3 chains involves considerable rearrangement of the anions. The fluoride is found at the interstitial site only.

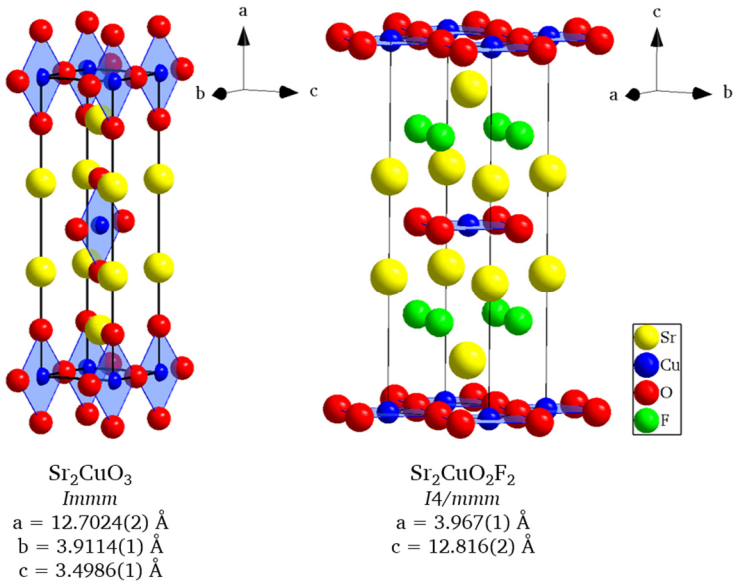

Sr_2CuO_3
Immm
a = 12.7024(2) Å
b = 3.9114(1) Å
c = 3.4986(1) Å

$Sr_2CuO_2F_2$
I4/mmm
a = 3.967(1) Å
c = 12.816(2) Å

Figure 2-5: Crystal structures of Sr_2CuO_3 [70] and $Sr_2CuO_2F_2$ [69].

2.2.1.2 Fluoride insertion into interstitial sites and/or substitution of apical sites

In many cases, the fluorination proceeds by oxide substitution at apical sites and fluoride intercalation into interstitial sites in the rock salt layers. Such a substitution and intercalation process has been observed for the fluorination of Sr_2TiO_4 to $Sr_2TiO_3F_2$. Various fluorination reagents including NH_4F and MF_2 (M = Cu, Zn) [71] as well as PVDF [63] have been applied. For all reagents, the fluorination results in a staged anion ordering, in which fluoride is inserted into one of the interstitial sites within the two rock salt layers. In contrast to $LaSrMnO_4F$, additionally one fluoride substitutes one apical oxide in a way that the substituted apical anions are furthest away from the interstitial anions. This leads also to a distortion of the TiO_5F octahedra. The assignment of the fluoride and oxide ions to the respective anion sites has been made based on bond-valance sum calculations. The crystal structure of $Sr_2TiO_3F_2$ is shown in Figure 2-6.

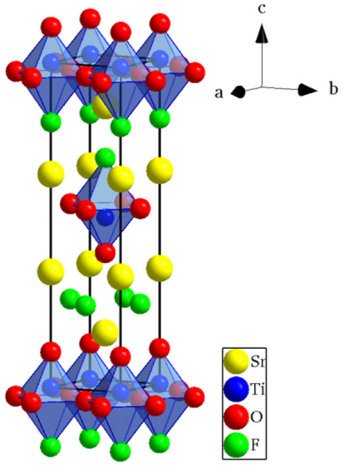

$Sr_2TiO_3F_2$
P4/nmm
a = 3.8017(1) Å
c = 15.5358(1) Å

Figure 2-6: Crystal structure of $Sr_2TiO_3F_2$ [71].

Low-temperature reactions between Ba_2SnO_4 and ZnF_2 in the presence of H_2O result in the formation of $Ba_2SnO_{2.5}F_3{\cdot}xH_2O$ ($x \sim 0.5$) [72]. Therefore, the compound cannot only be fluorinated to a large extent, but also water can be reversibly intercalated. From a combination of nuclear magnetic resonance, extended X-ray absorption and Mößbauer spectroscopy and diffraction studies, it has been followed that both interstitial layers are predominantly occupied by fluoride. Computer modelling studies have further predicted that substitution of apical sites by fluoride is favoured over the substitution of the equatorial site. Due to the indistinguishability of oxide and fluoride by means of diffraction (see section 2.4.1), a mixed occupation of oxide and fluoride anions has to be assumed for the apical anion site. Additionally, water is present in the crystal structure; however, it has not been possible to locate it. Within the structural analysis performed by the authors, its most likely position is at the apical or interlayer sites and it has, therefore, been equally distributed between these sites. The crystal structure of $Ba_2SnO_{2.5}F_3{\cdot}xH_2O$ ($x \sim 0.5$) is given in Figure 2-7.

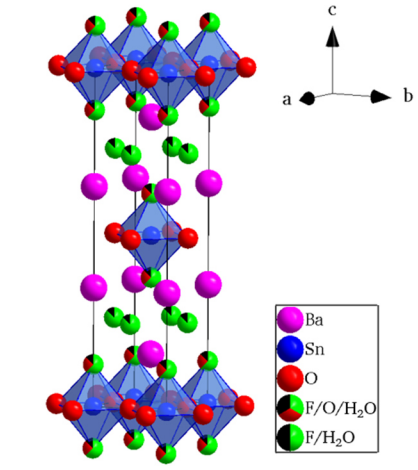

Figure 2-7: Crystal structure of $Ba_2SnO_{2.5}F_3{\cdot}xH_2O$ ($x \sim 0.5$) [72]. For better visualisation of $Ba_2SnO_{2.5}F_3{\cdot}xH_2O$, the description of the equatorial, apical and interstitial sites by split sites used in reference 73 was omitted und the sites were shifted to their corresponding un-split positions. The occupancies of the sites were merged to maintain the correct overall occupancies.

As already mentioned above, the presence of additional fluoride δ in $Sr_2CuO_2F_{2+\delta}$ and $Ca_2CuO_2F_{2+\delta}$ has a significant influence on the crystal structures of the compounds. Interestingly, for $Sr_2CuO_2F_{2+\delta}$, a structure more closely related to the T structure [63, 65, 68, 71] is obtained, whereas for $Ca_2CuO_2F_{2+\delta}$ [66], the structure is more similar to the T‘ structure. The crystal structures of $Sr_2CuO_2F_{2.57}$ and $Ca_2CuO_2F_{2.1}$ are depicted in Figure 2-8. In $Sr_2CuO_2F_{2+\delta}$, the apical site is occupied and excess fluoride is found at the interstitial site within the rock salt layer. Contrarily, in $Ca_2CuO_2F_{2+\delta}$, the interlayer site is predominantly filled and the additional fluoride occupies the apical anion site.

A comparison between the stoichiometric compounds $Ca_{2-x}Sr_xCuO_2F_2$ (T’ structure) and the over-stoichiometric $Sr_2CuO_2F_{2+\delta}$ (T structure) and $Ca_2CuO_2F_{2+\delta}$ (T’ structure) is interesting at this point. Usually, the transition between T and T’ structures is associated with the larger size of the Sr cation compared to the Ca cation. [14] This has also been observed in the rare earth cuprates, where La_2CuO_4 has the T structure and Nd_2CuO_4 the T’ structure. [50-53] According to this, a transition between T’ and T would be expected when going to the Sr-richer side in the

series $Ca_{2-x}Sr_xCuO_2F_2$ with $0 \leq x \leq 2$, which is, however, not observed. Therefore, the transition cannot only be due to cation size effects. [64] These effects do also not explain the structural transition of $Sr_2CuO_2F_{2+\delta}$ compounds when changing the anion stoichiometry from $\delta > 0$ to $\delta = 0$. It rather seems that the presence of additional fluoride on the interstitial site stabilises the T structure. [64, 69] Furthermore, different fluorination mechanisms leading to the formation of $Sr_2CuO_2F_2$ and $Sr_2CuO_2F_{2+\delta}$ have to be considered. The non-oxidative fluorination resulting in the formation of the stoichiometric compounds proceeds via a direct intercalation of fluoride into the interstitial site accompanied by the transformation of the CuO_4 chains (Niggli notation: $CuO_{2/4}O_{2/2}$) into CuO_2 layers (Niggli notation: $CuO_{4/2}$). [64] In the oxidative fluorination, on the other hand, fluoride is first formally intercalated into the vacant equatorial site to form CuO_4F_2 octahedra followed by an interchange of the oxide at the apical site and fluoride to form CuO_2 layers in the equatorial plane. Excess fluoride occupies the interstitial site. [65] Only the subsequent reduction of $Sr_2CuO_2F_{2+\delta}$ to $Sr_2CuO_2F_2$ enables the stabilisation of the T' structure due to the preference of corresponding anion rearrangements. [69]

Moreover, it should be pointed out that the fluorination of Sr_2CuO_3 leads to an expansion of the longest crystallographic axis (compare Figure 2-5 and Figure 2-8), whereas a compression is found when fluorinating Ca_2CuO_3 (space group: *Immm*, a = 12.208(1) Å, b = 3.768(1) Å, c = 3.249(1) Å) [73] to $Ca_2CuO_2F_2$ (space group: *I4/mmm*, a = 3.8567(4) Å, c = 11.8274(2) Å) [64] and $Ca_2CuO_2F_{2+\delta}$ (compare Figure 2-8). This relates to the cation sizes and to the structural transitions from the T-type structure of the precursor oxides to the T'-type or T-type structures of the respective fluorinated compounds. The strongest difference of the longest crystallographic axes are observed between $Sr_2CuO_2F_2$ and $Sr_2CuO_2F_{2+\delta}$. The structural transition from T' to T is associated with the filling of both apical and interstitial sites leads to a large extension. Only a small expansion is found between Sr_2CuO_3 and $Sr_2CuO_2F_2$ due to the transformation of the CuO_4 chains into CuO_2 layers corresponding to the removal of apical sites and filling of equatorial sites and due to the partial occupation of the interstitial site by fluoride. The latter also explains the compression observed in the fluorinated Ca compounds, even though the interstitial sites are stronger occupied and the apical sites are partially filled.

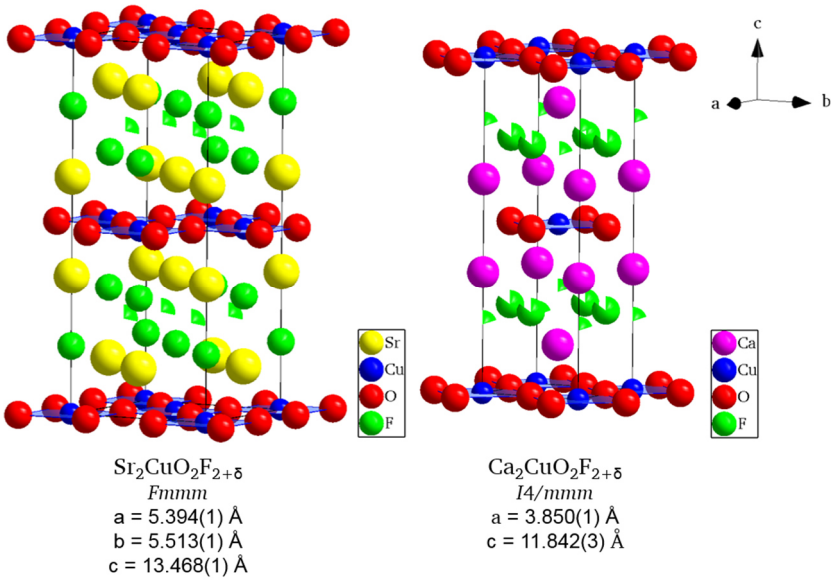

Figure 2-8: Crystal structures of $Sr_2CuO_2F_{2+\delta}$ ($\delta \sim 0.57$) [65] and $Ca_2CuO_2F_{2+\delta}$ ($\delta \sim 0.1$) [66]. For better visualisation of $Sr_2CuO_2F_{2+\delta}$, the description of the apical and interstitial sites by split sites used in reference 67 was omitted and the sites were shifted to their corresponding un-split positions.

High fluoride contents can be stabilised in $Sr_3Fe_2O_{7-x}$ (space group: *I4/mmm*, $a = 3.86543(2)$ Å, $c = 20.1633(1)$ Å) [74] when fluorinating the compound with PVDF. The phases $Sr_3Fe_2O_{5.28(4)}F_{1.72(4)}$ and $Sr_3Fe_2O_4F_4$ have been synthesised. Even tough partial decomposition has been found, even higher fluoride contents up to compositions of $\sim Sr_3Fe_2O_3F_6$ could be obtained. The phases show an increasing occupation of the interstitial anion site and a large increase in cell volume with increasing fluoride contents. In $Sr_3Fe_2O_4F_4$, an ordered half-occupation of the interstitial sites by fluoride has been observed. Additionally, all apical sites are occupied by fluoride. The main expansion takes place within the *ab* plane. In $Sr_3Fe_2O_3F_6$, it is presumed that the apical and interstitial sites are fully occupied and that ¼ of the equatorial sites are occupied by fluoride. The complete filling of the interstitial site results in an additional expansion along the *c* axis ($c = 22.217(2)$ Å). Since a detailed structural refinement could not be performed on $Sr_3Fe_2O_3F_6$, the crystal structure of $Sr_3Fe_2O_4F_4$ is shown in comparison to the structure of $Sr_3Fe_2O_{5.28(4)}F_{1.72(4)}$. $Sr_3Fe_2O_{5.28(4)}F_{1.72(4)}$ can also be regarded as an example for the substitution of oxide at the apical anion site by fluoride without the additional insertion of fluoride into the interstitial site.

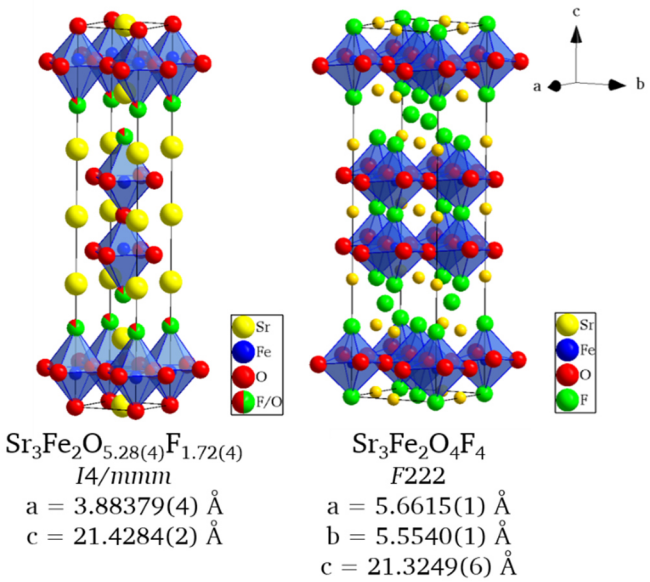

Figure 2-9: Crystal structures of $Sr_3Fe_2O_{5.28(4)}F_{1.72(4)}$ [74] and $Sr_3Fe_2O_4F_4$ [74].

2.2.2 Topochemical reductions and anion exchange reactions

The use of metal hydrides as reductants for perovskite and perovskite-related oxides for the synthesis of new oxygen defect structures has proven to be an important approach for topochemical modifications. Using this approach, oxides with pyrochlore structure can be also reduced. Metal hydrides enable controllable reductions at lower temperatures as compared to reactions in reductive atmospheres, e.g. in H_2 gas or gas mixtures containing H_2. In general, higher reactivities, leading to higher degrees of reduction, are found at increased temperatures; these higher temperatures result, however, in the decomposition of the precursor oxide, possibly leading to the formation of transition metals. Therefore, a compromise between these two factors has to be found. In addition, the choice of metal hydride is important. [12] The trend of reactivity of commonly used metal hydride reductants can be summarised according to the following [75]:

$$MgH_2 < SrH_2 < LiH \approx CaH_2 \approx BaH_2 < NaH$$

This trend also gives the ability to deduce reaction conditions and increases the reliability and reproducibility of the synthesis.

Hydride-based reductions can occur via deoxygenation processes resulting in oxygen-deficient products. The reaction can also take partly place via oxide-hydride exchange leading to the formation of oxyhydrides. Hydride anions or H_2 gas can act as active reductive species. Depending on the thermodynamics of the metal hydride and the formed side products, the hydride anion can be the reductant in a one- or two-electron reduction. The one-electron reduction may lead to the release of H_2. In addition, thermal decomposition can take place at elevated temperatures resulting in the formation of the pure metal and H_2. The metal can also act as reductant. [75-77] It should be further noted that it is often not possible to predict whether an oxygen-deficient or oxyhydride product will be formed. [76]

This can be illustrated when considering the topochemical reduction of different titania-based compounds that have been reduced using metal hydrides or H_2. For both cases, the formation of either oxygen-deficient oxides or oxyhydrides has been observed. The reduction of

pyrochlore-type $Ln_2Ti_2O_7$ (Ln = Y, La, Yb, Lu) with CaH_2 in a temperature range between 550 and 600 °C leads to a maximum reduction to $Y_2Ti_2O_{5.90}$ [78], $La_2Ti_2O_{6.73}$ [79], $Lu_2Ti_2O_{6.45}$ [80] and $Lu_2Ti_2O_{6.10}$ [80] corresponding to oxidation states of $Ti^{+2.9}$, $Ti^{+3.73}$, $Ti^{+3.45}$ and $Ti^{+3.1}$, respectively. Even though a strong reduction seems to be possible for $Y_2Ti_2O_7$, the strongest reduced phase $Y_2Ti_2O_{5.90}$ is only found in a phase mixture with less strongly reduced $Y_2Ti_2O_{6.48}$. This phase separation indicates that there is a phase gap in the compositional range $Y_2Ti_2O_{7-x}$ ($0.5 < x < 1.1$) and that the synthesis of phase pure samples is not always possible. [81] The stabilisation of hydride within these phases has been excluded; only for $La_2Ti_2O_{6.73}$, minute hydride contents of ~ 0.02 H per formula unit have been confirmed. The crystal structures of $La_2Ti_2O_7$ and $La_2Ti_2O_{6.73}$ are given for comparison in Figure 2-10.

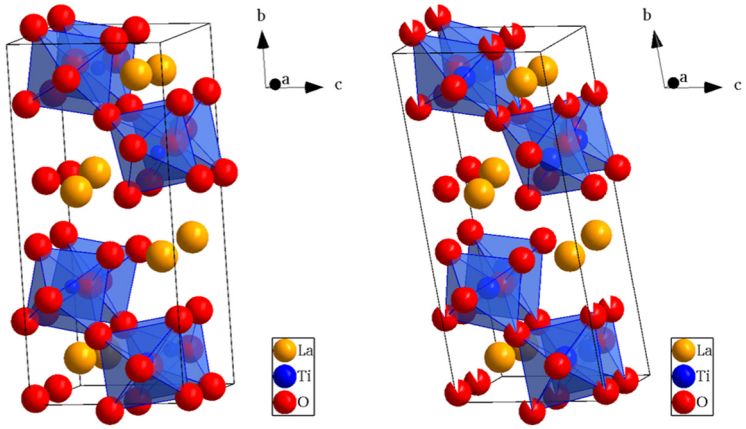

$La_2Ti_2O_7$
$P112_1$
a = 7.800(3) Å
b = 13.011(4) Å
c = 5.546(2) Å
γ = 98.60(2)°

$La_2Ti_2O_{6.73}$
$P112_1$
a = 7.8120(1) Å
b = 13.0144(2) Å
c = 5.5472(9) Å
γ = 90.00°

Figure 2-10: Crystal structure of $La_2Ti_2O_7$ [82]and $La_2Ti_2O_{6.73}$ [83]. The hydride content of ~ 0.02 H per formula unit is not included.

In contrast, an oxide-hydride exchange is observed for the reaction between $ATiO_3$ (A = Ca, Sr, Ba) [84-86] or the solid solutions $(Ca,Sr,Ba)TiO_3$ [87] with CaH_2 at 530 °C. The strongest reduction has been observed for $BaTiO_{3-x}H_x$ with $x \leq 0.6$ corresponding to a Ti oxidation state as low as +3.4. The crystal structure of $BaTiO_{2.5}H_{0.5}$ is shown in Figure 2-11.

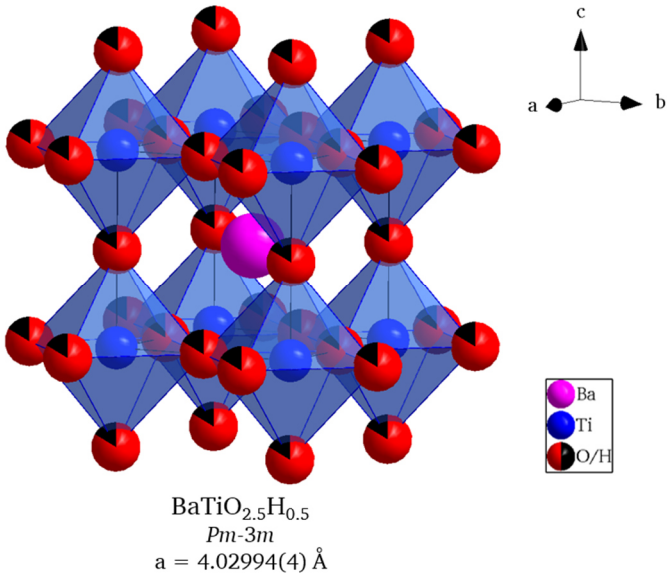

Figure 2-11: Crystal structure of $BaTi_{2.5}H_{0.5}$ [83].

The high-temperature reduction of RP-type $Ca_{n+1}Ti_nO_{3n+1}$ with n = 2, 3 and ∞ [88] under flowing H_2 at temperatures > 900 °C causes only minor reductions to $Ti^{+3.9}$. This shows that the stabilisation of low-valent Ti is difficult to achieve.

In general, the extent of the topochemical reduction of transition metal oxides resulting in the stabilisation of unusually low oxidation states is often limited. For the reduction of oxides containing early transition metals such as Ti, as described above, or V [89-91], high reaction temperatures are required; however, even then only a comparatively low degree of reduction is observed. For late transition metal oxides containing for example Mn [75, 92], Fe [93-95] or Ni significantly lower reaction temperatures are needed to achieve higher reductions. In the following, this is exemplified on Ni containing compounds.

The formation of low-valent Ni containing compounds with minimum oxidation states as low as +1 has been reported to be feasible. In particular, the deoxygenation of members of the $Ln_{n+1}Ni_nO_{3n+1}$ (Ln = La, Nd, Pr; n = 2, 3, ∞) homologous series have been investigated. [96-104] The reductions have been performed using H_2 gas, CaH_2 or NaH in a temperature range between 190 and 350 °C, which is considerably lower compared to reaction conditions used for titanate reductions. All reduced compounds of the series are members of the T'-type $Ln_{n+1}Ni_nO_{2n+2}$ homologous series with mixed-valent $Ni^{2+/+}$ with infinite NiO_2 square-planar layers (Niggli nation: $NiO_{4/2}$). The square-planar coordination of the Ni cation is favoured for d^9 Ni. [105] For example for lanthanum nickelates (Table 2-1 and Figure 2-12), the deoxygenation of the RP-type $La_3Ni_2O_7$ (space group: *Amam*, $a = 5.39283(11)$ Å, $b = 5.44856(11)$ Å, $c = 20.51849(50)$ Å) [106] and $La_4Ni_3O_{10}$ (space group *Bmeb*, $a = 5.41327(11)$ Å, b = 5.46233(11) Å, $c = 27.96049(70)$ Å) [106] leads to the formation of $La_3Ni_2O_6$ and $La_4Ni_3O_8$ with Ni oxidation states of +1.5 and +1.33, respectively. So far, only the reductive syntheses of so-called double (n=2) and triple (n =3) layer T'-type nickelates have been reported. [99, 100] Perovskite-type $LaNiO_3$ (space group: *R*-3*c*, $a = 5.4573(1)$ Å, $c = 13.1462(3)$ Å) [107] can be reduced to $LaNiO_2$ with a Ni oxidation state of +1. [96-98, 103, 104] After the observation of high-temperature superconductivity in topochemically modified cuprates [36-42, 108], such nickelates having infinite NiO_2 square-planar layers have been considered promising candidates for superconductivity due to the isoelectronic configuration

of Cu^{3+}/Cu^{2+} and Ni^{2+}/Ni^{+} (d^8/d^9). [109-111] In this context, the superconductivity of infinite-layer $Nd_{0.8}Sr_{0.2}NiO_2$ prepared via the reduction of $Nd_{0.8}Sr_{0.2}NiO_3$ films grown on $SrTiO_3$ (100) substrates using CaH_2 in a temperature range between 260 and 280 °C has been only recently reported. [112]

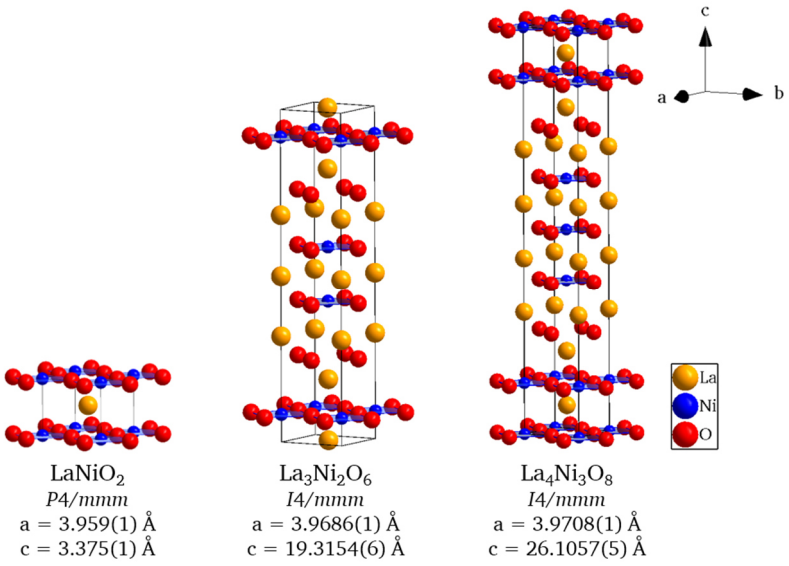

Figure 2-12: Crystal structures of La_2NiO_2 [98], $La_3Ni_2O_6$ [100] and $La_4Ni_3O_8$ [99].

Furthermore, the severe influence of the reaction temperature on the stabilisation of hydride within the structure becomes evident on the reduction of the RP-type compound $LaSr_3NiRuO_8$ (space group: *I4/mmm*, a = 3.8904(1) Å, c = 12.6297(1) Å). Depending on the reaction temperature, the reaction of this phase with CaH_2 takes place via a topochemical deintercaltion of oxide to form the body-centred orthorhombic phases $LaSr_3NiRuO_7$ (a = 3.907 Å, b = 3.789 Å, c = 12.689 Å) at 400 °C and $LaSr_3NiRuO_6$ (a = 3.853 Å, b = 3.593 Å, c = 13.011 Å) at 425 °C. For reactions performed at 450 °C, an anion exchange occurs, which leads to the formation of $LaSr_3NiRuO_4H_4$ (space group: *I4/mmm,* a = 3.6226(2) Å, c = 13.317(1) Å). [113]

The synthesis of other mixed-anion compounds starting from oxyhydrides via different anion exchange reactions offers additional opportunities for topochemial modifications. The hydride in $BaTiO_{2.5}H_{0.5}$ can be for example partially exchanged by nitride, fluoride or hydroxide to form $BaTi(O,H,N/F/OH)_3$. [76, 83, 114]

Besides the reduction of oxides via deoxygenations and anion exchange reactions, the selective extraction or exchange of fluoride from oxyfluorides using hydride-based or electrochemical (see section 2.2.3) approaches may also lead to considerable reductions of transition metal oxidation states. In order to do so, different topochemical modification methods have to be combined and performed consecutively (see also section 2.2.4). Sequences of non-oxidative fluorination and reductive defluorination reactions of RP-type oxides and derived oxyfluorides were investigated for the first time within the scope of this thesis. For the choice of suitable temperatures for the hydride-based reduction reactions, the metastability of the oxyfluorides have to be taken into consideration. This metastability makes a reaction temperature laying considerably below the decomposition temperature necessary. However, these low temperatures may limit the synthesis of phase pure reduced samples

significantly. Therefore, the reaction chemistry has to be balanced between the metastability of the educts, the energetic stability of the reaction products and the kinetic limitations impeding to reach the energetically most stable product.

Moreover, the structure and especially the dimensionality n of the RP-type precursor oxide and the oxyfluorides have a significant influence on the highest and lowest oxidation states, which can be obtained using fluorination and subsequent reduction reactions (see section 2.2.2), respectively. The higher the value of n, the more perovskite-like layers are present and the structures can be considered as being more closely related to the perovskite structure. This, in turn, means that the relative amount of rock salt layers and, therefore, interstitial vacancies, which can be filled by additional anions, decrease. The ratio between the additional anions, which can be extracted, and the number of B cations decreases with increasing n. This leads to smaller possible degrees of reduction for higher order members of the homologous series, which might in turn have an impact on the stability of the formed phases.

2.2.3 Topochemical modifications via electrochemical reactions in fluoride-ion batteries

Topochemical modifications of RP-type compounds can be also obtained using electrochemical approaches. The electrochemical oxidation utilising a three-electrode configuration in aqueous alkaline electrolytes leading to the intercalation of δ oxide ions into interstitial vacancies and the formation of over-stoichiometric oxides has been first demonstrated in the early 1990s. [115-118] The deintercalation of these additional oxide ions could also be confirmed. [119] Repeated intercalation and deinteralation steps have, however, not been investigated. The experiments have been performed using either potentiostatic or galvanostatic conditions. More recently, the electrochemical oxidation and fluorination in electrolytes of organic solvents and oxygen- or fluorine-containing salts have been demonstrated. [108, 120] The amount of additionally intercalated anions δ is, however, for both approaches relatively low ($0 < \delta < \sim 0.3$). Much stronger fluoride intercalation into RP-type oxides could be achieved with all-solid-state fluoride-ion batteries (FIBs) operating with the solid electrolyte $La_{0.9}Ba_{0.1}F_{2.9}$. [18-20] The increased fluoride intercalation is facilitated by the broad electrochemical stability window of the electrolyte as compared to the solution-based electrolytes. [26] Furthermore, this set-up allows for the reversible intercalation and deintercalation of fluoride ions upon charging and discharging of the cell over extended cycle numbers. [18-20] This reversibility offers possibilities for the reversible switching and/or tuning of material properties.

When considering the ‘reversed’ principle of electrochemical reduction due the extraction of additional anions leading to the formation of anion deficient compounds, the stability window of the electrolyte plays an important role. For example, due to the narrow stability window of the aqueous solutions on the reductive side, an early onset of decomposition of water under the formation of H_2 is observed. This makes a reductive deoxygenation difficult. Furthermore, this might explain why the preparation of compounds known to be accessible via hydride-based approaches have not yet been reported using electrochemical synthesis routes. The electrochemical defluorination using a FIB, might, however, be possible. This has been investigated for the first time within the scope of this work.

2.2.3.1 Basic working principle of fluoride-ion batteries

FIBs are all-solid-state batteries based on the shuttling of fluoride ions between two electrodes through a fluoride ion-conducting electrolyte. [27] Batteries are electrochemical energy storage devices, which convert and store chemical energy in electric energy, and vice versa. The underlying working principle can also be used to synthesise novel compounds by making use of the occurring reduction/oxidation (redox) reactions within the active materials of the battery electrodes. In general, batteries consist of two electrodes, i.e., an anode and a cathode, and an electrolyte. The electrodes are connected via an external circuit and via the electrolyte inside the cell. In all-solid-state batteries, the electrolyte serves additionally as separator between the electrodes. When charging or discharging, the active materials of the electrodes are subjected to redox reactions and mobile ions are transferred through the electrolyte to/from the respective electrode. The emerging electrons move through the external circuit.

Per definition, for discharging conditions, the reduction reaction takes place at the cathode (positive electrode) and the oxidation reaction at the anode (negative electrode). For FIBs, during discharging, i.e., when a consumer load is applied, electrons flow from the anode through the external circuit to the cathode and fluoride ions migrate through the electrolyte from the cathode to the anode. The reversed process describes the charging process. A schematic FIB cell and the directions of fluoride ion and electron flow during discharging and charging is shown in Figure 2-13.

The electrochemical reactions taking place at the anode and cathode of a FIB during discharging (forward direction) and charging (backward direction) can be described with the following equations. Exemplarily shown for n =1 RP-type compounds, when an intercalation-based oxyfluoride $A_2BO_3F_2$ obtained via a non-oxidative fluorination (representing the discharged state of the compound) is used as active materials in the anode and a conversion-based composite M/MF_2 containing a metal M and a metal fluoride MF_2 as cathode composites, the following reactions take place:

$$Anode: A_2BO_3F_{2-x} + xF^- \rightleftharpoons A_2BO_3F_2 + xe^- \; with \; 0 < x \leq 2$$

$$Cathode: MF_2 + 2e^- \rightleftharpoons M + 2F^-$$

In the opposite case, an intercalation-based RP-type oxide A_2BO_4 (representing the discharged state of the compound) is used as active materials in the cathode and a conversion-based composite M/MF_2 containing a metal M and a metal fluoride MF_2 as anode composites leads to the following electrochemical reactions:

$$Cathode: A_2BO_4F_2 + 2e^- \rightleftharpoons A_2BO_4 + 2F^-$$

$$Anode: M + 2F^- \rightleftharpoons MF_2 + 2e^-$$

As explain in section 2.2.4, the use of a non-oxidatively fluorinated compound $A_2BO_3F_2$ as active material in a cathode material might also enable an additional oxidative fluorination of $A_2BO_3F_2$ to $A_2BO_3F_3$.

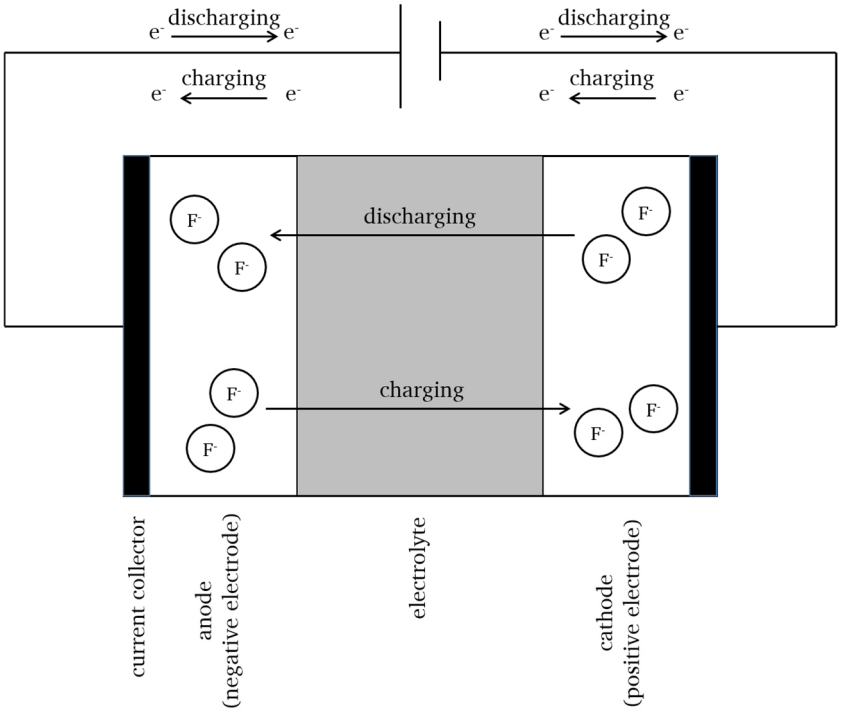

Figure 2-13: Schematic representation of the charge carrier flow in a fluoride-ion battery during discharging and charging.

Even though the term “fluoride-ion battery” and the underlying principles go back to studies performed in the 1970s/80s [121-126], interest into this research field was reawakened only after the reversibility of charging and discharging processes over several cycles within all-solid-state FIBs based on the electrolyte $La_{0.9}Ba_{0.1}F_{2.9}$ has been reported in 2011 [27]. Since then, considerable research efforts have been carried out on the development and improvement of electrolytes and electrode materials.

High ionic conductivities, which are the prerequisite for a well performing electrolyte of FIBs besides a broad electrochemical stability window, have been reported for compounds with fluorite-type or tysonite-type structure; especially, solid solutions of aliovalently-doped fluorides have shown to have improved conductivities. [127-133] One of the highest conductivities has been observed for nanocrystalline tysonite-type $La_{0.9}Ba_{0.1}F_{2.9}$ with $2.81 \cdot 10^{-4}$ S·cm^{-1} at 160 °C. This compound can be prepared via a simple ball milling process of stoichiometric mixtures of BaF_2 and LaF_3 at 600 RPM for 12 h. [27, 134] $La_{0.9}Ba_{0.1}F_{2.9}$ prepared accordingly has, therefore, been chosen as fluoride-conducting electrolyte for all studies performed within this thesis. It has to be pointed out that for this $La_{0.9}Ba_{0.1}F_{2.9}$ powder, sufficient ion conductivity is only achieved at elevated temperatures. However, in the meanwhile, it has also been reported that the synthesis via coprecipitation [100], further optimisation of milling conditions [135] and additional sintering steps of the obtained powder materials can result in higher conductivities, even though room-temperature applications are still not possible with $La_{0.9}Ba_{0.1}F_{2.9}$. The highest reported room-temperature conductivity is $4 \cdot 10^{-5}$ S·cm^{-1} for nanocrystalline $La_{0.95}Ba_{0.05}F_{2.95}$ powders sintered at 700 °C. [135] Recently, investigations have been also extended towards solid-state [136-141] and even liquid [142] room-temperature electrolytes in order to lower the temperatures for the electrochemical reactions.

Electrode materials can be classified based on the type of reaction taking place between the active material and the mobile ions and the resulting structural rearrangements as either

conversion or as intercalation materials. For the conversion mechanism, strong changes in the crystalline structure, often accompanied by large volume changes, which lead to poor cycling performances and strong capacity fading, are common. Intercalation reactions, as can be found when applying topochemical fluorination methods, result in considerably less pronounced structural changes and better cycling performances. The theoretical specific capacities of intercalation-based electrodes are, however, much lower as compared to conversion-based electrodes. [143] The same observations have been made for electrodes used in FIBs. All reported electrodes are composite materials consisting of a conversion- or intercalation-based active material, an electronically conductive additive (e.g. carbon black) and, if the ionic conductivity of the active materials is not sufficiently high, electrolyte to improve the conductivity. Various conversion-based anode and cathode systems containing a metal and/or metal fluoride have been investigated. [27-29] Systems based entirely on conversion-based electrodes suffer from fast capacity fading upon cycling due to large volume changes. Improved cycling behaviours have been found when cycling intercalation-based cathodes with an RP-type oxide as active material against conversion-based anodes. [18-20, 144] Additionally, the choice of suitable electrode couples, or more precisely, of the electrochemical potential of intercalation-based electrode against the counter electrode have to be taken into account when considering how much fluoride intercalation into RP-type oxides or deintercalation from RP-type oxyfluorides might be achievable within a charging or discharging process. Using the same counter electrode as reference, higher oxidising powers of the cathode materials can be expected for materials with higher electrochemical potentials. The other way around, stronger reductions within the anode material should be possible for materials with lower potentials. For the successful modifications of RP-type oxides and oxyfluorides, the appropriate combination of different electrode materials is, therefore, an important factor. As counter electrode for all conducted experiments, a conversion-based composite containing Pb and PbF_2 as active materials has been selected, which can be used as both cathode and anode. The Pb/PbF_2 composite has a potential of ~ 2.3 V against Li|LiF. [20]

2.2.4 Combination of topochemical modification methods

The targeted synthesis of compounds with specific transition metal oxidation states and structural arrangements are key for the development of novel materials with specific properties. In this respect, the combination of above described topochemical modification methods can be an important tool. Property engineering due to the choice of suitable experimental procedures is possible, since the sequence of different topochemical reactions can have significant influence on the resulting compound. This is exemplified below on the RP-type compound La_2NiO_{4+d} by means of hypothetical considerations.

It could be assumed that the topochemical reduction of La_2NiO_{4+d} to La_2NiO_{4-d} would lead to the formation of the single (n=1) layer T'-type structure in analogy to the double (n=2) and triple (n =3) layer T'-type nickelates $La_3Ni_2O_6$ and $La_4Ni_3O_8$ (see section 2.2.2). For this compound, the formation of significant amounts of monovalent Ni species would result in a considerable number of vacancies d. Despite the great research interest into low-valent nickelates in the field of high-temperature superconductors in the recent years, this T'-type structure has, however, not been reported for the n = 1 member of the Ruddlesden-Popper series $La_{n+1}Ni_nO_{3n+1}$ so far. This might be related to the fact that T' compounds with large anion deficiency d on the interstitial sites are not known, with a structural origin possibly lying in the resulting low coordination numbers of the A-site cation. For strongly reduced phases with the RP-type structure with n = 1 , e.g. $LaSrNiO_{3.1}$ [145] , anion vacancies on the

equatorial site have rather been observed, which results in chains of square-planar coordinated cations instead of layers.

In order to avoid such an anion deficiency, while still be able to reduce the compound and stabilise the T'-type structure, a topochemcial modification leading to the introduction of additional anions into the parent compound might be a suitable approach. A non-oxidative fluorination using PVDF could result in the formation of $La_2NiO_3F_2$ under the maintenance of the Ni^{2+} oxidation state. A subsequent reductive metal hydride-based defluorination might further allow for the synthesis of a single (n=1) layer T' type nickel oxyfluoride with a composition of La_2NiO_3F.

The introduction of additional anions (five anions per formula unit in $La_2NiO_3F_2$ instead of four anions per formula unit in La_2NiO_4) could be crucial to obtain the n = 1 T'-type structure. For $La_2NiO_3F_2$, one fluoride ion could be removed before an anion deficiency on the interstitial site (less than four anions per formula unit) would have to be generated (Table 2-1). Furthermore, by reducing $La_2NiO_3F_2$ to La_2NiO_3F, a Ni valence as low as +1 might be achieved. In contrast, only higher Ni valences of +1.5 and +1.33 can be achieved for previously studied $La_3Ni_2O_6$ and $La_4Ni_3O_8$. [99-101]

Table 2-1: Comparison between n = 1, 2, 3, ∞ Ruddlesden-Popper-type and reduced T'-type lanthanum nickelates and n = 1 Ruddlesden-Popper-type and reduced T'-type lanthanum nickel oxyfluorides. Additionally indicated are the Ni oxidation states and occupations of anion sites of the different compounds.

n	Ruddlesden-Popper structure of oxide	T' structure of reduced oxide	Ruddlesden-Popper structure of oxyfluoride	T' structure of reduced oxyfluoride
1	$La_2Ni^{2+}O_2^{eq}O_2^{ap}\square_2^{int}$	$La_2Ni^{(2-2d)+}O_2^{eq}\square_2^{ap}O_{2-d}^{int}$	$La_2Ni^{2+}O_2^{eq}O^{ap}F^{ap}F^{int}\square^{int}$	$La_2Ni^{+}O_2^{eq}\square_2^{ap}O^{int}F^{int}$
2	$La_3Ni_2^{2.5+}O_4^{eq}O_3^{ap}\square_2^{int}$	$La_3Ni_2^{1.5+}O_4^{eq}\square_3^{ap}O_2^{int}$		
3	$La_4Ni_3^{2.67+}O_6^{eq}O_4^{ap}\square_2^{int}$	$La_4Ni_3^{1.33+}O_6^{eq}\square_4^{ap}O_2^{int}$		
∞	$LaNi^{3+}O_3$	$LaNi^{+}O_2$		

In a similar fashion, a sequence of non-oxidative and oxidative fluorination of La_2NiO_{4+d} might allow for the synthesis of a Ni^{3+} containing compound. In a first step, the non-oxidative fluorination could again lead to $La_2NiO_3F_2$ under the maintenance of the Ni^{2+} oxidation state. After this fluorination, five anions per formula unit would be present in the compound. Since up to six anions per formula unit might be stabilised in the structure, additional vacancies at the anion sites could be filled oxidatively in an additional electrochemical fluorination step. Moreover, the electrochemical approach might also allow for the reductive deintercalation of fluoride ions out of $La_2NiO_3F_2$.

Besides other synthesis strategies, these approaches have been followed within this thesis (see sections 4.1 and 4.2.

2.3 Magnetism

The magnetic properties of RP-type oxides have attracted great interest for various technological applications. [43-48] With respect to this, the modification of magnetic properties of RP-type oxides and oxyfluorides through the control of transition metal oxidation states via different topochemical fluorination and defluorination approaches opens a wide scope for the development of new magnetic materials. The influence of defluorination reactions on the

magnetic behaviour of oxyfluorides was studied for the first time within this work. Furthermore, the reversibility of fluorination and deintercalation reactions in FIBs may allow for tuning and reversible switching of magnetic properties. The discussion of magnetic properties of materials requires an elementary understanding of magnetism and its diverse phenomena. Therefore, the basic concepts of magnetism and the indirect exchange interactions defining the magnetic properties in RP-type compounds are discussed. Except otherwise indicated, the information provided below has been obtained from fundamental textbooks [17, 146-148].

2.3.1 Basic principles of magnetism

Magnetism is a quantum mechanical phenomenon, which manifests itself in various types of magnetic behaviour, i.e., diamagnetism, paramagnetism, ferromagnetism, antiferromagnetism and ferrimagnetism. The different behaviours can be observed depending on the origin of the magnetic moments and their interactions. Since the magnetic moments of nuclei are small compared to the moments associated with electrons, only the latter will be considered. These moments are caused by the angular momentum of spins of unpaired electrons and the orbital angular momentum of electrons moving around nuclei. If no unpaired electrons are present, the magnetic moment only relates to the orbital motion and diamagnetism is observed. The application of an external field leads according to the Lenz's law to the induction of an electrical current, which produces an opposed magnetic field. The applied field is slightly repelled. The magnetic susceptibility χ defined as the ratio of magnetisation within a material to the externally applied field is, therefore, negative for diamagnetic materials. Even though diamagnetic contributions are found in all materials, they are weak and often outweighed by other much stronger magnetic contributions. Positive susceptibilities are characteristic for paramagnetic materials, in which permanent magnetic moments, originating from the spins of unpaired electrons, align with the applied magnetic field. The induced magnetic field has the same direction as the applied magnetic field. In the absence of an external field, the moments are randomly oriented.

Spontaneous magnetic ordering in the form of ferromagnetism, ferrimagnetism or anitferromagnetism is found depending on the kind of exchange interactions between spins of unpaired electrons (see section 2.3.2). Ordering is observed only below certain transition temperatures, called Curie temperature T_C for ferro- and ferromagnetic materials or Néel temperature T_N for antiferromagnetic materials. Above these temperatures, the samples become paramagnetic due to the increase of thermal energy, which leads to randomisation of the orientation of magnetic moments. The moments align parallel in ferromagnetic materials and antiparallel in antiferromagnetic materials leading to the exhibition of spontaneous magnetisation or not, respectively. Additionally, ferrimagnetic ordering is possible, in which antiparallel alignment of moments takes place. The opposing moments are, however, unequal and, therefore, a nonzero magnetisation remains.

The temperature dependence of the susceptibility of paramagnets can be described according to the Curie-law

$$\chi = \frac{C}{T}$$

where the Curie constant C is defined as

$$C = \frac{n \cdot \mu_B^2}{3k_B} \cdot J(J+1) \cdot g^2 = \frac{n \cdot \mu_B^2}{3k_B} \cdot \mu_{eff}^2.$$

Herein, n is the number of magnetic atoms, μ_B the Bohr magneton, J the total angular momentum quantum number and g the so-called g factor, which is ~ 2 for an electron spin.

Above T_C or T_N, the temperature dependency of ferro- and antiferromagnetic materials is characterised by the (modified) Curie-Weiss-law:

$$\text{Ferromagnetism: } \chi = \frac{C}{T - T_C}$$

$$\text{Antiferromagnetism: } \chi = \frac{C}{T + \theta}$$

θ is the Weiss constant. A linear fit of $\chi^{-1}(T)$ of the paramagnetic region can be used to determine the Curie constant and Curie temperature or Weiss constant, respectively. The effective magnetic moment μ_{eff} can be obtained when the Curie constant is known. Assuming spin-only moments only, i.e., neglecting the contributions of orbital angular momentum L to the total angular momentum J (L = 0, J = S), the number of unpaired electrons of a transition metal ion can be estimated using $2[S(S+1)]^{1/2}$ where S is the sum of spin quantum numbers of unpaired electrons.

2.3.2 Indirect exchange interactions

In transition metal oxides and oxyfluorides, the occurrence of ferro- and antiferromagnetic ordering requires indirect exchange interactions of the *d* orbital electrons of the transition metal cations via electrons of *p* orbitals of diamagnetic anions (e.g. oxide and/or fluoride ions). This involves virtual or real electron transfer of the *p* electrons. With respect to the investigated compounds, two mechanisms can be distinguished: i) *superexchange interactions* and ii) *double-exchange interactions*. [149]

Superexchange interactions: The strength and sign of the superexchange is dependent on the occupation and orbital degeneracy (see also section 2.1.2) of the involved *d* orbitals. The interaction involves virtual electron transfers leading to the formation of excited states. The so-called Goodenough-Kanamori-Anderson (GKA) rules [150-153], which can be used to predict the magnetic interactions, are based on the minimisation of Coulomb interactions and include the Pauli exclusion principle and the Hund's rules. In a qualitative manner, they can be summarised as the following:

1st GKA rule: The 180° exchange between two half-filled or empty orbitals is strong and antiferromagnetic.

2nd GKA rule: The 180° exchange between one half-filled and one empty or doubly-filled orbital is weak and ferromagnetic.

3rd GKA rule: The 90° exchange between two half-filled orbitals is weak and ferromagnetic.

Figure 2-14 illustrates the GKA rules based on the $d_{x^2-y^2}$ and d_{z^2} orbitals of Mn^{3+} and the p_z orbitals of O^{2-} of a Mn – O – Mn bond. In Mn^{3+}, the d_{z^2} orbital is energetically favoured due to the Jahn-Teller activity of Mn^{3+}; the occupation of the $d_{x^2-y^2}$ orbital is, however, discussed as well.

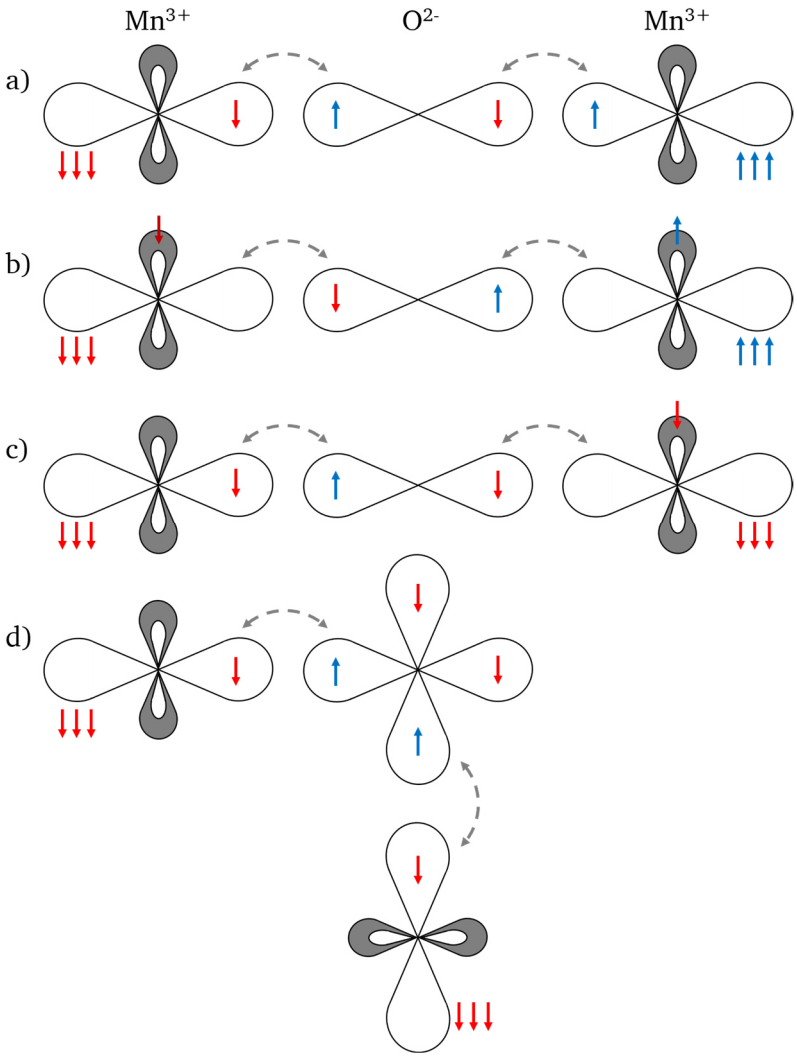

Figure 2-14: Illustration of superexchange and GKA rules based on the magnetic exchange between between Mn^{3+} ions and via a O^{2-} ion. The e_g orbitals of Mn^{3+} are shown: the $3d_{z^2}$ orbitals are represented in white and the $3d_{x^2-y^2}$ orbitals in grey (the part of the orbitals perpendicular to the drawing layer is not shown). The $2p_z$ orbital (a-c) and the $2p_y$ and $2p_z$ orbitals (d) of O^{2-} are given in the middle. The triplet of arrows symbolises the spin S=3/2 of the three half-occupied t_{2g} orbitals, which are not shown in the representation. Depending on the occupation of orbitals antiferromagnetic (a, b) or ferromagnetic (c, d) exchange takes place. The illustration has been redrawn with permission from reference 150. Copyright © 2012, IOP Publishing.

Double-exchange interactions: For a double-exchange, mixed valance configurations are required. If two valance states, for examples Mn^{3+} and Mn^{4+} (Figure 2-15) are present, the electron in the d_{z^2} orbital of Mn^{3+} can hop via the oxide ion to the empty e_g orbitals of the Mn^{4+}. In contrast to the superexchange, for a parallel orientation of the spins of the half-occupied t_{2g} orbitals of the transition metal ions, no Coulomb repulsion or Hund's coupling has to be taken into account and real jump processes can be carried out. If the spins of the t_{2g} orbitals are antiparallel, there is no hopping according to Hund's rules.

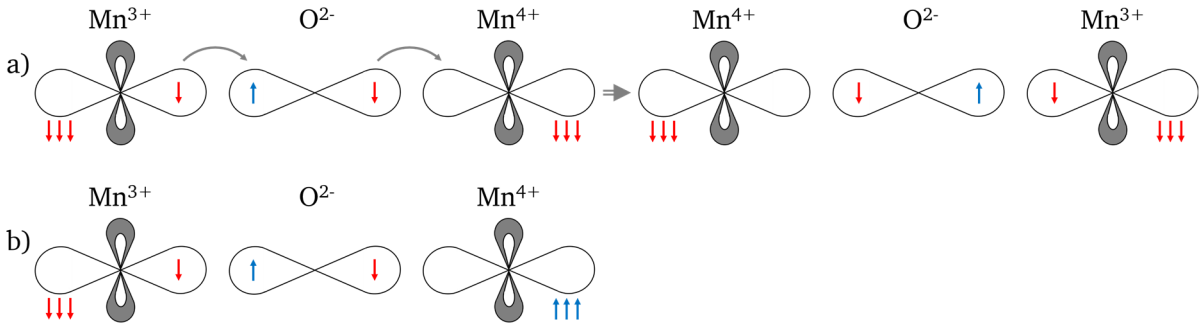

Figure 2-15: Illustration of double-exchange interactions between Mn^{3+} and Mn^{4+} ions via a O^{2-} ion. The e_g orbitals of Mn^{3+} and Mn^{4+} are shown: the d_{z2} orbitals are represented in white and the d_{x2-y2} orbitals in grey (the part of the orbitals perpendicular to the drawing layer is not shown). The p_z orbital of O^{2-} is given in the middle. The triplet of arrows symbolises the spin S=3/2 of the three half-occupied t_{2g} orbitals, which are not shown in the representation. For a ferromagnetic ordering of spins of Mn^{3+} and Mn^{4+}, real electron transfers are possible via a double-exchange (a); for an antiferromagnetic ordering of spins of Mn^{3+} and Mn^{4+}, no electron transfers are possible (b). The illustration has been redrawn with permission from reference 150. Copyright © 2012, IOP Publishing.

2.4 Diffraction

In the following section, fundamentals about powder diffraction and the Rietveld method are given. Common features and differences between different types of diffraction techniques based on the used radiation, i.e., X-rays, neutrons and electrons are discussed. Rietveld analysis can be performed on X-ray and neutron powder diffraction data sets. Each diffraction peak contains information about the sample and the instrument used for the measurement. In order to be able to perform Rietveld refinements, which involves the simulation of the measured data using a sufficiently good mathematical approximation, the different features have to be understood, separated and described by mathematical functions. In the following, the basic principles underlying diffraction are introduced, before the Rietveld method is examined. Unless otherwise specified, the given information has been extracted from textbooks about crystallography and diffraction [154-159] and the Rietveld method [160, 161].

2.4.1 Basic principles of powder diffraction

Powder diffraction is a powerful tool for the determination of crystal structures. The investigation of a crystal structure by means of diffraction is only possible when waves with wavelengths of the same order of magnitude as the interatomic distances interact with atoms in a crystal. Suitable wavelengths can be found for X-rays and particles such as neutrons and electrons. Important features of all three types of radiation are given in Table 2-2. The nature of interaction between X-rays, neutrons and electrons with nuclei and electrons of individual atoms varies and accordingly different information can be extracted depending on the type of radiation used. Moreover, complementary information can be gained by using different radiation as will be explained in the following.

Table 2-2: Comparison of three types of radiation used in diffraction experiments. [155]

	X-rays	Neutrons	Electrons
Nature	Wave	Particle	Particle
Scattered by	Electron density	Nuclei and magnetic spins of electrons	Electrostatic potential
Scattering function	$f(\sin\theta/\lambda) \propto Z$	f is constant	$f(\sin\theta/\lambda) \propto Z^{1/3}$
Wavelength range	~ 0.5 – 2.5 Å	~ 1 Å	~ 0.02 – 0.05 Å
Lattice image	Reciprocal	Reciprocal	Direct, reciprocal
Applicable theory of diffraction	Kinematical	Kinematical	Dynamical

For an infinite ideal crystal, diffraction can be geometrically described in a simplified way as specular reflections, i.e., the angle of incidence θ is equal to the angle of reflection, of parallel waves by a set of lattice planes with the same Miller indices *hkl* and distance *d* (Figure 2-16). The planes are treated as semi-transparent mirrors and, therefore, reflections at consecutive parallel planes can take place. Since all waves have the same direction after being reflected, they interfere. Constructive interference occurs only when the path difference Δ between waves scattered at successive planes is an integer multiple of the wavelength λ:

$$\Delta = n\lambda$$

In all other cases, destructive interference is observed.

Geometrically, the path difference Δ can also be described as:

$$\Delta = 2d \sin\theta$$

Combining both equations, the Bragg equation is obtained:

$$n\lambda = 2d \sin\theta$$

Thus, only for certain angles θ, intensity maxima appear, while for other angles no intensity is found.

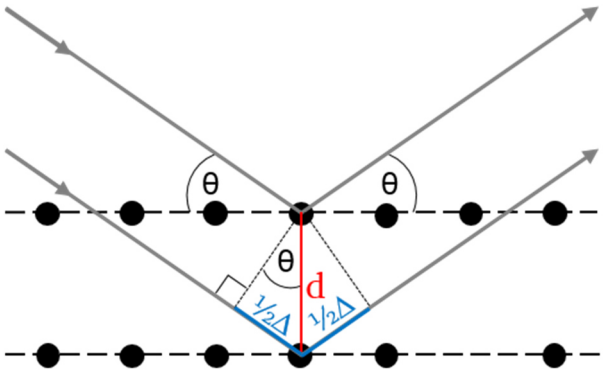

Figure 2-16: Illustration of the geometry used for the simplified derivation of Bragg's law.

A geometrical interpretation of the diffraction condition can be also given using the Ewald's sphere (Figure 2-17). It displays the relationship between diffraction patterns and the reciprocal space. The length of the incident wave $\overrightarrow{k_0}$ is in reciprocal space the inverse of the wavelength. An elastically scattered wave $\overrightarrow{k_f}$ has the identical length as $\overrightarrow{k_0}$. The angle between $\overrightarrow{k_0}$ and $\overrightarrow{k_f}$ is 2θ. Therefore, a sphere with the radius of $1/\lambda$ is delineated since $\overrightarrow{k_f}$ can be diffracted in all directions under different angles 2θ. For each reciprocal lattice point

located on this Ewald's sphere, the Bragg condition is fulfilled and diffraction takes place. Depending on the angle, different Debye-Scherrer cones with apex angles of 4θ are generated, which are characteristic for one set of lattice planes. The scattering vector $\vec{k}$ is given by

$$\vec{k} = \overrightarrow{k_f} - \overrightarrow{k_0}.$$

The length of the scattering vector is $1/d_{hkl}$.

For thin samples, for which sufficient transmission is possible, the diffraction patterns are recorded by projecting the 3-dimensional intensities on a 2-dimensional detector, which is oriented perpendicular to the incident beam. While for polycrystalline samples, Debye ring patterns are detected, single crystalline samples show spot patterns. In the middle of the patterns a centre spot from the non-diffracted beam is visible. The rings or spots can be indexed and interplanar distances and lattice parameters may be deducted.

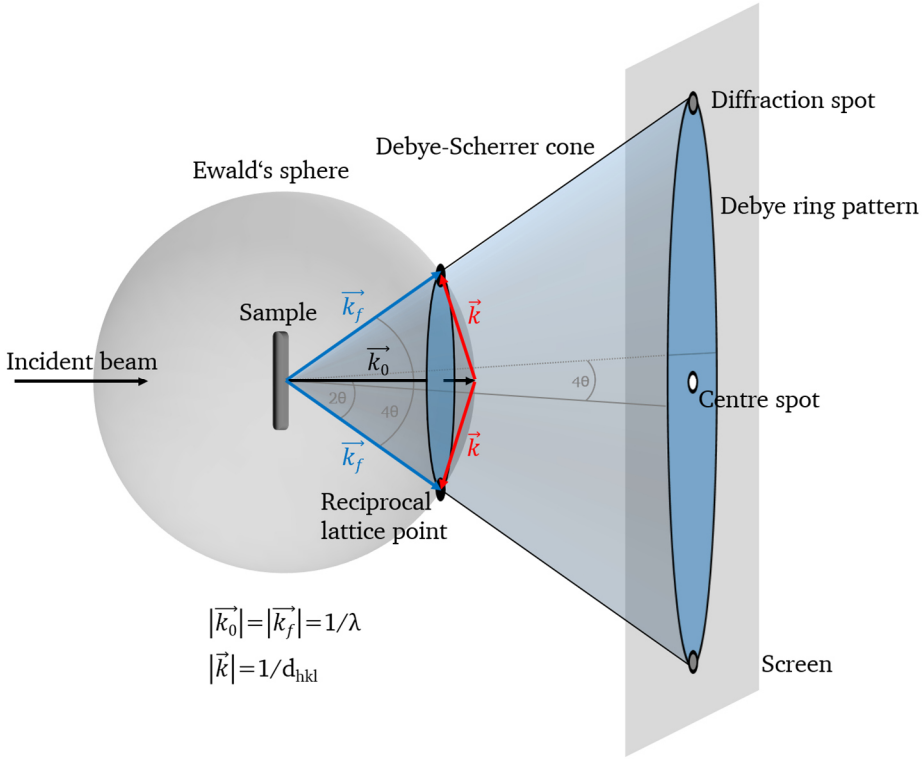

Figure 2-17: Illustration of the Ewald's sphere in reciprocal space. For reciprocal lattice points on the sphere, diffraction takes place and diffraction cones are formed, which can be detected on a screen as a spot pattern for single crystals or a ring pattern for polycrystalline samples.

Any diffraction experiment can be understood as a Fourier transformation of a crystal structure from direct space into reciprocal space. This results in 3-dimensional intensities in reciprocal space instead of a direct image of the crystal structure. The determination of the latter takes place via a transformation of the obtained diffraction patterns back into direct space, which is not straightforward as will be explained below. For the representation of X-ray and neutron powder diffraction data, the 3-dimensional intensities in reciprocal space are given as a 1-dimensional diffractogram as a function of the reflection position 2θ or the interplanar distance *d*, respectively. In electron diffraction, the 2-dimensional representation of measured intensity data leads to a reduced overlapping of peaks allowing a reconstruction of the 3-dimensional electron diffraction data in reciprocal space and indexing can be performed unambiguously. Compared to X-ray or neutron diffraction, the beam used in

electron diffraction experiments consists of high-energy electrons, which are accelerated in a strong electric potential of several hundred kV. Therefore, they have a wavelength, which is smaller than the interatomic distances in the sample. Due to the small wavelength, the scattering angles are small and the radius of the Ewald's sphere, which also corresponds with the lengths of $\overrightarrow{k_0}$ and $\overrightarrow{k_f}$, becomes quite large. Therefore, the curvature of the sphere degenerates practically into a plane and possibly many reflections can be measured at the same time. Additionally, direct imaging is possible using electron transmission techniques.

The measured intensity patterns obtained from X-ray, neutron or electron diffraction have multiple, potentially overlapping reflections of one or more phases within the sample superimposed on a background. Each peak is characterised by its *position, intensity, shape, width* and *asymmetry* all of which contain information about the crystal structure, properties of the sample and/or instrumental parameters. A closer examination of these features not only enables a better understanding about what information can be extracted from a diffractogram but also how to simulate a pattern to eventually determine crystal structures via structural refinement approaches like the Rietveld method (see section 2.4.2). The features are, therefore, examined in the following. In addition, the *fundamental parameter approach* is discussed, which is used to lower the influences of the instrument and the radiation source on the peak shape, width and asymmetry.

2.4.1.1 Peak position

As noted previously, diffraction peaks appear only at specific scattering angles θ, for which the Bragg equation is fulfilled. The position of the reflection is, therefore, dependent on the wavelength λ and the interplanar distance d. The latter is a function of the unit cell dimensions, e.g. the lattice parameters a, b, c, α, β, γ, and the Miller indices *h, k* and *l*, which define every set of lattice planes. For each crystal system, different relations can be geometrically deducted. Exemplarily, for the orthorhombic system the following is valid

$$\frac{1}{d^2} = \frac{h^2}{a^2} + \frac{k^2}{b^2} + \frac{l^2}{c^2}\,.$$

The peak position and the corresponding interplanar distances may allow determining the crystal system, lattice parameters and possibly the space group of an unknown phase. The possibilities for the space group determination can be reduced due to the systematic extinctions of reflections with certain *h, k* and *l* indices. Depending on the lattice type, e.g. body-centred or face-centred, or on present symmetry elements like glide planes or screw axes parallel to certain plains or axes, some reflections have no intensity. Therefore, the symmetry elements can be deduced and possible space groups can be determined. However, especially when the lattice parameters are unknown, the necessary indexing of all observed reflections, i.e., the assignment of the integer indices *h, k* and *l* is not trivial. The implementation of iterative indexing approaches into computer software (e.g. Topas V5.0 [162, 163]) facilitates the analysis, even though the solutions are often not unambiguous, especially for low symmetries.

Other factors affecting peak positions are various instrumental and sample related aspects. For example, preparative inaccuracies such as incorrect height adjustment influence peak positions.

2.4.1.2 Peak intensity

The integrated intensity I_{hkl} of a reflection caused by waves reflected from a set of lattice planes *hkl* (after subtraction of the background) is affected by the atomic structure and

several other factors including sample and instrument related parameters. Overall, it can be expressed as the following product:

$$I_{hkl} = s \cdot p_{hkl} \cdot LP_\theta \cdot A_\theta \cdot T_{hkl} \cdot E_{hkl} \cdot |F_{hkl}|^2.$$

Herein, s is the scaling factor, p_{hkl} the multiplicity factor, LP_θ the Lorentz-polarisation factor, A_θ the absorption correction, T_{hkl} the factor for preferred orientations and E_{hkl} the extinction correction. Preferred orientation effects have been not observed within the scope of this thesis and can, therefore, together with the extinction factor, which accounts for deviations from kinematical diffraction, be neglected. The parameters are all independent of the crystal structure of the sample. Only the structure factor $|F_{hkl}|^2$ correlates to the atomic structure, i.e., to the type of atoms and their positions within the unit cell. When a unit cell contains multiple atoms, the amplitude of the scattered wave is given by the structure amplitude

$$F_{hkl} = \sum_j f_j \cdot \exp(-B_j \cdot \frac{sin^2\theta}{\lambda^2}) \cdot N_j \cdot \exp(2\pi i(hx_j + ky_j + lz_j))$$

where f_j is the scattering factor of atom j, B_j the thermal displacement parameter of atom j and N_j is the occupation factor of atom j. In the second exponential term, $2\pi(hx_j + ky_j + lz_j)$ is the phase angle Φ_j of atom j with the Miller indices *h, k* and *l* of the reflection and the relative atomic positions x_j, y_j and z_j in the unit cell. The summation takes place over all atoms j in the unit cell. Since only $|F_{hkl}|^2$ can be deducted from the measurement of the scattered intensity, the phase information is lost. Consequently, crystal structures cannot be solved directly from experimental data.

The scattering factor f_j is contained in the expression for the structure amplitude F_{hkl} because the ability of an atom j to scatter radiation depends on the type of atom. Moreover, the scattering factor is dependent on the kind of incident radiation used in the experiment (e.g. X-rays or neutrons), because the radiation is scattered by different scattering objects such as electrons or nuclei. In all cases, the scattering factor has the form of a Fourier transform of the density distribution of scattering objects.

X-rays are almost exclusively scattered by the electron density surrounding the nuclei and, therefore, the scattering factor increases with the atomic number Z. The X-ray scattering factor depends strongly on the diffraction angle θ (expressed as $\sin\theta/\lambda$) (Figure 2-18) due to electron density around the nucleus. For $\sin\theta/\lambda = 0$, the values of f equals the atomic number Z.

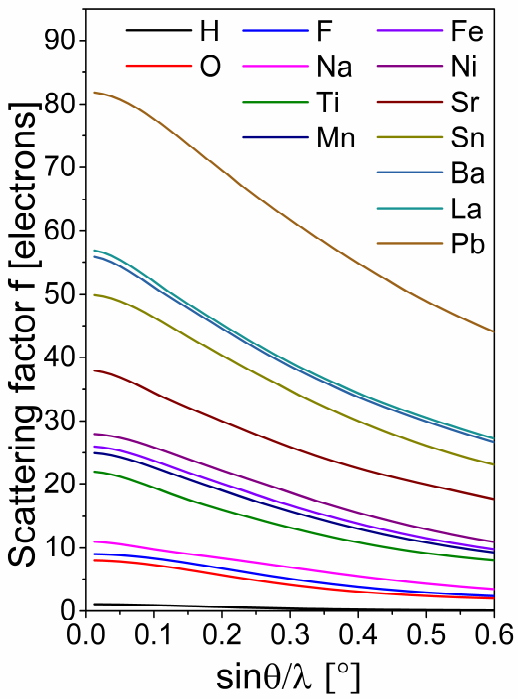

Figure 2-18: X-ray atomic scattering factors as a function of sinθ/λ. The strong decrease of the scattering factors is shown exemplary on the elements measured within this thesis. The scattering factors have been fitted to the analytical function $f\left(\frac{sin\theta}{\lambda}\right) = \sum_{i=1}^{4} a_i \cdot \exp\left(-b_i \cdot \frac{sin^2\theta}{\lambda^2}\right) + c$ with the coefficients a_i, b_i and c. [164] Thermal displacement has not been considered.

Neutrons are scattered by the nuclei. The Fourier transform of the density distribution of a nucleus, i.e., that of a delta function, is unity, which results in constant nuclear scattering factors over the complete angular range. Instead of scattering factors, they are referred to as scattering length b_j. The scattering lengths differ strongly for different atoms and isotopes and there is no progression with Z (Figure 2-19). Additionally, the scattering length can be positive or negative. A negative value corresponds to a 180° phase shift on scattering.

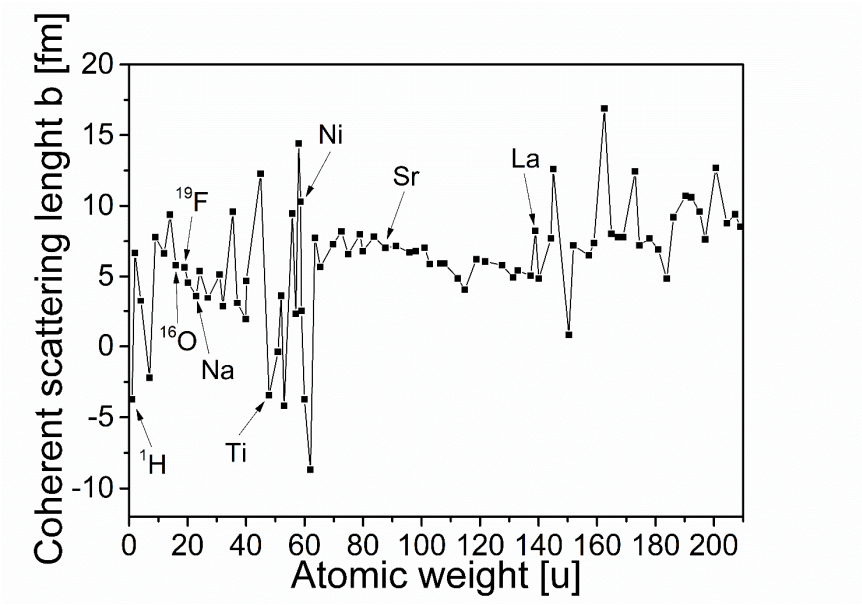

Figure 2-19: Nuclear scattering lengths of thermal neutrons as a function of atomic weight. The scattering lengths of the elements and their isotopes were taken from reference 166. The scattering lengths of the elements investigated by neutron diffraction within this thesis are labelled.

Furthermore, due to the nuclear spins of ½ and the corresponding magnetic moments of neutrons, magnetic interactions with magnetic moments of unpaired electrons of atoms of the sample can be observed. In this case, interactions take mostly place between the neutrons and outer-shell electrons. The Fourier transform of the spatial distribution of these outer-shell electrons and, therefore, the magnetic scattering factor decreases, consequently, faster than the X-ray scattering factor. Since the moments of atoms can be long-range ordered (see section 2.3), coherent magnetic scattering can take place. The magnetic scattering is superimposed on the nuclear scattering in magnetic samples. Magnetic structures can be commensurate or incommensurate. For commensurate structures, there is a close relationship between the magnetic unit cell and the underlying crystallographic nuclear unit cell. Depending on the ordering of atomic magnetic moments $\vec{\mu}$, magnetic unit cells may be doubled, tripled etc. along the axes, which is described by the scattering vector $\vec{k}$. The periodic change of the magnetic moment $\vec{\mu}$ is given by

$$\vec{\mu} = \overrightarrow{\mu_0} \cdot \exp(-2\pi i \cdot \vec{k} \cdot \vec{T})$$

where $\vec{T}$ is the nuclear translation vector. Thus, the scattering vector $\vec{k}$ describes how the magnetic moment $\vec{\mu}$ of a translatorically identical atom transforms between neighbouring unit cells. In incommensurate structures, such comparatively simple relationships are not found.

Likewise to the nuclear structure amplitude F_{hkl}, the magnetic structure amplitude can be defined as

$$\overrightarrow{F_{hkl}^{mag}} = \sum_j p_j \cdot \overrightarrow{q_j} \cdot \exp(2\pi i(hx_j + ky_j + lz_j)).$$

The magnetic structure amplitude is, however, a vectorial quantity and sums up all magnetic contributions within the unit cell. It depends on the orientation and length of the scattering vector $\vec{k}$ and the atomic magnetic moment $\vec{\mu}$. p_j is the magnetic scattering length of atom j and $\overrightarrow{q_j}$ is the magnetic interaction vector of atom j. The magnetic interaction vector $\vec{q}$ can be described in a geometrical form as

$$\vec{q} = \hat{k} \times (\hat{\mu} \times \hat{k}) = \hat{\mu} - (\hat{k} \cdot \hat{\mu}) \cdot \hat{k} \text{ with } |\vec{q}| = \sin\alpha.$$

Herein, $\hat{k}$ and $\hat{\mu}$ are the unit vectors parallel to the scattering vector $\vec{k}$ and atomic magnetic moments $\vec{\mu}$ and α is the angle between $\hat{k}$ and $\hat{\mu}$. The magnetic interaction vector $\vec{q}$ changes its sign, when the magnetic moment is reversed.

If there is an increase in the magnetic unit cell volume, i.e., $\vec{k} \neq \vec{0}$, additional reflections commonly at high d-spacings are observed. If magnetic and nuclear reflections overlap, the overall intensity is given by $|F_{hkl}|^2 + \left|F_{hkl}^{mag}\right|^2$. [166]

With respect to the RP-type oxides and oxyfluorides investigated within the scope of this thesis, some remarks have to be given about the implications originating from the use of different types of radiation on the crystal structure analysis. The direct proportionality between the X-ray scattering factor and the atomic number Z, resulting also in higher cross sections due to an approximate Z^2 relationship, leads to stronger scattering of heavier atoms than lighter atoms. Hence, X-ray diffraction gives mostly detailed information only about the cations in the compounds. Neutron diffraction, on the other hand, enables the investigation of the anion sublattice due to the particular nuclear scattering lengths and cross sections of each element. The cross sections are approximately $|b|^2$. The use of multiple data sets of different

kinds of radiation can, therefore, be beneficial for the crystal structure determination. The differentiation between oxide and fluoride ions by means of X-ray or neutron diffraction is, however, not possible due to the similar scattering factors or lengths of oxide and fluoride (^{16}O: 5.8 fm, ^{19}F: 5.7 fm) [165] (Figure 2-19). To distinguish between these anions, other empirical coordination chemistry related approaches like the bond-valance method [167, 168] have to be applied. For this, precise bond distances have to be known, which can be determined using diffraction experiments. Using neutron diffraction, it is, in principle, even possible to detect hydride ions, which have a negative scattering length of -3.7 fm [165] corresponding to an inversed scattering vector compared to oxide or fluoride ions. If, however, additional anion vacancies are present, it is difficult to assign precise oxide, fluoride or hydride ion contents to a certain anion site. To illustrate this problem two simple examples are considered: i) a site is only partially occupied by oxide ions (consequently, vacancies are present on this site as well); ii) a site is partially occupied by slightly more oxide ions and additionally a small amount of hydride ions (consequently, fewer vacancies are present on this site as compared to example i). In neutron diffraction, the mathematics behind both refinements would be the same and it is not possible to conclude, which occupation scenario would be valid. This also demonstrates that an over-parametrisation of refinements may be misleading. Even though the mathematics behind the refinements of X-ray and neutron diffraction data are different, due to the extremely low scattering factor of hydride ions in X-ray diffraction, coupled refinements of X-ray and neutron diffraction data do not necessarily provide additional information about the anion sublattice. Therefore, a detailed structural characterisation of compounds containing multiple anions and vacancies is difficult.

Similar to X-ray and neutron diffraction, the scattering amplitude of electron diffraction is dependent on the electron atomic scattering factor of the atoms within the unit cell. Since the accelerated electrons are charged particles, which interact with the Coulombic potential of the sample atoms, the factor is regarded as the Fourier transform of the electrostatic potential distribution. The scattering factor is proportional to $Z^{1/3}$ and a strong decrease in dependence of the diffraction angle is found. The cross sections of electrons are $\sim 10^4$ to 10^5 times larger than in X-ray or neutron diffraction, which allows measuring small sample volumes. Furthermore, high-resolution electron microscopy images can be obtained, since a focussing of electrons by magnetic lenses is possible. [169, 170]

2.4.1.3 Peak shape and width

The profile of a powder diffraction peak (corrected by the background), characterised by its shape and width, is dependent on instrumental parameters, the emission profile of the source used and sample contributions. It can be described by a peak profile function, which is a convolution of instrumental, wavelength dispersion and sample functions. Each of these contributions have their own angular dependency of the peak shapes, widths and asymmetries. In X-ray diffraction, the peak shape can be represented by a Pseudo-Voigt function, i.e. a summation of a Lorentzian and Gaussian function with scalable contributions. While in constant wavelength neutron diffraction, the convolution results in reflections with almost exactly Gaussian peak shape, strong asymmetries are often found in time-of-flight neutron diffraction.

The sample function and, therefore, the convoluted peak shape function is influenced by the physical state of the sample. Isotropic peak broadening β caused by crystal size τ and microstrain ε increases according to

$$\beta = \frac{\lambda}{\tau \cdot cos\theta}$$

and

$$\beta = k \cdot \varepsilon \cdot tan\theta \ .$$

Therefore, size and strain contributions can be distinguished as a function of the diffraction angle θ.

Apart from isotropic, angular dependent broadening, anisotropic, hkl dependent strain broadening might be observed. It can be described phenomenologically using the spherical harmonics [171, 172] or Stephens model [173].

In the spherical harmonics model, the anisotropic broadening is given by

$$W(\theta, \varphi) = \sum_{ijp} C_{ijp} \cdot Y_{ijp}(\theta, \varphi)$$

with $Y_{ijp}(\theta,\varphi)$ being the spherical harmonic functions of order i (i has to be even), j = 0, 1,…, i and the parity p, which can be "+" or "-". The orientation of the unit vector $\hat{x}$, which is parallel to the scattering vector, is described by the polar angles θ and φ. C_{ijp} are refined with restrictions imposed by symmetry invariance with respect to the Laue class. [174]

The Stephens models [173], which are also implemented in Topas V5.0, consider a multidimensional distribution of lattice parameters leading to the anisotropic broadening. Each crystallite has its own set of metric parameters A, B, C, D, E and F of the reciprocal lattice, which is correlated to the spacing *d* between lattice planes *hkl* in direct space according to

$$\frac{1}{d^2} = M_{hkl} = A \cdot h^2 + B \cdot k^2 + C \cdot l^2 + D \cdot k \cdot l + E \cdot h \cdot l + F \cdot h \cdot k.$$

The variance of M_{hkl} is given by

$$\sigma^2(M_{hkl}) = \sum_{HKL} S_{HKL} \cdot h^H \cdot k^K \cdot l^L$$

with terms for the anisotropic strain parameters S_{HKL} defined for H + K + L = 4. The anisotropic strain parameters S_{HKL} are refined. Depending on the crystal system, different restrictions for the anisotropic strain parameters S_{HKL} have to be considered. The anisotropic strain broadening contribution to the line width is

$$\Gamma_A = [\sigma^2(M_{hkl})]^{1/2} \cdot \frac{tan\theta}{M_{hkl}}.$$

2.4.1.4 Peak asymmetry

Asymmetry effects are usually observed on the low angle side of a reflections due to various instrumental factors. The major contribution is caused by axial divergence of the beam; other factors such as non-ideal sample geometry etc. have a smaller influence. The asymmetry is usually strongly dependent on the diffraction angle and is most pronounced at low angles.

A proper instrument configuration and alignment can reduce the peak asymmetry substantially. Additionally, the fundamental parameter approach, which is discussed below, can significantly lower the asymmetry.

2.4.1.5 Fundamental parameter approach

The influence of the instrument and the radiation source on the peak shape, width and asymmetry can be determined using the fundamental parameter approach. [175-177] This approach is based on a comprehensive description of experimental conditions and hardware configurations by measuring a crystalline standard sample (e.g. LaB_6), for which crystallite size and/or strain effects are known. This allows refining of all non-sample related parameters. For subsequent refinements of other samples, the obtained values are used. Therefore, less parameters have to be used and it can be excluded that sample related influences are wrongly described by too variable instrumental parameters. The fundamental parameter approach is also implemented into Topas V5.0.

2.4.2 The Rietveld method

The Rietveld method is a crystal structure analysis method [178-180], in which a least-squares minimisation procedure is conducted. A starting structural model, which is reasonably close to the final model, is needed. The quantity that is minimised is the residual S_y

$$S_y = \sum_i w_i \left(y_{i,obs} - y_{i,cal}\right)^2$$

where $w_i = 1/y_i$ is the weighting coefficient at step i, $y_{i,obs}$ the observed intensity at step i and $y_{i,cal}$ is the calculated intensity at step i. Hence, for each measured step intensity data point i, an intensity is calculated by means of mathematical functions (e.g. Gaussian, Lorentzian or Pseudo-Voigt functions). The calculated intensities are based on the calculation of $|F_K|^2$ values from the structural model by summing over all calculated contributions from neighbouring reflections plus the background:

$$y_{i,cal} = s \cdot \sum_K p_K \cdot LP_\theta \cdot A_\theta \cdot T_K \cdot E_K \cdot \phi(2\theta_i - 2\theta_K) \cdot |F_K|^2 + y_{i,bkg}.$$

Herein, s is the scaling factor, p_K the multiplicity factor, LP_θ the Lorentz-polarisation factor, A_θ the absorption correction, T_K the factor for preferred orientations, E_K the extinction correction, ϕ the reflection profile, $|F_K|^2$ the structure factor and $y_{i,bkg}$ the background intensity at step i. The summation is over K, which are the Miller indices h, k and l of a reflection. As is discussed in section 2.4.1, the reflection profile is dependent on several factors including instrumental and sample related parameters and is described by various mathematical functions; the fundamental parameter approach can, however, help to reduce parameters. For the description of the background, a polynomial of order m is used:

$$y_{i,bkg} = \sum_m b_m \cdot (2\theta_i)^m.$$

The least-squares minimisations leads to a set of normal equations, which contain the derivatives of all calculated intensities $y_{i,cal}$ with respect to each refinable parameter. The set of equations can be solved by inversion of the normal matrix $\mathbf{M_{jk}}$ given by

$$\boldsymbol{M_{jk}} = -\sum_i 2w_i \cdot \left[\left(y_{i,obs} - y_{i,cal}\right) \cdot \frac{\partial^2 y_{i,cal}}{\partial x_j \partial x_k} - \left(\frac{\partial y_{i,cal}}{\partial x_j}\right) \cdot \left(\frac{\partial y_{i,cal}}{\partial x_k}\right)\right]$$

where x_j and x_k are the set of refinable parameters. Therefore, an m x m matrix is created and inverted, where m is the number of refined parameters. Since the function for the residual S_y is non-linear, the solution has to be determined iteratively. The shifts Δx_k are

$$\Delta \boldsymbol{x_k} = \sum \boldsymbol{M_{jk}^{-1}} \cdot \frac{\boldsymbol{\partial S_y}}{\boldsymbol{\partial x_k}}.$$

The calculated shifts are applied to the parameters of the starting model to potentially improve the model. The whole procedure is then repeated until a certain convergence criterion is reached. To avoid false minima, constraints have to be chosen deliberately. Refinable parameters are compiled in Table 2-3.

Table 2-3: Refinable parameters within the analysis of powder diffraction data. [160]

For each phase present	**Global**
Atomic positions x_j, y_j and z_j	2θ-Zero
Isotropic thermal parameters B_j	Instrumental profile
Occupation factor N_j	Profile asymmetry
Scaling factor s	Background
Sample-profile width parameters	Wavelength
Lattice parameters a, b, c, α, β and γ	Sample displacement
Individual anisotropic thermal parameters	Sample transparency
Preferred orientation	Absorption
Crystallite size and microstrain	
Extinction	

Due to the high number of refinement parameters, strong correlation between parameters can occur if too many parameters are refined simultaneously. These correlations lead to similar effects on the calculated intensities when different parameters are changed. Highly correlated parameters are thermal parameters and occupation factors, occupation and scaling factors, thermal parameters and absorption, thermal parameters and X-ray scattering factors or neutron scattering lengths when using the wrong types of atoms as well as thermal parameters and multiplicity factors. To avoid correlations, special attention has to be given to the sequence of refinements steps and physically and chemically plausible constraints should be applied.

To judge refinement results, difference plots between the measured and calculated data and different R-indices can be employed. The R_{wp} and R_{Bragg} values are the most meaningful indices amongst others. They are defined as

$$R_{wp} = \sqrt{\frac{\sum_i wi \cdot (y_{i,obs} - y_{i,cal})^2}{\sum_i w_i \cdot (y_{i,obs})^2}}$$

and

$$R_{Bragg} = \frac{\sum_K \left|\sqrt{I_{K,obs}} - \sqrt{I_{K,cal}}\right|}{\sum_K \sqrt{I_{K,obs}}}$$

where I_K is the intensity of reflection K at the end of the refinement.

Another important criterion is the Goodness-of-fit (GOF) indicator

$$GOF = \frac{R_{wp}}{R_e} = \sqrt{\frac{\sum_i wi \cdot (y_{i,obs} - y_{i,cal})^2}{N - P}} = \sqrt{\frac{S_y}{N - P}}$$

with

$$R_e = 'R - expected' = \sqrt{\frac{N-P}{\sum_i wi \cdot {y_{i,obs}}^2}}$$

where N is the number of measurement points and P the number of refined parameters.

A quantitative analysis of multiphase mixtures is possible since the scaling factors derived from Rietveld analysis are related to the relative weight fraction w_p of phase p in a mixture of j phases according to

$$w_p = \frac{s_p \cdot (Z_p M_p V_p)}{\sum_j s_j \cdot (Z_j M_j V_j)}.$$

Herein, s are the scaling factors and Z, M and V the numbers of formula units per unit cell, the masses of the formula unit and the unit cell volumes of the involved phases, respectively. Quantification errors are typically in the order of 1 to 2 %.

For the quantification of amorphous phase fractions, an internal standard approach can be used. The sample is mixed with a well crystalline standard with a similar adsorption coefficient in a distinct weight ratio. If there is an amorphous phase, the weight fraction of the standard is overestimated and from the difference to the expected value, the phase fraction of the amorphous phase can be calculated.

2.5 Characterisation techniques

The following discussion is limited to fundamental principles of the techniques and relevant aspects concerning the experimental set-ups used within this thesis.

2.5.1 Diffraction

The most important principles underlying diffraction are discussed in section 2.4. Within this section, additional information related to the used experimental set-ups are given.

2.5.1.1 X-ray diffraction

For the X-ray diffraction experiments, Cu K_α radiation consisting of two wavelengths of Cu $K_{\alpha1}$ of 1.540596 Å and $K_{\alpha2}$ of 1.544443 Å were used. The peak shape of the Cu K_α radiation was modelled via a combination of Lorentzian functions. Cu K_β radiation with a wavelength of 1.392 Å was filtered using a Ni filter with a K absorption edge at 1.488 Å.

The polycrystalline powder samples were measured in the Bragg-Brentano geometry, in which the flat-plate sample is positioned in the centre of the goniometer circle. The foci of the X-ray source and the detector have a constant distance to the tangent of the sample surface and they are moved on the goniometer circle by –θ and θ. The divergence of the incident X-ray beam is controlled by slits. Fixed or variable slits can be used. The length of the irradiated area of the sample is dependent on the divergence and scattering angles and may overflow the sample at low scattering angles, especially when small samples areas are illuminated. The divergence of the diffracted beam is controlled using anti-scatter and divergence slits. Axial divergence is reduced using Soller slits on the source as well as the detector side.

A position sensitive detector consisting of multiple channels with micro-strip anodes is used for the detection of the diffracted beam. Each anode element is an individual detector with a fixed 2θ position relative to other anodes. In the detector, the incoming X-ray photons are

converted into electrical signals by ionisation of xenon atoms and amplification of the number of obtained electrons due to their acceleration in an electric field causing further ionisation processes. The electrons cause a charge pulse when reaching the anode, which propagates to both ends of the anode. By comparing the relative arrival times of the pulse at both ends, the position of the X-ray photon can be determined. Quenching gas can be used to minimise dead times. [154, 156]

2.5.1.2 Neutron diffraction

The neutron diffraction experiments were conducted at the ISIS high-resolution powder diffractometer (HRPD) [181] and general materials diffractometer (GEM) [182, 183] at the Rutherford Appleton Laboratory in Didcot, United Kingdom. The ISIS Neutron and Muon Source providing neutrons for the diffraction measurements is a spallation source. Protons are accelerated in a synchrotron and diverted toward a target station, where they collide with tungsten metal. The collision leads to the spallation of neutrons from the metal and the emitted neutrons are channelled through beamlines towards the ISIS instruments.

The powder diffraction measurement of both diffractometers used are based on the time-of-flight analysis of pulsed neutrons with varying wavelengths. By recording the time each neutron of a pulse takes to reach the detector, its wavelength and the corresponding d-spacing can be calculated according to

$$\lambda = \frac{h}{m_{neutron} \cdot v} = \frac{h \cdot t}{m_{neutron} \cdot L} = 2d \sin\theta$$

where t is the time of flight, $m_{neutron}$ the mass of a neutron and L the length of the flight path. The angle θ is herein constant, since the detector banks are stationary.

The relative uncertainty of the d-spacing δd/d is dependent on the uncertainties of the time of flight δt, the path length δL and the scattering angle δθ. It can be described as

$$\left(\frac{\delta d}{d}\right)^2 = \left(\frac{\delta t}{t}\right)^2 + \left(\frac{\delta L}{L}\right)^2 + (\cot\theta \cdot \delta\theta)^2$$

This is implemented in the HRPD, where a long flight path of ∼ 96 m and consequently a relatively long time of flight lead to very high resolutions. The GEM, which has a shorter flight path of ∼ 17 m, offers higher intensities at the cost of poorer resolution.

The detector banks, which cover different angular ranges, measure different, partly overlapping d-spacing ranges. The measurable d-spacing depends, furthermore, on the wavelength or flight path and time, respectively, of the incident neutron. In general, low-angle banks detect high d-spacing ranges and high-angle banks have the best resolution. [156] The HRPD has three detector banks and the GEM eight banks. [181, 182] For the acquisition of data of the different banks, ZnS/^{6}Li scintillators or He gas tubes are used.

2.5.1.3 Automated diffraction tomography

In order to determine crystal structures, an as complete sampling as possible of the reciprocal space is required. While in X-ray and neutron powder diffraction, the 3-dimensional reciprocal space is reduced to 1-dimensional diffraction data leading to the superposition of intensities, electron diffraction allows for the collection of 3-dimensional data sets. Moreover, the use of electron radiation enables the investigation of small crystals in the nanometre range

regardless of other phases potentially surrounding the considered particle. Traditionally, high-resolution electron microscopy (HRTEM) was used for the characterisation of nano-sized particles. However, this method usually requires strong illumination and thus large electron doses, which could cause modifications of the crystal structure or amorphisation due to beam damage. Electron diffraction offers a possibility to obtain high-resolution crystallographic data using significantly lower radiation levels. Conventionally, electron diffraction is based on the acquisition 2-dimensional in-zone electron diffraction patterns of oriented crystals, where several patterns including prominently oriented zones are collected by tilting of the crystal around special crystallographic axes. This method involves several problems: i) a perfect alignment of a zone is not possible and, therefore, it is not assured that intensities originate from a cut through the centre of the reflection, ii) high electron dose and possible beam damage due to long exposures while orienting, iii) dynamic effects are strongly enhanced for in-zone patterns, and iv) a large number of high indexed reflections of the sampled reciprocal space is not measured reducing the total number of measured reflections. [184] To overcome these problems, automated diffraction tomography (ADT) was developed. The collection of ADT data is based on a complete scan of the reciprocal space within the tilt range of the goniometer by tilting a crystal around an arbitrary axis in fixed tilt steps of 1°. This leads to the collection of more reflections including those of off-zone data, which lowers dynamical effects, and to the considerably higher coverage of reciprocal space as well as to shorter exposure times. Precession of the beam during diffraction pattern acquisitions also reduces the dynamical effects even more and integrates reflections hardware-wise. [185, 186] The differences in data acquisition geometry of conventional electron diffraction and ADT are shown in Figure 2-20. Due to the limited tilting range of the goniometer, the border of the grid, the holder or other crystals, there is still a part of the reciprocal space, the so-called missing cone that cannot be measured. This missing cone reduces the completeness, which corresponds to the percentage of independent reflections present in the dataset, depending on the crystal system, e.g. to 60 % for the triclinic system, 70-90 % for the monoclinic system and 90 % for the orthorhombic system. A charged-coupled device (CCD) camera and a specific module for a fast version of ADT can be used for data acquisition. [187] The collected 2-dimensional tilt series is used to reconstruct the 3-dimensional reciprocal space using the eADT software [188], which also determines cell vectors. Detailed crystal structure analysis from the recorded intensities is possible subsequently. [184, 186, 188-190]

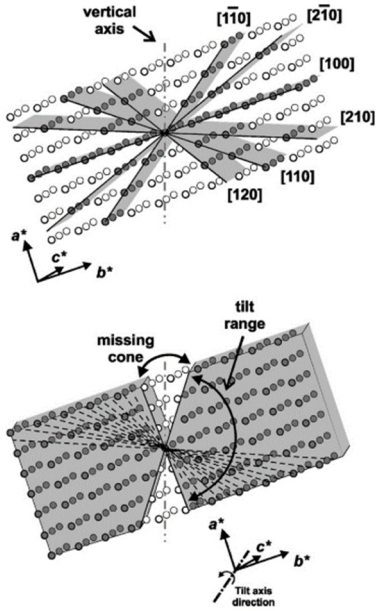

Figure 2-20: Data acquisition geometry of conventional electron diffraction (top) and ADT method (bottom). In conventional electron diffraction, only reflections of low index oriented zones (grey planes) in a tilt around c* are measured. In ADT, non-oriented patterns in a tilt with fixed steps of 1° around an arbitrary axis are measured. The filled spheres refer to measured reflections and the empty spheres to missing reflections in the reciprocal space. The figure has been reprinted with permission from reference 191. Copyright © 2013, Elsevier.

2.5.2 Magnetometric measurements

Magnetometric measurements can be conducted using a superconducting quantum interference device (SQUID). SQUIDs are the most sensitive devices available for the detection of the magnetic flux. Variations of the magnetic flux due to changes of external magnetic fields when periodically moving a sample through a superconducting input coil, which is inductively coupled to the SQUID sensor, are measured and translate into detectable voltage signals. The working principle is based on the phenomena of flux quantisation and Josephson tunnelling causing a periodic relationship between the voltage and the magnetic flux with a period of one flux quantum.

A DC SQUID sensor consists of a symmetric superconducting loop with two parallel Josephson junctions dividing the loop into two branches. When a constant current I_{bias} is applied to the loop, a supercurrent can only tunnel through the Josephson junctions as long as the critical current I_c of the both junctions is not exceeded, otherwise the junctions become resistive and a voltage is detected (Figure 2-21 left). SQUIDs are operated at a current in the I-V curve of the Josephson junction where the derivative $\frac{\partial V}{\partial \Phi}$ has a maximum and, thus, at a current slightly higher than the critical current I_c. For a DC SQUID with two junctions, the current I_{bias} is chosen to be twice this current ($I_{bias} > 2\ I_c$), which leads to a voltage drop across the junctions in both branch of the SQUID loop. When the sample causes an external flux Φ_{ext} in the detection coil, a current is induced, which compensates the magnetic flux. This current induces via inductively coupling screening currents I_{screen} in the SQUID loop that enhances or reduced the currents through the junctions depending on the direction of the external flux Φ_{ext}. Due to flux quantisation, if the magnetic flux changes by an integer multiple of one flux quantum Φ_0, the screening current I_{screen} is zero. If this is not the case, a screening current is induced with a maximum at $\Phi_0/2$. The screening current I_{screen} is, therefore, periodic with a period of one flux quantum Φ_0. Total currents I_{total} equal to $I_{bias} + I_{screen} > I_c$ for one junction

and $I_{bias} - I_{screen} < I_c$ for the other junction are found. Hence, as the external flux changes, the voltages across the junctions change in a periodical manner with a period of one flux quantum Φ_0 (Figure 2-21 right). [191, 192]

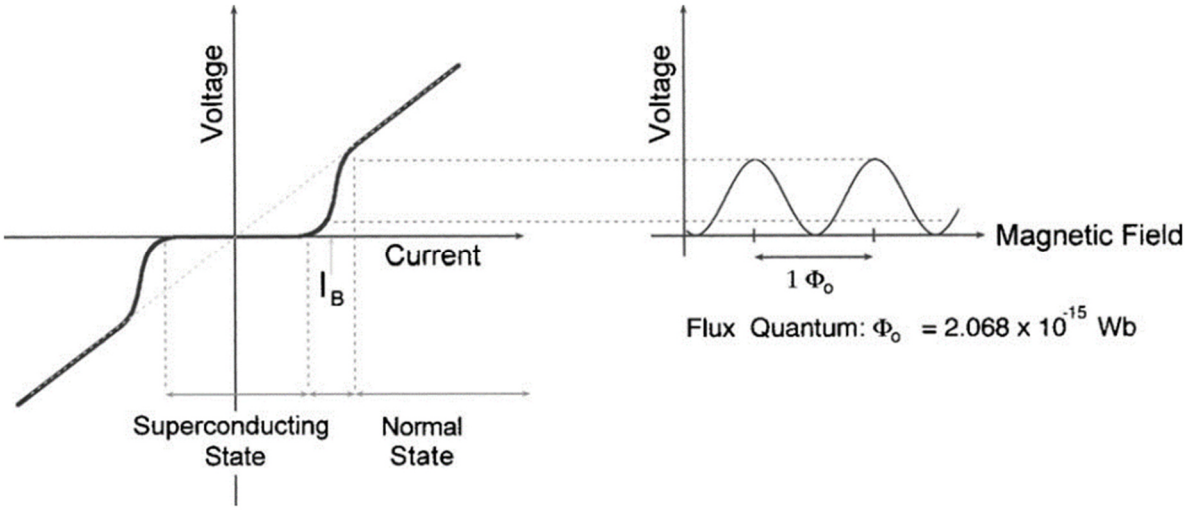

Figure 2-21: Current vs. voltage curve of a Josephson junction. The bias current is also indicated (left); voltage vs. externally applied magnetic field curve at a constant bias current (right). The figure has been reprinted with permission from reference192. Copyright © 2006, AIP Publishing.

2.5.3 X-ray absorption spectroscopy

The element-specific X-ray absorption spectroscopy (XAS) provides information about the chemical state and local atomic structure of selected atomic species. It is based on the absorption of monochromatic X-ray photons of high-intensity, energy-tuneable X-ray radiation usually provided from a synchrotron source by core electrons of the probed atomic species. Measurements can be conducted in transmission or fluorescence geometries. XAS was performed at PETRA III beamlines P64 and P65 at the Deutsches Elektron-Synchrotron (DESY) in Hamburg, Germany. The beamlines cover an X-ray energy range from 4 to 44 keV. [193, 194]

The attenuation of the intensity of X-rays due to absorption when passing through a material is according to the Lambert-Beer law

$$I = I_0 \cdot \exp(-\mu \cdot t).$$

Herein I is the attenuated X-ray intensity, I_0 the incident X-ray intensity and t the thickness of the sample. The absorption coefficient μ, which can be deduced from the intensity ratio, is a function of the energy of incident radiation. Only when the X-ray photon has an energy equal or higher than the binding energy of the core electrons of the atom, absorption takes place, i.e., a photoelectron is created leaving the atom in an excited state due to the photoelectric effect. Under the emission of either non-directional X-ray fluorescence or an Auger electron, the atom returns to its ground state. The sharp rise in adsorption is the adsorption edge. The edge position depends on the binding energy of the absorbing electrons and, thus, changes of the oxidation states and/or coordination chemistry of the atoms can be concluded.

The emitted photoelectron can be scattered from electrons of neighbouring atoms resulting in a backscattering to the absorbing atom. This backscattering of the photoelectron influences, however, the absorption of the next X-ray photon, since they partially interfere destructively leading to oscillations in the absorption coefficient. This fine-structure allows deducing the

type, number and distance of neighbouring atoms. The obtained spectra are divided into an X-ray absorption near-edge spectroscopy (XANES) region, typically within 30 eV of the absorption edge, and an extended X-ray absorption spectroscopy (EXAFS) region. XANES provides information about local symmetry, oxidation states and orbital occupancy; EXAFS examines the local structure including bond distances to neighbouring atoms, coordination numbers and determination of atom species. The detection of the intensity of the incident X-ray radiation and of the transmitted intensity in transmission geometry is conducted using ionisation chambers. For the detection in fluorescence mode, the semiconductor-based detectors are used.

The oscillations can be modelled according to the EXAFS equation

$$\chi(k) = \sum_j S_0 \cdot \frac{N_j}{k \cdot r_j^2} \cdot F_j(k) \cdot \exp(-2\sigma_j^2 k^2) \cdot \exp(\frac{2r}{\lambda(k)}) \cdot sin\left[2kr_j + \varphi_{ij}(k)\right]$$

where F_j and φ_j are the element-specific backscattering amplitude and phase shift of neighbouring atoms of kind j, respectively. N_j is the number of neighbouring atoms of kind j, r_j the distance to neighbouring atoms of kind j and σ^2 is the disorder in the neighbour distance. The amplitude reduction factor S_0 and the mean-free-path λ account for inelastic effects. [195-197]

The analysis of the data is carried out via the following steps:

i) Conversion of measured intensities to μ(E).

ii) Subtraction of a smooth pre-edge function from μ(E).

iii) Identification the adsorption edge energy E_0 and approximation of the increase of the absorption coefficient $\Delta\mu_0$ at E_0.

iv) Subtraction of a smooth post-edge background function μ_0(E) to approximate the absorption of an isolated atom from μ(E) and normalisation of μ(E) by $\Delta\mu_0$ according to obtain EXAFS fine-structure function χ(E):

$$\chi(E) = \frac{\mu(E) - \mu_0(E)}{\Delta\mu_0}.$$

v) Isolate χ(k), where the photon energy is converted to the wave number k given by

$$k = \sqrt{\frac{2m(E-E_0)}{\hbar^2}}.$$

vi) k-weight χ(k) and Fourier transform into R space.

2.5.4 X-ray photoelectron spectroscopy

With the surface-sensitive X-ray photoelectron spectroscopy (XPS), surface compositions and oxidation states can be investigated. It is based on the photoelectric effect. Monochromatic X-ray radiation with a characteristic energy (e.g. Al Kα with a wavelength of 8.36 Å corresponding to an energy of ~ 1.48 keV) interacts with the valence or core electrons of a sample by causing the ejection of photoelectrons due to the energy transfer of E_{photon} from the involved photon to the core electron. If the photon energy is equal or higher than the binding energy E_B, the electron can escape the sample and its kinetic energy E_{kin} is measured. The measured kinetic energy is a function of the binding energy, which is specific for the element and the atomic energy level from which the electron is emitted. If only elastic interactions take place, the relationship between the involved energy contributions including the

spectrometer specific work function W, which is a known constant, but has to be overcome as well, is given by

$$E_B = E_{photon} - E_{kin} - W.$$

The de-excitation of the excited state that follows the emission of the photoelectron can involve X-ray fluorescence or the ejection of an Auger electron. Auger electron emission is also observed in the measured spectra.

Spectra are usually given as counts per second versus the binding energy. Concentric hemispherical analysers (CHA) are used to focus emitted electrons. It consists of two concentric hemispheres with different applied negative potentials. By variation of the potentials, only electrons with a certain energy can pass the analyser since they are differently strong deflected depending on their kinetic energy. Slightly longer or shorter paths through the analyser can compensate small energy differences in a way that the electrons can also reach the detectors. Multi-channel electron multipliers collect the electrons of different energies, multiply them and convert them in a recordable signal.

The surface sensitivity of XPS originates from the limited mean free path of an electron before it loses a fraction of its kinetic energy in an inelastic collision. This leads to a maximum escape depth of $\sim$ 10 nm, from which discrete signals can be detected. If inelastic interactions take place, the signal contributes to the background. All elements from lithium to uranium can be detected. Hydrogen and helium are not detectable due to their small photoelectron cross section. [198]

2.5.5 Scanning electron microscopy

To investigate the morphology of samples, scanning electron microscopy can be used. The sample is scanned by a beam of focussed electrons. For imaging, low-energy secondary electrons are detected. They are formed due to inelastic interactions between the primary electron beam and the electrons of a sample. Due to their low energies and small mean free paths, secondary electrons only close to the surface are emitted. Consequently, very high resolutions can be obtained.

The detection of the secondary electrons is achieved using an Everhart-Thornley detector. The electrons are collected by attracting them to a cage with metal grid with an applied positive voltage. Further acceleration towards a metal-coated scintillator is achieved using higher potentials. The energy of the electrons is high enough to cause emission of photons by ionisation. The radiation is conducted to a photomultiplier, where photoelectrons are emitted from a photocathode and multiplied over a system of diodes. [199]

3 Experimental

This chapter describes the experimental procedures used to synthesise and characterise the RP-type compounds obtained within this work using different topochemical fluorination and defluorination methods.

3.1 Synthesis

3.1.1 Synthesis of precursor oxides and oxyfluorides

3.1.1.1 Solid-state synthesis

The synthesis of the RP-type precursor oxides with n = 1 and 2 was performed using solid-state reactions between suitable high-purity precursors. Stoichiometric amounts of the precursors were thoroughly mixed, heated to the respective calcination or sintering temperatures and hold for a certain duration in air. For parts of the precursor oxides, a pre-drying step was carried out. Between each heat treatment, a regrinding with mortar and pestle for 30 min was performed. For the sintering of $La_{1.3}Sr_{1.7}Mn_2O_7$, the powders were pressed to pellets. Details about the synthesis procedures are summarised in Table 3-1.

Table 3-1: Details about used precursors and applied mixing and heating procedures for the solid-state synthesis of RP-type oxides. Additionally, remarks about pre-drying steps of the precursors and pelletizing are given.

	Precursor	Mixing procedure	Heating procedure	Remarks
Sr_2TiO_4	$SrCO_3$ (≥ 98%, Sigma-Aldrich) TiO_2 (nanopowder, ≥ 99.7%, anatase, Sigma-Aldrich)	Ball milling at 250 RPM for 30 min	2x 1200 °C for 14 h with intermediate regrinding	
$Sr_3Ti_2O_7$	$SrCO_3$ (≥ 98%, Sigma-Aldrich) TiO_2 (nanopowder, ≥ 99.7%, anatase, Sigma-Aldrich)	Ball milling at 300 RPM for 1 h	2x 1250 °C for 24 h with intermediate regrinding	
La_2NiO_{4+d}	La_2O_3 (99.9%, Alfa Aesar) NiO (99%, Alfa Aesar)	Ball milling at 250 RPM for 30 min	2x 1200 °C for 12 h with intermediate regrinding	La_2O_3 and NiO were pre-dried at 700 °C for 4 h
$La_{1.3}Sr_{1.7}Mn_2O_7$	La_2O_3 (99.9%, Alfa Aesar) $SrCO_3$ (≥ 98%, Sigma-Aldrich) Mn_2O_3 (99%, Sigma-Aldrich)	Mortar and pestle for 30 min	800 °C for 12 h (calcination) and 3x 1350 °C for 24 h (sintering) with intermediate regrinding	La_2O_3 was pre-dried at 700 °C for 4 h After the calcination step, the powder was pelletised for the sintering steps

3.1.1.2 Topochemical fluorination using polyvinylidene fluoride

The obtained precursor oxides were mixed with the fluorination agent polyvinylidene fluoride $(CH_2CF_2)_n$ (PVDF, Sigma Aldrich) using mortar and pestle and heated to 370 °C for 24 h in air.

An excess of 2.5 to 5 % of PVDF was used. During heating up, a slow heating rate of 10 °C per h was applied for the temperature range between 250 and 370 °C.

3.1.2 Topochemical defluorination using sodium hydride

The chemical reductions were performed using sodium hydride (NaH, dry, 95 %, Sigma-Aldrich) as reducing agent. The oxides or oxyfluorides were intimately ground with NaH using mortar and pestle in an Ar-filled glovebox.

The molar ratios of the oxyfluoride and NaH were chosen according to

$$A_2BO_3F_2 + x\ NaH\ (0.25 \leq \mathrm{x} \leq 2.5, \Delta\mathrm{x} = 0.25)\ for\ n = 1$$

and

$$A_3B_2O_5F_4 + x\ NaH\ (0.5 \leq \mathrm{x} \leq 4, \Delta\mathrm{x} = 0.5)\ for\ n = 2.$$

For n =1, values of x > 2 correspond to an excess of NaH. Additionally, the reduction of Sr_2TiO_4 was attempted by mixing the oxide with NaH in a molar ratio of 1:2.

The different mixtures were subsequently placed into corundum crucibles and sealed in stainless steel vacuum-tight reactors equipped with oil bubblers filled with silicon oil to avoid the build-up of overpressure on heating and release of H_2. The closed reactors were taken out of the glovebox and flushed with Ar. Subsequently, they were placed in heating mantles and heated to 300 °C for 48 h. A photograph of a reactor placed in a heating mantle during the reaction is shown in Figure 3-1. The valve between the reactor and the oil bubblers was kept open during the heating treatment to facilitate the gas release. After the reaction, the reactors were flushed again with Ar and transferred into the glovebox, in which they were opened and the samples were removed.

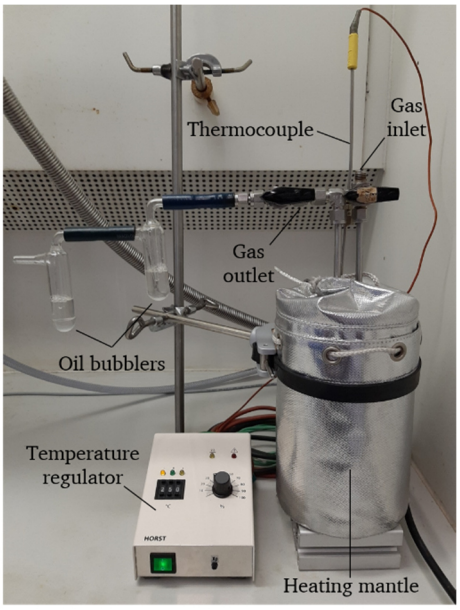

Figure 3-1: Photograph of a reactor used for the hydride-based reduction placed within a heating mantle during the reaction.

To remove the reaction side product sodium fluoride (NaF), washing of selected samples was attempted using 0.25 M NH_4Cl in dried methanol outside the glovebox.

3.1.3 Re-oxidations and re-fluorinations of the reduction reaction products

Selected reduction reaction products were intentionally re-oxidised by heating to 350 °C for 4 h in air.

Re-fluorination experiments were performed using flowing F_2 (10 % in N_2) at temperatures between 50 and 300 °C for durations of 15 min and 60 min. The schematic set-up of the F_2 gas furnace used can be found in Figure 3-2. After each heat treatment, the furnace was immediately purged with N_2.

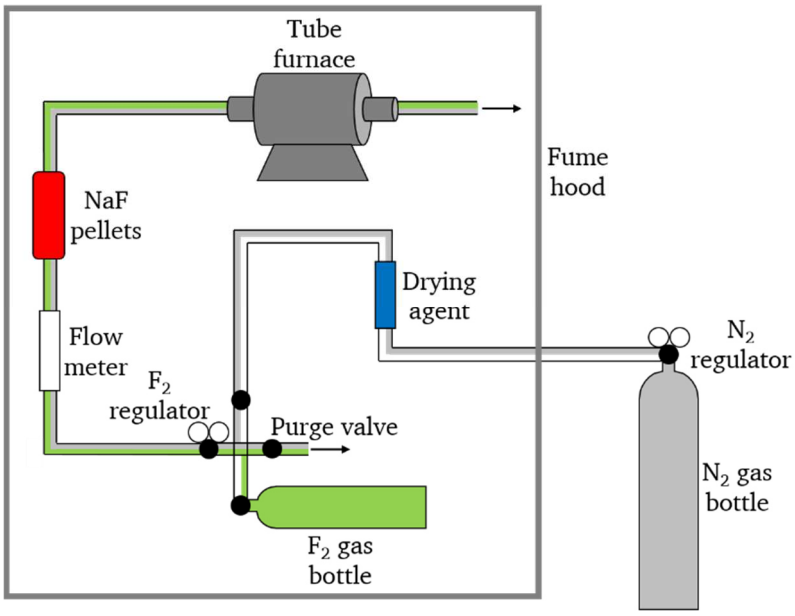

Figure 3-2: Schematic set-up of the F_2 gas furnace used.

3.1.4 Topochemical defluorination and fluorination via electrochemical reactions in fluoride-ion batteries

In the following subchapter, the experimental steps for the synthesis of topochemically modified oxides and oxyfluorides using the set-up of fluoride-ion batteries are presented.

3.1.4.1 Electrolyte and electrode material preparation

The preparation of the electrolyte and electrode composites containing intercalation-based RP-type oxides and oxyfluorides as active material was performed using ball milling. The respective educts were weighed and filled into a ZrO_2 grinding jar with ZrO_2 balls in an Ar-filled glovebox. The jar was sealed before taking it out of the glovebox in order to avoid direct contact to air.

For the electrolyte $La_{0.9}Ba_{0.1}F_{2.9}$, stoichiometric ratios of LaF_3 (99.9 %, STREM Chemicals) and BaF_2 (99 %, STREM Chemicals) were milled for 12 h at 600 RPM. LaF_3 and BaF_2 were dried prior to their use by heating them to 700 °C under Ar.

For the preparation of the electrode composites, 30 wt% of the RP-type oxides or oxyfluorides were milled with 60 wt% of $La_{0.9}Ba_{0.1}F_{2.9}$ and 10 wt% of dried carbon black (CB) (99.9+ %, abcr) for 1 h at 250 RPM. A mixture of thoroughly mixed $La_{0.9}Ba_{0.1}F_{2.9}$ and carbon black was prepared beforehand by milling for 3 h at 250 RPM. This mixture was also used as electrode composite for experiments without other active materials.

The electrode material containing $La_2NiO_3F_2$ as active material was used as anode or cathode depending on the conducted experiment. The titanium-containing oxyfluorides were investigated only in terms of their potential use as active anode materials. $La_{1.3}Sr_{1.7}Mn_2O_7$ was used as active cathode material. The terminology of anode or cathode is based on the role of the active material within the composite during discharge. The anode served always as reference electrode. Specific capacities were calculated with respect to the weight of the active material of the RP-type electrode composite.

As the counter electrode, a conversion-based electrode was used consisting of a metal M (M = Pb or Zn), a metal fluoride MF_2 (M =Pb or Zn) and CB. For the synthesis of the Pb/PbF_2 composite, 45 wt% Pb (≥99 %, Sigma Aldrich), 45 wt% PbF_2 (99+ %, STREM chemicals) were milled for 12 h at 600 RPM. The Zn/ZnF_2 composite was prepared using the same milling procedure using 20 wt% Zn (98 %, abcr), 20 wt% ZnF_2 (99 %, abcr) 50 wt% $La_{9.9}Ba_{0.1}F_{2.9}$ and 10 wt% dried CB. $La_{0.9}Ba_{0.1}F_{2.9}$ was used to increase the ionic conductivity within the composite. The counter electrode was always used in excess.

3.1.4.2 Cell preparation and electrochemical reduction and oxidation

For the cell preparation, pellets consisting of the anode composite, electrolyte and cathode composite were pressed using a hydraulic press from Specac with 2 t for 90 s in an Ar-filled glovebox. 5 mg of the electrode composite were used. Within this composite, 1.5 mg of the active material and 3.5 mg of $La_{0.9}Ba_{0.1}F_{2.9}$ and carbon black, which ensure sufficient ionic and electronic conductivity, are contained. For experiments on the $La_{0.9}Ba_{0.1}F_{2.9}$ and carbon black only, i.e., where no active material was present, 3.5 mg of the $La_{0.9}Ba_{0.1}F_{2.9}$ and carbon black mixture were used. 8 mg of the M/MF_2 composite corresponding to an excess were used. Specific capacities were calculated in relation to the amount of active material used in the composite.

The pellets were spring-loaded into a modified Swagelok-type cell with stainless steel current collectors (Figure 3-3). The cells were heated to 170 °C to achieve sufficient ionic conductivity of the electrolyte.

Electrochemical measurements were performed with a BioLogic Science Instruments VSP or SP-150 potentiostat. For galvanostatic charging and discharging causing electrochemical reduction and oxidation, constant currents corresponding to a C/25 rate were applied. For cells with the $La_{1.3}Sr_{1.7}Mn_2O_7$ cathode composite, a constant current corresponding to a C/20 rate were used. Cell cycling was performed between suitable cut-off capacities or voltages. Cyclic voltammetry was carried out at a scan rate of 0.01 mVs^{-1} between 3 and 0 V starting from the open cell voltage (OCV).

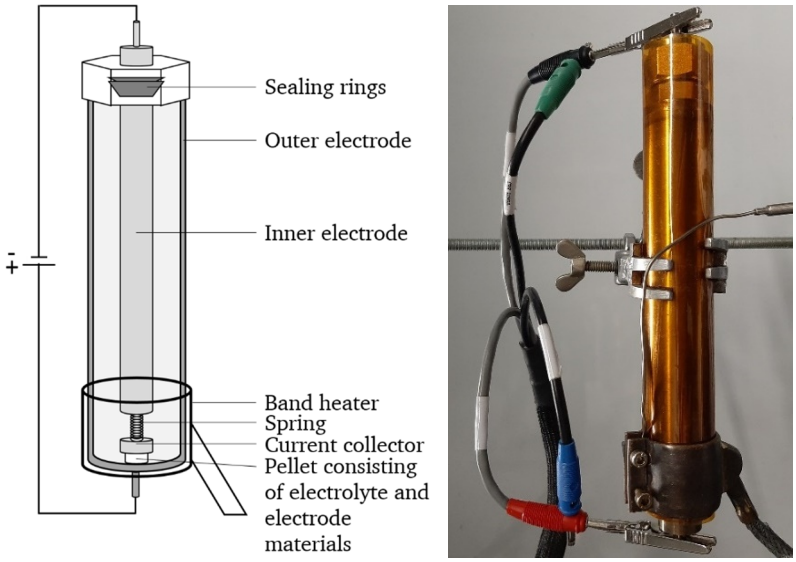

Figure 3-3: Schematic set-up (left) and a photograph (right) of a fluoride-ion battery.

3.2 Characterisation

3.2.1 X-ray and neutron diffraction experiments

X-ray diffraction (XRD) patterns were recorded on a Bruker D8 Advance in Bragg-Brentano geometry with Cu K_α radiation and a VANTEC detector. For phase quantification, samples were measured in the 2θ range between 20° and 70° using a fixed divergence slit for ~ 2 to 4 h. The high-quality data for the Rietveld refinements were recorded in the angular range of 20 to 130° using a variable divergence slit of 6 mm with measurement times of ~ 15 to 17.5 h. All air-sensitive samples were measured inside low background airtight specimen holders (Bruker A100B36/B37), which were sealed inside an Ar-filled glovebox.

High-temperature XRD patterns were recorded on the same setup equipped with an Anton Paar HTK 1200N high-temperature chamber in the angular range between 20° and 47° using a fixed divergence slit with a measurement time of ~ 0.5 h.

Time-of-flight (TOF) neutron powder diffraction (NPD) data [200] were recorded on the high-resolution powder diffractometer (HRPD) [181] and the general materials diffractometer (GEM) [182, 183] at the ISIS pulsed spallation source (Rutherford Appleton Laboratory, UK). For the measurement, ~ 1.5 g of the oxyfluorides or reduction products were loaded into 6 mm diameter thin-walled, air-tight sealed cylindrical vanadium sample cans. Depending on the sample, either only room-temperature data or additionally low-temperature data at 100, 55 and 10 K were recorded. The time-of-flight data were normalised to the incident spectrum and corrected for detector efficiency by reference to a V:Nb standard using the Mantid suite of diffraction utilities. [201]

Analysis of diffraction data was performed via the Rietveld method with the program TOPAS V. 5.0 [162, 163] using the whole XRD data 2θ range as well as the data recorded on all diffraction banks of the TOF neutron powder diffractometer. The instrumental intensity distribution of the XRD and NPD instruments were determined empirically from a sort of fundamental parameters set [176] using a reference scan of LaB_6 (NIST 660a) and silicon (NIST SRM640c), respectively. Microstructural parameters (e.g. crystallite size and strain broadening) were refined to adjust the peak shapes. If anisotropic line broadening was found, the peak shapes of the XRD and neutron data were additionally fitted with the aid of a Stephen's model and

spherical harmonics. [173, 174] Thermal displacement parameters were constrained to be the same for all atoms of all phases to minimise quantification errors and correlation with occupancy parameters. Note that quantification errors are of the order of 1-2 wt-% at least for the phase quantities given in the article; numerical errors obtained from the refinement are known for not representing a reasonable interval of trust, and so error bars of the numerical errors are omitted for the graphical representations of phase quantities.

For the determination of the magnetic structure of $La_2NiO_3F_2$ and its reduced phases, the magnitude and the orientation of magnetic moments, refinements were performed on GEM bank 3 data only.

For the determination of amorphous phase contents in the reduction reaction products, the samples were mixed in a defined weight ratio with the standard LaB_6 (Sigma-Aldrich, 99 %) and XRD patterns were recorded. The calculation of the respective amorphous fraction was performed using the internal standard method as implemented in TOPAS V. 5.0.

3.2.2 Transmission electron microscopy characterisation

Samples for the transmission electron microscopy characterisation were prepared by placing a drop of a dispersion of the respective powder in n-hexane on a carbon coated copper grid. A FEI Tecnai F30 S-TWIN transmission electron microscope (TEM) equipped with a field emission gun and operated at 300 kV was used. For fast and automated diffraction tomography (Fast-ADT) experiments [189]; a 10-μm condenser aperture, spot size 6 and gun lens 8 were set to produce a quasi-parallel beam of 200-nm in size. For the identification of Ni-containing particles, energy dispersive X-ray (EDX) spectroscopy measurements were conducted with a 50-μm condenser aperture, spot size 6 and gun lens 1 to increase the electron dose and have a reliable amount of counts on the EDX detector (EDAX EDAM III). STEM images were collected using a Fischione high-angle annular dark field (HAADF) detector. Electron diffraction patterns were acquired with an UltraScan4000 CCD camera provided by Gatan (16-bit, 4096 x 4096 pixels). Hardware binning 2 and exposure time of 1 seconds were used to acquire non-saturated diffraction reflections. Fast-ADT datasets were acquired with an automated acquisition module developed for FEI and JEOL microscopes, which allows the acquisition of electron diffraction tomographies in around 10 minutes for conventional CCD cameras and fixed tilt step of 1°. Precession electron diffraction (PED) [185] was coupled to the Fast-ADT data collection to minimise the dynamical effects and improve the reflection intensity integration quality. [202] PED was generated by means of the DigiStar system developed by NanoMegas SPRL and it was kept to 1°.

Three-dimensional processing of the Fast-ADT data was done by the eADT software package. [184] Sir2014 [203] was used for ab initio structure solution and Jana2006 [204] was later used for crystal structure refinement. Intensity extraction for dynamical refinement was done by PETS2 [205]. EDX peak identification was carried out by the ES Vision software.

Transition electron microscopy measurements and the analysis of the obtained data were performed in collaboration with Prof. Ute Kolb, Dr. Galina Matveeva and Sergi Plana-Ruiz (Technical University of Darmstadt and Johannes Gutenberg-Universität Mainz).

3.2.3 Elemental analysis

For the determination of the hydride content in the oxyfluorides and reduction reaction products, elemental analysis was performed on an Elementar VarioEL III CHN instrument. The

samples were burned in Sn boats under oxygen and the evolving gases were gas chromatographically separated and analysed quantitatively with a thermal conductivity detector. The hydrogen content was determined as the mean of four measurements.

3.2.4 Scanning electron microscopy

The scanning electron microscopy (SEM) images were recorded using the secondary electron detector of a Philips XL30 FEG scanning electron microscope operating at voltages between 10 and 15 keV. Prior to the measurements, a ~ 10 nm-thick layer of Au was sputtered onto the samples.

3.2.5 Magnetometric measurements

Magnetic characterisation was performed with a Quantum Design MPMS instrument. Powder samples were filled into gelatine capsules, which were mounted into straws. Field-cooled (FC) and zero-field-cooled (ZFC) M(T) curves were measured in a temperature range between 5 and 300 K with an applied field of $\mu_0 H = 1$ T. The measurements were corrected by the diamagnetic contributions of the phases that are present in the phase mixtures as well as by the contribution stemming from the gelatine capsule and straw used for sample mounting. [206] If not otherwise mentioned, no deviations between the FC and ZFC measurements were observed and only one of the measurements are shown. Field-dependent M(H) measurements were performed at different temperatures between 3 and -3 T for $La_2NiO_3F_2$ and 5 and -5 T for the reduced Ni-containing reduction products.

Magnetometric measurements were performed in collaboration with Supratik Dasgupta, Dr. Sami Vasala (Technical University of Darmstadt) and Dr. Ralph Witte (Karlsruhe Institute of Technology).

3.2.6 X-ray absorption spectroscopy

X-ray absorption experiments (XAS) were carried out at PETRA III beamlines P65 and P64 at Deutsches Elektronen-Synchrotron (DESY) in Hamburg, Germany [193, 194]. The measurements at the Ti K-edge (4966 eV) and the Ni K-edge (8333 eV) were performed using a Si(111) double-crystal monochromator and a maximum synchrotron beam current of 100 mA. Spectra of the Ti containing samples were recorded in transmission mode and on solid samples diluted with boron nitride. Due to the low Ni concentration, the spectra of the Ni containing samples were recorded in fluorescence mode. For energy calibration, a Ti and Ni foil, respectively, were measured before and after the sample measurement to account for possible energy shifts due to monochromator movements. The energy shifts were detected at the edge energies, which were determined by the maxima in the spectrum derivations, as well as in the energies of the pre-peaks. The complete handling of the samples, i.e., the preparation and measurement, was carried out under inert atmosphere.

While for the Ti containing samples sufficient amounts of powders were prepared via topochemical reduction using NaH, the electrochemical reduction allows only the synthesis of very small sample amounts. Therefore, 8 cells Pb/PbF_2 vs. $La_2NiO_3F_2$ were prepared by charging to 75 $mAhg^{-1}$ and the electrode sides containing the Ni phases were scratched off the pellets.

XAS measurements and the analysis of the obtained data were performed in collaboration with Dr. Roland Schoch and Prof. Dr. Matthias Bauer (Universität Paderborn).

3.2.7 X-ray photoelectron spectroscopy

The surface oxidation states were examined by XPS analysis using a Physical Electronic VersaProbe XPS unit (PHI 5000 spectrometer) with Al Kα radiation. All detailed spectra were recorded with a step size of 0.1 eV, a pass energy of 23.5 eV and a spot size of 200 x 200 μm. To confirm the calibration of the instrument, gold (Au $4f_{7/2}$ emission line at 84.0 eV) and silver (Ag $3d_{5/2}$ emission line at 368.3 eV) were measured as reference materials beforehand. A neutraliser was used for the compensation of surface charging.

Samples were transferred from an Ar-filled glovebox to the ultrahigh-vacuum system of the spectrometer in an Ar atmosphere using a sealed transfer chamber capable of in-vacuo transportation to minimise surface oxidation processes.

Depending on the sample, the binding energies were calibrated to one of the following absorption lines: carbon 1*s* (C 1*s*) emission line 284.8 eV, the sodium 1*s* (Na 1*s*) line at 1071.1 eV or to the fluorine 1*s* (F 1*s*) emission line at 686.1 eV. [207] To determine the integral intensity and the exact binding energies of the emission lines, the spectra were background-corrected according to Shirley.[208]

Magnetometric measurements were performed in collaboration with Dr. Alexander Benes, Manuel Donzelli and Tobias Vogel (Technical University of Darmstadt).

3.2.8 Titration

Average oxidation states were determined by iodometric titrations. Samples of ~50 mg were dissolved in 1 M HCl containing an excess of KI. Starch solution was added as an indicator. The titration was performed using a standardised $Na_2S_2O_3$ solution with a concentration of 0.01 mol/L. The average oxidation state was determined from three measurements.

Titration experiments were performed in collaboration with Aamir I. Waidha.

3.2.9 DFT+U calculations

Quantum mechanical calculations were performed using the projector-augmented wave (PAW) [209, 210] method for pseudopotenial and plane wave functions as implemented in the Vienna ab-initio simulation package (VASP) [211, 212]. To account for exchange and correlation, the Perdew-Burke-Ernzerhof (PBE) functional of a generalised gradient approximation (GGA) [213, 214] was used. To account for the strong localisation of the electrons of the *d* orbitals, a +U correction [215-217] was applied. The difference of the U and J parameters known as U_{eff} bears importance for the utilised + U model. In accordance with previous studies, the U_{eff} was chosen to be 2 eV [218] for the titanium compounds and 5 eV [219, 220] and 6 eV [109, 221] for the Ni compounds containing Ni^{2+} and low-valent Ni, respectively. Energy cut-offs of the plane wave basis sets of 500 eV for the Ti and Ni^{2+} compounds and 600 eV for the reduced Ni compounds were used. The reciprocal space was sampled in relation to the cells given later in this thesis by a Monkhorst-Pack-type [222] Γ-centred k-mesh $n_1 \times n_2 \times n_3$ of 8 × 8 × 4 for the Ti compounds, of 4 × 8 × 8 for the Ni^{2+} compounds and 2 × 4 × 5 for the reduced Ni compounds. Electronic self-consistency was considered to be reached when total energies varied by less than $1 \cdot 10^{-6}$ eV. Full structure optimisations were performed until forces converged to 0.001 eV/Å for the Ti and Ni^{2+} compounds and 0.01 eV/Å for the reduced Ni compounds.

DFT+U calculations were performed in collaboration with Prof. Dr. Oliver Clemens, Ali Muhammad Malik and Dr. Jochen Rohrer (Technical University of Darmstadt).

4 Results and Discussion

In this part, the scientific findings made within the scope of this thesis in the context of crystal structure and property changes of RP-type compounds due to chemical and electrochemical topochemical modification approaches are summarised and discussed. The chapter is divided into two subchapters.

In the first subchapter, the influence of consecutive *chemical fluorination and defluorination reactions based on reactions involving solid-state and gaseous reagents* are investigated. The following compounds are examined: the n = 1 RP-type compound Sr_2TiO_4, the n = 2 RP-type compound $Sr_3Ti_2O_7$ and the n =1 RP-type compound La_2NiO_{4+d}. Sr_2TiO_4 or rather $Sr_2TiO_3F_2$ were selected as starting point for the *development of a novel low-temperature reductive defluorination process* using a solid-state reduction reagent, since the crystal structure of the fluorinated compound has been already known. [71] The effect of stepwise increasing the amount of reducing agent on the reductive behaviour of the oxyfluoride is examined. Subsequently, the impact of the higher order of the n = 2 member of the RP strontium titanate homologous series as well as the choice of Ni as transition metal cation on the fluorination and defluorination behaviour are studied. As discussed previously (see section 2.2.3), in terms of electrode materials of FIBs, the RP-type oxyfluoride obtained after a non-oxidative fluorination represent the discharged state of the active material within an intercalation-based anode composite, while the defluorinated phase can be considered as the charged state. Therefore, the development of a defluorination process, enabling the *synthesis of the charged state of an anode material via topochemical reactions ex-situ*, would facilitate the in-depth *analysis of crystal structures as well as properties* of reduced phases. This aids gaining a deeper understanding, which is required for the development of such battery systems. In contrary to a reductive defluorination method, oxidative synthesis routes for the preparation of the charged state of intercalation-based RP-type cathode materials, for which the RP-type oxide and fluorinated oxyfluoride represent the discharged and charged states, respectively, are well known (see section 2.2.1).

In the second subchapter, *topochemical modifications based on electrochemical reactions within FIBs* are examined. A first focus is set on the investigation of the potential use of the oxyfluorides obtained after the polymer-based fluorination of Sr_2TiO_4, $Sr_3Ti_2O_7$ and La_2NiO_{4+d} as *intercalation-based active anode materials*. After testing the structural stability of the RP-type compounds in the anode composites under experimental conditions, stable candidates are examined in terms of their defluorination behaviour due to galvanostatic charging. Based on the findings made in the first subchapter, indication for a successful defluorination could be found mainly for the Ni-based compound by comparing structural changes of the phases obtained via both chemical and electrochemical synthesis approaches. Possible limitations with regards to the other compounds are discussed. Furthermore, the structural reversibility of the defluorination reaction upon discharging of the reduced Ni-compound are examined. Moreover, the application of the Ni-containing *oxyfluoride as potential active material in a cathode composite* in terms of structural reversibility of a post-oxidation and its cyclability is investigated. The occurrence of *undesirable side reactions* is addressed in addition.

Having demonstrated that a structural reversibly can be observed upon cycling of FIBs, it is interesting to investigate if the corresponding magnetic property changes, which were for the oxyfluorides mainly examined on the chemically synthesised phases, can be also reversibly switched. This is brought into focus in the second part of the subchapter. With respect to possible technological applications based on *tuning of the magnetisation when reversibly switching between two magnetic states via electrochemical reactions*, strong absolute changes of the magnetisation are desirable. The changes of the reduced oxyfluorides compared to their parent oxyfluorides are, however, found to be relatively small. To ensure a strong magnetisation change, the magnetic properties of a suitable RP-type compound should be highly sensitive to oxidation state changes of the transition metal cation and preferably undergo a change from a ferromagnetic interactions of magnetic moments to a non-ferromagnetic interactions (or vice versa) upon reversible fluoride deintercalation and re-intercalation or fluoride intercalation and re-deintercalation. Additionally, the selected compound should contain a transition metal cation with a high magnetic moment, which is related to the number of unpaired electrons. Since the oxidative fluorination behaviour of RP-type oxides via chemical methods and the resulting effects on magnetic properties have been already extensively studied in literature, the selection of an active RP-type cathode material with respective changes of magnetic properties for a proof-of-principle study seemed reasonable. Additionally, intercalation-based cathodes have shown to be cyclable over extended cycle numbers. [18-20] The reversible tuning is, therefore, demonstrated on the n = 2 RP-type oxide $La_{1.3}Sr_{1.7}Mn_2O_7$, which is ferromagnetic with a high magnetic moment of > 3 μ_B and a high Curie-temperature of ~ 120 K. [223, 224] It can be assumed that the intercalation of fluoride ions into this compounds leads to the formation of antiferromagnetically-ordered or paramagnetic phases with significantly reduced magnetisations. [21, 223, 224]

4.1 Topochemical fluorination and defluorination of Ruddlesden-Popper-type compounds using solid-state or gaseous reagents

The following chapter summarises and discusses the results reported previously in the following publications:

[1] **Wissel, K.**; Dasgupta, S.; Benes, A.; Schoch, R.; Bauer, M.; Witte, R.; Fortes, A. D.; Erdem, E.; Rohrer, J.; Clemens, O., Developing intercalation based anode materials for fluoride-ion batteries: topochemical reduction of $Sr_2TiO_3F_2$ via a hydride based defluorination process. *J. Mater. Chem. A* **2018,** *6* (44), 22013-22026.

[2] **Wissel, K.**; Vogel, T.; Dasgupta, S.; Fortes, A. D.; Slater, P. R.; Clemens, O., Topochemical Fluorination of n = 2 Ruddlesden-Popper Type $Sr_3Ti_2O_7$ to $Sr_3Ti_2O_5F_4$ and Its Reductive Defluorination. *Inorg. Chem.* **2020,** *59* (2), 1153-1163.

[3] **Wissel, K.**; Heldt, J.; Groszewicz, P. B.; Dasgupta, S.; Breitzke, H.; Donzelli, M.; Waidha, A. I.; Fortes, A. D.; Rohrer, J.; Slater, P. R.; Buntkowsky, G.; Clemens, O., Topochemical Fluorination of La_2NiO_{4+d}: Unprecedented Ordering of Oxide and Fluoride Ions in $La_2NiO_3F_2$. *Inorg. Chem.* **2018,** *57* (11), 6549-6560.

[4] **Wissel, K.**; Malik, A. M.; Vasala, S.; Plana-Ruiz, S.; Kolb, U.; Slater, P. R.; da Silva, I.; Alff, L.; Rohrer, J.; Clemens, O., Topochemical reduction of $La_2NiO_3F_2$: the first Ni-based Ruddlesden-Popper n = 1 T'-type structure and the impact of reduction on magnetic ordering. *Chem. Mater.* **2020**, *32* (7), 3160-3179.

In this chapter, a focus is set on the topochemical fluorination of Sr_2TiO_4, $Sr_3Ti_2O_7$ and La_2NiO_{4+d} using a polymer-based fluorination method and their subsequent defluorination via a newly developed metal-hydride-based approach. As reducing agent NaH was chosen as it has been reported to have the strongest reducing powers. [75]

For non-oxidative fluorination reactions of $A_{n+1}B_nO_{3n+1}$, in which one oxide ion is replaced by two fluoride ions via a substitution and intercalation, the formation of oxyfluorides with compositions of $A_{n+1}B_nO_{3n+1-x}F_{2x}$ with $0 < x \leq 2$, depending on the molar ratios of the oxide to the fluorine-containing polymer PVDF $(CH_2CF_2)_n$, takes place. It should be noted that stoichiometric amounts of PVDF refer in the following discussion to molar ratios of 1:1 for n = 1 and 1:2 for n = 2 RP-type compounds.

For the investigation of the topochemical defluorination behaviour of the obtained oxyfluorides, a series of experiments with varying NaH amounts was conducted. Neglecting decomposition and possible fluoride-hydride and fluoride-oxide substitution reactions during the reduction, the reaction equations of the desired reductions of n =1 and 2 RP-type compounds can be formulated as the following

$$A_2BO_3F_2 + x\ NaH \rightarrow A_2BO_3F_{2-x} + x\ NaF + \frac{x}{2}H_2\ (0.25 \leq x \leq 2)\ for\ n = 1$$

and

$$A_3B_2O_5F_4 + x\ NaH \rightarrow A_3B_2O_5F_{4-x} + x\ NaF + \frac{x}{2}H_2\ (0.5 \leq x \leq 4)\ for\ n = 2.$$

Property changes of the obtained reduced phases upon defluorination of the parent oxyfluorides were mainly examined in regards to changes of the magnetic states. Thoroughly, structural characterisation was performed to relate arising property changes to structural modifications.

The findings made in the studies on the different oxides and their respective oxyfluorides are given successively in separate subchapters for each system. For the analysis of the obtained oxyfluorides and their reduced phases various characterisation methods were combined. The combinations differ for the different systems. The underlying reaction mechanisms were studied using techniques such as X-ray and neutron powder diffraction, elemental analysis, magnetic measurements, X-ray absorption and X-ray photoelectron spectroscopy and titration experiments. For the structural analysis of the obtained phases, coupled Rietveld analyses of X-ray and neutron powder diffraction data were used. For the investigation of the magnetic structure, a low-temperature neutron diffraction study was performed. In addition, transition electron microscopy was performed for the confirmation of proposed structural models. Quantum chemical calculations helped further to gain insights into sturctural stabilites, reaction mechanisms, structural rearrangement processes and their impact on the magnetic interactions. After each subchapter, a short conclusion summarising the results is given. A concluding discussion, addressing similarities and differences of the studied systems and possible challenges, is carried out in a final conclusion (see section 5).

4.1.1 Topochemical fluorination of Sr_2TiO_4 to $Sr_2TiO_3F_2$ and its defluorination

4.1.1.1 Topochemical fluorination of Sr_2TiO_4 to $Sr_2TiO_3F_2$

4.1.1.1.1 Coupled Rietveld analysis of $Sr_2TiO_3F_2$

As reported by Slater et al.[71], the non-oxidative topochemical fluorination of Sr_2TiO_4 using PVDF as the fluorinating reagent proceeds via a substitution and intercalation process of fluoride, in which one oxide ion is replaced by two fluoride ions (see also section 2.2.1). The formed $Sr_2TiO_3F_2$ shows a strong expansion along the *c* axis of ~ 23 % (c = 15.509(5) Å) and a smaller expansion along the *a* axis of ~ 2 % (a = 3.8043(6) Å) compared to Sr_2TiO_4 with lattice parameters a = 3.8849(1) Å and c = 12.5946(1) Å (Figure 4-1). The coupled Rietveld refinement of X-ray and neutron powder data (see Figure 6-1 in the appendix) confirms to proposed symmetry lowering from *I4/mmm* to *P4/nmm* due to the presence of several superstructure reflections (e.g. $(016)_{P4/nmm}$ or $(113)_{P4/nmm}$ at d values of ~ 2.13 and 2.39 Å, respectively). The structural parameters as obtained from the refinement are given in Table 6-1. The crystal structure of $Sr_2TiO_3F_2$ is shown in Figure 2-6.

The metastability of $Sr_2TiO_3F_2$, which is linked to a low decomposition temperature, impedes the synthesis of phase pure samples and the formation of ~ 3 wt% of SrF_2 as an impurity phase is observed after the fluorination reaction. This phase remains present in all reduction reaction products. Its phase fraction stays relatively constant within errors in the reduction products.

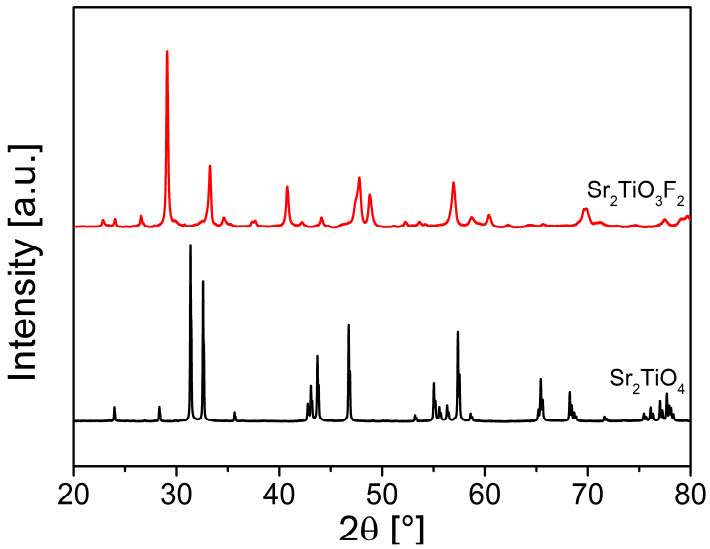

Figure 4-1: X-ray diffraction patterns of Sr_2TiO_4 to $Sr_2TiO_3F_2$.

4.1.1.2 Topochemical defluorination of $Sr_2TiO_3F_2$

4.1.1.2.1 Analysis of the reduction mechanism of $Sr_2TiO_3F_2$

As for the reduction of oxides [11, 12], the reaction temperature is an important factor for the successful reduction of oxyfluorides. Due to the metastability of oxyfluorides, the choice of the reaction temperature is crucial in order to find a compromise between reactivity and decomposition. To establish a suitable temperature for the reduction of $Sr_2TiO_3F_2$, different temperatures between 250 and 350 °C were examined. It was found that too low

temperatures (<280 °C) result in large amounts of unreacted NaH and $Sr_2TiO_3F_2$ due to the kinetic inhibition of the reaction. Higher temperatures, on the other hand, lead to an increased level of decomposition of the metastable oxyfluoride. The reaction temperature of 300 °C can be regarded as an optimised experimental setting for the defluorination reaction and, thus, it was chosen for the study. Remarkable, no considerable reduction of the parent oxide Sr_2TiO_4 is observed using NaH under the same reaction conditions (Figure 6-2), indicating that the introduction of fluoride ions affects the reduction behaviour strongly.

The temperature of 300 °C correlates also with the temperature, above which NaH decomposes to metallic Na and H_2. The thermal decomposition takes place between ~ 300 and 420 °C. [225] Attempts to perform the reduction with metallic sodium were not successful, which is related to the fact that the softness of the metal makes a homogeneous mixing of the metal and the oxyfluoride difficult.

Using the reaction temperature of 300 °C, various defluorination reactions were performed on mixtures with compositions of $Sr_2TiO_3F_2$ + x NaH with $0 \leq x \leq 2.5$ and $\Delta x = 0.25$. A directly visible indicator for a successful reduction of $Sr_2TiO_3F_2$, which results in a lowering of the Ti oxidation state, is given by the black colour of the reaction product (Figure 4-2). While $Sr_2TiO_3F_2$ contains only Ti^{4+}, giving rise to a white colour, compounds with low-valent Ti are known to be black. [79]

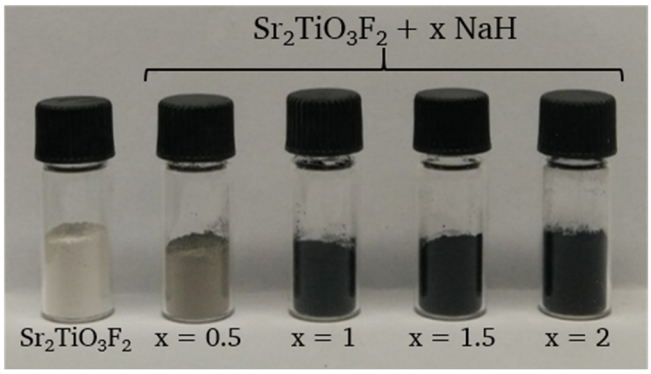

Figure 4-2: Photograph of $Sr_2TiO_3F_2$ and reaction products $Sr_2TiO_3F_2$ + x NaH with x = 0.5, 1, 1.5, 2.

To gain a deeper understanding about the reaction mechanism, X-ray diffraction data of the reduction products were collected (Figure 4-3).

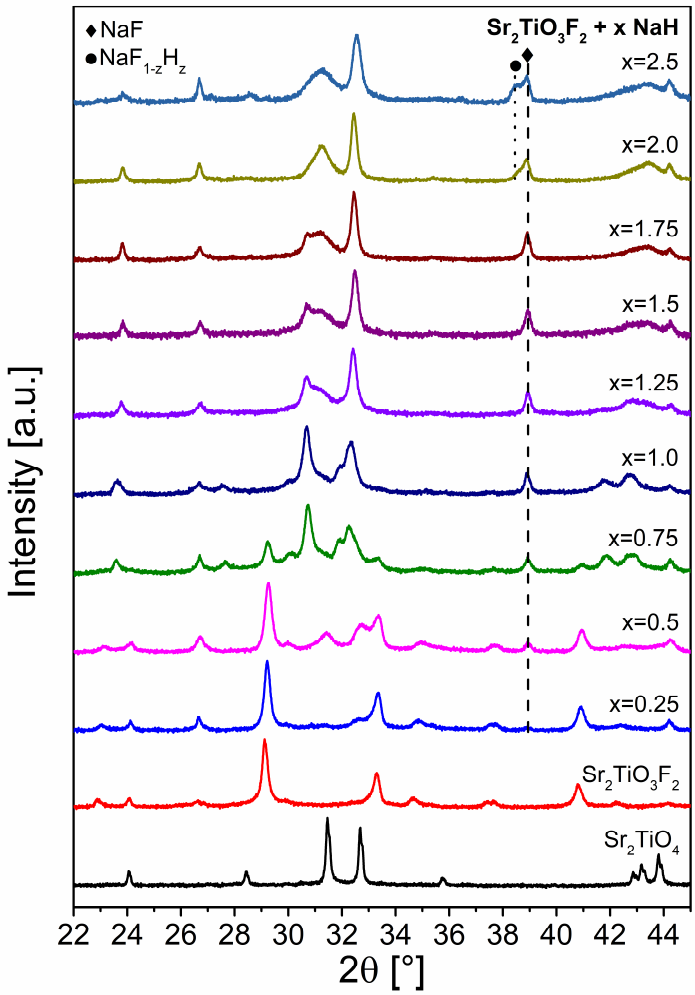

Figure 4-3: X-ray diffraction patterns of Sr_2TiO_4, $Sr_2TiO_3F_2$ and the reduction products $Sr_2TiO_3F_2$ + x NaH with 0.25 ≤ x ≤ 2.5. For the Rietveld refinements of the patterns shown together with an assignment of reflections, the reader is referred to Figure 6-3 in the Appendix.

The data show the formation of various RP-type phases. For x = 1 and 2, nearly single-phase compositions of RP-type phases, besides the reaction side products NaF and $NaF_{1-z}H_z$ (see below), are found. To determine the crystal structures of these RP-type phases, coupled Rietveld refinements of X-ray and neutron powder diffraction data were additionally performed (see section 4.1.1.2.2; the refined patterns are shown in Figure 4-6). All other compositions contain mixtures of multiple phases, including two intermediate phases found at lower NaH contents. Quantitative phase analysis was performed using the Rietveld method. The evolution of the relative phase fraction of the RP-type phases is shown in Figure 4-4 a.

In comparison to $Sr_2TiO_3F_2$, strong shifts of reflections *hkl* with $l \neq 0$ to higher diffraction angles, implying strong decreases of the *c* lattice parameters, can be observed for all reduced RP-type phases. These decreases lead to large unit cell volume changes. Higher amounts of NaH lead to larger volume reductions (Figure 4-4 b). While the *c* axis decreased considerably on reduction, the *ab*-plane undergoes a small expansion due to the formation of low-valent Ti species, which are larger than Ti^{4+} (ionic radii of 6-fold coordinated Ti^{3+}: 0.67 Å and Ti^{4+}: 0.42 Å) [54]. Overall, each phase has a distinctive set of lattice parameters and the unit cell volumes per formula unit stay relatively constant within their range of existence of the respective phase. The reflections *hkl* with $l \neq 0$ show, furthermore, a considerable anisotropic

strain broadening, which is significantly increased for the stronger reduced phase found in the range $1.25 \leq x \leq 2.5$.

After the reactions, NaF, which is formed as side product during the defluorination, is present in all reaction products. Since no other source of fluoride than $Sr_2TiO_3F_2$ is available for the formation of NaF from NaH, the degree of defluorination can be easily verified by comparing the phase fraction of measured NaF with the theoretical amounts of NaF. The latter can be calculated considering that all NaH used in the reaction mixture converts to NaF. For $0 \leq x \leq 2$, the amounts of measured NaF increases continuously and is in good agreement with theoretical amounts (Figure 4-4 c). When using an excess of NaH (x = 2.5), no significant increase of the formed NaF is found. This shows that higher amounts of NaH do not result in further topochemical modifications, which is also related to the fact that no additional fluoride ions are present. In addition, it indicates a negligible degree of decomposition/amorphisation, which is in strong contrast to the reduction of Ni-based oxyfluorides (see 4.1.3.2.1). For $x > 2$, unreacted NaH forms with NaF a mixed crystal $NaF_{1-z}H_z$, which can be identified as a broad shoulder next to all NaF reflections at lower diffraction angles. Assuming a linear relationship between the hydride content of the $NaF_{1-z}H_z$ formed and the lattice parameters of NaF ($a \approx 4.63$ Å [226]) and NaH ($a_{NaH} \approx 4.89$ Å [227]), an estimation of the hydride content of $NaF_{1-z}H_z$ is possible. For x = 2 and 2.5, approximate compositions of the mixed crystals of $NaF_{0.93}H_{0.07}$ and $NaF_{0.34}H_{0.66}$, respectively, can be derived.

Taking the phase fractions and the compositions of the reduced phases contained in the reduction products into account, an approximate value Δ with Δ being the fluoride extracted from $Sr_2TiO_3F_2$ upon reduction can be determine for a specific x (Figure 4-4 d). For the determination of the compositions of the reduced phases, a combination of coupled Rietveld refinements (see section 4.1.1.2.2), magnetic measurements (see section 4.1.1.3) and X-ray absorption (see section 4.1.1.4) and X-ray photoelectron spectroscopy (see section 4.1.1.5) was used. From the obtained values Δ, a nearly stoichiometric extraction of fluoride ions as a function of x can be concluded.

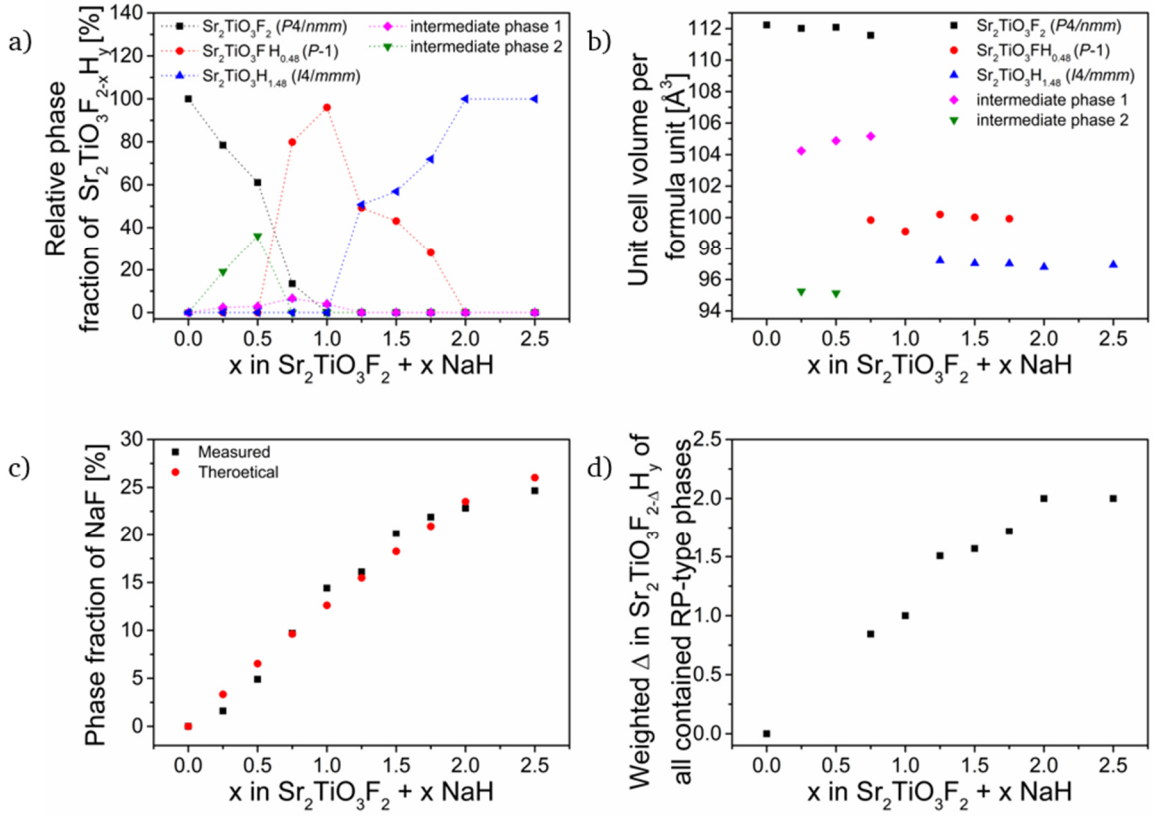

Figure 4-4: Relative phase fractions (a) and unit cell volumes per formula unit (b) of $Sr_2TiO_3F_2$ and the reduced RP-type phases in the reduction product $Sr_2TiO_3F_2$ + x NaH with 0.25 ≤ x ≤ 2.5 as a function of x. The relative phase fractions were calculated neglecting other side and decomposition phases, e.g. NaF or SrF_2. Measured phase fraction of NaF (c) in the reduction products $Sr_2TiO_3F_2$ + x NaH with 0.25 ≤ x ≤ 2.5 as a function of x. Also given are the theoretically expected values of NaF calculated assuming full conversion of the added NaH to NaF. Values of extracted fluoride Δ in $Sr_2TiO_3F_{2-\Delta}H_y$ (d) of all reduced RP-type phases contained in the reduction product $Sr_2TiO_3F_2$ + x NaH with 0.75≤ x ≤ 2.5 as a function of x. The values were calculated using the relative phase fractions and approximate compositions of the reduced phases as derived from the occupation factors determined via coupled Rietveld analyses of the found phases. For x = 0.25 and 0.5 no values are given, since the fluoride content of the intermediate phases is not known.

Elemental analysis of the reaction products with x = 1 and 2 suggests the presence of hydride ions in the reduction products and the formation of phases with formal compositions of $Sr_2TiO_3FH_{0.48(1)}$ + 1 NaF for x = 1 and $Sr_2TiO_3H_{1.48(10)}$ + 2 NaF for x = 2 can be followed. The presence of other (potentially amorphous) hydride-containing phases can be excluded. Additionally, for x = 2, only a minor fraction of the hydride ions is found within the $NaF_{1-z}H_z$ formed. Therefore, the most plausible hosts for the hydride ions are the single-phase RP-type phases obtained for x =1 and 2, which are in the following called $Sr_2TiO_3FH_{0.48}$ and $Sr_2TiO_3H_{1.48}$, respectively. This is, moreover, supported by the fact that substitution or insertion processes involving hydride ions are commonly observed in hydride-based reductions (see section 2.2.2). From this, it can be followed that the reaction mechanism is best described via reductive defluorination and partial fluoride-hydride substitution reactions according to

$$for\ x = 1: Sr_2TiO_3F_2 + NaH \rightarrow Sr_2TiO_3FH_{0.48} + NaF + 0.26H_2$$

and

$$for\ x = 2: Sr_2TiO_3F_2 + 2NaH \rightarrow Sr_2TiO_3H_{1.48} + 2NaF + 0.26H_2.$$

In previous studies [11], it has been reported that side products of deoxygenation reactions such as CaO or Na_2O can be removed by washing with dry methanolic solutions of NH_4Cl, which was also attempted to remove NaF from the reduction products. Even though NaF could be removed successfully, changes of the reflection positions and intensities indicate a (partial) re-oxidation (Figure 6-4). Scanning electron micrographs of $Sr_2TiO_3F_2$ in comparison to the unwashed and washed reaction products with x = 2 (Figure 4-5) indicate, furthermore, that the reaction leads to the formation of a rough surface layer on top of the reduced particles, which can be removed upon washing. This suggests that the layer consists of NaF. Additionally, larger particles show a layer-wise breaking after the washing step, which is in agreement with the strong anisotropic strain broadening observed in the diffraction patterns of the highly defluorinated phase.

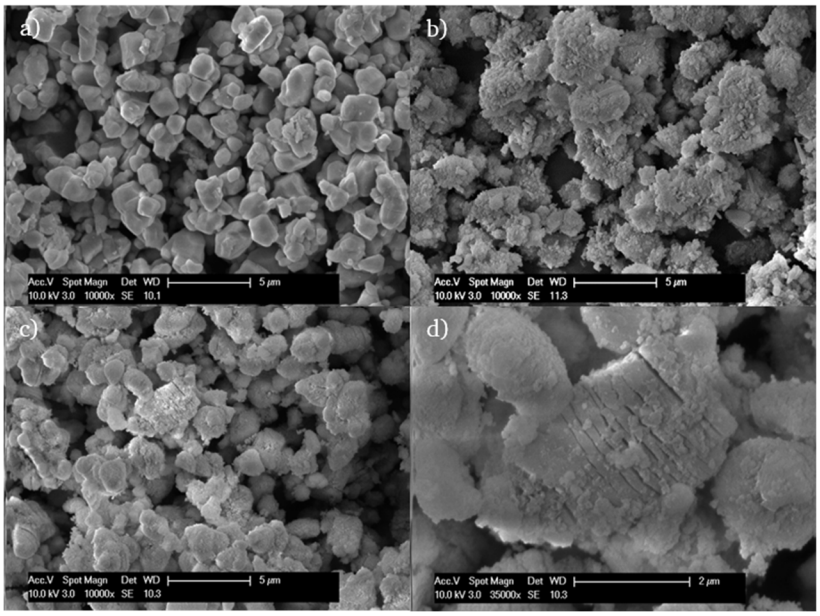

Figure 4-5: Scanning electron micrographs of $Sr_2TiO_3F_2$ (a), the unwashed reaction product of $Sr_2TiO_3F_2$ + x NaH with x =2 with rough porous layer of NaF on top of particles (b) and the washed reaction product of $Sr_2TiO_3F_2$ + x NaH with x =2 showing a layer-like breaking of particles at different magnifications (c and d).

Re-oxidation experiments on the reaction products of $Sr_2TiO_3F_2$ + x NaH with x =1 and 2, further corroborates the proposed reaction mechanism (Figure 6-5). The re-oxidation can be described by the following equations

$$for\ x = 1: Sr_2TiO_3FH_{0.48} + 0.74O_2 \rightarrow Sr_2TiO_3F_2 + Sr_2TiO_4 + 0.48H_2O$$

and

$$for\ x = 2: Sr_2TiO_3H_{1.48} + 1.74O_2 \rightarrow 2Sr_2TiO_4 + 1.48H_2O.$$

4.1.1.2.2 Coupled Rietveld analysis of the reduction products

Structural refinements were performed for the phases $Sr_2TiO_3FH_{0.48}$ and $Sr_2TiO_3H_{1.48}$ on room-temperature X-ray and neutron powder diffraction data of the reduction products of the reaction mixtures $Sr_2TiO_3F_2$ +NaH with x = 1 and 2 via coupled Rietveld analyses. For each composition, only one of these RP-type phases is present in nearly phase-pure product mixtures with side and decomposition products. For both RP-type phases, significant anisotropic broadening of reflections was observed. Therefore, a very detailed structural

analysis including the determination of many structural parameters such as anisotropic displacements parameters has not been possible due to the strong correlations of these parameters. Furthermore, the determined structural models take the findings from the other characterisation methods used within this study into account. The models should be considered as the best approximation of the structures. The Rietveld refinements of $Sr_2TiO_3FH_{0.48}$ and $Sr_2TiO_3H_{1.48}$ are shown in Figure 4-6.

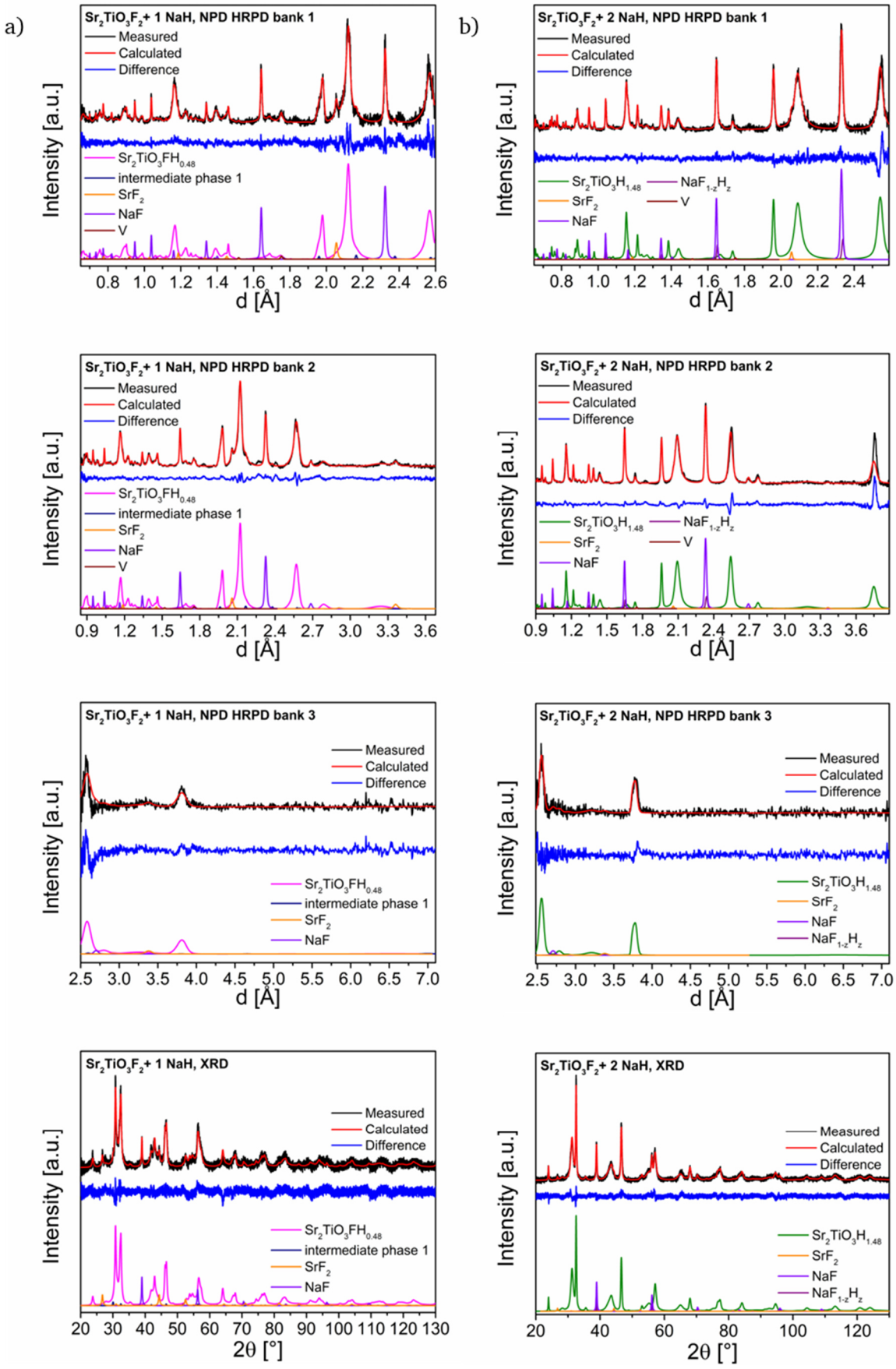

Figure 4-6: Coupled Rietveld refinements of the reduction products of $Sr_2TiO_3F_2$ + x NaH with x = 1 (a) and x = 2 (b) of NPD HRPD banks 1-3 and XRD data.

For the diffraction patterns of the reduction product of $Sr_2TiO_3F_2$ + x NaH with x = 1, containing the largest phase fraction of $Sr_2TiO_3FH_{0.48}$ of the series, some of the reflections of $Sr_2TiO_3FH_{0.48}$ show a splitting. With respect to the reflections of the aristotype structure with *I*4/*mmm* symmetry of the RP-type phases, this splitting can be best observed at the $(020)_{I4/mmm}$ reflection at a d-spacing of ~ 1.96 Å. Superstructure reflections, which would indicate an increase of the unit cell size of the primitive cell, are not found. Therefore, various structural models of *translationengleiche* subgroups with orthorhombic, monoclinic and triclinic lattices were tested. Other fitting strategies, such as mixtures of more than one RP-type phase with higher symmetry were also employed, resulted, however, in a bad description of the shapes of the reflections. Significantly improved fitting is obtained using monoclinic subgroups (e.g. *C*12/*m*1), for which the equivalency of the *a* and *b* lattice parameters of the tetragonal aristotype cell is removed and the angle γ is $\neq 90°$. Additional lowering of the symmetry to the triclinic spacegroup *P*-1 further improved the fitting of some reflection groups considerably and can be regarded as the best approximation of the structural distortion. The symmetry tree for the symmetry lowering from the arisotype structure of *I*4/*mmm* to *P*-1 is given in Figure 6-6.

Oxide and fluoride ions are indistinguishable by X-ray and neutron diffraction due to their nearly identical scattering factors and lengths (see section 2.4.1.2). Nevertheless, the neutron diffraction data can give valuable information about the structure and composition of the anion sublattice by analysing the occupation factors of the different anion sites. While in $Sr_2TiO_3F_2$ the interstitial ($X3a^{int}$) site is fully occupied by fluoride ($X3b^{int}$ is vacant, see Table 6-1), the interstitial sites are completely vacant in $Sr_2TiO_3FH_{0.48}$, indicating that one fluoride ion per formula unit was successfully extracted from $Sr_2TiO_3F_2$. When additionally refining the equatorial ($X1^{eq}$) and apical ($X2^{ap}$) anion sites, they are nearly fully occupied by oxide and/or fluoride ions. Consequently, their occupation factors were fixed to 1 for the refinement. Since it is not possible to distinguish between oxide and fluoride ions at the apical anion site, a random 0.5/0.5 O/F occupation was assumed in accordance with the composition $Sr_2TiO_3FH_{0.48}$. To take also the fluoride-hydride substitution as indicated by elemental analysis into account, the localisation of hydride ions at the vacant interstitial sites was attempted without meaningful improvement of the fits. Even though hydride ions have a negative scattering length as opposed to oxide and fluoride ions, a differentiation between different anions in a compound is not always possible. Furthermore, the fact that hydride ions could not be localised may indicate that they have an overall bad localisation within the structure. Additionally, the structural analysis of $Sr_2TiO_3FH_{0.48}$ shows that all ions are located close to their ideal positions of the tetragonal aristotype structure, not resulting in a tilting of the TiO_5F octahedra. The structural parameters of $Sr_2TiO_3FH_{0.48}$ are given in Table 4-1.

Table 4-1: Structural parameters of the reduced phase $Sr_2TiO_3FH_{0.48}$ (space group: *P*-1) derived from coupled Rietveld analysis of XRD and NPD data of the reduction product of $Sr_2TiO_3F_2$ + x NaH with x = 1. The cell was transformed for easier comparability into a larger triclinic cell of the size √2 x √2 x 1 of the original cell; atomic positions were constrained in order to maintain translational symmetry between the sites. The presence of hydride ions as determined from a combination of elemental analysis, magnetic measurements and XAS could not be confirmed. This is most likely related to the fact that a detailed structural characterisation of compounds containing multiple anions and vacancies is difficult (see section 2.4.1.2). The anion sites $X1^{eq}$, $X2^{ap}$ and $X3^{int}$ refer to the equatorial, apical and interstitial sites, respectively.

Atom	**Wyckoff position**	**x**	**y**	**z**	**Occupancy**	**B [Å²]**
Sr1	2*i*	0.005(1)	0.494(1)	0.8574(2)	**1**	0.39(2)
Sr2	2*i*	**=x(Sr1)+0**	**=y(Sr1)+0.5**	**=z(Sr1)+0.5**	**1**	0.39(2)
Sr3	2*i*	**=x(Sr1)+0.5**	**=y(Sr1)+0**	**=z(Sr1)+0.5**	**1**	0.39(2)
Sr4	2*i*	**=x(Sr1)+0.5**	**=y(Sr1)+0.5**	**=z(Sr1)+0**	**1**	0.39(2)
Ti1	1*a*	**0**	**0**	**0**	**1**	0.39(2)
Ti2	1*g*	**0**	½	½	**1**	0.39(2)
Ti3	1*e*	½	½	**0**	**1**	0.39(2)
Ti4	1*f*	½	**0**	½	**1**	0.39(2)
O1 at X1a^{eq}	2*i*	0.25	0.25	0	**1**	0.39(2)
O2 at X1b^{eq}	2*i*	**=x(O1) +0.5**	**=y(O1) +0.5**	**=z(O1) +0.5**	**1**	0.39(2)
O3 at X1c^{eq}	2*i*	**=x(O1) +0.25**	**=y(O1) +0.75**	**=z(O1) +0.5**	**1**	0.39(2)
O4 at X1d^{eq}	2*i*	**=x(O1)+0.75**	**=y(O1) +0.25**	**=z(O1) +0**	**1**	0.39(2)
(O/F)1 at X2a^{ap}	2*i*	0.005(2)	0.492(1)	0.6578(3)	**0.5/0.5**	0.39(2)
(O/F)2 at X2b^{ap}	2*i*	**=x(O/F)1+0**	**=y(O/F)1+0.5**	**=z(O/F)1+0.5**	**0.5/0.5**	0.39(2)
(O/F)3 at X2c^{ap}	2*i*	**=x(O/F)1+0.5**	**=y(O/F)1+0**	**=z(O/F)1+0.5**	**0.5/0.5**	0.39(2)
(O/F)4 at X2d^{ap}	2*i*	**=x(O/F)1+0.5**	**=y(O/F)1+0.5**	**=z(O/F)1+0**	**0.5/0.5**	0.39(2)
X3a^{int}	2*i*	0.25	0.25	0	**0**	0.39(2)
X3b^{int}	2*i*	**=x(F1)+0.5**	**=y(F1)+0.75**	**=z(F1)+0.5**	**0**	0.39(2)
X3c^{int}	2*i*	**=x(F1)+0.25**	**=y(F1)+0.75**	**=z(F1)+0.5**	**0**	0.39(2)
X3d^{int}	2*i*	**=x(F1)+0.75**	**=y(F1)+0.25**	**=z(F1)+0**	**0**	0.39(2)
***a* [Å]**	5.585(1)		***b* [Å]**	5.541(1)		
***c* [Å]**	12.919(2)		***α* [°]**	90.83(1)		
***β* [°]**	89.78(1)		***γ* [°]**	89.52(1)		
R_{wp}(XRD+NPD) [%]	3.10		**GOF(XRD+NPD)**	1.56	**R_{Bragg} [%]**	0.92 (XRD) 1.39 (NPD, bank 2)

The diffraction patterns of the reduction product $Sr_2TiO_3F_2$ + x NaH with x = 2, containing only one RP-type compound with an approximate composition of $Sr_2TiO_3H_{1.48}$, can be well described with a structural model with *I4/mmm* symmetry. Compared to the pattern of $Sr_2TiO_3FH_{0.48}$, an even higher degree of anisotropic broadening is found. Such broadening, although less severe, has been also observed for other reduced RP-type compounds, e.g. $Sr_3Fe_2O_5$ [94]. Refinements of the occupation factors of the apical ($X2^{ap}$) and interstitial ($X3^{int}$) anion sites show a significant amount of anion vacancies. While the interstitial site is completely vacant, a partial occupation of the apical anion site is observed. This partial occupation indicates that additional fluoride ions are extracted as compared to $Sr_2TiO_3FH_{0.48}$. As indicated by elemental analysis, the presence of hydride ions at the vacant apical ($X2^{ap}$) and/or interstitial ($X3^{int}$) sites has to be also taken into consideration. A minor fraction of hydride ions can be localised at the apical site only. However, the hydride content is still too low for the proposed composition of $Sr_2TiO_3H_{1.48}$, as can be seen from the determined structural parameters given in Table 4-2. Additionally, the occupation of the apical site $X2^{ap}$

by oxide is too high (occupation when hydride ions are not considered is still ~ 0.7), which is further enhanced by the placement of hydride ions on this site due to the negative scattering length of hydride. A partial occupation of this site by fluoride ions can be largely excluded since both fluoride ions are extracted (see section 4.1.1.2.1). A potential partial re-oxidation might explain, however, the observed filling of the apical site. Alternatively, the deviation to the composition of $Sr_2TiO_3H_{1.48}$ might be a result of a limited quality of the data set.

Table 4-2: Structural parameters of the reduced phase $Sr_2TiO_3H_{1.48}$ (space group: *I4/mmm*) derived from coupled Rietveld analysis of XRD and NPD data of the reduction product of $Sr_2TiO_3F_2$ + x NaH with x = 1. The anion sites $X1^{eq}$, $X2^{ap}$ and $X3^{int}$ refer to the equatorial, apical and interstitial sites, respectively.

Atom	**Wyckoff position**	**x**	**y**	**z**	**Occupancy**	**B [Å²]**
Sr1	4*e*	**0**	**0**	0.3550(2)	**1**	0.79(2)
Ti1	2*a*	½	½	½	**1**	0.79(2)
O1 at $X1^{eq}$	4*c*	½	**0**	½	**1**	0.79(2)
O2 at $X2^{ap}$	4*e*	**0**	**0**	0.155(1)	0.83(1)	0.79(2)
H1 at $X2^{ap}$	4*e*	**0**	**0**	0.155(1)	0.17(1)	0.79(2)
$X3^{int}$	4*d*	**0**	½	¼	**0**	0.79(2)
***a* [Å]**	3.9100(2)		***c* [Å]**	12.722(1)		
R_{wp}(XRD+NPD) [%]	2.80		**GOF(XRD+NPD)**	1.66	**R_{Bragg} [%]**	0.66 (XRD) 1.01 (NPD, bank 1)

The obtained bond distances of $Sr_2TiO_3FH_{0.48}$ and $Sr_2TiO_3H_{1.48}$ are listed in comparison to $Sr_2TiO_3F_2$ [71] in Table 4-3. Due to the defluorination, considerable changes of the bond distances are observed. In particular, the bond distances between Ti and its surrounding ions suggests the formation of low-valent Ti species. The crystal structures of $Sr_2TiO_3FH_{0.48}$ and $Sr_2TiO_3H_{1.48}$ as determined from the coupled Rietveld analysis are shown in Figure 4-7.

Table 4-3: Bond distances of the reduced phases $Sr_2TiO_3FH_{0.48}$ and $Sr_2TiO_3H_{1.48}$ in comparison to $Sr_2TiO_3F_2$. The anion sites $X1^{eq}$, $X2^{ap}$ and $X3^{int}$ refer to the equatorial, apical and interstitial sites, respectively.

			Bond distance [Å]		
Bond	**$Sr_2TiO_3F_2$ [71]**	**Bond**	**$Sr_2TiO_3FH_{0.48}$**	**Bond**	**$Sr_2TiO_3H_{1.48}$**
Sr2-O1 at $X1^{eq}$	2.497(2) [4x]	**Sr-O at $X1^{eq}$**	2.672(4) [1x] 2.693(4) [1x] 2.703(4) [1x] 2.707(4) [1x]	**Sr1-O1 at $X1^{eq}$**	2.692(2) [4x]
Sr1-O2 at $X2a^{ap}$	2.815(2) [4x]	**Sr-(O/F) at $X2^{ap}$**	2.581(5) [1x]	**Sr1-O2 at $X2^{ap}$**	2.539(5) [~0.83]
Sr2-F1 at $X2b^{ap}$	2.773(2) [4x]		2.694(8) [1x]		2.7677(2) [~3.32]
	2.503(5) [1x]		2.798(12) [1x]	**Sr1-H2 at $X2^{ap}$**	2.539(5) [~0.17]
			2.803(12) [1x]		2.7677(2) [~0.68]
			2.861(8) [1x]		
Sr1-F2 at $X3^{int}$	2.423(2) [4x]				
Ti-O1 at $X1^{eq}$	1.973(2) [4x]	**Ti-O at $X1^{eq}$**	1.958(1) [2x] 1.975(1) [2x]	**Ti1-O1 at $X1^{eq}$**	1.955(1) [4x]
Ti-O2 at $X2a^{ap}$	1.691(7) [1x]	**Ti-(O/F) at $X2^{ap}$**	2.040(4) [2x]	**Ti1-O2 at $X2^{ap}$**	1.974(5) [~1.66x]
Ti-F1 at $X2b^{ap}$	2.829(7) [1x]			**Ti1-H2 at $X2^{ap}$**	1.974(5) [~0.34x]

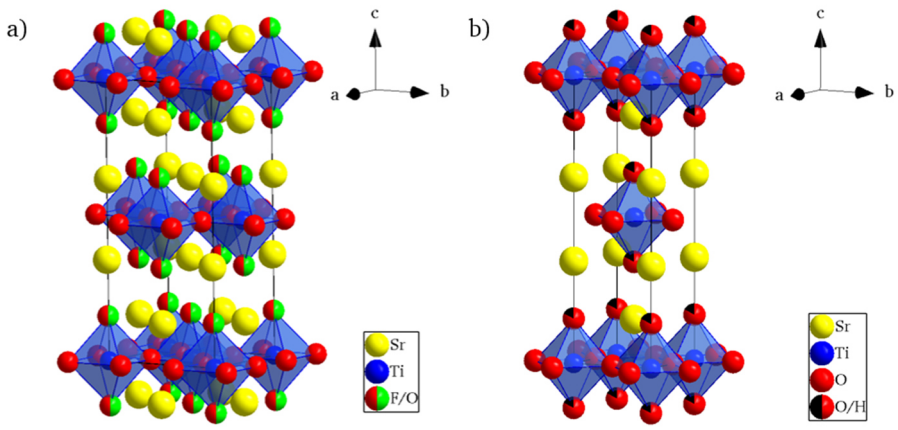

Figure 4-7: Crystal structures of the reduced phases $Sr_2TiO_3FH_{0.48}$ and $Sr_2TiO_3H_{1.48}$ as determined from the coupled Rietveld analysis.

4.1.1.3 Magnetisation study of $Sr_2TiO_3F_2$ and the reduction products

The ZFC M(T) curves of $Sr_2TiO_3F_2$ and the reduction products of $Sr_2TiO_3F_2$ + x NaH with x = 1 and 2 containing $Sr_2TiO_3FH_{0.48}$ and $Sr_2TiO_3H_{1.48}$, respectively, are shown in Figure 4-8. $Sr_2TiO_3F_2$ is diamagnetic for temperatures > 25 K. At lower temperatures, a minor trace of an unidentified paramagnetic phase seems to be present, resulting in a deviation from the diamagnetic behaviour. The otherwise diamagnetic behaviour is characteristic for an oxidation state of the Ti cations in $Sr_2TiO_3F_2$ of +4, corresponding to a d^0 electron configuration. In contrast to this, for the reduction products, a paramagnetic behaviour is observed. This can only be related to the RP-type phases $Sr_2TiO_3FH_{0.48}$ and $Sr_2TiO_3H_{1.48}$, since NaF and SrF_2 are diamagnetic. The paramagnetic behaviour confirms again the successful extraction of fluoride ions upon the reaction with NaH. The related reduction leads the formation of low-valent Ti species with unpaired electrons. These electrons are decisive for the manifestation of magnetic interactions (see also section 2.3). Ti^{3+} and Ti^{2+} have d^1 and d^2 electron configurations, respectively.

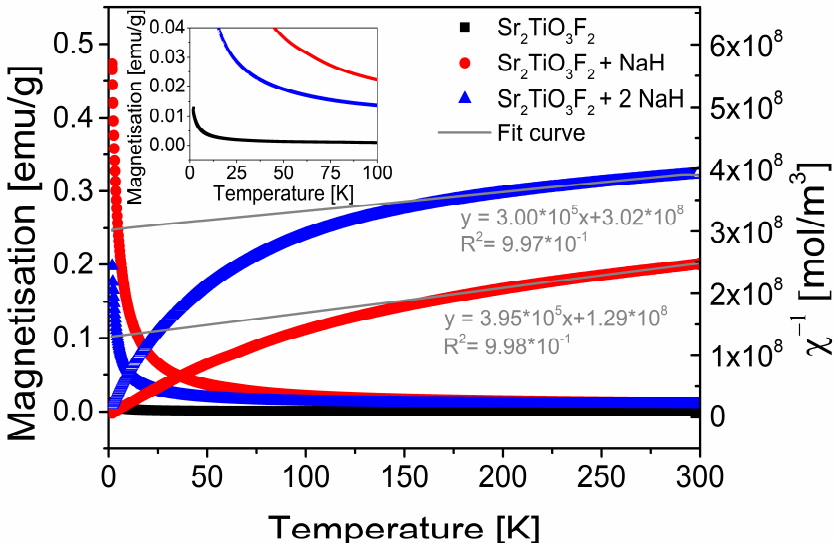

Figure 4-8: ZFC M(T) (closed symbols) and χ^{-1}(T) (open symbols) curves of $Sr_2TiO_3F_2$ and the reduction products of $Sr_2TiO_3F_2$ + x NaH with x = 1 and 2 containing the reduced phases $Sr_2TiO_3FH_{0.48}$ and $Sr_2TiO_3H_{1.48}$, respectively, measured at μ_0 = 1 T. The inset shows a magnification of the M(T) curves at low temperatures. The fitting curves of the Curie-Weiss fits, the corresponding linear functions and the coefficients of determination are also given. The curves are corrected from the diamagnetic contributions of the present phases and the gelatinee capsules and straws used for the measurements.

The plots of the χ^{-1}(T) of the reduction products deviate significantly from the ideal linear paramagnetic behaviour at low temperatures. Similar behaviours have been also found upon the topochemical reduction of other titanates with pyrochlore [80] and layered perovskite [79] structures. In these reports, different Curie-Weiss law-related fitting strategies have been employed. One strategy, as reported by Blundred et al. [80], is based on the limitation of the fitting temperature range to temperatures above the paramagnetic transition temperature, i.e., to high temperatures. In this temperature range, an ideally paramagnetic behaviour should be observed resulting in a linear χ^{-1}(T) curve. However, for the χ^{-1}(T) curves of the reduction products, a linear curve progression is only observed in a very narrow temperature range at high temperatures. This suggests that no ideal paramagnetism is found in the reduction products.

To take deviations from the ideal paramagnetic behaviour due to diamagnetic contributions into account, the susceptibility data were in a first approach corrected by these contributions. An estimation of the diamagnetic contributions can be obtained from listed diamagnetic susceptibilities of the contained ions. [206] Additionally, the diamagnetic contributions of the gelatine capsules and straws used during the measurements were taken into account. The correction leads to χ^{-1}(T) curves with approximately linear behaviours in the temperature range of 200 to 300 K. It has to be acknowledged that this range is still very limited; extending the range to lower temperatures results, however, in considerably worse fits. This demonstrates again that the reduced phases are not ideally paramagnetic and the determined spin-only magnetic moments should be perceived as estimations. Curie-Weiss fits in the linear regions (Figure 4-8) reveal magnetic moments of ~ 1.27 and 1.46 μ_B per Ti, corresponding to ~ 0.61 and 0.77 unpaired electrons, for $Sr_2TiO_3FH_{0.48}$ and $Sr_2TiO_3H_{1.48}$, respectively. For the reduced RP-type phases with proposed compositions of $Sr_2TiO_3FH_{0.48}$ and $Sr_2TiO_3H_{1.48}$ based on the findings of section 4.1.1.2.1, including the presence of significant amounts of hydride ions as obtained from elemental analysis, Ti oxidation states close to +3.5 are expected.

Therefore, the oxidation states determined using this fitting approach are in good agreement with the suggested compositions.

Another fitting approach discussed in literature is based on a modified Curie-Weiss model according to $\chi = C/(T - \Theta) + \chi_0$ where χ_0 is a term to assign for diamagnetic and/or other temperature-independent magnetic contributions. This fitting strategy has been for example reported by Pussacq et al. [79]. When performing the fitting accordingly over the entire temperature range of the susceptibility data, significantly lower magnetic moments of ~ 0.39 and 0.20 μ_B per Ti are obtained for $Sr_2TiO_3FH_{0.48}$ and $Sr_2TiO_3H_{1.48}$, respectively. However, the strongest deviations of the fits are found at higher temperatures, i.e., in the temperature regions, in which paramagnetic behaviour should be predominant. In the high temperature region of the $\chi^{-1}(T)$ curves, the slope of the fitting curve is considerably higher than the slope of the measurement data. Since the magnetic moment is inversely proportional to the slope of the curves, overall lower magnetic moments are obtained. This might in part explain the strong discrepancies between the magnetic moments derived using the two applied fitting strategies. However, it can be assumed that the spin-only moments of the reduced compounds lay between the values derived from both fitting strategies. It should, however, be noted, that the complex fitting procedure dependency of the obtained magnetic moments shows that the magnetic behaviour cannot be interpreted as purely paramagnetic with only spin-only moments.

4.1.1.4 X-ray absorption spectroscopy of $Sr_2TiO_3F_2$ and the reduction products

The element-specific XAS can be used as alternative technique for the determination of the Ti oxidation state. With respect to this, XANES is a powerful tool, which can give additional information about the local symmetry and the orbital occupancy. Moreover, EXAFS provides detailed information about the local structure around Ti including bond distances to neighbouring atoms and coordination numbers. The atom species of the neighbouring atoms can also be determined.

The normalized Ti K-edge XANES spectra of $Sr_2TiO_3F_2$ and the reduction products of $Sr_2TiO_3F_2$ + x NaH with x = 1 and 2 containing $Sr_2TiO_3FH_{0.48}$ and $Sr_2TiO_3H_{1.48}$, respectively, are given in Figure 4-9. A spectrum of TiO_2 is provided as reference. Since $Sr_2TiO_3FH_{0.48}$ and $Sr_2TiO_3H_{1.48}$ are the only Ti-containing compounds in the reduction mixtures, all observed changes of their spectra in relation to $Sr_2TiO_3F_2$ are related to the defluorination of the phases. In general, Ti has five pre-edge features, i.e., A_1, A_2, A_3, B and C, which are all located between 4960 and 4980 eV, even though it is not always possible to separate them due to their small energy separation. [228-230] Their intensities are strongly dependent on surrounding atoms in a short to medium range (< 100 atoms) and the size of the investigated particles. [228] The pre-edge features can be assigned to transitions of electrons to bound excited states of the absorbing atom. The origin of the A_1 feature is still debated in literature. [231] The most plausible explanations are core hole effects coupled with dipolar and quadrupole transitions [232] and 3*d*-4*p* hybridized states [228]. The A_2 and A_3 are correlated to transitions into t_{2g} and e_g orbitals, which are a result of hybridisation reactions of mainly Ti 3*d* and minor O 2*p*. [231, 233] This blend-in of an O 2*p* character is only possible for non-centrosymmetric coordination of Ti. Consequently, the A_2 and A_3 have a higher intensity, when a high distortion from centrosymmetry is present. In contrast to this, for perfect centrosymmetry, no Ti 3*d*-O 2*p* but only Ti 3*d*-O 1*s* hybridisation would be possible. For the latter case, no pre-edge related features would be visible, since these transitions are electric dipole forbidden. [229, 231] A

comparison of the A_2 pre-edge feature of $Sr_2TiO_3F_2$, $Sr_2TiO_3FH_{0.48}$ and $Sr_2TiO_3H_{1.48}$ provides, therefore, structural information. In $Sr_2TiO_3F_2$, the features is very pronounced, indicating a higher distortion of the octahedra and shorter distances between Ti and apical oxide ions [234] than in $Sr_2TiO_3FH_{0.48}$ and $Sr_2TiO_3H_{1.48}$. This is in agreement with the structural analysis of $Sr_2TiO_3F_2$ based on diffraction data [71] (see section 2.2.1 and 4.1.1.1). The reduced compounds show drastically decreased intensities of the A_2 feature related to a more centrosymmetric coordination around the Ti cations. The lowest intensity is obtained for $Sr_2TiO_3H_{1.48}$, which agrees well with the fact that no fluoride ions, which would distort a perfect inversion symmetry on the local scale, remain in the structure after the defluorination.

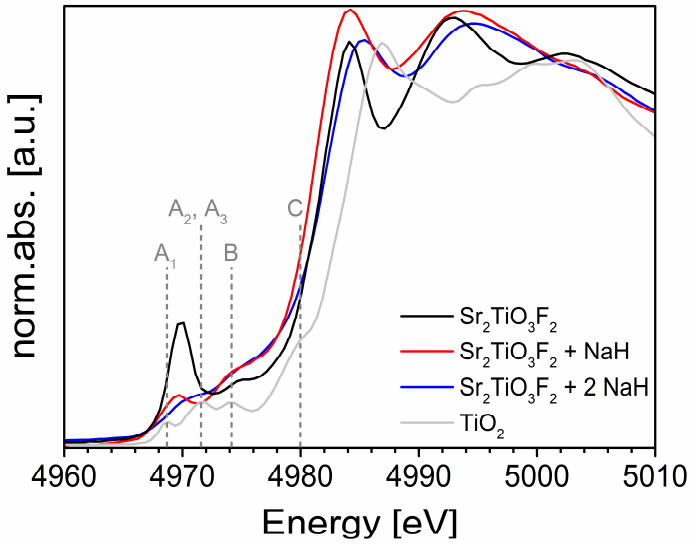

Figure 4-9: Normalized Ti K-edge X-ray absorption spectra of $Sr_2TiO_3F_2$ and the reduction products of $Sr_2TiO_3F_2$ + x NaH with x = 1 and 2 containing the reduced phases $Sr_2TiO_3FH_{0.48}$ and $Sr_2TiO_3H_{1.48}$, respectively. As a reference, the spectrum of TiO_2 is plotted.

Due to a complex shifting of the pre-edge features and the absorption edges positions in the spectra of $Sr_2TiO_3F_2$, and the reduction products $Sr_2TiO_3F_2$ + x NaH with x = 1 and 2, a precise determination of the oxidation states of Ti of the reduced compounds is not possible. In comparison to TiO_2, the spectra are shifted towards lower energies, indicating a comparative increase of the electron density at the Ti centre. This is further supported by an energy shift of ~ 2 eV of the most-intense pre-edge features of the reduction products $Sr_2TiO_3F_2$ + x NaH with x = 1 and 2. This shift can be assigned to a reduction of the Ti oxidation state to values between +3.5 and +3. [234]

More detailed information about the local structure around Ti in $Sr_2TiO_3F_2$, $Sr_2TiO_3FH_{0.48}$ and $Sr_2TiO_3H_{1.48}$ is gained via an EXAFS analysis. The spectra and obtained structural parameters are given in Figure 4-10 and Table 4-4, respectively. The determined coordination spheres, the atom species of backscattering atoms, their numbers and the distances between the absorbing Ti and the backscattering atoms are in good agreement with the structural models obtained from the coupled Rietveld analysis. Similar tendencies of bond distance changes (compare Table 4-3) upon defluorination can be found. Additionally, the proposed composition can be in principle confirmed, however, since hydride ions are weak backscatterers in EXAFS, they cannot not be located within the structures.

Furthermore, the increase of centrosymmetry based on the intensities of the A_2 pre-edge features of $Sr_2TiO_3F_2$, $Sr_2TiO_3FH_{0.48}$ and $Sr_2TiO_3H_{1.48}$ of the XANES measurements can be confirmed by the EXAFS analysis.

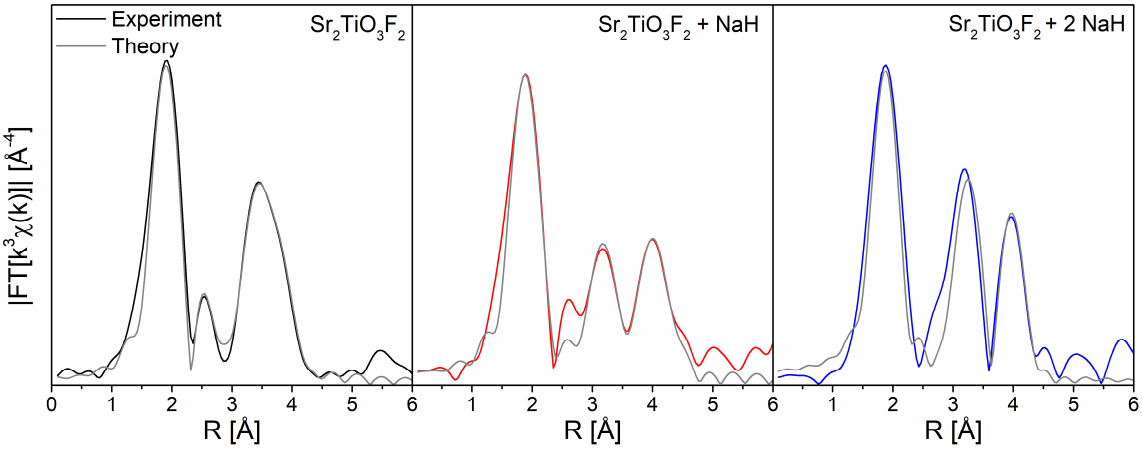

Figure 4-10: Ti K-edge EXAFS spectra of $Sr_2TiO_3F_2$ and the reduction products of $Sr_2TiO_3F_2$ +x NaH with x =1 and 2 containing the reduced phases $Sr_2TiO_3FH_{0.48}$ and $Sr_2TiO_3H_{1.48}$, respectively, after Fourier transformation.

Table 4-4: Structural parameters of $Sr_2TiO_3F_2$ and the reduction products $Sr_2TiO_3F_2$ +x NaH with x =1 and 2 containing reduced phases $Sr_2TiO_3FH_{0.48}$ and $Sr_2TiO_3H_{1.48}$, respectively, obtained from EXAFS analysis.

Sample	**Bs**[a]	**N(Bs)**[b]	**R(Abs-Bs) [Å]**[c]	**σ [Å^{-1}]**[d]	**R [%]**[e] **χ^2_{red}**[f] **E_f [eV]**[g] **A_{fac}**[h]
$Sr_2TiO_3F_2$	O	1.1 ± 0.1	1.819 ± 0.018	0.032 ± 0.003	24.42
	O	4.0 ± 0.2	1.939 ± 0.019	0.032 ± 0.003	4.75x10^{-5}
	F	1.2 ± 0.1	2.634 ± 0.026	0.032 ± 0.003	7.505
	Sr	6.9 ± 1.4	3.341 ± 0.033	0.112 ± 0.011	0.5311
	Sr	2.6 ± 0.5	3.688 ± 0.036	0.055 ± 0.005	
	Ti	1.0 ± 0.2	3.800 ± 0.038	0.115 0.011	
$Sr_2TiO_3FH_{0.48}$ in	O/F	4.9 ± 0.5	1.931 ± 0.019	0.087 ± 0.008	42.33
$Sr_2TiO_3F_2$ + NaH	Sr	4.0 ± 0.8	3.256 ± 0.032	0.112 ± 0.011	1.34x10^{-5}
	Ti	4.9 ± 1.0	4.023 ± 0.040	0.089 ± 0.008	9.775
					0.8
$Sr_2TiO_3H_{1.48}$ in	O	4.9 ± 0.5	1.920 ± 0.019	0.077 ± 0.007	35.07
$Sr_2TiO_3F_2$ + 2 NaH	Sr	3.7 ± 0.7	3.234 ± 0.032	0.087 ± 0.008	8.02x10^{-6}
	Ti	3.7 ± 0.7	3.978 ± 0.039	0.063 ± 0.006	10.81
					0.8

[a] Bs: backscattering atom; [b] Number of backscattering atoms; [c] Distance of absorbing atom to backscattering atom; [d] Debye-Waller like factor; [e] Fit index; [f] Reduced χ^2; [g] Fermi energy, which accounts for the shift between theory and experiment; [h] Amplitude reducing factor.

4.1.1.5 X-ray photoelectron spectroscopy of $Sr_2TiO_3F_2$ and the reduction products

The Ti surface oxidation states of $Sr_2TiO_3F_2$ and $Sr_2TiO_3FH_{0.48}$ and $Sr_2TiO_3H_{1.48}$ in the reduction products of $Sr_2TiO_3F_2$ + x NaH with x = 1 and 2 were additionally analysed using XPS. The Ti $2p_{3/2}$ XPS spectra are shown in Figure 4-11. The poor signal-to-noise ration of the spectra of the reduction products in comparison to the spectrum of $Sr_2TiO_3F_2$ is due to the layer of NaF, which is formed on the surface of particles of the RP-type phases upon defluorination (see also Figure 4-5).

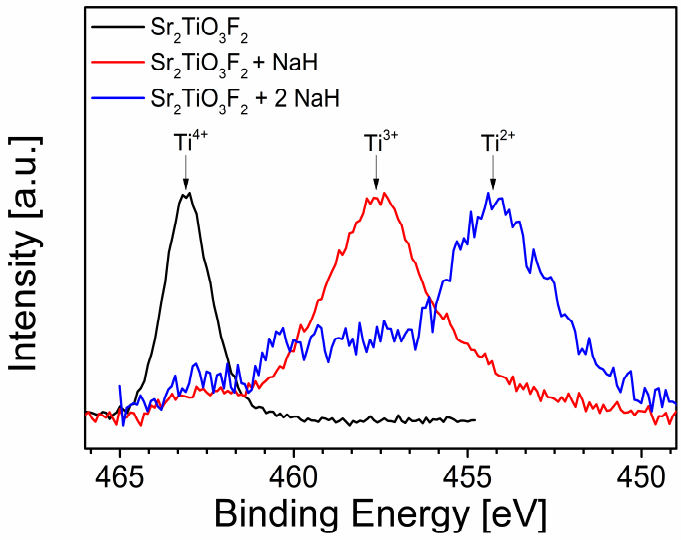

Figure 4-11: Ti $2p_{3/2}$ XPS spectra of $Sr_2TiO_3F_2$ and the reduction products $Sr_2TiO_3F_2$ + x NaH with x = 1 and 2 containing the reduced phases $Sr_2TiO_3FH_{0.48}$ and $Sr_2TiO_3H_{1.48}$, respectively. Due to the release of hydrogen on the particle surface of the bulk materials with compositions of $Sr_2TiO_3FH_{0.48}$ and $Sr_2TiO_3H_{1.48}$, the formation of phases with compositions of Sr_2TiO_3F and Sr_2TiO_3 is indicated.

The Ti $2p_{3/2}$ spectrum of $Sr_2TiO_3F_2$ features a peak at ~ 463.1 eV, pointing to a surface oxidation state of Ti^{4+}. Due to the presence of more electronegative fluoride ions in $Sr_2TiO_3F_2$, the observed binding energy is higher than the reported binding energies of Ti^{4+}-containing oxides (e.g. $SrTiO_3$: Ti $2p_{3/2}$ at 457.9 – 458.2 eV [207, 235]) due to the presence of more electronegative fluoride ions. In the spectra of the reduction products, considerable shifts of the peaks towards lower binding energies are observed. Additionally, the signals appear to be broader. This clearly indicates that a strong reduction of the RP-type phases has taken place on the surface of the particles. Characteristic binding energies of Ti^{3+}- and Ti^{2+}-containing oxides have been reported to be ~ 457.7 and 454.7 eV, respectively. [235] For the reduction product of $Sr_2TiO_3F_2$ +NaH, the signal found at ~ 457.6 eV can be, therefore, assigned to Ti^{3+}. In the reduction product $Sr_2TiO_3F_2$ +2 NaH, the strongest signal is found at even lower binding energies suggesting an even stronger reduction and the presence of Ti ions with an oxidation state as low as +2. In addition, lower signals at higher binding energies indicate the presence of residual Ti^{4+} and Ti^{3+} species.

The found surface oxidation states of the reduced RP-type phases are in strong contrast to the bulk oxidation states of $Sr_2TiO_3FH_{0.48}$ and $Sr_2TiO_3H_{1.48}$, for which for both an average oxidation state of $Ti^{3.5+}$ can be estimated. This indicates that a release of hydrogen takes place at the particle surfaces according to the following equations

$$for\ x = 1: Sr_2TiO_3FH_{0.48} \rightarrow Sr_2TiO_3F + 0.24H_2$$

and

$$for\ x = 2: Sr_2TiO_3H_{1.48} \rightarrow 2Sr_2TiO_3 + 0.74H_2.$$

This shows that defluorination can result in very low Ti oxidation states, which are significantly lower compared to those found for hydride-based reductions of oxide compounds (see section 2.2.2).

Moreover, the observation of hydrogen release at the particle surface suggests that the particle size or respectively the surface area of the parent oxyfluorides, may have also an important role in the achievable degree of reduction. It may be assumed that higher surface areas might result in the release of hydrogen from higher relative fractions of the particle volumes as compared to larger particles with smaller surface areas. This in turn, might allow for an increased overall reduction resulting in lower bulk oxidation states. With respect to this, attempts to prepare $Sr_2TiO_3F_2$ with increased surface areas via the topochemical fluorination of nano-sized Sr_2TiO_4 were made. The precursor oxide Sr_2TiO_4 was synthesised using a sol-gel process based on reports of Ge et al. [236] and Lee et al. [237] as well as by a nebulized-spray pyrolysis process adapted from Shih et al. [238]. However, the fluorination of the obtained powders results in the formation of large phase fractions of only partially fluorinated RP-type oxyfluoride phases and strong decomposition leading to the formation of SrF_2 and $SrTiO_3$. It is, therefore, indicated that a particle size reduction impedes the fluorination of the nano-sized Sr_2TiO_4 and facilitates decomposition. A further optimization of the reaction conditions for the fluorination is required in order to obtain nano-crystalline, preferably phase-pure $Sr_2TiO_3F_2$.

4.1.1.6 DFT calculations

4.1.1.6.1 Theoretical insights into the crystal structures of $Sr_2TiO_3F_2$ and the hypothetical phases Sr_2TiO_3F and Sr_2TiO_3

To examine the most stable crystal structures and the ion configurations of the anion sublattice of $Sr_2TiO_3F_2$ and reduced phases Sr_2TiO_3F and Sr_2TiO_3 found at the particle surfaces, different ordering scenarios of oxide and fluoride ions and/or vacancies were studied via DFT-based calculations. The structures of the phases with compositions of Sr_2TiO_3F and Sr_2TiO_3 should be regarded as idealized structures, which can be obtained upon purely reductive defluorination, i.e., if no fluoride-hydride substitution takes place.

For $Sr_2TiO_3F_2$, the ordering scenario proposed by Slater et al. [71] based on neutron powder diffraction data can be confirmed to be the energetically most favourable (Figure 4-12 a). After the removal of one fluoride ion from $Sr_2TiO_3F_2$, corresponding to a composition of Sr_2TiO_3F, the energetically most stable configurations show vacant interstitial sites. Configurations with the remaining fluoride ion at the apical sites are energetically favourable by ~ 0.6-0.7 eV per formula unit as compared to configurations, in which the fluoride ions occupy the equatorial site and oxide ions the apical sites. The most stable configuration is shown in Figure 4-12 b). This is in agreement with bond-valance sum [71] or Madelung energy [46] calculations of previous studies on Fe-based RP-type oxyfluorides. For Sr_2TiO_3, configurations, in which vacancies are present at the equatorial site are energetically more favourable by ~ 0.25-0.4 eV per formula unit in comparison to configurations with vacancies at the apical sites. This has been also observed experimentally for $Sr_3Fe_2O_5$. [74] The most stable configuration of anion vacancies at the equatorial site results in a strong orthorhombic distortion of $\Delta(a\text{-}b) \approx 0.33$ Å (Figure 4-12 c), which is, however, not observed experimentally. Other configurations with higher energies do not show these strong structural distortions, better reflecting the experimentally observed structure. The second most stable configuration with an energy higher by ~ 0.12 eV per formula unit is given in addition (Figure 4-12 d). For this structure, no orthorhombic distortion is found. Furthermore, it has to be acknowledged that the energy differences between different configurations of anion vacancies in Sr_2TiO_3 are much smaller compared to different distributions of fluoride ions in Sr_2TiO_3F.

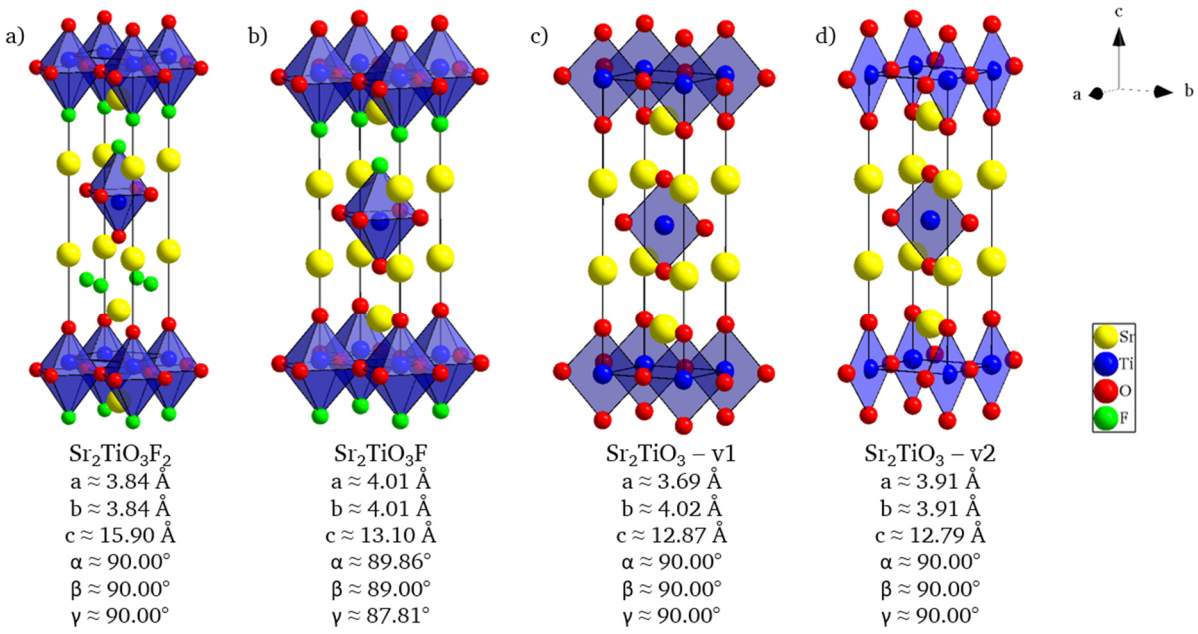

Figure 4-12: Most stable crystal structures of $Sr_2TiO_3F_2$ (a), Sr_2TiO_3F (b) and Sr_2TiO_3 (c and d) after structural relaxation. For Sr_2TiO_3, two versions (v1 (c) and v2 (d)) are given, which differ in ~ 0.12 eV per formula unit to each other.

4.1.1.6.2 Investigation of the reaction energetics

The determination of the change of the Gibb's free energy ΔG allows assessing whether a reaction is exergonic or endergonic. Therefore, it provides information about thermodynamically favourable or unfavourable reactions. ΔG can be calculated according to $\Delta G = \Delta H - T\Delta S$, where ΔH is the enthalpy of reaction, T the temperature and ΔS the change in reaction entropy. ΔH can be calculated from the difference of the energies of the reaction products and educts obtained from DFT calculations of their structures. The entropic contribution TΔS can be calculated from standard formation entropies at the respective temperatures. For T, a reaction temperature of 300 °C was used.

The fluoride-hydride substitution process was found to be of high importance regarding the formation of bulk reduction products with compositions of $Sr_2TiO_3FH_{0.48}$ and $Sr_2TiO_3H_{1.48}$. In contrast to this, pure reduction reactions under the release of hydrogen seem to be favoured at the particle surfaces. To estimate the energetics of a fluoride-hydride substitution in comparison to the hydrogen release, the energies for the compositions Sr_2TiO_3FH, Sr_2TiO_3H and $Sr_2TiO_3H_2$ were calculated in addition to the energies of the most stable configurations of $Sr_2TiO_3F_2$, Sr_2TiO_3F and Sr_2TiO_3 (see section 4.1.1.6.1). The models of Sr_2TiO_3FH, Sr_2TiO_3H and $Sr_2TiO_3H_2$ were chosen according to the most stable configurations of Sr_2TiO_3F and Sr_2TiO_3 and hydrogen was added to different vacant sites. The energies of the most stable configurations of Sr_2TiO_3FH, Sr_2TiO_3H and $Sr_2TiO_3H_2$ were used for the following considerations.

Reactions leading to the formation of Sr_2TiO_3FH, Sr_2TiO_3H and $Sr_2TiO_3H_2$ are strongly exergonic and the substitution of fluoride by hydride seem to be a strong driving force for the reaction (Table 4-5). The (partial) release of hydrogen from the hydride-substituted structures can neither be confirmed nor ruled out energetically. Depending on the proposed reaction, the release is either weakly exergonic or endergonic. This is in good agreement with the experimental observations. It should, however, be pointed out that other factors might affect

the compositions of the experimentally observed phases, which cannot be taken into considerations in DFT calculations. Such factors are the fast kinetics of the fluoride-hydride substitution, the slow kinetics of the hydrogen release and/or effects of configurational entropy (e.g. partial F/H disorder) in combination with complex structural distortions. Furthermore, the stabilisation of hydride ions within the structures could also be due to a potential surface passivation effect, which reduces the hydride mobility and hinders the additional release of hydrogen.

Table 4-5: Change of Gibb's free energies ΔG of defluorination reactions considering hydride substitution or hydrogen release calculated with enthalpies of reaction ΔH of optimized structures obtained using the DFT + U method. The entropic contribution ΔS was calculated from the standard entropy of formation of hydrogen at a reaction temperature of 573 K [239].

	Reaction equation	**ΔH [eV]** **< 0: exothermal** **> 0: endothermal**	**-TΔS [eV]** **at T = 573 K = 300 °C** [239]	**ΔG [eV]** **< 0: exergonic** **> 0: endergonic**
Substitution	$Sr_2TiO_3F_2$ + NaH → Sr_2TiO_3FH + NaF	-0.38	0	-0.38
H_2 Release	Sr_2TiO_3FH → Sr_2TiO_3F + ½ H_2	+0.58	-0.45	+0.13
Substitution	$Sr_2TiO_3F_2$ + 2 NaH → $Sr_2TiO_3H_2$ + 2 NaF	-0.58	0	-0.58
H_2 Release	$Sr_2TiO_3H_2$ → Sr_2TiO_3 + H_2	+0.88	-0.90	-0.02
	$Sr_2TiO_3H_2$ → Sr_2TiO_3H + ½ H_2	+0.45	-0.45	0
Substitution	Sr_2TiO_3F + NaH → Sr_2TiO_3H + NaF	-0.33	0	-0.33
H_2 Release	Sr_2TiO_3H → Sr_2TiO_3 + ½ H_2	+0.43	-0.45	-0.02

4.1.1.6.3 Reactivities of oxides and oxyfluorides in NaH-based reductions

When comparing the reductive deintercalation of oxide ions (deoxygenation) and fluoride ions (defluorination) using hydride-based reducing agents, it is obvious that kinetic and thermodynamic factors influence the reactivity. Fluoride ions possess a much higher mobility than oxide ions [240] and with regards to the kinetics, defluorination reactions should be more favourable. To distinguish between energetic and kinetic driving forces of deoxygenations and defluorinations, it is important to compare the change of the Gibb's free energies for both types of reactions. Different defluorination reactions of Ti-based RP-type oxyfluorides and deoxygenation reactions of Ti-based RP-type oxides are considered. The results are listed in Table 4-6.

In accordance with the starting point of the decomposition of NaH to metallic Na and hydrogen at 300 °C, the ΔG values of the reduction reactions using NaH (i.e., ΔG of reactions F_A, F_B, F_c, O_A, O_B, O_c) and Na (i.e., ΔG of reactions $F_{A'}$, $F_{B'}$, $F_{c'}$, $O_{A'}$, $O_{B'}$, $O_{c'}$) are almost identical. This shows that Na ($E^0(Na|Na^+)$ = -2.71 V vs. SHE, $E^0(Na|Na^+)$ ≈ 0.29 V vs. Li|LiF) could also be the reductive species in the reduction reactions at 300 °C.

Interestingly, only the defluorination reactions are exergonic, while the deoxygenations are endergonic. The differences in the reaction energetics is strongly related to the different lattice energies of the reduction side products NaF and Na_2O formed during the defluorination and deoxygenation reactions, respectively. While NaF has a rock salt structure, Na_2O crystallises in the antifluorite structure with a much higher lattice energy. Therefore, it can be concluded that the energetic contribution of the side product plays an important role in the reactivity of oxides and oxyfluorides in hydride-based reductions. It should be mentioned that a deoxygenation of RP-type oxyfluorides, leading to the presence of Na_2O in the reduction

products, is also not observed. It can be assumed that the extraction of oxide ions from oxyfluorides is energetically similar to the extraction of oxide ions from the respective oxide and, therefore, the respective reactions would be expected to be endergonic.

Moreover, the endergonic character of the deoxygenation reactions at 300 °C is in good agreement with the experimental findings made in the attempts to reduce Sr_2TiO_4 using NaH (see section 4.1.1.2.1). In these experiments, neither a considerable reduction nor the formation of Na_2O is observed. This is, further, in agreement with the considerably higher reaction temperatures reported for deoxygenation reactions of various titanate oxides (see section 2.2.2).

Table 4-6: Change of Gibb's free energies ΔG of defluorination and deoxygenation reactions calculated with enthalpies of reaction ΔH of optimized structures obtained using the DFT + U method. The entropic contribution was calculated from the standard formation entropy of hydrogen at a reaction temperature of 573 K [239].

	Reaction equation	**ΔH [eV] < 0: exothermal > 0: endothermal**	**-TΔS [eV] at T = 573 K = 300 °C [239]**	**ΔG [eV] < 0: exergonic > 0: endergonic**
(F_A)	$Sr_2TiO_3F_2$ + NaH → Sr_2TiO_3F + NaF + ½ H_2	+0.10	-0.45	-0.35
($F_{A'}$)	$Sr_2TiO_3F_2$ + Na → Sr_2TiO_3F + NaF	-0.34	0	-0.34
(F_B)	$Sr_2TiO_3F_2$ + 2 NaH → Sr_2TiO_3 + 2 NaF + H_2	+0.31	-0.90	-0.59
($F_{B'}$)	$Sr_2TiO_3F_2$ + 2 Na → Sr_2TiO_3 + 2 NaF	-0.57	0	-0.57
(F_C) = (F_B)-(F_A)	Sr_2TiO_3F + NaH → Sr_2TiO_3 + NaF + ½ H_2	+0.21	-0.45	-0.24
($F_{C'}$) = ($F_{B'}$)-($F_{A'}$)	Sr_2TiO_3F + Na → Sr_2TiO_3 + NaF	-0.23	0	-0.23
(O_A)	Sr_2TiO_4 + NaH → $Sr_2TiO_{3.5}$ + ½ Na_2O + ½ H_2	+1.09	-0.45	+0.63
($O_{A'}$)	Sr_2TiO_4 + Na → $Sr_2TiO_{3.5}$ + ½ Na_2O	+0.66	0	+0.66
(O_B)	Sr_2TiO_4 + 2 NaH → Sr_2TiO_3 + Na_2O + H_2	+2.13	-0.90	+1.23
($O_{B'}$)	Sr_2TiO_4 + 2 Na → Sr_2TiO_3 + Na_2O	+1.25	0	+1.25
(O_C) = (O_B)-(O_A)	$Sr_2TiO_{3.5}$ + NaH → $Sr_2TiO_{3.5}$ + ½ Na_2O + ½ H_2	+1.04	-0.45	+0.59
($O_{C'}$) = ($O_{B'}$)-($O_{A'}$)	$Sr_2TiO_{3.5}$ + Na → $Sr_2TiO_{3.5}$ + ½ Na_2O	+0.59	0	+0.59

At reaction temperatures of 300 °C, the formation of gaseous HF and water via an additional reduction can be ruled out due to the strongly endergonic character of these reactions (Table 4-7). Such reactions would involve the redox couple $H_2|2H^+$ ($E^0(H_2|2H^+) = 0$ V vs. SHE, $E^0(H_2|2H^+) \approx 3$ V vs. Li|LiF), which does not provide sufficient reductive power to reduce Ti further since the calculated change of the Gibb's free energies of the defluorinated phases correspond to low potential range of ~ 0.5-0.7 V vs. Li|LiF for both consecutive defluorination steps. At considerably higher temperatures, the entropic contributions related to the formation of HF and water could, however, compensate for the endothermic enthalpy terms, making a hydrogen reduction feasible.

Table 4-7: Change of Gibb's free energies ΔG of defluorination and deoxygenation reactions considering the formation of H_2O and HF calculated with enthalpies of reaction ΔH of optimized structures obtained using the DFT + U method. The entropic contributions were calculated from the standard formation enthalpies of hydrogen, HF and H_2O at a reaction temperature of 573 K [239].

	Reaction equation	**ΔH [eV]** **< 0: exothermal** **> 0: endothermal**	**-TΔS [eV]** **at T = 573 K** **= 300 °C [239]** **for gaseous species**	**ΔG [eV]** **< 0 → exergonic** **> 0 → endergonic**
HF Release	$Sr_2TiO_3F_2$ + NaH → Sr_2TiO_3 + NaF + HF(g)	+2.72	-1.07	+1.65
H_2O Release	Sr_2TiO_4 + NaH → Sr_2TiO_3 + ½ Na_2O + ½ H_2O(g)	+2.31	-0.64	+1.67

4.1.1.7 Summary

A comprehensive study on the reduction behaviour of the n = 1 RP-type oxyfluoride $Sr_2TiO_3F_2$ with *P*4/*nmm* symmetry was performed using varying amounts of the reducing agent NaH according to $Sr_2TiO_3F_2$ + x NaH with $0 \leq x \leq 2.5$ ($\Delta x = 0.25$) at reaction temperatures as low as 300 °C. Based on a combination of various characterisation methods, the newly developed topochemical defluorination method allows for the selective extraction of fluoride ions from $Sr_2TiO_3F_2$, accompanied by fluoride-hydride exchange. Therefore, the reduction mechanism can be best explained by a combination of a reductive defluorination and partial fluoride-hydride substitution. The substitution process takes increasingly place for increasing NaH contents. A nearly stoichiometric reductive reaction between $Sr_2TiO_3F_2$ and NaH can be assumed and only negligibly small degrees of decomposition or amorphisation occur.

Reduction products, containing almost only one of the RP-type phases with approximate compositions $Sr_2TiO_3FH_{0.48}$ or $Sr_2TiO_3H_{1.48}$, were obtained for x = 1 and 2, respectively. For other values of $x \geq 1$, phase mixtures of these phases were found. Strong structural changes within the reduced phases in comparison to the parent oxyfluoride, expressed by a considerable decrease of the *c* axis from ~ 15.5 Å to ~ 12.9 Å and ~ 12.7 Å for increasing degrees of reduction, with additional symmetry lowering for $Sr_2TiO_3FH_{0.48}$ to *P*-1, were observed. $Sr_2TiO_3H_{0.48}$ crystallises in the aristotype structure *I*4/*mmm*. Additionally, strong anisotropic strain broadening was observed for the stronger defluorinated phase. Structural models of the reduced phases were derived from coupled Rietveld analyses of X-ray and neutron powder diffraction data. No significant phase fractions of decomposition or amorphisation phases were found in the reduction products and the extraction of fluoride takes place nearly stoichiometrically. Changes of coordination environments were further examined by means X-ray absorption spectroscopy, confirming the proposed structural changes. Magnetic measurements in combination with X-ray absorption and X-ray photoelectron spectroscopy revealed significant changes in the Ti oxidation states, confirming again a successful reductive defluorination. A transition from diamagnetic to paramagnetic behaviour upon the reduction of $Sr_2TiO_3F_2$ confirmed further the presence of unpaired electrons in the reduced phases. Interestingly, the surface oxidation states of the reduced compounds were found to differ from the bulk with Ti oxidation states of ~ +3.5. For the particle surfaces of reduced phases, compositions of Sr_2TiO_3F and Sr_2TiO_3 with Ti^{3+} and Ti^{2+} species, respectively, could be deduced, suggesting a hydrogen release at the particle surfaces. The most stable crystal structures of $Sr_2TiO_3F_2$, Sr_2TiO_3F and Sr_2TiO_3 were in addition examined using DFT-based calculations. Such calculations were also conducted to investigate

the influence of the fluoride-hydride substitution on the driving forces of the reaction and it was found that such substitutions lead to strongly exergonic reactions. A (partial) release of hydrogen from the hydride-substituted structures could neither be confirmed nor ruled out energetically. The reactivities of oxides and oxyfluorides towards reductions in hydride-based reactions were examined in addition. It could be shown that the formation of NaF is a strong energetic driving force for the overall exergonic defluorination reactions, whereas the deoxygenation reactions are endergonic. This is related to the different lattice energies of NaF and Na_2O formed as side products during the reductions and confirms that much higher reaction temperatures (> 530 °C) are needed to obtain a considerable reduction in deoxygenations, as was also shown experimentally when attempting to reduce Sr_2TiO_4 under the same reaction conditions as $Sr_2TiO_3F_2$. In addition to thermodynamically considerations, the fluoride ions show a higher mobility than oxide ions correlated to improved kinetics in the defluorination reactions. Moreover, the formation of HF or H_2O in an additional reduction step can be ruled out due to the strongly endergonic character of these reactions and the need to access the $H_2|2H^+$ redox potential. The predicted low redox potential of the $Sr_2TiO_3F_{2-x}|Sr_2TiO_3F_2$ redox couple of ~ 0.5-0.7 V vs. Li|LiF additionally highlight the potential of $Sr_2TiO_3F_2$ as intercalation-based anode material (see section 4.2.1). Due to this low potential, the use of $Sr_2TiO_3F_2$ would enable high energy densities, with a comparatively high theoretical gravimetric capacity of ~ 190 $mAhg^{-1}$, corresponding to the extraction of two fluoride ions.

Overall, it is shown that a sequence of topochemical non-oxidative fluorination and hydride-based defluorination reactions opens up a new avenue of research for the development of novel materials with defined intrinsic properties due to the possibilities to alter oxidation states and coordination environments of transition metals in transition metal oxyfluorides. Significantly lowered reaction temperatures and stronger degrees of reduction as for comparable reductions of respective oxides facilitate the synthesis of materials with interesting properties.

4.1.2 Topochemical fluorination of $Sr_3Ti_2O_7$ to $Sr_3Ti_2O_5F_4$ and its defluorination

4.1.2.1 Topochemical fluorination of $Sr_3Ti_2O_7$ to $Sr_3Ti_2O_5F_4$

4.1.2.1.1 Coupled Rietveld analysis of $Sr_3Ti_2O_5F_4$

The topochemical fluorination of $Sr_3Ti_2O_7$ using a stoichiometric amount of PVDF as the fluorination reagent results in a significant cell expansion of ~ 15.8 %. The XRD pattern of the fluorination product is shown in Figure 2-1 in comparison to the pattern of $Sr_3Ti_2O_7$ (a = 3.89890(15) Å, c = 20.3125(10) Å). This is due to a strong expansion along the c axis of ~ 15.0 % (c = 23.372(5) Å), while the a axis remains almost constant (a = 3.9059(8) Å). In agreement with previously fluorinated n = 2 RP compounds with high filling degrees of the interstitial layers [46, 59], good refinements could be obtained within the aristotype space group of *I*4/*mmm*. Symmetry lowering is not indicated due to the absence of reflection splitting and superstructure reflections. Additionally, ~ 5 wt% of SrF_2 and ~ 7 wt% of $SrTiO_3$ are formed due to partial decomposition (variations in the levels of decomposition between different synthesis batches of the oxyfluoride lead to slightly varying amounts of SrF_2 and $SrTiO_3$). These impurity phases remain present in all defluorination products, and their relative phase fractions do not show strong changes within errors. Moreover, the presence of higher amounts of SrF_2 and $SrTiO_3$ in the fluorinated product in comparison to the fluorination of Sr_2TiO_4 suggests that the fluorinated RP-type strontium titanium oxyfluoride with n = 2 is less stable than the lower-order oxyfluoride.

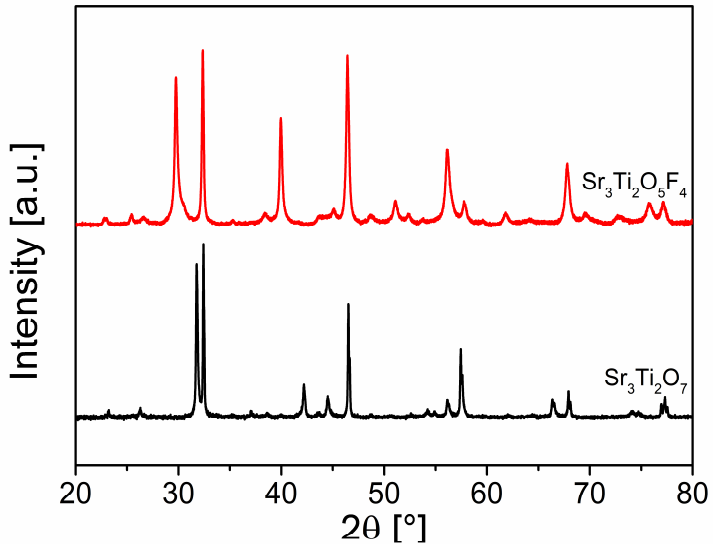

Figure 4-13: X-ray diffraction patterns of $Sr_3Ti_2O_7$ and $Sr_3Ti_2O_7$ fluorinated with PVDF $(CH_2CF_2)_n$ in a molar ratio of $Sr_3Ti_2O_7$:CH_2CF_2 of 1:2.

The structural refinement of the fluorinated phase was performed via a coupled Rietveld analysis of XRD and NPD data (Figure 4-14). The obtained structural parameters are given in Table 4-8. The bond distances are listed in Table 4-11 in comparison to the obtained reduced phase (see section 4.1.2.2). It is found that all anion sites are fully occupied within errors, suggesting a composition of $Sr_3Ti_2X_9$ with X being oxide or fluoride ions. Due to the indistinguishability of oxide and fluoride ions by powder diffraction methods, neither the quantity of the respective ion within the oxyfluoride can be determined nor is an assignment of the type of ion to a specific site directly possible. The diamagnetic nature of the sample

after fluorination supports the presence of Ti^{4+} (see section 4.1.2.3), which is in good agreement with the assumed composition of $Sr_3Ti_2O_5F_4$. In accordance with the used amount of PVDF, this composition corresponds to a stoichiometric incorporation of the fluoride ions from the polymer as it has been also previously reported for other perovskite-type and RP-type oxyfluorides [241-244]. Therefore, the fluorination reaction proceeds via a non-oxidative substitution and insertion process, in which two oxide ions are replaced by four fluoride ions. The same has been found for the formation of $Sr_2TiO_3F_2$. [71]

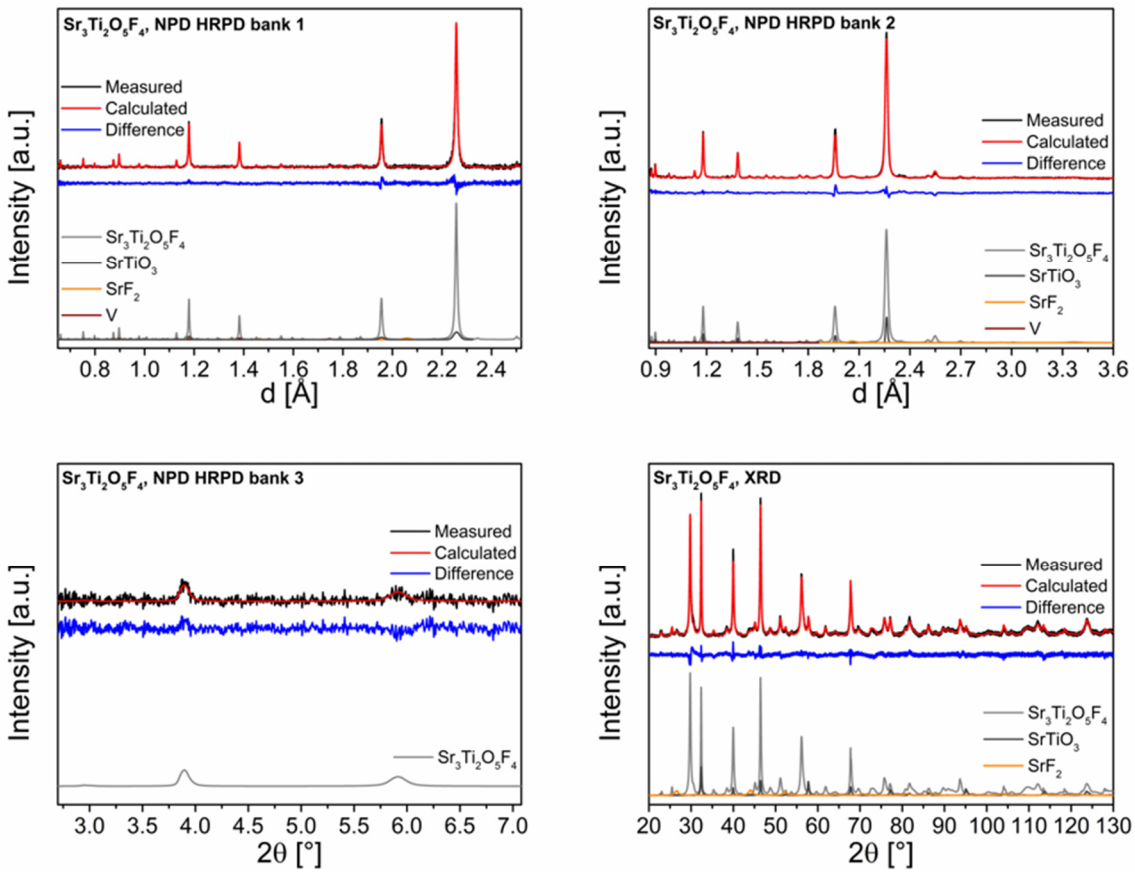

Figure 4-14: Coupled Rietveld refinements of $Sr_3Ti_2O_5F_4$ of NPD HRPD banks 1-3 and XRD data.

Table 4-8: Structural parameters of $Sr_3Ti_2O_5F_4$ (space group: *I4/mmm*) derived from coupled Rietveld analysis of XRD and NPD data. The anion sites $X1^{eq}$, $X2^{ap,central}$, $X3^{ap,terminal}$ and $X4^{int}$ refer to the equatorial, central apical, terminal apical and interstitial sites, respectively.

Atom	**Wyckoff position**	**x**	**y**	**z**	**Occupancy**	**B [Å²]**
Sr1	2*b*	**0**	**0**	½	**1**	1.07(2)
Sr2	4*e*	**0**	**0**	0.31381(5)	**1**	1.07(2)
Ti1	4*e*	**0**	**0**	0.0804(1)	**1**	1.07(2)
O1 at $X1^{eq}$	8*g*	**0**	½	0.0822(1)	**1**	1.07(2)
O2 at $X2^{ap,central}$	2*a*	**0**	**0**	**0**	**1**	1.07(2)
F1 at $X3^{ap,terminal}$	4*e*	**0**	**0**	0.8335(1)	**1**	1.07(2)
F2 at $X4^{int}$	4*d*	½	**0**	¼	**1**	1.07(2)
a [Å]	3.9059(8)		***c*** [Å]	23.372(5)		
R_{wp}(XRD+NPD) [%]	2.98	**GOF(XRD+NPD)**		1.83	**R_{Bragg} [%]**	0.98 (XRD) 2.75 (NPD, bank 1)

Bond-valence sum calculations were used to assign the anions to their respective crystallographic sites. Different possible anion distribution models of oxide and fluoride ions were tested and the results are listed in Table 4-9. The global instability index (GII) can be used to judge the structural stability of the different distributions. [167, 168] The lowest GII and, therefore, the most stable configuration is found when fluoride ions are located at the interstitial site $X4^{int}$ and the terminal apical site $X3^{ap,terminal}$, which is in good agreement with previous studies on RP-type compounds [46]. This configuration is also found to be the most stable in DFT-based calculations. The refined crystal structure of $Sr_3Ti_2O_5F_4$ with the most stable anion configuration is given in Figure 4-15.

Table 4-9: Results of bond-valance sum calculations of $Sr_3Ti_2O_5F_4$ for different oxide and fluoride ion distributions at the anion sites $X1^{eq}$, $X2^{ap,central}$, $X3^{ap,terminal}$ and $X4^{int}$. The anion sites $X1^{eq}$, $X2^{ap,central}$, $X3^{ap,terminal}$ and $X4^{int}$ refer to the equatorial, central apical, terminal apical and interstitial sites, respectively.

Arrangement of oxide and fluoride ions at anion sites $X1^{eq}$, $X2^{ap,central}$, $X3^{ap,terminal}$ and $X4^{int}$	**Bond valance sum**	**Global instability index (GII)**
$O1_{X1}$ – $O2_{X2}$ – $F1_{X3}$ – $F2_{X4}$	O1: 2.0482 O2: 1.6843 F1: 0.9924 F2: 1.1048	0.2541
$O1_{X1}$ – $F1_{X2}$ – $O2_{X3}$ – $O3_{X4}$	O1: 2.0482 O2: 1.3438 O3: 1.1801 F1: 1.4388	0.4811
$O1_{X1}$ – $(0.5O2/0.5F2)_{X2}$ – $O3_{X3}$ – $F4_{X4}$	O1: 2.0482 O2: 1.6843 F2: 1.1048 O3: 1.1801 F1: 1.4388	0.3981
$F1_{X1}$ – $O2_{X2}$ – $(0.5O3/0.5F3)_{X3}$ – $F4_{X4}$	F1: 1.7471 O2: 1.6843 O3: 1.1801 F2: 0.9924 F3: 1.1048	0.4095
$O1_{X1}$ – $(0.5O2/0.5F2)_{X2}$ – $F3_{X3}$ – $O4_{X4}$	F1: 2.0482 O2: 1.6843 F2: 1.4388 F3: 0.9942 O4: 1.3471	0.3575
$F1_{X1}$ – $(0.75O2/0.25F2)_{X2}$ – $O3_{X3}$ – $F4_{X4}$	F1: 1.7471 O2: 1.6843 F2: 1.4388 O3: 1.1801 F1: 1.1048	0.4342
$F1_{X1}$ – $(0.25O2/0.75F2)_{X2}$ – $O3_{X3}$ – $O4_{X4}$	F1: 1.7471 O2: 1.6843 F2: 1.4388 O3: 1.1801 O4: 1.3438	0.4839

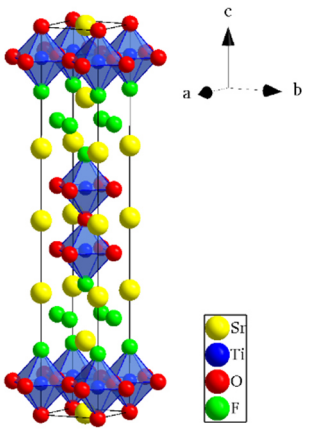

Figure 4-15: Crystal structure of $Sr_3Ti_2O_5F_4$ as determined from the coupled Rietveld analysis. The assignment of anions to different anion sites is based on bond-valance calculations.

4.1.2.2 Topochemical defluorination of $Sr_3Ti_2O_5F_4$

4.1.2.2.1 Analysis of the reduction mechanism of $Sr_3Ti_2O_5F_4$

To study the behaviour of $Sr_3Ti_2O_5F_4$ on the reductive deintercalation of fluoride ions, defluorination reactions between various mixtures of $Sr_3Ti_2O_5F_4$ + x NaH with $0.5 \leq x \leq 4$ and $\Delta x = 0.5$ were performed. The X-ray diffraction data show a complex behaviour with several partially overlapping and/or splitting reflections indicating the formation of various coexisting RP-type phases in the reduction products (Figure 4-16). Over the entire range of x, none of the patterns can be sufficiently accurately described using a single RP-type phase or one with lowered symmetry. This is in strong contrast to the reduction products $Sr_2TiO_3F_2$ + x NaH, for which for x = 1 and 2 nearly phase-pure RP-type phase mixtures are obtained. Due to the broad range of compositions studied, suitable compositions can be determined, for which an individual phase is predominant. In summary, five different phases can be identified, namely four tetragonal phases and one orthorhombic phase. The obtained phases were quantitatively evaluated using the Rietveld method. The evolution of the phase fractions of the different phases is depicted in Figure 4-17 a). In addition, coupled Rietveld refinements of X-ray and neutron powder diffraction data of $Sr_3Ti_2O_5F_4$ + x NaH with x = 2 and 4 were performed to determine suitable structural models of the contained phases (see section 4.1.2.2.1; refined patterns are shown in Figure 4-19 and Figure 6-9).

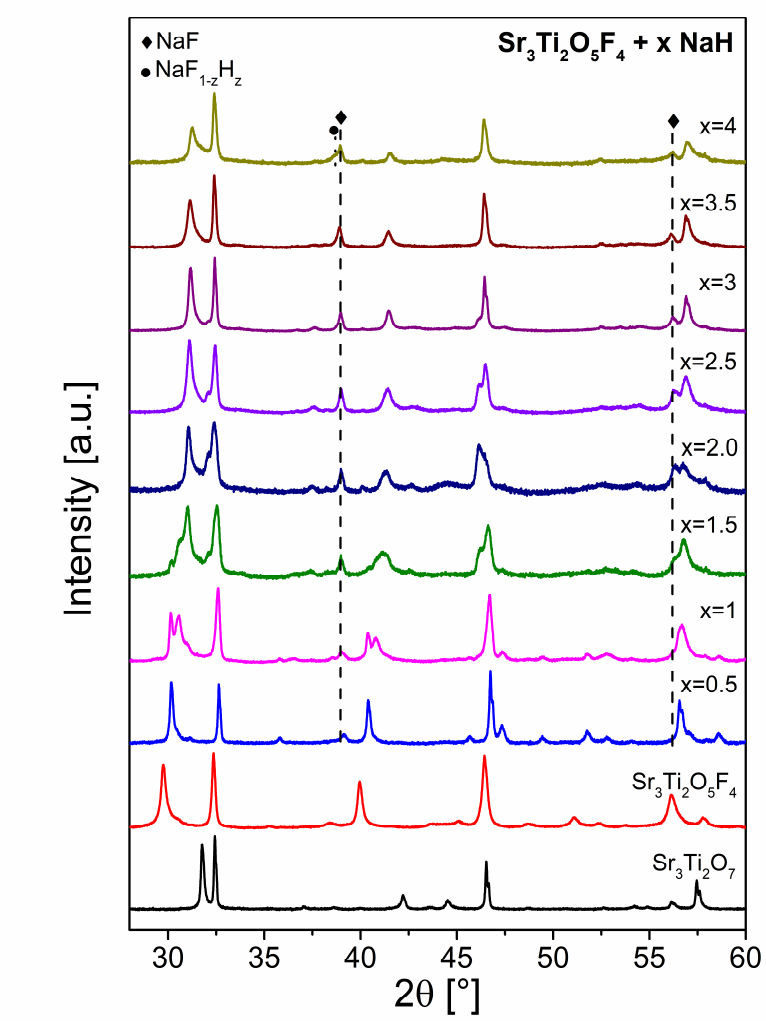

Figure 4-16: X-ray diffraction patterns of $Sr_3Ti_2O_7$, $Sr_3Ti_2O_5F_4$ and the reduction products $Sr_3Ti_2O_5F_4$ + x NaH with 0.5 ≤ x ≤ 4. For the Rietveld refinements of the patterns shown together with an assignment of reflections, the reader is referred to Figure 6-7 in the Appendix.

As for the reduction products $Sr_2TiO_3F_2$ + x NaH, strong shifts of reflections (*hkl*) with $l \neq 0$ can be observed for all phases contained in reduction products $Sr_3Ti_2O_5F_4$ + x NaH in comparison to the parent oxyfluoride $Sr_3Ti_2O_5F_4$. These changes are due to strong decreases of the *c* lattice parameters, resulting in considerable unit cell volume changes (Figure 4-17 b). Higher amounts of added NaH result in higher reductions in the cell volumes. When considering a particular phase, the unit cell volume stays relatively constant, although smaller changes of lattice parameters indicate some degree of compositional flexibility for each phase. Smaller changes are also observed for the lattice parameters *a* and *b,* which undergo a comparatively small expansion, which is related to the formation of low-valent Ti species. [54]

When increasing the amount of reductant, a stronger degree of disorder is also introduced into the obtained RP-type phases. This can be best assessed based on reflections (*hkl*) with $l \neq 0$ of the tetragonal #3 and #4 phases, which show, in comparison to the tetragonal #1 and #2 phases and the orthorhombic phase, significantly increased anisotropic broadening. This broadening is commonly observed for the reduction of RP-type compounds [94], indicating the flexibility of the lattice to adopt compositional variations in a broader range. This also implies that the phases obtained in the reduction products with lower values of x, i.e., the tetragonal #1 and #2 phases as well as the orthorhombic phase, are highly ordered.

After the reactions, NaF (Figure 4-17 c) is present in all reaction products. The measured and theoretically predicted amounts of NaF are in good agreement. This also confirms that the multi-phase model, which was used to describe the reflections of the RP-type phases, gives an excellent approximation of the relative amount of each phase fraction. Furthermore, it indicates a negligible degree of decomposition on reduction showing the stability of the phases upon defluorination. Small amounts of the mixed crystals $NaF_{1-z}H_z$ can be identified as a shoulder next to the NaF reflection at ~ 38.8° in the XRD pattern of $Sr_3Ti_2O_5F_4$ + x NaH with x = 4. Approximately 13.9 wt% of $NaF_{0.93}H_{0.07}$ and 12.1 wt% of $NaF_{0.8}H_{0.2}$ are present. For $Sr_3Ti_2O_5F_4$ + x NaH with x = 2, while no shoulder next to the NaF reflections are visible in the XRD pattern, the neutron diffraction suggests the formation 8.2 wt% of $NaF_{0.91}H_{0.09}$ in the reduction product. When comparing SEM micrographs of $Sr_3Ti_2O_7$ and $Sr_3Ti_2O_5F_4$ to the reduction products $Sr_3Ti_2O_5F_4$ + x NaH with x = 2 and 4 (Figure 4-18), it appears that the particles of the reduced particles are covered by a surface layer. Surface-sensitive XPS measurements (see section 4.1.2.4) suggest that this layer consists of NaF since very high Na and F signals are observed. This is also in agreement with the finding that the layer can be removed upon washing of the reduction product $Sr_2TiO_3F_2$ + x NaH with x = 2 (see section 4.1.1.2.1).

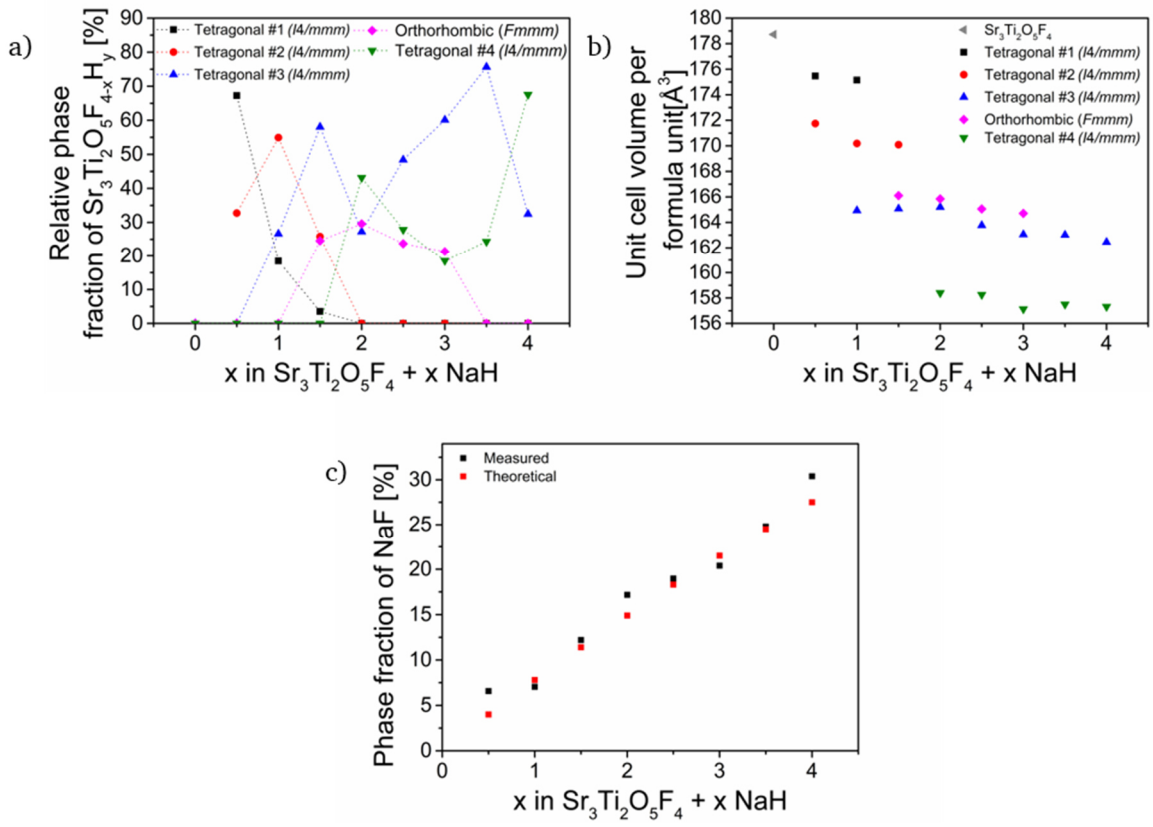

Figure 4-17: Relative phase fractions (a) and unit cell volumes per formula unit (b) of $Sr_3Ti_2O_5F_4$ and the reduced RP-type phases in the reduction product $Sr_3Ti_2O_5F_4$ + x NaH with $0.5 \leq x \leq 4$ as a function of x. The relative phase fractions were calculated neglecting other side and decomposition phases, e.g. NaF or SrF_2. Measured phase fraction of NaF (c) in the reduction products $Sr_3Ti_2O_5F_4$ + x NaH with $0.5 \leq x \leq 4$ as a function of x. Also given are the theoretically expected values of NaF calculated assuming full conversion of the added NaH to NaF.

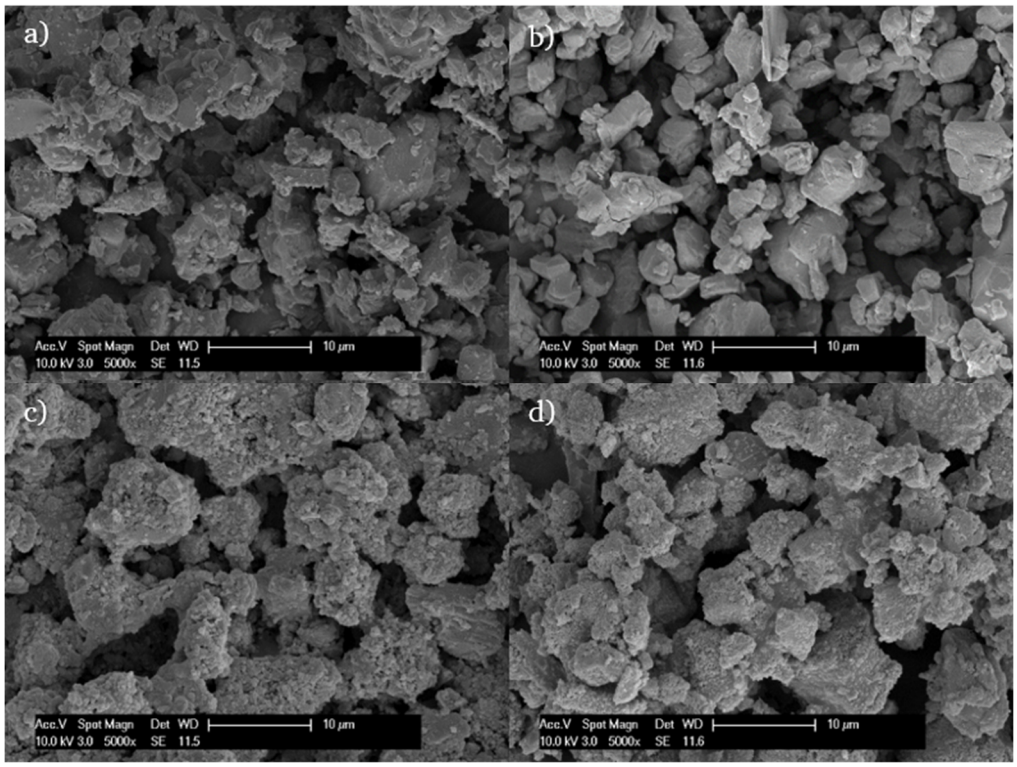

Figure 4-18: Scanning electron micrographs of $Sr_3Ti_2O_7$ (a), $Sr_3Ti2O_5F_4$ (b), the unwashed reaction product of $Sr_3Ti2O_5F_4$ + x NaH with x = 2 (c) and x = 4 (d) with rough porous layers of NaF on top of particles.

Elemental analysis confirms again the presence of hydride ions within the reaction products and the formation of compounds with formal compositions of $Sr_3Ti_2O_5F_2H_{0.42(2)}$ + 2 NaF for x = 2 and $Sr_3Ti_2O_5H_{1.26(10)}$ + 4 NaF for x = 4 can be derived. As discussed, a small amount of the hydride ions is located in $NaF_{1-z}H_z$. Since the presence of other hydride-containing side and decomposition products or substantial amorphisation, leading to the formation of amorphous hydride-containing products can be ruled out, the most plausible host for a major part of the hydride ions are the reduced RP-type phases. However, because two-phase mixtures of RP-type oxyfluoride hydrides are found for values of x = 2 and 4, the exact hydride content of each individual RP-type phase cannot be determined.

Regardless of this, the overall degree of fluoride-hydride substitution in comparison to the reductive defluorination under formation of H_2 is lower compared to those of $Sr_2TiO_3FH_{0.48(1)}$ and $Sr_2TiO_3H_{1.48(10)}$ contained in the reduction products $Sr_2TiO_3F_2$ + x NaH with x = 1 and 2 (see section 4.1.1.2.1). For the reductions of both n = 1 and n = 2 RP-type strontium titanium oxyfluorides, the reductive defluorination is the predominant reaction mechanism for low NaH equivalents, and fluoride-hydride substitution becomes dominant for increasing amounts of NaH.

Re-oxidation experiments on $Sr_3Ti_2O_5F_4$ + x NaH with x = 2 and 4 were performed, which can also serve to confirm the successful defluorination. On exposure of the compounds to air at elevated temperatures, phase mixtures containing several re-oxidised phases as well as side and decomposition products (NaF, increased amounts of $SrTiO_3$, TiO_2 and SrF_2) are found (Figure 6-5). The lattice parameters of the re-oxidised phases have *c* lattice parameters between those of $Sr_3Ti_2O_7$ and $Sr_3Ti_2O_5F_4$, showing that a certain oxide-fluoride disorder is present in the phases. The fact that $Sr_3Ti_2O_7$ is not formed on re-oxidation suggests that a complete defluorination of $Sr_3Ti_2O_5F_4$ to $Sr_3Ti_2O_5$ has not taken place for the highest amount

of NaH added, which is in agreement with the observation of $NaF_{1-z}H_z$. However, the phase fractions of the phases with smaller *c* lattice parameters increase considerably when the re-oxidation is performed on the higher-reduced phases, which contain less fluoride. Overall, the phase fractions and the lattice parameters of the re-oxidised oxyfluorides are in good agreement with the assumed degree of defluorination.

4.1.2.2.2 Coupled Rietveld analysis of the reduction products

Structural analyses of the reduction products $Sr_3Ti_2O_5F_4$ + x NaH with x = 2 and 4 were performed via coupled analysis of XRD and NPD data. The refined patterns of $Sr_3Ti_2O_5F_4$ + x NaH with x = 2 and 4 are shown in Figure 4-19 and Figure 6-9, respectively.

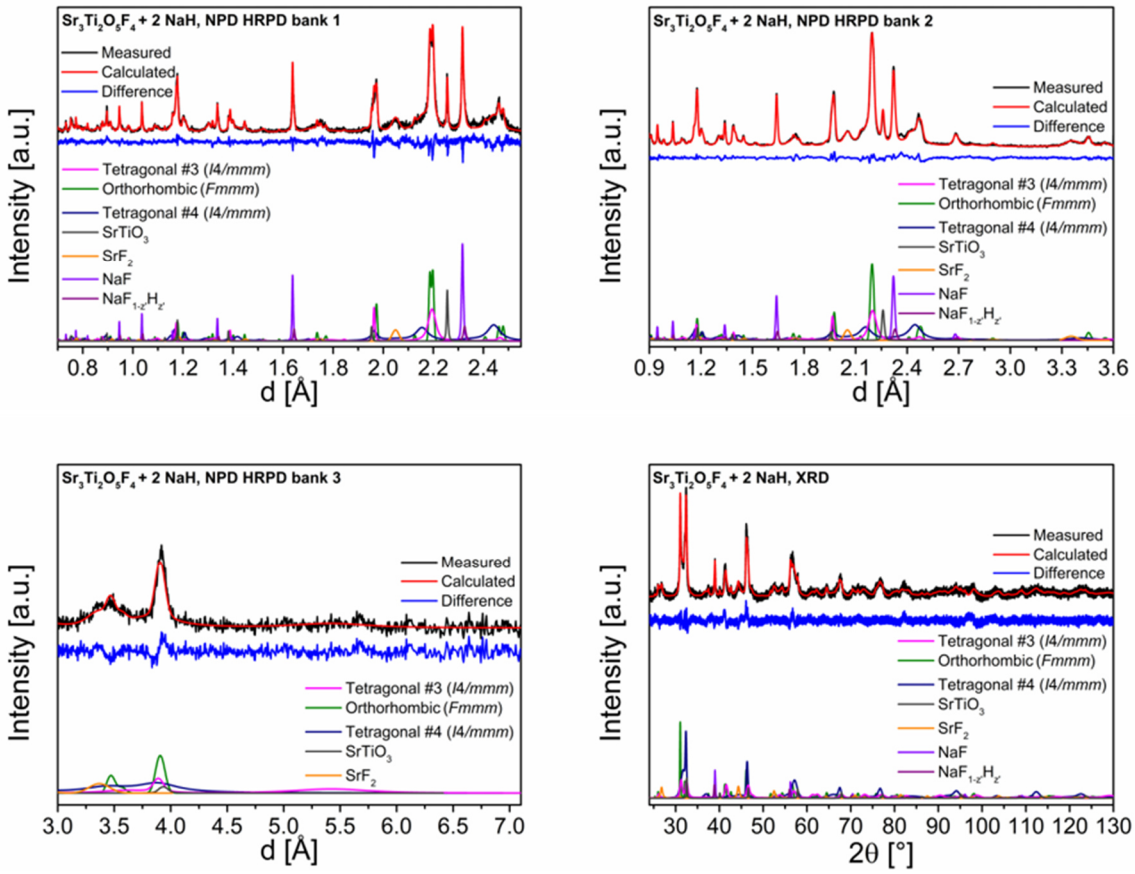

Figure 4-19: Coupled Rietveld refinements of the reduction product of $Sr_3Ti_2O_5F_4$ + x NaH with x = 2 of NPD HRPD banks 1-3 and XRD data.

In $Sr_3Ti_2O_5F_4$ + x NaH with x = 2, three RP-type phases, i.e., two tetragonal phases (called tetragonal #3 and #4) and an orthorhombic phase are found. The highest phase fraction of the latter phase of the whole series is found within this reduction product. In $Sr_3Ti_2O_5F_4$ + x NaH with x = 4, only the tetragonal #3 and #4 phases are present. Since only multi-phase mixtures were obtained within this study, it is not possible to assign an unambiguous anion contents to each phase. Moreover, it is also not possible to distinguish between hydride and oxide/fluoride ions at sites, which contain anion vacancies in addition (see section 2.4.1.2).

A very detailed structural analysis of the tetragonal phases is not possible due to a strong correlation of the parameters. The intensity patterns can be accurately described with

structural models of the aristotype n = 2 RP structure with *I4/mmm* symmetry. The analysis of this phase, especially of the tetragonal #4 phase, is further impeded by strong anisotropic reflection broadening. This is indicative for the presence of a distribution of multiple phases with slightly varying *c* lattice parameters. Regardless of these implications, the structural refinements indicate that considerable amounts of vacancies are present at the interstitial site $X4^{int}$ of both phases and on the terminal apical site $X3^{ap,terminal}$ of the tetragonal phase #4. Moreover, decreasing occupation factors of these sites in $Sr_3Ti_2O_5F_4$ + x NaH with x = 4 as compared to x = 2 are plausible, considering that higher degrees of defluorination should be expected when using higher NaH amounts. Structural parameters of the tetragonal #3 phase are given in the Table 6-2.

For the patterns of $Sr_3Ti_2O_5F_4$ + x NaH with x = 2, some of the sharper reflections, e.g. $(116)_{I4/mmm}$ or $(110)_{I4/mmm}$ at d values of ~ 2.25 and 2.76 Å, respectively, show reflection splitting suggesting the presence of a phase, which has undergone a symmetry lowering to an orthorhombic symmetry. A model within the *translationengleiche* supgroup *Fmmm* with a cell size of $\sqrt{2} \times \sqrt{2} \times 1$ of the aristotype structure allows for a good fitting of the reflections. Further loss of translational symmetry is not indicated due to the absence of superstructure reflections. The neutron diffraction data can, moreover, give valuable information about the approximate structure and composition of the anion sublattice, since, while oxide and fluoride cannot be distinguished from each other, they can be differentiated from anion vacancies. The equatorial ($X1^{eq}$) and central apical ($X2^{ap,central}$) sites are found to be fully occupied by oxide and/or fluoride within errors and their occupations was, therefore, fixed to 100 %. The occupation factors of the terminal apical ($X3^{ap,terminal}$) and the interstitial ($X4^{int}$) sites, on the other hand, are significantly decreased due to the extraction of fluoride upon defluorination, resulting in a formal composition of the orthorhombic phase of $Sr_3Ti_2O_5F_{1.86}H_y$. It was not possible to assign the residual hydride ions, as determined from elemental analysis (see 4.1.2.2.1), to the $X3^{ap,terminal}$ or $X4^{int}$ site. The refined structural parameters and bond distances are given in Table 4-10 and Table 4-11, respectively. The crystal structure of the orthorhombic phase is shown in Figure 4-20. The assignment of the oxide and fluoride to the different anion sites was done based on the most stable anion configuration of $Sr_3Ti_2O_5F_4$ obtained from bond-valence sum calculations (see section 4.1.2.1.1), supported by the fact that, due to fluoride extraction, only the terminal apical ($X3^{ap,terminal}$) and interstitial ($X4^{int}$) anion sites are not fully occupied.

Table 4-10: Structural parameters of the reduced phase $Sr_3Ti_2O_5F_{1.86}H_y$ (space group: *Fmmm*) derived from coupled Rietveld analysis of XRD and NPD data of the reduction product of $Sr_3Ti_2O_5F_4$ + x NaH with x = 2. The anion sites $X1^{eq}$, $X2^{ap,central}$, $X3^{ap,terminal}$ and $X4^{int}$ refer to the equatorial, central apical, terminal apical and interstitial sites, respectively.

Atom	**Wyckoff position**	**x**	**y**	**z**	**Occupany**	**B [Å²]**
Sr1	4*b*	**0**	**0**	½	**1**	0.87(6)
Sr2	8*i*	**0**	**0**	0.6818(2)	**1**	0.87(6)
Ti1	8*i*	**0**	**0**	0.9147(4)	**1**	0.87(6)
O1 at $X1^{eq}$	16*j*	¼	¼	0.4024(2)	**1**	0.87(6)
O2 at $X2^{ap,central}$	4*a*	**0**	**0**	**0**	**1**	0.87(6)
F1 at $X3^{ap,terminal}$	8*i*	**0**	**0**	0.1721(9)	0.30(1)	0.87(6)
F2 at $X4^{int}$	8*f*	¼	¼	¼	0.63(2)	0.87(6)
***a* [Å]**	5.6083(4)	***b* [Å]**		5.5596(9)	***c* [Å]**	21.275(3)
R_{wp} (XRD+NPD) [%]	3.09	**GOF(XRD+NPD)**		1.71	**R_{Bragg} [%]**	0.99 (XRD) 3.61 (NPD, bank 1)

Table 4-11: Bond distances of $Sr_3Ti_2O_5F_4$ the reduced phase $Sr_3Ti_2O_5F_{1.86}H_y$. The anion sites $X1^{eq}$, $X2^{ap,central}$, $X3^{ap,terminal}$ and $X4^{int}$ refer to the equatorial, central apical, terminal apical and interstitial sites, respectively.

	Bond distance [Å]	
Bond	**$Sr_3Ti_2O_5F_4$**	**$Sr_3Ti_2O_5F_{1.86}H_y$**
Sr1-O1 at $X1^{eq}$	2.750(2) [8x]	2.865(3) [8x]
Sr1-O2 at $X2^{ap,central}$	2.7723(3) [4x]	2.8042(2) [4x]
Sr2-O1 at $X1^{eq}$	3.130(2) [4x]	2.666(4) [4x]
Sr2-F1 at $X3^{ap,terminal}$	2.8105(6) [4x]	2.787(2) [~1.2x] 2.812(2) [~1.2x]
Sr2-F2 at $X4^{int}$	2.4666(8) [4x]	2.450(3) [~2.52x]
Ti-O1 at $X1^{eq}$	1.9608(4) [4x]	1.992(1) [4x]
Ti-O2 at $X2^{ap,central}$	1.886(2) [1x]	1.815(9) [1x]
Ti-F1 at $X3^{ap,terminal}$	2.020(3) [4x]	1.897(5) [~1.2x]

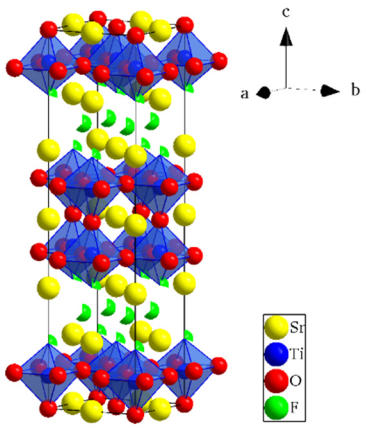

Figure 4-20: Crystal structure of the reduced phase $Sr_3Ti_2O_5F_{1.86}H_y$ as determined from the coupled Rietveld analysis. The assignment of anions to different anion sites is based on bond-valance calculations.

4.1.2.3 Magnetisation study of $Sr_3Ti_2O_5F_4$ and the reduction products

The ZFC M(T) curves of $Sr_3Ti_2O_5F_4$ and reduction reaction products $Sr_3Ti_2O_5F_4$ + x NaH with x = 2 and 4, respectively, are shown in Figure 4-21. $Sr_3Ti_2O_5F_4$ is diamagnetic in the whole temperature range. This is due to the presence of diamagnetic Ti^{4+} cations with d^0 configuration only. In contrast to this, the reduction products show predominantly paramagnetic behaviour, reflecting the presence of unpaired electrons (d^1 and d^2 electron configurations of Ti^{3+} and Ti^{2+}, respectively) and, thus, confirming a successful defluorination and reduction of the Ti oxidation state.

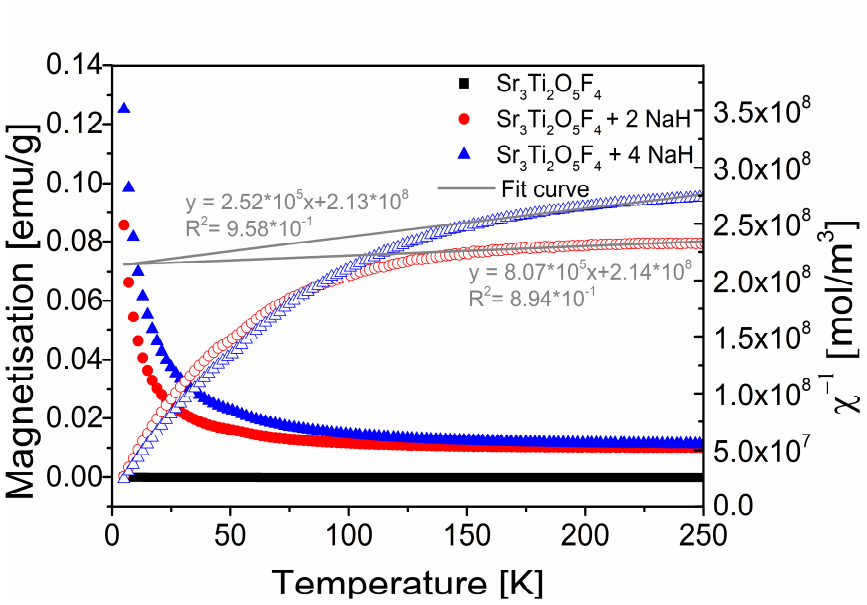

Figure 4-21: ZFC M(T) (closed symbols) and χ^{-1}(T) (open symbols) curves of $Sr_3Ti_2O_5F_4$ and the reduction products of $Sr_3Ti_2O_5F_4$ + x NaH with x = 2 and 4 measured at μ_0 = 1 T. The fitting curves of the Curie-Weiss fits, the corresponding linear functions and the coefficients of determination are also given. The curves are corrected from the diamagnetic contributions of the present phases and the gelatine capsules and straws used for the measurements.

As is discussed in section 4.1.1.3, different fitting strategies can be applied to describe the temperature dependency of the magnetisation of reduced Ti-containing compounds and to correct for diamagnetic and/or other temperature-independent magnetic contributions possibly causing a deviation from ideal paramagnetic behaviour. After the correction of the measured data from diamagnetic contributions, nearly linear regions of the χ^{-1}(T) curves of the reduction products can be found in the limited temperature range between 150 and 250 K. Curie-Weis fits in this range (Figure 4-21) result in spin-only magnetic moments of ~ 2.01 and 1.12 μ_B for $Sr_3Ti_2O_5F_4$ + x NaH with x = 2 and 4, respectively. These moments correspond to ~ 1.25 and 0.50 unpaired electrons. The correlating oxidation states differ strongly from the expected oxidation states based on the formal compositions of $Sr_3Ti_2O_5F_2H_{0.42}$ and $Sr_3Ti_2O_5H_{1.26}$ of the RP-type phases in the reduction products determined in section 4.1.2.2.1. Additionally, it would be expected that the oxidation state of the reduction product, for which a higher amount of NaH was used, would be lower. Modified Curie-Weiss fits over the whole temperature range reveal considerable smaller spin-only moments of ~ 0.24 and 0.26 μ_B for $Sr_3Ti_2O_5F_4$ + x NaH with x = 2 and 4, respectively. Therefore, an unambiguous interpretation of the obtained moments and the corresponding oxidation states is not possible and an ideally paramagnetic behaviour with spin-only moments only can be excluded.

4.1.2.4 X-ray photoelectron spectroscopy $Sr_3Ti_2O_5F_4$ and the reduction products

Surface sensitive XPS measurements of $Sr_3Ti_2O_5F_4$ and the reduction products $Sr_3Ti_2O_5F_4$ + x NaH with x = 2 and 4 allow to draw conclusions about the Ti oxidation states on the surface of the particles. The Ti $2p_{3/2}$ spectra are given in Figure 4-22. The poor signal-to-noise ratio of the Ti $2p_{3/2}$ spectra of the reduction products in comparison to the spectrum of $Sr_3Ti_2O_5F_4$ is due to a layer of NaF, which is formed upon defluorination on the surface of the particles of the RP-type phases. The presence of this layer can be confirmed by the high

intensities of the Na 1*s* and F 1*s* spectra (Figure 6-10), which is also in agreement with the obtained SEM images (Figure 4-18).

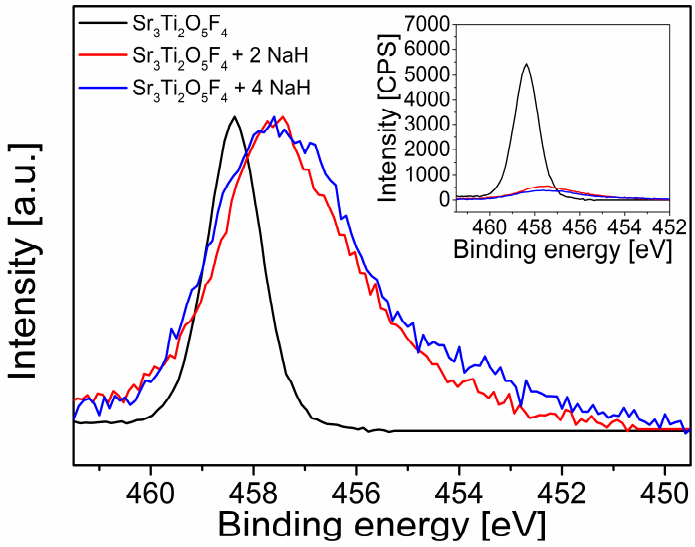

Figure 4-22: Ti 2$p_{3/2}$ XPS spectra of $Sr_3Ti_2O_5F_4$ and the reduction products $Sr_3Ti_2O_5F_4$ + x NaH with x = 2 and 4. Due to the release of hydrogen on the particle surface of the bulk materials a considerable reduction leading to the formation of Ti^{3+} and Ti^{2+} species is found.

The spectrum of $Sr_3Ti_2O_5F_4$ features a peak at ~ 458.4 eV with a FWHM of ~ 1.25 eV, which is typical for Ti^{4+} and suggests the existence of this oxidation state only. [245] In the spectra of the reduced compounds, considerable shifts towards lower binding energies and broader signals are observed. Characteristic binding energies of Ti^{3+} and Ti^{2+} containing oxides have been reported at ~ 457.7 eV and ~ 454.7 eV [235], respectively, corresponding well to the found signals. Therefore, it can be concluded that a strong reduction with the co-existence of different oxidation states has taken place on the surface of the particles of the reduced RP-type phases. A precise quantification of the intensities of the different signals is hindered by the poor quality of the spectra. However, the strongest reduction seems to have occurred in $Sr_3Ti_2O_5F_4$ + 4 NaH, which is indicated by the extended tail to lower binding energies.

4.1.2.5 Summary

The topochemical fluorination of the n = 2 RP-type oxide $Sr_3Ti_2O_7$ using stoichiometric amounts of PVDF as fluorination reagent resulted in the formation of $Sr_3Ti_2O_5F_4$, suggesting that the reaction proceeds via a non-oxidative substitution and insertion process, in which two oxide ions are replaced by four fluoride ions. As determined via a coupled Rietveld analysis of X-ray and neutron powder diffraction data, the fluorination results in a full occupation of all anion sites and the *I*4/*mmm* aristotype structure of the oxide is maintained in the fluorinated compound. The assignment of oxide and fluoride ions to the fully occupied anion sites was achieved using bond-valance sum calculations, further confirmed by DFT-based calculations. The most stable configuration is found when fluoride ions are located at the interstitial and terminal apical sites, while the equatorial and central apical site are occupied by oxide ions. Furthermore, it was found, that the fluorination of $Sr_3Ti_2O_7$ leads to a higher degree of decomposition in comparison to the fluorination of Sr_2TiO_4.

The reduction of $Sr_3Ti_2O_5F_4$ according to $Sr_3Ti_2O_5F_4$ + x NaH with $0 \leq x \leq 4$ ($\Delta x = 0.5$) performed at 300 °C was found to take place in a similar fashion as the reduction of Sr_2TiO_4 via a reductive defluorination and a fluoride-hydride substitution. In comparison to the reduction of Sr_2TiO_4, the fluoride-hydride substitution is less pronounced, which should in principle enable the synthesis of phases with lower Ti oxidation states. After the reactions, for all values of x, phase mixtures of various reduced RP-type phases were found. This indicates a more complex reduction behaviour with either a variety of phases of similar stability or limited reaction kinetics, hampering the compositional equilibration of the reduced phases in the reduction products. Considerable unit cell volume reductions, primarily due to decreases in the *c* lattice parameters of the reduced phases, were observed compared to the parent oxyfluoride ($c \approx 23.4$ Å). The crystal structures of the reduced phases were investigated via coupled Rietveld refinements of X-ray and neutron diffraction data of the reduction products. For $Sr_3Ti_2O_5F_{1.86}H_y$ ($c \approx 21.3$ Å) obtained in the reduction product with $x = 2$, in addition to the decrease in cell volume, a symmetry reduction to *Fmmm* was observed. For higher degrees of defluorination, phases with *I4/mmm* symmetry and strong anisotropic broadening were observed. No considerable decomposition or amorphisation reaction were found to take place upon reduction. The formation of low-valent Ti was confirmed by magnetic and X-ray photoelectron spectroscopy measurements. A transition from a diamagnetic to a paramagnetic states was found upon the defluorination of $Sr_3Ti_2O_5F_4$, confirming the presence of unpaired electrons and, therefore, the successful defluorination of the RP-type phases in the reduction products.

4.1.3 Topochemical fluorination of La_2NiO_{4+d} to $La_2NiO_3F_2$ and its defluorination

4.1.3.1 Topochemical fluorination of La_2NiO_{4+d} to $La_2NiO_3F_2$

4.1.3.1.1 Analysis of the fluorination mechanism of La_2NiO_{4+d}

The fluorination behaviour of La_2NiO_{4+d} was studied for a variety of different molar ratios of La_2NiO_{4+d}:CH_2CF_2 (PVDF) (Figure 4-23). A nearly single-phase product is obtained using a stoichiometric ratio of 1:1 (only a marginal excess of ~ 2.5 % PVDF was used). For lower fluorine contents (molar ratio of 1:0.5), a two-phase mixture with a partially fluorinated phase and the phase obtained when using the stoichiometric ratio of 1:1 is found. For higher amounts of PVDF (molar ratios of 1:1.5 and 1:2), again the phase obtained when using the stoichiometric ratio of 1:1 and increasing degrees of decomposition, leading to the formation of LaF_3, is observed. The phase fraction of LaF_3 increases with increasing amounts of PVDF. Additionally, amorphisation takes place.

The found partially fluorinated phase has been reported previously by Hancock [246]. It has been found that the topochemical fluorination with 0.4 molar equivalents of PVDF results in the formation of a nearly phase-pure sample with orthorhombic *Fmmm* symmetry (a = 5.36781(7) Å, b = 5.60196(8) Å, c = 12.6887(2) Å). In accordance to what is observed for a ratio of 1:0.5 in the current study, a ratio of 1:0.6 has resulted in the formation of a phase mixture with a lower and higher fluorinated phase. However, in the previous study, it has not been possible to synthesise phase-pure samples of the higher fluorinated phase since higher levels of PVDF (> 0.6 molar equivalents of PVDF) have led to large LaF_3 impurities.

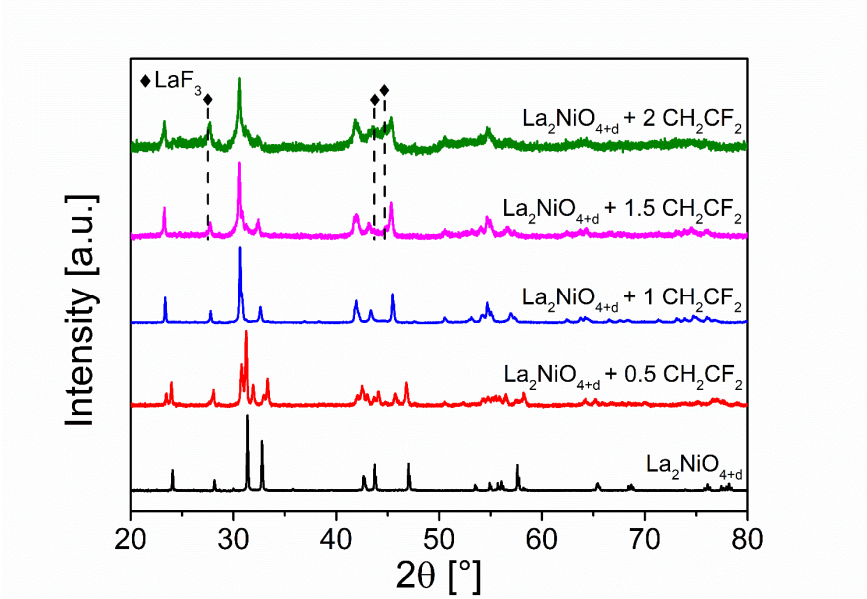

Figure 4-23: X-ray diffraction patterns of La_2NiO_{4+d} and La_2NiO_{4+d} fluorinated with different amounts of PVDF $(CH_2CF_2)_n$ in molar ratios of La_2NiO_{4+d}:CH_2CF_2 of 1:0.5, 1:1, 1:1.5 and 1:2.

To determine the composition of the product obtained at a ratio of 1:1, the La_2NiO_{4+d} and the fluorination product were further investigated using iodometric titration and XPS (Figure 4-24) to determine the bulk and surface oxidations state of Ni, respectively. The titration indicates an average Ni oxidation state of Ni^{2+} for both compounds (+2.10(1) for La_2NiO_{4+d} (d ≈ 0.05) and +2.06(1) for the fluorinated compound). Thus, a small reduction of the oxidation state is found. This reductive character of the fluorination has been observed

previously for PVDF-based fluorination reactions even in air, e.g. for the synthesis of $SrFeO_2F$ from $SrFeO_{3-d}$. [247, 248] For the investigation of the surface oxidation states via XPS, the Ni 3*p* peak was chosen, since the higher-intensity peaks of the Ni $2p_{3/2}$ and La $3d_{3/2}$ overlap; it should be noted that the Ni $3p_{1/2}$ and $3p_{3/2}$ are in general not well resolved. [207, 249] The found signals at ~ 67.7 and 67.0 eV can be assigned to the 3*p* signal of Ni^{2+} of La_2NiO_{4+d} and of the fluorinated compound, respectively. [250-252] This is also in agreement with a reduction of the oxidation state of the fluorinated compound as obtained from titration. In combination with the determined anion content derived from the Rietveld analysis of diffraction data (see section 4.1.3.1.2), it can be concluded that the fluorinated compound has an approximate composition of $La_2NiO_3F_2$ (more precisely $La_2NiO_{3.06}F_{1.94}$). This corresponds to a nearly stoichiometric incorporation of fluoride ions from the polymer into the RP-type oxide under the substitution of one oxide ion by two fluoride ions. Assuming the same reaction mechanism for the fluorination with lower amounts of PVDF, oxyfluorides with compositions $La_2NiO_{3+d/2}F_{2-d}$ should be formed.

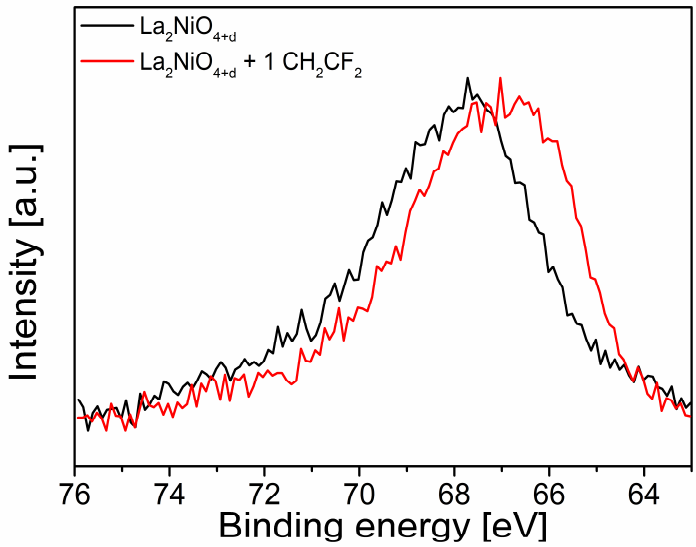

Figure 4-24: Ni 3*p* XPS spectra of La_2NiO_{4+d} and La_2NiO_{4+d} fluorinated with PVDF in a molar ratio of 1:1.

4.1.3.1.2 Coupled Rietveld analysis of $La_2NiO_3F_2$

$LaNiO_{4+d}$ crystallizes in the tetragonal aristotype structure of n = 1 RP-type phases with space group *I4/mmm* (a = 3.86279(5) Å and c = 12.6746(2) Å), in good agreement with previous work. [253] Depending on the synthesis batch of the parent oxide, either phase pure samples are formed or additionally a small amount of $La_{0.5}Zr_{0.5}O_{1.75}$ (~ 1 wt%) is found. Presumably, the impurity phase is formed due to the use of a ZrO_2 grinding jar and balls during the ball milling process. The phase fraction of this impurity phase, if found in La_2NiO_{4+d} and $La_2NiO_3F_2$, remains constant in the defluorinated products. When comparing the XRD patterns of La_2NiO_{4+d} to $La_2NiO_3F_2$ (Figure 4-25), significant changes can be observed. The pattern of $La_2NiO_3F_2$ shows a clear splitting of some reflections (e.g. $(011)_{I4/mmm}$ reflection at a d-spacing of ~ 2.92 Å), indicating symmetry lowering to an orthorhombic symmetry.

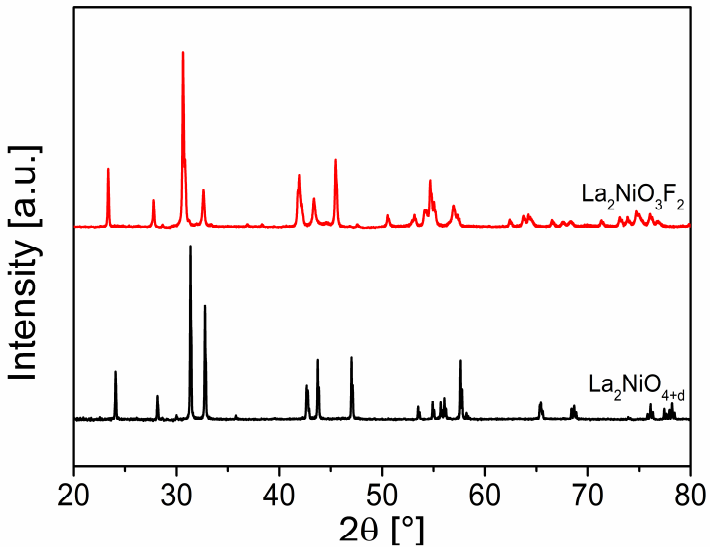

Figure 4-25: X-ray diffraction patterns of La_2NiO_{4+d} to $La_2NiO_3F_2$.

The structural refinement of $La_2NiO_3F_2$ was performed via a coupled Rietveld analysis of XRD and NPD data (Figure 4-26). Fits of the patterns were attempted using a face-centred unit cell (space group: *Fmmm*) with a size $\sqrt{2} \times \sqrt{2} \times 1$ of the parent unit cell with *I*4/*mmm* symmetry, which allows fitting of the main reflections. In contrast to what was found previously for fluorinations of other RP-type compounds, no strong increase of the *c* axis is observed and the orthorhombic distortion results mainly form a strong straining within the *ab* plane with axis lengths of $a \approx 5.79$ Å and $b \approx 5.49$ Å. This orthorhombic straining is one of the highest, if not the highest, straining found for anion excess RP-type compounds A_2BX_{4+y}.

Further loss of translational symmetry is indicated from the presence of superstructure reflections. The patterns could be best fitted using a structural model with space group *Cccm* ($a = 12.8364(3)$ Å, $b = 5.7940(2)$ Å, $c = 5.4871(2)$ Å). The corresponding symmetry tree is shown in Figure 4-27. Other *klassengleiche* subgroups of *Fmmm* (e.g. different settings of *Cmce*) were also examined but lead to significantly worse fits due to the systematic absence of certain reflections (e.g. $(130)_{Cccm}$, $(510)_{Cccm}$, $(221)_{Cccm}$ and $(112)_{Cccm}$, at d values of ~ 1.91 Å, ~ 2.35 Å, ~ 2.38 Å and ~ 2.43 Å, respectively).

The analysis of the neutron diffraction data facilitates the detailed determination of the structure and composition of the anion sublattice. Both the equatorial ($X1^{eq}$) and apical ($X2^{ap}$) anion sites, which are fully occupied in the tetragonal precursor oxide La_2NiO_{4+d}, are also fully occupied in $La_2NiO_3F_2$. The symmetry reduction from *I*4/*mmm* to *Cccm* results in a splitting of the interlayer anion site into two independent crystallographic sites $X3a^{int}$ and $X3b^{int}$ (Figure 4-27). Only the $X3b^{int}$ (4*b*) site is fully occupied with anion species, while the $X3a^{int}$ (4*a*) site is not occupied. From this, an overall composition of La_2NiX_5 can be derived for the fluorinated compound. Taking the presence of single-valent Ni^{2+} (see section 4.1.3.1.1) into account, the composition $La_2NiO_3F_2$ can be derived. The refined structural parameters are listed in Table 4-12. Bond distances are given in Table 4-18.

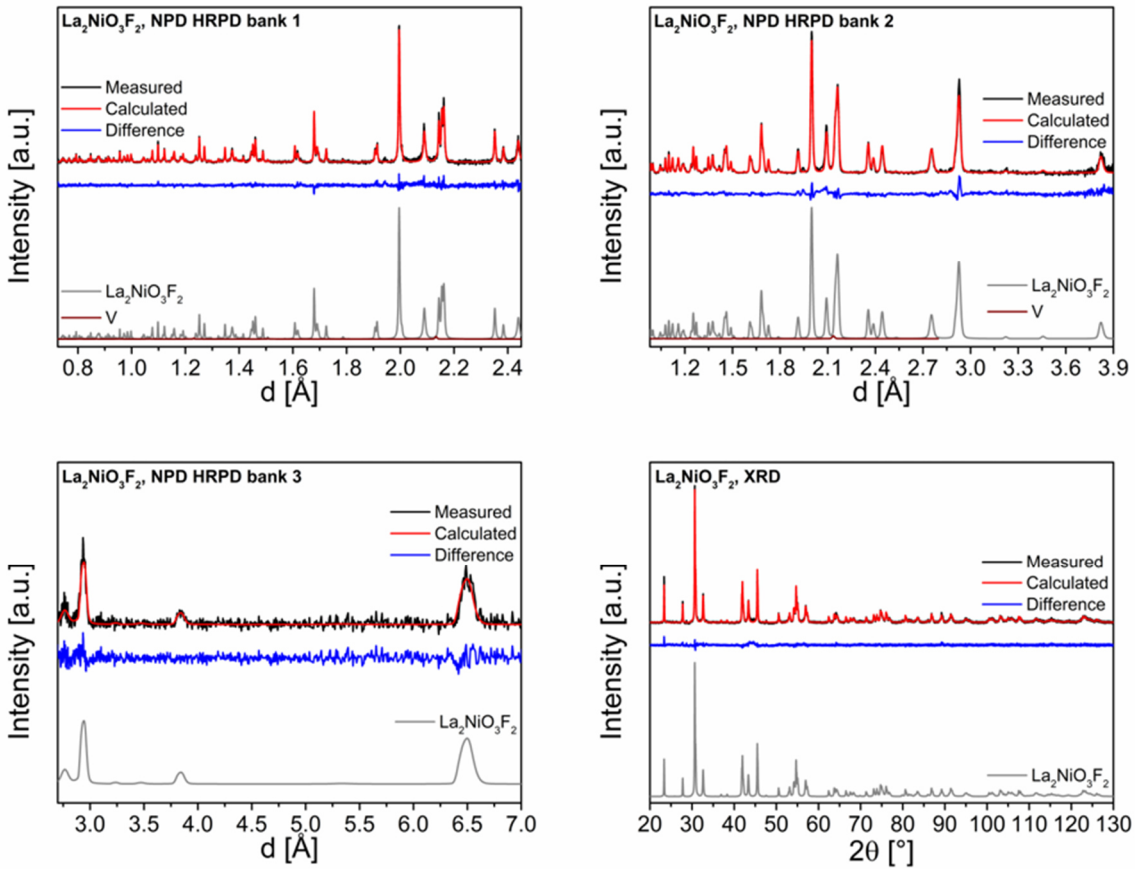

Figure 4-26: Coupled Rietveld refinements of $La_2NiO_3F_2$ of NPD HRPD banks 1-3 and XRD data.

Tetragonal
I4/mmm (139)
$a_1 \approx 3.99$ Å
$c_1 \approx 12.84$ Å

*t*2: $a_2 = a_1 - b_1$, $b_2 = a_1 + b_1$, $c_2 = c_1$

Orthorhombic
Fmmm (69)
$a_2 \approx 5.79$ Å
$b_2 \approx 5.49$ Å
$c_2 \approx 12.84$ Å

k2: $a_3 = c_2$, $b_3 = a_2$, $c_3 = b_2$

Orthorhombic
Cccm (66)
$a_3 \approx 12.84$ Å
$b_3 \approx 5.79$ Å
$c_3 \approx 5.49$ Å

		equitorial	apical	interstitial
La1: 4*e*	Ni1: 2*a*	X1^{eq}: 4*c*	X2^{ap}: 4*e*	X3^{int}: 4*d*
0 0 z $z \sim 0.61$	0 0 0	0 ½ 0	0 0 *z* $z \sim 0.84$	0 ½ ¼

La1: 8*i*	Ni1: 4*a*	X1^{eq}: 8*e*	X2^{ap}: 8*i*	X3^{int}: 8*f*
0 0 z $z \sim 0.61$	0 0 0	¼ ¼ 0	0 0 *z* $z \sim 0.84$	¼ ¼ ¼

La1: 8*l*	Ni1: 4*e*	X1^{eq}: 8*g*	X2^{eq}: 8*l*	X3^{int}a: 4a	X3^{int}b: 4*b*
x y 0 $x \sim 0.14$ $y \sim 0.75$	¼ ¼ 0	x 0 ¼ $x \sim 0.25$	x y 0 $x \sim 0.91$ $y \sim 0.75$	0 0 ¼	0 ½ ¼

Figure 4-27: Symmetry tree for the symmetry reduction from *I*4/*mmm* to *Cccm*. The different anion sites X1^{eq}, X2^{ap} and X3^{int} refer to the equatorial, apical and interstitial sites, respectively.

Table 4-12: Structural parameters of $La_2NiO_3F_2$ (space group: *Cccm*) derived from coupled Rietveld analysis of XRD and NPD data. The anion sites $X1^{eq}$, $X2^{ap}$ and $X3^{int}$ refer to the equatorial, central apical, terminal apical and interstitial sites, respectively.

Atom	**Wyckoff position**	**x**	**y**	**z**	**Occupany**	**B [Å²]**
La1	8*l*	0.38826(4)	0.7458(2)	**0**	**1**	1.05(3)
Ni1	4*e*	¼	¼	**0**	**1**	1.61(4)
O1 at $X1^{eq}$	8*g*	0.2673(2)	**0**	¼	**1**	1.26(4)
F1 at $X2^{ap}$	8*l*	0.5869(2)	0.6576(3)	**0**	**1**	2.34(6)
$X3a^{int}$	4*a*	**0**	**0**	¼	**0**	1.26(4)
O2 at $X3b^{int}$	4*b*	**0**	½	¼	**1**	1.26(4)
a [Å]	12.8350(4)	***b*** [Å]		5.7935(2)	***c*** [Å]	5.4864(2)
R_{wp} (XRD+NPD) [%]	3.12	**GOF(XRD+NPD)**	1.58		**R_{Bragg} [%]**	1.13 (XRD) 3.55 (NPD, bank 1)

In previous reports on oxyfluorides with RP-type structure (e.g. $Sr_2TiO_3F_2$ [63, 71] or $LaSrMnO_4F$ [20, 21, 60]), a layer-wise occupation of every second anion layer was observed, resulting in a symmetry lowering to *P*4/*nmm*. This was found to result in a strong increase of the *c* axis (see section 2.2.1), without any significant tilting of the TiO_5F or MnO_6 octahedra. This layer-wise ordering is symmetry-forbidden in *Cccm* and the site splitting within this space group implies half filling of every interstitial layer in a channel-like manner, accompanied by a tilting of the octahedra. This appears to be the origin of the orthorhombic distortion. This ordering scenario does not result in a strong increase of the long crystallographic axis $c_{I4/mmm}$ respectively a_{Cccm}. Instead, a strong expansion along the $[110]_{I4/mmm}$ direction, along which the tilting of the octahedra takes place, and a contraction along the $[-110]_{I4/mmm}$ direction, along which channels of interstitial anions are formed are observed.

Bond-valance sum calculations were performed to assess different distribution models of oxide and fluoride ions. Table 4-13 lists the results of the calculations for different arrangements on equatorial ($X1^{eq}$) and apical ($X2^{ap}$) sites of the octahedra as well as at the occupied interstitial site $X3b^{int}$ for the determined composition $La_2NiO_3F_2$. The highest GIIs were found for anion distributions, for which the equatorial anion site $X1^{eq}$ is (partially) substituted by fluoride ions. Thus, these configurations can be excluded, which agrees well with previous studies on RP-type oxyfluorides. [7] For an occupation of the equatorial anion site $X1^{ap}$ by oxide ions, two different distributions of oxide and fluoride ions at the remaining sites $X2^{ap}$ and $X3b^{int}$ can be considered: One configuration with an occupation of the interstitial site $X3b^{int}$ by oxide ions and an occupation of the apical anion site $X2^{ap}$ by fluoride ions, and a second configuration with an occupation of the interstitial site $X3b^{int}$ by fluoride ions and a mixed occupation of the apical site $X2^{ap}$ by oxide and fluoride ions. For the latter configuration an occupation with 50 % oxide and 50 % fluoride ions is assumed. The most stable configuration is found for the configuration with the interlayer site $X3b^{int}$ being occupied by oxide ions and the apical site $X2^{ap}$ being occupied by fluoride ions. This result is surprising, since a significant occupation of the interlayer site by oxide ions instead of fluoride ions has never been observed before for oxyfluoride with RP-type structure. The crystal structure of $La_2NiO_3F_2$ as derived from the coupled Rietveld analysis with an assignment of the oxide and fluoride ions based on the performed bond-valance sum calculations is shown for different viewing directions in Figure 4-28.

Table 4-13: Results of bond-valance sum calculations of $La_2NiO_3F_2$ for different oxide and fluoride ion distributions at the anion sites X1, X2 and X3. The anion sites X1, X2 and X3 refer to the equatorial, central apical, terminal apical and interstitial sites, respectively.

Arrangement of oxide and fluoride ions at anion sites $X1^{eq}$, $X2^{ap}$ and $X3^{int}$	**Bond valance sum**	**Global instability index (GII)**
$O1_{X1}$ – $F1_{X2}$ – $O2_{X3}$	O1: 1.83 F2: 1.25 O3: 1.67	0.19
$(0.5O1/0.5F1)_{X1}$ – $(0.5O2/0.5F2)_{X2}$ – $O3_{X3}$	O1: 1.83 F1: 1.52 O2: 1.54 F2: 1.25 O3: 1.67	0.33
$F1_{X1}$ – $O2_{X2}$ – $O3_{X3}$	F1: 0.52 O2: 1.54 O3: 1.67	0.37
$O1_{X1}$ – $(0.5O2/0.5F2)_{X2}$ – $F3_{X3}$	O1: 1.84 O2: 1.54 F2: 1.25 F3: 1.33	0.27
$(0.5O1/0.5F1)_{X1}$ – $O2_{X2}$ – $F3_{X3}$	O1: 1.83 F1: 1.52 O2: 1.54 F3: 1.33	0.34

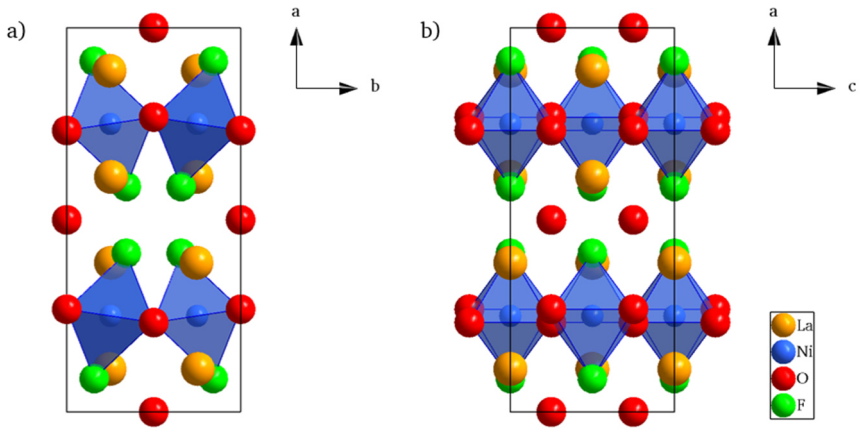

Figure 4-28: Crystal structure of $La_2NiO_3F_2$ as determined from the coupled Rietveld analysis. The assignment of anions to different anion sites is based on bond-valence calculations. To illustrate the tilting of the NiO_4F_2 octahedra, the structure is show along the *c* axis (a) and the *b* axis (b).

When comparing the tilt pattern of the NiO_4F_2 octahedra of $La_2NiO_3F_2$ to reported tilt patterns of La_2NiO_{4+d} with varying values d, interesting observations can be made. The presence of interstitial oxide anions affects the symmetry of La_2NiO_{4+d} significantly and a broad range of oxygen-over-stoichiometry dependent phases with different space groups can be identified. At room temperature, stoichiometric La_2NiO_4 crystallises in the orthorhombic space group *Bmeb*. [44] For increasing values of interstitial oxide ions d, several phases have been reported: a tetragonal phase with space group $P4_2/nmc$ for $0.02 < d < 0.03$ [44, 254], a tetragonal phase with $I4/mmm$ $0.05 \lesssim d \lesssim 0.11$ [253], a orthorhombic phase with space group *Fmmm* for $0.13 \lesssim d \lesssim 0.18$ [255] and a monoclinic phase with space group *C*2 for $d = 0.25$ [256, 257]. Additionally, several structural transitions have been observed at lower temperatures. [44, 253, 255] It should be noted that the orthorhombic distortion within the *Fmmm* phase in comparison to

the *I4/mmm* phase is relatively small and the splitting of the reflections can be very subtle, depending on the quality of the powder diffraction data.

With regards to the tilting pattern of the NiO_4F_2 octahedra of $La_2NiO_3F_2$, a closer examination of the orthorhombic structure with *Bmeb* symmetry when intercalating anions into the interstitial site is interesting. As described by Tranquada et al. [253] conceptually, starting from the ideal tetragonal *I4/mmm* aristotype symmetry of RP-type compounds, assuming relatively rigid NiO_6 octahedra with the Ni ions remaining on their special site, tilting of single polyhedra would affect the whole crystal structure. If only one apical oxide ion would be displaced along $[1\text{-}10]_{I4/mmm}$, a tilting of the octahedron along the $[110]_{I4/mmm}$ axis of the unit cell with the equatorial anions moving accordingly would be expected. Since the octahedra are connected via the equatorial anions, the neighbouring octahedra would align in a zigzag-fashion within the layer. In the layers above and below this plane, the octahedra would align in phase to minimise Coulombic repulsion between the apical ions of adjacent layers. This also requires the doubling of the unit cell to a size of $\sqrt{2} \times \sqrt{2} \times 1$ and an orthorhombic distortion with a longer axis along the tilt direction is observed. This tilt pattern is found for the *Bmeb* structure of La_2NiO_4.[44] Figure 4-29 shows this tilt pattern in the non-conventional setting *Becm* for easier comparability to the pattern of $La_2NiO_3F_2$ with *Cccm* symmetry. The formed interstitial cavities have the identical size.

Such a tilting of the octahedra is not possible for the higher symmetrical phases with higher values of d due to symmetry restrictions. For the *Fmmm* symmetry, Jorgensen et al. [255] have alternatively proposed that the intercalation of an additional anion into the interstitial site leads to the formation of a local defect, which displaces the four closest apical oxide ions from their ideal position. In this defect model, the apical oxide ion site is split into two sites. The first site remains at its regular position and is filled by oxide ions, which are not neighbouring the defect. The other site is in direct proximity to the defect anion at the interstitial site and has been given positional flexibility in x, y and z direction with a sensible displacement away from this intercalated anion. Final refinements provide reasonable atomic positions and overall occupancies. The bond distance between the apical and interstitial oxide ions are $\sim$ 2.54 and 2.71 Å (ionic radius of O^{2-}: 1.40 Å) [54]. Each distance is found twice. If the apical anions would not be displaced around the interstitial anion, too short distances of $\sim$ 2.07 and 2.28 Å would be obtained, making intercalation unfeasible. Moreover, small local displacements of the La cations are also likely, which might give rise to the observed small orthorhombic distortion. Within the defect model, the average *Fmmm* symmetry is maintained when the interstitial anions are distributed randomly.

The allocation of one oxide ion at the interstitial site of the *Bmeb* structure [253], as opposed to what is found for the *Fmmm* symmetry, results in an displacement of the apical ions in the adjacent perovskite-type layers away from the interstitial ion accompanied by a tilting of the octahedra (for the conventional setting of *Bmeb* along the $[010]_{Bmeb}$ of the cell). The tilting propagates through the layers of octahedra and disturbs the tilting pattern on a local scale. The *Bmeb* pattern is still found in the layer above and below the plane containing the interstitial anion, although the pattern is reversed on crossing this plane. Thus, an antiphase domain boundary is created. Furthermore, the tilting within the intercalated layer facilitates the intercalation of additional anions into the resulting large cavities, leading to a staged ordering. The small cavities next to the large cavities are energetically unfavourable for the

intercalation of additional anions. The stage-3 ordering scenario of the *Becm* structure is given exemplarily in Figure 4-29 b.

In $La_2NiO_3F_2$ (Figure 4-29 c), the octahedra align similar to the octahedra closest to the intercalated interstitial anions in the staged intercalation process. However, no *Becm*-like ordering is found in the adjacent layers. Instead, the tilting pattern can be understood as a stage-1 ordering of interstitial oxide ions of the *Becm* structure. The size difference of the formed interstitial cavities is well represented by the distance of the apical fluoride ions to the interstitial sites 4*a* and 4*b*, which are 1.995(2) and 2.654(2) Å, respectively. With respect to the size of oxide and fluoride ions of ~1.40 and 1.33 Å [54], the distortion of the octahedra avoids the formation of very short anion-anion distances. It further explains why the 4*a* site is not occupied. As a consequence of this energetical inequivalence of the interstitial sites in the *Cccm* symmetry, it follows that the filling of the vacant site due to the intercalation of additional fluoride ions in an additional topochemical fluorination step (see Figure 4-74) or due to the introduction of anion disorder (see Figure 4-90) can only occur if the site energies approach each other. For this, the tilting has to be significantly reduced.

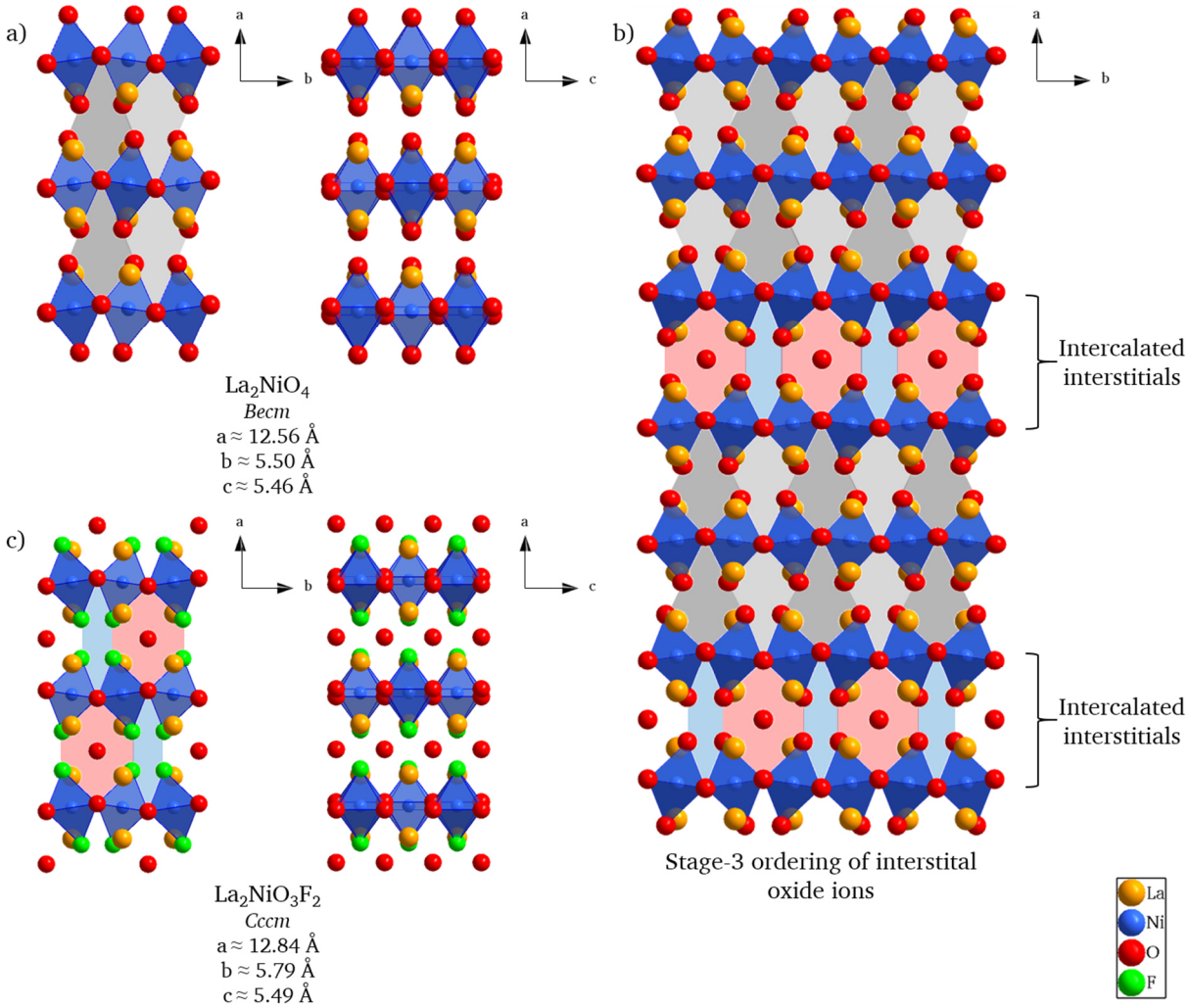

Figure 4-29: Comparison of the tilting of the octahedra in La_2NiO_4 with space group *Bmeb* [44] (the structure is shown in the non-conventional setting *Becm* for easier comparability to $La_2NiO_3F_2$) (a), stage-3 ordered La_2NiO_{4+d} as proposed by reference 254 (b) and $La_2NiO_3F_2$ with space group *Cccm* (c).

4.1.3.1.3 Investigation of the anion sublattice of $La_2NiO_3F_2$ by DFT calculations

To elucidate the structure of the anion sublattice and to provide an understanding for stabilities of different anion ordering scenarios, DFT calculations on different ordering scenarios were tested for $La_2NiO_3F_2$ (Figure 4-30). Interestingly, the experimentally most stable anion distribution $O_{X1}-F_{X2}-O_{X3}$ is not found to be energetically most favourable (Table 4-14). The configurations of $O_{X1}-(0.5O/0.5F)_{X2}-F_{X3}$ v1 and v2 are found to show lower energies per $La_2NiO_3F_2$ formula unit ($\Delta \approx -0.06$ to -0.04 eV) and a strong structural distortion to monoclinic symmetry. However, these energy differences are small (and "0 K energies"), being in the same order of magnitude as the thermal energy at the synthesis temperature of 370 °C ($\sim$ 50 meV). Remarkably, bond valence sum calculations were able to predict the ordering of oxide and fluoride ions correctly, which can be understood from the fact that they originate from the evaluation of experimentally obtained bond distances. The structural distortions found for the structures after DFT optimization strongly differ for the different anion configurations. In this respect, it should be emphasized that the $O_{X1}-F_{X2}-O_{X3}$ configuration is the one with lowest energy while maintaining the highest possible orthorhombic symmetry, i.e., without transforming to monoclinic. An orthorhombic symmetry is only obtained for the $O_{X1}-(0.5O/0.5F)_{X2}-F_{X3}$ v3 configuration, which has a considerably higher energy than the $O_{X1}-F_{X2}-O_{X3}$ configuration ($\Delta = +0.18$ eV per $La_2NiO_3F_2$ formula unit, corresponding to $\sim$ 3.5x of the thermal energy at the synthesis temperature). Taking the calculated structural distortions and energies into account, the experimentally observed structure might be understood as the best compromise between energy and symmetry.

Furthermore, it should be noted that the models $O_{X1}-(0.5O/0.5F)_{X2}-F_{X3}$ v1, v2 and v3 show strong off-center shift of the Ni ion of the NiO_5F octahedra towards the apical oxide ion. This is not indicated from the refinement of XRD and NPD data with a structural model, which allows for off-center displacement of the Ni cations.

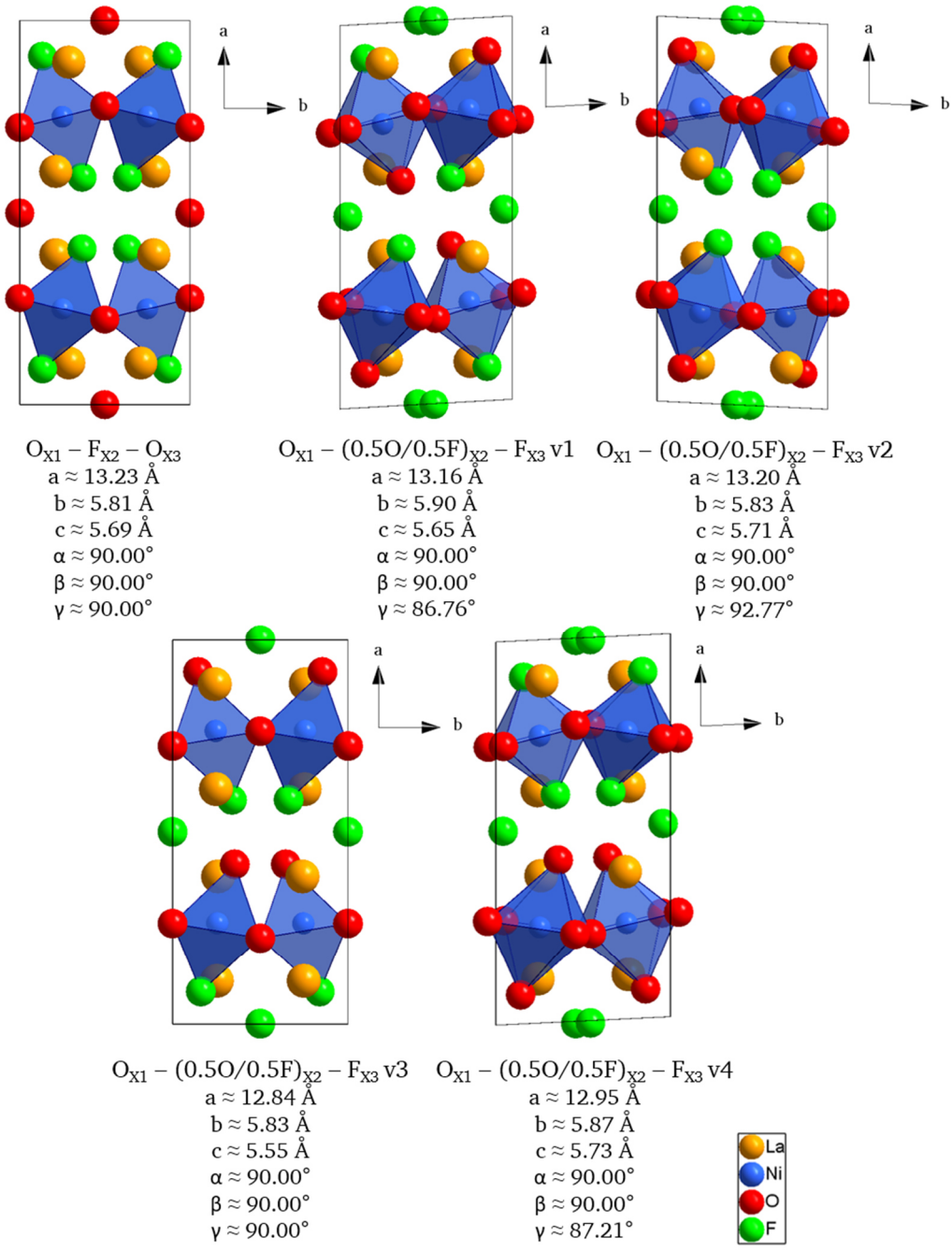

Figure 4-30: Crystal structures of $La_2NiO_3F_2$ for different oxide and fluoride ion distributions at the anion sites X1, X2 and X3 after structural relaxation. The anion sites X1, X2 and X3 refer to the equatorial, central apical, terminal apical and interstitial sites, respectively.

Table 4-14: Energy differences per formula unit of $La_2NiO_3F_2$ of different oxide and fluoride ion distributions at the anion sites X1, X2 and X3 to the most stable configuration $O_{X1} - F_{X2} - O_{X3}$. The anion sites X1, X2 and X3 refer to the equatorial, central apical, terminal apical and interstitial sites, respectively.

Arrangement of oxide and fluoride ions at anion sites $X1^{eq}$, $X2^{ap}$ and $X3^{int}$	**Energy difference per formula unit of $La_2NiO_3F_2$ [eV] to the most stable configuration $O_{X1} - F_{X2} - O_{X3}$**
$O_{X1} - F_{X2} - O_{X3}$	0
$O_{X1} - (0.5O/0.5F)_{X2} - F_{X3}$ v1	-0.06
$O_{X1} - (0.5O/0.5F)_{X2} - F_{X3}$ v2	-0.04
$O_{X1} - (0.5O/0.5F)_{X2} - F_{X3}$ v3	+0.018
$O_{X1} - (0.5O/0.5F)_{X2} - F_{X3}$ v4	+0.22

4.1.3.1.4 High-temperature X-ray diffraction study on $La_2NiO_3F_2$

To investigate the decomposition behaviour and the temperature stability of $La_2NiO_3F_2$, a high-temperature X-ray diffraction study was performed (Figure 4-31). With increasing temperature, reflections shift toward lower diffraction angles due to thermal lattice expansion. Apart from the presence of a very small phase fraction of the impurity phase LaF_3, LaOF is formed as a decomposition product starting from ~ 500 °C, which is a well-known behaviour found for the heating of oxyfluoride materials. [258] Between 500 and 650 °C, increasing phase fractions of LaOF are found. A crystalline Ni-containing decomposition product is not observed.

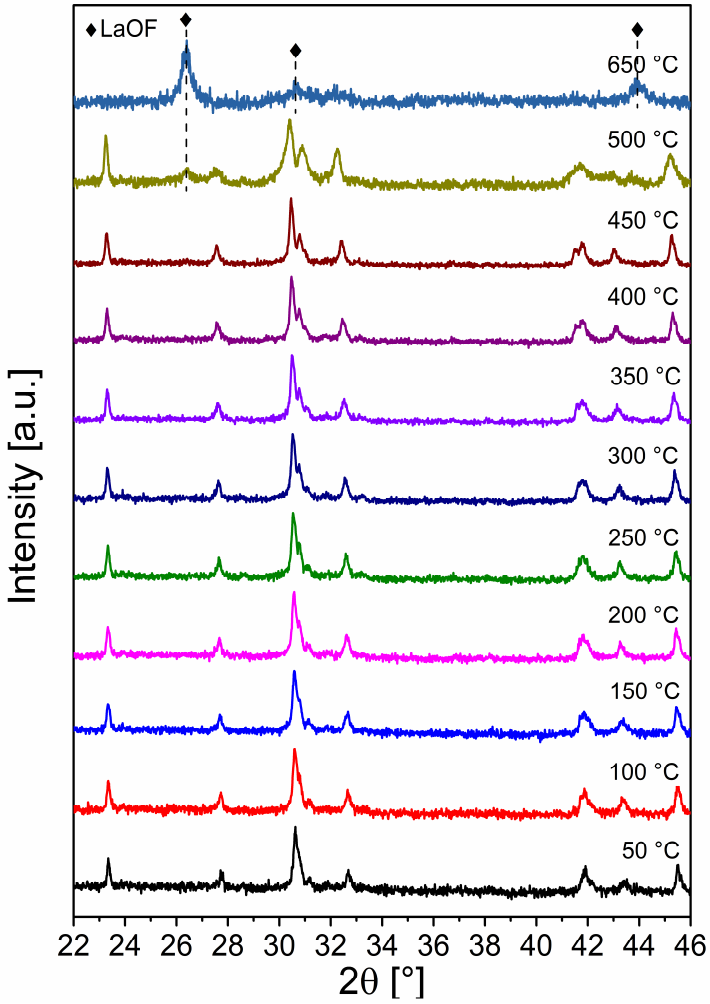

Figure 4-31: High-temperature XRD patterns of $La_2NiO_3F_2$ in the temperature range from 50 °C to 650 °C. A strong increase of the phase fraction of the decomposition product LaOF is found starting from ~ 500 °C.

From the shifts of different reflections on heating, reflected in the trend of the determined lattice parameters (Figure 4-32), it becomes apparent that the thermal expansion is anisotropic. While the increase of each of the three lattice parameters is fairly linear with temperature (the lattice parameters obtained at 500 °C have to be excluded due to the onset of decomposition), *a* and *c* show a significantly stronger increase than *b*. Thus, the orthorhombic distortion decreases on heating of the compound. However, a complete transition toward the tetragonal crystal system cannot be achieved prior to the decomposition,

suggesting that the ordering of the oxide ions on the interstitial sites has a high thermal stability.

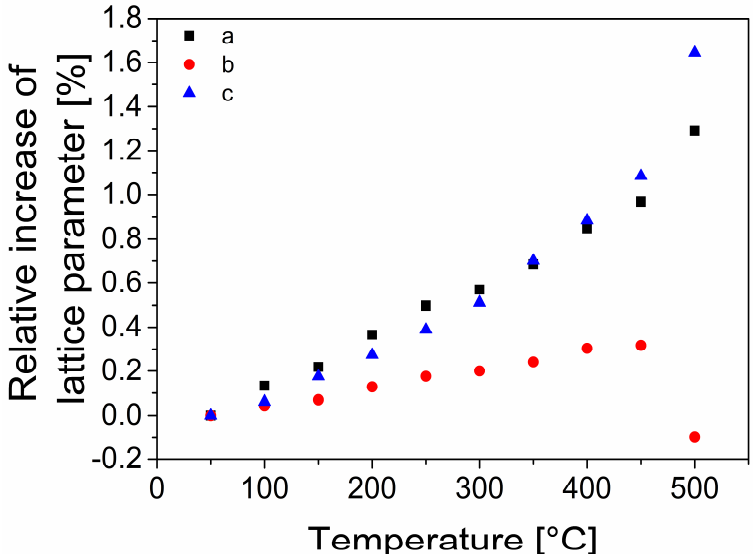

Figure 4-32: Relative increase of the lattice parameters *a*, *b* and *c* as a function of temperature.

4.1.3.2 Topochemical defluorination of $La_2NiO_3F_2$

4.1.3.2.1 Analysis of the reduction mechanism of $La_2NiO_3F_2$

For the topochemical reduction of $La_2NiO_3F_2$, various mixtures of $La_2NiO_3F_2$ + x NaH with $0 \leq x \leq 2.5$ and $\Delta x = 0.25$ were reacted and investigated by means of X-ray diffraction (Figure 4-33). Depending on the amount x of NaH added, phase mixtures of phases with different fluoride contents and strongly differing structures are formed in the reduction products, visually evident from the strong shifts and splitting of reflections in comparison to $La_2NiO_3F_2$. By studying the broad range of compositions, the following four phases (given in the order of appearance in the reduction products for increasing x) can be identified: one monoclinic, two orthorhombic phases, labelled 'orthorhombic #1' and 'orthorhombic #2', and one tetragonal phase. The monoclinic phase found after the reduction should not be mistaken for the monoclinic phases discussed in the context of different anion ordering scenarios in $La_2NiO_3F_2$ based on DFT calculations (section 4.1.3.1.3).

Quantitative Rietveld analysis of XRD data was performed for all compositions studied. The crystal structures of the reduced phases were additionally analysed by coupled analyses of X-ray and neutron powder diffraction data (see section 4.1.2.2.2; the refinements of the reduction products of $La_2NiO_3F_2$ + 0.25 NaH, $La_2NiO_3F_2$ + 0.5 NaH and $La_2NiO_3F_2$ + 1.5 NaH, from which the used structural models of the four phases were deducted, are shown in Figure 4-37, Figure 4-38 and Figure 4-39).

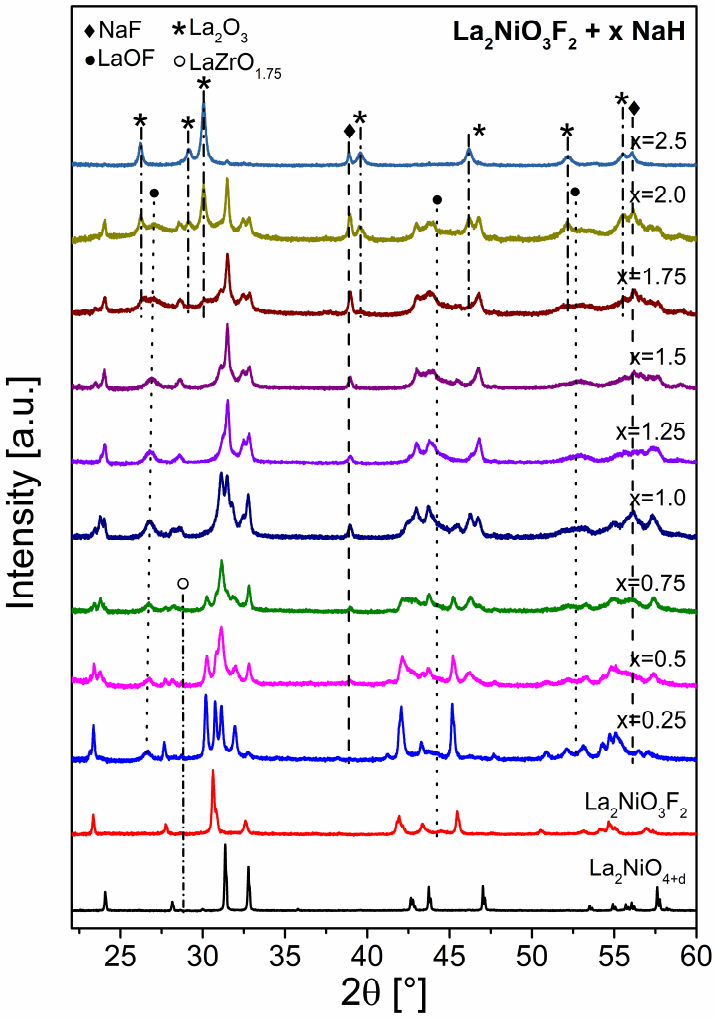

Figure 4-33: X-ray diffraction patterns of La2NiO$_{4+d}$, $La_2NiO_3F_2$ and the reduction products $La_2NiO_3F_2$ + x NaH with 0.25 ≤ x ≤ 2.5. For the Rietveld refinements of the patterns shown together with an assignment of reflections, the reader is referred to Figure 6-11 in the Appendix.

The evolution of the phase fractions of obtained reduced phases as a function of the NaH amount is given in Figure 4-35 a. It should be emphasised that the absolute phase fractions of the RP-type phases are given instead of the relative fractions (compared to Figure 4-4 and Figure 4-17 of the titanium-based RP-type compounds). For x = 0.25, the majority of the sample consists of the monoclinic phase, with the orthorhombic #1 phase being present in addition. While the phase fraction of the monoclinic phase is continuously decreasing for increasing values of $0.25 \leq x \leq 0.75$, the orthorhombic #1 phase becomes the main phase. For $x \geq 1$, the phase fraction of the orthorhombic #1 phase is reduced and additionally the orthorhombic #2 phase and the tetragonal phase are formed. The phase fractions of these phases increase for increasing NaH amounts, before they decrease drastically. This strong decrease for $x \geq 1.75$ suggests a substantial decomposition of the previously present RP-type phases. It can be ruled out that the decomposition is due to water and a resulting HF release, since the samples were prepared, stored and characterized under Ar atmosphere (< 0.1 ppm H_2O). It is rather indicated that the reaction temperature of 300 °C is slightly too high to ensure the structural stability of the metastable $La_2NiO_3F_2$ upon reduction. As discussed above (see section 2.2.2), a balance between the metastability of the parent oxyfluoride and kinetic

as well as thermodynamic factors concerning the reduction products has to be found. This also imply that the synthesis of phase-pure samples might be limited.

Each RP-type phase, formed during the reduction, has a distinctive set of lattice parameters with a nearly constant volume per formula unit (Figure 4-35 b) within its range of existence. Compared to $La_2NiO_3F_2$, the volumes of the orthorhombic phases decrease significantly with increasing degrees of defluorination. The monoclinic phase has an increased volume and the tetragonal phase shows a slightly decreased volume, although strong changes of lattice parameters are found.

The increasing decomposition is also apparent with respect to the increasing phase fractions of LaOF, La_2O_3 and NiO in the reduction products (Figure 4-35 c). Besides these crystalline decomposition products, the formation of amorphous decomposition products has to be taken additionally into consideration. This becomes particularly clear when comparing the amounts of formed NaF to the theoretical amounts of it in the reduction products (assuming again a complete reaction of the used NaH to NaF (in accordance with the absence of NaH or NaOH) as well as crystalline phases only) (Figure 4-35 d). The measured NaF phase fractions are significantly higher than the theoretical fractions, which can only be explained by the presence of one or more non-crystalline phases, which leads to an overestimation of the phase fractions of crystalline phases in the reduction products, since the phase fractions of amorphous phases cannot be directly measured by means of diffraction (see also below). The strong increase of LaOF and the divergence between the phase fraction of measured and theoretical NaF starts already at $x = 1$. The formation of La_2O_3 is observed for $x \geq 1.75$. For $x = 2.5$, besides La_2O_3, only ~ 7 wt% of the orthorhombic #2 phase is found. The presence of crystalline Ni (or NiO), which should also be formed during the decomposition cannot be confirmed by means of diffraction (except for the reduction products with $x = 1.75$ and 2, in which a very small phase fraction of NiO is observed) possibly since it may form amorphous or nano-crystalline clusters. Indication for the formation of an amorphous Ni containing phase is only given in the reduction product with a large excess of NaH ($x = 2.5$), in which, even though no crystalline Ni phase can be found at all, a very broad bump is found between ~ 43 and 46° 2θ (Figure 4-36). This angular range coincides with the range, in which the scattering of amorphous Ni has been reported. [259] The highest-intense (111) reflection of crystalline Ni would be expected at ~ 44° 2θ. [260] However, magnetic measurements (see section 4.1.3.4.1) give clear indication for the existence of ferromagnetic Ni, especially with regards to the antiferromagnetic ordering found for the reduced compounds (see section 4.1.3.4.2).

The partial decomposition leading also to the formation of amorphous phases on reduction can be confirmed further by determining the amorphous phase fractions (Figure 4-35 e) within the reaction products using the method of an internal standard. For $0.25 \leq x \leq 1.5$, a continuous increase of the amorphous weight fractions is found (it has to be emphasized that the outlier of the reduction product with $x = 1$ could be reproduced within 3 attempts). Remarkably, for $1.75 \leq x \leq 2.5$, the amorphous phase fractions decrease again, indicating a re-crystallization on the formation of the final decomposition product La_2O_3. Such strong decomposition and amorphisation processes are not observed in the reduction series of the $Sr_2TiO_3F_2$ (section 4.1.1.2) and $Sr_3Ti_2O_5F_4$ (section 4.1.2.2). This could be related to differences in the degree of exothermicity of the reduction reactions and of the metastability of the RP-type Ti- and Ni-based compounds. If the reduction reaction is highly exothermic, the released thermal energy is high enough to overcome the activation barrier for the

decomposition of the metastable oxyfluorides into the stable decomposition products. In accordance with the higher redox potential of $Ni^{+}|Ni^{2+}$ in comparison to $Ti^{3+}|Ti^{4+}$ vs. Li|LiF in the electrochemical series [261] (for the reduction of both RP-type compounds, H^{-} ions ($E^{0}(2H^{-}|H_2) = -2.23$ V vs. SHE, $E^{0}(2H^{-}|H_2) \approx 0.77$ V vs. Li|LiF) are the reductive species), ΔG of the reduction of $La_2NiO_3F_2$ is more negative, which is also related to a higher enthalpic contribution (Ni^{2+} is a stronger oxidant than Ti^{4+}). Therefore, the exothermic enthalpic contribution is higher, which could facilitate the decomposition of $La_2NiO_3F_2$.

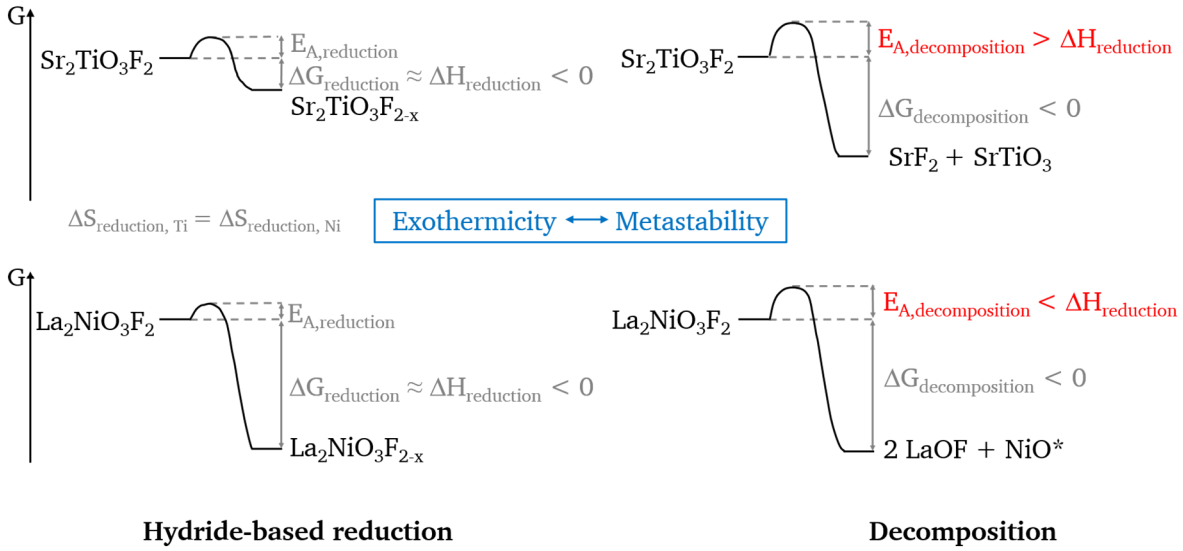

Figure 4-34: Schematic illustration of the interdependency of the exothermicity of the hydride-based reductions and the metastability of $Sr_2TiO_3F_2$ and $La_2NiO_3F_2$. ΔG is assumed to be approximately ΔH (ΔS is equal in both reductions and was, therefore, neglected in this consideration). *The detailed decomposition products of the decomposition of $La_2NiO_3F_2$ are not known.

From the broad range of samples measured, a set of competing reactions including reductive defluorination, decomposition and anion exchange reactions can be formulated, which explain the variety of phases found, highlighting also the most plausible reaction mechanism:

Reductive defluorination reaction:

$$La_2NiO_3F_2 + x\ NaH \rightarrow La_2NiO_3F_{2-x} + x\ NaF + \frac{x}{2}H_2$$

Decomposition reactions:

$$La_2NiO_3F_2 + x\ NaH \rightarrow 2\ LaOF + Ni + x\ NaOH + \frac{1-x}{2}O_2$$

$$La_2NiO_3F_2 + 2\ NaH \rightarrow La_2O_3 + Ni + 2\ NaF + H_2$$

Partial fluoride-oxide exchange:

$$La_2NiO_3F_{2-x} + y\ La_2O_3 \rightarrow La_2NiO_{3+y}F_{2-x-2y} + 2y\ LaOF$$

Since NaOH is not observed in the reduction products, a reaction according to the first decomposition reaction equation seems unlikely. This can be also understood with regard to the $H_2|2H^{+}$ potential, which would be involved in the formation of NaOH. This potential reduces the enthalpic contribution to the change of the Gibb's free energy considerably due to its lower reductive power as compared to $2H^{-}|H_2$. This phase is also not observed in the

studies on the reduction of $Sr_2TiO_3F_2$ and $Sr_3Ti_2O_5F_4$, which do not show significant decomposition or amorphisation. The other decomposition reaction involving the formation of NaF as observed experimentally seems also not probable, since La_2O_3 is only formed for $x \geq 1.75$, while LaOF is obtained for $x \leq 1.75$. However, a partial fluoride-oxide exchange between $La_2NiO_3F_{2-x}$ and La_2O_3 according to the partial fluoride-oxide exchange reaction equation might explain the formation of the reduced RP-type phases and LaOF at low values of x. Taking this into account, together with the fact that more than one RP-type phase is present especially for high values of x, it is clear that a detailed determination of the anion composition, i.e. the oxide/fluoride ratio, of the reduced phases is not possible, since oxide and fluoride ions are indistinguishable by diffraction. However, the neutron diffraction studies allow for the approximate determination of an overall anion content of each phase. Nevertheless, the consistency of the structural changes together with the quantification of the phases in the reduction products renders the above described defluorination mechanism involving reductive defluorination and partial fluoride-oxide exchange the most likely scenario.

The determination of occupation factors of the anion sites of the reduced phases (see section 4.1.3.2.2) allows a rough estimation of the composition of each individual phase. It should be emphasised that for the estimation of the compositions, the proposed fluoride-oxide exchange is not considered and changes of the occupation factor of an anion site were correlated only to the extraction of fluoride ions due to the reaction with NaH, i.e., the reductive defluorination. Weighted by the relative phase fraction of the reduced phases (not taking decomposition and side products, fluoride-hydride substitution (see below) or amorphisation into account) an approximate overall value of Δ in $La_2NiO_3F_{2-\Delta}$ can be determined for a specific x (Figure 4-35 f). While for values $0.25 \leq x \leq 0.75$, a steady increase in Δ can be observed, Δ adopts values between $\sim$ 0.81 and 0.94 for higher x. This seems to be reasonable since a theoretical extraction of more than one fluoride ion from $La_2NiO_3F_2$ would correspond to the formation of metallic nickel (or an average nickel oxidation state below +1, respectively) within the reduced phase, which is chemically implausible. It might be, further, possible to extract more fluoride if a (partial) fluoride-hydride substitution takes place. Elemental analysis indicates, however, relatively low hydride contents in the reduction products (formal compositions: $La_2NiO_3F_{1.75}H_{0.12(2)}$ + 0.25 NaF for $x = 0.25$, $La_2NiO_3F_{1.5}H_{0.12(2)}$ + 0.5 NaF for $x = 0.5$; $La_2NiO_3FH_{0.17(2)}$ + 1 NaF for $x = 1$; $La_2NiO_3F_{0.5}H_{0.21(4)}$ +1.5 NaF for $x = 1.5$). In comparison to the reductions of $Sr_2TiO_3F_2$ and $Sr_3Ti_2O_5F_4$, the hydride contents are significantly lower. Assuming that the RP-type phases are the hosts of these hydride ions, such a fluoride-hydride substitution can have occurred in addition to the reductive defluorination and fluoride-oxide exchange, as explained previously, only to a small extent. From the Rietveld analysis, it was not possible to assign the residual hydride ions to one of the RP-type phases or to other crystalline or amorphous phases (see section 2.4.1.2).

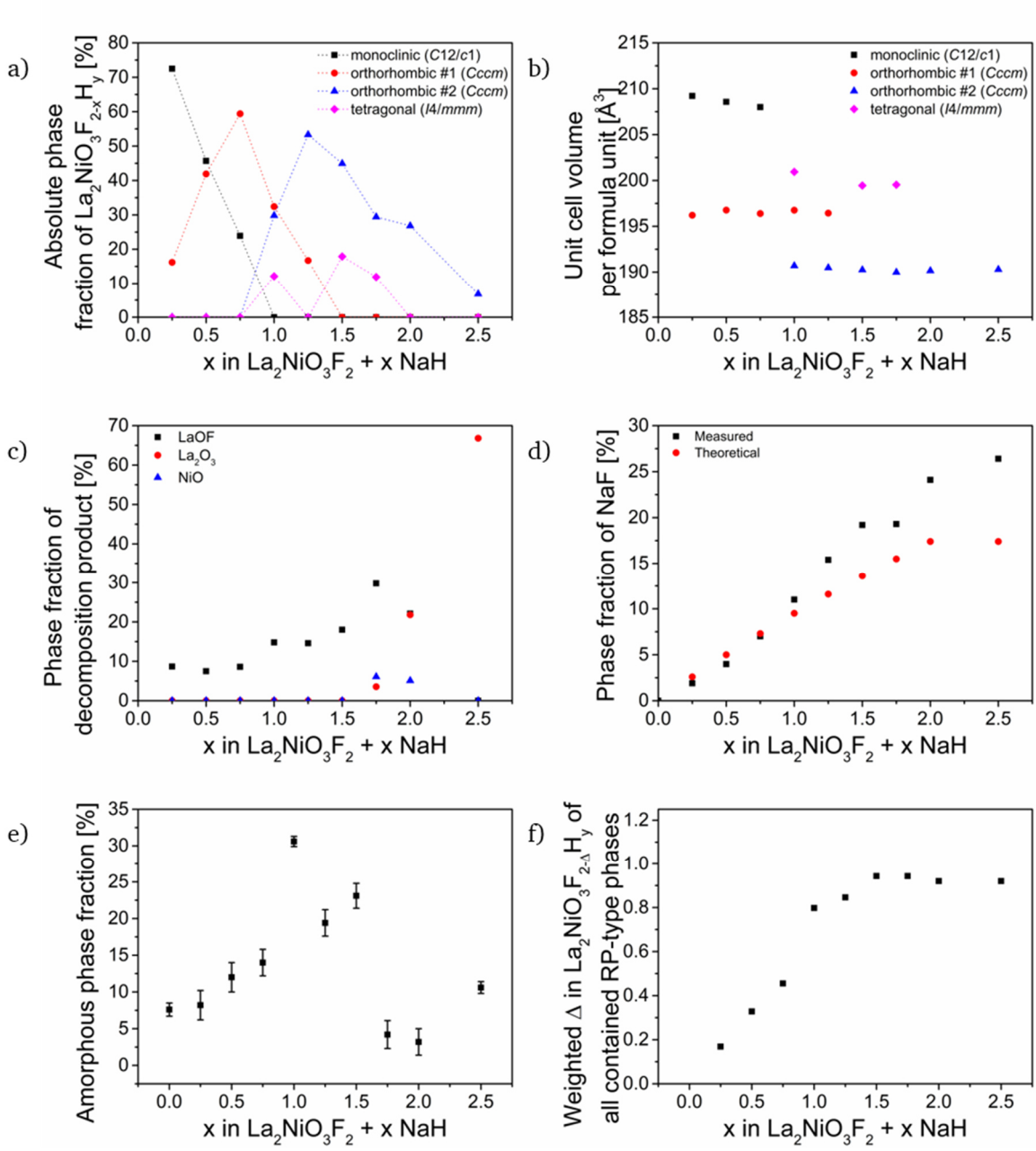

Figure 4-35: Absolute phase fractions (a) and unit cell volumes per formula unit (b) of $La_2NiO_3F_2$ and the reduced RP-type phases in the reduction product $La_2NiO_3F_2$ + x NaH with 0.25 ≤ x ≤ 2.5 as a function of x. Due to the strong decomposition and amorphisation observed, the absolute phase fractions are given here. This is in contrast to the reduction series on $Sr_2TiO_3F_2$ and $Sr_3Ti_2O_5F_4$, for which the relative phase fractions are given. Measured phase fraction of the decomposition phases (c), NaF (d) and amorphous phases (e) in the reduction products $La_2NiO_3F_2$ + x NaH with 0.25 ≤ x ≤ 2.5 as a function of x. Also given are the theoretically expected values of NaF calculated assuming full conversion of the added NaH to NaF. Values of extracted fluoride Δ in $La_2NiO_3F_{2-\Delta}H_y$ (f) of all reduced RP-type phases in the reduction product $La_2NiO_3F_2$ + x NaH as a function of x. The values were calculated using the relative phase fractions and approximate compositions of the reduced phases as derived from the occupation factors determined via coupled Rietveld analyses of the found phases.

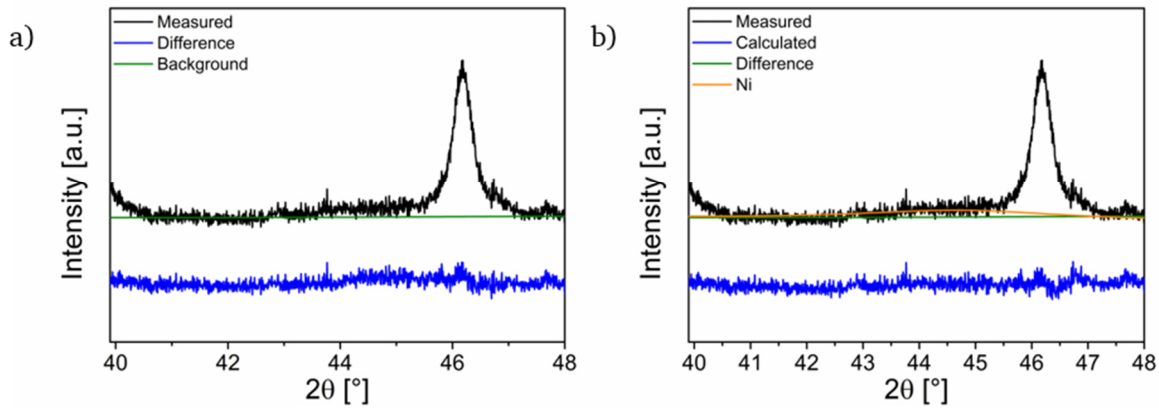

Figure 4-36: Comparison of selected angular ranges of $La_2NiO_3F_2$ + 2.5 NaH indicating the presence of amorphous or nanocrystalline Ni. When Ni is not included in the refinement (a), a systematic deviation in the difference curve due to missing intensity related to amorphous or nanocrystalline Ni is observed. Taking Ni into account (b), this intensity is described by a broad bump. The crystallite size of the Ni is small (~ 2-3 nm).

Further support for the proposed reaction mechanism can be obtained by re-oxidation and re-fluorination experiments on the reduction products. After the exposure of the products $La_2NiO_3F_2$ + x NaH with x = 0.5, 1 and 1.5 to air at elevated temperatures, phase mixtures with several re-oxidised phases are found (Figure 6-12). Phases with similar lattice parameters have been found when the parent oxide La_2NiO_{4+d} has been fluorinated with varying non-stoichiometric amounts of PVDF to $La_2NiO_{3+x/2}F_{2-x}$ [246]; this, together with the fact that $La_2NiO_3F_2$ cannot be reformed on re-oxidation supports the extraction of fluoride, which is also in agreement with the NaF formation. Moreover, the re-fluorination of the reduction reaction products $La_2NiO_3F_2$ + x NaH with x = 1 and 1.5 were attempted using F_2 gas at various temperatures (Figure 6-13). A considerable re-fluorination with progressive decomposition occurring in parallel could only be achieved in a narrow temperature range. However, instead of the synthesis of desired $La_2NiO_3F_2$, a monoclinic phase $La_2NiO_3F_{2+x}$ with a considerably increased c lattice parameter ($c \approx 14.92$ Å) is found due to difficulties in controlling the extent of fluorination using F_2 gas. Nevertheless, the successful fluorination demonstrates the reversibility of the reduction process and confirms the reaction mechanism.

4.1.3.2.2 Coupled Rietveld analysis of the reduction products

For the determination of the nuclear structures of the four reduced phases, coupled Rietveld analyses of room-temperature XRD and NPD data were performed on the reduction products of $La_2NiO_3F_2$ + x NaH with x = 0.25, 0.5, 1 and 1.5. The refinements of $La_2NiO_3F_2$ + x NaH with x = 0.25, 0.5 and 1.5 are given in Figure 4-37, Figure 4-38 and Figure 4-39, respectively (the refinements of $La_2NiO_3F_2$ + x NaH with x = 1 are given in Figure 6-14). Due to the presence of two to three reduced phases within each sample, a structural model of a particular phase was deduced from the measurement showing the highest phase fraction of this phase. The obtained model was then used to refine the other measurements with lower phase fractions of the respective phase. While doing so, no significant changes in structural parameters (lattice parameters, atom positions, site occupations etc.) of the phase and stable convergence of the refinements were observed. Although structural characterisation was performed on phase mixtures, the large d-spacing range covered in the measurements in combination with the changes of resolution of the diffraction detector banks, and sufficient peak separation of the phases enables the determination of a concise picture of the structural changes.

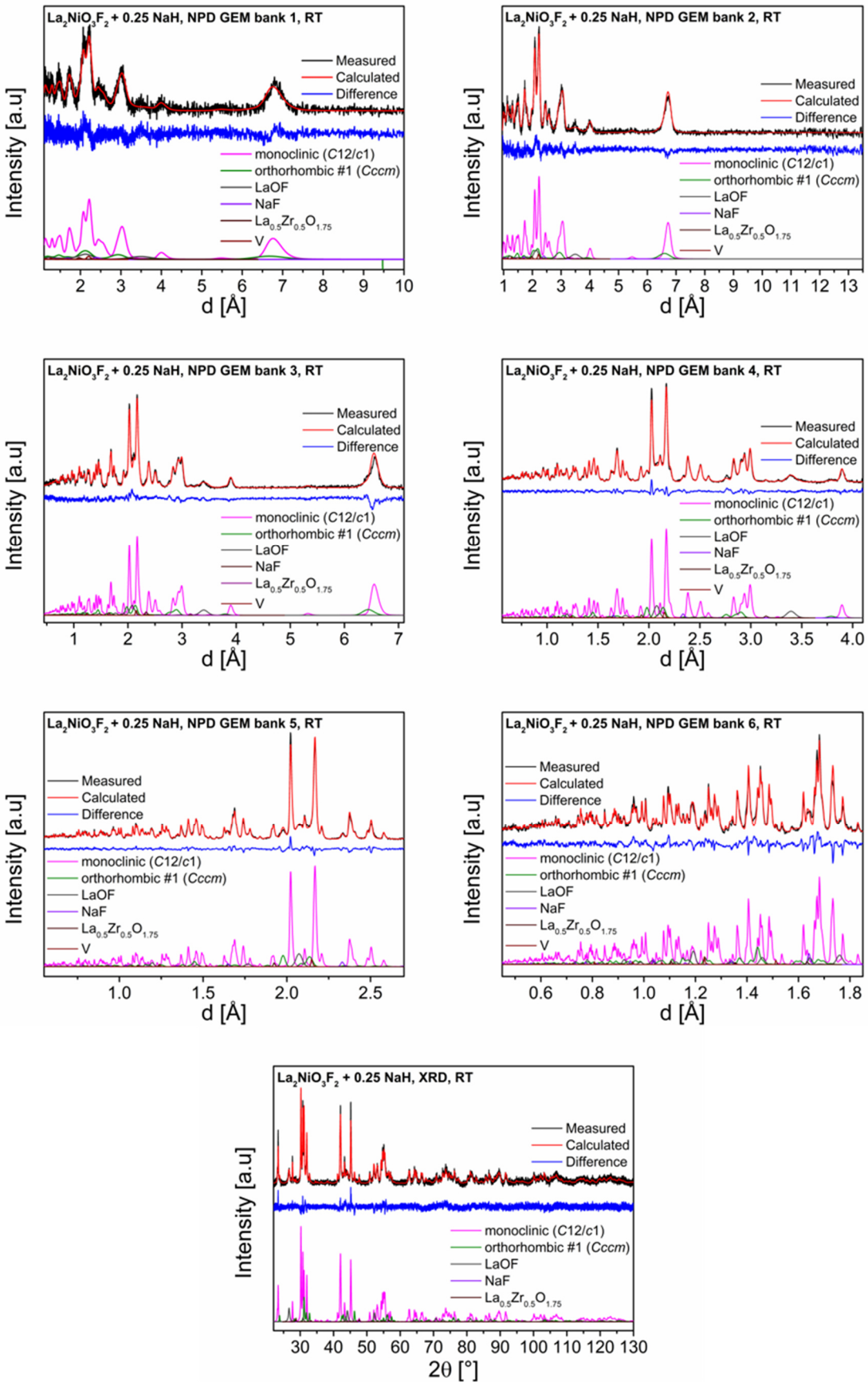

Figure 4-37: Coupled Rietveld refinement of the reduction product of $La_2NiO_3F_2$ + x NaH with x = 0.25 of NPD GEM banks 1-6 and XRD data measured at room-temperature (RT).

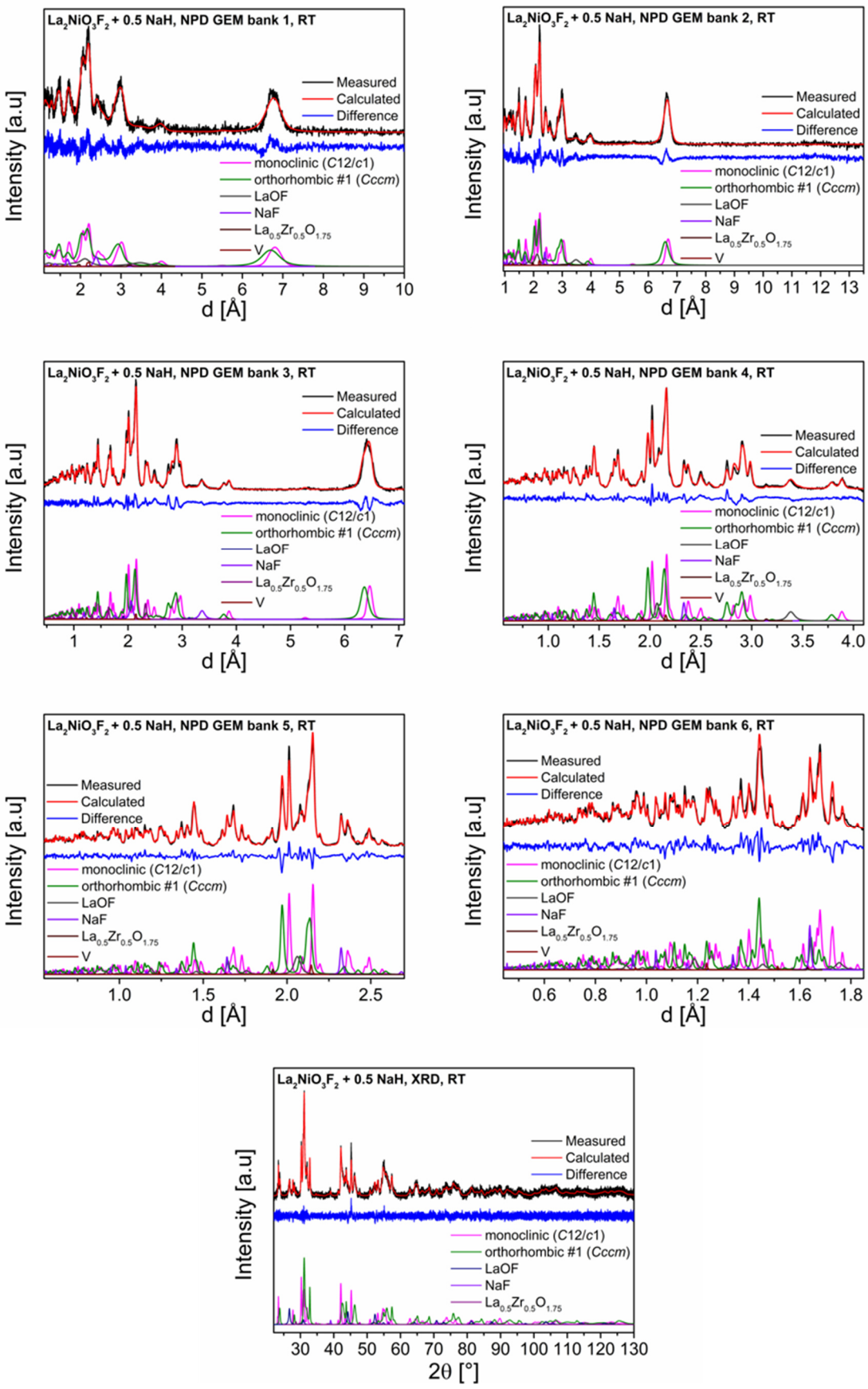

Figure 4-38: Coupled Rietveld refinement of the reduction product of La_2NiO3F_2 + x NaH with x = 0.5 of NPD GEM banks 1-6 and XRD data measured at room-temperature (RT).

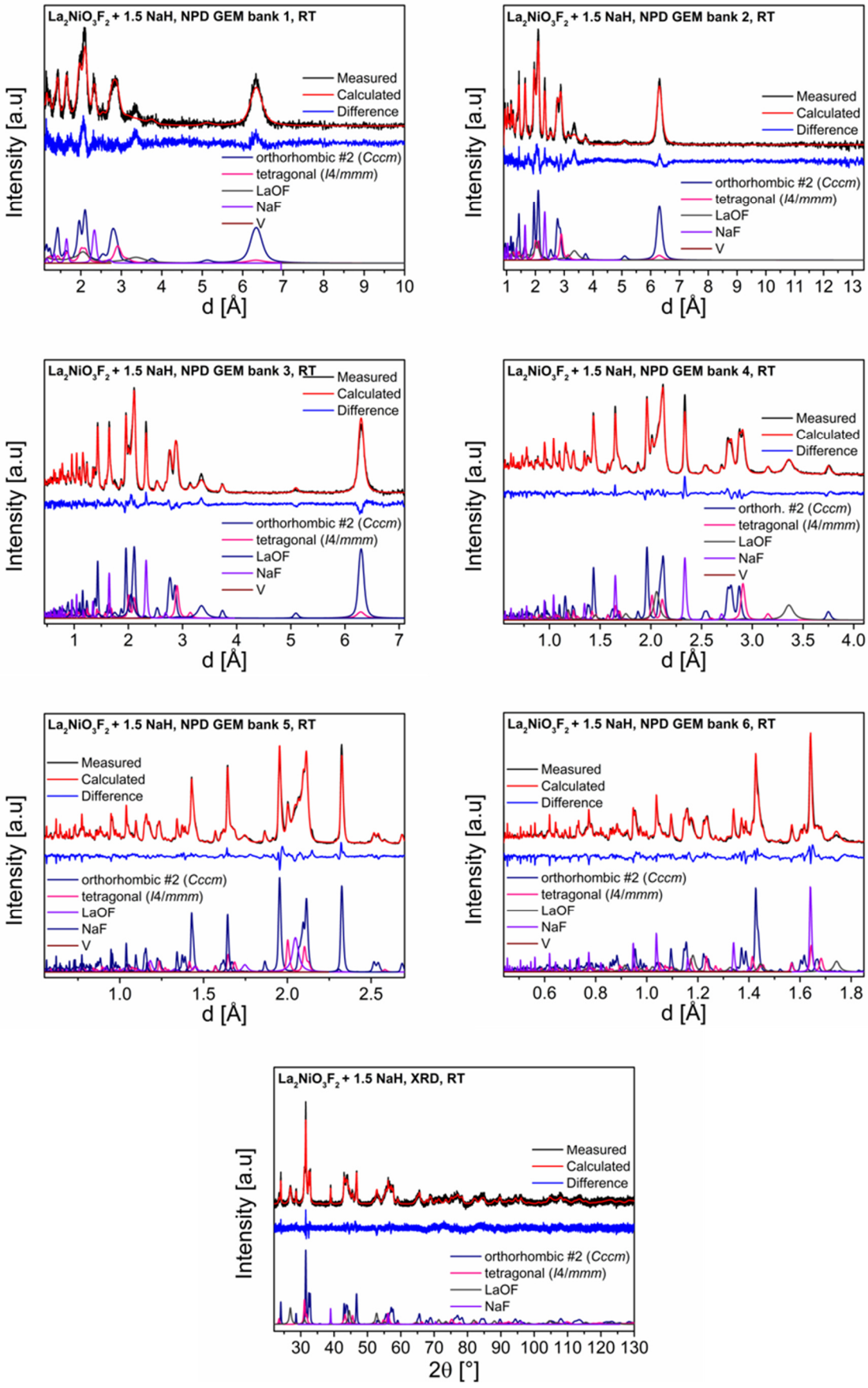

Figure 4-39: Coupled Rietveld refinement of the reduction product of $La_2NiO_3F_2$ + x NaH with x = 1.5 of GEM banks 1-6 and XRD data measured at room-temperature (RT).

Facilitated by the high phase fraction of the monoclinic phase (~ 73 wt%) within the reduction product, its structural model was derived from the measurement of $La_2NiO_3F_2 + 0.25$ NaH (Figure 4-37). Indexing can be performed with a base-centered $\sqrt{2} \times \sqrt{2} \times 1$ supercell of the tetragonal aristotype RP-type structure. Different structural models were tested, and a close structural relationship between the orthorhombic $La_2NiO_3F_2$ (space group: *Cccm*) and the reduced monoclinic phase is observed. It is found that the reduction of the symmetry from the orthorhombic space group *Cccm* towards a monoclinic distortion with *C* centering is only possible for the *translationengleiche* subgroups *C*12/*m*1 or *C*12/*c*1, with superior fit for the model with *C*12/*c*1 symmetry. The corresponding symmetry tree of the symmetry reduction from *Cccm* to *C*12/*c*1 and the refined structural parameters are given in Figure 4-40 and Table 4-15, respectively.

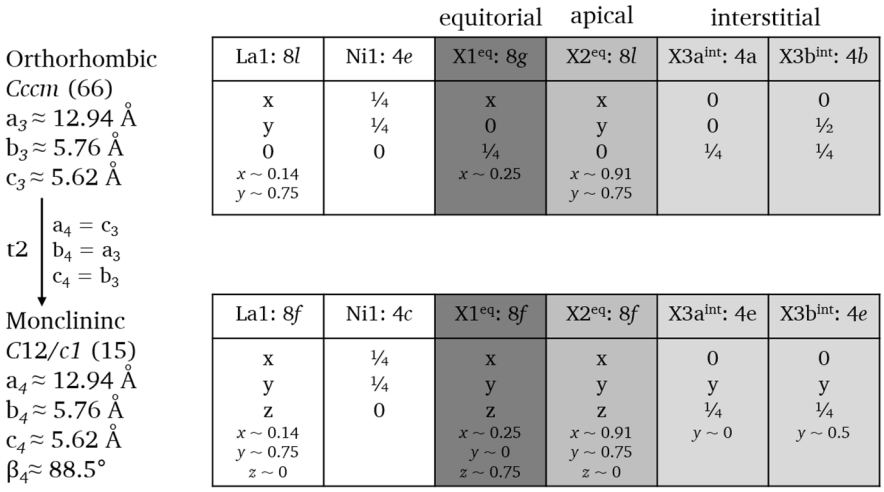

Figure 4-40: Symmetry tree for the symmetry reduction from *Cccm* to *C*12/*c*1. The different anion sites $X1^{eq}$, $X2^{ap}$ and $X3^{int}$ refer to the equatorial, apical and interstitial sites, respectively. The symmetry tree for the symmetry reduction from *I*4/*mmm* to *Cccm* is given in Figure 4-27.

Table 4-15: Structural parameters of the monoclinic phase with approximate composition $La_2NiO_3F_{1.93}$ (space group: *C*12/*c*1) derived from coupled Rietveld analysis of XRD and NPD data of the reduction product of $La_2NiO_3F_2$ + x NaH with x = 0.25. The anion sites $X1^{eq}$, $X2^{ap}$ and $X3^{int}$ refer to the equatorial, apical and interstitial sites, respectively.

Atom	**Wyckoff position**	**x**	**y**	**z**	**Occupancy**	**B [Å²]**
La1	8*f*	0.1123(7)	0.7483(3)	-0.0236(2)	**1**	0.88(1)
Ni1	4*c*	¼	¼	**0**	**1**	0.88(1)
O1 at $X1^{eq}$	8*f*	0.2704(1)	-0.0317(3)	0.7771(3)	**1**	0.88(1)
F1 at $X2^{ap}$	8*f*	0.9118(1)	0.8445(2)	-0.0330(3)	0.964(3)	0.88(1)
$X3a^{int}$	4*e*	**0**	**0**	¼	**0**	0.88(1)
O2 at $X3b^{int}$	4*e*	**0**	0.5177(5)	¼	**1**	0.88(1)
a [Å]	12.9413(4)		***b*** [Å]	5.7608(2)		
c [Å]	5.6186(2)		***β*** [°]	88.509(2)		
R_{wp}(XRD+NPD) [%]	3.40		**GOF(XRD+NPD)**	1.66	**R_{Bragg} [%]**	1.73 (XRD) 3.70 (NPD, bank 3)

Even though oxide and fluoride ions are indistinguishable by neutron and X-ray diffraction, the neutron diffraction data can be used to investigate the structure and composition of the anion sublattice in more detail by analysis of the occupation factors of anion sites. The symmetry reduction from *I*4/*mmm* to *C*12/*c*1 leads to a splitting of the interlayer anion site

into two 4e crystallographic sites X3a^{int} and X3b^{int} (Figure 4-27 and Figure 4-40). Similar to what is found for $La_2NiO_3F_2$, only the X3b^{int} site is occupied resulting in a channel-like half-filling of the interstitial sites. When also refining the occupation factors of the equatorial (X1^{eq}) and apical (X2^{ap}) anion sites, a small but considerable decrease of the occupancy of the apical anion site is observed, while the equatorial anion site remains fully occupied. From this, an overall composition of approximately $La_2NiX_{4.93}$ or of $La_2NiO_3F_{1.93}$ (assuming that only fluoride is extracted in the reduction process) can be derived. Furthermore, this indicates that the fluoride is, as in $La_2NiO_3F_2$, occupying the apical anion site. Major structural rearrangements of the oxide and fluoride ions between different anion sites upon the reduction with low amounts of NaH can, therefore, be excluded. This can be confirmed by bond-valence-sum calculations, for which, similar to calculations made on $La_2NiO_3F_2$, more stable configurations are found when fluoride is occupying the apical site. In comparison to the orthorhombic parent phase $La_2NiO_3F_2$, the slight reduction results in a change of the *b/c* ratio towards unity accompanied by a monoclinic distortion. For orthorhombic $La_2NiO_3F_2$, the distortion originates from a considerable tilting of the NiO_4F_2 octahedra along the *b* axis. The additional degrees of freedom of the monoclinic phase enable also a tilting of the octahedra along the *c* axis. This tilting leads to an increase of the distance of F^{ap}-F^{ap} (d(X2^{ap}-X2^{ap} ($La_2NiO_3F_2$)) ≈ 2.88 Å, d(X2^{ap}-X2^{ap} ($La_2NiO_3F_{1.93}$)) ≈ 2.93 Å) between two neighbouring perovskite building blocks. As it will be shown in section 4.1.3.2.3, this structural behaviour on extraction of comparatively small amounts of fluoride ions can be well confirmed from DFT-based calculations of a phase with composition $La_2NiO_3F_{1.75}$ and is explained there in detail. The crystal structure of the monoclinic phase with the approximate composition of $La_2NiO_3F_{1.93}$ is shown in Figure 4-41 a.

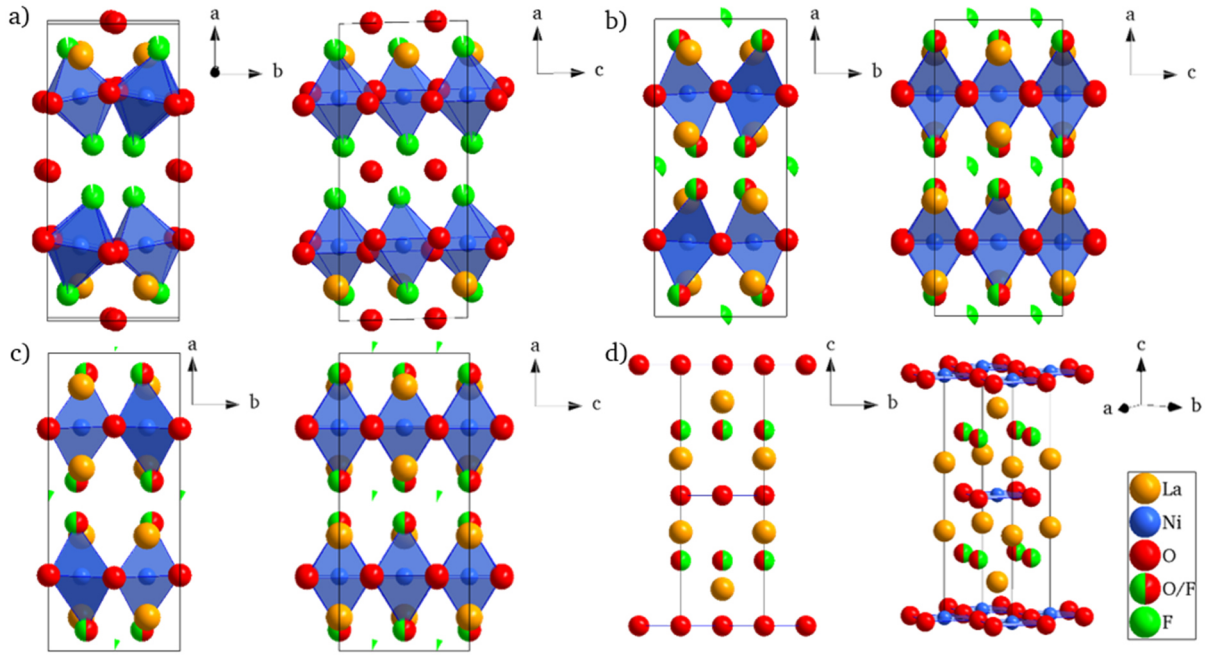

Figure 4-41: Crystal structures of the reduced monoclinic (a), orthorhombic #1 (b), orthorhombic #2 (c) and tetragonal (d) phases as determined from the coupled Rietveld analysis. To illustrate the tilting of the octahedra in the monoclinic, orthorhombic #1 and orthorhombic #2 phases, the structures are show along the *c* axis and the *b* axis. The structure of the tetragonal phase is shown along the *a* axis and twisted around the *c* axis to show the infinite NiO_2 square-planar layers.

In the reduction product $La_2NiO_3F_2$ + 0.25 NaH, besides the main monoclinic phase, additionally the orthorhombic #1 phase (~ 14 wt%) is present. The structural model of this phase was derived from $La_2NiO_3F_2$ + x NaH with x = 0.5 (Figure 4-38), since it has a higher phase fraction of the phase (~ 42 wt%). The highest weight fractions of the orthorhombic #2 (~ 45 wt%) and the tetragonal (~ 18 wt%) phases were found in the reduction product $La_2NiO_3F_2$ + 1.5 NaH (Figure 4-39) and their structural models were derived from its refinement.

For both orthorhombic phases, best fits could be achieved using structural models with space group *Cccm*. Higher symmetries such as *Fmmm* or other orthorhombic space groups, which show different tilting patterns of the NiX_6 octahedra (e.g. *Cmce* [44]), were tested in addition. These models can, however, not explain some superstructure reflections (e.g. $(110)_{Cccm}$ at a d value of ~ 5.1 Å), which can be described using the *Cccm* model. The structural parameters are given in Table 4-16 and Table 4-17.

Table 4-16: Structural parameters of the orthorhombic #1 phase with approximate composition $La_2NiO_3F_{1.39}$ (space group: *Cccm*) derived from coupled Rietveld analysis of XRD and NPD data of the reduction product of $La_2NiO_3F_2$ + x NaH with x = 0.5. The anion sites $X1^{eq}$, $X2^{ap}$ and $X3^{int}$ refer to the equatorial, central apical, terminal apical and interstitial sites, respectively.

Atom	**Wyckoff position**	**x**	**y**	**z**	**Occupany**	**B [Å²]**
La1	8*l*	0.1117(2)	0.7416(5)	**0**	**1**	0.73(1)
Ni1	4*e*	¼	¼	**0**	**1**	0.73(1)
O1 at $X1^{eq}$	8*g*	0.2430(4)	**0**	¼	**1**	0.73(1)
O2/F1 at $X2^{ap}$	8*l*	0.9271(3)	0.8153(4)	**0**	**1**	0.73(1)
$X3a^{int}$	4*a*	**0**	**0**	¼	**0**	0.73(1)
F2 at $X3b^{int}$	4*b*	**0**	½	¼	0.386(9)	0.73(1)
a [Å]	12.698(1)	***b*** [Å]		5.6484(5)	***c*** [Å]	5.4675(5)
R_{wp} (XRD+NPD) [%]	4.44	**GOF(XRD+NPD)**	2.36		**R_{Bragg} [%]**	0.34 (XRD) 1.65 (NPD, bank 3)

Table 4-17: Structural parameters of the orthorhombic #2 phase with approximate composition $La_2NiO_3F_{1.08}$ (space group: *Cccm*) derived from coupled Rietveld analysis of XRD and NPD data of the reduction product of $La_2NiO_3F_2$ + x NaH with x = 1.5. The anion sites $X1^{eq}$, $X2^{ap}$and $X3^{int}$ refer to the equatorial, central apical, terminal apical and interstitial sites, respectively.

Atom	**Wyckoff position**	**x**	**y**	**z**	**Occupany**	**B [Å²]**
La1	8*l*	0.1134(1)	0.7500(5)	**0**	**1**	0.44(1)
Ni1	4*e*	¼	¼	**0**	**1**	0.44(1)
O1 at $X1^{eq}$	8*g*	0.2558(4)	**0**	¼	**1**	0.44(1)
O2/F1 at $X2^{ap}$	8*l*	0.9284(2)	0.7875(3)	**0**	**1**	0.44(1)
$X3a^{int}$	4*a*	**0**	**0**	¼	**0**	0.44(1)
F2 at $X3b^{int}$	4*b*	**0**	½	¼	0.077(5)	0.44(1)
a [Å]	12.5309(3)	***b*** [Å]		5.5427(1)	***c*** [Å]	5.4758(1)
R_{wp} (XRD+NPD) [%]	4.31	**GOF(XRD+NPD)**	2.28		**R_{Bragg} [%]**	1.35 (XRD) 2.46 (NPD, bank 3)

When refining the occupation factors of the equatorial ($X1^{eq}$), apical ($X2^{ap}$) and interstitial ($X3b^{int}$) sites of the orthorhombic phases, the occupation factor of the $X3b^{int}$ interstitial site, which is fully occupied in $La_2NiO_3F_2$, decreases considerably resulting in compositions of $La_2NiX_{4.39}$ ($La_2NiO_3F_{1.39}$) for the orthorhombic #1 phase and of $La_2NiX_{4.08}$ ($La_2NiO_3F_{1.08}$) for the orthorhombic #2 phase. In the monoclinic phase, vacancies are formed at the apical site, i.e., at the site, at which the fluoride ions are located in the parent phase $La_2NiO_3F_2$. In contrast, no indication is given for the presence of vacancies at the apical sites for the orthorhombic

phases. This shows that at least a partial rearrangement of anions between the apical and interstitial sites can take place, which is also accompanied by a lowering of the tilting of the NiX_6 polyhedra. This lowering of the tilting leads to a decrease of the bond valance sums of the interstitial anion site, which renders the allocation of fluoride ions at it more plausible. This correlates with a change in the bond distances of Ni to the apical ($X2^{ap}$) and equatorial ($X1^{eq}$) anions, showing increased stretching of the octahedra for increasing amounts of NaH used (Table 4-18 and Figure 4-41 b and c). This is in plausible agreement with the formation of Jahn-Teller active Ni^{+} with d^9 electron configuration and is also observed in DFT-based calculations (see section 4.1.3.2.3). Furthermore, when comparing the bond distances between apical ($X2^{ap}$) and interstitial anions ($X3b^{int}$) of $La_2NiO_3F_2$ with the reduced monoclinic and orthorhombic phases, it can be seen that the distances decrease considerably, indicating that the tilting of the octahedra decreases for stronger reduced phases. These distances are relatively short, but it has to be taken into account that the occupancies of this interstitial site in these phases decrease significantly. This also shows that refinements can only serve to determine an average structure of the disordered state, in which local adaptations have to be expected. Furthermore, considerable disorder is most likely to be present within the reduced orthorhombic phases. The unrealistic small distances between the apical ($X2^{ap}$) and the unoccupied interstitial anions ($X3a^{int}$) highlight, moreover, that this interstitial site cannot be occupied. The distances between two apical sites ($X2^{ap}$) of neighbouring perovskite building blocks are also given.

Table 4-18: Bond distances of $La_2NiO_3F_2$ and the reduced monoclinic, orthorhombic #1, orthorhombic #2 and tetragonal phases. The anion sites $X1^{eq}$, $X2^{ap}$ and $X3^{int}$ refer to the equatorial, central apical, terminal apical and interstitial sites, respectively.

		Bond distance [Å]			
Bond	**$La_2NiO_3F_2$**	**monoclinic**	**orthorh. #1**	**orthorh. #2**	**tetragonal**
La1 – O1 at $X1^{eq}$	2.539(2) [2x] 2.813(2) [2x]	2.423(2) [1x] 2.621(2) [1x] 2.626(2) [1x] 3.145(2) [1x]	2.552(4) [2x] 2.721(4) [2x]	2.546(3) [2x] 2.642(3) [2x]	2.665(2) [4x]
La1 – F1 at $X2^{ap}$ **or** **La1 – O2/F1 at $X2^{ap}$**	2.356(2) [1x] 2.602(2) [1x] 2.809(1) [2x]	2.379(2) [1x] 2.577(2) [1x] 3.176(2) [1x] 3.450(2) [1x]	2.551(4) [1x] 2.809(1) [2x] 3.184(4) [1x]	2.617(3) [1x] 2.7953(6) [2x] 3.025(3) [1x]	
La1 – O2 at $X3b^{int}_{Cccm}$ or $C12/c1$ **or** **La1 – F2 at $X3b^{int}_{Cccm}$** **or** **La1 – O2/F1 at $X3^{int}_{I4/mmm}$**	2.4718(8) [2x]	2.486(2) [1x] 2.487(2) [1x]	2.396(2) [2x]	2.411(2) [2x]	2.417(1) [4x]
Ni1 – O1 at $X1^{eq}$	2.0076(2) [4x]	2.071(2) [2x] 2.019(2) [2x]	1.9673(3) [4x]	1.9492(1) [4x]	1.9962(1) [4x]
Ni1 – F1 at $X2^{ap}$ **or** **Ni1 – (O2/F1) at $X2^{ap}$**	2.160(2) [2x]	2.152(3) [2x]	2.279(4) [2x]	2.245(3) [2x]	
$X2^{ap}$ – $X3a^{int}_{Cccm}$ or $C12/c1$ **or** **$X2^{ap}$ – $X3^{int}_{I4/mmm}$**	1.990(2) [2x] ($X3^{int}a_{Cccm}$ is unoccupied)	1.876(1) [1x] 2.174(2) [1x] ($X3^{int}a_{C12/c1}$ is unoccupied)	1.953(2) [2x] ($X3^{int}a_{Cccm}$ is unoccupied)	2.017(2) [2x] ($X3^{int}a_{Cccm}$ is unoccupied)	2.2921(1) [4x] ($X2^{ap}$ is unoccupied)
$X2^{ap}$ – $X3b^{int}_{Cccm}$ or $C12/c1$	2.657(2) [2x]	2.659(3) [1x] 2.733(2) [1x]	2.428(2) [2x]	2.284(2) [2x]	
$X2^{ap}$– $X2^{ap}$	2.883(2) [1x] 3.536(2) [2x] 4.552(3) [1x]	2.933(2) [1x] 3.297(2) [1x] 3.963(2) [1x] 4.599(2) [1x]	2.790(5) [1x] 3.302(3) [1x] 4.014(4) [2x]	2.961(3) [1x] 3.274(2) [1x] 3.658(2) [2x]	3.6117(1) [4x] ($X2^{ap}$ is unoccupied)

On increasing of the amount of NaH further, a tetragonal phase (Figure 4-39) is formed. This phase is found to possess a completely different neutron diffraction intensity pattern with strong changes in the relative reflection intensities compared to the T-related orthorhombic phases (Figure 4-42). This intensity pattern is indicative for the formation of a tetragonal phase with T'-type structure (space group: *I*4/*mmm*), in which the apical site X2^{ap} is empty and the interstitial site X3^{int} is filled, suggesting an approximate composition of La_2NiO_3F. The Ni cations have a square planar coordination in this structure (Figure 4-41 d). The structural parameters are listed in Table 4-19. DFT calculations (see section 4.1.3.2.3) support this observation, showing that this is the most stable structure for a phase with a composition of La_2NiO_3F. Such T'-type RP phases have only been found for compounds containing high amounts of Jahn-Teller active cations, e.g. for the Nd_2CuO_4 [50], $La_3Ni_2O_6$ [100, 101], $La_4Ni_3O_8$ [99, 101], giving further support that a composition close to La_2NiO_3F is obtained here. Additionally, the reduction of $La_2NiO_3F_2$ to La_2NiO_3F leads to a lower average Ni oxidation state as compared to the previously reported reductions of $La_3Ni_2O_7$ and $La_4Ni_3O_{10}$ to $La_3Ni_2O_6$ and $La_4Ni_3O_8$, respectively. For La_2NiO_3F, a Ni valence of +1 is achieved, while only higher Ni valences of +1.5 and +1.33 can be obtained for in $La_3Ni_2O_6$ and $La_4Ni_3O_8$. [99-101]

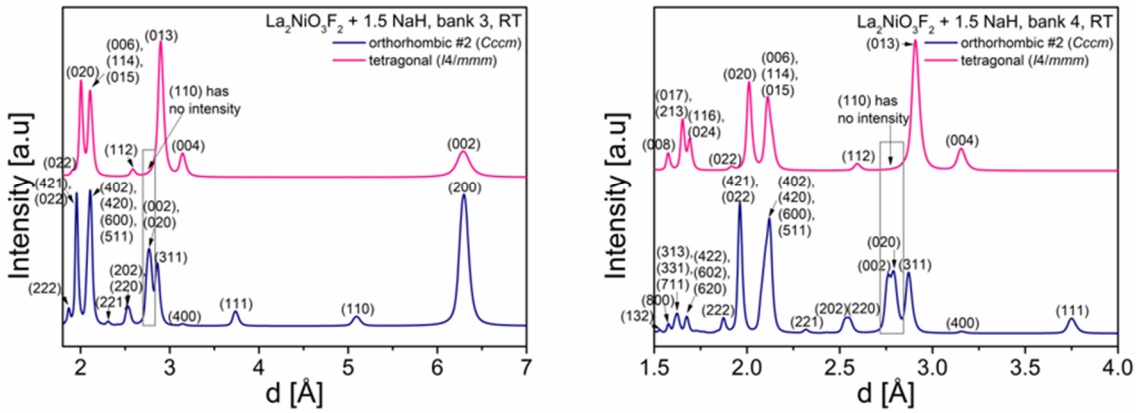

Figure 4-42: Comparison between refined diffraction patterns of reduced orthorhombic #2 (T-type structure) and tetragonal (T'-type structure) phase of the reduction product $La_2NiO_3F_2$ + x NaH with x = 1.5 of NPD GEM banks 3 and 4 measured at room-temperature (RT). The differences in the relative reflections intensities of the patterns are indicative for the formation of T- and T'-type structures due to different occupied and unoccupied anion sites. Additionally, characteristic reflections are indexed. The reader should be aware that the different indexes result from the increased unit cell size from the transition from tetragonal to orthorhombic (lattice parameters of orthorhombic cell: $a_{ortho} = c_{tetra}$, $b_{ortho} = a_{tetra}-b_{tetra}$, $c_{ortho} = a_{tetra}+b_{tetra}$). The groups of reflections corresponding to the same set of lattice planes, e. g. $(013)_{tetra}$ and $(311)_{ortho}$ as well as $(110)_{tetra}$ and $(020)_{ortho}/(002)_{ortho}$, are found at similar overall d-spacings.

Table 4-19: Structural parameters of the tetragonal phase with approximate composition La_2NiO_3F (space group: *I*4/*mmm*) derived from coupled Rietveld analysis of XRD and NPD data of the reduction product of $La_2NiO_3F_2$ + x NaH with x = 1.5. The anion sites X1^{eq}, X2^{ap} and X3^{int} refer to the equatorial, central apical, terminal apical and interstitial sites, respectively.

Atom	**Wyckoff position**	**x**	**y**	**z**	**Occupany**	**B [Å²]**
La1	4*e*	**0**	**0**	0.6411(2)	**1**	0.54(1)
Ni1	2*q*	**0**	**0**	**0**	**1**	0.54(1)
O1 at X1^{eq}	4*c*	**0**	½	**0**	**1**	0.54(1)
X2^{ap}	4*e*	**0**	**0**	**0.84**	**0**	0.54(1)
O2/F1 at X3^{int}	2*d*	**0**	½	¼	**1**	0.54(1)
a [Å]	3.9925(2) (a·√2 = 5.6462(3))			***c*** [Å]		12.5150(9)
R_{wp} (XRD+NPD) [%]	4.61	**GOF(XRD+NPD)**	2.70		**R_{Bragg} [%]**	1.25 (XRD) 2.23 (NPD, bank 3)

As discussed in section 2.2.4, the introduction of additional anions into La_2NiO_{4+d} via the non-oxidative fluorination reaction using PVDF seems to be crucial to obtain the single (n=1) layer T'-type structure with infinite NiO_2 square-planar layers after the reductive defluorination. For the stabilisation of the T'-type structure it seems further important that not more than 2n+2 anions are present within the compound. As has been also observed for $Sr_2CuO_2F_{2+\delta}$ [64, 69] (see section 2.2.1.2), excess anions lead to the formation of T-type structures, which is also found for the orthorhombic #1 and #2 phases. Especially for the orthorhombic #2 phase with its approximate composition of $La_2NiO_3F_{1.08}$, only a small over-stoichiometry is observed, highlighting the high sensitivity of the stability of different structure types towards small compositional differences.

Interestingly, a strong collapse of the long crystallographic axis, as it occurs for the transition from the T- to T'-type structure of $Sr_2CuO_2F_{2+\delta}$ and $Sr_2CuO_2F_2$, is already observed for the orthorhombic #2 phase ($a \approx 12.53$ Å). For comparison, the parent oxyfluoride $La_2NiO_3F_2$, which has, as the orthorhombic #2 phase, a T-type related structure, has an *a* lattice parameter of ~ 12.84 Å. The tetragonal phase with T'-type structure shows only a small additional decrease of the *c* axis to ~ 12.52 Å compared to the orthorhombic #2 phase. The observed collapse in the orthorhombic #2 phase seems to be related to significant decreases of the $X2^{ap}$-$X3b^{int}$ and $X2^{ap}$-$X2^{ap}$ bond distances (even to an extent, for which in particular the distance between $X2^{ap}$ and the slightly filled $X3b^{int}$ sites becomes too short) (Table 4-18). The atomic rearrangements of anions from the apical to the interstitial anion site in the tetragonal phase, on the other hand, result in a potentially more favourable structure with more reasonable bond distances. The transition from the T- to T'-type structure gives rise to the strong reduction of the *c* lattice parameter.

4.1.3.2.3 Towards understanding of the structural distortions in the reduced phases by DFT calculations

As shown in the previous section, obtaining a complete structural understanding of the anion chemistry of the reduced phases is difficult to achieve experimentally. Therefore, DFT calculations were performed to develop a deeper understanding of the most favourable structural relaxations of the anion sublattice on reductive defluorination of $La_2NiO_3F_2$. To do so, the structural model of $La_2NiO_3F_2$ was considered as a starting point. Then, one to four fluoride ions per unit cell were successively removed, corresponding to compositions of $La_2NiO_3F_{1.75}$ to La_2NiO_3F, and the structure was allowed to relax. In addition, various different relative orientations of the introduced vacancies were examined together with different distributions of oxide and fluoride ions at the apical and/or interstitial sites. The equatorial site was always occupied by oxide ions. In the following, the discussion is limited to the changes of the initial to the most stable relaxed structures of the reduced phases.

For calculations on compounds $La_2NiO_3F_{2-\Delta}$ with high values of Δ, it was found that the remaining anions show a very high mobility, although no molecular dynamics was chosen (i.e., a structure optimization at 0 K). This is exemplified for the defluorinated phase with the composition La_2NiO_3F (Figure 4-43 vacancy configuration 1). For this composition, a complete relaxation to the T' structure can be observed for suitable initial vacancy configurations, which is due to the movement of apical fluoride ions to the interstitial site, leading to a fully unoccupied apical site and a filled interstitial site (an occupation with 50 % fluoride and 50 % oxide ions is assumed). This is in agreement with the experimental observation of the T'-type tetragonal phase (see section 4.1.3.2.2). It is found that the principle relaxation of the lattice

parameters on transition to the T'-type structure can also be reproduced: the *b* and *c* lattice parameters after relaxation are found to be of the order of 5.7 to 5.8 Å, which is close to the experimental value 5.65 Å, whereas the lattice parameter *a* decreases to 12.67 Å (12.52 Å experimentally). Furthermore, it is found that a relaxation to the T' structure is independent on the initial anion configuration; both, $La_2Ni(O_2)^{eq}(F)^{ap}(O)^{int}$ and $La_2Ni(O_2)^{eq}(O)^{ap}(F)^{int}$ relax to T'-type $La_2Ni(O_2)^{eq}(\square)^{ap}(OF)^{int}$. It should be emphasized that a relaxation to a T'-type structure seems to be hindered, if the relative location of the vacancies towards each other are unfavourable (Figure 4-43 vacancy configuration 2). This might also explain why both, T and T'-type phase can be observed at the same time in the reduction products. This behaviour is in principle also found for intermediate compositions $La_2NiO_3F_{1.25}$ and $La_2NiO_3F_{1.5}$.

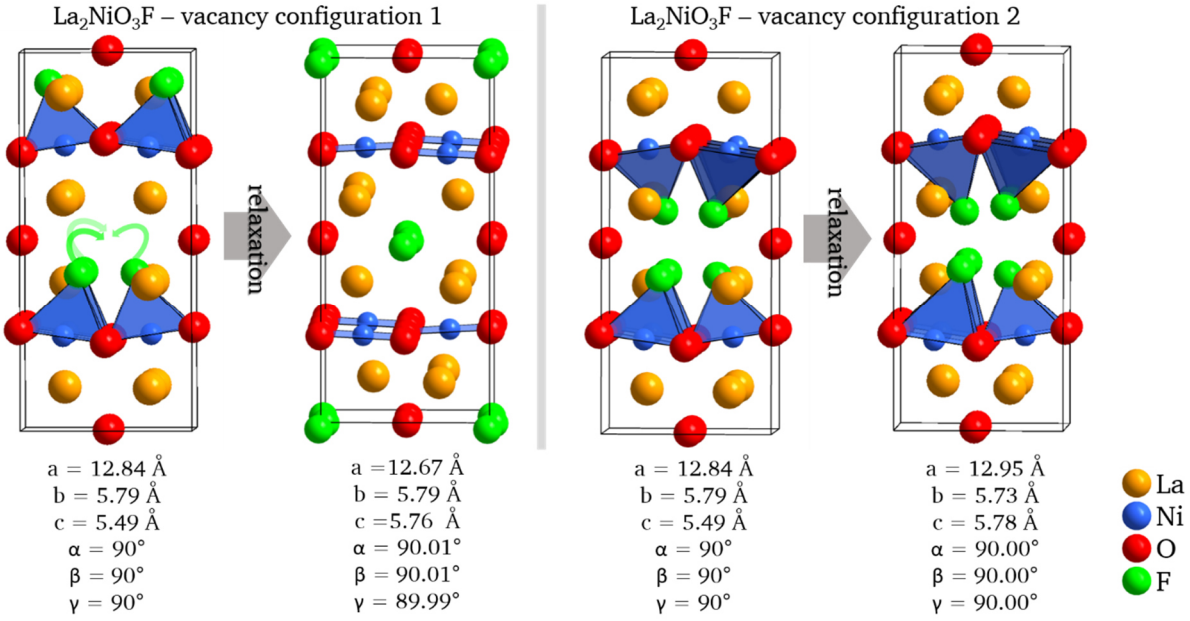

Figure 4-43: Structural relaxation of different vacancy ordered starting models of La_2NiO_3F. The starting models were derived from the experimentally determined orthorhombic structure of $La_2NiO_3F_2$, from which four different fluoride ions were removed to create different vacancy configurations. Configuration 1 was found to relax to a T' type structure, whereas configuration 2 does not.

Removing only one fluoride ion from the unit cell of $La_2NiO_3F_2$ results in a composition of $La_2NiO_3F_{1.75}$. With respect to the subgroups of *Cccm*, this corresponds to a monoclinic ordering variant (isomorphic subgroups which maintain the orthorhombic symmetry for a similar composition require a 3- to 5-fold increase of the unit cell size, which was computationally too costly to be considered). A deviation from the orthorhombic symmetry is also found in a partly relaxed structure (compare Figure 4-44 a and b), where the angle γ changes due to this artificial ordering of fluoride ions and vacancies. On fully relaxing the structure by inducing further strain, it is found that the energetically most stable structure has a similar distortion and tilting pattern as the experimentally found structure of the monoclinic phase with an approximate composition $La_2NiO_3F_{1.93}$ (compare Figure 4-44 c and d), which is expressed by the deviation of the angle β from 90°. The structural distortion is complicated and can be explained as follows: the reductive defluorination results in a change of the electronic structure to a d^9 Jahn-Teller-active electron configuration of the formed Ni^+. This Ni^+ ion is located in the NiO_4F polyhedron, and, consequently, close to the anion vacancy. The polyhedron distorts towards square planar coordination by shifting the remaining fluoride ion away from the apical site towards the position of the interstitial site. However, this shift is energetically costly due to the proximity to the fluoride ion of the polyhedron with identical

tilting in the layer above. By inducing the tilting along the *c* axis, the apical fluoride ion of the NiO_4F polyhedron can move further away from the central Ni-ion by an additional increment of ~ 0.12 Å (= $\Delta(d(Ni\text{-}X2^{ap}) = d(Ni\text{-}X2^{ap}(c)) - d(Ni\text{-}X2^{ap}(a))$, while additionally increasing the distance to the next closest fluoride ion $d(X2^{ap}\text{-}X2^{ap})$ by ~ 0.05 Å. This has a strong energetic impact of -0.39 eV per unit cell (u. c.).

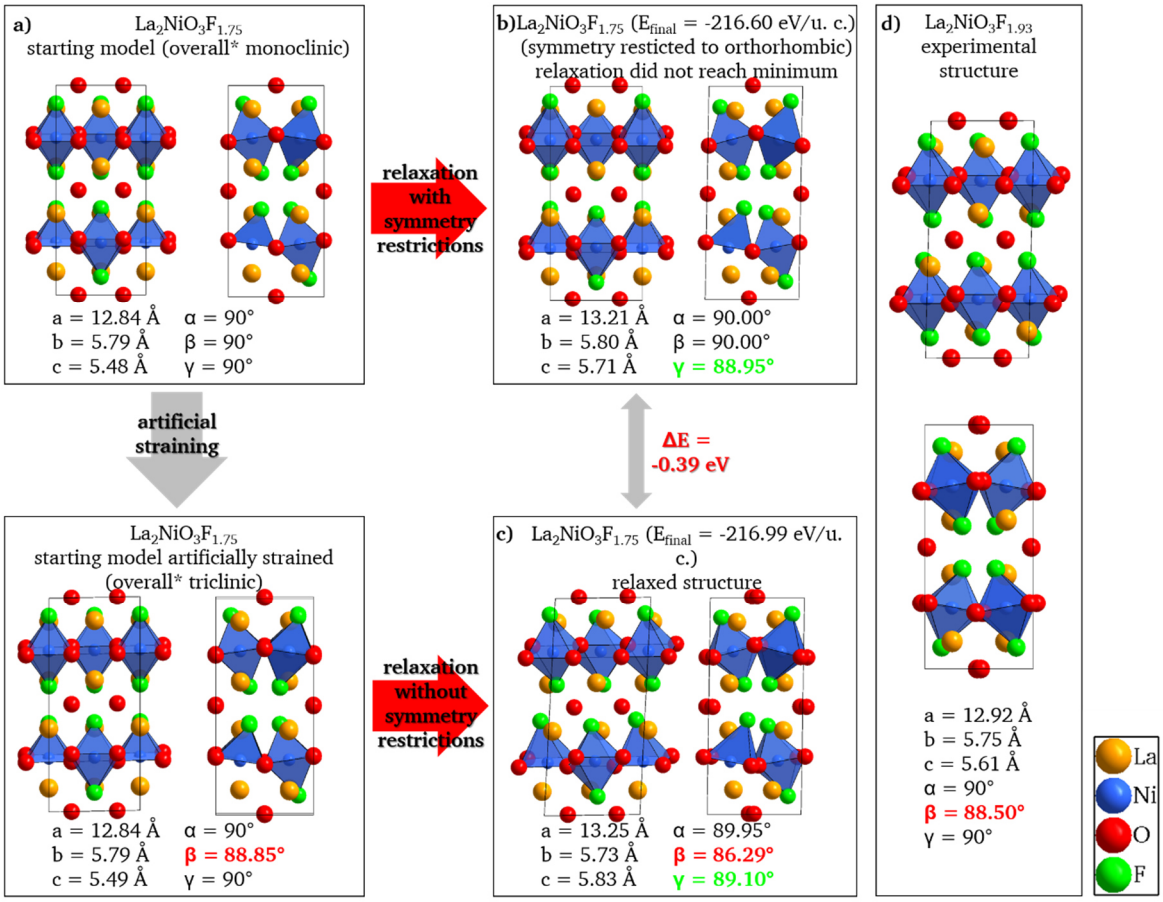

Figure 4-44: Scheme of the DFT-based calculations performed to determine the most stable structure of the reduced monoclinic phase with approximate composition of $La_2NiO_3F_{1.93}$ by performing calculations on non-strained and strained $La_2NiO_3F_{1.75}$. The starting model (a) was derived from the experimentally determined orthorhombic structure of $La_2NiO_3F_2$ by removing one fluoride ion. Calculations were performed on a non-strained model with symmetry restrictions (c) and strained model without symmetry restrictions (d). For reference, the experimentally obtained crystal structure of $La_2NiO_3F_{1.93}$ is shown (e). The viewing directions of the left and right representations corresponding to one relaxed structure are along the *b* axis and *c* axis, respectively. (*: "Overall" refers to the combination of cell metrics and inner symmetry of the atoms.)

The electronic origin of the monoclinic distortion can also be verified by comparing with results for the structure of $La_2NiO_3F_2$, obtained using similar calculation strategy. Even after inducing a monoclinic straining to $La_2NiO_3F_2$, a relaxation back to the orthorhombic symmetry with negligible orthorhombic distortion ($\beta = 89.94°$) and no energy difference ($\Delta E = 0.00$ eV per unit cell) can be observed (Figure 4-45). This indicates the absence of a structural driving force for the lowering of the symmetry in stoichiometric, well-ordered $La_2NiO_3F_2$, highlighting the strong impact of small compositional changes in materials containing elements with d^9 electron configuration.

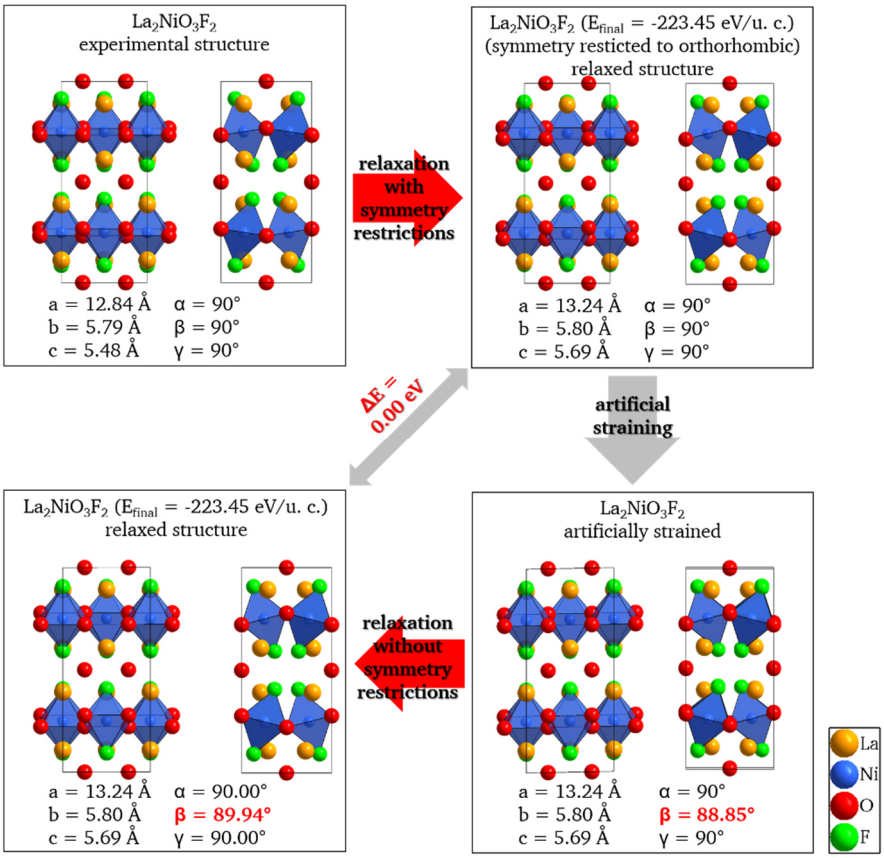

Figure 4-45: Scheme of the DFT-based calculations performed to corroborate the experimentally found crystal structure of $La_2NiO_3F_2$ is the most stable structure by comparing the relaxed structures obtained after straining and non-straining. Calculations were performed with and without symmetry restrictions.

4.1.3.3 Transmission electron microscopy study of $La_2NiO_3F_2$ and the reduction products

High-resolution-TEM imaging can be a powerful technique to investigate structural changes in phase mixtures. However, this type of analysis is impeded by the fact that the crystals obtained in this study are generally quite thick and can be composed of multiple domains of different RP-type phases as well as decomposition and side products. Therefore, an alternative approach was used to confirm the structures observed via X-ray and neutron powder diffraction methods by independent means using the Fast-ADT technique. This relatively new tool is based on the sequential acquisition of electron diffraction patterns from preferably mono-domain crystals at different consecutives tilt angles, which are separated by a fixed tilt step. The 3-dimensional reconstruction of the diffraction space data facilitates the determination of crystal structures in a similar way as in single crystal X-ray methods.

In order to reinforce the proposed structures of $La_2NiO_3F_2$ and the reduced phases derived from X-ray and neutron powder diffraction, Fast-ADT measurements were performed on $La_2NiO_3F_2$ and the reduction products with x = 0.25 and 1.5. The selection of suitable crystals for the measurements turned out to be very difficult because they have to be reasonably thin in order to obtain good quality data sets. Although thinner particles (Figure 4-46) were chosen for the acquisition of the Fast-ADT data, these crystals are still relatively thick. Most of the analysed particles contain twins, other domains or large amounts of the side product NaF and/or the decomposition product LaOF, which hamper the successful structure determination of the reported phases (Figure 4-47). Furthermore, it cannot be excluded that a

(partial) re-oxidation of the phases took place during the preparation of the samples. Especially isolated particles, which were deliberately selected for the measurements, should be more prone towards oxidation. However, the deduction of unit-cell and space group information was possible for all phases. The obtained lattice parameters (Table 4-20) are in agreement within the accuracy of this method with the results obtained from X-ray and neutron diffraction reported in the previous sections.

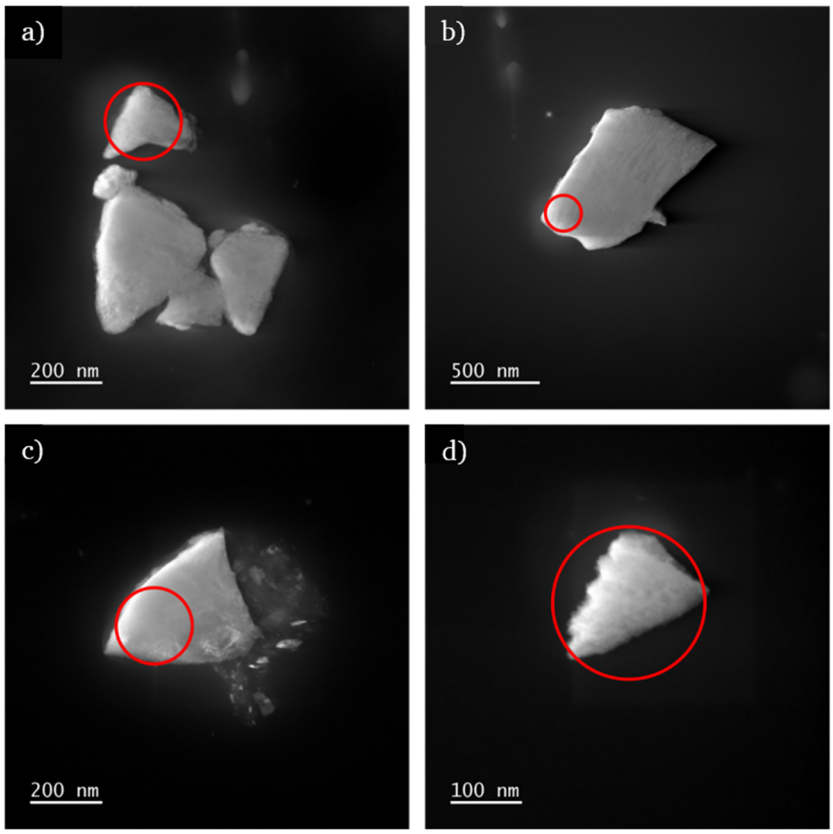

Figure 4-46: High-angle annular dark field (HAADF) images of crystals with the monoclinic structure (a) and orthorhombic #1 of structure (b) of the reduction product $La_2NiO_3F_2$ + x NaH with x = 0.25 and of crystals with the orthorhombic #2 structure (c) and tetragonal structure (d) of the reduction product $La_2NiO_3F_2$ + x NaH with x = 1.5. The red circles point out the size of the electron beam and its position for the Fast-ADT measurements.

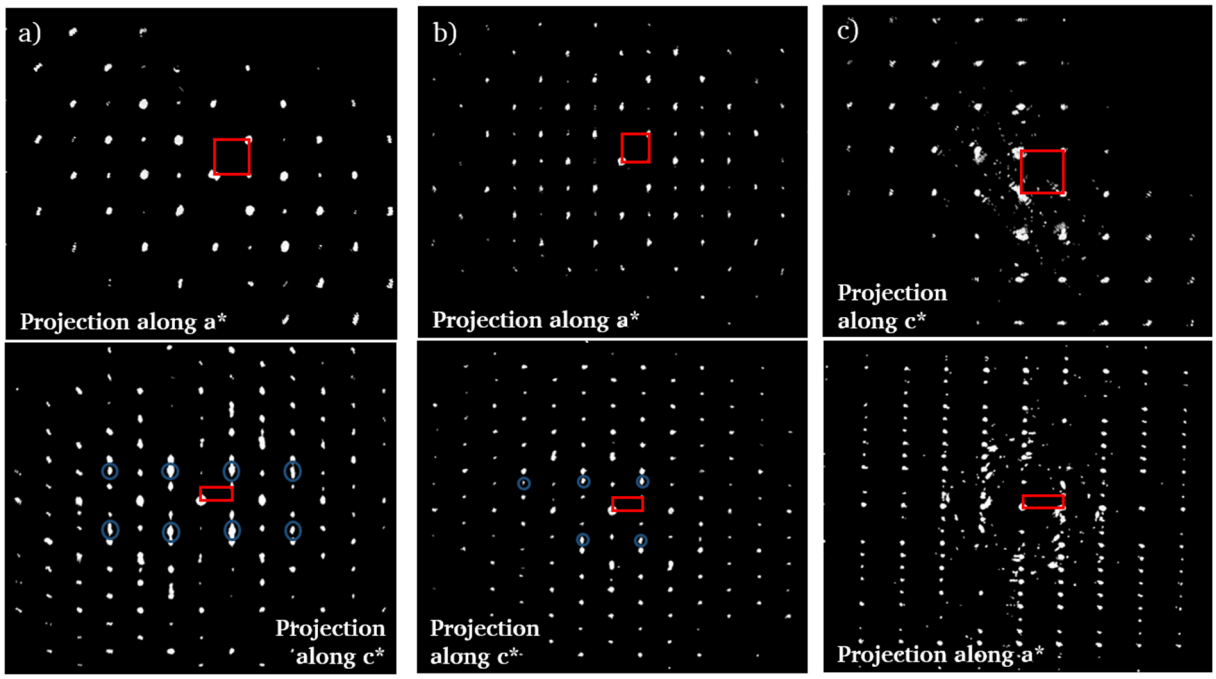

Figure 4-47: Views of the reciprocal space along the a* and c* axes of a crystal with monoclinic (a), orthorhombic #2 (b) and the tetragonal (c) structure. The reflections highlighted with blue circles correspond to LaOF, growing presumably expitaxially on the RP-type phases.

Table 4-20: Unit cell parameters of $La_2NiO_3F_2$ and reduced phases within the reduction products $La_2NiO_3F_2$ + x NaH with x = 0.25 and 1.5 determined from Fast-ADT measurements. Crystal structure determination was performed on the crystals which are marked with *.

		Phase	Lattice parameters					
			a **[Å]**	***b*** **[Å]**	***c*** **[Å]**	**α [°]**	**β [°]**	**γ [°]**
$La_2NiO_3F_2$	Crystal 1 *	$La_2NiO_3F_2$	13.13	5.79	5.56	90.2	91.0	89.6
$La_2NiO_3F_2$+ 0.25 NaH	Crystal 1	orthorhombic #1	12.95	5.76	5.68	90.1	90.4	89.9
	Crystal 2	monoclinic	12.83	5.79	5.63	90.2	88.3	89.9
	Crystal 3 *	monoclinic	12.92	5.80	5.65	90.1	88.0	90.1
$La_2NiO_3F_2$ + 1.5 NaH	Crystal 1	tetragonal	3.96	3.99	12.62	90.5	89.8	90.4
	Crystal 2	tetragonal	3.97	4.01	12.65	89.7	90.2	90.0
	Crystal 3	orthorhombic #2	12.97	5.72	5.64	89.9	90.8	90.2
	Crystal 4	tetragonal	3.90	3.88	12.52	89.6	90.2	86.5
	Crystal 5	tetragonal	3.92	3.89	12.61	90.0	90.5	90.0

Using dynamical refinement approaches, it was also possible to confirm the *Cccm* structure of $La_2NiO_3F_2$ and the *C*12/*c*1 structure of the monoclinic phase present within the reduction product with x = 0.25 (Table 4-21). Data acquisition, structural solution and dynamical refinement parameters are given in Table 6-3. It was also attempted to refine the structures of the orthorhombic #1 and #2 phases as well as the tetragonal phase found in the products with x = 0.25 and x = 1.5. Although the centering of these phases could be confirmed (Figure 4-47), accurate structural analyses of these phases were not possible. This is presumably due to an epitaxial growth of the decomposition product LaOF on the reduced RP-type phases, which biases the obtained reflection intensities significantly. This epitaxy gives an indication of the decomposition mechanism of the metastable oxyfluoride phases. Therefore, it is not possible to confirm the structural models of the stronger reduced phase determined from coupled Rietveld analysis of X-ray and neutron diffraction data by means of electron

diffraction methods. It has to be pointed out that the coupled Rietveld refinement of X-ray and neutron diffraction data provides a more robust analysis of the anion sublattice, especially with respect to small details in anion occupancies found for $La_2NiO_3F_2$ and the monoclinic phase.

Table 4-21: Atomic positions of structural models of $La_2NiO_3F_2$ and the reduced monoclinic phase refined from Fast-ADT measurements by the dynamical approach implemented into the Jana2006 program. Note that some of the oxygen positions have negative or too high U_{iso} values. Such deviations as well as their high R1 values may be explained from the presence of other domains in the data sets with reflections partially overlapping with reflections of the main phase. The U_{iso} of the monoclinic crystal structure is given as the equivalent U (U_{eq}) since it was refined anisotropically ($U_{eq} = \frac{1}{3}\sum\sum U_{ij} a_i^* a_j^* \mathbf{a_i} \cdot \mathbf{a_j}$). Furthermore, the occupation factors of the reduced monoclinic phase have not been refined.

$La_2NiO_3F_2$ (space group: *Cccm*)

Atom	Wyckoff position	x	y	z	Occupancy	U_{iso} [Å^2]
La1	8*l*	0.3927(4)	0.7513(5)	**0**	**1**	0.0197(9)
Ni1	4*e*	¼	¼	**0**	**1**	0.013(1)
O1 at X1^{eq}	8*g*	0.281(1)	**0**	¼	**1**	-0.011(1)
F1 at X2^{ap}	8*l*	0.592(2)	0.658(4)	**0**	**1**	0.053(5)
O2 at X3b^{int}	4*b*	**0**	½	¼	**1**	0.17(3)
Monoclinic phase with approximate composition $La_2NiO_3F_{1.93}$ (space group: *C*12/*c*1)						
Atom	**Wyckoff position**	**x**	**y**	**z**	**Occupancy**	**U_{iso} [Å^2]**
La1	8*f*	0.1131(1)	0.7472(3)	0.9740(4)	**1**	0.0114(6)
Ni1	4*c*	¼	¼	**0**	**1**	0.014(1)
O1 at X1^{eq}	8*f*	0.2292(5)	0.525(1)	0.223(2)	**1**	0.012(3)
F1 at X2^{ap}	8*f*	0.4152(2)	0.658(2)	0.466(2)	**1**	0.013(3)
O2 at X3b^{int}	4*e*	**0**	0.522(2)	¼	**1**	0.005(4)

4.1.3.4 Magnetic characterisation of $La_2NiO_3F_2$ and the reduction products

4.1.3.4.1 Magnetisation study of $La_2NiO_3F_2$ and the reduction products

The ZFC M(T) and χ^{-1}(T) curves of $La_2NiO_3F_2$ are shown in Figure 4-48 a. The difference between the ZFC and FC M(T) curves is shown in Figure 6-15. Above 49 K, a paramagnetic behaviour is observed. Between 150 and 300 K, χ^{-1}(T) data are nearly linear and can be fitted in accordance with the Curie−Weiss law. The obtained paramagnetic moment of 2.82 μ_B agrees well with the expected spin-only magnetic moment of high-spin Ni^{2+} (2.83 μ_B). A Weiss constant Θ of ∼ −469 K indicates strong antiferromagnetic interactions.

At 49 K, a transition from paramagnetic to antiferromagnetic behaviour is observed. The increase of the magnetisation at temperatures below 30 K suggests the contribution of a weak ferromagnetic component, which could originate from a magnetic canting within the compound on antiferromagnetic ordering. [44]

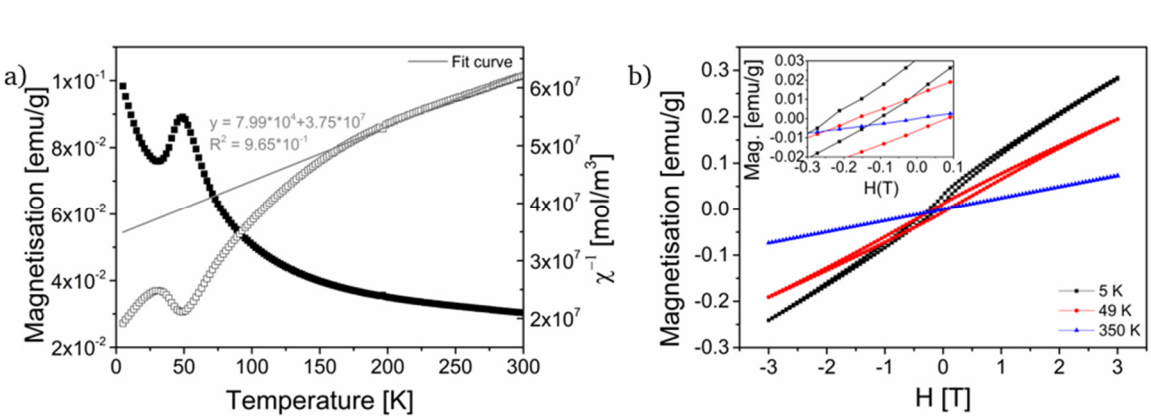

Figure 4-48: a) ZFC M(T) (closed symbols) and χ^{-1}(T) (open symbols) curves of $La_2NiO_3F_2$ measured at μ_0 = 1 T. The fitting curve of the Curie-Weiss fit, the corresponding linear function and the coefficient of determination are also given. The curves are corrected from the diamagnetic contributions of the present phases and the gelatine capsules and straws used for the measurements; (b) M(H) curves measured at 5, 49 and 350 K of $La_2NiO_3F_2$. The inset shows the exchange bias observed at 5 K in comparison to the measurements at 49 and 350 K. The fitting curves of the Curie-Weiss fits, the corresponding linear functions and the coefficients of determination are also given.

To confirm the origin of ferromagnetism below 30 K, a field-dependent M(H) measurement was performed at 5 K (Figure 4-48 b). The observed weak hysteresis confirms an intrinsic ferromagnetic component. In addition, an exchange bias with an exchange bias field of −0.17 T is observed. The presence of such an exchange anisotropy can be explained by coexistence of ferromagnetic and antiferromagnetic components in the system. The predominant hard antiferromagnetic component pins the soft ferromagnetic component, resulting in a shift of the hysteresis curve from its origin. This shift is, however, found to reduce significantly when measured at 49 K, due to a strong antiferromagnetic coupling at the Néel temperature and temperature-dependent decay of the ferromagnetic component. Furthermore, a similar FC and ZFC temperature-dependent magnetisation rules out the possibility of exchange-bias via spin-glass.

The ZFC M(T) curves of the reduction reaction products $La_2NiO_3F_2$ + x NaH with x = 0.25, 0.5, 1 and 1.5 (Figure 4-49 a) show an entirely different behaviour compared to their parent oxyfluoride $La_2NiO_3F_2$. Over the whole temperature range, the magnetisation of all reduction products is significantly higher as compared to the magnetisation of $La_2NiO_3F_2$ and increases additionally strongly when higher amounts of NaH were used in the reaction. This provides an indication for a magnetic contribution of a decomposition product to the otherwise antiferromagnetic or paramagnetic phases formed upon the reduction of $La_2NiO_3F_2$ (see also section 4.1.3.4.2). Due to a weak hysteresis in field-dependent measurements (Figure 4-49 b), the presence of a ferromagnetic component can be assumed. The analysis of the reduction mechanism (see section 4.1.3.2.1) suggests that the ferromagnetic contribution originates from metallic Ni which is formed due to the partial decomposition of $La_2NiO_3F_2$ during the defluorination process. This is also in accordance with previous findings made on the reduction of $LaNiO_3$ to $LaNiO_2$. [22] This ferromagnetic contribution of Ni with its high susceptibility dominates the overall magnetic signal and renders a deconvolution of the contribution of the reduced RP-type phases impossible. Therefore, the magnetic measurements on their own cannot reveal changes of the magnetic properties of the phases obtained on reduction of $La_2NiO_3F_2$.

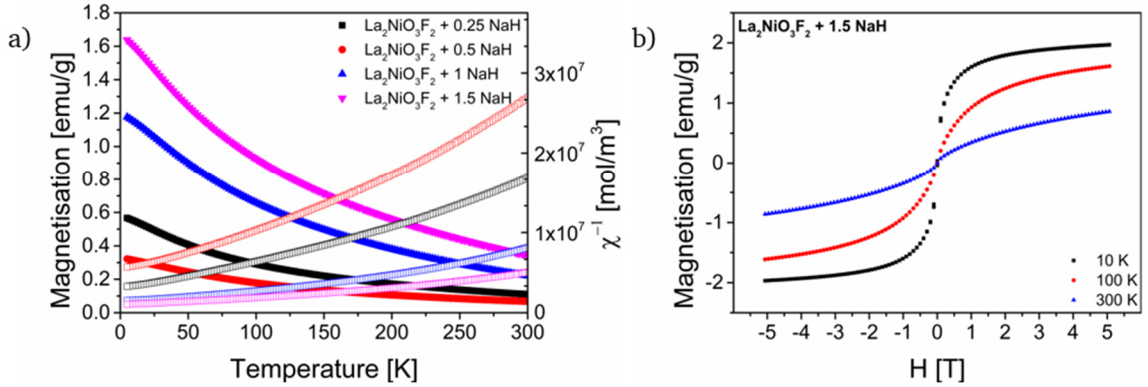

Figure 4-49: ZFC M(T) (closed symbols) and χ^{-1}(T) (open symbols) curve of reduction products of $La_2NiO_3F_2$ + x NaH with x = 0.25, 0.5, 1 and 1.5 measured at μ_0 = 1 T (a) and M(H) curves measured at 10, 100 and 300 K of reduction product of $La_2NiO_3F_2$ + x NaH with x = 1.5 (b).

4.1.3.4.2 Analysis of magnetic structure of $La_2NiO_3F_2$ and the reduction products

In order to develop a deeper understanding of the magnetic properties of $La_2NiO_3F_2$ and the reduced RP-type phases found in the reduction products $La_2NiO_3F_2$ +x NaH with x = 0.25, 0.5, 1 and 1.5, neutron diffraction data were recorded at low temperatures. The comparison between data measured at room-temperature and at 10 K (Figure 4-50) shows the appearance of additional reflections in all diffraction patterns. Since Ni^+ and Ni^{2+} ions do not possess large spin moments, the intensity of the magnetic reflections is low and only two reflections are clearly visible.

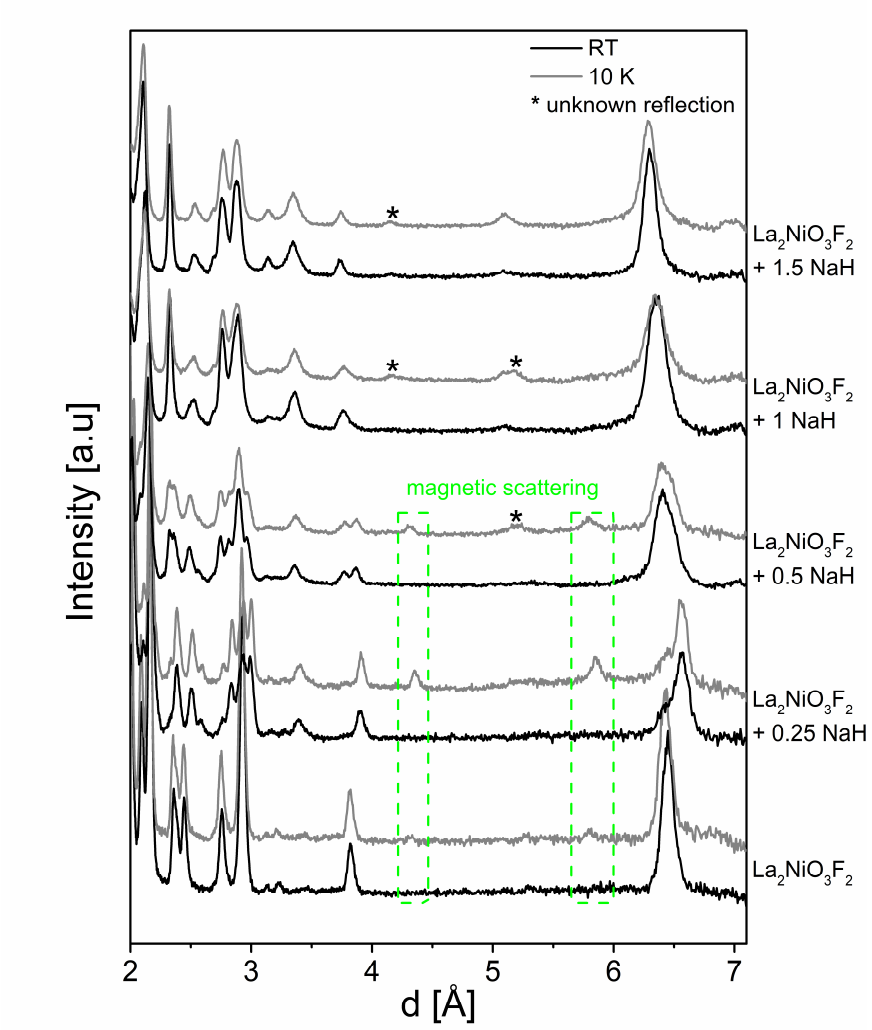

Figure 4-50: Comparison between NPD GEM bank 3 data measured at room-temperature (RT) and 10K of $La_2NiO_3F_2$ and the reduction products of $La_2NiO_3F_2$ + x NaH with x = 0.25, 0.5, 1 and 1.5. Reflections attributed to magnetic scattering are highlighted. Reflections, which could not be identified, are marked with *.

For the parent oxyfluoride $La_2NiO_3F_2$ and the reduction products $La_2NiO_3F_2$ + x NaH with x = 0.25 and 0.5, the additional reflections could be indexed with a k-vector of [1 0 0] based on the nuclear structures determined in section 4.1.3.2.2. The magnetic reflections in $La_2NiO_3F_2$ + x NaH with x = 0.25 and 0.5 can be attributed to the reduced monoclinic phase with an approximate composition of $La_2NiO_3F_{1.93}$. Since the number of additional reflections is low, the amount of additional refinement parameters was limited by using a magnetic subgroup approach, i.e., refining the magnetic intensities within one of the maximal magnetic subgroups of the nuclear structures. [262] By this approach, it is possible to limit the additional refinement parameters to a single parameter. This is due to the fact that the magnetic space group implies certain relative orientations of the magnetic moments of the Ni atoms. Robust refinements (Figure 4-51) could be achieved based on the magnetic subgroups $C_Pc'cm$ (66.9.572) and P_C2_1/c (14.84) of the space groups $Cccm$ and $C12/c1$, respectively. The magnetic vectors of the Ni ions align parallel to the c axis with G-type antiferromagnetic (AFM) ordering of the magnetic moments within the perovskite building blocks. The corresponding magnetic structures are shown in Figure 4-52. It is also worth emphasizing that this inter- and intra-layer ordering of magnetic moments has been also found for La_2NiO_4

experimentally [44] and for the stronger reduced n = 3 $La_4Ni_3O_8$ (67 % Ni^+) by DFT based calculations [263].

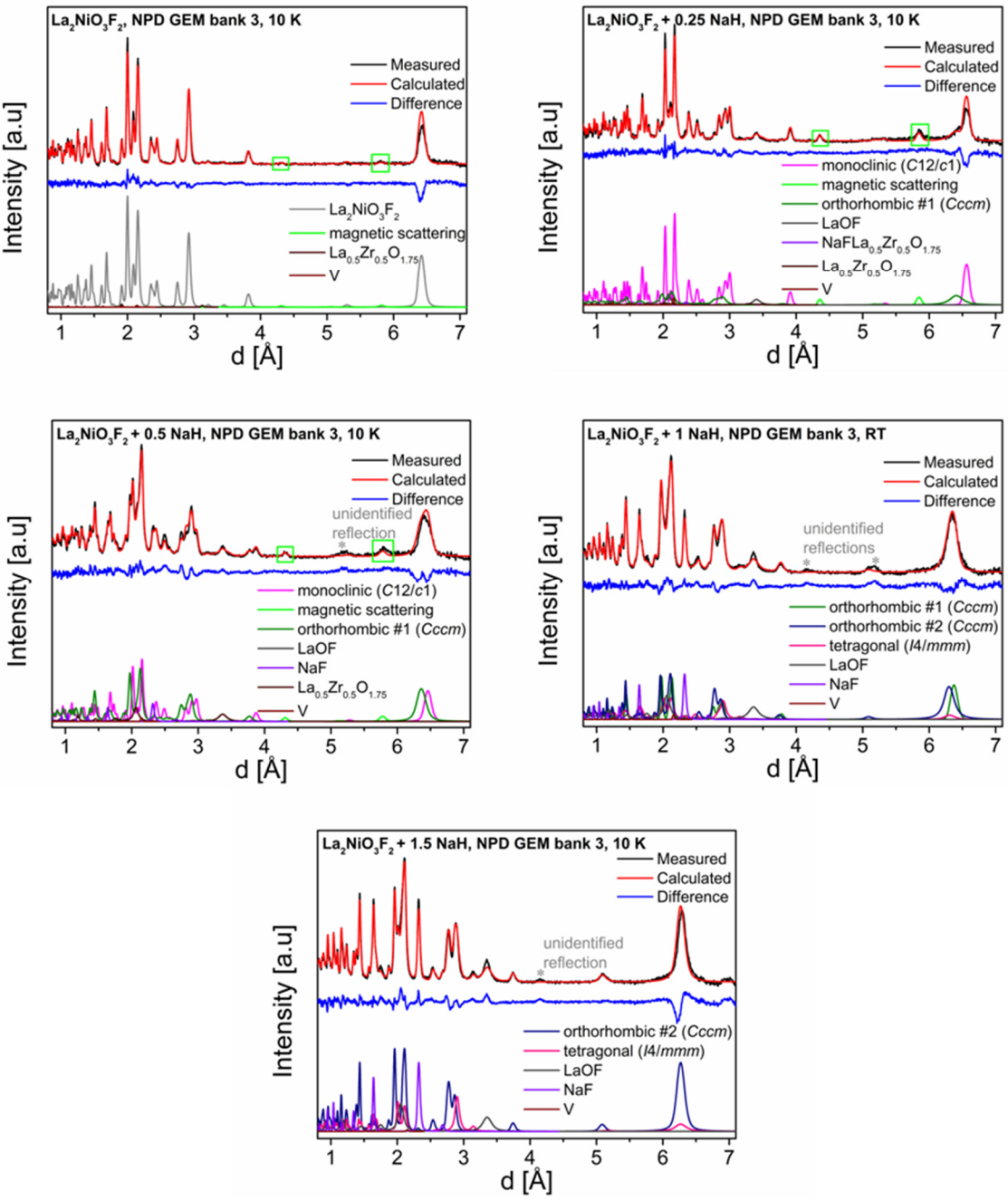

Figure 4-51: Rietveld refinements of $La_2NiO_3F_2$ and the reduction products of $La_2NiO_3F_2$ + x NaH with x = 0.25, 0.5, 1 and 1.5 of NPD GEM bank 3 and XRD data measured at 10 K.

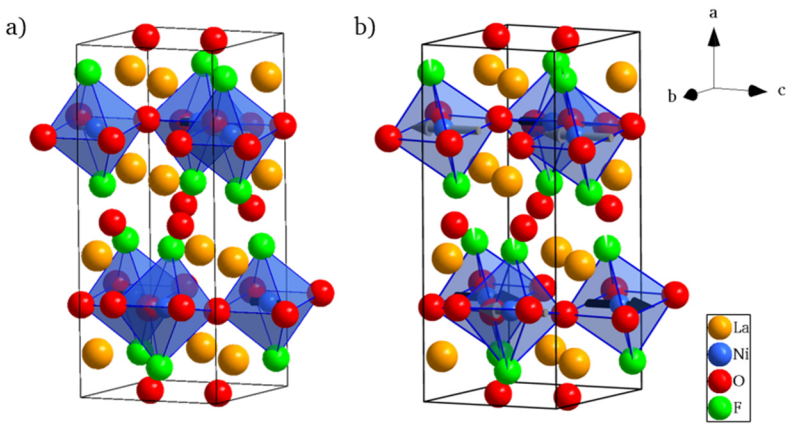

Figure 4-52: Magnetic structures of $La_2NiO_3F_2$ and the reduced monoclinic phase as determined from the Rietveld analysis of NPD data 3 at 10 K. The arrows indicate the length and directions of the magnetic vectors.

Remarkably, at 10 K, a strong difference is observed for the magnitudes of the magnetic moments refined for $La_2NiO_3F_2$ and for $La_2NiO_3F_{1.93}$ of 0.7(1) μ_B and 1.62(7) μ_B, respectively. This is surprising, since it would be assumed that a higher magnetic moment (2.83 μ_B for Ni^{2+} (d^8), 1.73 μ_B for Ni^{+} (d^9)) would be found in the phase with a higher fraction of Ni^{2+}, i.e., for $La_2NiO_3F_2$. It is known that superexchange interactions between adjacent layers are weak, and especially for the layered perovskite-related compounds of the n = 1 RP structure family A_2BO_4 with quasi-two-dimensional B-O-B networks, highly anisotropic magnetic interactions can be expected. [23, 24, 25] Furthermore, superexchange interactions via fluoride ions are weaker as compared to oxide ions. [56]

In this respect, a comparison of the magnetic properties and structures of $La_2NiO_3F_2$ and the reduced RP-type phase to La_2NiO_{4+d} might help to understand the observed differences. In La_2NiO_{4+d}, only the stoichiometric samples with d = 0 are reported to possess 3-dimensional antiferromagnetic ordering up to temperatures of 300 K [44], while slightly over-stoichiometric compounds (d > 0) show considerably lower transition temperatures. [43] For $La_2NiO_3F_2$, where the oxidation state is maintained with regard to La_2NiO_4, no 3-dimensional AFM ordering is present at ambient temperature and the moments found at 10 K are significantly lower than the moment of La_2NiO_4 of 1.68 μ_B (measured at 4 K) [44]. This highlights that the introduction of additional anions into the interstitial site weakens magnetic interactions between adjacent layers. Surprisingly, for $La_2NiO_3F_{1.93}$, ordering is found at least at up to 100 K without a significant decrease of the magnetic moment compared to lower temperature (Figure 4-53). Furthermore, the moment is close to the moment found for La_2NiO_4 at 4 K.

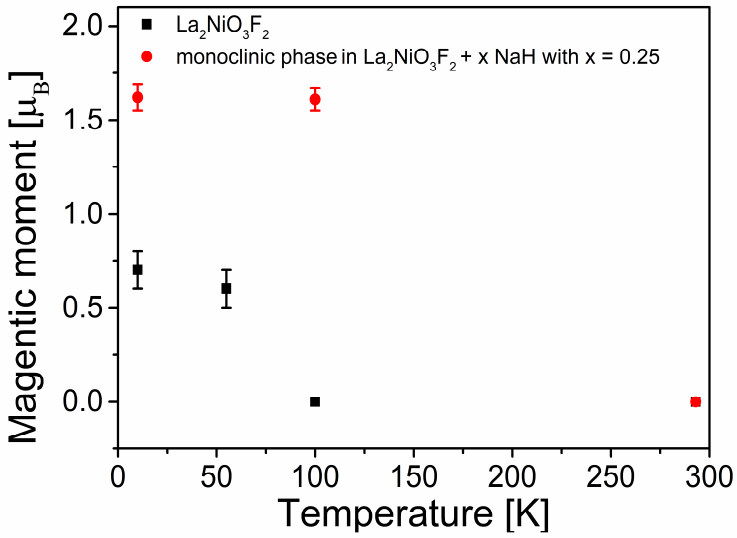

Figure 4-53: Magnetic moments of $La_2NiO_3F_2$ and the reduced monoclinic phase in the reduction products of $La_2NiO_3F_2$ + x NaH with x = 0.25 as a function of measurement temperature. For $La_2NiO_3F_2$, FC and ZFC M(T) measurements show a Néel temperature of 49 K [29], the neutron powder diffraction data suggests a higher transition temperature (> 55 K); the exact Néel temperature could, however, not be determined.

For monoclinically distorted $La_2NiO_3F_{1.93}$, it appears that the structural distortion in combination with the change of the electron configuration strengthens the exchange between adjacent perovskite building blocks. The Ni-F-F-Ni super-superexchange, found in $La_2NiO_3F_2$ only, is partly replaced by Ni-F-Ni superexchange interactions (Figure 4-54).

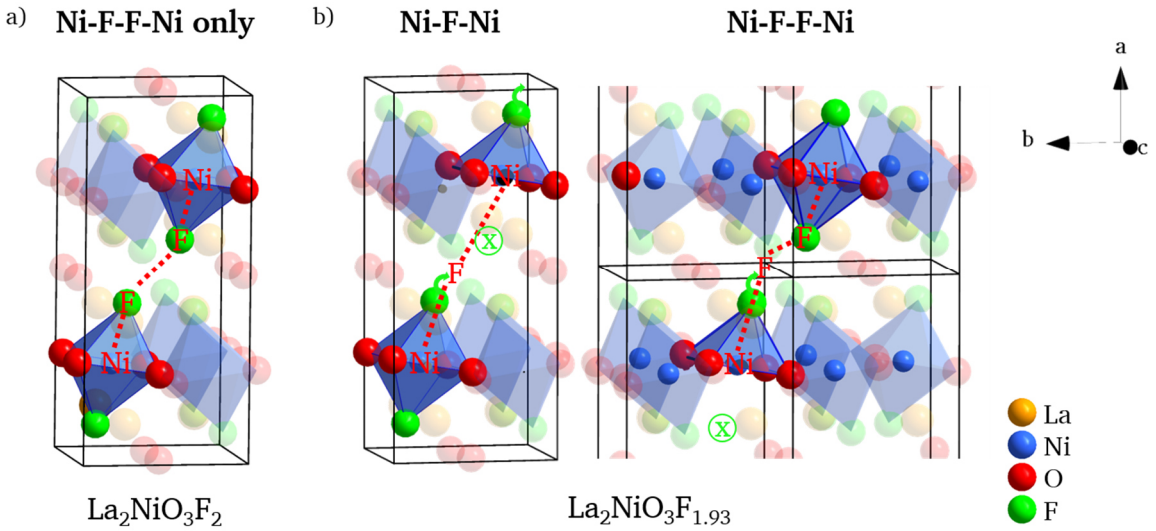

Figure 4-54: Illustration of the Ni-F-F-Ni super-superexchange between Ni^{2+} and and F^- ions of adjacent perovskite-type building blocks in $La_2NiO_3F_2$ (a) and of the Ni-F-Ni superexchange between Ni^+ and and F^- ions ions of adjacent perovskite-type building blocks and Ni-F-F-Ni super-superexchange between $Ni^{+/2+}$ and F^- ions of adjacent perovskite-type building blocks in $La_2NiO_3F_{1.93}$ (b). On a local scale, the extraction of one fluoride ion (its former position is indicated by the green X in the circle), the fluoride ion located oppositely in the adjacent perovskite-type building blocks moves slightly away from its apical site, resulting in an increase of the distance between the Ni^{2+} and the fluoride ion (compare section 4.1.3.2.3) and Ni-F-Ni interactions are found. For the composition $La_2NiO_3F_{1.93}$, it can be assumed that every ~16^{th} fluoride ion is extracted. The remaining fluoride ions of the formed NiO_4F polyhedron is also shifted slightly due to formation of Ni^+, which leads to an increase of the distance between the Ni^+ and the fluoride ion and strengthened Ni-F-F-Ni interactions are expected.

It has to be noted that it was not possible to draw robust and reliable conclusions about the magnetic properties and/or ordering scenarios for the stronger reduced phases. Even though additional reflections (marked with *) are present in the samples $La_2NiO_3F_2$ + x NaH with x = 0.5, 1 and 1.5 (Figure 4-50 and Figure 4-51), they could not be indexed successfully by testing different $n \times m \times l$ superstructures with reasonably small n, m, l ∈ ℕ. Their analysis is impeded by the small number of identifiable reflections with low intensities, which show in one case additionally overlapping with one neighbouring nuclear reflection of another phase. The absence of these additional reflections in the ambient temperature measurements renders possible that they belong to a magnetic ordering process. However, a clear assignment would require that the higher reduced phases could be prepared in a purer state.

4.1.3.5 Summary

The topochemical fluorination of the n = 1 RP-type oxide La_2NiO_{4+d} performed using stoichiometric molar ratios of the oxide and the fluorination reagent PVDF leads to the synthesis of $La_2NiO_3F_2$. Therefore, the fluorination mechanism can be described as nearly non-oxidative reaction, in which one oxide ion is replaced by two fluoride ions. However, a small reduction of the oxidation state was found. A coupled Rietveld analysis of X-ray and neutron diffraction data reveals an unusually strong orthorhombic distortion within the *ab* plane with lattice parameters of $a \approx 5.79$ Å and b ≈ 5.49 Å of the fluorinated compound. This is in contrast to the typically observed expansion along the long crystallographic axis of other RP-type compounds upon fluoride intercalation. Such an expansion was also observed for the previously discussed oxyfluorides $Sr_2TiO_3F_2$ and $Sr_3Ti_2O_5F_4$. Furthermore, a symmetry lowering to *Cccm* with a half filling of both interstitial layers in the unit cell due to the occupation of only one of the two available interstitial sites is found to take place. This results in a channel-like filling of the interstitial site by anions, accompanied by a strong tilting of the octahedra. The structure of the anion sublattice, i.e., the oxide and fluoride ion configuration leading to the most stable structure, was investigated by bond-valance sum and DFT-based calculations. The bond-valance sum calculations, being based on the experimentally obtained crystal structure, suggests an unprecedented anion ordering with oxide ions filling the interstitial site and fluoride ions occupying the apical site. In contrast to this, DFT-based calculations of different anion ordering scenarios predicted slightly more stable crystal structures with a mixed apical anion site occupation and fluoride ions filling the interstitial sites after structural relaxation. These structures showed, however, a further symmetry lowering to monoclinic lattices. It can be followed that the experimentally observed orthorhombic structure is the best compromise of energy and symmetry. Moreover, a high-temperature X-ray diffraction study on $La_2NiO_3F_2$ showed that the orthorhombic distortion has a higher thermal stability.

The investigation of the defluorination products of $La_2NiO_3F_2$ obtained using NaH as reducing agent according to $La_2NiO_3F_2$ + x NaH with $0 \leq x \leq 2.5$ ($\Delta x = 0.25$) at reaction temperatures of 300 °C revealed a complex reduction behaviour with reductive defluorination taking place in parallel to substantial decomposition processes and anion exchange reactions in the form of partial fluoride-oxide substitutions. The strong decomposition is accompanied by considerable amorphisation, which is strongly increasing with increasing NaH contents. The occurrence of this increased decomposition in comparison to the reductions of $Sr_2TiO_3F_2$ and $Sr_3Ti_2O_5F_4$ could be explained by a higher exothermicity of the defluorination reactions of $La_2NiO_3F_2$. Moreover, substitution reactions are of importance to understand the formation of the experimentally observed reduced RP-type phases and the decomposition product LaOF via the

exchange of fluoride and oxide ions between the reductively formed $La_2NiO_3F_{2-x}$ and La_2O_3. The decomposition reaction, causing the formation of La_2O_3 and a subsequent fluoride-oxide exchange reaction, leading to the formation LaOF, is more likely than a direct formation of LaOF upon decomposition, since the initial formation of La_2O_3 and the other side products of this decomposition reaction are more plausible concerning the experimentally observed phases. In addition to these reactions, minor degrees of fluoride-hydride substitutions within the reduced RP-type phases were found as compared to the reduced Ti-based phases. Overall, multiple RP-type phases, forming different phase mixtures in the reaction products were obtained. The reduced phases underwent significant structural changes upon reduction. A chemically plausible maximum extraction of approximately one fluoride ion per formula unit was found to take place. The coupled Rietveld analyses of room-temperature X-ray and neutron powder diffraction data of the reaction products were performed to derive the structural models of the reduced phases. The extraction of small amounts of fluoride-ions leads to the formation of a monoclinic phase with *C*12/*c*1 symmetry. The reduction leads to a decrease of the occupation of the apical anion site. An approximate composition of $La_2NiO_3F_{1.93}$ was determined. For increasing NaH amounts, two orthorhombic phases with approximate compositions of $La_2NiO_3F_{1.39}$ and $La_2NiO_3F_{1.08}$ were found. Both phases crystallise in space group *Cccm*. Vacancies are formed at the interstitial anion sites. This also suggests an anion rearrangement within the unit cell, since the interstitial site of $La_2NiO_3F_2$ is filled with oxide ions, which cannot be extracted within the defluorination reaction. Further increase of the equivalents of NaH used, finally led to the formation of a tetragonal phase (space group: *I*4/*mmm*) with an approximate composition of La_2NiO_3F. Interestingly, for this phase a transition from a T-related RP-type structure, as observed for all other phases within this work, to a T'-type structure was found. In a T'-type structure the apical anion site is not occupied and the interstitial site is fully filled. Similar structural transitions have been previously only observed for compounds containing high amounts of Jahn-Teller active cations, e.g. $La_3Ni_2O_6$ [100, 101] or $La_4Ni_3O_8$ [99, 101], confirming a strong reduction leading to the formation of large contents of d^9 Ni^+ ions. Furthermore, the obtained La_2NiO_3F can be considered as the first single (n=1) layer T'-type structure with infinite NiO_2 square-planar layers. By means of DFT-based calculations, the origin of the structural distortions within the monoclinic phase and the T'-type structure of La_2NiO_3F was examined and could confirm the proposed structural changes. For the monoclinic phase it was found that the introduction of the monoclinic distortion, expressed by a deviation of the angle β from 90° leads to an energetically favourable configuration. The tilting of the polyhedra along the *c* axis facilitates longer bond distances between the apical anions of adjacent perovskite building blocks, while also ensuring that a longer distance between the apical fluoride ion of a polyhedron to the Jahn-Teller active central Ni^+ cation can be formed, which is the driving force for the structural distortion. Moreover, the crystal structures of the reduced phases were studied by means of electron diffraction using automated diffraction tomography, confirming the crystal structures derived from the coupled Rietveld analysis of X-ray and neutron powder diffraction data.

While the temperature-dependent magnetisation measurement of $La_2NiO_3F_2$ revealed an antiferromagnetic character of the parent oxyfluoride below a transition temperature of 49 K, only the presence of the ferromagnetic decomposition product Ni, could be confirmed using such measurements. This ferromagnetic contribution made the determination of magnetic properties of the reduced RP-type phases impossible. In order to be able to relate structural changes of $La_2NiO_3F_2$ and the reduced RP-type phases to potential changes in magnetic

properties, the magnetic structures were additionally investigated using coupled Rietveld analyses of low-temperature X-ray and neutron powder diffraction data of the reaction products. For all examined reduction products, additional reflections were observed in the low-temperature measurements. The reflections, correlated to the nuclear structures of $La_2NiO_3F_2$ and the reduced monoclinic phase $La_2NiO_3F_{1.93}$, could be successfully fitted based on a magnetic subgroup approach. For the stronger reduced phases, the magnetic structures could not be indexed unambiguously. Using the magnetic subgroups $C_Pc'cm$ (66.9.572) and P_C2_1/c (14.84) of the space groups *Cccm* and *C*12/*c*1, respectively, magnetic moments of 0.7(1) μ_B for $La_2NiO_3F_2$ and 1.62(7) μ_B for the monoclinic phase were determined. For these magnetic subgroups, the magnetic vectors of the Ni ions align parallel to the *c* axis with G-type antiferromagnetic ordering of the magnetic moments within the perovskite layers. Remarkably, the magnetic moment of the monoclinic phase is considerably higher as in $La_2NiO_3F_2$ and is even comparable to the moment of La_2NiO_4, for which a moment of 1.68 μ_B has been measured at comparable temperatures [62]. Due to the higher moment of Ni^{2+}, it would be expected that $La_2NiO_3F_2$ possesses a higher magnetic moment. With respect to La_2NiO_4, the occurrence of weaker magnetic interactions between the perovskite layers of the fluorinated compounds would be expected, as the interaction over several anion and, in particular, via fluoride ions is found to be weaker. [35] However, it seems that the introduction of the structural distortion in the monoclinic phase combined with the change of Ni electron configuration to that of a Jahn-Teller active d^9 Ni^+ strengthens the exchange between neighbouring perovskite building blocks. In addition, the transition temperature of the monoclinic phase in comparison to $La_2NiO_3F_2$ increases significantly.

4.2 Topochemical modifications of Ruddlesden-Popper-type compounds via electrochemical reactions in fluoride-ion batteries

A part of the following chapter summarises the findings reported previously in the following publication:

> [5] Vasala, S.; Jakob, A.; **Wissel, K.**; Waidha, A. I.; Alff, L.; Clemens, O., Reversible Tuning of Magnetization in a Ferromagnetic Ruddlesden–Popper-Type Manganite by electrochemical Fluoride-Ion Intercalation. *Adv. Electron. Mater.*, **2019**, *6* (2), 1900974.

When considering the feasiblity of electrochemical reactions within a battery, the redox potentials of the used anode and cathode materials play an important role. An anode material should have a high reducing power in its charged state, i.e., an unsually low oxidation state of the transition metal cation and comparatively low potential against Li|LiF (E^0(Li|LiF) ≈ -3 V vs. $H_2|2H^+$). Therefore, RP-type oxyfluorides $A_{n+1}B_nO_{3n+1-x}F_{2x}$ with $0 < x \leq 2$, synthesised via a non-oxidative fluorination of $A_{n+1}B_nO_{3n+1}$, can be regarded as the discharged states of potential anode materials, while the corresponding defluorinated phases present the charged states (Figure 4-55).

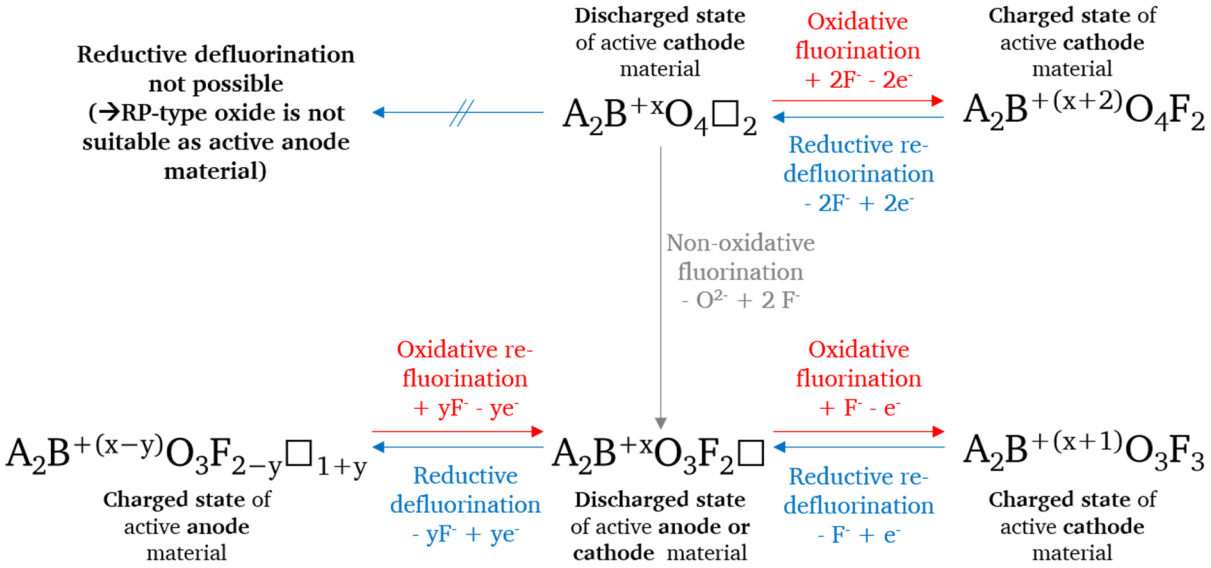

Figure 4-55: Illustration of the effect of reductive defluorination and oxidative fluorination reactions on the composition and oxidation states of the formed phases derived from n = 1 RP-type oxides and non-oxidatively fluorinated oxyfluorides phases in terms of their potential use as electrode materials in FIBs. The reversible processes are denoted as oxidative re-fluorination and reductive re-defluorination. In addition it is pointed out, which phases can be regarded as the charged and discharged states of the respective electrode material.

As shown in section 4.1, the hydride-based defluorinations of $Sr_2TiO_3F_2$, $Sr_3Ti_2O_5F_4$ and $La_2NiO_3F_2$ result in the formation of various reduced RP-type phases with differing fluoride ion contents. If the topochemical modifications via an electrochemical defluorination lead to similar structural distortions within the oxyfluorides, the emerging phases would be relatable to the chemically formed phases in terms of structural characteristics and fluoride contents. Additionally, changes in the magnetic properties could be deduced from the chemically

formed equivalent phases. Therefore, the comparison to the equivalents obtain using the hydride-based defluorination would make an in-depth analysis of the electrochemically reduced phases possible. Furthermore, the DFT-based calculations performed to investigate the most stable crystal structures of $Sr_2TiO_3F_2$ and $La_2NiO_3F_2$ and their chemically reduced phases enable a prediction of redox potentials from the determined changes of the Gibb's free energies. The obtained potentials are illustrated in Figure 4-56. Potential ranges are given since different anion configurations within the oxyfluorides with slightly differing energies are taken into account. For $Sr_3Ti_2O_5F_4$ and its reduced phases no DFT calculations were performed. However, it can be assumed that the redox potential is close to the potential of $Sr_2TiO_3F_{2-x}|Sr_2TiO_3F_2$.

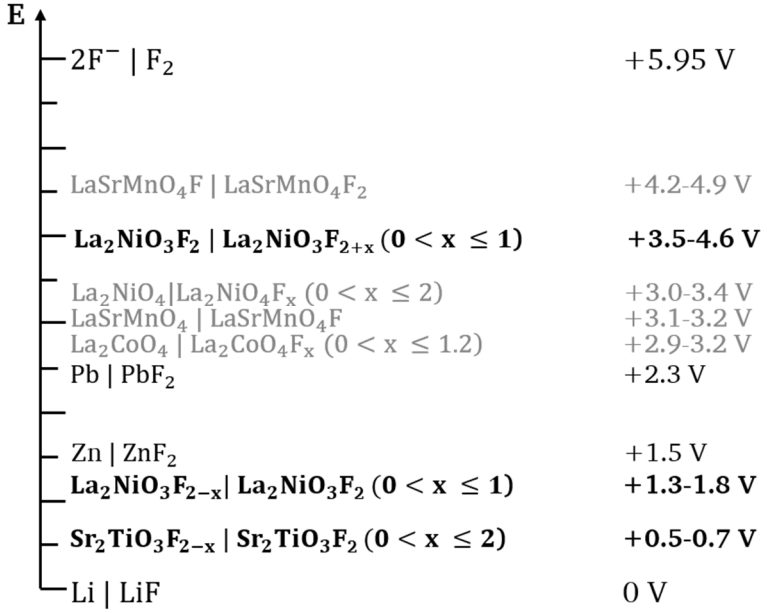

Figure 4-56: Predicted redox potentials of RP-type oxyfluorides investigated in terms of their potential application as active materials in intercalation-based electrode materials in FIBs within this work in relation to Li|LiF. The potentials were calculated based on DFT calculations. Additionally given are the potentials of the redox couples of the used conversion-based counter electrodes Zn|ZnF_2 and Pb|PbF_2 [20] and of other RP-type compounds, which have been studied previously as active cathode materials. [18-20, 264] The potential of Zn|ZnF_2 was derived from reference 262. The redox potentials of $La_{1.3}Sr_{1.7}Mn_2O_7|La_{1.3}Sr_{1.7}Mn_2O_7F$ and $La_{1.3}Sr_{1.7}Mn_2O_7F|\ La_{1.3}Sr_{1.7}Mn_2O_7F_2$ were not calculated.

In contrast to anode materials, cathode materials should have a high oxidising power in the charged state corresponding to high potentials against Li|LiF. RP-type oxides $A_{n+1}B_nO_{3n+1}$ and oxidative fluorinated $A_{n+1}B_nO_{3n+1}F_x$ with $0 < x \leq 2$ can be, therefore, considered to be the discharged and charged states of active cathode materials, respectively. Various RP-type oxides have been investigated as intercalation-based cathode materials previously. [18-20, 264] The potentials of the respective redox couples are also shown in Figure 4-56. Moreover, n = 1 RP-type oxyfluorides $A_2BO_3F_2$ might also be suitable as cathode materials (Figure 4-55) due to the presence of vacancies at the anion sites, which might be filled in an oxidative post-fluorination step using electrochemical approaches. So far, alternative topochemical fluorination methods require the use of highly oxidising fluorination reagents for an additional oxidative fluorination. These are, however, often difficult to handle and extensive safety measures have to be followed. [8] Therefore, the electrochemical modification method could present a viable and safer approach for the synthesis of $A_2BO_3F_{2+x}$ obtained from

$A_2BO_3F_2$ via an additionally fluorination. In this context, the redox potential of $La_2NiO_3F_2|La_2NiO_3F_{2+x}$ is given in addition in Figure 4-56.

Not only could the topochemical modification via electrochemical reactions allow for the synthesis of new, otherwise inaccessible materials, but also drive the development of FIBs forward. The cell potential and consequently the energy density of a cell depends on the choice of the electrode materials. For the development of a FIB battery with a preferentially high energy density, suitable low potential anodes and high potential cathodes would be need to be found. So far, only conversion-based anode materials containing Zn/ZnF_2 and Pb/PbF_2 have been combined with intercalation-based RP-type cathode materials. [18-20, 264] In order to realise a high energy density FIB, the use of intercalation-based anode composites containing the above-mentioned RP-type oxyfluorides as active material might, therefore, be a promising strategy.

With respect to this, the behaviour of the potential active anode materials $Sr_2TiO_3F_2$, $Sr_3Ti_2O_5F_4$ and $La_2NiO_3F_2$ is examined in the following two subchapters. In particular, the Ti-based RP-type oxyfluorides should be suitable active anode materials due to their low potential against Li|LiF. The redox couple $La_2NiO_3F_{2-x}|La_2NiO_3F_2$ has a slightly higher redox potential than the Ti-based oxyfluorides (Figure 4-56). After testing the structural stability of the RP-type oxyfluorides used within the anode composites under experimental conditions, the reversibility of structural changes within the RP-type phases upon galvanostatic charging and discharging, also upon cycling, is investigated. Furthermore, the reversible electrochemical fluorination of $La_2NiO_3F_2$ when used as cathode material is studied. As counter electrodes either a Pb/PbF_2, Zn/ZnF_2 or La_2NiO_{4+d} composite was used. The structural characterisation is mainly based on the Rietveld analysis of X-ray diffraction data. For the structural analysis, electron diffraction techniques were used in addition. Oxidation states were analysed using X-ray photoelectron and X-ray absorption spectroscopy.

All redox potentials included in Figure 4-56 lay within the stability window of the used electrolyte $La_{0.9}Ba_{0.1}F_{2.9}$ [26], so that substantial side reactions involving the electrolyte can be ruled out. However, as shown by Nowroozi et al. [18-20] based on studies on the reversible electrochemical fluorination of RP-type oxides used as active materials in cathode composites, side reactions affecting the conductive carbon additive within the electrode composites occur in parallel to the desired fluoride intercalation reactions during charging. Especially when addressing an extended cyclability of FIBs, these side reactions gain importance, as they lead to a progressive decrease of the electrical conductivity due to the formation of insulating CF_x species within the electrode composites. In order to limit these side reactions, the selection of suitable cut-off criteria for the charging and discharging processes has been found to be important. In particular, relatively low charging cut-off potentials, correlating with low charging capacities, have been shown to increase the cyclability tremendously, since the carbon fluorination is less pronounced at such low potentials. Additionally, it has been found that the comparatively low Coulombic efficiencies, observed in the first cycles due to the irreversible side reactions taking place during charging, increase considerably upon cycling. This indicates that the influence of the side reactions decreases and that the desired reversible intercalation of fluoride ions into the RP-type materials becomes more dominant, possibly related to the formation of stable interfaces between the active material and the carbon additive, which impede additional irreversible reactions. The occurrence of such carbon oxidations due to the reaction with fluoride is also likely to be found for the cathode composites investigated within this work. Moreover, side reaction could also take place when

reducing RP-type oxyfluorides within anode composites due to a possible reduction of the carbon additive. Therefore, special attention is given to the investigation of carbon oxidation and potential carbon reduction reactions. The influence of these reactions is investigated on the $La_2NiO_3F_2$-containing electrode composites and resulting implications are discussed.

To ease to differentiation between experiments involving electrode composites, either used as active anode or cathode material, the cells are referred to by the name of the respective active RP-type phase in the material in relation to the active material in the counter electrode (i.e., M/MF_2 vs. $La_2NiO_3F_2$ ($La_2NiO_3F_2$ is active material in anode composite), $La_2NiO_3F_2$ vs. M/MF_2 ($La_2NiO_3F_2$ is active material in cathode composite). The anode composite is always used as reference. Cells with electrode materials without RP-type phases are labelled as M/MF_2 vs. $La_{0.9}Ba_{0.1}F_{2.9}$ + CB or $La_{0.9}Ba_{0.1}F_{2.9}$ + CB vs. M/MF_2.

As demonstrated for the chemically reduced equivalents, along with structural changes, the electrochemical reactions should lead to magnetic property changes of the obtained phases in comparison to their parent oxyfluorides. Due to the reversibility of structural changes upon charging and discharging within the FIBs, it should be also possible to switch reversibly between the magnetic states of the obtained phases. For a technological application, high absolute changes of the magnetisation between two magnetic states are desirable. Since the differences in magnetisation of the reduced oxyfluorides and their parent oxyfluorides are comparatively small, the potential of reversible magnetic tuning is demonstrated on n = 2 RP-type $La_{1.3}Sr_{1.7}Mn_2O_7$. When using this compound as active material in a cathode composite, an oxidative fluorination should take place, which leads to a transition from a three-dimensional ferromagnetic to a non-ferromagnetic ordering of the magnetic moments of the Mn ions. The made findings are presented in the last subchapter of this part of the work.

4.2.1 Screening for suitable Ruddlesden-Popper-type oxyfluorides as active anode materials – Stabilities and defluorination feasibilities of anode composites

As active materials in the anode composites, the RP-type oxyfluorides $Sr_2TiO_3F_2$, $Sr_3Ti_2O_5F_4$ and $La_2NiO_3F_2$ were investigated within the scope of this work. The anode composites were prepared via ball milling of 30 wt% of the respective oxyfluoride with 60 wt% of the electrolyte $La_{0.9}Ba_{0.1}F_{2.9}$ and 10 wt% of carbon black. The electrolyte and the carbon black were used to ensure sufficient ionic and electronic conductivity, respectively. To investigate the stability of the RP-type oxyfluorides within the anode composites after the milling step and of pressed cell pellets consisting of the respective anode composite, the electrolyte and the cathode composite after heating to 170 °C, Rietveld refinements were performed. A composite containing Pb/PbF_2 was used as cathode material. For the heating, a duration of approximately 72 h was chosen, which is the average duration of the conducted galvanostatic charging experiments. If the oxyfluorides were found to be stable, cells Pb/PbF_2 against the respective anode composite were galvanostatically charged to ~ 3 V using a slow C-rate of C/25 in a Swagelok-type cell (see section 3.1.4.2) and a Rietveld analysis of the anode side after charging was conducted. The charging was also performed at 170 °C. To give an impression about the dimensions of the electrode and electrolyte layers within a pressed pellet, a SEM cross-section of a pellet is given in Figure 4-57.

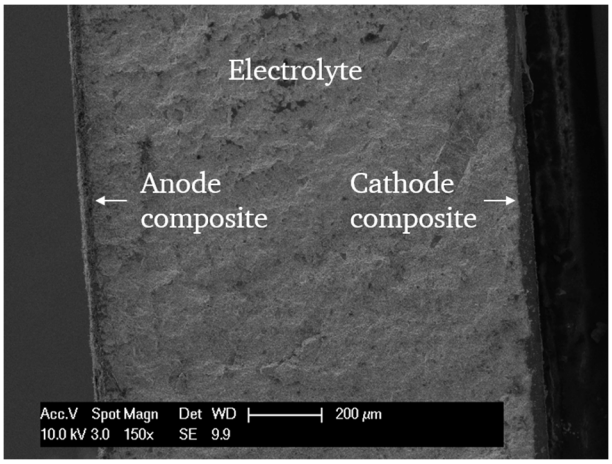

Figure 4-57: SEM cross-section of a pressed pellet consisting of the anode composite containing $La_2NiO_3F_2$, the electrolyte $La_{0.9}Ba_{0.1}F_{2.9}$ and the cathode composite containing Pb/PbF_2.

Figure 4-58 shows the Rietveld analysis of XRD data of $Sr_2TiO_3F_2$, as obtained after the topochemical fluorination of Sr_2TiO_4 using PVDF (see section 4.1.1.1), the anode composite containing this $Sr_2TiO_3F_2$ after milling and the anode side of a cell after heating. The comparison of reflection positions of the fluorination product and the milled anode composite reveals that no reactions between the electrolyte $La_{0.9}Ba_{0.1}F_{2.9}$ and $Sr_2TiO_3F_2$, which would possibly lead to shifts of the reflections, have taken place during the milling procedure. The obtained phase fractions of the electrolyte $La_{0.9}Ba_{0.1}F_{2.9}$ and $Sr_2TiO_3F_2$ in the anode composite are in good agreement with the used amounts and, therefore, major decomposition or amorphisation can be ruled out. The relative phase fractions of $Sr_2TiO_3F_2$ and SrF_2 in the fluorination product and the anode composite stay also constant, indicating only a minor influence of decomposition. However, after the heating, significant changes in the XRD pattern of the anode side of the pressed pellet can be observed. This becomes most evident by the disappearance of the reflections corresponding to $Sr_2TiO_3F_2$ and the appearance of additional reflections of a new phase, which could not be identified. Moreover, increased phase fractions of SrF_2, related to a substantial decomposition of $Sr_2TiO_3F_2$, and of the electrolyte, suggesting significant amorphisation of $Sr_2TiO_3F_2$ upon heating, are found. Due to the formation of SrF_2, it would be reasonable to expect also the presence of $SrTiO_3$. This phase is, however, not found. Assuming that the additional reflections belong to one phase, it could be followed that an orthorhombic phase with higher lattice parameters is formed, since a shift of the reflection positions towards lower diffraction angles in comparison to the positions of the (013) and (110) reflections of $Sr_2TiO_3F_2$ at 29.1° and 33.3°, respectively, and the splitting of the (110) reflection is observed. However, no phase, which would describe the missing reflection intensities could be found.

Due to the observed instability of $Sr_2TiO_3F_2$ within the anode composite under the experimental conditions applied within the test cells, no galvanostatic charging experiments were conducted using this anode composite.

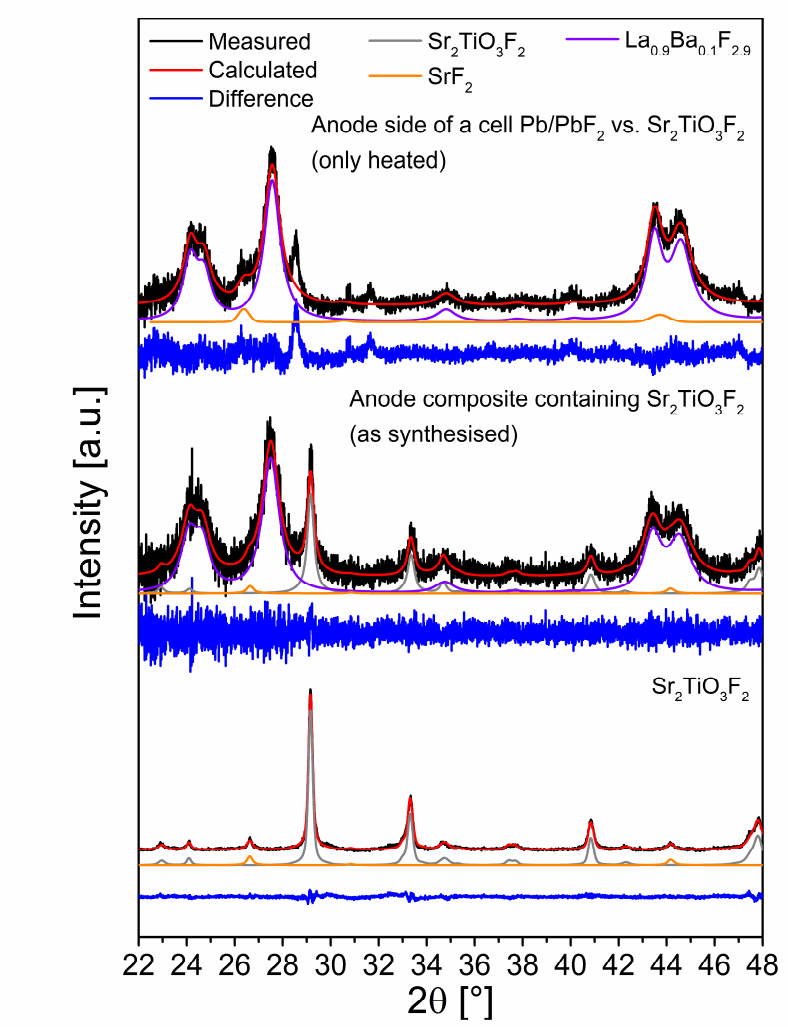

Figure 4-58: Comparison between Rietveld refinements of X-ray diffraction data of $Sr_2TiO_3F_2$ used in the anode composite, of the anode composite containing $Sr_2TiO_3F_2$ after milling and of the anode side of a cell Pb/PbF_2 against $Sr_2TiO_3F_2$ heated to 170 °C for 72 h.

The same procedure was followed for the $Sr_3Ti_2O_5F_4$-containing anode composite. In contrast to the $Sr_2TiO_3F_2$-containing anode composite, no reactions involving $Sr_3Ti_2O_5F_4$ are observed when heating the pellets to 170 °C (Figure 4-59). The relative phase fractions of $Sr_3Ti_2O_5F_4$, SrF_2 and $SrTiO_3$ found within the fluorination product, the milled anode composite and the anode side of the heated pellet remain relative constant within errors. Only a marginal increase of the decomposition phases SrF_2 and $SrTiO_3$ by ~ 1 and 2 wt%, respectively, are observed in comparison to the fluorination product, which contains ~ 5 wt% SrF_2 and ~ 7 wt% $SrTiO_3$. Furthermore, the phase fractions of $La_{0.9}Ba_{0.1}F_{2.9}$, $Sr_3Ti_2O_5F_4$, SrF_2 and $SrTiO_3$ in the anode composite and the anode side of the heated pellet correspond well with the expected phase fractions. This suggests that no major decomposition or amorphisation is taking place upon milling or heating. With respect to this, the observed instability of $Sr_2TiO_3F_2$ within the heated electrode composite is rather surprising. In both composites, the same ions with the same oxidation states are present. Based on this, a higher redox activity of one of the RP-type phases when in contact with of $La_{0.9}Ba_{0.1}F_{2.9}$ and carbon at elevated temperatures, potentially leading to the formation of other phases, can be ruled out. However, small compositional and/or structural distortions in $Sr_2TiO_3F_2$ might possibly facilitate its decomposition.

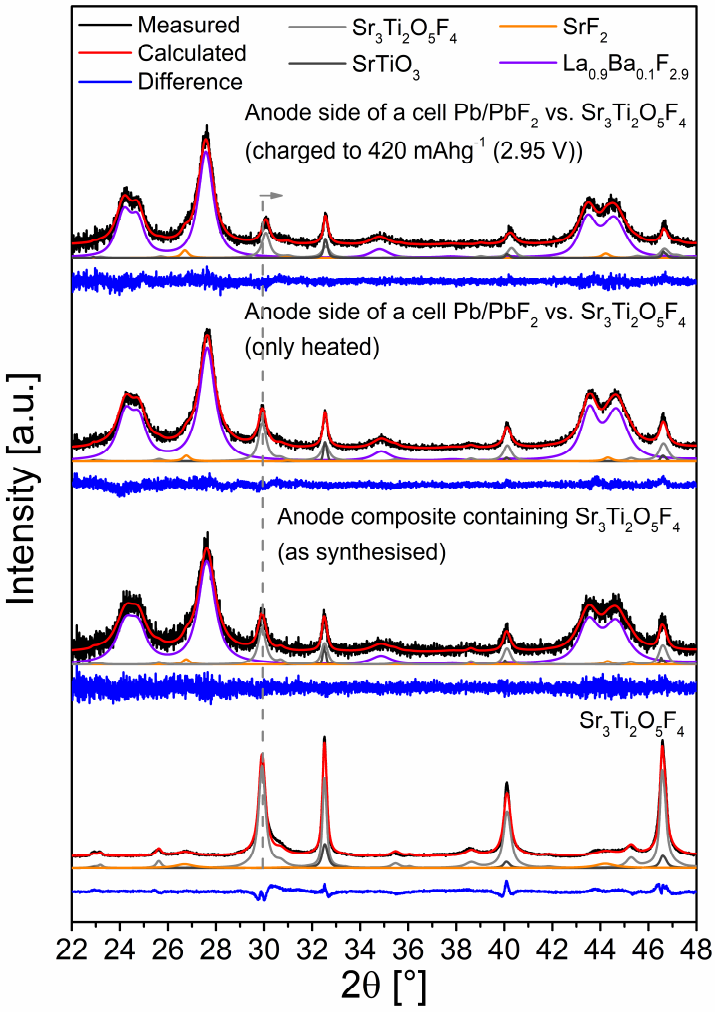

Figure 4-59: Comparison between Rietveld refinements of X-ray diffraction data of $Sr_3Ti_2O_5F_4$ used in the anode composite, of the anode composite containing $Sr_3Ti_2O_5F_4$ after milling, of the anode side of a cell Pb/PbF_2 against $Sr_2TiO_3F_2$ heated to 170 °C for 72 h and of the anode side of a cell Pb/PbF_2 against $Sr_3Ti_2O_5F_4$ charged to 420 $mAhg^{-1}$ (2.95 V).

The stability $Sr_3Ti_2O_5F_4$ in the anode composite encouraged further electrochemical testing. Therefore, a cell Pb/PbF_2 vs. $Sr_3Ti_2O_5F_4$ was galvanostatically charged to 2.95 V. The galvanostatic charging curve is shown in Figure 4-60. Since no changes of the RP-type phase within the anode composite is observed after the heating process, changes of the reflections of phases in the anode side of the cell have to be related to occurring redox reactions taking place within the cell during electrochemical charging. No distinctive, ideally horizontal plateaus are observed. Instead, sloping plateaus are found above ~ 0.55 V. These plateaus cover a capacity of ~ 420 $mAhg^{-1}$, which indicates that side reactions have a substantial contribution to the observed capacity (see section 4.2.2.5). This becomes, in particular, evident when considering that the gravimetric capacity for the extraction of one fluoride ion from $Sr_3Ti_2O_5F_4$ is ~ 54 $mAhg^{-1}$. Furthermore, assuming similar redox potentials of the n = 1 and n = 2 strontium titanium oxyfluorides, a possible reduction of $Sr_3Ti_2O_5F_4$ should occur in a potential range above ~ 1.5 V vs. $Sr_3Ti_2O_5F_{4-x}|Sr_3Ti_2O_5F_4$, which can be estimated based on the predicted redox potentials of $Sr_2TiO_3F_{2-x}|Sr_2TiO_3F_2$ and $Pb|PbF_2$ (Figure 4-56). This assumption does not consider any over-potentials. Due to the low potential of the titanium-containing RP-type phases vs. Li|LiF, the reduction of $Sr_3Ti_2O_5F_4$ would take place at potentials, which lay significantly above the potentials, at which the onset of the side

reactions is located. These side reactions impede, however, the reduction of the RP-type phases as they most likely affect the electronic conductivity of the carbon additive. This aspect is discussed in detail based on the example of the reduction of $La_2NiO_3F_2$ in section 4.2.2.5 and is assumed to take place for titanates in an analogous manner. Nevertheless, when comparing the XRD patterns of the fluorination product, the anode composite and the anode side of a heated cell to the charged cell (Figure 4-59), a small shift of the (015) reflection at ~ 29.7° 2θ towards higher angles is found, which indicates a small chemical modification of $Sr_3Ti_2O_5F_4$. This shift is related to a decrease of the *c* lattice parameter from 23.372(5) Å of the starting $Sr_3Ti_2O_5F_4$ used within the anode composite (see also section 4.1.2.1.1) to 23.152(8) Å of the electrochemically reduced $Sr_3Ti_2O_5F_4$. The *a* lattice parameter decreases also slightly ($Sr_3Ti_2O_5F_4$: $a = 3.9059(8)$ Å, reduced phase: $a = 3.9024(7)$ Å). The obtained lattice parameters and the cell volume per formula unit of 176.3(2) $Å^3$ of the reduced $Sr_3Ti_2O_5F_4$ phase after the electrochemical charging are similar to those of the tetragonal #1 phase found after the hydride-based reduction using low amounts of NaH (x = 0.5 and 1) (compare section 4.1.2.2 and Figure 4-17 b). As is shown for the chemically reduced equivalents, the formation of considerable amounts of Ti^{3+} species in the reduced RP-type compound due to the extraction of fluoride would lead to a stronger decrease of the *c* lattice parameter and an increase within the *ab* plane. A small degree of defluorination of $Sr_3Ti_2O_5F_4$ would plausibly explain the described findings. The quantification of the phases within the anode side of the charged cell based on a Rietveld analysis reveals in addition, that the relative phase fractions of the decomposition products SrF_2 and $SrTiO_3$ increase to ~ 11 and 16 wt% with respect to the phase fraction of $Sr_3Ti_2O_5F_4$. Its phase fraction decreases accordingly. Therefore, considerable decomposition of $Sr_3Ti_2O_5F_4$ is also taking place upon charging of the cell.

In order to investigate the reduction and decomposition behaviour of $Sr_3Ti_2O_5F_4$ within a FIB in more detail, clearly additional experiments are required. By applying another conductive additive, less prone to side reactions below or in the potential range of the reduction of $Sr_3Ti_2O_5F_4$, it might be possible to achieve a stronger reduction of the RP-type phase. Furthermore, by choosing suitable cut-off voltages it might be also possible to prevent the decomposition of $Sr_3Ti_2O_5F_4$, if the decomposition is not taking place in parallel to the reduction. In the latter case, a potential extended cycling of the cells would be highly limited.

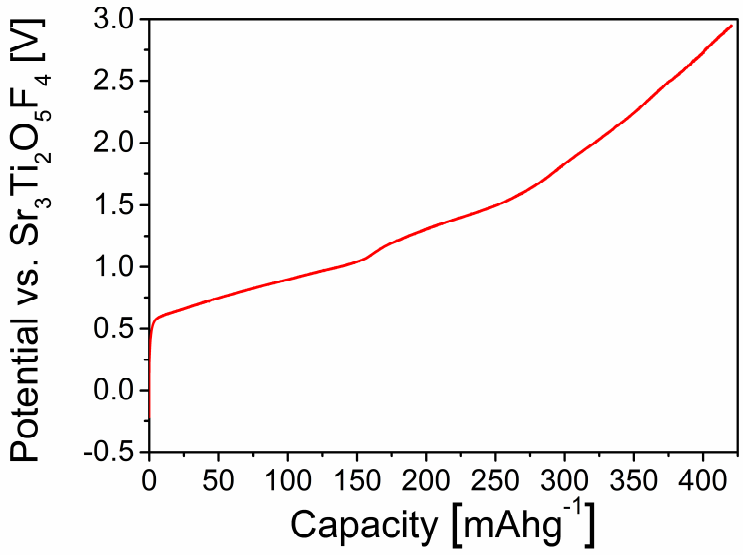

Figure 4-60: Charging curve of a cell Pb/PbF_2 against $Sr_3Ti_2O_5F_4$ charged to 420 $mAhg^{-1}$ (2.95 V).

Since only a minor degree of defluorination and a substantial decomposition was observed upon charging of $Sr_3Ti_2O_5F_4$, $La_2NiO_3F_2$ was also investigated as potential anode material. The redox potential of $La_2NiO_3F_{2-x}|La_2NiO_3F_2$ is with ~ 0.6 to 1.1 V vs- Li|LiF higher in comparison to the potential of the Ti-containing RP-type compounds (Figure 4-56), which might give the possibility to separate the potential ranges, in which the reduction of $La_2NiO_3F_2$ and the side reactions are taking place. Ideally, the side reactions would occur at higher potentials than the desired reduction and the side reactions could be avoided by setting suitable cut-off potentials.

Similar to what is found for the $Sr_3Ti_2O_5F_4$-containing anode material, no change of reflection positions of $La_2NiO_3F_2$ can be found for the synthesised and heated anode composite in comparison to sample obtained after chemical fluorination of La_2NiO_{4+d} containing $La_2NiO_3F_2$ and $La_2NiO_{3-d/2}F_{2-d}$ (Figure 4-61). In addition, the relative phase fractions of the RP-type phases to each other as well as the phase fraction of $La_{0.9}Ba_{0.1}F_{2.9}$ to the RP-type phases stay relatively constant within errors. This suggests that no decomposition or amorphisation takes place during the synthesis or heating process. When charging a cell Pb/PbF_2 vs. $La_2NiO_3F_2$, significant changes in the reflection patterns of the RP-type phases can be observed, which can be related to the successful reduction of $La_2NiO_3F_2$ based on the result obtained after the hydride-based reductions (see section 4.1.3.2). Therefore, a detailed investigation of the reduction behaviour of $La_2NiO_3F_2$ is given in the following subchapter (section 4.2.2). Furthermore, the fluorination behaviour of $La_2NiO_3F_2$, when used in a cathode composite, is studied.

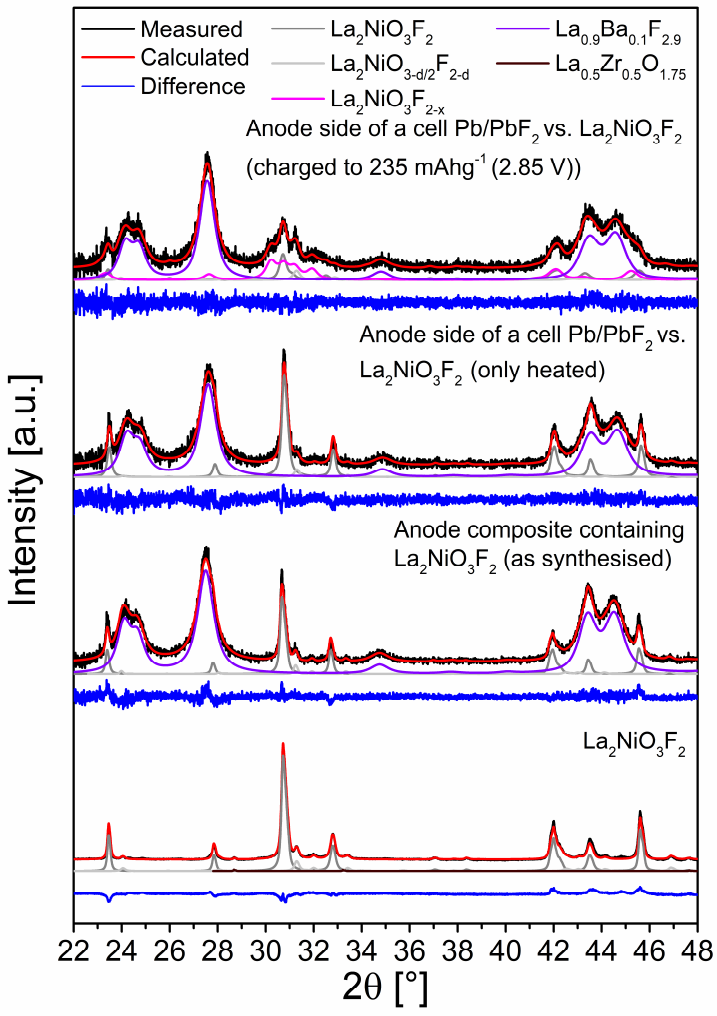

Figure 4-61: Comparison between Rietveld refinements of X-ray diffraction data of $La_2Ni_2O_3F_2$ used in the anode composite, of the anode composite containing $La_2Ni_2O_3F_2$ after milling, of the anode side of a cell Pb/PbF_2 against $La_2Ni_2O_3F_2$ heated to 170 °C for 72 h and of the anode side of a cell Pb/PbF_2 against $La_2Ni_2O_3F_2$ charged to 235 $mAhg^{-1}$ (2.85 V).

4.2.2 Electrochemical defluorination and additional fluorination of $La_2NiO_3F_2$

4.2.2.1 Electrochemical defluorination of $La_2NiO_3F_2$

4.2.2.1.1 Electrochemical defluorination behaviour of $La_2NiO_3F_2$

A typical charging curve of a cell Pb/PbF_2 vs. $La_2NiO_3F_2$ is shown in Figure 4-62. The first sloping plateau extends over a potential range from ~ 0.6 to 1.1 V vs. $La_2NiO_3F_2$ and covers ~ 75 $mAhg^{-1}$. This plateau is followed by a second steeper sloping plateau until 2.85 V (235 $mAhg^{-1}$). The potential range of the first plateau is in good agreement with the expected one based on the redox potentials of the electrode materials (compare Figure 4-56). Since the theoretical capacity for the extraction of one fluoride ion from $La_2NiO_3F_2$ is ~ 67 $mAhg^{-1}$, it is indicated that besides the desired reduction of $La_2NiO_3F_2$ other redox processes occur. Moreover, a topochemical extraction of more than one fluoride ion would be chemically implausible without the formation of metallic Ni.

In order to obtain an insight into the structural changes of the RP-type phases at different charging states, several cells were charged to different cut-off capacities (Figure 4-62) and X-

ray diffraction patterns (Figure 4-63) were collected ex-situ and analysed using the Rietveld method. Structural models were derived from the chemical equivalents. It should be noted that an extensive investigation of structural changes and phase fraction evolutions of the phases obtained upon charging and discharging has shown a significantly improved reproducibility when specific cut-off capacities were chosen as opposed to usually applied potential limitations. This is most likely due to slightly varying over-potentials observed for different cells, which are not yet fully understood.

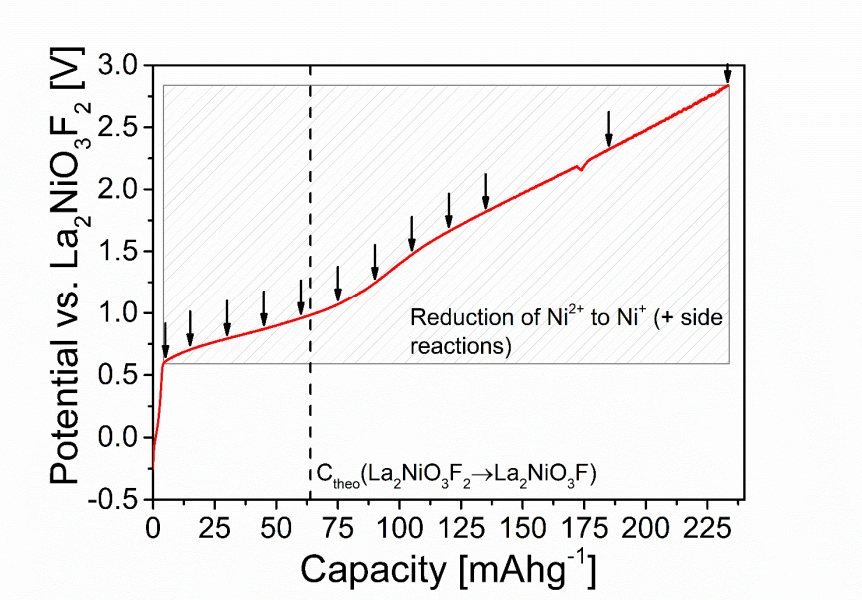

Figure 4-62: Charging curve of a cell Pb/PbF_2 against $La_2Ni_2O_3F_2$ charged to 235 $mAhg^{-1}$ (2.85 V). The arrows show various cut-off capacities, to which different cells were charged.

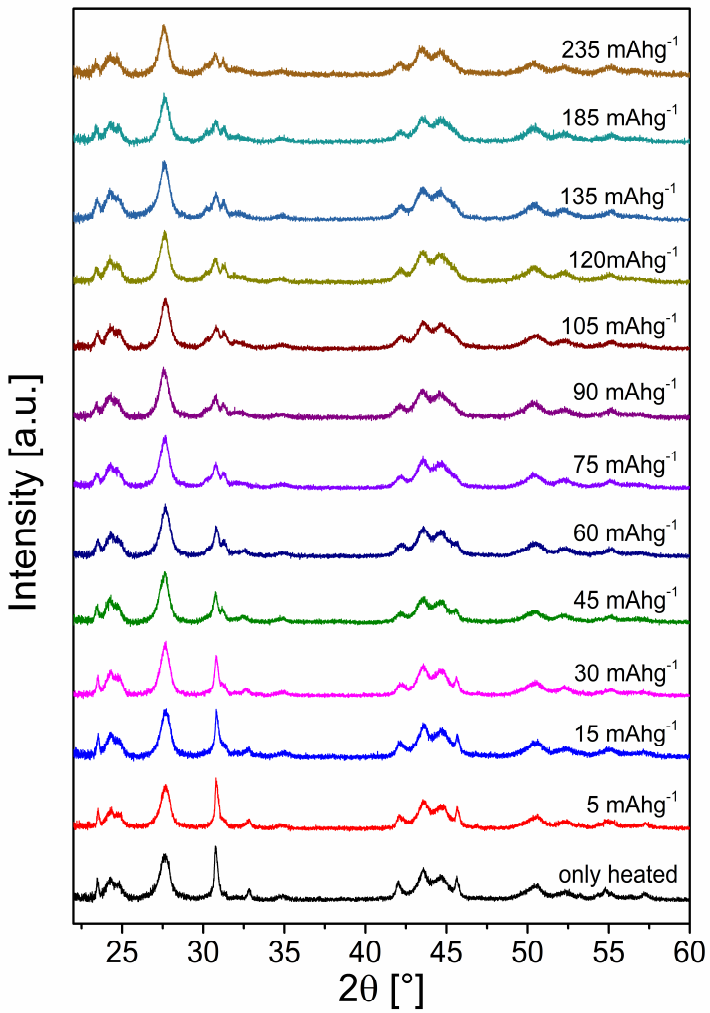

Figure 4-63: X-ray diffraction patterns of anode sides of different cells Pb/PbF_2 against $La_2NiO_3F_2$ charged to various cut-off capacities. For reference, a cell, which was only heated, is given.

Besides the electrolyte $La_{0.9}Ba_{0.1}F_{2.9}$ and amorphous CB, the main starting phase is the fully fluorinated $La_2NiO_3F_2$ (called 'orthorhombic #1', space group: *Cccm*, a = 12.8414(16) Å, b = 5.8013(6) Å, c = 5.4724(6) Å). Additionally, ~ 2 wt% of partly fluorinated $La_2NiO_{3+d/2}F_{2-d}$ (called 'orthorhombic #2', space group: *Fmmm*, a = 12.731(7) Å, b = 5.605(3) Å, c = 5.372(3) Å) are found. The lattice parameters of the latter phase are in accordance with the previously reported parameters obtained in a fluorination of the parent oxide La_2NiO_{4+d} with slightly lower fluorine amounts [74] (compare also section 4.1.3.1). Its formation is hard to be avoided completely.

When electrochemically defluorinating on charging, the phase fraction of the orthorhombic #1 phase decreases (Figure 4-64 a) and the lattice parameters change continuously on further charging up to ~ 45 $mAhg^{-1}$ (Figure 4-64 c-e). For the orthorhombic #2 phase, the phase fraction remains relatively constant (note that the phase fraction of this phase is in the order of quantification errors of the Rietveld method), while the lattice parameters change significantly. For both phases, the changes of the lattice parameters b and c are indicative for the extraction of fluoride ions. With increasing degree of reductive defluorination (C > 30 $mAhg^{-1}$), a monoclinic phase (Figure 4-63 and Figure 4-65) (called 'monoclinic #1', space group: *C*12/*c*1, lattice parameters at 90 $mAhg^{-1}$: a = 12.976(3) Å, b = 5.7422(13) Å,

c = 5.6231(9) Å, β = 88.798(15)°) occurs. Its phase fraction increases strongly up to ~ 75 mAhg^{-1} and remains comparatively constant at higher charging states.

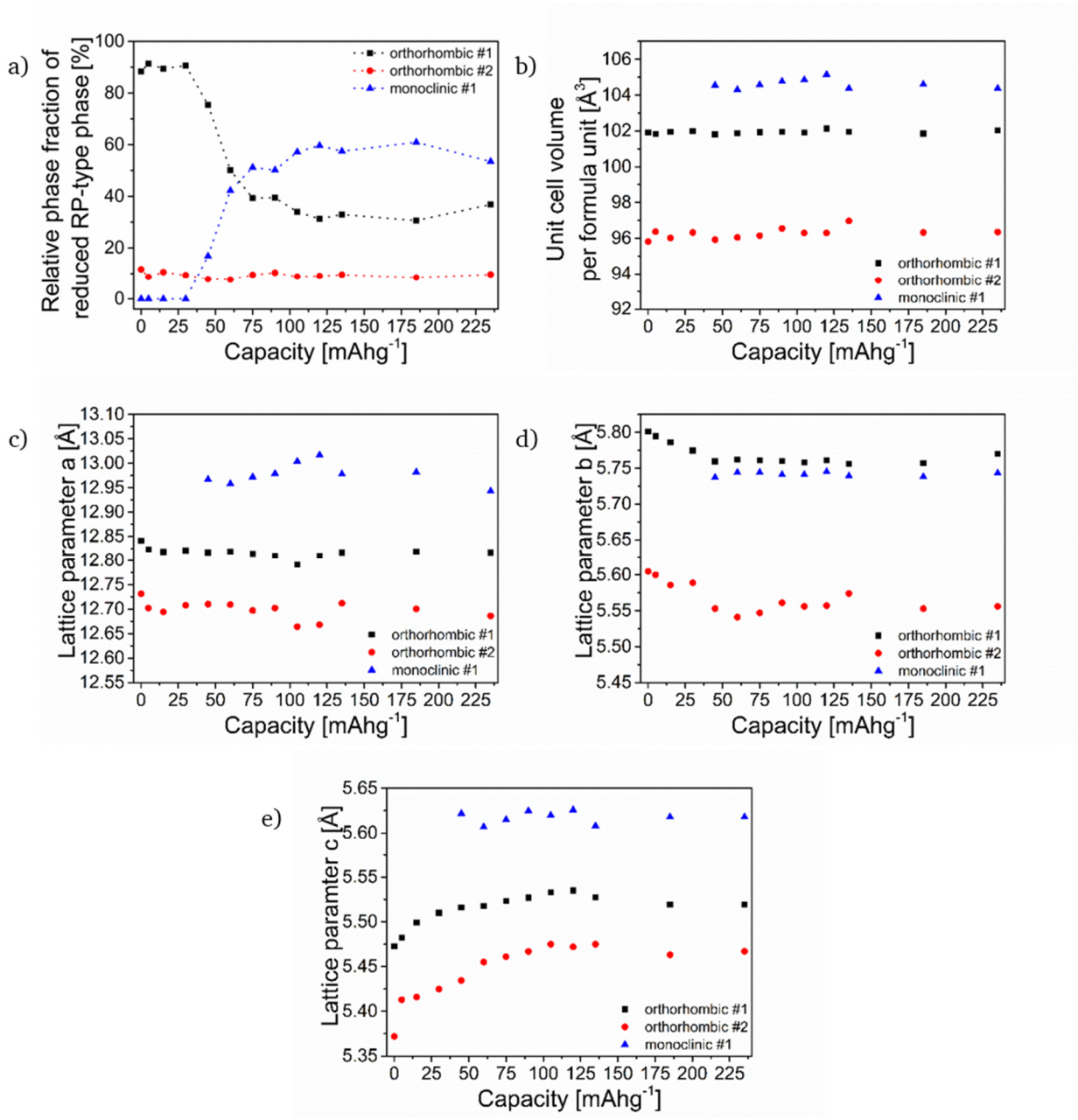

Figure 4-64: Relative phase fractions (a), unit cell volume per formula unit (b) and lattice parameters *a* (c), *b* (d) and *c* (e) of reduced RP-type orthorhombic #1, orthorhombic #2 and monoclinic #1 phases in the anode sides of cells Pb/PbF_2 against $La_2NiO_3F_2$ charged to different cut-off capacities. For the calculation of the relative phase fractions of the RP-type phases, the phase fraction of $La_{0.9}Ba_{0.1}F_{2.9}$ was not taken into account.

For each individual phase the unit cell volumes per formula unit remain relatively constant over the whole capacity range (Figure 4-64 b), while the lattice parameters undergo considerable changes in all three phases (Figure 4-64 c-e), which might indicate that the tilting of the octahedra is affected due to the introduction of defects. The highest unit cell volume is observed for the monoclinic #1 phase, and on formation of this phase from the orthorhombic #1 phase a steep increase in cell volume of ~ 3 Å^3 per formula unit is found. Strong expansions along the *a* axis and within the *bc* plane are observed. The latter mainly affects the equatorial Ni-O bonds. This is in agreement with the structural analysis of this

compound obtained via the hydride-based reductions (see section 4.1.3.2). Furthermore, for the orthorhombic #1 and #2 phases, strong changes in the *b* and *c* lattice parameters are found, leading to significantly smaller orthorhombic distortions. The observed changes in symmetry could result from changes of the ordering of anions and/or the tilting of polyhedra, which could, however, not be resolved with the structural analysis methods used.

A comparison between the X-ray diffraction patterns of the uncharged (only heated) anode side of a cell, the anode side of a cell charged to 90 $mAhg^{-1}$ and the reduction product $La_2NiO_3F_2$ + x NaH with x = 0.25 obtained via the hydride-based chemical defluorination (see section 4.1.3.2) is given in Figure 4-65. The electrochemically formed monoclinic #1 phase is in excellent agreement with the monoclinic phase found on reducing $La_2NiO_3F_2$ via hydride-based reactions. No indication is given for the formation of stronger defluorinated, orthorhombic phases, found when reducing $La_2NiO_3F_2$ chemically, in the electrochemically reduced anode composite, even when charging to the highest charging capacities.

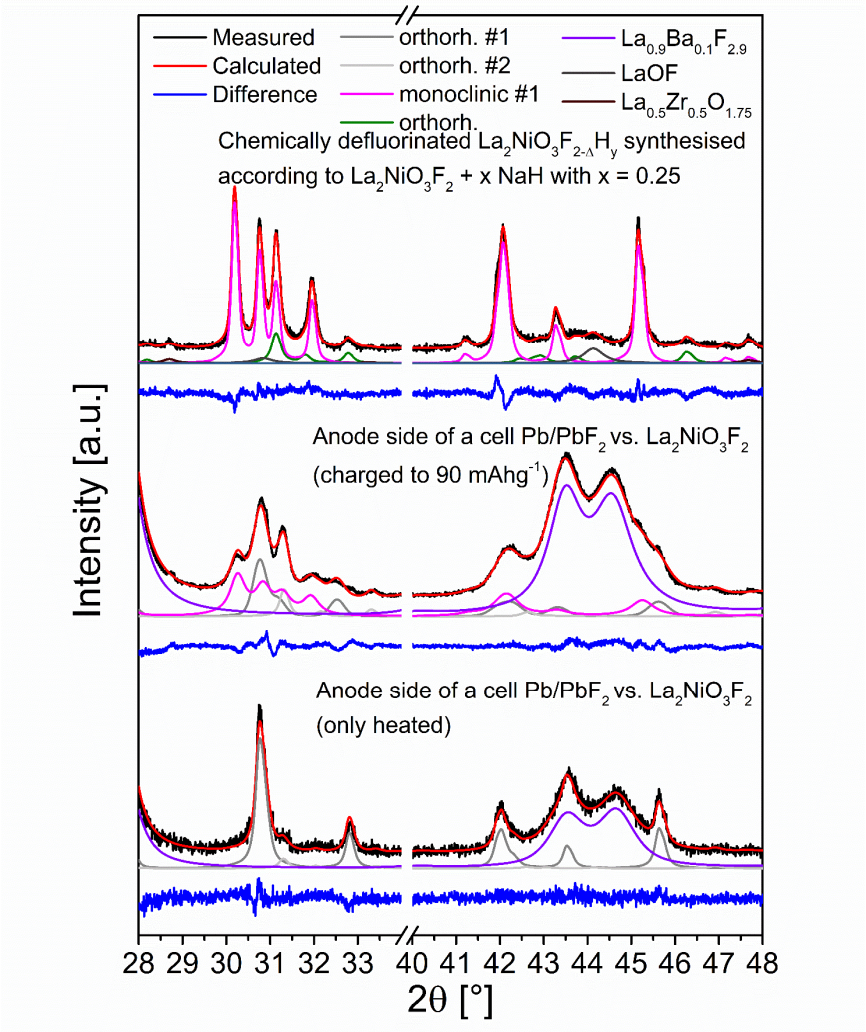

Figure 4-65: Comparison between selected angular ranges of Rietveld refinements of X-ray diffraction data of the anode side of a cell Pb/PbF_2 against $La_2Ni_2O_3F_2$ heated to 170 °C for 72 h, of the anode side of a cell Pb/PbF_2 against $La_2Ni_2O_3F_2$ charged to 90 $mAhg^{-1}$ and of chemically defluorinated $La_2NiO_3F_{2-\Delta}H_y$ synthesised via a hydride-based reduction according to the reaction equation $La_2NiO_3F_2$ + x NaH with x = 0.25. For full refinements, see Figure 4-37 and Figure 6-16 in the appendix.

4.2.2.1.2 X-ray photoelectron and X-ray adsorption spectroscopy of $La_2NiO_3F_2$, the anode composite and the reduced phases

The determination of the detailed oxidation state after the electrochemical reactions has proven to be difficult. XPS spectra (see Figure 6-17) give no meaningful information about the oxidation state of Ni of the electrochemically reduced RP-type phases due to the small energy separation between the La *3d* and Ni *2p* (or La *4d* and Ni *3s* signals). [250, 251] These signals are, moreover, dominated by the La signals, which are majorly originating from large amount of the electrolyte $La_{0.9}Ba_{0.1}F_{2.9}$ used within the composite electrode. Only the low-intensity Ni *3p* signals are not overlapping with other signals. Their intensities are, however, too low to make a meaningful analysis possible. The same observations were made for the oxidised RP-type phases obtained after electrochemical oxidation of $La_2NiO_3F_2$ (see section 4.2.2.2). Even though the Ni oxidation states of the RP-type phases could not be determined based on XPS measurements, this technique could be used to gain insights into the nature of the side reactions occurring during charging. In this context, C 1*s* spectra were recorded to investigate changes of the carbon additive used within the electrodes composites (see section 4.2.2.6).

To further examine the oxidation state of the reduced RP-type phases, XAS spectra of pure $La_2NiO_3F_2$ and of the electrochemically reduced anode composite (charged to 75 $mAhg^{-1}$) (Figure 4-66) were measured and compared. For the scratched-off anode sides of the charged cells, a small energy shift of the adsorption edge of ~ 0.5 eV to lower binding energies is observed and confirms that a partial reduction of $La_2NiO_3F_2$ to $La_2NiO_3F_{2-\Delta}$ has occurred. The shift is substantially smaller to what would be expected for a complete reduction from Ni^{2+} to Ni^{+} species. For the reduction of n = 2 and 3 RP-type nickelates, shifts of $\sim$ 2 - 3 eV upon the deoxygenation of $La_3Ni_2O_{6.9}$ to $La_3Ni_2O_6$ and $La_4Ni_3O_{10}$ to $La_4Ni_3O_8$, correlated to the reduction of the Ni oxidation state from +2.4 to +1.5 and +2.67 to +1.33, respectively, have been reported. [99, 100] An exact quantification of the oxidation state from the shift is not possible due to the lack of reference systems with similar coordinated Ni^{+} and due to the fact that changes in the coordination environment, e.g. the number of coordinating O/F ions also influences the edge in terms of energy position and shape. Moreover, it should be noted that in the scratched-off charged anode composite (for the quantification see Figure 6-18), only $\sim$ 37 % of the Ni cations are contained in the reduced monoclinic RP-type phase, while the remaining $\sim$ 63 % are found in the orthorhombic #1 phase. The latter undergoes a smaller reduction compared to the monoclinic phase, which causes a smaller edge shift in the spectrum, since the Ni ions of both phases are measured simultaneously. From the coupled Rietveld refinement of X-ray and powder neutron diffraction of the monoclinic #1 phase found after the chemical reduction, a composition of the phase of approximately $La_2NiO_3F_{1.93}$ (not considering possible hydride substitution processes) has been derived and it can be assumed that the monoclinic phase obtained electrochemically has a similar composition. Considering this, the small but noteworthy shift is in good agreement with the expected oxidation states of the obtained RP-type phases.

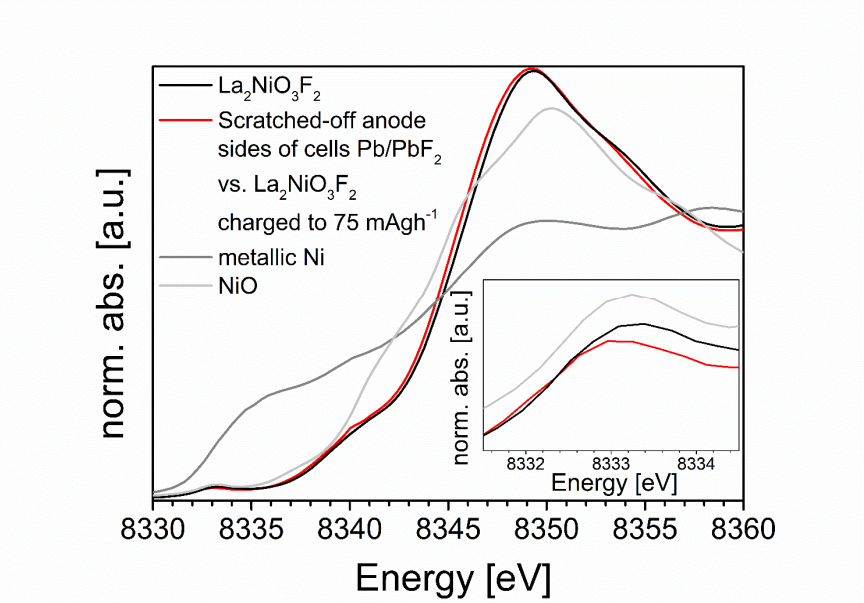

Figure 4-66: Normalized Ni K-edge X-ray absorption spectra of $La_2NiO_3F_2$ and the scratched-off anode sides of cells Pb/PbF_2 against $La_2NiO_3F_2$ charged to 75 $mAhg^{-1}$. As references, the spectrum of metallic Ni and NiO are plotted.

Furthermore, it should be noted that minor changes of the sample on scratching-off the electrode for measuring the composite and on handling the as obtained small amounts is indicated (see Figure 6-18).

4.2.2.2 Electrochemical fluorination of $La_2NiO_3F_2$

4.2.2.2.1 Electrochemical fluorination behaviour of $La_2NiO_3F_2$

The charging curve of a cell $La_2NiO_3F_2$ vs. Pb/PbF_2 composite ($La_2NiO_3F_2$ is used as active cathode material in this nomenclature) is shown in Figure 4-67. Between potentials of ~ 1.1 to 1.4 V vs. Pb/PbF_2, a first plateau covers ~ 320 $mAhg^{-1}$. After a steep potential increase to ~ 2 V, a second sloping plateau is found until the cut-off voltage of 3 V (739 $mAhg^{-1}$) is reached. The potential range, in which redox reactions occur, are again in good agreement with the expected potentials (see Figure 4-56). As for the electrochemical reduction of $La_2NiO_3F_2$, the observed capacities strongly exceed the theoretical capacity of ~ 64 $mAhg^{-1}$ for the intercalation of one fluoride ion leading to the formation of $La_2NiO_3F_3$. Therefore, undesired side reactions have to take place, as has been previously reported for the electrochemical fluorination of intercalation-based RP-type cathodes. [18-20]

In the same fashion as for the defluorination of $La_2NiO_3F_2$, X-ray diffraction patterns of cathode sides of cells charged to different cut-off capacities (Figure 4-68) being differently strongly oxidized were measured and analysed.

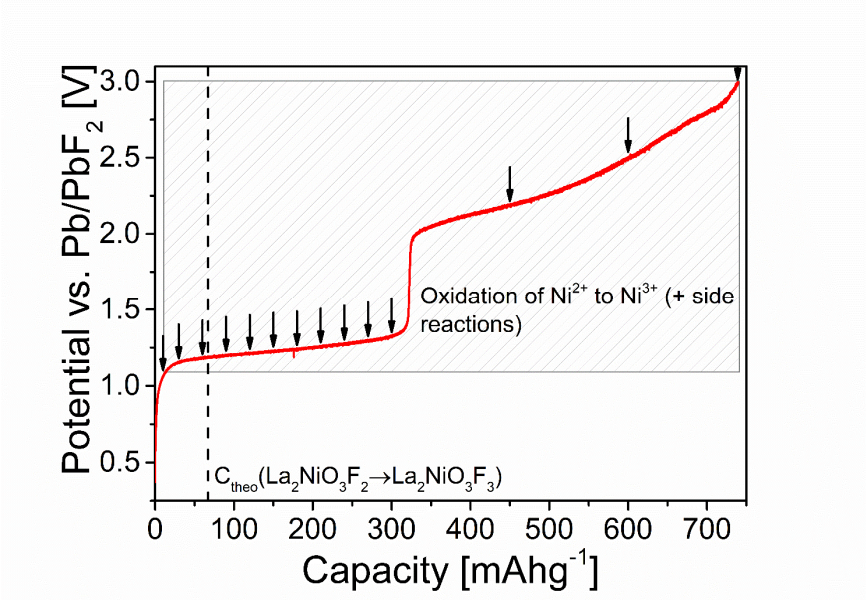

Figure 4-67: Charging curve of a cell $La_2Ni_2O_3F_2$ against Pb/PbF_2 charged to 739 $mAhg^{-1}$ (3 V). The arrows show various cut-off capacities, to which different cells were charged.

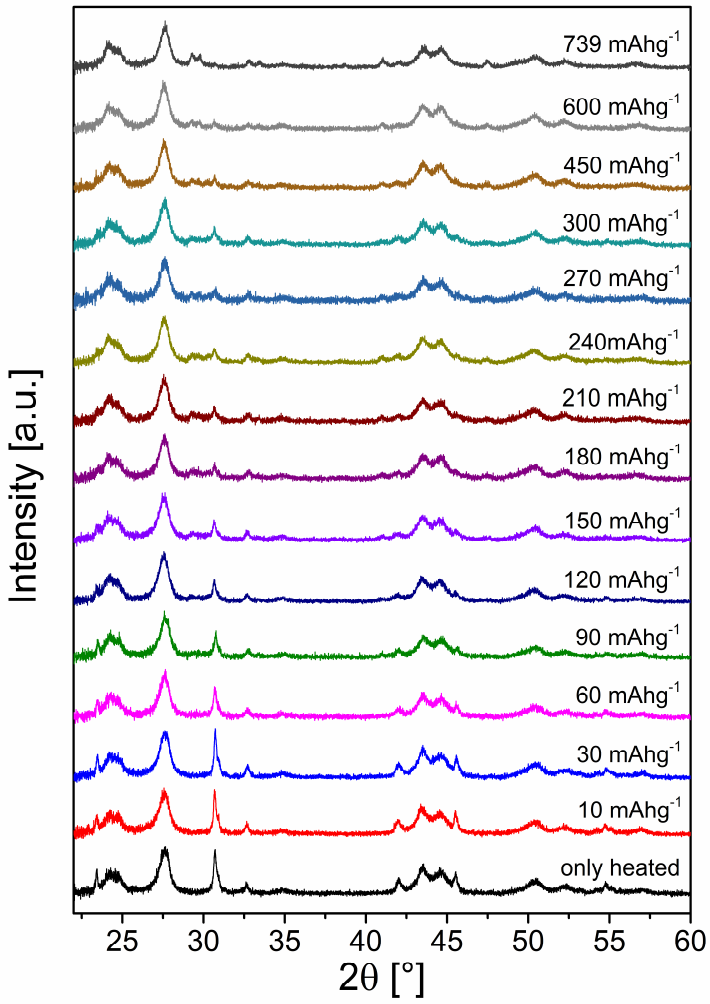

Figure 4-68: X-ray diffraction patterns of cathode side of different cells $La_2NiO_3F_2$ against Pb/PbF_2 charged to various cut-off capacities. For reference, a cell, which was only heated, is given.

The starting cathode composite contains, besides the electrolyte $La_{0.9}Ba_{0.1}F_{2.9}$ and CB, only $La_2NiO_3F_2$ (called 'orthorhombic #1', space group: *Cccm*, a = 12.8381(12) Å, b = 5.7978(4) Å, c = 5.4964(5) Å). Electrochemically fluorination upon charging (Figure 4-69 a) leads for capacities above 30 $mAhg^{-1}$ to the appearance of a monoclinic phase (called 'monoclinic #2', presumable space group: *C*12/*c*1, lattice parameters at 739 $mAhg^{-1}$: a = 14.890(5) Å, b = 5.4759(13) Å, c = 5.3811(13) Å, β = 91.238(16)°) and an orthorhombic phase (called 'orthorhombic #3', space group: *Cccm*, lattice parameters at 739 $mAhg^{-1}$: a = 13.44(3) Å, b = 5.648(12) Å, c = 5.496(13) Å). Along with these observations, a continuous decrease of the phase fraction of the orthorhombic #1 phase up to ~ 150 $mAhg^{-1}$ takes place. For higher capacities, its phase fraction remains constant. Further small decrease in the phase fraction of the orthorhombic #1 phase is observed for high capacities corresponding to the second charging plateau. The unit cell volume and lattice parameters of the phase are independent of the state of charging (Figure 4-69 b-e).

The relative phase fraction of the monoclinic #2 phase increases up to ~ 150 $mAhg^{-1}$ to ~ 45 wt%. Similar to the phase fraction of the orthorhombic #1 phase, it remains relatively constant until ~ 450 $mAhg^{-1}$. A strong increase of the relative phase fraction to ~ 90 wt% is found only for much higher capacities. For this phase, a considerable change in the lattice parameter a is found for capacities up to ~ 150 $mAhg^{-1}$. This increase of a can only be explained by a strong change of the anion sublattice, which is most likely due to the filling of the vacant interstitial site, present in $La_2NiO_3F_2$, by fluoride under formation of $La_2NiO_3F_3$ (see Figure 4-69). The orthorhombic #3 phase appears at higher capacities than the monoclinic #2 phase and its phase fraction is comparatively constant between ~ 180 and 300 $mAhg^{-1}$. The decrease of its phase fraction due to the increased formation of the monoclinic #2 phase at high capacities suggests that the monoclinic #2 phase is partly formed from the orthorhombic #3 phase. This also implies that the monoclinic #2 phase has a higher fluoride content than the orthorhombic #3 phase. The lattice parameters are relatively constant within errors.

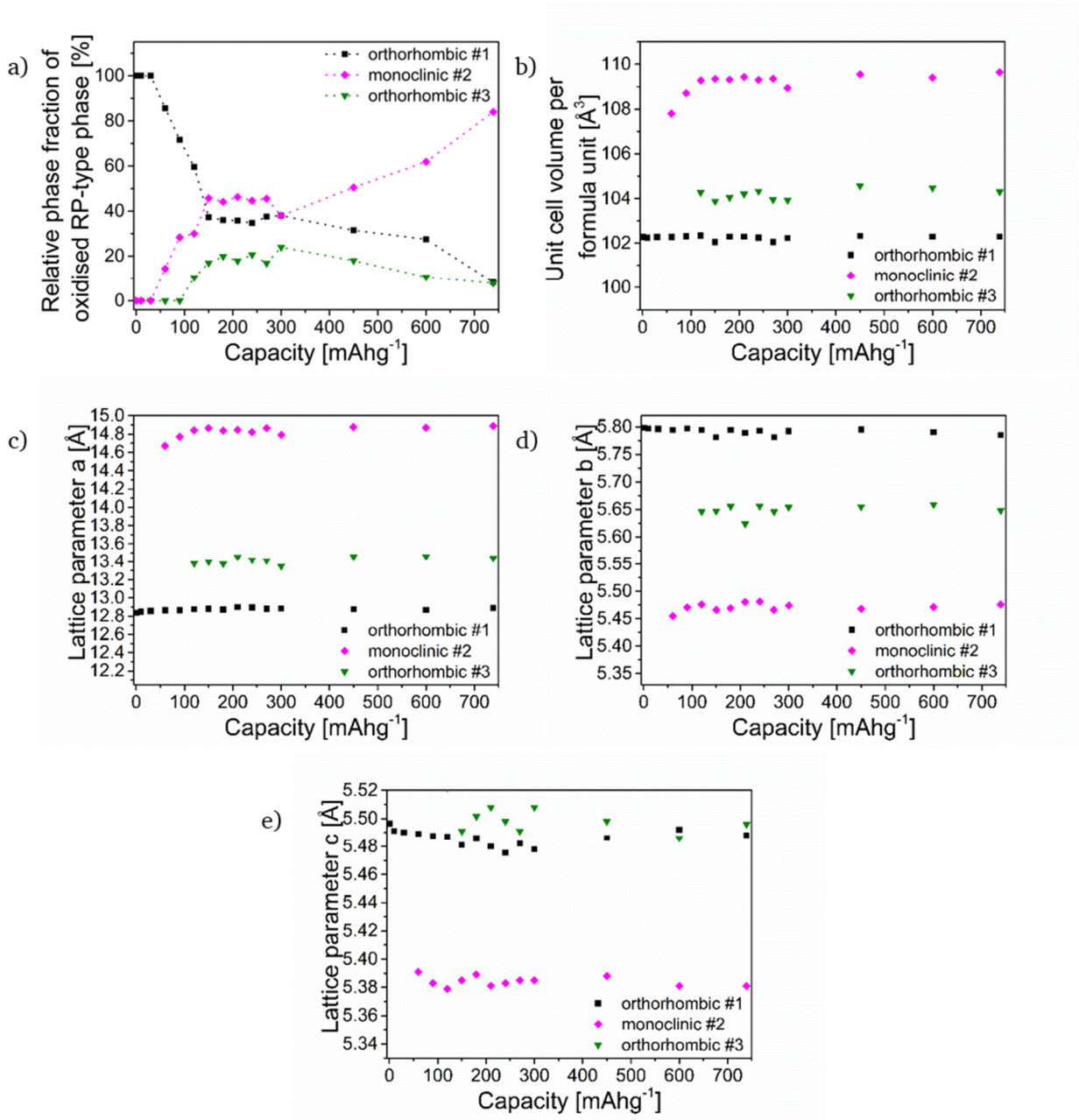

Figure 4-69: Relative phase fractions (a), unit cell volume per formula unit (b) and lattice parameters *a* (c), *b* (d) and *c* (e) of oxidised RP-type orthorhombic #1, monoclinic #2 and orthorhombic #3 phases in the cathode sides of cells $La_2NiO_3F_2$ against Pb/PbF_2 charged to different cut-off capacities. For the calculation of the relative phase fractions of the RP-type phases, the phase fraction of $La_{0.9}Ba_{0.1}F_{2.9}$ was not taken into account.

The unit cell volumes per formula unit of the found RP-type phases remain also relatively constant over the entire capacity range (Figure 4-69 b). Only for the monoclinic #2 phase an increase of the volume is found for capacities up to ~ 150 $mAhg^{-1}$, which is related to changes in the lattice parameter *a*. The highest unit cell volume is observed for the monoclinic #2 phase, which undergoes a volume increase of up to ~ 7 $Å^3$ per A_2BX_y formula unit as compared to the orthorhombic #1 phase due to fluoride intercalation within interstitial vacancies upon charging. The increase is caused from an expansion of the *a* lattice parameter, while the *b* and *c* lattice parameters contract. The contraction of the *bc* plane suggests strong changes of bond distances of equatorial Ni-O bonds, which would be expected for an oxidation to Ni^{3+}, since Ni^{2+} is larger than Ni^{3+} (ionic radii: Ni^{2+}: 0.63 Å, Ni^{3+}: 0.56 Å (high-spin configuration) or 0.6 (low-spin configuration))[54]. The orthorhombic #3 phase possesses

a cell volume between that of the orthorhombic #1 and the monoclinic #2 phases. The volume increase is again due to an expansion along the *a* axis. The smaller *b* lattice parameter, which also results in smaller orthorhombic distortions, is again consistent with an increase of the Ni oxidation state.

At this point a comparison between the X-ray diffraction patterns of the uncharged (only heated) and charged (to 739 $mAhg^{-1}$) cathode sides of cells $La_2NiO_3F_2$ vs. Pb/PbF_2 and chemically fluorinated $La_2NiO_3F_{2+x}$ is interesting. The additional chemical fluorination of $La_2NiO_3F_2$ in a post-fluorination step using highly oxidizing F_2 gas was attempted for the first time in this work. Various reaction temperatures were investigated (Figure 4-70). The best results in terms of yield of $La_2NiO_3F_{2+x}$ are obtained when using a reaction temperature of 190 °C for a duration of 15 min. However, the additional chemical fluorination results only in a very small fraction of $La_2NiO_3F_{2+x}$, while the predominant phase (~ 90 wt%) is still unreacted $La_2NiO_3F_2$. Longer exposure to F_2 (Figure 4-71) or higher reaction temperatures (Figure 4-70) cause a progressive decomposition of $La_2NiO_3F_2$ under formation of LaF_3. Lower reaction temperatures at increased reaction times do not lead to any changes of the parent phase. The positions of the additional reflections of the chemically fluorinated $La_2NiO_3F_{2+x}$ are in good agreement to the positions of the reflections found for the electrochemically formed monoclinic #2 phase, indicating a chemical similarity of both products.

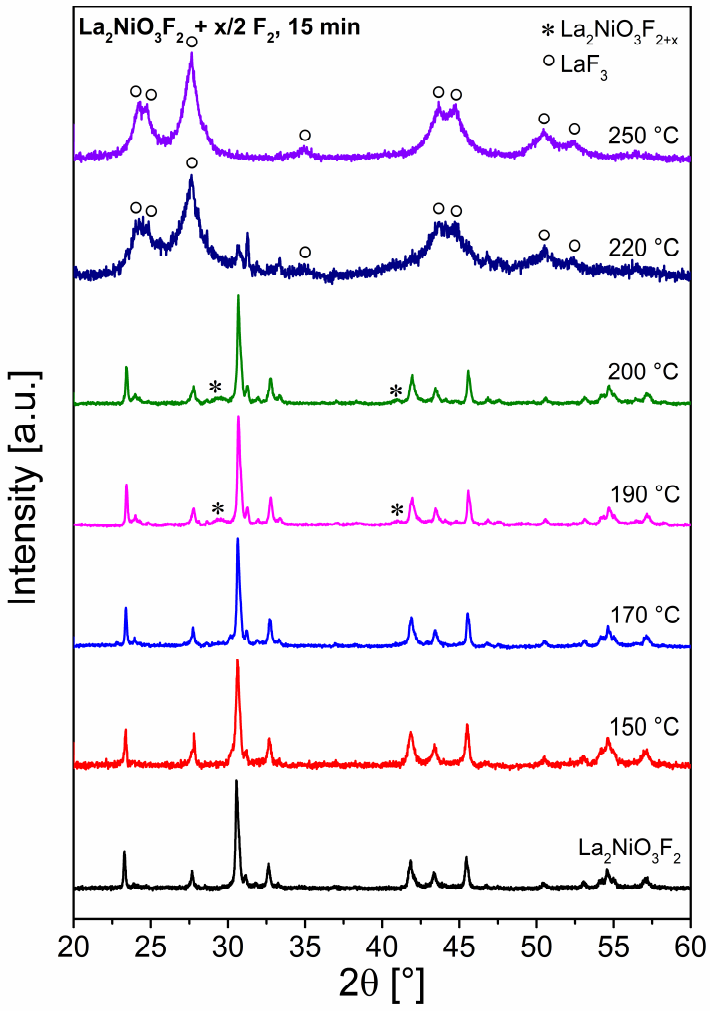

Figure 4-70: XRD patterns of the fluorination products containing additionally fluorinated $La_2NiO_3F_{2+x}$. The post-fluorination was performed using F_2 gas at various reaction temperatures for 15 min.

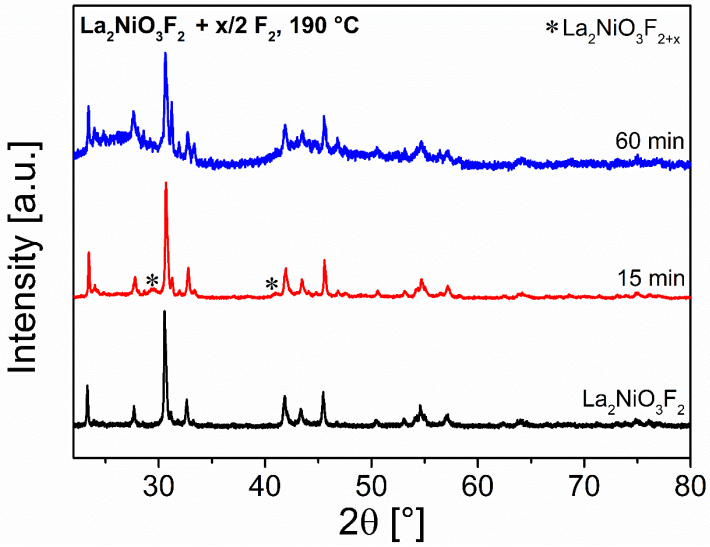

Figure 4-71: XRD patterns of the fluorination products containing additionally fluorinated $La_2NiO_3F_{2+x}$. The post-fluorination was performed using F_2 gas for different reaction times at 190 °C, which was found to be the best temperature for the reaction.

A direct comparison between the XRD patterns of the cathode side of the cell $La_2NiO_3F_2$ against Pb/PbF_2 charged to 739 $mAhg^{-1}$ and the additionally fluorinated $La_2NiO_3F_{2+x}$ obtained after chemical fluorination confirms this (Figure 4-72). The electrochemical fluorination results, however, in considerably higher phase fractions of the monoclinic #2 phase. Therefore, electrochemical routes can present viable, safe and easily controllable methods for the synthesis of fluorinated compounds, which cannot be obtained via other routes.

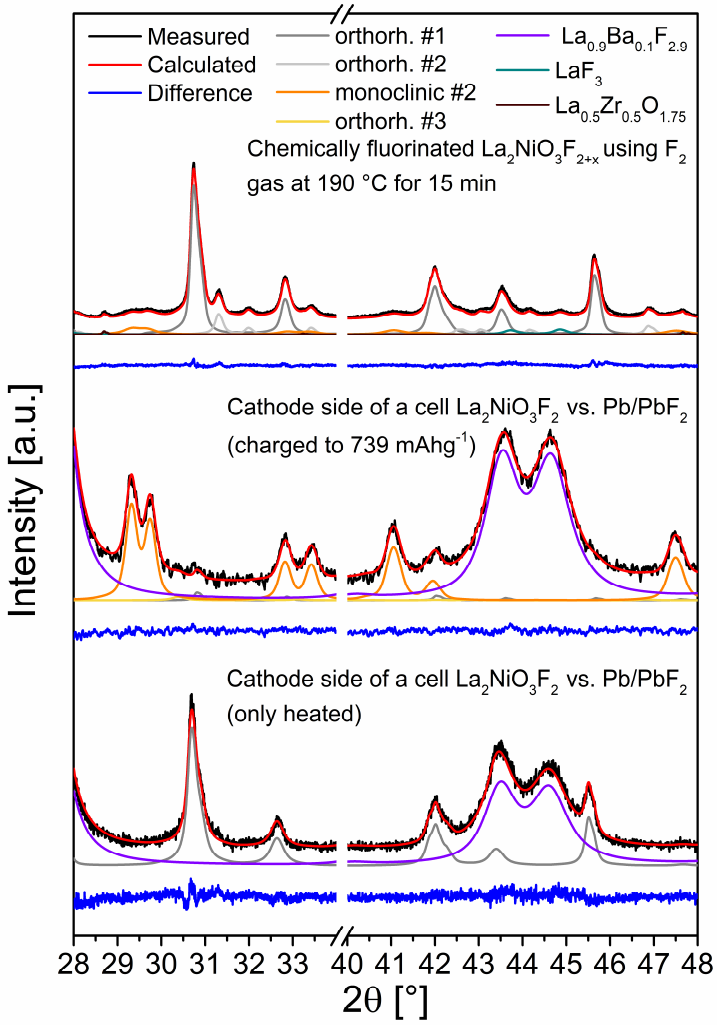

Figure 4-72: Comparison between selected angular ranges of Rietveld refinements of X-ray diffraction data of the cathode side of a cell $La_2Ni_2O_3F_2$ against Pb/PbF_2 heated to 170 °C for 72 h, of the cathode side of a cell $La_2Ni_2O_3F_2$ against Pb/PbF_2 charged to 739 $mAhg^{-1}$ and of chemically fluorinated $La_2NiO_3F_{2+x}$ synthesised via a post-fluorination using F_2 gas at 190 °C for 15 min. For full refinements, see Figure 6-16 and Figure 6-19 in the appendix.

4.2.2.2.2 Transmission electron characterisation of the oxidised $La_2NiO_2F_{2+x}$

Since the synthesis of sufficiently high amounts of $La_2NiO_2F_{2+x}$, necessary for a structural analysis using neutron diffraction, via the oxidation approach using F_2 gas was not possible, an alternative approach based on electron transmission microscopy was attempted for the structural characterisation. This approach has been successfully used previously for the determination of the structure $La_2NiO_{4.13}F_{1.59}$ obtained via electrochemical fluorination of $La_2NiO_{4.13}$ within FIBs. [19]

In contrast to this previous study, it was much harder to identify suitable crystals in the polycrystalline sample for the ADT analysis. In analogy to the previously used approach for

the identification of Ni-containing crystals, consisting, therefore, of the targeted RP-type phase, EDX spectroscopy was performed. However, after the EDX spectroscopy measurements, a strong amorphisation of the investigated crystals, making ADT measurements unfeasible, is found. It can be assumed that the relatively high electron dose applied during the spectroscopy leads to a destruction of the phase and strong amorphisation. This is of special interest with respect to the metastability of such phases; since $La_2NiO_{4.13}F_{1.59}$ did not decompose under such conditions, it is indicated that the fluorinated phase $La_2NiO_3F_{2+x}$ suffers from a lower stability as compared to $La_2NiO_{4.13}F_{1.59}$. Due to this instability, it was also not possible to use EDX spectroscopy to estimate the composition of $La_2NiO_3F_{2+x}$. In order to assure the presence of Ni within the investigated particles, EDX measurements were, therefore, performed after the ADT measurements. An exemplary EDX spectrum is shown in Figure 6-20.

Only one of the crystals, on which measurements were attempted, was finally found to to provide diffraction and contain Ni. This is also in agreement with our previous findings, which showed that agglomerates of $La_{0.9}Ba_{0.1}F_{2.9}$ are hardly distinguishable from RP-type particles from a morphological point of view; the RP-type particles are, additionally, partly covered with $La_{0.9}Ba_{0.1}F_{2.9}$. The reconstructed ADT diffraction volumes of this crystal is shown in Figure 4-73. Due to the comparatively small data set of the obtained data, i.e., a limited reflection coverage, a detailed structural analysis was not possible. Missing *b* and *c* axes result in a certain uncertainty of the atomic positions of the ions in the *bc* plane, therefore, the derived structure can only give general indications about structural changes occurring upon electrochemical fluorination.

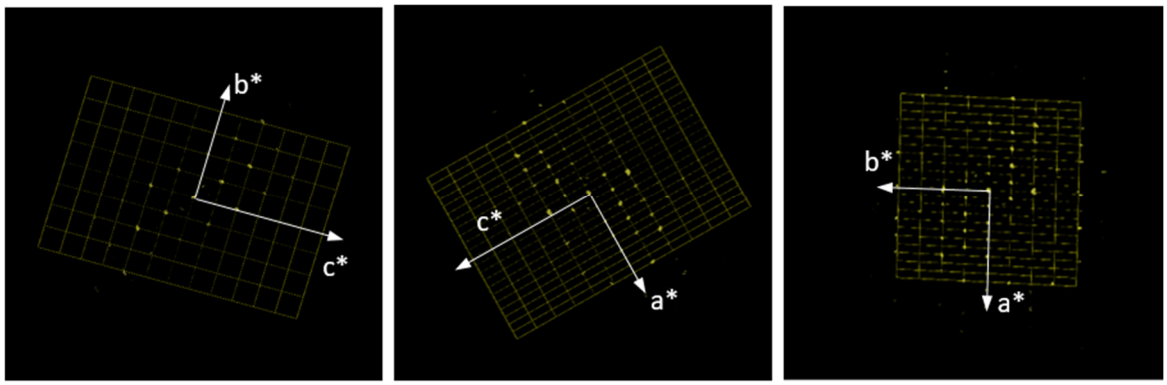

Figure 4-73: Views of the reciprocal space along the directions from left to right (100), (010), (001) of the measured crystal with monoclinic #2 structure obtained via galvanostatic charging of a cell $La_2NiO_3F_2$ vs. Pb/PbF_2.

The derived lattice parameters are given in Table 4-22. The change of the lattice parameters with a strong expansion of the *a* axis as observed in the X-ray diffraction study could be well confirmed by the ADT method within the expected errors. Furthermore, a symmetry lowering to a monoclinic C-centered cell is indicated and atomic positions corresponding to a C12/c1 symmetry could be derived (Table 6-4 and Table 6-5). The refined atomic positions are also in principle agreement with the structural model used for the Rietveld refinements.

Table 4-22: Unit cell parameters of the monoclinic #2 RP-type phase of two crystals obtained via galvanostatic charging of a cell $La_2NiO_3F_2$ vs. Pb/PbF_2 determined from Fast-ADT measurements.

Phase	**Lattice parameters**					
	a **[Å]**	***b*** **[Å]**	***c*** **[Å]**	**α [°]**	**β [°]**	**γ [°]**
monoclinic #2	14.74	5.57	5.31	90.8	91.4	90.0

A successful topochemical post-fluorination of $La_2NiO_3F_2$ requires the intercalation of up to one additional fluoride ions per formula unit into the vacant interstitial site of $La_2NiO_3F_2$. The presence of structurally inequivalent interstitial anion sites as found in *C*12/*c*1 would be in principle justified upon the intercalation of these additional fluoride ions, in particular when considering that the occupied interstitial site in $La_2NiO_3F_2$ is filled by oxide ions. It has to be emphasised that structural solutions were also attempted based on other C-centred groups such as *C*12/*m*1. A *C*12/*m*1 symmetry would allow for a single interstitial anion site, which would be structurally plausible for a fully fluorinated phase $La_2NiO_3F_3$ if reorganization of anions would take place (e.g. only fluoride ions occupy the interstitial layer or fluoride-oxide disorder within the interstitial layer arises). These structural models differ with respect to the relative orientation of the tilting patterns of the NiX_6 octahedra of adjacent perovskite-type layers (Figure 4-74 a and b), which leads to different shapes and possibly sizes of the interstitial cavities due to the different underlying symmetry elements. In Figure 4-74 a, the tilting of the octahedra in the oxidised phase is illustrated for the structural model with *C*12/*c*1 symmetry derived from the electron diffraction data. From the relative coordination around the interstitial ions, it becomes evident that two independent crystallographic interstitial sites are present in this symmetry. When viewing along the *c* axis, the differences between the red and blue hexagons, from which the three-dimensional shape of the polyeder filling the interstitial cavities can be derived, are obvious. In contrast to this, the differences between the red and blue hexagons, when viewing along the *b* axis are quite subtle. Close inspections of the bond distances between the anions at the apical and at both interstitial sites showed that distances differ, which is related to the different atomic positions of the anions in the interstitial sites. In comparison to the parent phase $La_2NiO_3F_2$ with *Cccm* symmetry (see section 4.1.3.1.2), the longer bond distances between the apical and interstitial anions make an occupation of the former vacant site in this monoclinic space group energetically more feasible. The shortest distance present is $\sim$ 2.5 Å. This is also related to a less pronounced tilting of the octahedra. Similar considerations can be made for the introduction of disorder at the interstitial sites due to the repeated electrochemical fluoride intercalation and deintercalation (see Figure 4-90). Nevertheless, the relative orientation of the octahedra of neighbouring perovskite-type layers of $La_2NiO_3F_2$ and the additionally fluorinated phase is still comparable.

For the structural model with *C*12/*m*1 symmetry (structural parameters are given in Table 6-6), on the other hand, the tilting patterns is changed significantly (Figure 4-74 b), i.e., the octahedra of different perovskite-type layers align in the same fashion as the octahedra of adjacent layers above and below. A comparison of the sizes of the interstitial cavities shows that only one interstitial site is present, making a complete filling of this site plausible. For each viewing direction, only one shape and size of the hexagons is observed and the lighter and darker hexagons can be transferred into each other by mirror or rotation operations.

In strong contrast to the tilting of the octahedra found for these two structural models with monoclinic space groups, a tilting of the octahedra is not possible for their supergroup with *Fmmm* symmetry. This symmetry has been, however, observed when electrochemically fluorinating $La_2NiO_{4.13}$, leading also to a composition close to La_2NiX_6 (Figure 4-74 c). [19] Only one interstitial site is present within this space group. The sizes of the hexagons differ slightly for both viewing directions, which is in accordance with the independency of the lattice parameters *a* and *b*. Relatively short bond distances between the apical and interstitial anions, related to the absence of octahedra tilting, are partly compensated by an additional expansion

along the *c* axis. Moreover, the shapes of the octahedra identified for the monoclinic space groups can be all related to the regular shape of the octahedra found in *Fmmm* symmetry by pulling at opposite corners and/or edges, illustrating the structural relationship between the space groups.

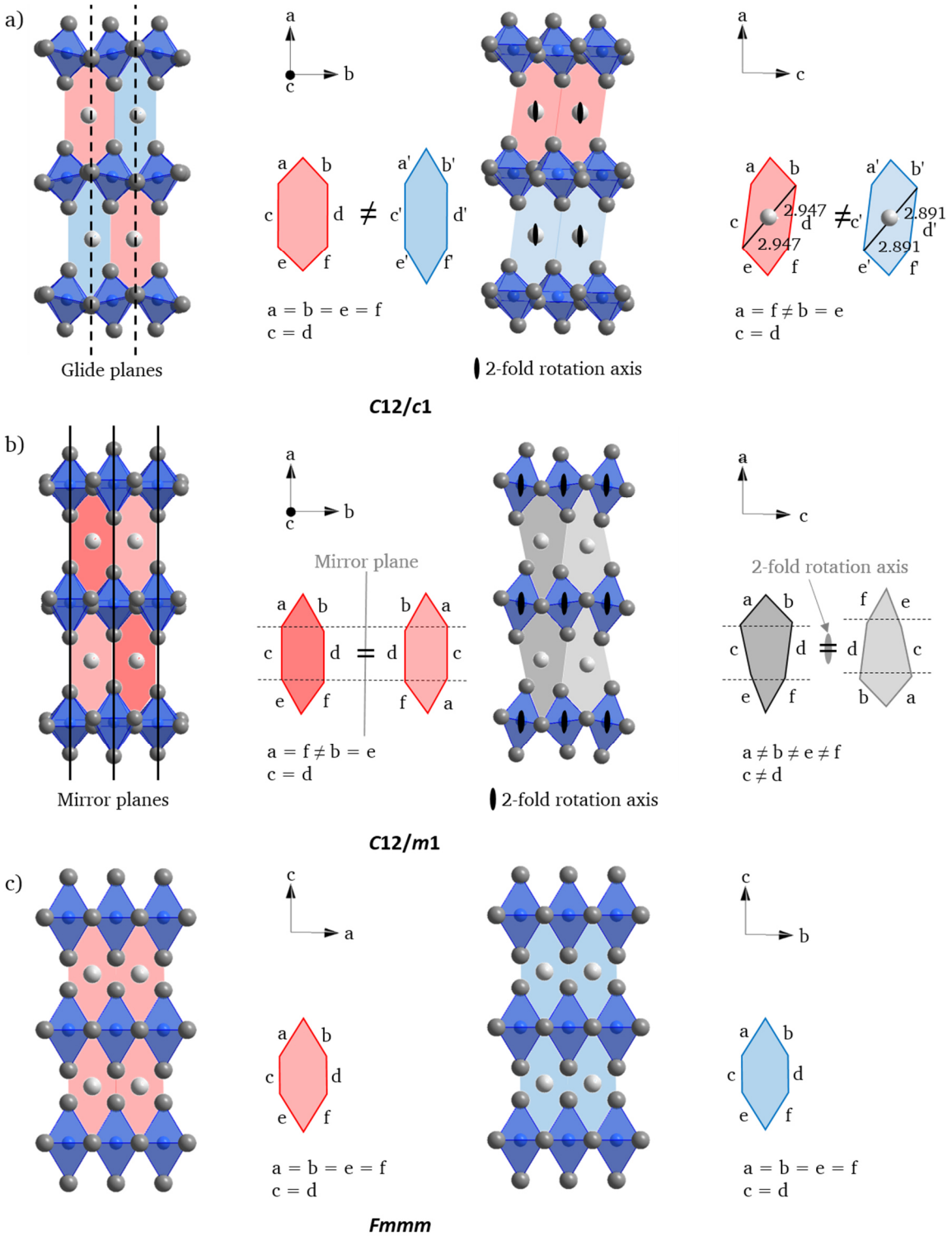

Figure 4-74: Comparison of the tilting pattern of the NiX_6 octahedra of La_2NiX_6 (respectively $La_2NiO_3F_3$) in space group *C*12/*c*1 (a), *C*12/*m*1 (b) and *Fmmm* (c). For a better visualisation, only three edge-sharing NiX_6 octahedra per perovskite-type layer and the corresponding interstitial anions are shown (La^{3+} ions are not included). The letters next to edges of the hexagons and the given relationships indicate whether a symmetric equivalency or not is present between the edges (respectively the ions at the corners of the hexagons). The symmetry elements (glide and mirror planes and 2-fold rotational axes) are only included in the representation of the monoclinic structures.

From the structural changes of the cells in dependence of the charging state observed using X-ray diffraction combined with the additional information gained from ADT, a composition close to $La_2NiO_3F_3$ can be assumed for the monoclinic #2 phase.

4.2.2.3 Electrochemical re-fluorination of the reduced $La_2NiO_2F_{2-x}$

Re-oxidation of reduced RP-type phases was performed in Pb/PbF_2 vs. $La_2NiO_3F_2$ cells, which were previously charged to 90 $mAhg^{-1}$. Due to strong over-potentials, a considerable discharging can only be obtained when the cells are discharged to negative potentials (Figure 4-75). A first discharging plateau is found between ~ -0.8 and -1.1 V against $La_2NiO_3F_2$ covering ~ 80 $mAhg^{-1}$ of discharge capacity. Within this plateau, the orthorhombic #1 and #2 starting phases $La_2NiO_3F_2$ and $La_2NiO_{3+d/2}F_{2-d}$ are regained and the monoclinic #1 phase vanishes completely (Figure 4-76 and Figure 4-77 a). This confirms the reversibility of the structural changes on re-fluorination. Considering that the charging of the cell to 90 $mAhg^{-1}$ results in the formation of a relative phase fraction of ~ 50 % of the reduced monoclinic #1 phase containing Ni^+ in addition to large percentage of $La_2NiO_3F_2$ containing Ni^{2+}, the first discharging plateau related to the re-oxidation of the Ni^+ species is too long, suggesting that side reactions take place as well.

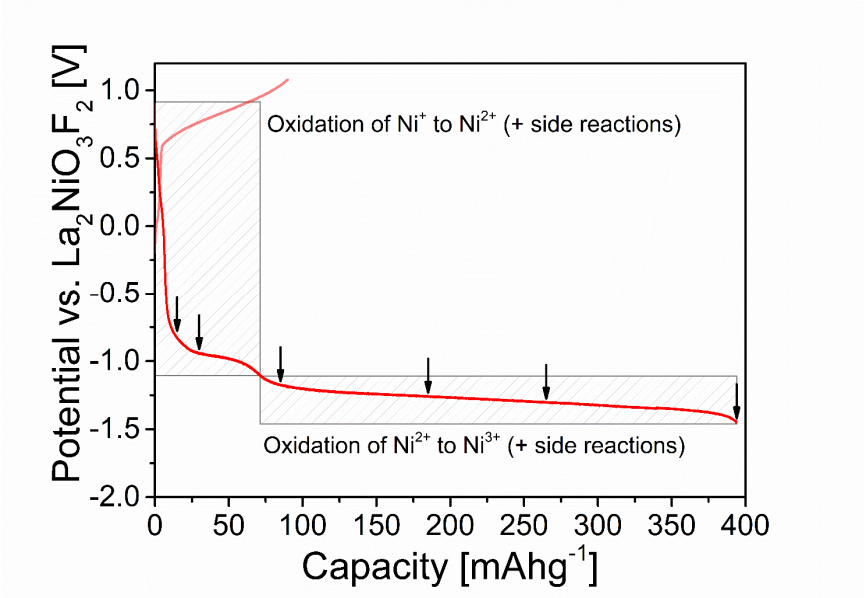

Figure 4-75: Charging and discharging curves of a cell Pb/PbF_2 against $La_2NiO_3F_2$ charged to 90 $mAhg^{-1}$ and subsequently discharged to 395 $mAhg^{-1}$. The arrows show various cut-off capacities, to which different cells were discharged.

Forcing the cells to discharge beyond this first discharging plateau, a second extended plateau extending ~ 310 $mAhg^{-1}$ in the voltage range of ~ -1.2 and -1.45 V occurs. In the diffraction patterns (Figure 4-76) strong changes resulting from the formation of the monoclinic #2 phase (presumable space group: $C12/c1$, lattice parameters at 395 $mAhg^{-1}$: a = 14.906(3) Å, b = 5.4646(9) Å, c = 5.3709(9) Å, = 91.074(1)°) are observed. The same phase is observed for a direct fluorination of the respective cathode composite. The phase fraction of $La_2NiO_3F_{2+}$ increases continuously while the other phases diminish. For all phases, the unit cell volumes and lattice parameters (Figure 4-77 b-f) are in good agreement with what is found in the sections 4.2.2.1 and 4.2.2.2. Interestingly, the orthorhombic #3 phase, which is observed for a direct oxidation when charging the cathode composite (see Figure 4-69), seems, not to be formed.

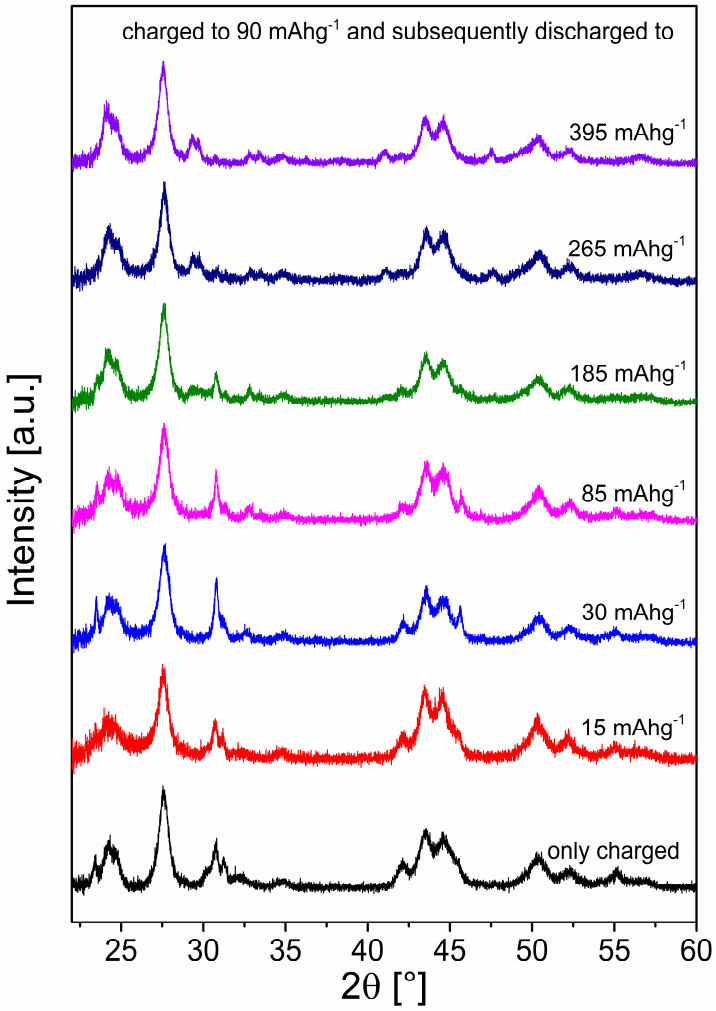

Figure 4-76: X-ray diffraction patterns of anode sides of different cells Pb/PbF_2 against $La_2NiO_3F_2$ charged to 90 $mAhg^{-1}$ and subsequently discharged to various cut-off capacities. For reference, a cell, which was only charged to 90 $mAhg^{-1}$, is given.

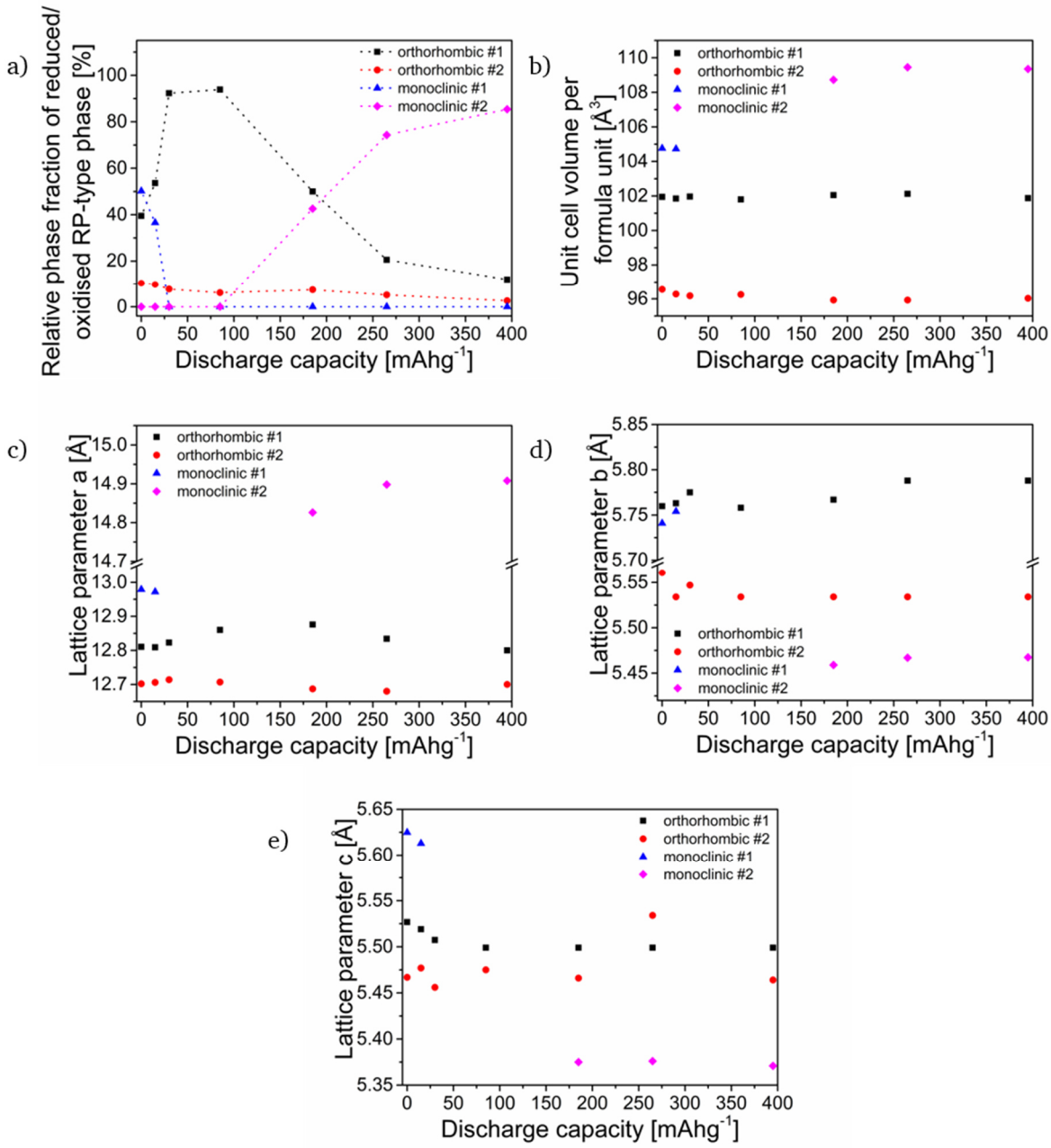

Figure 4-77: Relative phase fractions (a), unit cell volume per formula unit (b) and lattice parameters *a* (c), *b* (d) and *c* (e) of reduced/oxidised RP-type orthorhombic #1,orthorhombic #2, monoclinic #1 and monoclinic #2 phases in the anode sides of cells Pb/PbF_2 against $La_2NiO_3F_2$ charged to 90 $mAhg^{-1}$ and subsequently discharged to different cut-off capacities. For the calculation of the relative phase fractions of the RP-type phases, the phase fraction of $La_{0.9}Ba_{0.1}F_{2.9}$ was not taken into account.

A comparison of the diffraction patterns of an oxidized cathode side (charged to 739 $mAgh^{-1}$) of a $La_2NiO_3F_2$ against Pb/PbF_2 cell and a reduced and subsequently oxidized (charged to 90 $mAhg^{-1}$ and subsequently discharged to 395 $mAhg^{-1}$) anode side of a Pb/PbF_2 against $La_2NiO_3F_2$ cell is given in Figure 4-78. The reduction of $La_2NiO_3F_2$ followed by its oxidation leads to a smaller phase fraction of the orthorhombic #1 starting phase and considerably higher phase fractions of the monoclinic #2 phase at lower capacities and potentials compared to the direct oxidation (for better comparability of phase fractions at other charging capacities of $La_2NiO_3F_2$ against Pb/PbF_2 cells, see also Figure 4-69 a). The results suggest that a prior defluorination facilitates the electrochemical fluorination process under formation of Ni^{3+}. This might result from anion disorder introduced on the defluorination of the starting

material, aiding anion migration and thus facilitating the formation of the highly fluorinated state. Comparable phase fractions of the orthorhombic #1 and monoclinic #2 phases are only obtained at much higher charging capacities in the direct oxidation of the cathode material.

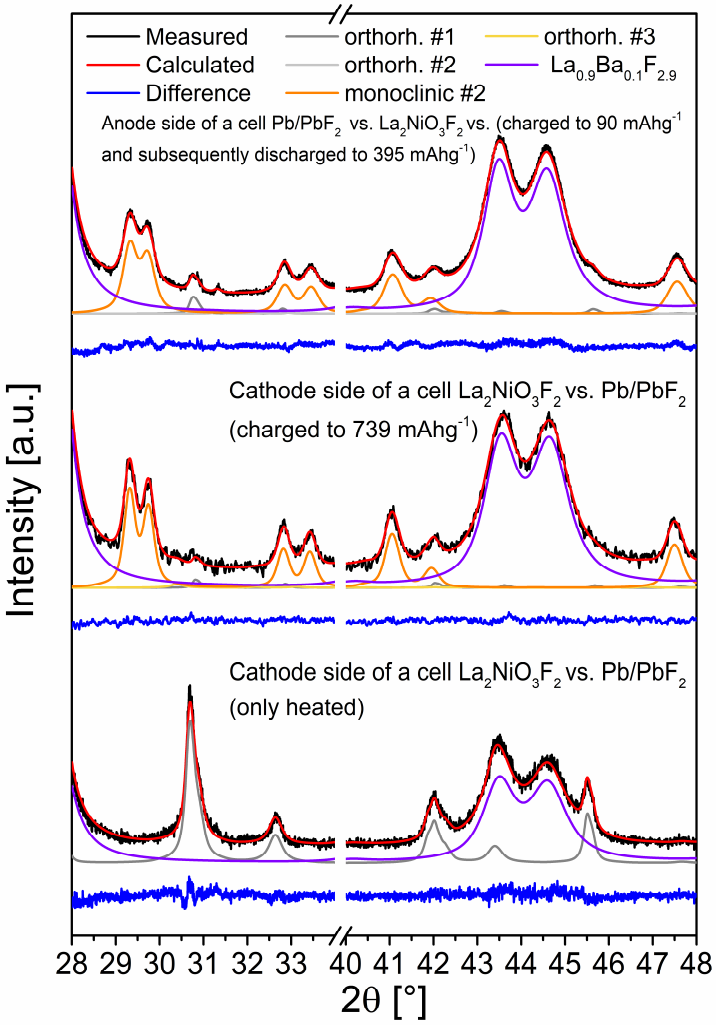

Figure 4-78: Comparison between selected angular ranges of Rietveld refinements of X-ray diffraction data of the cathode side of a cell $La_2Ni_2O_3F_2$ against Pb/PbF_2 heated to 170 °C for 72 h, of the cathode side of a cell $La_2Ni_2O_3F_2$ against Pb/PbF_2 charged to 739 $mAhg^{-1}$ and of the anode side of a cell Pb/PbF_2 against $La_2Ni_2O_3F_2$ charged to 90 $mAhg^{-1}$ and subsequently discharged to 395 $mAhg^{-1}$. For full refinements, see Figure 6-16 in the appendix.

4.2.2.4 Electrochemical re-defluorination of the oxidised $La_2NiO_2F_{2+x}$

Similar to the re-oxidation of the reduced RP-type phases, re-reduction experiments on the oxidized phases were performed via discharging of previously defluorinated (charged to 90$mAhg^{-1}$) $La_2NiO_3F_2$ against Pb/PbF_2 cells. A first discharging plateau is located between ~ 0.55 and 0.45 V against Pb/PbF_2 covering ~ 20 $mAhg^{-1}$ of discharge capacity (Figure 4-79). Within this plateau, the orthorhombic #1 starting phase $La_2NiO_3F_2$ is fully regained and the monoclinic #2 phase disappears (Figure 4-80 and Figure 4-81 a). This shows that full structural reversibility is found for charging and discharging within the positive potential range making the cathode composite a promising candidate for its application in reversible intercalation-based FIBs (see section 4.2.2.6). The changes in unit cell volumes and lattice parameters of the orthorhombic #1 and monoclinic #2 phases (Figure 4-81 b-e) indicate that the discharging in this potential range leads to an extraction of fluoride ions and, therefore, to

a reduction of the Ni^{3+} to Ni^{2+}. With respect to the relative phase fraction of the monoclinic #2 phase of ~30 % found within the cathode side of the cell after charging and its composition close to $La_2NiO_3F_3$, the corresponding theoretical discharge capacity for the reduction of Ni^{3+} to Ni^{2+} is in good agreement with the observed length of the first discharging plateau. Since the potential of this plateau is relatively high, side reactions seem to play a minor role.

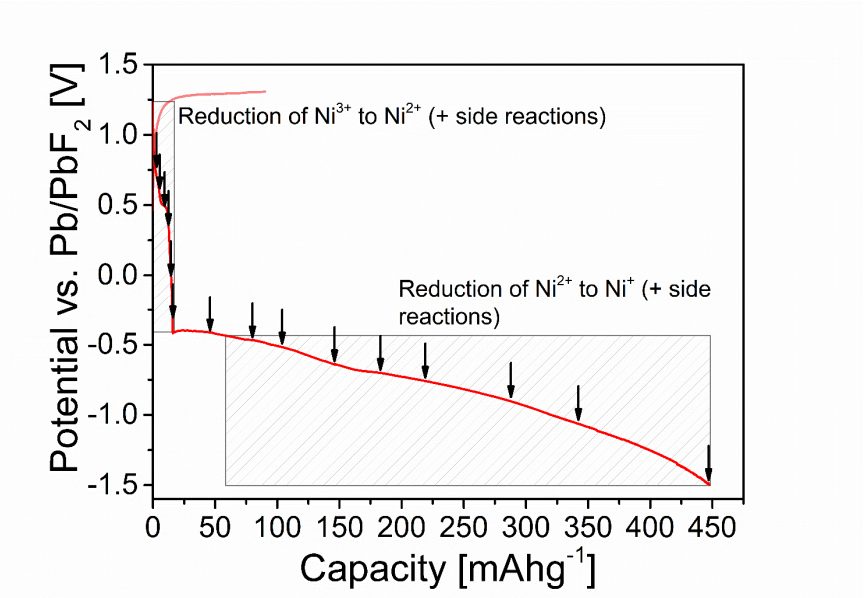

Figure 4-79: Charging and discharging curve of a cell $La_2NiO_3F_2$ against Pb/PbF_2 charged to 90 $mAhg^{-1}$ and subsequently discharged to 448 $mAhg^{-1}$. The arrows show various cut-off capacities, to which different cells were discharged.

Discharging the cells to negative potentials, a second extended sloping plateau occurs between ~ -0.35 and -1.5 V, where a discharge capacity of ~ 448 $mAhg^{-1}$ is obtained. The formation of the orthorhombic #1 phase (space group: *Cccm*, lattice parameters at 448 $mAhg^{-1}$: a = 12.917(9) Å, b = 5.750(2) Å, c = 5.591(2) Å, = 88.99(4)°) can be followed from the changes of the X-ray diffraction patterns of cells, which were discharged to different cut-off capacities (Figure 4-80). The same phase with similar lattice parameters has also been observed for a direct defluorination of the anode composite (see section 4.2.2.1). The evolutions of phase fractions, unit cell volumes and lattice parameters are given in Figure 4-81 a-e.

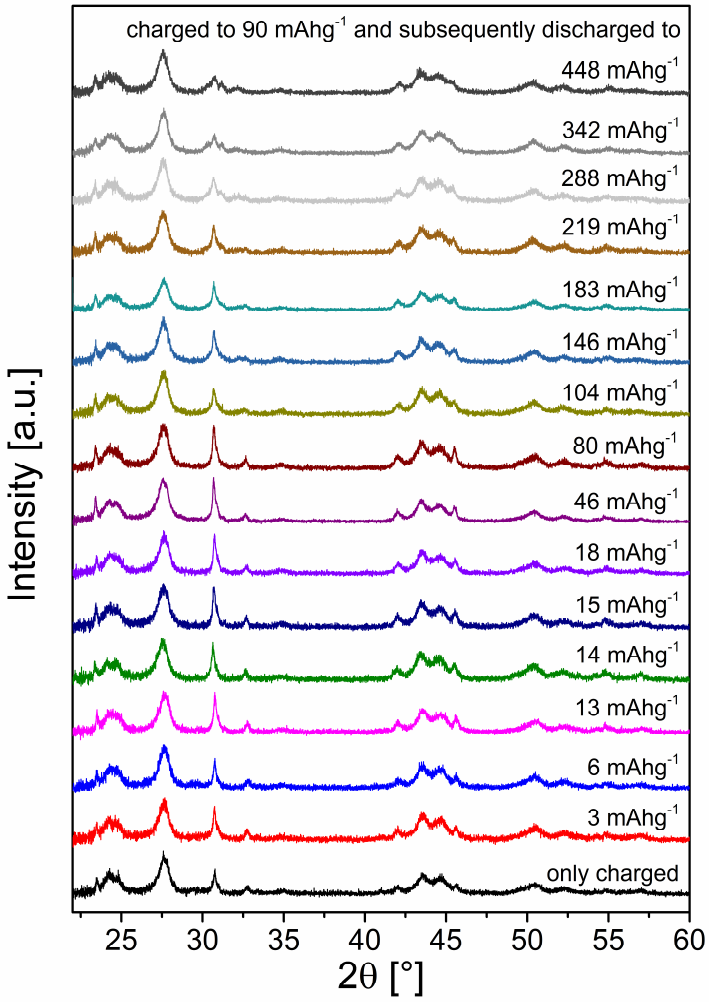

Figure 4-80: X-ray diffraction patterns of cathode sides of different cells $La_2NiO_3F_2$ against Pb/PbF_2 charged to 90 $mAhg^{-1}$ and subsequently discharged to various cut-off capacities. For reference, a cell, which was only charged to 90 $mAhg^{-1}$, is given.

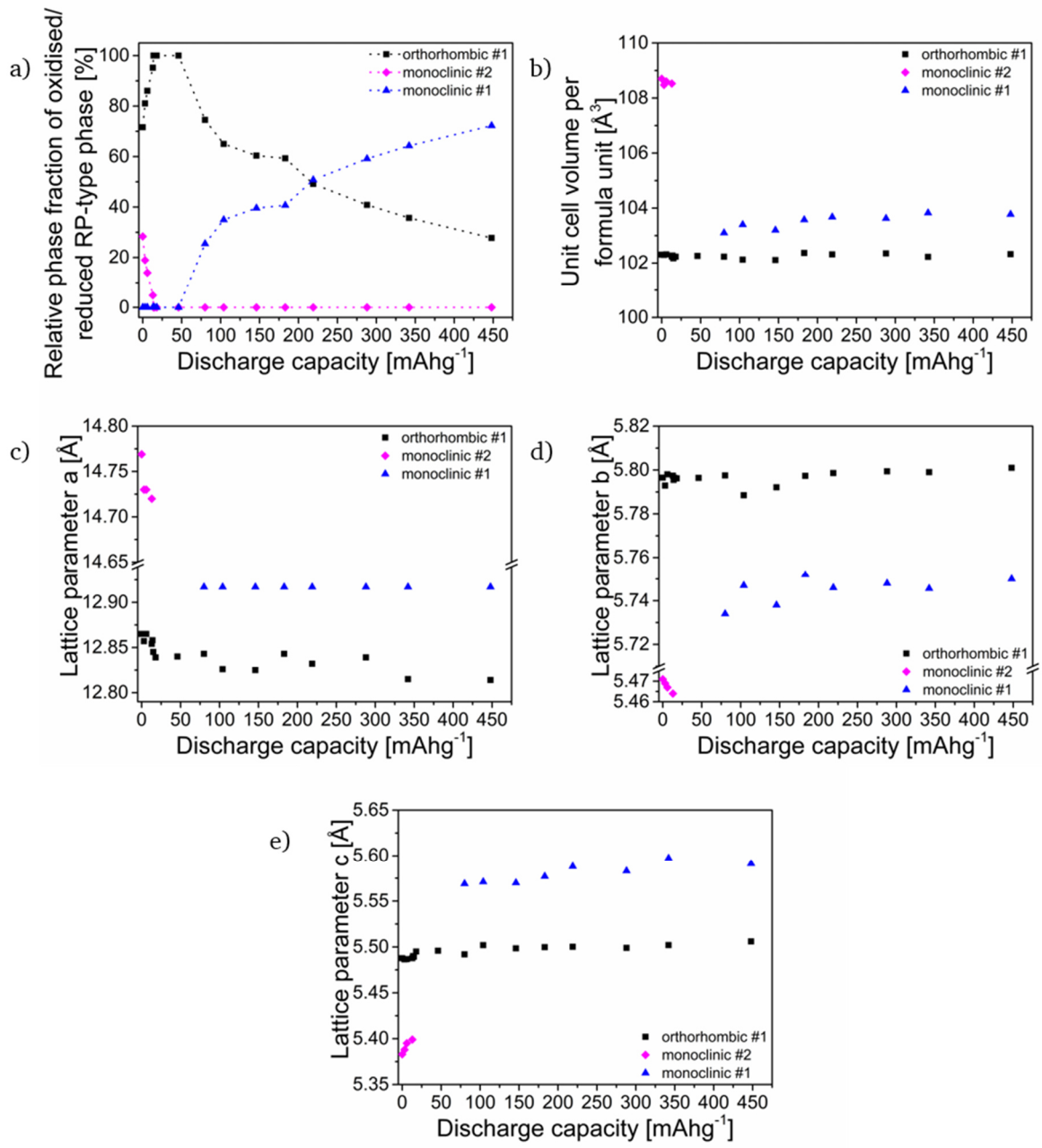

Figure 4-81: Relative phase fractions (a), unit cell volume per formula unit (b) and lattice parameters *a* (c), *b* (d) and *c* (e) of reduced/oxidised RP-type orthorhombic #1, monoclinic #2 and monoclinic #1 phases in the cathode sides of cells $La_2NiO_3F_2$ against Pb/PbF_2 charged to 90 $mAhg^{-1}$ and subsequently discharged to different cut-off capacities. For the calculation of the relative phase fractions of the RP-type phases, the phase fraction of $La_{0.9}Ba_{0.1}F_{2.9}$ was not taken into account.

A comparison between diffraction patterns of a directly reduced anode side (charged to 90 $mAhg^{-1}$) of a Pb/PbF_2 against $La_2NiO_3F_2$ cell and an oxidized and subsequently reduced (charged to 90 $mAhg^{-1}$ and subsequently discharged to 448 $mAhg^{-1}$) cathode side of a $La_2NiO_3F_2$ against Pb/PbF_2 cell is given in Figure 4-82. Even though smaller phase fractions of the orthorhombic #1 phase (as well as no orthorhombic #2 phase) and larger phase fractions of the monoclinic #1 phase are obtained after discharging to 448 $mAhg^{-1}$, the influence of the previous oxidation of $La_2NiO_3F_2$ on the formation of the reduced monoclinic #1 phase seems to be not as severe as for the opposite sequence of reduction followed by oxidation (see section 4.2.2.3). Especially, since the much higher discharge capacity of 448 $mAhg^{-1}$ as compared to 90 $mAhg^{-1}$ of a directly reduced cell has to be taken into account. This limited

influence of the previously performed slight fluorination might be related to a smaller extent of introduced disorder.

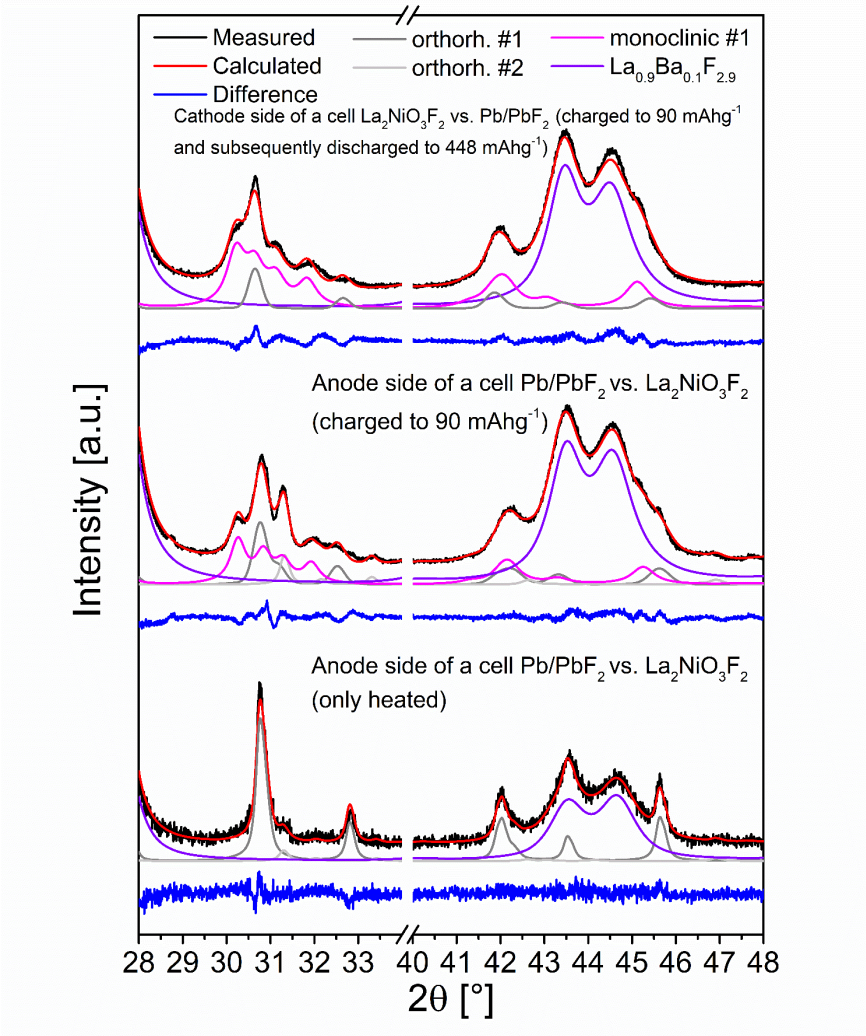

Figure 4-82: Comparison between selected angular ranges of Rietveld refinements of X-ray diffraction data of the anode side of a cell Pb/PbF_2 against $La_2Ni_2O_3F_2$ heated to 170 °C for 72 h, of the anode side of a cell Pb/PbF_2 against $La_2Ni_2O_3F_2$ charged to 739 $mAhg^{-1}$ and of the cathode side of a cell $La_2Ni_2O_3F_2$ against Pb/PbF_2 charged to 90 $mAhg^{-1}$ and subsequently discharged to 448 $mAhg^{-1}$. For full refinements, see Figure 6-16 in the appendix.

4.2.2.5 Investigation of side reactions

When comparing theoretical capacities for the extraction and intercalation of one fluoride ion to the obtained capacities of the reduction and oxidation experiments, it becomes apparent that side reactions are taking place, which do not affect the RP-type phases.

Grenier et al. [26] investigated the electrochemical stability of an electrolyte $La_{1-x}Ba_xF_{3-x}$ in its pure form and in a composite with carbon. It has been shown that the pure electrolyte starts to decompose at potentials beyond ~ 5 V vs. Li (~ 2.7 V vs. Pb/PbF_2), showing the large electrochemical window of the electrolyte. Potentials > 5 V are much higher than the used potentials in electrochemical fluorination experiments. The electrochemical activity of the carbon within a composite with the electrolyte was observed at lower potentials of ~ 4.2 to 4.8 V vs. Li (~ 1.9 to 2.5 V vs. Pb/PbF_2), which is related to an early onset of the irreversible fluorination of C leading to the formation of electronic insulating CF_x species and minor

degrees of electrolyte decomposition. This shows that the electrochemical window needs to be narrowed to avoid the carbon fluorination.

In order to differentiate, in which potential range the fluorination of the active material and/or the carbon additive occurs, cyclic voltammograms of cells $La_2NiO_3F_2$ vs. Pb/PbF_2 and $La_{0.9}Ba_{0.1}F_{2.9}$ + CB vs. Pb/PbF_2 were recorded (Figure 4-83). It should be emphasised that the used cathode composite, containing the active RP-type $La_2NiO_3F_2$, contains also $La_{0.9}Ba_{0.1}F_{2.9}$ and CB, while the cathode composite denoted as '$La_{0.9}Ba_{0.1}F_{2.9}$ + CB' is only comprised of $La_{0.9}Ba_{0.1}F_{2.9}$ and CB. It can be followed that a clear separation between the oxidation of the active material and the carbon additive is not possible. Moreover, in the cell $La_{0.9}Ba_{0.1}F_{2.9}$ + CB vs. Pb/PbF_2, the fluorination of carbon seems to be largely irreversible since no current is observed in the anodic branch, whereas a certain reversibility is found for the $La_2NiO_3F_2$ vs. Pb/PbF_2 cell. This suggests that the carbon fluorination is also irreversible in cells containing the active material. It has also to be taken into account that $La_2NiO_3F_2$ (or $La_2NiO_{4.13}$) used here in a composite with $La_{0.9}Ba_{0.1}F_{2.9}$ and CB could have an additional catalytic effect on the fluorination of carbon resulting in the formation of CF_x at lower potentials. [19] In comparison to the reported onset of carbon fluorination and electrolyte decomposition [26], reactions at lower potentials are observed in the electrode composite containing only $La_{0.9}Ba_{0.1}F_{2.9}$ and CB.

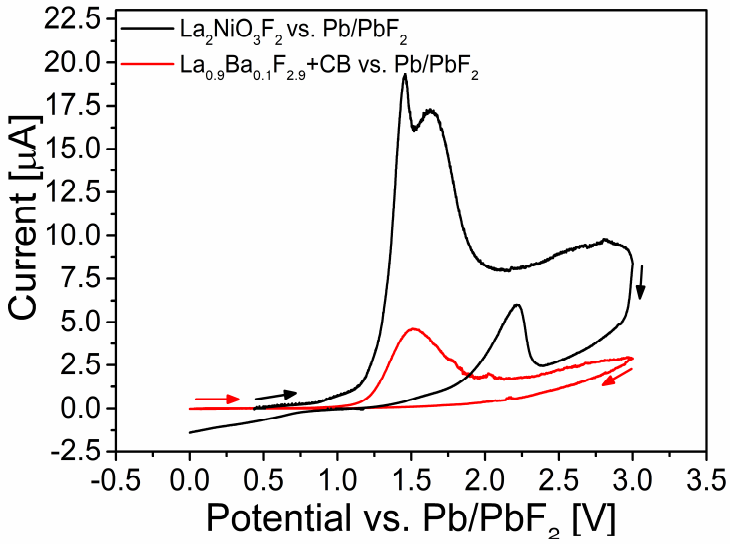

Figure 4-83: Cyclic voltammograms of cells $La_2NiO_3F_2$ against Pb/PbF_2 and $La_{0.9}Ba_{0.1}F_{2.9}$ + CB against Pb/PbF_2. A scan rate of 0.01 mVs^{-1} between 3 and 0 V starting from the OCV.

A possible reduction of the carbon additive, presumably due to a release of surface-adsorbed oxygen or via a reaction with La or Ba of the electrolyte $La_{0.9}Ba_{0.1}F_{2.9}$, could also cause side reactions alongside the actual reduction of the active material. A potential reduction involving a reaction between carbon and the electrolyte (simplified to the expression LaF_3) could be imagined to take place via the following reaction equation

$$C^{+0} + x\ La^{+3}F_3^{-1} \xrightarrow{+3x\cdot e^-} C^{-\frac{3}{x}}La_x^{+3} + 3\ F^-.$$

Different reaction mechanisms for this proposed reaction are conceivable. With respect to the size of La^{3+} (ionic radius of La^{3+}: 1.032 Å)[54], the intercalation of La^{3+} between the graphene layers of graphite-like carbon in carbon black might be possible since the interlayer spacing in

graphite is 3.35 Å [265]. As has been shown for other cations (e.g. Na^+, K^+ (ionic radii of Na^+: 1.02 Å and of K^+: 1.38 Å)[54]) [266, 267], such an intercalation of La^{3+} could be assumed to result in a staged intercalation. While the graphite lattice can host the larger K^+ ions up to a concentration of KC_8 [268], which corresponds to a capacity of ~ 279 $mAhg^{-1}$, only NaC_{64} [269] can be formed due to the intercalation of Na^+. This low Na^+ contents corresponds to a low capacity of ~ 35 $mAhg^{-1}$. This shows that not only the size of the cation, but also thermodynamic considerations have to be taken into account. [270, 271] In addition to this, stronger electrostatic interactions of the trivalent lanthanum cation in comparison to the monovalent alkali metal ions should have a strong influence on the feasibility of intercalation reactions. For example, Al^{3+} cannot be intercalated into graphite. [272] Therefore, more reasonably would be insertion into distorted parts and adsorption into pores of the carbon black particles or reactions at grain boundaries or defect sides. These could lead to an absorption and clustering of La^{3+} in pores and/or adsorption processes at the surfaces and defects, as it is also found for the sodiation of hard carbon. [273]

The presence of such side reactions becomes also evident on investigating the reduction of $La_2NiO_{4.13}$ within Pb/PbF_2 against $La_2NiO_{4.13}$ cells (Figure 4-84). Here, only the reduction to La_2NiO_4 (space group: *Bmeb*) [44], i.e., the reduction from Ni^{3+} to Ni^{2+}, is observed between ~ -0.3 and 0.3 V vs. $La_2NiO_{4.13}$ showing that interstitial oxide can be also deintercalated using the FIB set-up. No additional structural changes of the RP-type phase (Figure 4-84 b) occur when charging beyond a subsequent plateau (~ 0.6 to 1.5 V vs. $La_2NiO_{4.13}$). Since no further reduction of La_2NiO_4 to La_2NiO_{4-x}, i.e., the formation of Ni^+, can be observed, this also highlights the importance of the presence of interstitial oxide or fluoride anions, for the facilitation of the electrochemical reductions. In contrast to La_2NiO_4, $La_2NiO_3F_2$ is rich in interstitial anions making a reduction from Ni^{2+} to Ni^+ feasible. Moreover, the much higher cell potentials of > 0.6 V of cells Pb/PbF_2 vs. $La_2NiO_3F_2$, needed to access the reaction under the deintercalation of fluoride in comparison to the reduction of $La_2NiO_{4.13}$, point to the formation of low-valent Ni.

The observed plateau between ~ 0.6 to 1.5 V vs. $La_2NiO_{4.13}$, which is purely related to side reactions, coincides with the first plateau observed for the electrochemical reduction of $La_2NiO_3F_2$. This indicates that alongside the actual reduction of $La_2NiO_3F_2$ side reactions take place, which do not affect the RP-type phases further.

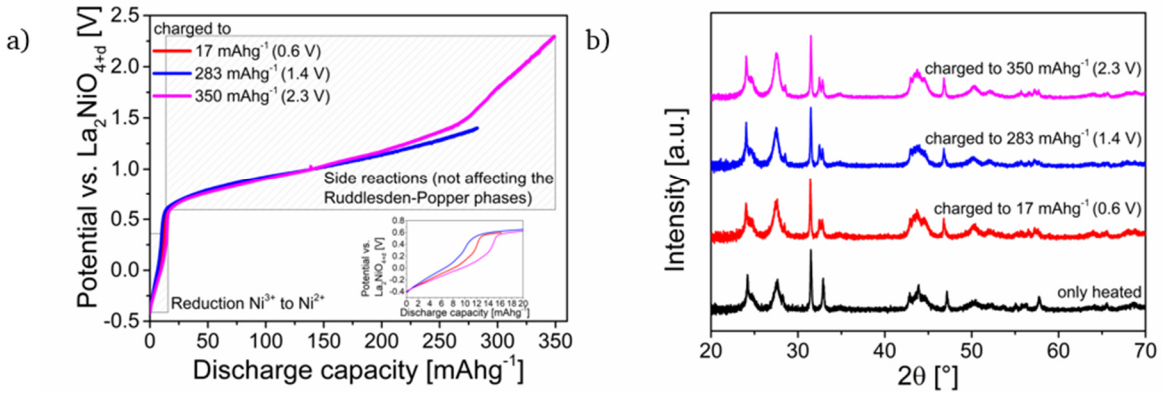

Figure 4-84: a) Charging curves of cells Pb/PbF_2 against $La_2NiO_{4.13}$ charged to of 17, 283 and 350 $mAhg^{-1}$; b) XRD diffraction patterns of the anode sides of different cells Pb/PbF_2 against $La_2NiO_{4.13}$ charged to 17, 283 and 350 $mAhg^{-1}$. For reference, a cell, which was only heated, is given. For the Rietveld refinements, see Figure 6-21 in the appendix.

Cyclic voltammograms of cells Pb/PbF_2 against $La_2NiO_3F_2$ and Pb/PbF_2 vs. $La_{0.9}Ba_{0.1}F_{2.9}$ + CB (Figure 4-85) confirm the findings obtained for the reduction of the $La_2NiO_{4.13}$. Again, the reduction of the CB in the cell Pb/PbF_2 vs. $La_{0.9}Ba_{0.1}F_{2.9}$ + CB seems to be widely overlapping with the electrochemical activity recorded for the cell Pb/PbF_2 against $La_2NiO_3F_2$ containing $La_2NiO_3F_2$ and CB. For both cells, no reversibility can be observed.

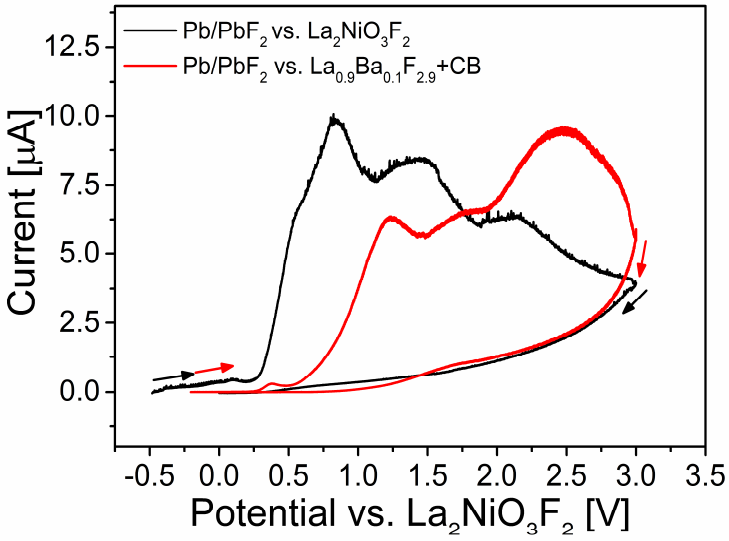

Figure 4-85: Cyclic voltammograms of cells Pb/PbF_2 against $La_2NiO_3F_2$ and Pb/PbF_2 against $La_{0.9}Ba_{0.1}F_{2.9}$ + CB.

Even though the separation of the electrochemical signals belonging to the fluorination or defluorination of $La_2NiO_3F_2$ and the oxidation or reduction of the carbon additive, respectively, is not possible, surface sensitive XPS measurements show clear changes of the carbon C *1s* signals, which are related to the oxidation and reduction of the carbon (Figure 4-86). The pristine anode composite possesses a C *1s* signal at ~ 284.4 eV, which is characteristic for carbon black. [207] The spectrum of the reduced anode composite features a shoulder at lower binding energies indicating a partial reduction of the carbon species. For the oxidized cathode composite, a shift of the main signal of ~ 0.5 eV towards higher binding energies suggests the oxidation of the carbon. This is also in accordance with previous findings made when electrochemically fluorinating $La_2NiO_{4.13}$. [19]

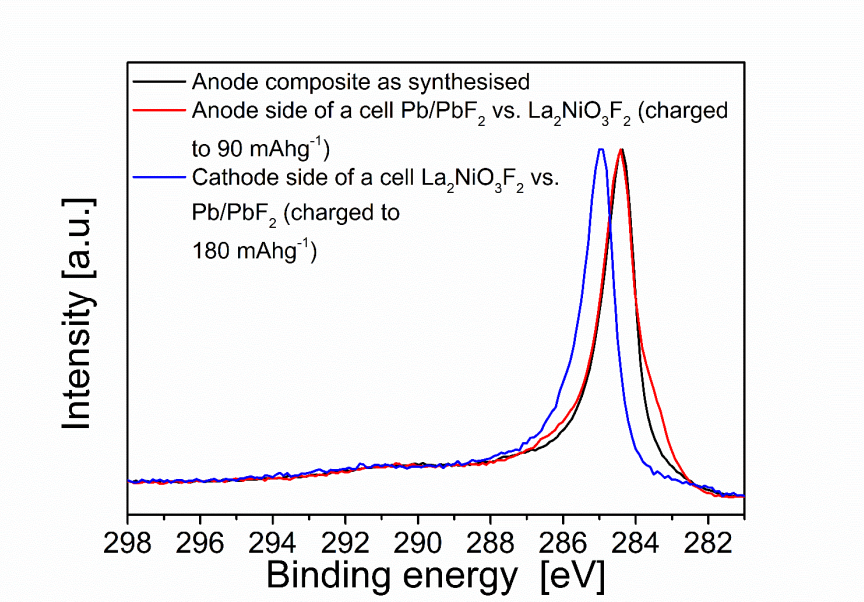

Figure 4-86: C 1*s* XPS spectra of the anode composite containing $La_2NiO_3F_2$ after milling, of the anode side of a cell Pb/PbF_2 against $La_2NiO_3F_2$ charged to 90 $mAhg^{-1}$ and of the cathode side of a cell $La_2NiO_3F_2$ against Pb/PbF_2 charged to 180 $mAhg^{-1}$.

4.2.2.6 Cycling of cells containing $La_2NiO_3F_2$-based electrodes

Since the structural reversibility of the charged $La_2NiO_3F_{2+x}$ is observed within the positive potential range upon discharging when using $La_2NiO_3F_2$ as active cathode material (see 4.2.2.2.2), the application of it in a reversible FIB might be possible. To address the cycling performance on extended cycling, cells $La_2NiO_3F_2$ vs. Pb/PbF_2 were cycled between different charging cut-off capacities of 30, 60 and 90 $mAhg^{-1}$ and subsequently discharged to 0 V against Pb/PbF_2. The cycling curves are given in Figure 4-87 a-c. As has been also found for the reversible cycling of $La_2NiO_{4.13}$ vs. M/MF_2 with M = Pb, Zn [19], the choice of suitable charging cut-off capacities plays herein an important role. The best charging behaviour is found for low charging capacities of 30 $mAhg^{-1}$, while the cells with higher charging capacities fail significantly faster. This becomes apparent when comparing the charging capacities needed to reach the second charging plateau at potentials above 2 V of the cycled cells and of the cell that was only charged once (see section 4.2.2.2). The early onset of the second plateau at such low capacities after a few cycles could show that considerable amounts of the cathode composite containing the electrochemically active $La_2NiO_3F_2$ peel-off, possibly due to larger volume changes related to higher charging states. A major role could also play side reactions, which lead to the increasing formation of diffusion barriers for fluoride ions and electrons at the interface between the active material and carbon black. These barriers hinder the reversible intercalation of fluoride ions into the RP-type phases via the ionically conductive electrolyte due to progressive deterioration of the carbon matrix within the composite, which is needed to ensure sufficient electron conduction for the occurring redox reactions, resulting in higher over-potentials in consecutive cycles during charging. On the other hand, these barriers may result in a stable interface between the active material and carbon black, as soon as the fluoride ion incorporation into the carbon additive, resulting in the increasing formation of insulating CF_x species [19], is effectively suppressed. The formation of these CF_x species seems to take place largely simultaneously with the fluorination of the RP-type phase and becomes more dominant at higher capacities, which impedes the long-term cycling performance. Interestingly, increasing over-potentials are only observed during

charging, indicating that the destruction of the carbon matrix impedes only the intercalation of fluoride, while the re-defluorination process seems to be widely unaffected. For cells only charged to the cut-off capacity of 30 $mAhg^{-1}$, the side reactions seem to be less pronounced, leading to a longer cyclability over at least 50 cycles. This is further confirmed by the Coulombic efficiencies (Figure 4-87 d), which give information about the extent of irreversible side reactions. Even though the efficiencies are relatively low for the cells charged to 30 $mAhg^{-1}$, the cells charged to 60 and 90 $mAhg^{-1}$ possess significantly lower efficiencies. This suggests that more side reactions are taking place within these cells. Interestingly, the Coulombic efficiencies increase for all cells for increasing cycle numbers before they fail. Especially for the cell charged to 30 $mAhg^{-1}$, a significant increase of the efficiency of ~ 36 % over the first 50 cycles can be observed.

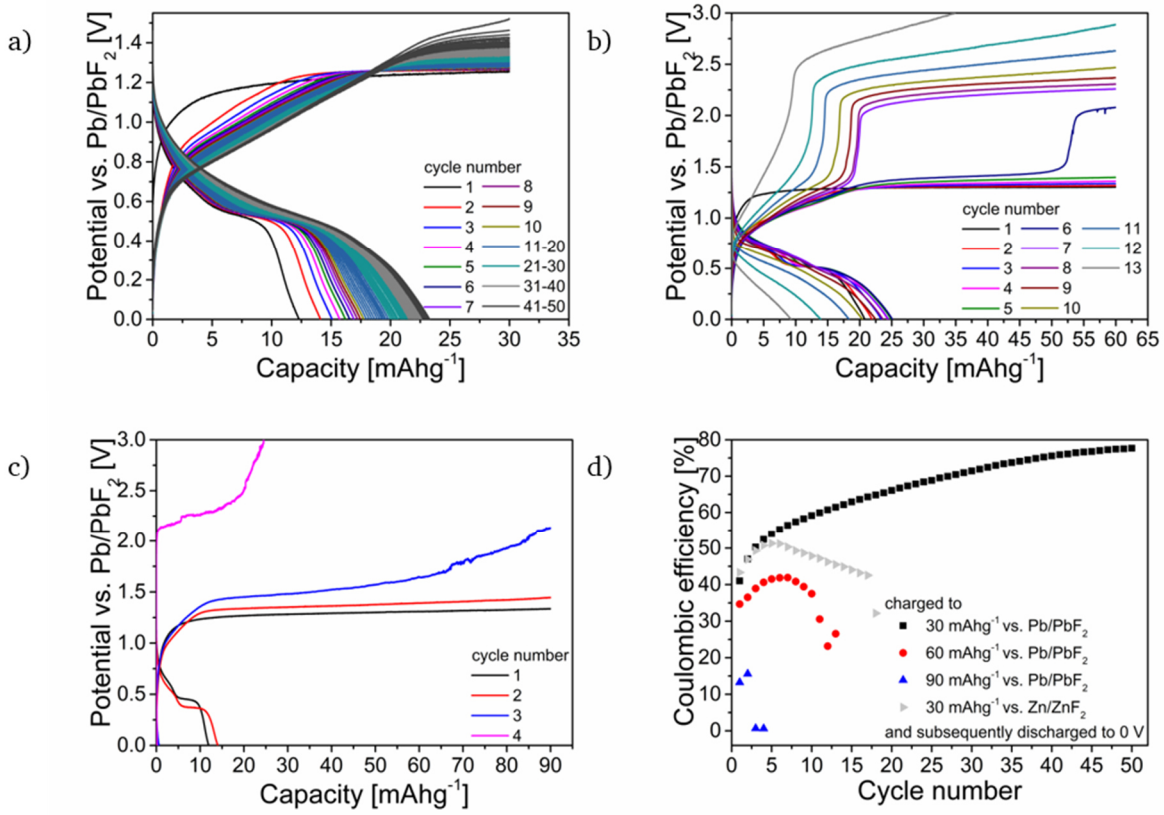

Figure 4-87: Cycling curves of cells $La_2NiO_3F_2$ against Pb/PbF_2 cycled between the charging cut-off capacity 30 $mAhg^{-1}$ (a), 60 $mAhg^{-1}$ (b) and 90 $mAhg^{-1}$ (c) and the discharging cut-off voltage 0 V. Coulombic efficiencies of cells (c) are additionally given. For comparison, the Coulombic efficiencies of a cell $La_2NiO_3F_2$ against Zn/ZnF_2 cycled between the charging cut-off capacities of 30 $mAhg^{-1}$ and the discharging cut-off voltage of 0 V is given.

It has been also shown that the use of Zn/ZnF_2 as counter electrode can improve the cycling performance of intercalation-based RP-type cathode materials, e.g. La_2CoO_4 or $La_2NiO_{4.13}$. [19, 29] When, however, charging $La_2NiO_3F_2$ against Zn/ZnF_2 instead of Pb/PbF_2 considerably worse cycling performances are obtained with increasing over-potentials and significant capacity fading after the fifth cycle (Figure 4-87 d). The cycling curves and the Rietveld refinement of a cell $La_2NiO_3F_2$ against Zn/ZnF_2 can be found in Figure 6-22. This increase in over-potentials might be related to the lower redox potential of $Zn|ZnF_2$ compared to $Pb|PbF_2$ (see Figure 4-56), leading to higher potentials needed to oxidise the RP-type phases and a potentially stronger carbon fluorination at lower potentials or an increased overlapping with the desired fluorinated reaction of the RP-type phases. The fluorinated carbon could then cause a

progressive increase of the over-potentials due to the decreasing electronic conductivity within the cathode composite.

To investigate structural changes of cells cycled between the cut-off conditions of 30 $mAhg^{-1}$ and 0 V with respect to the cycle number, cells were cycled for various cycle numbers. Additionally, some cells were cycled over several cycles followed by a charging step to analyse the charged state after several cycles (Figure 4-88). In accordance with section 4.2.2.2, after the first charging to 30 $mAhg^{-1}$, no significant structural changes are observed (see Figure 6-23). For higher cycle numbers, cells in the charged state show considerable amounts of the fluorinated monoclinic #2 and orthorhombic #3 phases (Figure 4-89). This indicates that substantial fluorination is only obtained after a few cycles. The reversible formation of the orthorhombic #3 phase, which seems to have a smaller fluoride content than the monoclinic #2 phase becomes more dominant for higher cycle numbers within the first 10 cycles. This is in contrast to the cells, which were only charged once (see section 4.2.2.2), in which the monoclinic #2 phase is dominating. Diffraction data of cells in their charged state, which were cycled for more than 10 cycles, would be a useful addition at this point to see which of the fluorinated phases is formed at higher cycle numbers. These cells could, however, not be prepared due to time limitations.

The discharged state of cycled cells could, on the other hand, also be investigated for higher cycle number (Figure 4-88 and Figure 4-89). For low cycle numbers (at least in the first ten cycles), the starting phase orthorhombic #1 is regained and the fluorinated monoclinic #2 and orthorhombic #3 phases disappear. The overall intensity of the reflections of the RP-type phases decreases, however, compared to the intensity of the reflection of the unaffected electrolyte $La_{0.9}Ba_{0.1}F_{2.9}$ for higher cycle numbers. This suggests that the structural changes in the RP-type phases are not fully reversible after prolonged cycling and the cycling results in partial decomposition and amorphisation. Moreover, after cycling over 20 and 50 cycles, an additional intermediate phase is found besides the orthorhombic #1 phase in the discharged state of the cell. This phase exhibits a unit cell volume slightly higher than the volume of the orthorhombic #1 phase, which confirms that major fractions of the intercalated fluoride ions present in the fluorinated phases after charging can be extracted upon discharging. However, a complete defluorination under the re-formation of the orthorhombic #1 phase seems to be impossible after extended cycling, potentially related to the introduction of significant disorder in the anion sublattice. Additionally, the phase fraction and the unit cell volume of the intermediate phase is found to increase between the 20^{th} and the 50^{th} cycle significantly. This likely indicates that more fluoride ions are trapped within the host lattice of the intermediate phase for higher cycle numbers and/or that the effect of disorder becomes more pronounced.

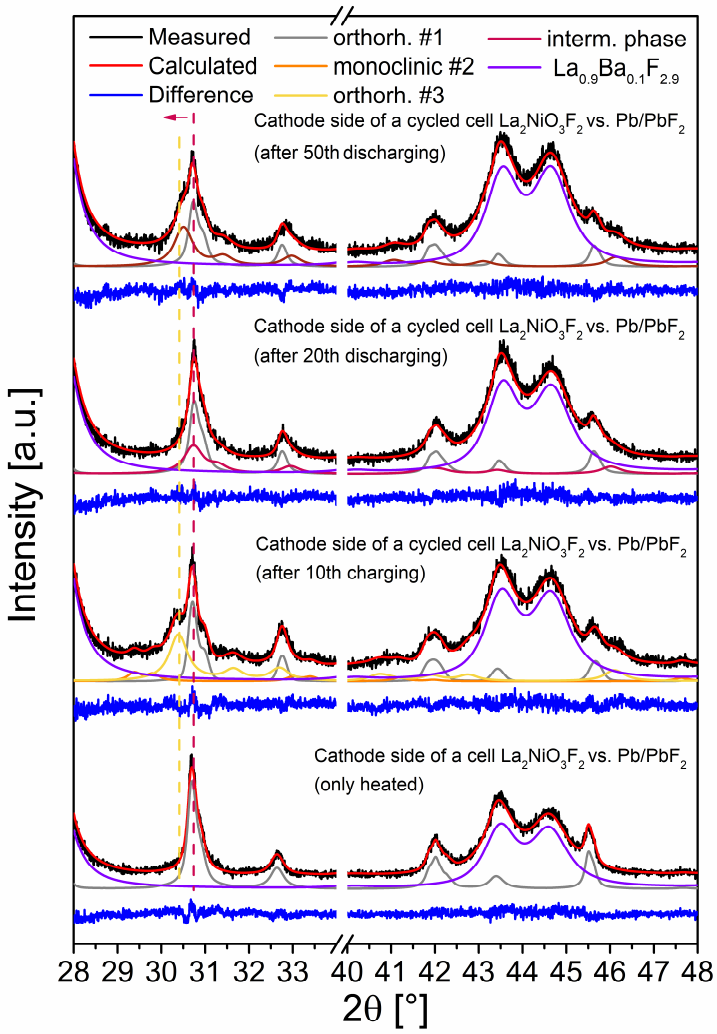

Figure 4-88: Comparison of Rietveld refinements of XRD data of cathode sides of a cell $La_2NiO_3F_2$ against Pb/PbF_2 heated to 170 °C for 72 h (discharged state) and of cycled cells $La_2NiO_3F_2$ against Pb/PbF_2 after the 10th charging (charged state), after the 20th discharging (discharged state) and after the 50th discharging (discharged state). For full refinements, see Figure 6-23 in the appendix.

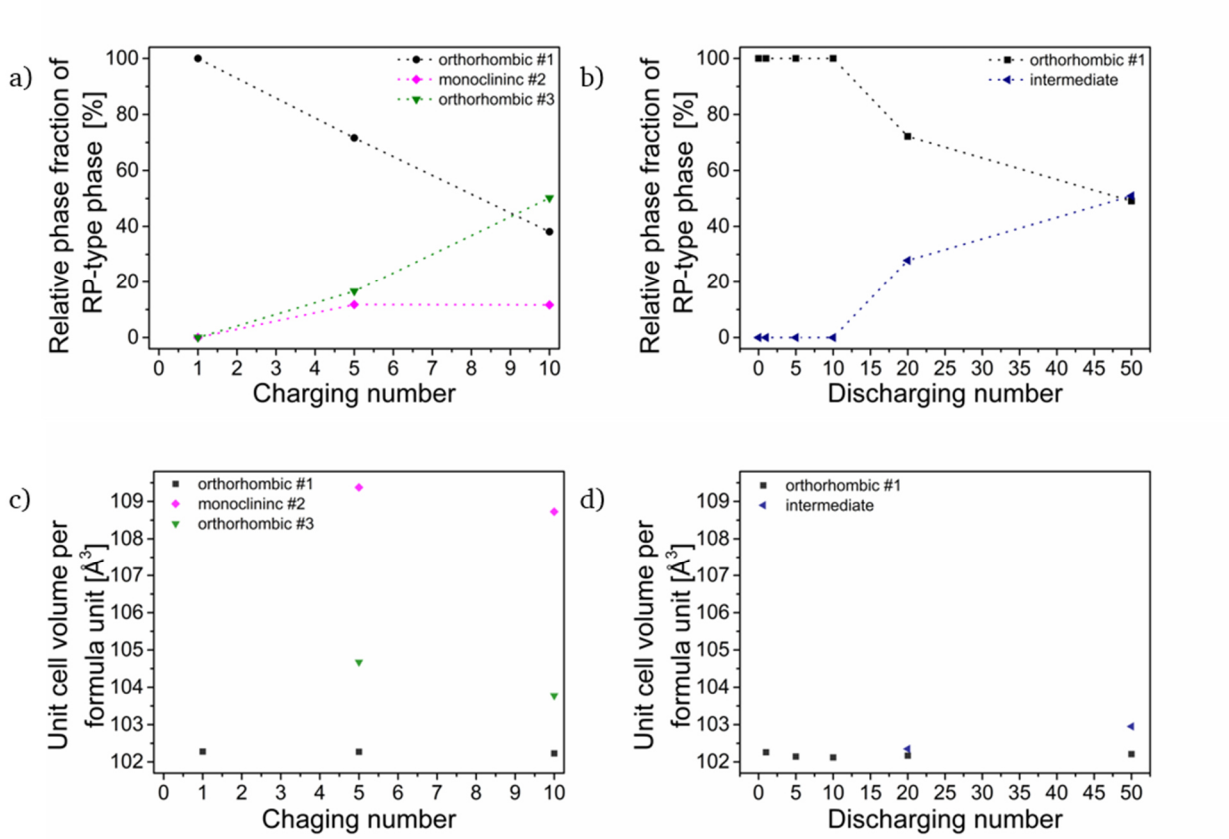

Figure 4-89: Relative phase fractions of RP-type orthorhombic #1, monoclinic #2 and orthorhombic #3 phases as well as an intermediate phase in the cathode sides of cells $La_2NiO_3F_2$ against Pb/PbF_2 cycled for various cycle numbers between the charging cut-off capacity 90 $mAhg^{-1}$ and the discharging cut-off potential 0 V. The fractions of cathode sides of cells within the charged (a) and discharged (b) state and the volumes within the charged (c) and discharged (d) state are shown. For the calculation of the relative phase fractions of the RP-type phases , the phase fraction of $La_{0.9}Ba_{0.1}F_{2.9}$ was not taken into account. Lattice parameters are given in Figure 6-24 and Figure 6-25 in the appendix.

This shows that for high cycle numbers a cycling between the fluorinated orthorhombic #3 and monoclinic #2 phases formed during charging and the intermediate phase formed during discharging takes place. Interestingly, the Coulombic efficiencies of these higher cycle numbers increase significantly compared to the cycles, in which the fluorinated phases are completely re-defluorinated to the orthorhombic #1 phase. It can be concluded that the cyclability between the intermediate phase and the orthorhombic #3 and monoclinic #2 phases is significantly improved. This could be related to a higher degree of anion disorder in the intermediate phase and the correlated structural distortions in comparison to the orthorhombic #1 phase, which facilitates the fluoride intercalation during the subsequent charging. For the anion-ordered orthorhombic #1 phase with orthorhombic Cccm symmetry it was shown (see section 4.1.3.1.2) that anions (no differentiation is made between oxide and fluoride ions at the apical and interstitial sites here) occupy the 4*b* interstitial anion site in a channel-like manner, which is accompanied by a strong tilting of the NiO_4F_2 octahedra. An occupation of the vacant 4*a* site would be unfeasible, i.e., energetically unfavourable, due to the short distances to the apical anions. Within an energy scheme, this would be reflected in a higher site energy of the 4*a* interstitial site in comparison to the 4*b* site in the ordered $La_2NiO_3F_2$ (Figure 4-90). In partly disordered $La_2NiO_3F_2$, which could be formed upon repeated cycling between the fluorinated phases and the re-defluorinated phases, the site energies of the two interstitial sites approach each other, as the 4*b* site becomes less

favourable and the 4*a* site more favourable. This can only take place if the strong tilting observed in the ordered $La_2NiO_3F_2$ is less pronounced in the disordered state in order to make a filling of the previously unoccupied interstitial site by fluoride feasible, as is also observed for the highly fluorinated phases (see section 4.2.2.2.1 and 4.2.2.2.2). Strong structural anion movements related to the tilting of the octahedra upon repeated fluorination and complete re-defluorination are energetically costly. Therefore, cycling between the fluorinated and the intermediate phase are more efficient and a better cyclability can be found. Similar considerations concerning the site energies can be made for the defluorination of $La_2NiO_3F_2$. It should be mentioned that in such a disordered phase not only two distinctive energy levels of the interstitial sites are present, but rather a continuous distribution of energies. This is related to different local environments of the individual interstitial anions and vacancies. This could also explain the transition from a plateau-like to more sloping charging and discharging plateaus in the cycling curves (see Figure 4-88).

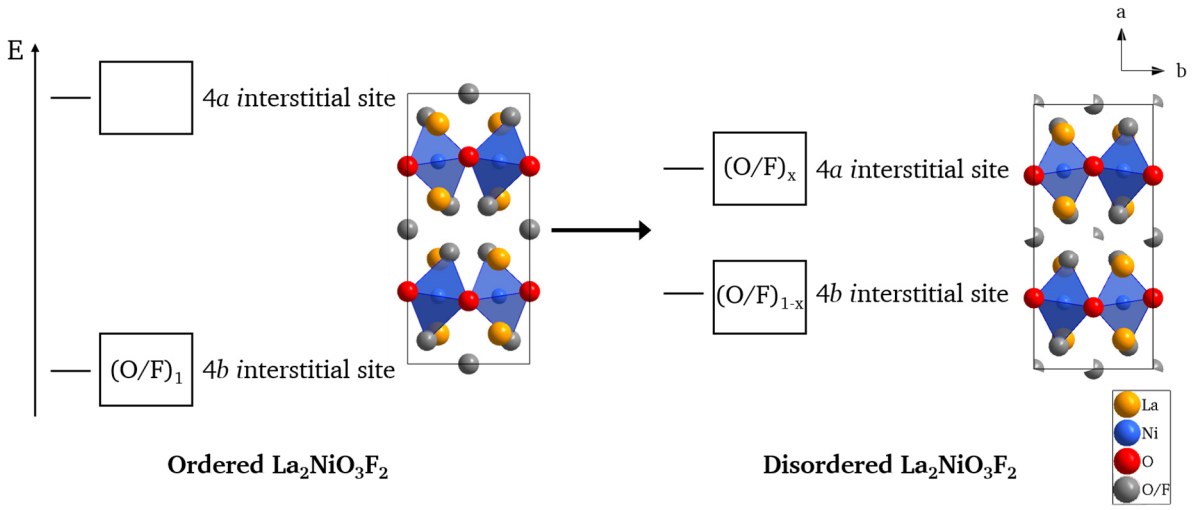

Figure 4-90: Illustration of energies of the 4a and 4b interstitial sites in ordered and disordered $La_2NiO_3F_2$.

A comparable influence of repeated charging and discharging, leading to the introduction of disorder in anion ordered compounds, can be ruled out for RP-type oxides or oxyfluorides with symmetries, which result in the presence of a single interstitial site. For example, in the study on the oxidative electrochemical fluorination of $La_2NiO_{4.13}$ to $La_2NiO_{4.13}F_y$, only phases with tetragonal *I*4/*mmm* or orthorhombic *Fmmm* symmetry have been observed. [19] In these phases, only one interstitial site with one specific energy is present, which is related to the absence of tilting of the NiO_6 octahedra (compare Figure 4-74 c). Therefore, all anions at the interstitial site have, in principle, the same energy.

When using $La_2NiO_3F_2$ as active anode material, the reversibility of the RP-type phases after charging is only observed after discharging to negative potentials (see section 4.2.2.3). Therefore, the application of this anode material in combination with a Pb/PbF_2-based cathode material is not feasible for the energy storage in FIBs. However, the FIB setup might be usable to evoke reversible property changes related to the structural changes observed upon charging and discharging of the cell. As for the cells $La_2NiO_3F_2$ vs. Pb/PbF_2, the cut-off conditions are of great importance for an extended cycling life. In analogy to the previously investigated cells, charging cut-off capacities of 30 and 60 $mAhg^{-1}$ were used. The choice of a suitable discharging cut-off condition is difficult. Based on the experiments conducted in section 4.2.2.3, the starting RP-type phases in the anode composite are regained after

discharging to ~ -1.1 V against $La_2NiO_3F_2$. It can, however, be expected that the over-potentials increase with each cycle. This would require to lower the discharging cut-off condition accordingly, in order to ensure that the end of the plateau related to the oxidation of the reduced RP-type phases is reached, though avoiding an additional oxidation to $La_2NiO_3F_{2+x}$. Especially, the latter point is difficult to achieve due to the small potential separation between the associated plateaus. Since an adjustment of the cut-off potential is not possible, a constant potential of - 1.15 V was chosen as cut-off criterion. Nevertheless, it should be emphasised that lower potentials seem reasonable with regards to the obtained results. The cycling curves for the first ten cycles are shown in Figure 4-91. Progressively increasing over-potentials, in particular during charging, are observed. When charging to the higher charging cut-off capacity of 60 $mAhg^{-1}$, larger increases in the over-potentials are found. For the cell charged to 30 $mAhg^{-1}$, only relatively small discharge capacities are found with almost no distinctive plateau visible within the first cycles. Even if ignoring the capacity related to fluorination reactions of carbon additive, which might also take place in this potential range during discharging, only a small capacity, which can be assigned to the re-fluorination of the RP-type phases obtained during charging, is observed. Therefore, it can be concluded that only a limited reduction of the RP-type phases occurs during charging in the first cycles. A considerable increase of the discharge capacities is, however, observed for higher cycle numbers. Similar to what is observed for the cells $La_2NiO_3F_2$ against Pb/PbF_2 charged to 30 $mAhg^{-1}$, this indicates that substantial defluorination during charging and the respective fluorination during discharging is only obtained after a few cycles, i.e., only after the anion disorder introduced in the starting material on the defluorination is increased cycle by cycle above a certain level, facilitating then the subsequent reduction. For the cell charged to 60 $mAhg^{-1}$, due to the increased reduction of the RP-type phases as a result of the higher charging cut-off capacity, the discharging capacities are higher starting from the first cycle and increase up to the third cycle, before fading significantly in the following cycles. This fading suggests that the reversible reduction and re-oxidation of the RP-type phases decrease. This can be assigned to the occurring side reactions, which should also take place increasingly during discharging. A strong interdependence between the decrease of the desired reactions involving the RP-type phases and the increase of side reactions is found. Since the Coulombic efficiencies are relatively low, especially for the cell charged to 60 $mAhg^{-1}$, irreversible side reactions seem to play a major role, destroying the conductive carbon matrix and leading to increasing over-potentials during charging. Interestingly, during discharging, the plateau does not seem to be shifted towards more negative potentials. It might, however, be possible that a full re-oxidation of the reduced RP-type phase obtained during charging is not achieved before the discharging is cut-off at -1.15 V, i.e., before the end of the re-oxidation plateau is reached. Since only a limited reduction of the RP-type phases can be achieved upon charging, it can be expected that the repeated charging causes at some point mainly side reactions, which in turn cause even higher over-potentials. Therefore, limiting the charging capacity further might be of a high relevance in order to limit the side reactions as much as possible. In addition, a lower discharging cut-off potential might be favourable. A detailed analysis of diffraction data of anode sides of cells in the charged and discharged state cycled for different cycle numbers would be clearly informative, was, however, not performed due to time restrictions and the fairly poor cycling performances observed in comparison to previously discussed cells, in which $La_2NiO_3F_2$ was used as active cathode material.

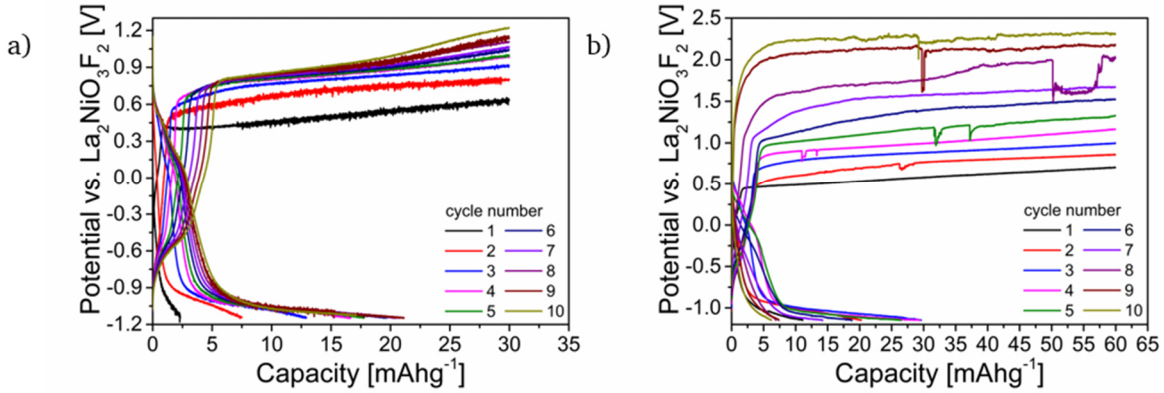

Figure 4-91: Cycling curves of cells Pb/PbF_2 against $La_2NiO_3F_2$ cycled between the charging cut-off capacity 30 $mAhg^{-1}$ (a) and 60 $mAhg^{-1}$ (b) and the discharging cut-off voltage -1.15 V

The use of intercalation-based electrodes, e.g. a La_2NiO_{4+d}-containing cathode composite and a $La_2NiO_3F_2$-containg anode composite, might result in high energy densities due to the comparatively high cell potential of such a FIB cell (compare Figure 4-56). First attempts to cycle cells La_2NiO_{4+d} against $La_2NiO_3F_2$ were performed. As it is discussed above, the side reactions, occurring in both electrode composites, could limit the cycling performance substantially, especially since the side reactions would potentially take place before or simultaneously with the desired reactions involving the RP-type phases. The charging cut-off capacity was chosen to be 30 $mAhg^{-1}$. The discharging cut-off condition was selected based on preliminary discharging experiments (see Figure 6-26 and Figure 6-27). For potentials below ~ -1.7 V against $La_2NiO_3F_2$, it is found that the substantial additional fluorination of $La_2NiO_3F_2$ to $La_2NiO_3F_{2+x}$ and reduction of La_2NiO_{4+d} to La_2NiO_4 take place. Therefore, a discharging cut-off potential of -1.6 V was used. It should, however, be mentioned that a higher potential (e.g. ~ -1.1 V) might be also suitable. When using this higher cut-off potential, the second discharging plateau observed in the first cycle (Figure 4-92), potentially already related to the additional fluorination of $La_2NiO_3F_2$ and reduction of La_2NiO_{4+d}, would also not be obtained. The structural changes taking place in this capacity range, especially within the first cycle, are, however, very subtle and additional experiments need to be conducted to determine the optimal cut-off potential.

Nevertheless, when cycling a cell La_2NiO_{4+d} against $La_2NiO_3F_2$ between 30 $mAhg^{-1}$ and -1.6 V, a comparatively good cycling performance is found over at least 40 cycles. Even though higher over-potentials between the charging and discharging plateaus are observed compared to cells La_2NiO_{4+d} against Pb/PbF_2 [19], continuously increasing Coulombic efficiencies are obtained. For the use of cells La_2NiO_{4+d} against $La_2NiO_3F_2$ for effective reversible energy storage, these high over-potentials, allowing only for substantial discharging in the negative potential range, are detrimental and a significant reduction of the over-potentials is required. For cells La_2NiO_{4+d} against Pb/PbF_2 [19], on the other hand, the discharging has been found to take place in the positive potential range. This shows that the use of the intercalation-based $La_2NiO_3F_2$ anode composite instead of the conversion-based Pb/PbF_2 has a significant influence on the observed over-potentials. The exact origin and nature of these over-potentials are not known yet. However, in comparison to cells Pb/PbF_2 against $La_2NiO_3F_2$, a significantly better performance with an overall lower increase of the over-potentials after 40 cycles and comparatively good efficiencies is observed. This could be related to the fact that the major discharging takes place at higher potentials compared to the Pb/PbF_2 against $La_2NiO_3F_2$ cells,

suggesting fewer side reactions, leading to the destruction of the carbon matrix. Therefore, it can be concluded that a higher degree of the desired redox reactions involving the PR-type phases is found. This demonstrates the strengths and weaknesses of FIBs purely made from intercalation-based electrode materials.

If the discharging below ~ -1.1 V leads actually already to the additional fluorination of $La_2NiO_3F_2$ and reduction of La_2NiO_{4+d}, this might explain the additional charging plateau between ~ 0.2 and 0.6 V, most distinctly pronounced in the second cycle, since it could be related to the re-reduction of $La_2NiO_3F_{2+x}$ and partial fluorination of La_2NiO_4. Further investigations are clearly required to relate the observed plateaus to the respective redox reactions involving the RP-type phases. Furthermore, the absence of the second discharging plateau after the first cycle, while the charging plateau between ~ 0.2 and 0.6 V is still present for charging numbers equal or larger than 3, needs to be addressed.

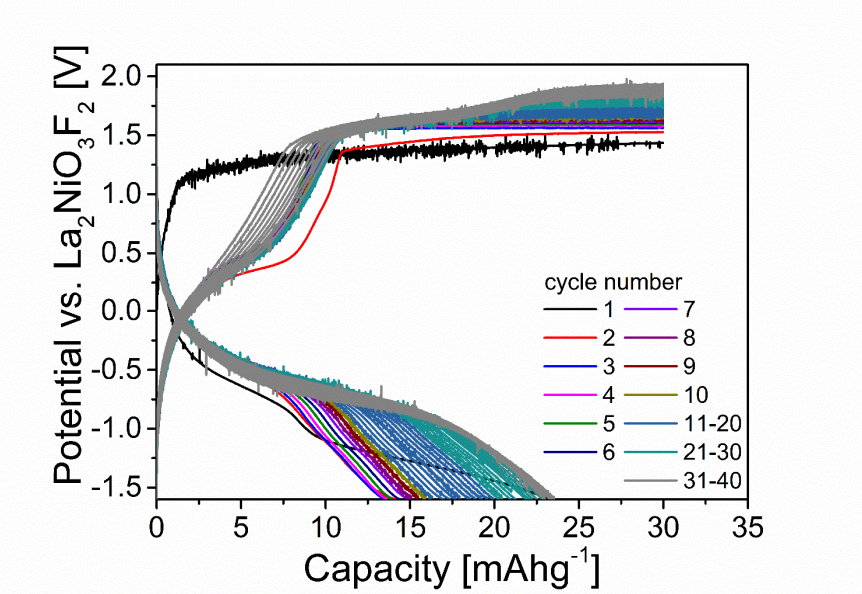

Figure 4-92: Cycling curves of cells La_2NiO_{4+d} against $La_2NiO_3F_2$ cycled for 40 cycles between the charging cut-off capacity 30 $mAhg^{-1}$ and the discharging cut-off voltage -1.6 V

4.2.2.7 A critical assessment of magnetisation studies on electrochemically obtained $La_2NiO_2F_{2-x}$ and $La_2NiO_2F_{2+x}$ phases

Reversible electrochemical reactions as observed for $La_2NiO_3F_2$ should also result in the change of magnetic properties and a switching between distinctive magnetic states of the obtained phases should be possible. Such a switching between the magnetic states of $La_2NiO_3F_2$ and $La_2NiO_3F_{2-x}$ or of $La_2NiO_3F_2$ and $La_2NiO_3F_{2+x}$, are certainly conceivable. For example, the reversible electrochemical defluorination and re-fluorination of $La_2NiO_3F_2$ and $La_2NiO_3F_{2-x}$, respectively, should allow for a switching between the antiferromagnetic state of $La_2NiO_3F_{2-x}$ and the paramagnetic state of $La_2NiO_3F_2$, since $La_2NiO_3F_2$ orders antiferromagnetically at lower temperatures compared to $La_2NiO_3F_{2-x}$ (see section 4.1.3.4). For a temperature below the transition temperature of $La_2NiO_3F_2$, a switching between the antiferromagnetic states of $La_2NiO_3F_2$ and $La_2NiO_3F_{2-x}$ might be potentially observed. For $La_2NiO_3F_{2+x}$, depending on its magnetic behaviour, similar switching processes could be possible. Since only phase transitions between paramagnetic and/or antiferromagnetic states occur, the correlated magnetisation changes can be expected to be small for all considered

cases, especially when phase mixtures of two (or more) RP-type phases in addition to large phase fractions of the electrolyte are present in the electrodes of the cells.

In order to asses, which magnetic transitions occur at which temperature, the intrinsic magnetic properties of these phase have to be known. The magnetic behaviours of $La_2NiO_3F_2$ and $La_2NiO_3F_{2-x}$ are discussed in section 4.1.3.4. For these samples, detailed analyses were possible based on SQUID and/or neutron diffraction measurements. The possibility to synthesise the reduced RP-type phase via the proposed topochemical defluorination method enables its analysis. The found magnetic characteristics should be transferrable to the phases present within the cell after the galvanostatic charging. It is, however, not possible to synthesise $La_2NiO_3F_{2+x}$ by any method other than the used electrochemical approach and even then contains the scratched-off electrode composite several RP-type phases, which order potentially magnetically, and only small sample amounts of 2 to 3 mg can be obtained. Nevertheless, it was attempted to investigate the magnetic properties of $La_2NiO_3F_{2+x}$ via a M(T) measurement of a scratched-off cathode side of a charged cell $La_2NiO_3F_2$ vs. Pb/PbF_2 (Figure 4-93). The Rietveld analysis of the cathode side on the intact pellet reveals relative phase fractions of the RP-type phases of $\sim$ 90 % of the oxidized monoclinic #2 phase and $\sim$ 10 % of $La_2NiO_3F_2$. In addition to the RP-type phases, a large part of the sample consists of diamagnetic $La_{0.9}Ba_{0.1}F_{2.9}$ and CB. Their contributions to the magnetisation were subtracted from the measurements. [206] The divergence between the ZFC and FC curves indicate that a weak antiferromagnetic transition takes place. Above $\sim$ 56 K, a paramagnetic behaviour is found for both measurements. The increase of the magnetisation at lower temperatures suggests the contribution of a weak ferromagnetic component. The presence of this ferromagnetic component could be confirmed by a field-dependent measurement at 10 K, showing a weak hysteresis. A Curie-Weiss fit (Figure 6-28) in the paramagnetic temperature range from 150 to 250 K of the FC measurement (the ZFC measurements show unfortunately a few jumps of the measurement data in this temperature range) reveals a magnetic moment of $\sim$ 2.79 μ_B per Ni ion. This moment corresponds to approximately two unpaired electrons. This would, however, suggests that the spin-only moment of the RP-type phases within the cathode materials has not changed significantly after charging in comparison to the starting RP-type phase $La_2NiO_3F_2$.

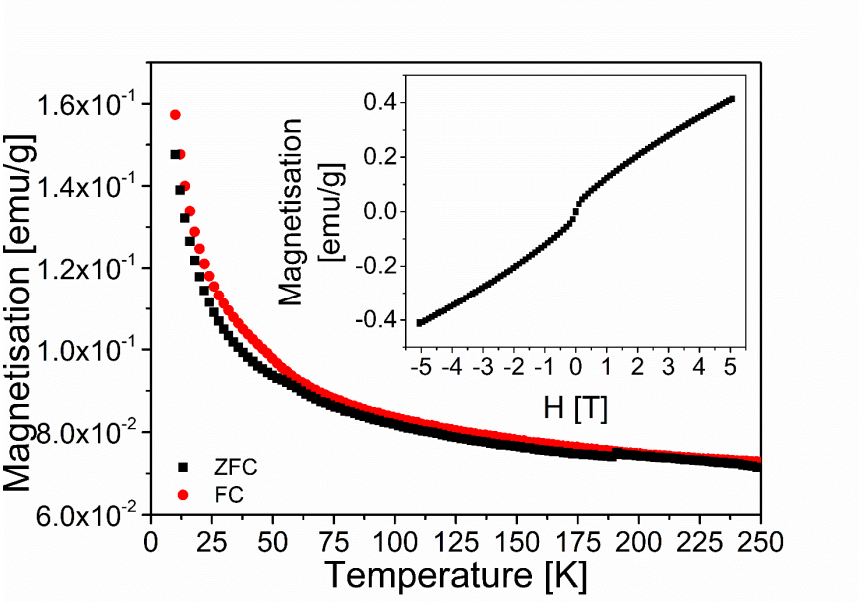

Figure 4-93: ZFC and FC M(T) curves of a charged and scratched-off cathode side of a charged cell $La_2NiO_3F_2$ vs. Pb/PbF_2 containing a large relative phase fraction of the monoclinic #2 phase. The inset shows the M(H) curve measured at 10 K.

For the residual $La_2NiO_3F_2$ within the cathode, no significant changes of the magnetic properties compared to the measurements on pure $La_2NiO_3F_2$ are expected. The M(T) curve of pure $La_2NiO_3F_2$ (Figure 4-21) shows, in principle, a similar behaviour, but with a much stronger change in magnetisation above and below the Néel temperature, which could be related to the much higher phase fraction of the phase in the pure sample. This suggests that the measured transition is related to $La_2NiO_3F_2$. Moreover, the small shift of the transition temperature towards slightly higher temperatures in comparison to the measured transition temperature of pure $La_2NiO_3F_2$ at ~ 49 K indicates changes within the RP-type phases. To what extent the transition temperature of the starting phase is changed due to the electrochemical treatment, which also causes smaller compositional changes, is difficult to determine and additional experiments would be required.

Considering the higher phase fraction of $La_2NiO_3F_{2+x}$ in the cathode composite, $La_2NiO_3F_{2+x}$ should have a considerable contribution to the magnetisation. Assuming that a complete additional fluorination of $La_2NiO_3F_2$ to $La_2NiO_3F_3$ takes place upon charging of cells $La_2NiO_3F_2$ vs. Pb/PbF_2, the d^7 electron configuration of Ni^{3+} indicates an antiferromagnetic ordering between the magnetic moments of the Ni ions below a certain transition temperature T_N. Depending on the spin state of Ni^{3+}, either one (low-spin configuration) or three (high-spin configuration) unpaired electrons can be expected. For the low-spin configuration, a Jahn-Teller distortion would be additionally expected. However, the superexchange interactions might be reduced due the strongly increased distance between the perovskite-type building blocks, caused by the intercalation of additional fluoride ions in comparison to $La_2NiO_3F_2$, which might even inhibit a three-dimensional ordering completely. [23-25] It becomes evident that, as long as the magnetic properties of $La_2NiO_3F_{2+x}$ are not fully understood, an unambiguous assignment of the found antiferromagnetic transition to one of the contained RP-type phases is not possible, even though there are strong evidence for a predominant contribution from the residual $La_2NiO_3F_2$.

In addition, a comparison between the XRD pattern of the scratched-off cathode side after the SQUID measurement to the pattern of the intact pellet (Figure 6-29) shows the appearance of additional reflections with relative high intensities, suggesting the presence of a relative large phase fraction of an additional phase. This could suggest that a partial decomposition takes place either during the scratching-off of the cathode side or the SQUID measurement. As this phase could have a significant influence on the measured M(T) curve, its origin should be discussed. This phase is presumably $La_{0.5}Zr_{0.5}O_{1.75}$, which has been also found in very small phase fractions (< 0.5 wt%) in other samples through this work (for example, in chemically fluorinated $La_2NiO_3F_{2+x}$ (see Figure 4-72)). It is assumed that it is formed during the ball milling process applied for the mixing of the precursor oxides for the synthesis of the RP-type oxides. Over time, abrasion of ZrO_2 from the used ball milling vial and balls could be observed, resulting in the introduction of ZrO_2 into the precursor mixture, leading finally to the marginal formation of $La_{0.5}Zr_{0.5}O_{1.75}$ upon sintering. The formation of this phase during the scratching-off or the SQUID measurement, even if a partial decomposition takes place, can be ruled out. The relatively high phase fraction of $La_{0.5}Zr_{0.5}O_{1.75}$ found within the scratched-off powder after the SQUID measurement is instead most probably related to the small sample amount (~ 3 mg) and the resulting poor particle statistics of the XRD measurement. In addition, the relative phase fractions of the RP-type phases and the electrolyte found suggest that no major decomposition or amorphisation took place.

This shows that the changes of magnetic properties due to electrochemical fluoride deintercalation or intercalation from or into $La_2NiO_3F_2$ within FIBs are difficult to determine based on SQUID measurements only. These changes could be only observed if strong alterations of the magnetisation due to strong changes of the magnetic moments of the investigated RP-type phases would occur. Chemical approaches to obtain the same topochemical modifications, allowing the analysis of phase pure samples using other characterisation techniques, are indispensable. The absolute change in magnetisation is limited by the type of magnetic transitions observed in the investigated RP-type phases. In addition, the small phase fractions of the RP-type phases in comparison to the phase fraction of the diamagnetic electrolyte results in small changes of the magnetisation. With respect to potential technological applications, higher absolute changes of the magnetisation are clearly required and, therefore, reversible magnetic tuning is discussed in section 4.2.3 based on a ferromagnetic RP-type oxides, which shows a considerably reduced magnetisation due to the formation of antiferromagnetic or paramagnetic fluorinated phases upon electrochemical fluorination within a FIB.

4.2.2.8 Summary

The topochemical modification of $La_2NiO_3F_2$ can be achieved via electrochemical reactions in FIBs when using $La_2NiO_3F_2$ as active material in intercalation-based electrode composites. It is shown that the reduction to $La_2NiO_3F_{2-x}$, which contains Ni^+, as well as the post-oxidation to $La_2NiO_3F_{2+x}$, which contains Ni^{3+}, is possible. The successful defluorination using electrochemical approaches was demonstrated for the first time. This is facilitated by the high stability of the solid electrolyte $La_{0.9}Ba_{0.1}F_{2.9}$ used in FIBs. Several reduced and oxidised RP-type phases can be identified. Charging and discharging state-dependent studies reveal the appearance of these new phases and the occurring structural changes.

The electrochemical defluorination upon galvanostatic charging when using $La_2NiO_3F_2$ as active anode material in cells Pb/PbF_2 vs. $La_2NiO_3F_2$ results in the partial formation of a

reduced phase with a similar monoclinic distortion and lattice parameters as found when reducing $La_2NiO_3F_2$ in a hydride-based defluorination reaction according to $La_2NiO_3F_2 + x\,NaH$ with $x = 0.25$. In addition, less strongly reduced phases, undergoing comparatively small structural changes compared to the starting RP-type phases and retaining their symmetry (space group: *Cccm*), are found, suggesting a minor degree of defluorination. It can be assumed that the similar structural changes of the monoclinic phases (space group: *C*12/*c*1) obtained via both topochemical modification routes are related to similar degrees of defluorination. As is determined via the coupled Rietveld analysis of the chemically reduced phase, an approximate composition of $La_2NiO_3F_{1.9}$ can be expected for the electrochemically reduced phase. Therefore, it can be concluded that the reduction of $La_2NiO_3F_2$ via galvanostatic charging causes a partial defluorination of a fraction of the RP-type phases within the anode composite. A stronger reduction could not be obtained when charging to higher potentials/capacities. The investigation of the Ni oxidation state by means of X-ray absorption spectroscopy confirms this partial reduction.

The use of $La_2NiO_3F_2$ as active cathode material in cells $La_2NiO_3F_2$ vs. Pb/PbF_2 results in the formation of differently strong oxidised phases upon charging. The strongest oxidised phase undergoes a large volume expansion of ~ 7 Å³ due to an increase of the *a* lattice parameter. This strong increase of *a* indicates that a significant change of the anion sublattice occurs, which is most likely due to the filling of the vacant interstitial site, present in $La_2NiO_3F_2$, by fluoride leading to the formation of $La_2NiO_3F_{2+x}$. This filling leads also to a symmetry reduction to *C*12/*c*1. Moreover, significant phase fractions of the relatively unchanged starting RP-type phase and of a less strongly oxidised orthorhombic phase with a unit cell volume between that of the starting RP-type phase and the highly oxidised phases are found. To investigate the crystal structure of the highly oxidised monoclinic phase by an independent approach, automated diffraction tomography was used, confirming the proposed crystal structure. The findings made by means of the used diffraction methods suggest a composition of the highly oxidised phase of approximately $La_2NiO_3F_3$. This phase could be prepared chemically only in a limited phase fraction via a highly oxidising F_2 gas oxidation approach. The electrochemical fluorination leads to significantly higher phase fractions of $La_2NiO_3F_{2+x}$ by a factor of ~ 7. This highlights the potential of electrochemical routes as alternatives for topochemical modifications, which are exceedingly difficult to obtain using chemical routes.

The structural reversibility of the reduced and oxidised phases on re-fluorination and re-reduction is also demonstrated. Furthermore, continued discharging to potentials lower than the potentials needed for the re-fluorination and re-defluorination leads to the formation of the respective additionally fluorinated or defluorinated phases from the re-fluorinated or re-defluorinated phases. Especially when re-fluorinating the pre-reduced RP-type phases, the continued fluorination leads to the formation of higher phase fractions of $La_2NiO_3F_{2+x}$, compared to the direct electrochemical fluorination of $La_2NiO_3F_2$. This highlights the influence of the synthesis strategy with a potential role of the introduction of anion disorder on the resulting products.

The fact that the charging and discharging capacities are observed, which are well beyond the theoretical capacities related to the intercalation and deintercalation of one fluoride ion into/from $La_2NiO_3F_2$, shows that undesired side reactions are taking place. Since these side reactions seem not to affect the RP-type phases, reactions related to the conductive oxidation or reduction carbon additive and/or the electrolyte $La_{0.9}Ba_{0.1}F_{2.9}$ used could explain the

observed large capacities. By means of cyclic voltammography it was found that these reactions are mostly irreversible and occur largely simultaneously with the desired reactions involving the RP-type phases. X-ray photoelectron spectroscopy measurements show further that the oxidation and reduction of the carbon takes place largely in parallel to the fluorination and defluorination of $La_2NiO_3F_2$, respectively. Since these reactions involving the carbon hamper the further reversible fluorination or defluorination reactions of the RP-type phases due to a decreased electronic conductivity in the electrode composite, increasing over-potentials are found. To avoid such irreversible reactions as much as possible and to maintain the facilitation of the fluorination or defluorination reactions of the RP-type phases, the electrochemical window has to be narrowed.

This is also reflected in the cycling performance of cells Pb/PbF_2 vs. $La_2NiO_3F_2$, $La_2NiO_3F_2$ vs. Pb/PbF_2 and La_2NiO_{4+d} vs. $La_2NiO_3F_2$. Considerable changes of the charging and discharging curves with increasing cycling numbers are found when charging to higher cut-off capacities, especially at low cycles, and a limitation of the cut-off capacity to 30 $mAhg^{-1}$ are found with respect to the investigated cut-off capacities to be most favourable. For higher cut-off capacities considerably worse Coulombic efficiencies, suggesting more irreversible reactions, resulting in the destruction of the conductive carbon matrix and higher over-potentials in the following charging steps with decreased reactions involving the RP-type phases, are observed. In particular, for the cells Pb/PbF_2 vs. $La_2NiO_3F_2$ and La_2NiO_{4+d} vs. $La_2NiO_3F_2$, large over-potentials are observed between the charging and the discharging plateaus, making a discharging to the negative potential range for a substantial re-defluorination of the oxidised La_2NiO_{4+d} composite or re-fluorination of the reduced $La_2NiO_3F_2$ composite necessary. Interestingly, a comparison between cells Pb/PbF_2 vs. $La_2NiO_3F_2$ and La_2NiO_{4+d} vs. $La_2NiO_3F_2$ shows that a better cycling performance is obtained for the latter cells, showing the potential of such purely intercalation-based cells.

For cells $La_2NiO_3F_2$ vs. Pb/PbF_2 a good cyclability over at least 50 cycles is found. Only for these cells, a meaningful discharging, leading to a structural reversibility, is observed in the positive potential range, making it a promising system for energy storage in FIBs. The influence of increasing disorder of the interstitial anion sites, present in the re-defluorinated $La_2NiO_3F_2$, on the cyclability and Coulombic efficiencies of consecutive cycles is discussed in addition. It is found that the changed energetics of the interstitial anion sites of disordered $La_2NiO_3F_2$ in comparison to ordered $La_2NiO_3F_2$ have a considerable effect, which is also correlated with more favourable structural distortions with respect to a subsequent electrochemical fluorination.

Moreover, it can be assumed that the reversible electrochemical reactions involving $La_2NiO_3F_2$ result also in the change of magnetic properties and a switching between distinctive magnetic states of the obtained phases is possible. However, for $La_2NiO_3F_2$ and $La_2NiO_3F_{2-x}$, for which magnetic properties could be investigated based on the analysis of their chemically prepared equivalents, only paramagnetic to antiferromagnetic transitions are observed. For $La_2NiO_3F_{2+x}$, assuming a complete fluorination to $La_2NiO_3F_3$, also a paramagnetic to antiferromagnetic transition can be expected based on its d^7 electron configuration. The intercalation of fluoride ions into the vacant interstitial site could, however, also inhibit a three-dimensional magnetic ordering completely. Therefore, the expected absolute magnetisation changes within the electrode composites when switching between $La_2NiO_3F_2$ and $La_2NiO_3F_{2-x}$ or $La_2NiO_3F_{2+x}$ upon charging and discharging are small. With respect to potential technological applications, higher absolute changes of the magnetisation are clearly

required and, therefore, reversible magnetic tuning is discussed based on a ferromagnetic RP-type oxide in the following subchapter (section 4.2.3).

4.2.3 Approaching reversible tuning of magnetic properties within fluoride-ion batteries - Electrochemical fluorination of $La_{1.3}Sr_{1.7}Mn_2O_7$

Tuning of magnetic properties via the reversible electrochemical intercalation or deintercalation of ions into or out of a host lattice is not only of great fundamental interest. It is also of relevance for various technological applications such as spin-based electronics, magnetic data storage or magnetic actuation. [34, 35, 31] A system showing such a magnetoelectric coupling should meet, depending on the application, different requirements. Besides a high magnetic on/off ratio due to large changes of the magnetisation when switching between two magnetic states, long-term stability and reversibility also the operating voltage, the speed of switching and the operation temperature are important. [30, 34, 35] A special focus lies on materials with a high magnetoelectric voltage coefficient $\alpha = \Delta M/(\Delta V \cdot M)$, i.e., high change of the relative magnetisation $\Delta M/M$ per applied field ΔV. A high magnetoelectric voltage coefficient relates, therefore, to a high energy efficiency in the application. [34, 35] In this context, a reversible on/off switching of ferromagnetism at ideally low potentials can offer interesting possibilities for possible future applications.

As has been shown previously in literature [18-20] and is also demonstrated within this thesis, the electrochemical modification of RP-type oxides and oxyfluorides is achieved within FIBs. Especially, the cycling performance of intercalation-based cathode composites containing RP-type oxides with a good reversibility of the electrochemical fluorination upon charging and re-defluorination upon discharging is promising, considering a reversible changing of magnetic properties. In addition, RP-type oxides have been intensively investigated with respect to their chemical fluorination behaviour and the structural changes occurring in the fluorinated phases. These phases are also known for their wide range of magnetic properties, which are highly dependent on the fluoride content. A substantial research effort has been made for the n =2 RP-type system $La_{2-2x}Sr_{1+2x}Mn_2O_7$. [23, 24, 47, 61, 223, 224, 274-278] The magnetic states of this system range from double-exchange mediated ferromagnetism to antiferromagnetism and are highly sensitive towards the oxidation state of Mn and the distance between adjacent perovskite building blocks within the structure, making it an optimal system for the tuning of magnetic properties. It can be expected that fluoride intercalation results in considerable changes in the magnetic properties due to compositional and structural changes. [21] In particular, magnetic interactions between Mn ions along the *c* axis should be affected, resulting in highly anisotropic magnetic properties. [23-25] The topochemical fluorination of $La_{1.2}Sr_{1.8}Mn_2O_7$ using F_2 gas or CuF_2 as fluorination reagents has been investigated previously. It has been shown that a staged intercalation of fluoride ions into the RP-type structure under the formation of $La_{1.2}Sr_{1.8}Mn_2O_7F$ and $La_{1.2}Sr_{1.8}Mn_2O_7F_2$ takes place.[21, 22] An investigation of magnetic behaviour of $La_{1.2}Sr_{1.8}Mn_2O_7F$ revealed, furthermore, the absence of long-range magnetic order at low temperatures. [21] Due to the staged intercalation, only one of the rock salt interstitial layers is filled in $La_{1.2}Sr_{1.8}Mn_2O_7F$, while both layers are occupied in $La_{1.2}Sr_{1.8}Mn_2O_7F_2$. For this work, the composition $La_{1.3}Sr_{1.7}Mn_2O_7$ with an average Mn oxidation state of +3.35 was selected, as it is reported to be ferromagnetic with a high magnetic moment of $> 3\ \mu_B$ per Mn cation and the highest Curie temperature of $\sim$ 120 K within the system. [223, 224]

To investigate if a magnetoelectric coupling can be achieved in $La_{1.3}Sr_{1.7}Mn_2O_7$ when using it as active cathode material in FIBs, the stability of it within the composites under experimental conditions, followed by the galvanostatic charging and discharging behaviour and the

resulting compositional and structural changes are investigated. The related magnetic properties of the obtained RP-type phases in the charged and discharged state are examined using SQUID measurements. In a final step, the reversible changes of the structures and the magnetic properties are studied after cycling the cells for various cycle numbers.

4.2.3.1 $La_{1.3}Sr_{1.7}Mn_2O_7$ and cathode composite

4.2.3.1.1 Rietveld analysis of $La_{1.3}Sr_{1.7}Mn_2O_7$

The starting RP-type phase $La_{1.3}Sr_{1.7}Mn_2O_7$ was synthesised via a solid-state synthesis. For its Rietveld refinement (Figure 4-94), a structural model with the n = 2 RP aristotype structure and space group *I*4/*mmm* proposed by Kubota et al. [224] was used. The obtained lattice parameters ($a = 3.8745(1)$ Å, $c = 20.1673(5)$ Å) and atomic parameters are in good agreements with the reported ones [224]. The structural parameters of $La_{1.3}Sr_{1.7}Mn_2O_7$ are given in Table 6-7. Titration experiments confirmed an oxidation state of Mn of +3.35, as expected for a composition of $La_{1.3}Sr_{1.7}Mn_2O_7$.

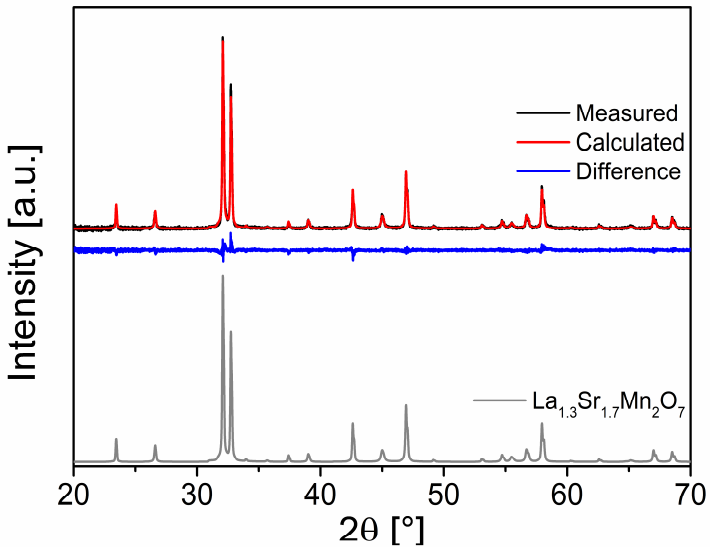

Figure 4-94: Rietveld refinement of XRD pattern of $La_{1.3}Sr_{1.7}Mn_2O_7$.

4.2.3.1.2 Stability and fluorination feasibility of the cathode composite containing $La_{1.3}Sr_{1.7}Mn_2O_7$

To examine the structural stability of $La_{1.3}Sr_{1.7}Mn_2O_7$ within the cathode composite after milling and of a pellet, consisting of a cathode composite, a $La_{0.9}Ba_{0.1}F_{2.9}$ and an anode composite layer, after heating to 170 °C, X-ray diffraction patterns of $La_{1.3}Sr_{1.7}Mn_2O_7$, the milled composite and the cathode side of a heated pellet, are compared in Figure 4-95. No reactions between $La_{1.3}Sr_{1.7}Mn_2O_7$ and the electrolyte $La_{0.9}Ba_{0.1}F_{2.9}$, potentially causing shifts of the $La_{1.3}Sr_{1.7}Mn_2O_7$ reflections, are found after the synthesis of the composite or heating. Moreover, the phase fractions of $La_{0.9}Ba_{0.1}F_{2.9}$ and the RP-type phase stay relatively constant within errors, which suggests that no decomposition or amorphisation takes place. This also shows that the crystal structure of $La_{1.3}Sr_{1.7}Mn_2O_7$ is stable during the heating process and that the application of a current or a voltage is necessary to evoke reactions.

After the application of a current during the charging of a cell $La_{1.3}Sr_{1.7}Mn_2O_7$ against Pb/PbF_2 to 3 V, significant changes in the reflection pattern related to the reflections of the RP-type phase are found. These shifts of reflections correspond to a considerable expansion of the *c* axis and a contraction of the *a* axis, which indicates the feasibility of the fluorination of $La_{1.3}Sr_{1.7}Mn_2O_7$ upon charging. Therefore, the electrochemical fluorination behaviour of $La_{1.3}Sr_{1.7}Mn_2O_7$ is analysed in detail in section 4.2.3.2.1.

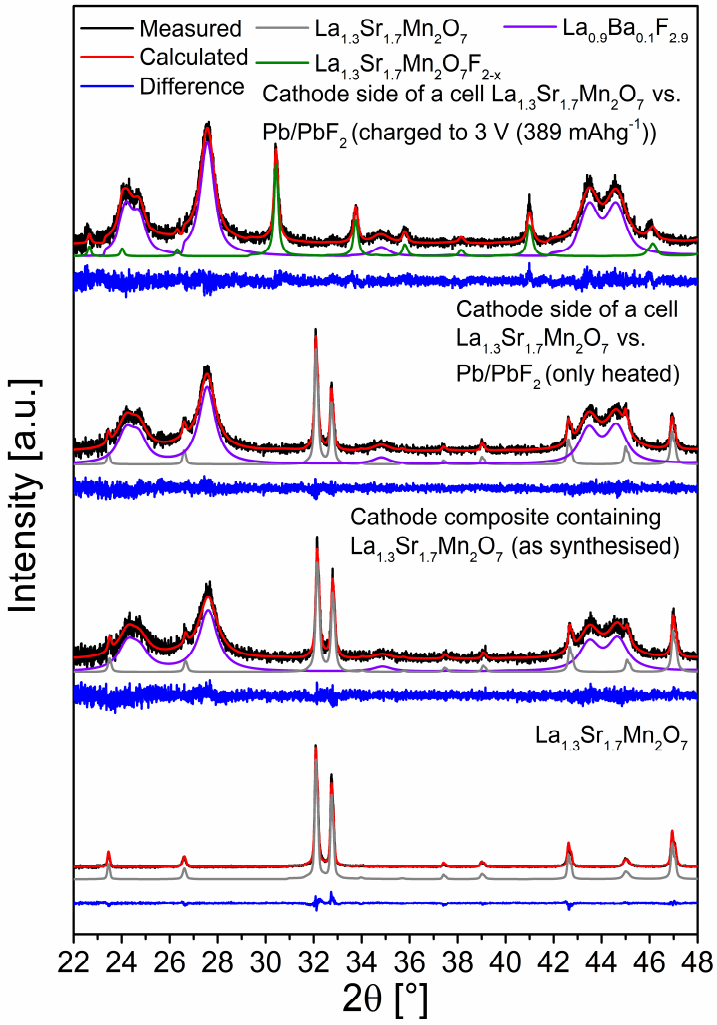

Figure 4-95: Comparison between Rietveld refinements of X-ray diffraction data of $La_{1.3}Sr_{1.7}Mn_2O_7$ used in the cathode composite, of the cathode composite containing $La_{1.3}Sr_{1.7}Mn_2O_7$ after milling, of the cathode side of a cell $La_{1.3}Sr_{1.7}Mn_2O_7$ against Pb/PbF_2 heated to 170 °C for 240 h and of the cathode side of a cell $La_{1.3}Sr_{1.7}Mn_2O_7$ against Pb/PbF_2 charged to 3 V (389 $mAhg^{-1}$).

4.2.3.1.3 Magnetisation study of $La_{1.3}Sr_{1.7}Mn_2O_7$ and the cathode composite

For the magnetic characterisation of the starting RP-type phase $La_{1.3}Sr_{1.7}Mn_2O_7$, M(T) and M(H) measurements were conducted. The obtained curves are shown in Figure 4-96 a and b, respetively. Both measurements were corrected from diamagnetic contributions [206], which are comparatively small and are not considered for all other measurements shown. The M(T) curve reveals two magnetic transitions at a T_c of ~ 117 K and a T_c' of ~ 246 K. An exact determination of the transition temperatures is possible using the derivative dM/dT shown in Figure 4-96 c. The transition at T_c' is related to a two-dimensional short-range ferromagnetic ordering due to stronger exchange interactions between the Mn ions in the quasi-two-

dimensional Mn-O-Mn networks within perovskite-type planes. A three-dimensional long-range magnetic ordering is obtained after cooling further to T_c, which is correlated to weaker inter-plane exchange interactions. [277] The M(H) measurement shows at 10 K a saturation magnetisation of ~ 3.6 μ_B per Mn ion, which corresponds well with the expected value based on the oxidation state of $La_{1.3}Sr_{1.7}Mn_2O_7$ ($0.65 \cdot 4\,\mu_B + 0.35 \cdot 3\mu_B = 3.65\,\mu_B$).

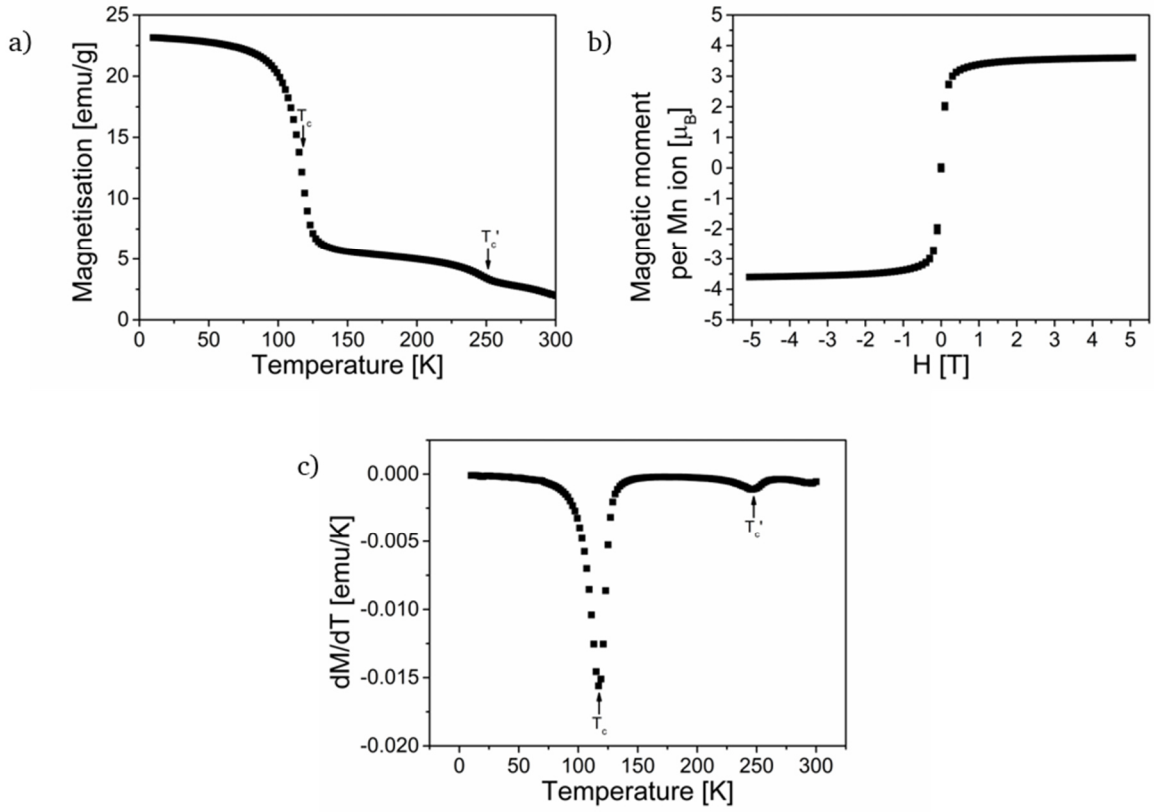

Figure 4-96: FC M(T) curve of $La_{1.3}Sr_{1.7}Mn_2O_7$ measured at μ_0 = 0.05 T (a), M(H) curves measured at 10 K (b) and dM/dT curve of $La_{1.3}Sr_{1.7}Mn_2O_7$, from which the transition temperatures T_c and T_c' were determined.

To ensure that the magnetic properties of $La_{1.3}Sr_{1.7}Mn_2O_7$ are not modified when preparing the cathode composite, M(T) and M(H) curves of the cathode composite after milling were performed. In addition, the cathode side of a heated pellet was scratched-off and magnetic measurements were conducted on the obtained powder. The comparison of the M(T) and M(H) curves (Figure 4-97 a and b) reveals no significant differences between both samples. There is also no difference to the M(H) measurement of pure $La_{1.3}Sr_{1.7}Mn_2O_7$ (Figure 4-96 b), showing that the RP-type phase is stable under experimental conditions. Furthermore, this confirms the results of the XRD study (see section 4.2.3.1.2) and it can be ruled out that reactions between $La_{1.3}Sr_{1.7}Mn_2O_7$, $La_{0.9}Ba_{0.1}F_{2.9}$ and/or CB occur, which would lead to alterations of the Mn oxidation state, resulting in changed saturation magnetisations. This also allows the conclusion that any observed magnetic changes of $La_{1.3}Sr_{1.7}Mn_2O_7$ within the cathode composite of cells are related to electrochemical redox reactions, taking place during charging or discharging.

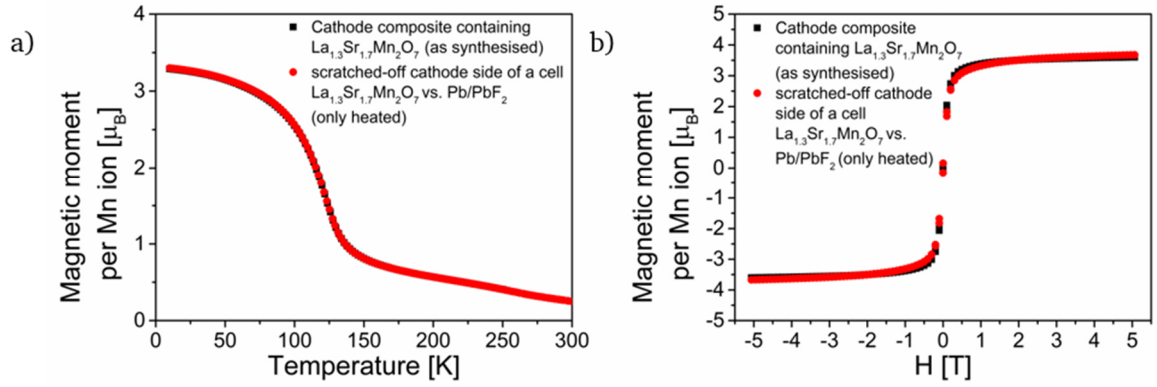

Figure 4-97: FC M(T) curves of the cathode composite containing $La_{1.3}Sr_{1.7}Mn_2O_7$ after milling and a scratched-off cathode side of a cell $La_{1.3}Sr_{1.7}Mn_2O_7$ against Pb/PbF_2 heated measured at μ_0 = 1 T (a), M(H) curves of the cathode composite containing $La_{1.3}Sr_{1.7}Mn_2O_7$ after milling and a scratched-off cathode side of a cell $La_{1.3}Sr_{1.7}Mn_2O_7$ against Pb/PbF_2 heated measured at 10 K (b).

4.2.3.2 Electrochemical fluorination of $La_{1.3}Sr_{1.7}Mn_2O_7$

4.2.3.2.1 Electrochemical fluorination behaviour of $La_{1.3}Sr_{1.7}Mn_2O_7$

As it is shown in section 4.2.3.1.2, the galvanostatic charging of a cell $La_{1.3}Sr_{1.7}Mn_2O_7$ against Pb/PbF_2 to 3 V leads to a considerable fluorination of $La_{1.3}Sr_{1.7}Mn_2O_7$ with a strong expansion of the *c* lattice parameter. The corresponding charging curve is shown in Figure 4-98. Its progression can be regarded to be typical for all conducted experiments. Three plateaus below the capacity of 60 $mAhg^{-1}$ are observed: the first plateau extends over a potential range of ~ 0.34 to 0.37 V and covers ~ 20 $mAhg^{-1}$; the second plateau is found between ~ 0.45 to 0.5 V, spanning over ~ 5 $mAhg^{-1}$; the third plateaus lies between ~ 0.8 and 0.85 V and extends ~ 10 $mAhg^{-1}$. In addition, a long plateau starts at ~ 1.3 V and a sloping plateau is found at potentials higher ~ 2.1 V. The capacities of the plateaus at higher voltages exceed the theoretical capacity of ~ 98 $mAhg^{-1}$ by far, suggesting that the undesired fluorination of carbon takes predominantly place in this potential region. This agrees well with findings reported in section 4.2.2.5 and in studies on the electrochemical fluorination of other RP-type oxides performed by Nowroozi at al. [18-20]

In order to investigate structural changes upon charging, different cells $La_{1.3}Sr_{1.7}Mn_2O_7$ against Pb/PbF_2 were charged to various cut-off potentials (Figure 4-98) and the X-ray diffraction patterns of the cathode sides of the charged cells were collected ex-situ (Figure 4-99).

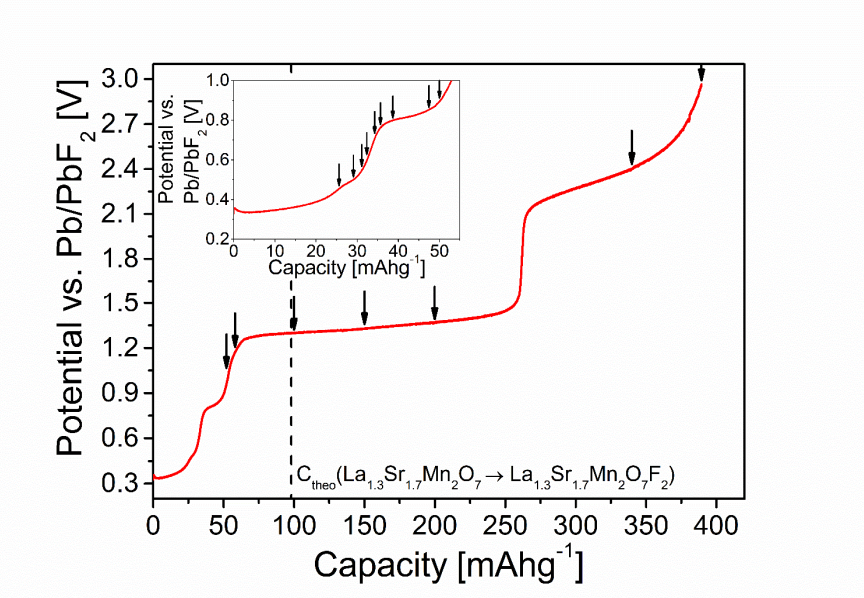

Figure 4-98: Charging curve of a cell $La_{1.3}Sr_{1.7}Mn_2O_7$ against Pb/PbF_2 charged to 3 V (389 $mAhg^{-1}$). The arrows show various cut-off potentials, to which different cells were charged.

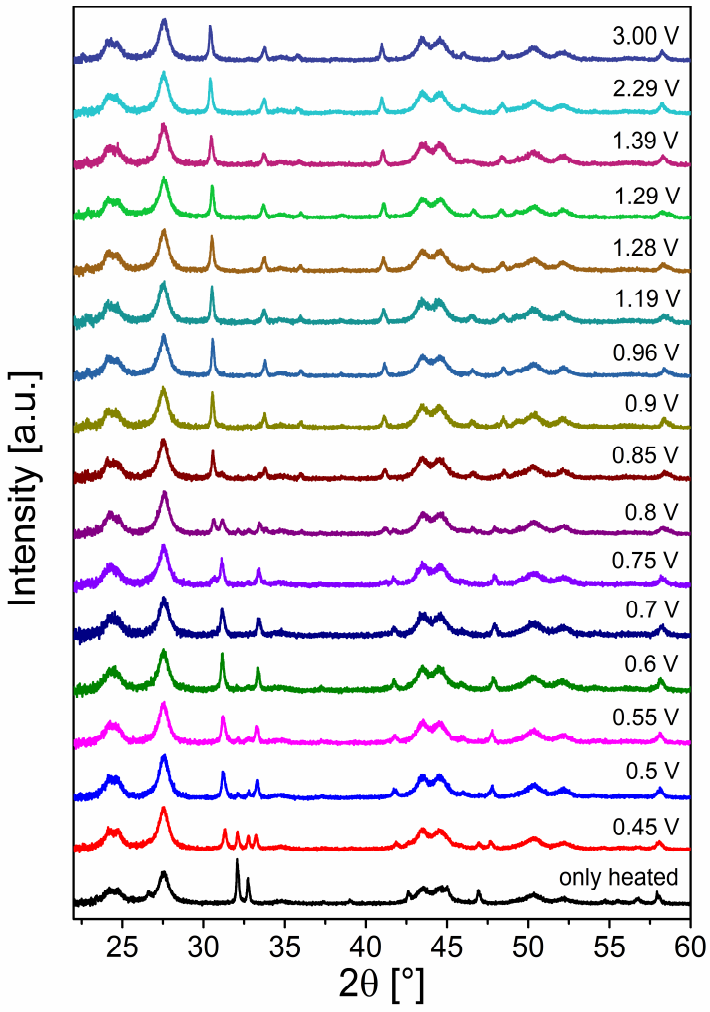

Figure 4-99: X-ray diffraction patterns of cathode sides of different cells $La_{1.3}Sr_{1.7}Mn_2O_7$ against Pb/PbF_2 charged to various cut-off capacities. For reference, a cell, which was only heated, is given. Rietveld refinements of selected patterns are shown in Figure 6-30 in the appendix.

The XRD pattern of the cathode side of a heated cell, used as reference, shows besides the electrolyte $La_{0.9}Ba_{0.1}F_{2.9}$ only the presence of the starting RP-type phase $La_{1.3}Sr_{1.7}Mn_2O_7$ (space group: *I4/mmm*, lattice parameters: a = 3.8755(2) Å, c = 20.165(1) Å). The amorphous CB cannot be detected. At comparatively low potentials, electrochemical charging leads to the appearance of a new phase at the cost of the initial RP-type phase. Starting at ~ 0.75 V, this newly formed phase is transformed into another phase. No indication is given for the formation of further phases at higher potentials. In agreement with chemical fluorination experiments [21, 22], Rietveld refinements of the patterns obtained after charging to 0.7 and 3 V, containing the highest phase fractions of the respective phases, indicate that the phases with compositions close to $La_{1.3}Sr_{1.7}Mn_2O_7F$ and $La_{1.3}Sr_{1.7}Mn_2O_7F_2$ are formed. As has been also observed by Aikens et al. [21], the fluorination results in a staged occupation of first only one of the interstitial rock salt layer. This is corresponding to a symmetry lowering from *I4/mmm* found for $La_{1.3}Sr_{1.7}Mn_2O_7$ to *P4/nmm* in the partially fluorinated phase (called '$La_{1.3}Sr_{1.7}Mn_2O_7F_{1-y}$', space group: *P4/nmm,* lattice parameters after charging to 0.7 V: a = 3.8019(5) Å, c = 21.974(5) Å). The loss of the body-centering leads to the presence of superstructure reflections, e.g. the $(0011)_{P4/nmm}$ reflections at a 2θ value of ~ 45.8°. When both interstitial layers are filled in the highly fluorinated phase (called '$La_{1.3}Sr_{1.7}Mn_2O_7F_{2-x}$', space group: I4/*mmm,* lattice parameters after charging to 3 V: a = 3.7649(3) Å, c = 23.639(3) Å), the body-centered symmetry is re-established. [22] It should be mentioned that the reflection of $La_{1.3}Sr_{1.7}Mn_2O_7F_{2-x}$, which is visible in a similar 2θ range as the (0011) superstructure reflection of $La_{1.3}Sr_{1.7}Mn_2O_7F_{1-y}$, is a (0012) reflection. This (0012) reflection shifts in all XRD patterns, containing the highly fluorinated phase, in accordance with an increase of the c lattice parameter progressively towards lower 2θ value, when charging to higher potentials. The structural parameters of the two fluorinated phases are given in Table 6-8 and Table 6-9. The crystal structures of the phases are shown in Figure 4-100.

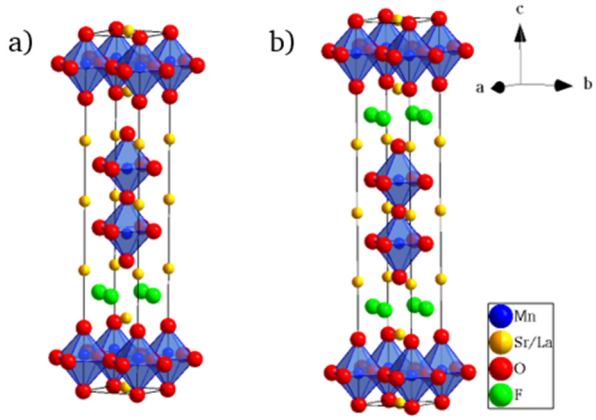

Figure 4-100: Crystal structures of $La_{1.3}Sr_{1.7}Mn_2O_7F$ (a) and $La_{1.3}Sr_{1.7}Mn_2O_7F_2$ (b).

When looking at the evolution of the relative phase fractions of the RP-type phases (Figure 4-101 a) in dependence of the cut-off potential, it can be concluded that the first two charging plateaus starting at ~ 0.34 and 0.45 V are related to redox reactions leading to the formation of $La_{1.3}Sr_{1.7}Mn_2O_7F_{1-y}$, while the formation of $La_{1.3}Sr_{1.7}Mn_2O_7F_{2-x}$ takes predominantly place at potentials higher than ~ 0.8 V. Increasing the potentials further does not lead to additional changes of the phase fractions. The maximum relative phase fractions of $La_{1.3}Sr_{1.7}Mn_2O_7F_{1-y}$ is found at 0.7 V. At lower potentials, the initial $La_{1.3}Sr_{1.7}Mn_2O_7$ and $La_{1.3}Sr_{1.7}Mn_2O_7F_{1-y}$ are found. Therefore, instead of forming a single phase with an average fluoride content and an

intermediate oxidation state of the Mn ions, the system seems to prefer to exist in a fluorinated phase with an increased oxidation state and a non-fluorinated phase with a lower oxidation state. Based on the obtained charging capacities of the cells with cut-off potentials ≤ 0.7 V, assuming that the observed capacity is only related to the desired redox reactions, and based on the relative phase fractions of the different RP-type phases, an estimation of the fluoride content of $La_{1.3}Sr_{1.7}Mn_2O_7F_{1-y}$ can be made (Table 6-10). It appears that fluoride contents smaller than ~ 0.6 per formula unit are unfavourable, resulting in the formation of a phase mixture of the starting phase and $La_{1.3}Sr_{1.7}Mn_2O_7F_{1-y}$ with $y < 0.4$. For a cut-off voltage of 0.7 V, the average fluoride content is ~ 0.65. At further increased potentials, the fluorination of the second rock salt-type layer starts. In addition, the initial RP-type phase reappears, before disappearing again at ~ 0.85 V. This suggests that a certain stability range of the fluoride content of $La_{1.3}Sr_{1.7}Mn_2O_7F_{2-x}$ exists, which leads also to the preference of a phase separation into the initial phase and $La_{1.3}Sr_{1.7}Mn_2O_7F_{2-x}$, instead of a single phase with an average fluoride content. The exact determination of this stability range is impeded by the presence of two fluorinated phases with unknown fluoride contents. This phase separation could be caused by redox disproportion, i.e., a conversion of one phase with intermediate oxidation state into two different phases with different oxidation states, or by structural changes that make phases with an average fluoride content energetically unfavourable.

The unit cell volumes per formula unit and the lattice parameters of the initial and fluorinated RP-type phases are shown in Figure 4-100 b-d. The layer-wise intercalation of fluoride ions into the interstitial layers leads to significant increases of the unit cell volumes, which is related to the strong expansion of *c* axis. Due to the oxidation of the Mn ions (ionic radii: Mn^{3+}: 0.645 Å (high-spin configuration), Mn^{4+}: 0.53 Å, Mn^{5+}: 0.33 Å, Mn^{6+}: 0.255 Å)[54], the *a* lattice parameter decreases. Within the existence range of each fluorinated phase, charging to higher potentials causes further smaller changes of the lattice parameters. This suggests that additional fluoride intercalation takes place, leading to higher fluoride contents in $La_{1.3}Sr_{1.7}Mn_2O_7F_{1-y}$ and $La_{1.3}Sr_{1.7}Mn_2O_7F_{2-x}$, i.e., a continuous decrease of y and x. This is also in agreement with the estimated average fluoride contents of $La_{1.3}Sr_{1.7}Mn_2O_7F_{1-y}$ calculated for cut-off potentials ≤ 0.7 V.

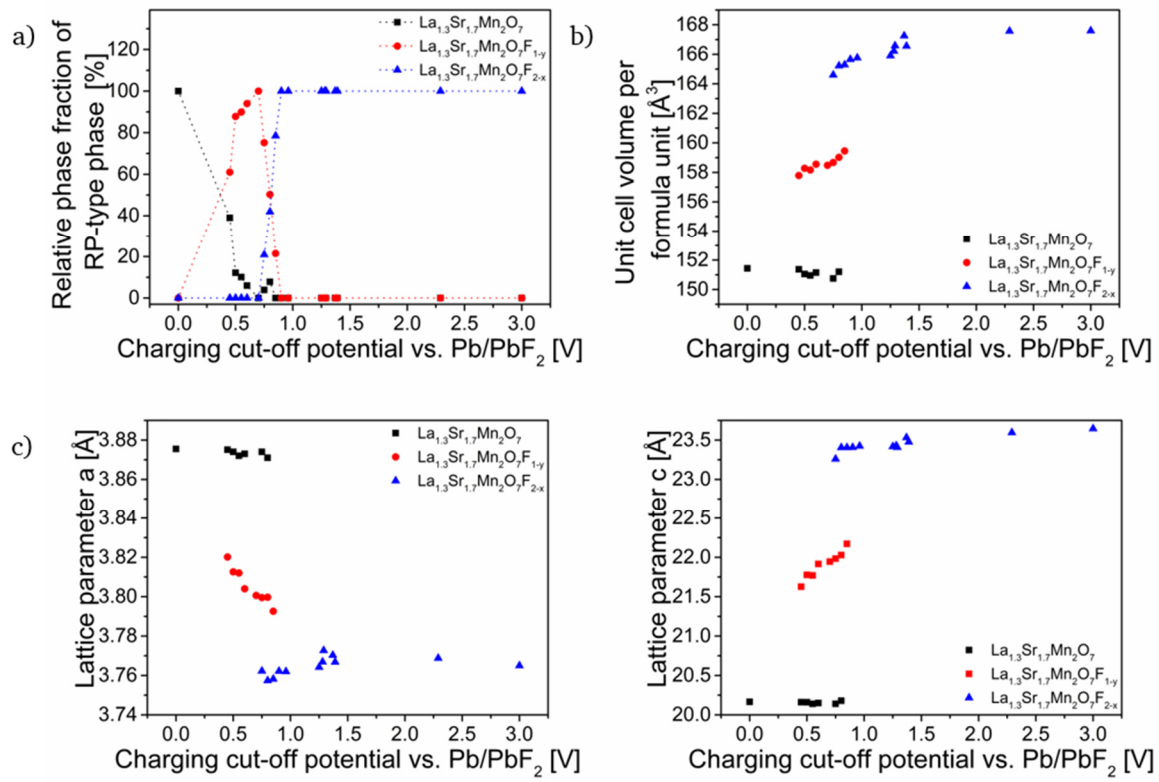

Figure 4-101: Relative phase fractions (a), unit cell volume per formula unit (b) and lattice parameters *a* (c) and *c* (d) of $La_{1.3}Sr_{1.7}Mn_2O_7$, $La_{1.3}Sr_{1.7}Mn_2O_7F_{1-y}$ and $La_{1.3}Sr_{1.7}Mn_2O_7F_{2-x}$ in the cathode sides of cells $La_{1.3}Sr_{1.7}Mn_2O_7$ against Pb/PbF_2 charged to different cut-off capacities. For the calculation of the relative phase fractions of the RP-type phases, the phase fraction of $La_{0.9}Ba_{0.1}F_{2.9}$ was not taken into account.

For a successful tuning of magnetic properties based on $La_{1.3}Sr_{1.7}Mn_2O_7$, the change in magnetisation due to intercalation and re-deintercalation of fluoride ions should be high; ideally, a complete on/off switching should be possible. This would correspond to a switching between the ferromagnetic ordering of $La_{1.3}Sr_{1.7}Mn_2O_7$ and an un-ordered or an antiferromagnetic state of the fluorinated phases. Doping-dependent studies on $La_{2-2x}Sr_{1+2x}Mn_2O_7$ [223, 224] have shown that a transition to antiferromagnetism occurs for doping levels correlated to a Mn oxidation state of +3.48 or higher. Assuming that this transition could be in analogy evoked by intercalating fluoride ions into $La_{1.3}Sr_{1.7}Mn_2O_7$, an intercalation of only 0.26 fluoride ions per formula unit would be sufficient to achieve the same oxidation state. The performed charging study shows, however, that a phase with a composition of $La_{1.3}Sr_{1.7}Mn_2O_7F_{0.26}$ cannot be stabilised upon charging. Therefore only phases with higher fluoride contents can be formed. These higher fluoride contents could have a considerable influence on the magnetic exchange interactions, potentially supressing a ferromagnetic or antiferromagnetic ordering even completely. It has to be emphasised that not only the electronic structure of the Mn ions influence the magnetic properties, but also other effects are relevant. These effects include the increased distance between adjacent perovskite-type building blocks due to the fluoride intercalation and other structural distortions, which lead to reduced overlapping of the orbitals. [279-281] Moreover, interactions have to be mediated over an increased number of anions. Exchange via fluoride ions instead of oxide ions affect also the strength of the exchange interactions in $La_{1.3}Sr_{1.7}Mn_2O_7F_x$. [56]

The highest possible reversible transformation of the initial RP-type phase into one of the fluorinated phases should be crucial to obtain a maximum change in the magnetisation.

Therefore, a charging cut-off potential, for which predominantly one of the fluorinated phases is formed seems to be beneficial. On the other hand, it should be considered that larger volume changes of the RP-type phases, especially during cycling, can lead to a poor reversibility due to the loss of the contact between the RP-type phases and the electrolyte and CB, which ensure good ionic and electronic conductivities, respectively. Consequently, the formation of $La_{1.3}Sr_{1.7}Mn_2O_7F_{2-x}$ should be avoided. Furthermore, the cut-off potential should be as low as possible to allow for high efficiencies and the shortest possible charging times.

4.2.3.2.2 Magnetisation study of the oxidised $La_{1.3}Sr_{1.7}Mn_2O_7F_x$

To investigate, for which cut-off potentials a maximal change in magnetisation in comparison to a reference cell, which was only heated, can be found, M(T) curves of the scratched-off cathode sides of various charged cells were recorded. The curves are shown in Figure 4-102. As expected, the electrochemical fluorination of $La_{1.3}Sr_{1.7}Mn_2O_7$ causes a significant change in the magnetic properties. Even charging to a cut-off capacity of only 0.45 V, leads to a decrease of the magnetic moment per Mn ion to ~ 37 % of the moment of the reference cell. For this comparison, the magnetic moments measured at 10 K are used. For all other cut-off potentials above 0.45 V, only very weak magnetic moments ($\leq 0.2\ \mu_B$) exist at 10 K. There seems to be a strong correlation between the relative phase fractions of the RP-type phases and the magnetic properties. In the cell, which was charged to 0.45 V, ~ 39 % of $La_{1.3}Sr_{1.7}Mn_2O_7$ is still present within the cathode composite. This decrease of the phase fraction of $La_{1.3}Sr_{1.7}Mn_2O_7$ is in accordance with the decrease in the observed magnetic moment. Moreover, the cells charged to 0.6 and 0.8 V only show very weak ferromagnetic transitions, while the cells charged to 1.28 and 3 V do not exhibit this feature. This corresponds also well to the presence of ~ 6 and 8 % of the initial RP-type phase in the cells charged to 0.6 and 0.8 V, respectively, whereas the higher charged cells contain only $La_{1.3}Sr_{1.7}Mn_2O_7F_{2-x}$. Therefore, it can be concluded that the fluorinated phases are not ferromagnetic and any ferromagnetic behaviour observed in the charged cells are due to residual $La_{1.3}Sr_{1.7}Mn_2O_7$. This is further confirmed by the fact that the Curie temperatures observed for the cells charged to 0.45, 0.6 and 0.8 V remains unchanged compared to the reference cell.

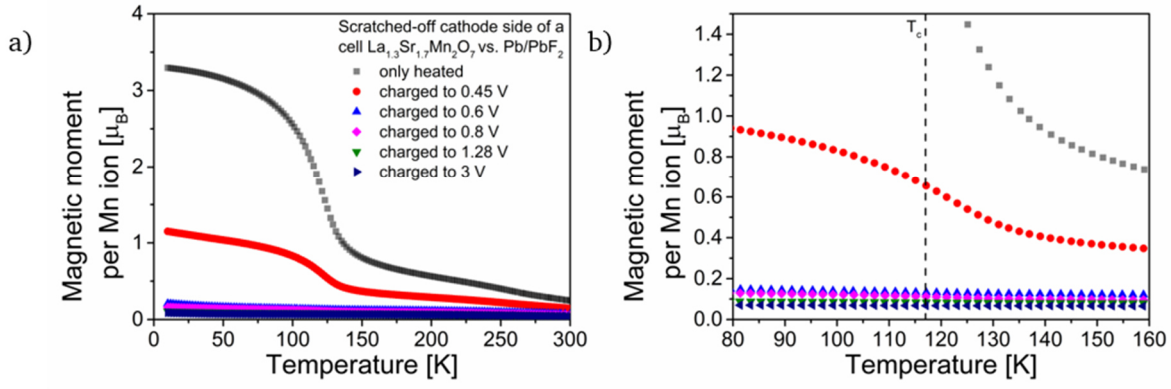

Figure 4-102: FC M(T) curves of scratched-off cathode side of cells $La_{1.3}Sr_{1.7}Mn_2O_7$ against Pb/PbF_2 charged to different cut-off potentials measured at μ_0 = 1 T (a) and a magnification of the M(T) curves in the T_c temperature region (b).

Taking the magnetisation measurements and the criteria discussed in section 4.2.3.2.1 into account, charging cut-off potentials of 0.45 and 0.6 V were chosen for the following experiments. Even though, residual ferromagnetic $La_{1.3}Sr_{1.7}Mn_2O_7$ is still present within the

cathode composite of the cells charged to these potentials, the change in magnetisation is comparatively high. Moreover, the formation of $La_{1.3}Sr_{1.7}Mn_2O_7F_{2-x}$ and a substantial fluorination of the conductive carbon additive can be avoided when using these charging cut-off conditions.

4.2.3.3 Electrochemical re-defluorination of the oxidised $La_{1.3}Sr_{1.7}Mn_2O_7F_x$

4.2.3.3.1 Electrochemical re-defluorination behaviour of the oxidised $La_{1.3}Sr_{1.7}Mn_2O_7F_x$

The typical charging and discharging curves of cells $La_{1.3}Sr_{1.7}Mn_2O_7$ against Pb/PbF_2, which were charged to 0.45 and 0.6 V, respectively, and subsequently discharged to -3 V are shown in Figure 4-103. The discharging curves feature several differently distinctive plateaus. For the cell charged to 0.45 V (Figure 4-103 a), in the potential range between ~ 0.13 and 0.8 V, a clear plateau, covering ~ 15 $mAhg^{-1}$, is visible. For the cell, which was charged to 0.6 V (Figure 4-103 b), a relatively short additional plateau between 0.2 and 0.14 V, extending over ~ 4 $mAhg^{-1}$, is observed. This plateau is followed by a plateau in the potential range between ~ 0.13 and -0.05 V, covering ~ 13 $mAhg^{-1}$. The two plateaus cover approximately the same specific capacity as the one plateau observed in the discharging curve of the cell, which was charged to 0.45 V. This indicates that relative changes of the phase fractions of the RP-type phases might be in the same order of magnitude. When further discharging to potentials below 0 V, only sloping plateaus can be found in both discharging curves. The more detailed investigation of the effect of discharging to the negative potential range on structural changes was motivated by the fact that no meaningful discharging of charged cells $LaSrMnO_4$ against Pb/PbF_2 has been observed in a previous study by Nowroozi et al. [20].

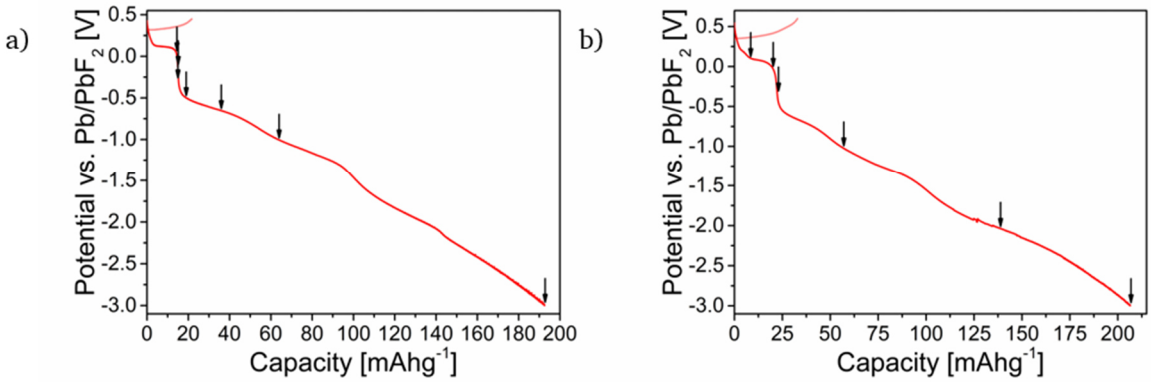

Figure 4-103: Charging and discharging curves of a cell $La_{1.3}Sr_{1.7}Mn_2O_7$ against Pb/PbF_2. The cells were charged to 0.45 V (a) and 0.6 V (b) and subsequently discharged to -3 V. The arrows show various cut-off potentials, to which different cells were discharged.

The XRD patterns of the cathode sides of the cells $La_{1.3}Sr_{1.7}Mn_2O_7$ against Pb/PbF_2 charged to 0.45 V and subsequently discharged to selected discharging cut-off potentials are shown in Figure 4-104. A complete re-defluorination of $La_{1.3}Sr_{1.7}Mn_2O_7F_{1-y}$ under the formation of only $La_{1.3}Sr_{1.7}Mn_2O_7$ is not observed. The derived relative phase fractions, unit cell volumes per formula unit and lattice parameters of the found RP-type phases are given in Figure 4-105. The discharged cells show a relatively strong decrease of the relative phase fraction of the fluorinated phase $La_{1.3}Sr_{1.7}Mn_2O_7F_{1-y}$ when discharging to 0 V. While the phase fraction of $La_{1.3}Sr_{1.7}Mn_2O_7$ increases only slightly in comparison to its phase fraction in the charged cells upon the electrochemical defluorination of $La_{1.3}Sr_{1.7}Mn_2O_7F_{1-y}$ during the discharging to 0 V, a

large phase fraction of an intermediate phase is found. This phase has a unit cell volume and lattice parameters between those of $La_{1.3}Sr_{1.7}Mn_2O_7$ and $La_{1.3}Sr_{1.7}Mn_2O_7F_{1-y}$. This suggests that in the intermediate phase residual fluoride ions are trapped within the host lattice, which cannot be extracted upon discharging. Only comparatively small changes of the relative phase fractions of the RP-type phases within errors are found in the potential range between 0 and -1 V. A slight increase of the phase fraction of the intermediate phase at the cost of $La_{1.3}Sr_{1.7}Mn_2O_7F_{1-y}$ is observed. This shows that the major achievable defluorination of $La_{1.3}Sr_{1.7}Mn_2O_7F_{1-y}$ takes place within the positive potential range, which is in contrast to the discharging behaviour of cells $LaSrMnO_4$ against Pb/PbF_2 [20]. However, in the study on $LaSrMnO_4$, the cells have been charged to much higher potentials, which should lead to a strong destruction of the electronically conductive carbon matrix, having a negative influence on the reversibility of electrochemical reactions. This highlights again that the choice of cut-off conditions has a decisive impact on the charging and discharging behaviour.

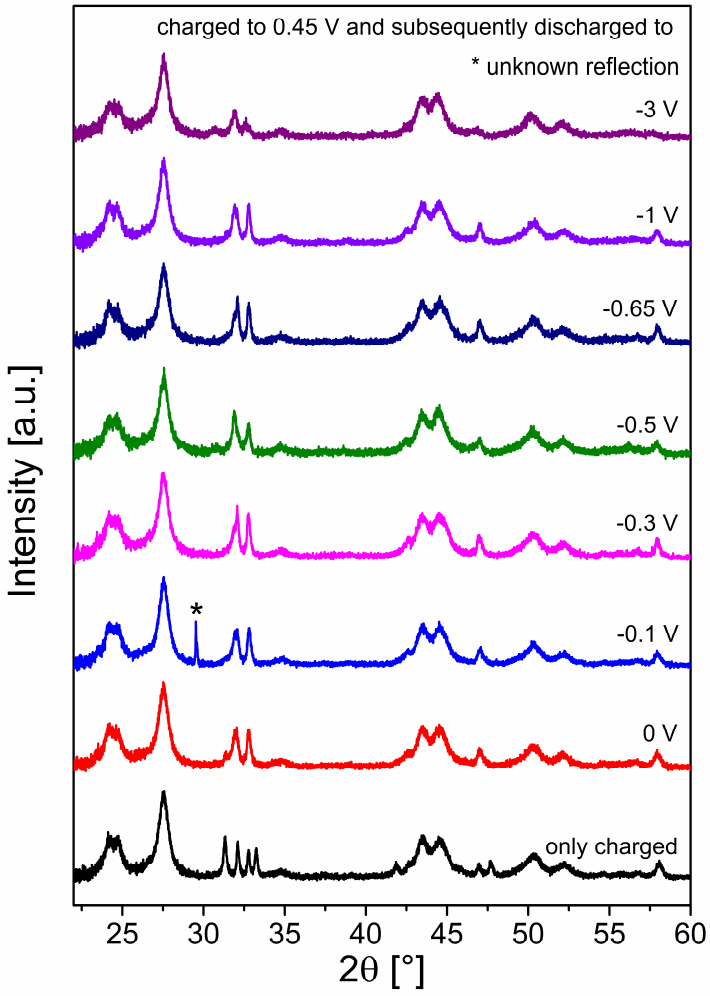

Figure 4-104: X-ray diffraction patterns of cathode sides of cells $La_{1.3}Sr_{1.7}Mn_2O_7$ against Pb/PbF_2 charged to 0.45 V and subsequently discharged to various cut-off potentials. For reference, a cell, which was only charged to 0.45 V, is given. The unknown reflection (marked with *) at ~ 29.5° is probably due to an impurity on the sample holder used for measuring of the sample. The Rietveld refinement of the cell discharged to -0.3 V is given in Figure 6-30.

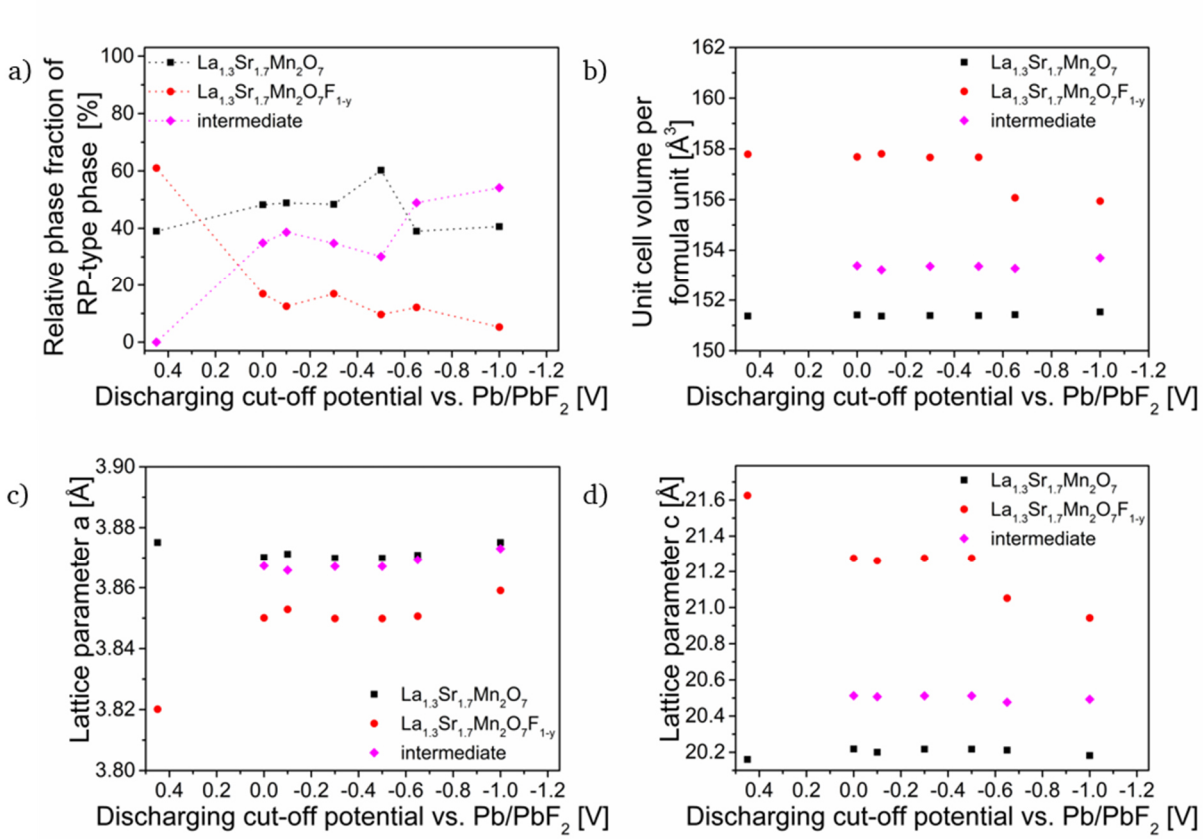

Figure 4-105: Relative phase fractions (a), unit cell volume per formula unit (b) and lattice parameters *a* (c) and *c* (d) of $La_{1.3}Sr_{1.7}Mn_2O_7$, $La_{1.3}Sr_{1.7}Mn_2O_7F_{1-y}$ and an intermediate phase in the cathode sides of cells $La_{1.3}Sr_{1.7}Mn_2O_7$ against Pb/PbF_2 charged to 0.45 V and subsequently discharged to different cut-off potentials. For the calculation of the relative phase fractions of the RP-type phases, the phase fraction of $La_{0.9}Ba_{0.1}F_{2.9}$ was not taken into account.

Similar observations can be made for the cells charged to 0.6 V. The XRD patterns of the cathodes charged to the cut-off potential of 0.6 V and subsequently discharged to various cut-off potentials are shown Figure 4-106. The discharging causes a strong decrease of the phase fraction of $La_{1.3}Sr_{1.7}Mn_2O_7F_{1-y}$ and an increase of $La_{1.3}Sr_{1.7}Mn_2O_7$ in the potential range between 0.6 and 0 V (Figure 4-107 a). In the cell discharged to 0 V, in addition to $La_{1.3}Sr_{1.7}Mn_2O_7$, a large fraction of the intermediate phase is formed, which is not observed at 0.11 V. With respect to this, additional experiments in the positive potential range are required in order to get a more detailed understanding about ongoing structural changes. At negative potentials, an increasing formation of the intermediate phase is observed, while the phase fraction of $La_{1.3}Sr_{1.7}Mn_2O_7$ remains relatively constant.

The unit cell volumes and lattice parameters *c* of the remaining $La_{1.3}Sr_{1.7}Mn_2O_7F_{1-y}$ and the intermediate phase of the cells with a charging cut-off condition of 0.6 V (Figure 4-107 b and d) are larger compared to those of the discharged cells with the lower cut-off potential of 0.45 V (Figure 4-105 b and d). This shows that higher fluoride contents are found within these phases after discharging. The lattice parameters *a* (Figure 4-105 c and Figure 4-107 c) provide for both charging conditions evidence for changing oxidation states. The intermediate phase possesses smaller lattice parameters than the initial RP-type phase. Therefore, a higher oxidation state of the Mn ions due to intercalated fluoride ions can be assumed.

In agreement to what was observed during the formation of $La_{1.3}Sr_{1.7}Mn_2O_7F_{1-y}$, during the defluorination of $La_{1.3}Sr_{1.7}Mn_2O_7F_{1-y}$ an increase of the lattice parameter *a* and the decrease of the lattice parameter *c* when discharging to more negative potentials is observed (Figure

4-105 and Figure 4-107 c and d). This show that also during discharging a progressive extraction of fluoride ions from $La_{1.3}Sr_{1.7}Mn_2O_7F_{1-y}$ within its range of existence takes place, leading to an increase of y and a respective reduction of the Mn oxidation state.

Overall, it is indicated that a full structural reversibility is, at least during the first charging and discharging step, not possible. In addition, more fluoride ions are trapped within the host lattices and higher phase fractions of the intermediate phase are found after discharging when higher charging cut-off potentials are selected.

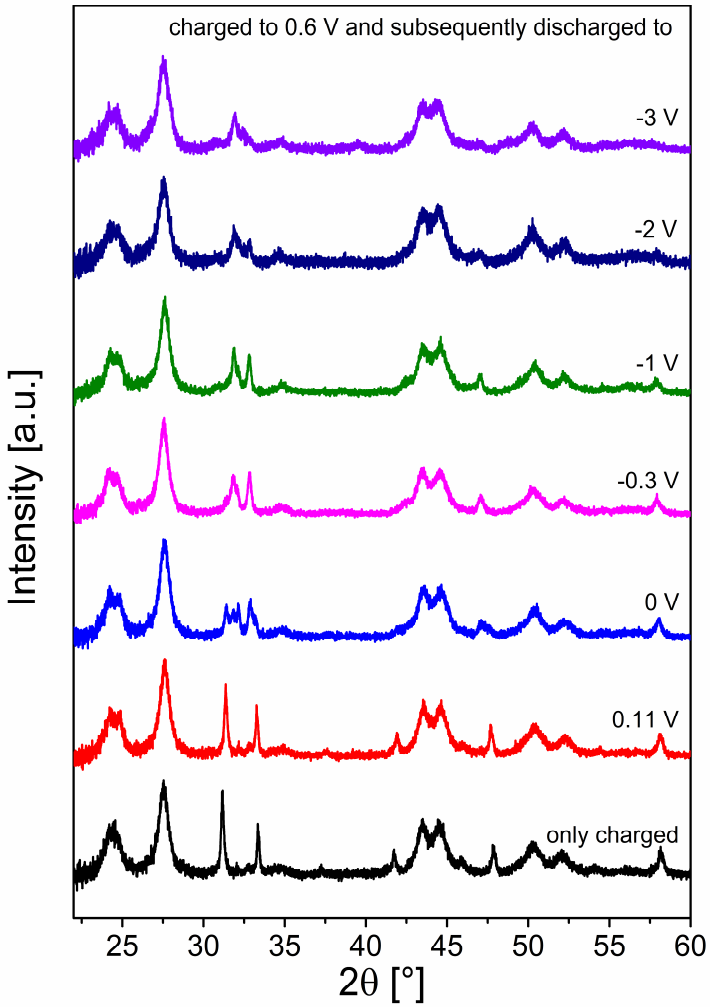

Figure 4-106: X-ray diffraction patterns of cathode sides of cells $La_{1.3}Sr_{1.7}Mn_2O_7$ against Pb/PbF_2 charged to 0.6 V and subsequently discharged to various cut-off potentials. For reference, a cell, which was only charged to 0.6 V, is given.

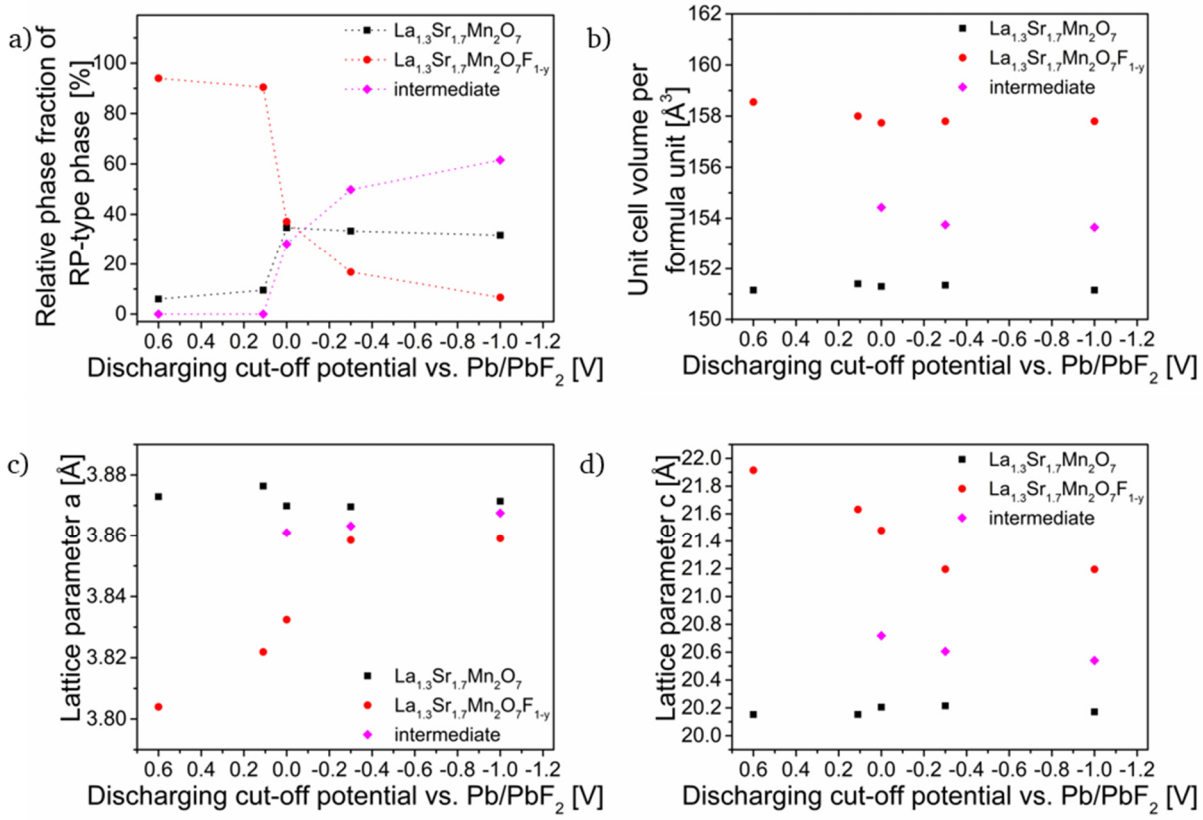

Figure 4-107: Relative phase fractions (a), unit cell volume per formula unit (b) and lattice parameters *a* (c) and *c* (d) of $La_{1.3}Sr_{1.7}Mn_2O_7$, $La_{1.3}Sr_{1.7}Mn_2O_7F_{1-y}$ and an intermediate phase in the cathode sides of cells $La_{1.3}Sr_{1.7}Mn_2O_7$ against Pb/PbF_2 charged to 0.6 V and subsequently discharged to different cut-off potentials. For the calculation of the relative phase fractions of the RP-type phases, the phase fraction of $La_{0.9}Ba_{0.1}F_{2.9}$ was not taken into account.

A discharging cut-off condition of -0.3 V was selected for the following experiments. At this potential a relative high phase fraction of ferromagnetic $La_{1.3}Sr_{1.7}Mn_2O_7$ is regained, which should result in a high magnetisation change. The stabilisation of a large phase fraction of the intermediate phase instead of $La_{1.3}Sr_{1.7}Mn_2O_7$ might, however, reduce the overall change of magnetisation between the charged and discharged state drastically. For the intermediate phase, it can be assumed that the residual fluoride ions within the interstitial rock salt layers has an influence on the strength of the magnetic interaction between the perovskite-type building blocks, which could possibly impede a three-dimensional ferromagnetic ordering. The effect of this phase on the magnetisation is examined below.

4.2.3.3.2 Magnetisation study of the re-reduced $La_{1.3}Sr_{1.7}Mn_2O_7$

The M(T) curves of scratched-off cathode sides of cells, which were charged to 0.45 and 0.6 V, respectively, and subsequently discharged to -0.3 V are shown, in Figure 4-108 in comparison to a cells, which were only charged. In addition, a measurement of a cell, which was only heated, is given. This heated cell can serve as a reference since it represents the ideally discharged state of the fully re-defluorinated cathode composite. It becomes evident that the ferromagnetic interaction can be partially restored after discharging. Compared to the initial magnetic moment of the heated cell at 10 K, ~ 57 and 20 % can be restored when a charging cut-off condition of 0.45 and 0.6 V, respectively, is used. In particular for the cell charged only to 0.45 V, the measured magnetic moment corresponds well with the relative phase fractions of $La_{1.3}Sr_{1.7}Mn_2O_7$ found within this cell. This shows that the ferromagnetic

contribution to the magnetisation is mainly caused by $La_{1.3}Sr_{1.7}Mn_2O_7$, while the intermediate phase and $La_{1.3}Sr_{1.7}Mn_2O_7F_{1-y}$ are not ferromagnetic. The increased distance between the perovskite-type layers due to the residual fluoride ions within the interstitial sites of the intermediate phase seems to be sufficient to distort the ferromagnetic coupling. The Curie temperatures of the cell charged to 0.45 V and subsequently discharged to -0.3 V remains unchanged compared to the reference cell and the cell, which was only heated. This indicates that the formed $La_{1.3}Sr_{1.7}Mn_2O_7$ is only slightly modified during the charging and discharging cycle. In contrast to this, the cell charged to 0.6 V and subsequently discharged to -0.3 V shows a widened transition temperature range and the Curie temperature is found at lower temperatures of ~ 60 K. This change could be due to chemical and/or structural inhomogeneities, caused by trapped fluoride ions, which might lead to a wide distribution of ferromagnetic transition temperatures. These inhomogeneities might be also responsible for the comparatively small magnetic moment, which can be restored after the discharging of this cell, even though a relatively high phase fraction of $La_{1.3}Sr_{1.7}Mn_2O_7$ is found. The still trapped fluoride ions in this phase might already of a negative influence on the strength of magnetic interactions, which would lead to lower magnetic moments.

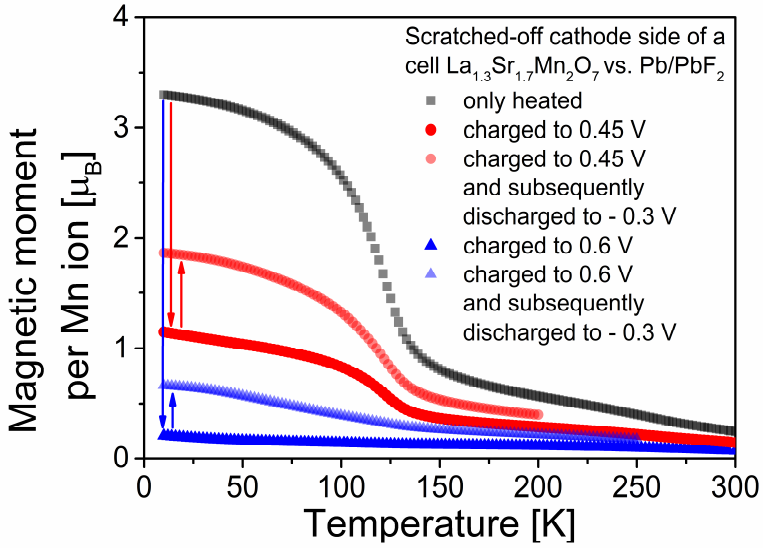

Figure 4-108: Comparison of FC M(T) curves of scratched-off cathode side of cells $La_{1.3}Sr_{1.7}Mn_2O_7$ against Pb/PbF_2 charged to 0.45 and 0.6 V, respectively, and subsequently discharged to -0.3 V measured at μ_0 = 1 T. For reference, a cell, which was only heated, is given.

4.2.3.4 Cycling of cells containing $La_{1.3}Sr_{1.7}Mn_2O_7$-based cathodes

4.2.3.4.1 Cycling behaviour

To verify the reversibility of the observed structural changes upon cycling, cells were operated between the charging cut-off conditions of 0.45 or 0.6 V and the discharging cut-off condition of -0.3 V for various cycles. Exemplarily, the charging and discharging curves of cells, which were cycled for ten cycles, are shown in Figure 4-109. For both charging conditions, after the first cycle, the plateaus of the redox reactions taking place during charging shift to lower potentials by ~ 0.12 V. The second smaller plateau observed in the charging curve of the cells charged to 0.6 V shifts by ~ 0.05 V. The charging capacities decrease by ~ 35 %. It appears that side reactions occur during the first charging step, which reduce over-potentials and facilitate fluorination reactions in the subsequent cycles. Similar to the solid-electrolyte-

interfaces found in lithium-ion batteries [282, 283], this might be related to the formation of interfaces between the active material with RP-type structure and the electrolyte within the cathode composite. Such interfacial reactions, which can influence the electric and ionic conductivities substantially, are known to have a significant effect on good battery performances. The over-potentials of the discharging step are not significantly affected.

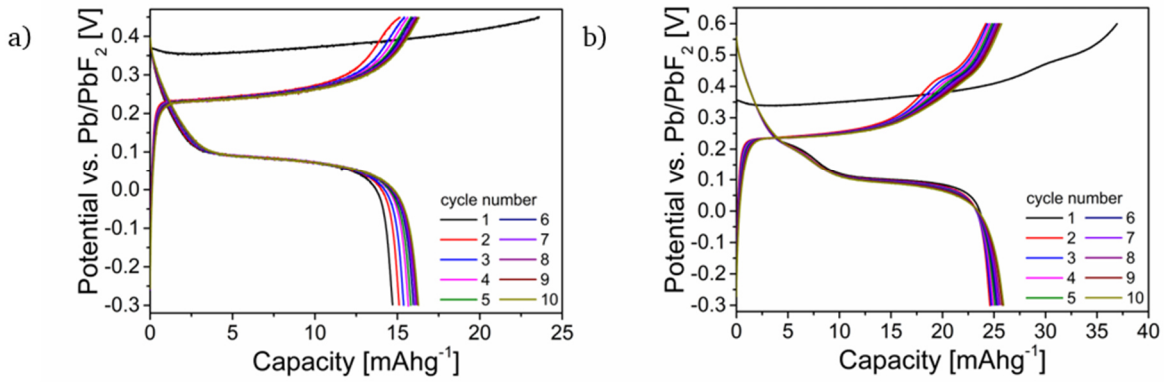

Figure 4-109: Cycling curves of cells $La_{1.3}Sr_{1.7}Mn_2O_7$ against Pb/PbF_2 cycled for 10 cycles between the charging cut-off potential 0.45 V (a) and 0.6 V (b) and the discharging cut-off potential -0.3 V.

After the first cycle, the cycling behaviour stays highly stable. Instead of a capacity fading, continuous increase of the capacities are observed. A cumulative increase of ~ 2 $mAhg^{-1}$ is found after ten cycles. While the Coulombic efficiencies of the first cycles are only ~ 65-75 %, starting from the second cycle, efficiencies of 101(2) % are reached. Efficiencies above 100 % could be explained by a reactivation of $La_{1.3}Sr_{1.7}Mn_2O_7F_{1-y}$ formed during the first cycle.

For the detailed investigation of structural changes of the RP-type phases during cycling, different cells were cycled for various cycle numbers. The cells were stopped either at the charged or discharged state. The XRD patterns of the cathode sides of the cycled cells charged to 0.45 V are shown in Figure 4-110. It becomes evident that the diffraction patterns of the cells in the charged state, with exception of the pattern obtained after the initial charging, are very similar. The same is found for the patterns of the cells in the discharged states. In Figure 4-111 the relative phase fractions of the RP-type phases are given in dependence of the number of charging and discharging steps conducted on the cells. Starting from the second cycle, relatively constant phase fractions of $La_{1.3}Sr_{1.7}Mn_2O_7$ and $La_{1.3}Sr_{1.7}Mn_2O_7F_{1-y}$ are found within the charged cells. Only ~ 10 % of residual $La_{1.3}Sr_{1.7}Mn_2O_7$ is found, whereas after the first cycle still ~ 40 % are present. After discharging, all cells contain a mixture of $La_{1.3}Sr_{1.7}Mn_2O_7$, $La_{1.3}Sr_{1.7}Mn_2O_7F_{1-y}$ and the intermediate phase. The strong decrease of the phase fractions of $La_{1.3}Sr_{1.7}Mn_2O_7F_{1-y}$ and the increase of $La_{1.3}Sr_{1.7}Mn_2O_7$ and the intermediate phase demonstrates the successful partial re-defluorination upon discharging. Higher fractions of $La_{1.3}Sr_{1.7}Mn_2O_7$ are found compared to the intermediate phase. Furthermore, the phase fractions of these phases remain almost constant within differently long cycled cells, starting directly form the first cycle. Between the charged and discharged states, an average increase of $La_{1.3}Sr_{1.7}Mn_2O_7$ from ~ 10 to 50 % and an average decrease of $La_{1.3}Sr_{1.7}Mn_2O_7F_{1-y}$ from ~ 90 to 15 % takes place. The remaining fraction of ~ 35 % forms the intermediate phase in the discharged cells. Overall, the strong changes in relative phase fractions show that high amounts of the active material contribute to the redox reactions during charging and discharging.

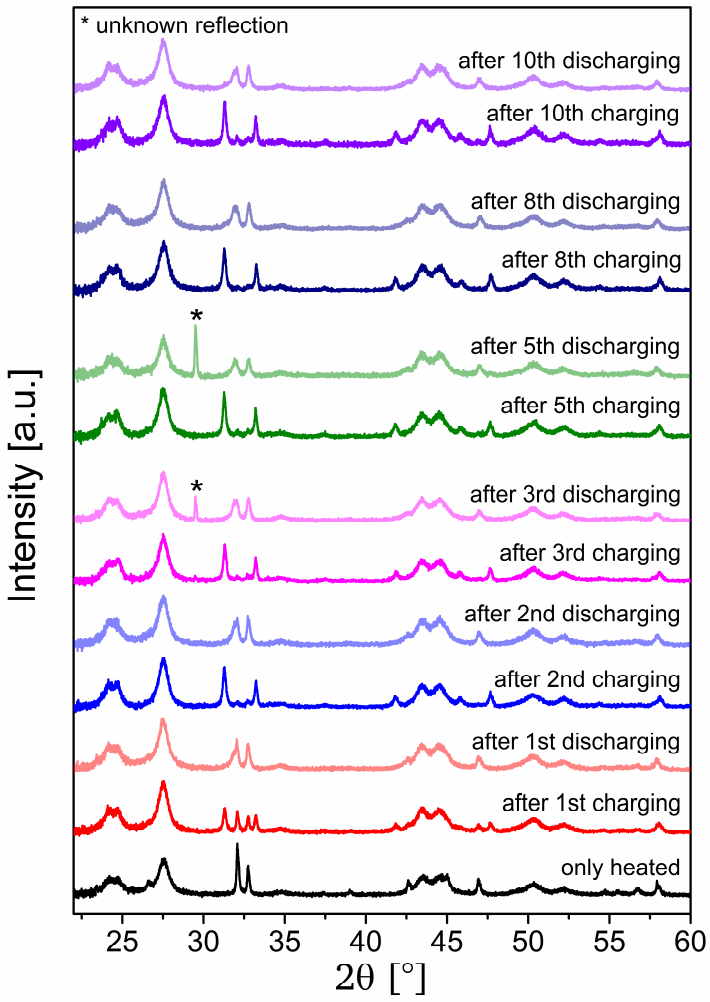

Figure 4-110: X-ray diffraction patterns of cathode sides of cells $La_{1.3}Sr_{1.7}Mn_2O_7$ against Pb/PbF_2 cycled for various cycle numbers between the charging cut-off potential 0.45 V and the discharging cut-off potential -0.3 V. Patterns of cathode sides of cells within the charged and discharged states are shown. The unknown reflection (marked with *) at ~ 29.5° is probably due to an impurity on the sample holder used for measuring of the sample. For reference, a cell, which was only heated (discharged state), is given.

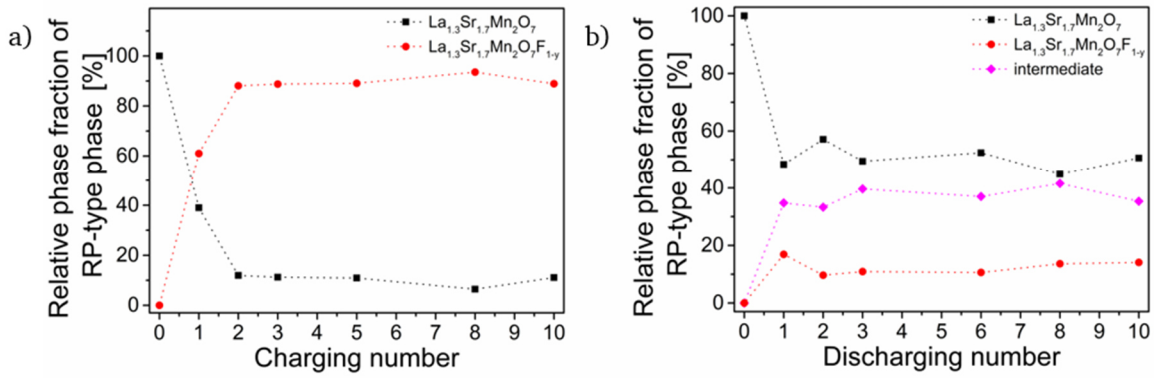

Figure 4-111: Relative phase fractions of $La_{1.3}Sr_{1.7}Mn_2O_7$, $La_{1.3}Sr_{1.7}Mn_2O_7F_{1-y}$ and an intermediate phase in the cathode sides of cells $La_{1.3}Sr_{1.7}Mn_2O_7$ against Pb/PbF_2 cycled for various cycle numbers between the charging cut-off potential 0.45 V and the discharging cut-off potential -0.3 V. The fractions of cathode sides of cells within the charged (a) and discharged (b) state are shown. For the calculation of the relative phase fractions of the RP-type phases, the phase fraction of $La_{0.9}Ba_{0.1}F_{2.9}$ was not taken into account. The unit cell volumes and lattice parameters of the RP-type phases are given in Figure 6-31 and Figure 6-32 in the appendix.

The XRD patterns of the cycled cells charged to 0.6 V are shown in Figure 4-112. As for the cycled cell charged to the cut-off potential of 0.45 V, the changes in the diffraction patterns of the cathode sides of the cells are consistent for all cells in the charged or discharged state. Remarkably, no differences between the first and the subsequent cycles can be observed. The obtained relative phase fractions of the RP-type phases (Figure 4-113) confirm this observation. Starting from the first cycle, the phase fractions of $La_{1.3}Sr_{1.7}Mn_2O_7$ and $La_{1.3}Sr_{1.7}Mn_2O_7F_{1-y}$ remain with ~ 5 and 95 % relatively constant within the charged cells. After the tenth charging, additionally ~ 10 % $La_{1.3}Sr_{1.7}Mn_2O_7F_{2-x}$ are found at the costs of $La_{1.3}Sr_{1.7}Mn_2O_7F_{1-y}$, indicating an increased fluorination of a part of the RP-type phases. After discharging, all cells contain again a mixture of $La_{1.3}Sr_{1.7}Mn_2O_7$, $La_{1.3}Sr_{1.7}Mn_2O_7F_{1-y}$ and the intermediate phase. However, higher average fractions of the intermediate phase of ~ 55 % and lower phase fractions of $La_{1.3}Sr_{1.7}Mn_2O_7$ and $La_{1.3}Sr_{1.7}Mn_2O_7F_{1-y}$ of ~ 30 and 15 %, respectively, are found compared to the cycled cells, which were only charged to 0.45 V. Therefore, less ferromagnetic $La_{1.3}Sr_{1.7}Mn_2O_7$ is obtained after discharging. In addition to the higher phase fractions of these phases, also the unit cell volumes and lattice parameters *c* are again higher compared to the cycled cells charged to 0.45 V (Figure 6-31 and Figure 6-34), suggesting higher fluoride contents.

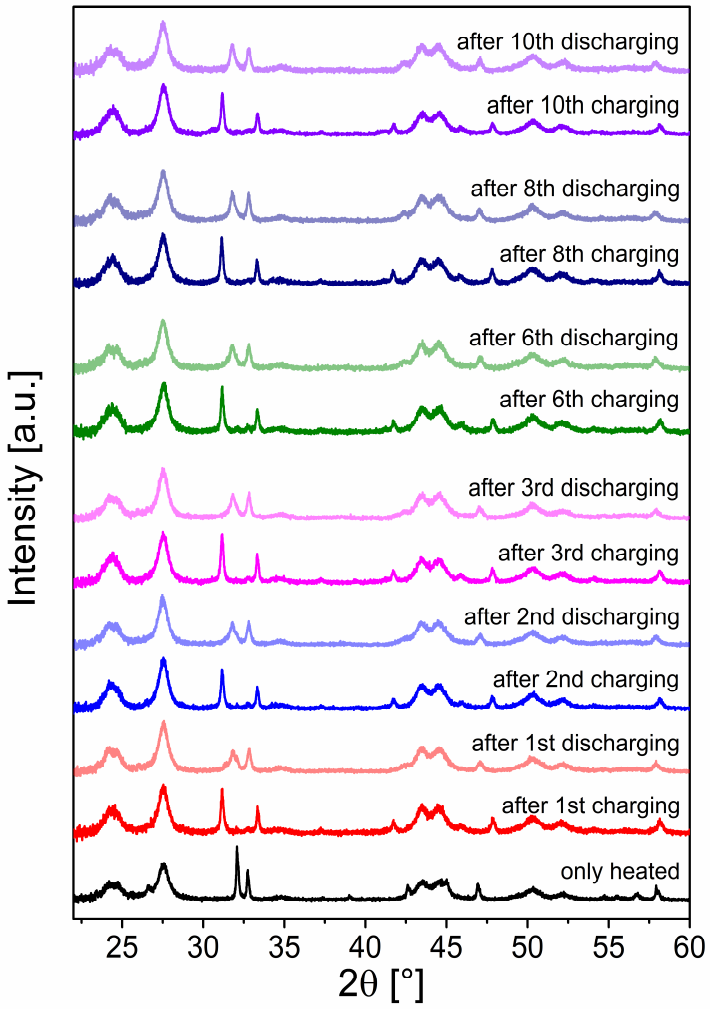

Figure 4-112: X-ray diffraction patterns of cathode sides of cells $La_{1.3}Sr_{1.7}Mn_2O_7$ against Pb/PbF_2 cycled for various cycle numbers between the charging cut-off potential 0.6 V and the discharging cut-off potential -0.3 V. Patterns of cathode sides of cells within the charged and discharged states are shown. For reference, a cell, which was only heated (discharged state), is given.

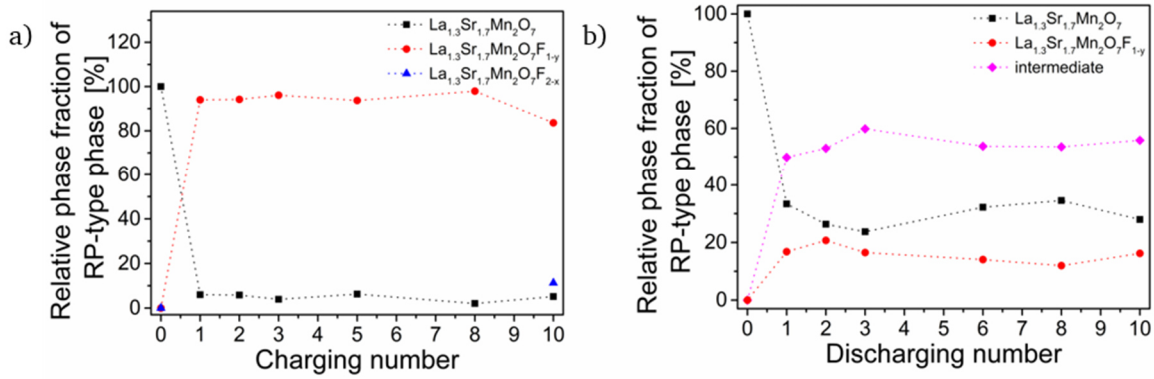

Figure 4-113: Relative phase fractions of $La_{1.3}Sr_{1.7}Mn_2O_7$, $La_{1.3}Sr_{1.7}Mn_2O_7F_{1-y}$ and an intermediate phase in the cathode sides of cells $La_{1.3}Sr_{1.7}Mn_2O_7$ against Pb/PbF_2 cycled for various cycle numbers between the charging cut-off potential 0.6 V and the discharging cut-off potential -0.3 V. The fractions of cathode sides of cells within in the charged (a) and discharged (b) state are shown. For the calculation of the relative phase fractions of the RP-type phases, the phase fraction of $La_{0.9}Ba_{0.1}F_{2.9}$ was not taken into account. The unit cell volumes and lattice parameters of the RP-type phases are given in Figure 6-33 and Figure 6-34 in the appendix.

In addition to the cycling over ten cycles, another cell was cycled between the cut-off conditions of 0.45 and -0.3 V for 45 cycles. With increasing cycle numbers, the discharging plateau becomes less distinctive, but no significant capacity fading or lower Coulombic efficiencies are found. With respect to reversible magnetisation tuning via continuous cycling, these findings are promising.

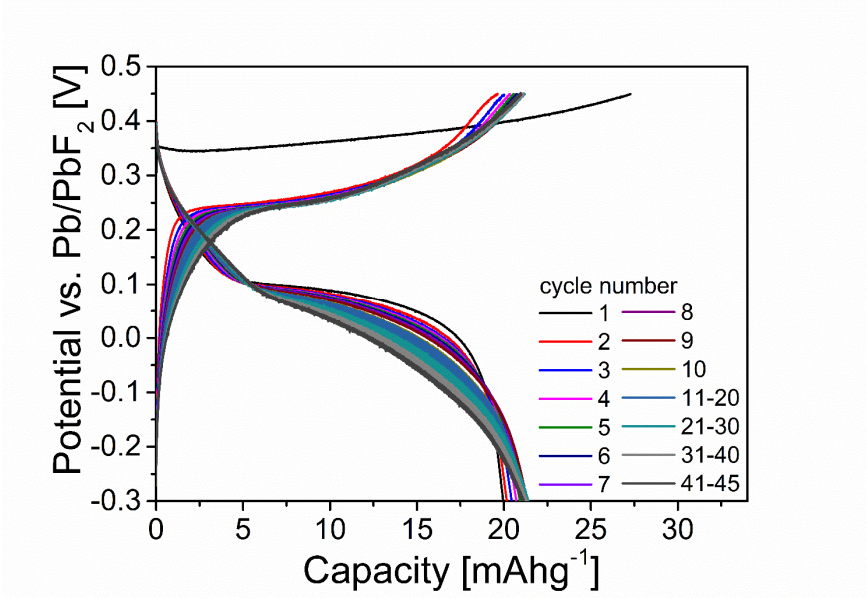

Figure 4-114: Cycling curves of cells $La_{1.3}Sr_{1.7}Mn_2O_7$ against Pb/PbF_2 cycled for 45 cycles between the charging cut-off potential 0.6 V and the discharging cut-off potential -0.3 V.

4.2.3.4.2 Magnetisation study of the cycled phases

The M(T) curves of cells, which were operated between the cut-off conditions of 0.45 and -0.3 V for various cycle numbers and stopped either in the charged or discharged state are shown in Figure 4-115. After the first cycle, the subsequent cycling appears to lead to the stabilisation of two states due to the different magnetic contributions of the RP-type phases present within the scratched-off cathode sides of the charged or discharged cells. During the first cycle, the system seems to stabilise, which explains the deviations of the magnetic

moments to the other cycles (see also section 4.2.3.4.1). The charged cells show significantly lower magnetic moments over the entire temperature range compared to the discharged cells. Since the discharged cells contain considerably higher phase fractions of ferromagnetic $La_{1.3}Sr_{1.7}Mn_2O_7$, higher overall magnetic moments per Mn ion are measured and the increase is stronger at T_c. The Curie temperatures of all cells remain close to the temperature of the heated reference cell.

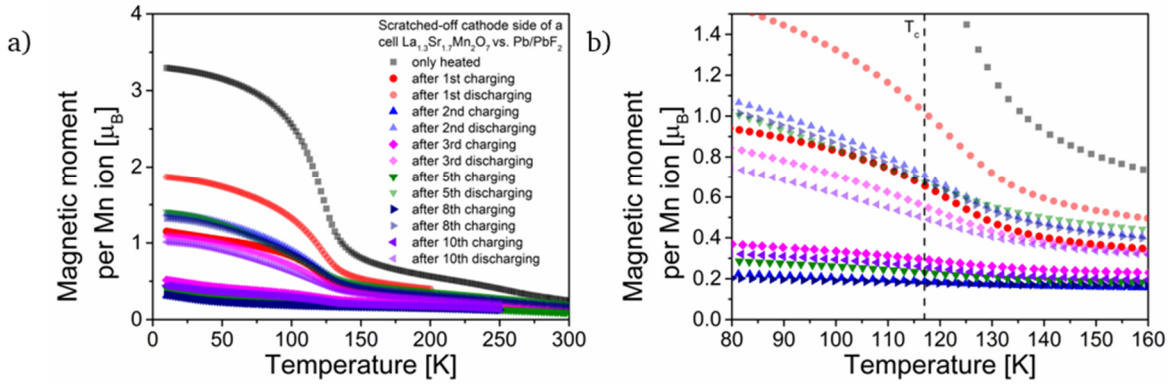

Figure 4-115: Comparison of FC M(T) curves of scratched-off cathode side of cells $La_{1.3}Sr_{1.7}Mn_2O_7$ against Pb/PbF_2 cycled for various cycle numbers between the charging cut-off potential 0.45 V and the discharging cut-off potential -0.3 V measured at μ_0 = 1 T (a) and a magnification of the M(T) curves in the T_c temperature region (b). Measurements of scratched-off cathode sides of cells within the charged and discharged states are shown. For reference, a cell, which was only heated (discharged state), is given.

It is also interesting to mention that M(H) curves of the cycled cells show a change in the hysteresis curves with slightly higher coercivity compared to the heated reference cell (Figure 6-35 and Figure 6-36). This coercivity remains stable within errors comparing different cycled cells and seems to be independent on the charging cut-off conditions and the charging or discharging state.

A comparison of the magnetic moments per Mn ion measured at 10 K in dependence of the charging and discharging state as well as the cycling number is given in Figure 4-116. The potential vs. time curve of the cell, which was cycled over ten cycles, illustrates at which points of the charging and discharging process the individual cells were stopped. Starting from the second cycle, the change in the magnetic moments within the charged and discharged states remains relatively constant and is well reproducible with respect to the increasing cycle numbers. The variations within one state of the cells are most likely related to errors introduced on weighing of the small sample amounts for the subsequent calculation of the magnetic moments. The moments fluctuate between ~ 0.3 to 0.5 μ_B per Mn ion for the charged cells and ~ 1 to 1.4 μ_B per Mn ion for the discharged cells, resulting in an average magnetic moment change of 0.84 μ_B per Mn ion. The relative magnetisation change is ~ 67 %.

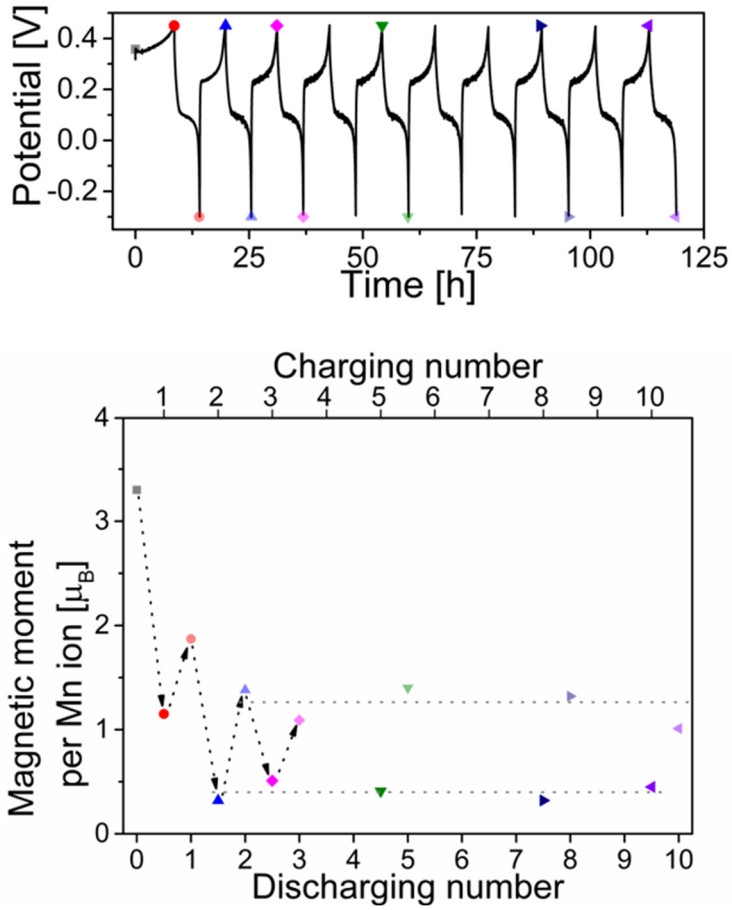

Figure 4-116: Magnetic moments per Mn ion of scratched-off cathode side of cells $La_{1.3}Sr_{1.7}Mn_2O_7$ against Pb/PbF_2 cycled for various cycle numbers between the charging cut-off potential 0.45 V and the discharging cut-off potential -0.3 V measured at 10 K and μ_0 = 1 T. The moments are given in dependence of the number of charging and discharging steps. The potential vs. time curve shows at which cycling states the cells were stopped.

The M(T) curves of the cells, which were cycled between 0.6 and -0.3 V (Figure 4-117), reveal also significant differences between the magnetisation of the charged and discharged cells. As is observed in section 4.2.3.3.2, a broadening of the transition with a shift towards lower temperatures between ~ 55 and 68 K is observed for the discharged cells.

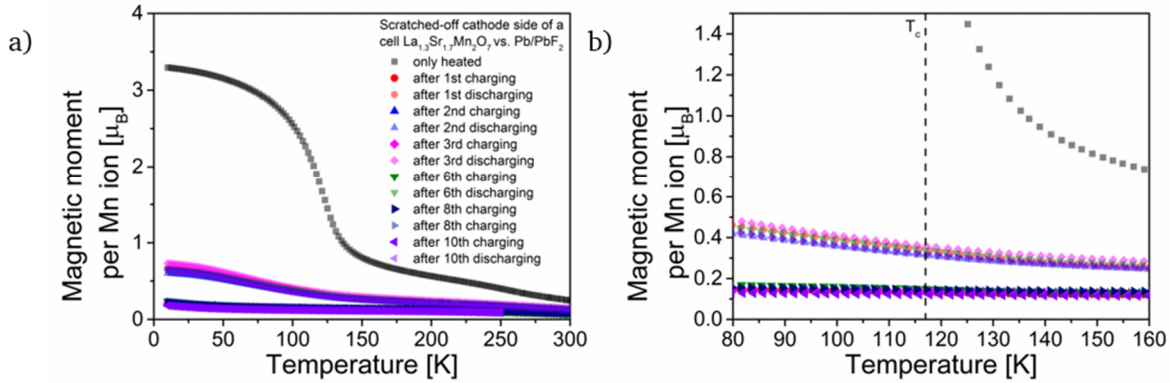

Figure 4-117: Comparison of FC M(T) curves of scratched-off cathode side of cells $La_{1.3}Sr_{1.7}Mn_2O_7$ against Pb/PbF_2 cycled for various cycle numbers between the charging cut-off potential 0.6 V and the discharging cut-off potential -0.3 V measured at μ_0 = 1 T (a) and a magnification of the M(T) curves in the T_c temperature region (b). Measurements of scratched-off cathode side of cells within the charged and discharged states are shown. For reference, a cell, which was only heated (discharged state), is given.

The magnetic moments per Mn ion (Figure 4-118) derived from the M(T) curves at 10 K stay relatively stable for the charged and discharged states over the first ten cycles. The moments lay between ~ 0.17 and 0.23 μ_B per Mn ion for the charged cells and between ~ 0.60 and 0.73 μ_B per Mn ion for the discharged cells. Therefore, the moments found in the charged and discharged states for the cells with the cut-off charging potential of 0.45 V are approximatly twice as high as the moments observed for the cells charged to the higher cut-off potential. Neverthless, the relative magnetisation changes are nearly the same, since it is ~ 68 % for the higher charged cells.

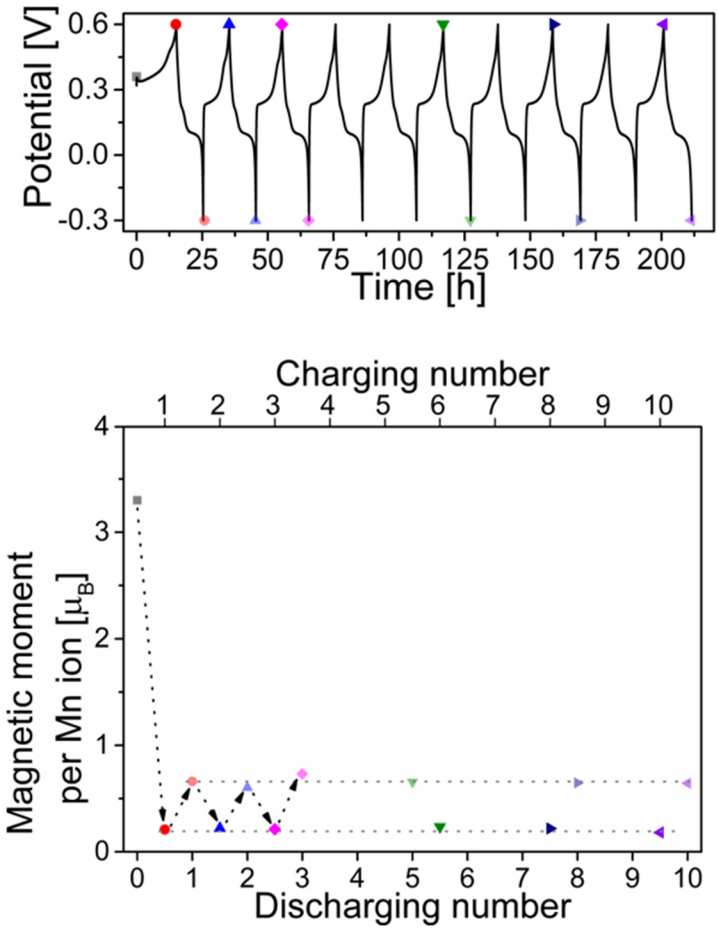

Figure 4-118: Magnetic moments per Mn ion of scratched-off cathode side of cells $La_{1.3}Sr_{1.7}Mn_2O_7$ against Pb/PbF_2 cycled for various cycle numbers between the charging cut-off potential 0.6 V and the discharging cut-off potential -0.3 V measured at 10 K and μ_0 = 1 T. The moments are given in dependence of the number of charging and discharging steps. The potential vs. time curve shows at which cycling states the cells were stopped.

This shows that by choosing the lower charging cut-off potential, the absolute magnetic moments, observed after discharging, can be increased, but the relative change between the charged and discharged state remains nearly the same. Since the cells can be operated at very low potentials, the presented cells possess the highest magnetoelectric voltage couplings with high magnetoelectric voltage coefficients $\alpha = \Delta M/(\Delta V \cdot M)$ for tuneable magnetic systems, which has been reported so far [34, 35].

4.2.3.5 Summary

It is demonstrated that the topochemical modification of the n = 2 RP-type compound $La_{1.3}Sr_{1.7}Mn_2O_7$ to $La_{1.3}Sr_{1.7}Mn_2O_7F_x$ is possible within the cathode composite containing $La_{1.3}Sr_{1.7}Mn_2O_7$ in FIBs. In agreement with previous reports on chemically prepared equivalents [6, 21], the obtained fluorinated phases $La_{1.3}Sr_{1.7}Mn_2O_7F_{1-y}$ and $La_{1.3}Sr_{1.7}Mn_2O_7F_{2-x}$ undergo a staged fluorination process with a consecutive filling of the two interstitial layers. This leads to step-wise expansions of the *c* lattice parameters from ~ 20.2 Å in $La_{1.3}Sr_{1.7}Mn_2O_7$ to ~ 22.0 Å in $La_{1.3}Sr_{1.7}Mn_2O_7F_1$ and finally to ~ 23.6 Å in $La_{1.3}Sr_{1.7}Mn_2O_7F_1$, which is accompanied by corresponding contractions of the *a* lattice parameters, caused by the increased oxidation state of Mn. The major part of the electrochemical fluorination takes place at potentials below 1 V. The formation of $La_{1.3}Sr_{1.7}Mn_2O_7F_{1-y}$ is observed for potentials ≤ 0.7 V, whereas the formation of $La_{1.3}Sr_{1.7}Mn_2O_7F_{2-x}$ took place at potentials > 0.7 V. Phase separation into the initial RP-type phase $La_{1.3}Sr_{1.7}Mn_2O_7$ and the respective fluorinated phases suggests the presence of certain stability ranges for $La_{1.3}Sr_{1.7}Mn_2O_7F_{1-y}$ and $La_{1.3}Sr_{1.7}Mn_2O_7F_{2-x}$. For the stability of $La_{1.3}Sr_{1.7}Mn_2O_7F_{1-y}$, a minimum fluoride content per formula unit of ~ 0.6 is determined. The fluorination leads to significant changes of the magnetisation in the cathode composite. Charging to higher potentials results in lower magnetic moments per Mn ion. These decreases are directly related to the decreasing relative phase fraction of the ferromagnetic phase $La_{1.3}Sr_{1.7}Mn_2O_7$ [224]. The fluorinated phases appear to have no significant contribution to the magnetisation in relation to the ferromagnetic phase. The transition temperatures remain constant for all samples containing residual $La_{1.3}Sr_{1.7}Mn_2O_7$. The charging experiments show that charging cut-off potentials of 0.45 and 0.6 V are suitable. These potentials can be regarded as the best compromises between a strong decrease of the phase fractions of remaining $La_{1.3}Sr_{1.7}Mn_2O_7$, while no $La_{1.3}Sr_{1.7}Mn_2O_7F_{2-x}$ is formed yet, which would lead to larger volume changes upon re-defluorination. In addition, these low potentials ensure high efficiencies and the shortest possible charging times.

The discharging of cells, which were charged to 0.45 and 0.6 V, respectively, shows that a partial re-defluorination of $La_{1.3}Sr_{1.7}Mn_2O_7F_{1-y}$ is possible. However, the complete re-formation of $La_{1.3}Sr_{1.7}Mn_2O_7$ is not observed and instead a large fraction of the re-defluorinated phases found after discharging is made up of an intermediate phase, which has a unit cell volume between those of the initial $La_{1.3}Sr_{1.7}Mn_2O_7$ and $La_{1.3}Sr_{1.7}Mn_2O_7F_{1-y}$. This shows that residual fluoride ions are present within the host lattice of the intermediate phase. Its phase fraction increases when the cells are charged to higher potentials. Moreover, more fluoride ions remain in the RP-type phases after charging to higher potentials. Slightly changed lattice parameters of $La_{1.3}Sr_{1.7}Mn_2O_7$, in particular found in the higher charged cells, reveal that even a few fluoride ions remain within the structure. Additionally, $La_{1.3}Sr_{1.7}Mn_2O_7F_{1-y}$ remains present. Therefore, it can be concluded that no full structural reversibility is obtained after discharging. Magnetic measurements show that the ferromagnetic interactions are partly restored upon the re-formation of $La_{1.3}Sr_{1.7}Mn_2O_7$ after discharging. For the cells with a charging cut-off condition of 0.45 V, the obtained magnetic moments can be directly related to the phase fraction of $La_{1.3}Sr_{1.7}Mn_2O_7$ within the cathode composite. For the higher charged cells, a shift of the transition temperatures of the starting phase to lower temperatures is found, which is due to the trapped fluoride ions, causing a wide distribution of ferromagnetic transition temperatures. These fluoride ions could cause reduced magnetic interactions, explaining to lower magnetic moments found within the higher charged cells after discharging.

For cycling experiments a discharging cut-off potential of -0.3 V was chosen and the cycling behaviour for both charging cut-off potentials was investigated for the first ten cycles. Interestingly, after the first cycle, the redox reactions, taking place during charging, occur at lower potentials compared to the first charging step. No other significant shifts are observed in the consecutive cycles. This reduction in over-potential might be related to beneficial side reactions, taking place during the first charging, which facilitate the fluorination in the subsequent cycles. In addition, starting from the second cycle, Coulombic efficiencies close to 100 % are observed, suggesting the absence of irreversible reactions. Several cells were charged between the cut-off potentials for various cycle numbers and the structure and magnetisation changes were examined in dependence of the cycle number as well as the charging or discharging state. Different observations are made for the cycled cells depending on the charging cut-off condition. Starting from the second cycle, the cells, which were only charged to 0.45 V, shows average phase fractions of ~ 10 % of $La_{1.3}Sr_{1.7}Mn_2O_7$ and ~ 90 % of $La_{1.3}Sr_{1.7}Mn_2O_7F_{1-y}$ in their charged state, independent of the cycle number. The discharging leads to the formation of relatively stable average phase fractions of ~ 50 % of $La_{1.3}Sr_{1.7}Mn_2O_7$, ~ 35 % of the intermediate phase and ~ 15 % of $La_{1.3}Sr_{1.7}Mn_2O_7F_{1-y}$. The cycled cells, which were charged to 0.65 V, possess, in contrast, average phase fractions of ~ 5 % of $La_{1.3}Sr_{1.7}Mn_2O_7$ and ~ 95 % of $La_{1.3}Sr_{1.7}Mn_2O_7F_{1-y}$. In their discharged state, ~ 30 % of $La_{1.3}Sr_{1.7}Mn_2O_7$, ~ 55 % of the intermediate phase and ~ 15 % of $La_{1.3}Sr_{1.7}Mn_2O_7F_{1-y}$ are found. In addition, the phases seem to contain more fluoride ions in comparison to the phases obtained after cycling between the lower charging cut-off potential and -0.3 V. Even though the charging to higher potentials results in lower phase fractions of $La_{1.3}Sr_{1.7}Mn_2O_7$, which leads to lower magnetisations of the cells in the charged state, the difference between its phase fractions in the charged and discharged states is smaller compared to the cycled cells with the lower charging cut-off condition. This results also in lower magnetisation changes for the cells with the higher charging cut-off condition. For the cells charged to 0.45 V, starting from the second cycle, relatively stable oscillations of the magnetic moments per Mn ion between ~ 0.3 to 0.5 μ_B and ~ 1 to 1.4 μ_B for the charged and discharged states of the cycled cells, respectively, in dependence of the cycle number are found. These fluctuations correspond to a relative magnetisation change of ~ 67 %. For the cycled cells, which were charged to 0.65 V, significantly lower moments and lower absolute magnetisation changes are found. The moments vary between ~ 0.17 to 0.23 μ_B and ~ 0.60 to 0.73 μ_B between the charged and discharged states, respectively. This corresponds to a relative change of ~ 68 % and shows that charging to lower potentials results in higher absolute changes of the magnetisation, while the relative changes stay nearly the same.

It is shown that a cycling between a strong and a weak ferromagnetic state is possible due to the fluorination of $La_{1.3}Sr_{1.7}Mn_2O_7$ and its partial re-defluorination. The comparatively small potential range at overall low potentials, in which the reactions occur, results in one of the highest reported magnetoelectric voltage coefficient for tuneable magnetic systems. This illustrates the potential of reversible electrochemical fluorination reactions for the tuning of material properties.

5 Conclusions and Outlook

Within this work, it is demonstrated that topochemical fluorination and defluorination methods based on different chemical and electrochemical approaches can be used for the successful synthesis of Ruddlesden-Popper-type phases with changed crystal and electronic structures as compared to their precursor phases. A (reversible) tuning of magnetic properties is also found to be possible due to the (reversible) intercalation and deintercalation of fluoride ions. In particular, the combination of consecutively performed topochemical modification methods are shown to results in the formation of otherwise inaccessible materials, opening up a widely unexplored research field.

Different two-step modification routes of Ruddlesden-Popper-type oxides $A_{n+1}B_nO_{3n+1}$ via a non-oxidative fluorination, leading to the formation of metastable compounds with compositions $A_{n+1}B_nO_{3n+1-x}F_{2x}$ with $0 < x \leq 2$, followed by a reductive defluorination or an oxidative post-fluorination were investigated. The following material systems were studied: Sr_2TiO_4, $Sr_3Ti_2O_7$ and La_2NiO_{4+d}. For the second step, in each case, chemical and electrochemical approaches, the latter based on the reduction or oxidation within a fluoride-ion battery were applied. For the chemical defluorination, a process via a sodium hydride-based reduction was developed and successfully applied. The chemical post-fluorination was attempted using highly oxidising F_2 gas. A variety of Ruddlesden-Popper-type oxyfluorides with different fluoride contents were synthesised and examined using a combination of several characterisation techniques to determine their structural and magnetic properties. The chemical defluorination process facilitates the in-depth analysis of the reduced phases and the obtained characteristics could be used to gain, in addition, an understanding about the electrochemically formed phases, as similar structural and property changes were found to occur for both investigated topochemical defluorination routes. Furthermore, the reversible magnetoelectric tuning based on the reversible electrochemical fluorination of ferromagnetic $La_{1.3}Sr_{1.7}Mn_2O_7$ in a fluoride-ion battery was examined.

It is interesting to relate the manifold and complex findings made for the different material systems and to discuss resulting implications for future investigations. This chapter does not primarily aim to summarize all findings; for a more detailed overview over the separate material systems investigated with respect to the used chemical or electrochemical modification method, the reader is referred to the summaries provided at the end of every subchapter in the previous chapter. The following section, is divided into three segments, in which a comparative reflection is provided upon (i) the chemical fluorination of Ruddlesden-Popper-type oxides $A_{n+1}B_nO_{3n+1}$ to oxyfluorides $A_{n+1}B_nO_{3n+1-x}F_{2x}$ and their chemical hydride-based defluorination, (ii) the reversible electrochemical defluorination and fluorination of oxyfluorides $A_{n+1}B_nO_{3n+1-x}F_{2x}$ and the resulting consequences for a further development of intercalation-based fluoride-ion batteries, as well as (iii) the (reversible) tuning of magnetic properties, in particular, in the context of the reversible electrochemical defluorination and/or fluorination of $La_2NiO_3F_2$ and $La_{1.3}Sr_{1.7}Mn_2O_7$.

i. *Chemical fluorination of Ruddlesden-Popper-type oxides $A_{n+1}B_nO_{3n+1}$ to oxyfluorides $A_{n+1}B_nO_{3n+1-x}F_{2x}$ and their chemical hydride-based defluorination:* The non-oxidative fluorination of the investigated Ruddlesden-Popper-type oxides using a fluorine-

containing polymer took place via a coupled substitution and insertion process, in which for each replaced oxide ion two fluoride ions were inserted. The obtained oxyfluorides $Sr_2TiO_3F_2$ and $Sr_3Ti_2O_5F_4$ showed strong expansions along the *c* axis due to the substitution of apical oxide ions by fluoride ions and the intercalation of fluoride into the interstitial sites, which is commonly observed in such reactions. In contrast to this, in $La_2NiO_3F_2$, a strong orthorhombic distortion with a half-occupation of every interstitial layer in a channel-like manner, which is accompanied by a strong tilting of NiX_6 octahedra, was found. The origins of these differences in tilting are best understood adopting the concept of Goldschmidt's tolerance factor, which is significantly smaller for the nickelate system compared to the titanate system.

The subsequently performed studies on the chemical defluorination behaviour of the synthesised oxyfluorides in dependence of the amount of reducing agent NaH revealed different reduction mechanisms of the Ti-based oxyfluorides in comparison to the Ni-based oxyfluoride. The Ti-based oxyfluorides showed a similar reduction behaviour and the reduction mechanism can be best described as a combination of a reductive defluorination and partial fluoride-hydride substitution, resulting in the formation of mixtures of Ruddlesden-Popper-type phases with different crystal structures and fluoride contents. The reduction of $Sr_3Ti_2O_5F_4$ led to phase mixtures of reduced phases, indicating similar stabilities of these phases in their range of existence. For the defluorination of $Sr_2TiO_3F_2$, however, two reduced phases were identified, which were found for certain NaH amounts to be nearly the only Ruddlesden-Popper-type phase in the reduction products besides the side products. For all other NaH amounts, phase mixtures of these two phases were found. Furthermore, it was shown that varying degrees of fluoride-hydride substitution occurred during the reactions of the different oxyfluorides with NaH. While the hydride contents in the reduced Ni-based oxyfluorides are only minor, higher degrees of such substitution reactions were found in the reduced Ti-based oxyfluorides. In this context, the dehydration of the obtained phases under vacuum could lead to a significant further reduction of the Ti oxidation states. Such experiments would be clearly interesting for future investigations. In addition, a complete dehydration would allow for a better comparability of chemically and electrochemically obtained phases, especially when relatively high hydride contents are found. For both Ti-based oxyfluorides, no significant decomposition or amorphisation and a nearly stoichiometric extraction of fluoride were observed during the defluorination process.

The reduction of $La_2NiO_3F_2$, on the other hand, led to a substantial decomposition and amorphisation. A complex reduction behaviour with reductive defluorination taking place in parallel to substantial decomposition and partial fluoride-oxide substitution reactions was observed. This difference in the observed degree of decomposition between Ti-based and Ni-based oxyfluorides is related to different exothermicities of the defluorination reactions, which can enhance the decomposition of the metastable oxyfluorides. As is qualitatively depicted in Figure 5-1, the change of the Gibb's free energy ΔG of the defluorination reaction of the Ni-based oxyfluoride is more negative than ΔG of the respective defluorination of the Ti-based oxyfluorides. The difference is represented with a blue arrow. This can be also explained based on the relation of ΔG to ΔE with ΔE being the difference between the redox potentials of the Ti-based Ruddlesden-Popper-type oxyfluorides ($Ti^{3+}|Ti^{4+}$) or of the Ni-based oxyfluoride

($Ni^{+}|Ni^{2+}$) to the potential of the reductive H^{-} species ($2H^{-}|H_2$). Since the potential of $Ti^{3+}|Ti^{4+}$ is more negative than the potential of $Ni^{+}|Ni^{2+}$, a more negative ΔG value for the reduction of the Ni-based oxyfluoride is found. The change of entropy ΔS is dominated by the formation of gaseous H_2 and, therefore, similar for both defluorination processes. When neglecting these almost equal contributions of ΔS to ΔG in both processes, it can be assumed that ΔG of the respective defluorination is in first approximation equal to the enthalpy of reaction ΔH and it follows that the defluorination of the Ni-based oxyfluoride is stronger exothermal compared to the defluorination of Ti-based oxyfluorides. Due to the metastability of the RP-type oxyfluorides, this exothermicity might lead to a significant decomposition. Especially, for the Ni-based oxyfluoride, the enthalpic contribution seems to be high enough to overcome the activation barrier for the decomposition.

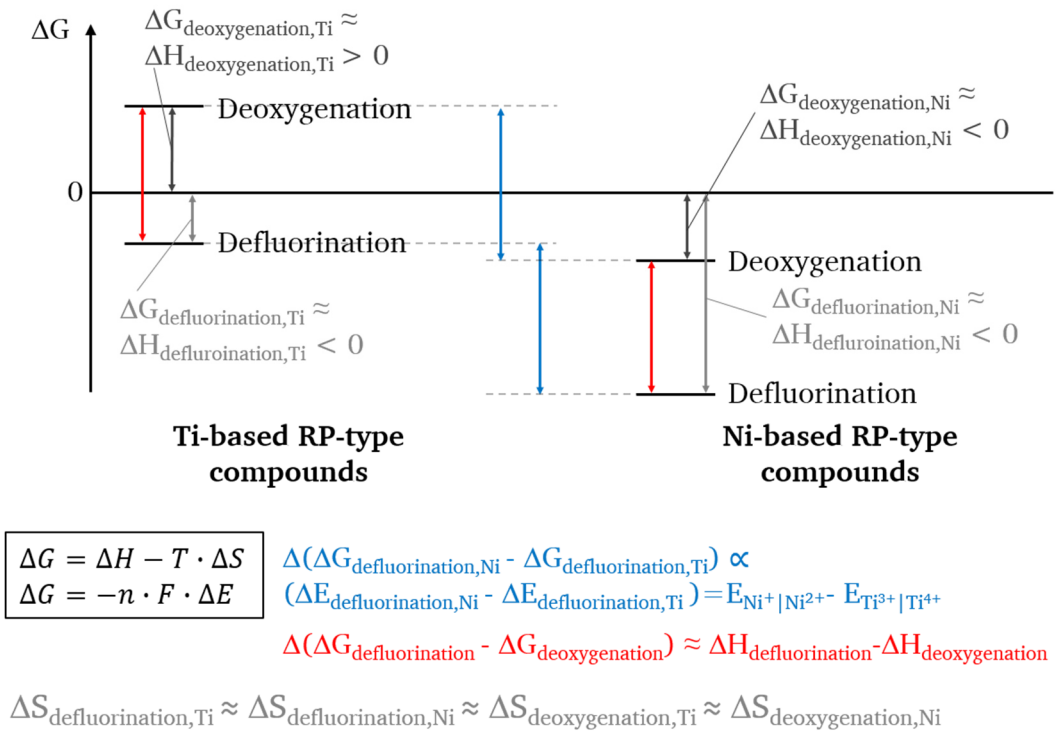

Figure 5-1: Schematic illustration of the relationships between the Gibb's free energy ΔG, the enthalpy of reaction ΔH, the change in entropy ΔS and the difference between redox potentials ΔE of defluorination and deoxygenation reactions of Ti- and Ni-based Ruddlesden-Popper-type oxides and oxyfluorides.

The same considerations can be made for the respective deoxygenation reactions of the Ruddlesden-Popper-type oxides. While it was shown within this work that a deoxygenation of Sr_2TiO_4 is not possible using NaH at an reaction temperature of 300 °C, the deoxygenation of higher-order Ruddlesden-Popper-type lanthanum nickelates with n = 2, 3 and ∞ [96-100, 103, 104] has been shown to be possible at even lower or comparable temperatures. Therefore, it can be concluded that ΔG of the deoxygenation of Ti-based oxides is endergonic, whereas the deoxygenation of Ni-based oxides is exergonic. The difference between the ΔG values of the deoxygenations and the defluorinations (red arrow in Figure 5-1) is mainly related to the differences of ΔH of the involved reactions. ΔH is dependent on the energetic contributions of the Ruddlesden-Popper-type parent oxyfluorides or oxides and of the respective reduced phases formed during the reactions. These energies are related to the structures of the

involved phases, the type of anion, which is extracted, and the site of this anion. Additionally, the energetic contributions of the side products NaF and Na_2O formed during the defluorination and deoxygenation, respectively, have a considerable influence on ΔH. This is related to the much higher lattice energy of Na_2O in comparison to NaF. A reductive deoxygenation under the formation of NaOH can be, moreover, excluded since the involved $H_2|2H^+$ redox potential does not provide sufficient reductive power, which is due to a higher potential of the $H_2|2H^+$ redox couple in relation to $Ti^{3+}|Ti^{4+}$ and $Ni^+|Ni^{2+}$.

These conceptual consideration can provide a path for additional research: For future investigations of the defluorination behaviour of Ruddlesden-Popper-type oxyfluorides it becomes clear that a complex balancing between the metastability and thermodynamic factors has to be performed. In order to prevent considerable decomposition, a selection of a parent oxyfluoride with a redox potential of the transition metal cation between those of $Ti^{3+}|Ti^{4+}$ and $Ni^+|Ni^{2+}$ might be suitable. This should result in a less negative ΔG value compared to the defluorination of the Ni-based oxyfluoride and, consequently, a reduced exothermicity. In addition to this, it was shown that ΔH and, in particular the enthalpy contribution of the side product, has a significant influence. A different metal hydride, leading to the formation of another metal fluoride, could be used as reducing agent to obtain less negative ΔG values. The selection of a metal hydride with a smaller enthalpy difference to the metal fluoride would lead to a less negative ΔG value with a lower absolute magnitude. In this context, for example KH (Δ_fH^0(KH): -57.7 kJ/mol) [284] and KF (Δ_fH^0(KF): -567.3 kJ/mol) [284] might be suitable candidates. For comparison, NaH and NaF possess standard enthalpies of formation of -56.3 and -576.6 kJ/mol, respectively. The use of KH instead of NaH could, therefore, reduce the enthalpic contribution from the side product by 10.4 kJ/mol. [284]

ii. *Reversible electrochemical defluorination and fluorination of oxyfluorides $A_{n+1}B_nO_{3n+1-x}F_{2x}$ and the resulting consequences for a further development of intercalation-based fluoride-ion batteries:* The feasibility of topochemical modifications of the Ruddlesden-Popper-type oxyfluorides via electrochemical defluorination and post-fluorination in fluoride-ion batteries was also investigated. Arising changes in the crystal structures due to the successful deintercalation and/or intercalation of fluoride ions were related to the chemically formed phases, since the chemically prepared phases can be regarded as the charged states of the Ruddlesden-Popper-type oxyfluorides. A stability of the oxyfluorides within the electrode composite upon heating could only be observed for $Sr_3Ti_2O_5F_4$ and $La_2NiO_3F_2$. Significant decomposition and amorphisation of $Sr_2TiO_3F_2$ was found after the heating of the respective electrode composite under the experimental conditions.

When using $Sr_3Ti_2O_5F_4$ as active anode material, minor changes upon galvanostatic charging, suggesting a small degree of defluorination, were observed. The use of $La_2NiO_3F_2$ as active anode material, having a higher potential against Li|LiF than the Ti-based oxyfluoride, led to a higher degree of defluorination, even though only a partial defluorination of a fraction of the RP-type phases within the anode composite took place. Based on the coupled Rietveld analysis of the chemically reduced $La_2NiO_3F_2$, an approximate composition of $La_2NiO_3F_{1.9}$ could be determined for the

electrochemically reduced phase. A stronger reduction could not be obtained upon prolonged charging. In addition to the defluorination of $La_2NiO_3F_2$, its post-fluorination, when using $La_2NiO_3F_2$ as active cathode material, was investigated. A significant oxidation of $La_2NiO_3F_2$ to a phase with a composition close to $La_2NiO_3F_3$ was observed. Though attempts to prepare this phase via a chemical approach using F_2 gas were performed, only minor phase fractions of the oxidised phase could be obtained and a strong decomposition was observed additionally. This highlights the potential of electrochemical routes as easily controllable synthesis alternatives for topochemical modifications, which are exceedingly difficult to obtain using chemical routes. The structural reversibility of the obtained reduced and oxidised phases upon discharging due to the re-fluorination and re-defluorination could be demonstrated. Continued discharging caused the formation of the respective post-fluorinated or defluorinated phase. Furthermore, sequences of reduction and oxidation reactions were found to facilitate the formation of $La_2NiO_3F_3$ compared to the direct fluorination of $La_2NiO_3F_2$, which suggested an influence of anion disorder, introduced during the prior reduction process, on the resulting product. The influence of disorder is discussed below in more detail.

Motivated by the observed reversibility of the structural changes upon charging and discharging, an investigation of the cycling behaviour was carried out. The performance of cells containing $La_2NiO_3F_2$ in the anode or cathode composites in combination with a Pb/PbF_2 counter electrode were tested. Moreover, the use of the intercalation-based cathode and anode containing La_2NiO_{4+d} and $La_2NiO_3F_2$, respectively, resulted in better cycling stabilities compared to cells with conversion-based Pb/PbF_2 cathodes. However, when using $La_2NiO_3F_2$ as active anode material, a meaningful discharging was only found in the negative potential range due to large over-potentials between the charging and discharging processes. These over-potentials increased further upon cycling of the cells with each subsequent cycle, giving indication for the presence of undesired side reactions, affecting the electronic conductivity of the carbon additive. These irreversible side reactions were found to take place largely in parallel with the desired reactions involving $La_2NiO_3F_2$ during the charging of the electrode composites (Figure 5-2). When using the electrode composite containing $La_2NiO_3F_2$ as anode, a reduction of the conductive additive carbon black was found to take place; when using it as cathode, an oxidation of the carbon black was observed. An effective limitation of these irreversible reactions, facilitating reversible defluorination or fluorination reactions of the Ruddlesden-Popper-type phases even upon extended cycling, could be achieved by narrowing the potential window significantly.

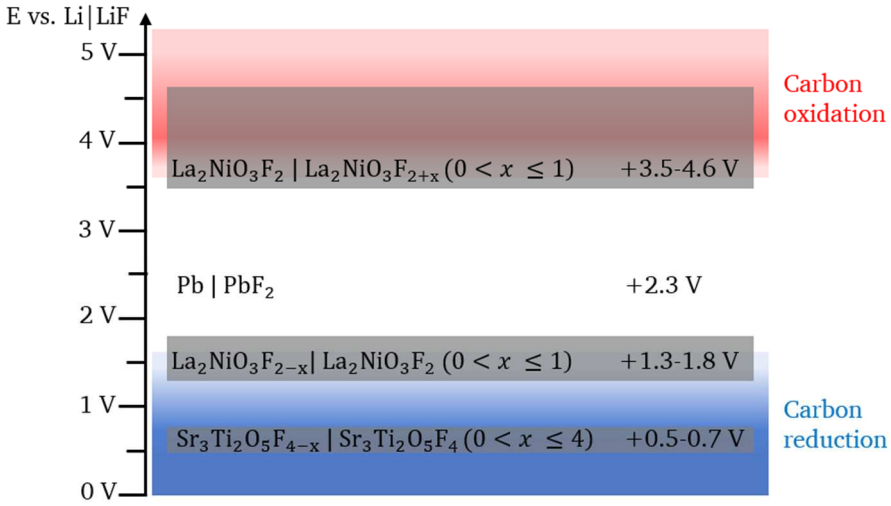

Figure 5-2: Predicted redox potentials of Ruddlesden-Popper-type oxyfluorides investigated as active electrode materials in fluoride-ion batteries in relation to Li|LiF. In addition, the potential ranges, in which the carbon side reactions take place, are shown. It is assumed that the redox potentials of $Sr_2TiO_3F_{2-x}$|$Sr_2TiO_3F_2$ and $Sr_3Ti_2O_5F_{4-x}$|$Sr_3Ti_2O_5F_4$ are comparable.

Figure 5-2 illustrates the influence of the carbon side reactions on the degree of defluorination, which could be obtained when charging the electrode composite containing the stable Ti-based oxyfluoride $Sr_3Ti_2O_5F_4$. The onset of the carbon reduction reaction at lower potentials than would be needed to achieve a reduction of the Ti-based compound might lead to a considerable destruction of the carbon matrix before the desired defluorination of the Ruddlesden-Popper-type compound can take place. Therefore, this defluorination might only occur to a very limited extent, since the electronic conductivity might be already significantly reduced after the first charging step.

In contrast to this detrimental influence of the carbon side reaction, the introduction of anion disorder was found to be beneficial for the reversible deintercalation and intercalation of fluoride ions from/into Ruddlesden-Popper-type $La_2NiO_3F_2$. For the cells containing $La_2NiO_3F_2$ as active cathode composite, continuously improving cycling performances with increasing Coulombic efficiencies were observed with each successive cycle. This might be related to disorder introduced at the interstitial anion sites, created due to the repeated reversible intercalation into $La_2NiO_3F_2$. Additionally, a prior defluorination was also found to be beneficial for a subsequent additional fluorination of $La_2NiO_3F_2$. In contrast to other intercalation-based Ruddlesden-Popper-type active cathode materials such as La_2NiO_{4+d} [19], $La_2NiO_3F_2$ has two independent crystallographic interstitial sites. One of them is energetically much more favourable than the other and an anion ordering is observed. The progressive formation of anion disorder might lead to an approaching of the energetic levels of the interstitial sites, possibly facilitating a subsequent intercalation of fluoride ions into the site with the higher energy upon the fluorination of $La_2NiO_3F_2$. For the defluorination of $La_2NiO_3F_2$, a corresponding effect was already observed after the first deintercalation during to re-intercalation of fluoride ions. The approaching of the site energies is also linked to structural changes, i.e., a reduced degree of tilting of NiX_6 octahedra.

In connection with the findings made for the chemical defluorination of Ruddlesden-Popper-type oxyfluorides, conclusions for future studies on active electrode materials can be drawn. To avoid the carbon oxidation, oxyfluorides based on transition metal cations with lower redox potentials than the onset of the carbon oxidation have to be used as active cathode materials, since this might result in an adequate separation of the redox potentials. On the anode side, a transition metal cation with a higher redox potential compared to the carbon reduction potential has to be used. This separation of the potentials would, however, lead to lower energy densities. In addition, for anode materials with higher potentials, higher ΔG values of the defluorination reactions would be observed. As was shown above, this would potentially lead to a substantial decomposition of the oxyfluoride due to the higher exothermicity of the reaction. The use of carbon black as conductive additive seems to be the biggest issue for the reversible electrochemical defluorination and post-fluorination within fluoride-ion batteries. The deterioration of the carbon matrix due to the undesired reactions, leading to a decrease of the electronic conductivity, is detrimental for a more complete reversible deintercalation or intercalation of fluoride ions and impairs the cycling performance considerably. The replacement of carbon black by a more redox stable material or strategies to limit the contact between the active material and carbon might be beneficial. For the latter aspect, the coating of the active cathode material with a thin layer of electrolyte $La_{1-x}Ba_xF_{3-x}$ might result in less carbon fluorination. Such core-shell structures have been previously examined based on conversion-based cathodes containing Cu particles coated with LaF_3. [142] Additionally, initial studies on the influence of such coatings on the fluorination behaviour of intercalation-based La_2NiO_{4+d} have been performed in our group. However, for the anode composite, such strategies might not be suitable since the carbon reduction is presumable based on a reaction between carbon and La^{3+} or Ba^{2+} cations of the electrolyte. With respect to this, thin film configurations could make the use of an electronic conductive additive unnecessary.

Furthermore, primary results on the cycling behaviour of cells entirely based on intercalation-based electrodes are promising and deserve additional attention. However, a considerable reduction of over-potentials between the charging and discharging process is required in order to use such systems for an efficient energy storage. This could be achieved by improving the ionic conductivity of the electrolyte. A size reduction may also help to overcome limitations related to the ionic conductivity within the Ruddlesden-Popper-type particles.

iii. *(Reversible) tuning of magnetic properties, in particular, in the context of the reversible electrochemical defluorination and/or fluorination of $La_2NiO_3F_2$ and $La_{1.3}Sr_{1.7}Mn_2O_7$:* Topochemical modifications of Ruddlesden-Popper-type oxides and of derived oxyfluorides were found to have a substantial influence on the magnetic properties of the obtained phases. It could be shown that the chemical defluorination of $Sr_2TiO_3F_2$ and $Sr_3Ti_2O_5F_4$, led to a transition from a diamagnetic to paramagnetic behaviour, which is related to the presence of unpaired electrons in the reduced phases. This transition is, in principle, also interesting for an electrochemical switching between magnetic states in fluoride-ion batteries, but was inaccessible by electrochemical means.

Magnetic ordering in the form of antiferromagnetism and ferromagnetism below a certain transition temperature was observed for the phases derived from La_2NiO_{4+d} and $La_{1.3}Sr_{1.7}Mn_2O_7$, respectively. In general, the ordering is dependent on the type of indirect exchange interactions (superexchange or double-exchange) between unpaired electrons of orbitals of the transition metal cations via electrons of orbitals of diamagnetic anions. For Ruddlesden-Popper-type oxyfluorides, these anions can be oxide or fluoride ions, depending on the structure of the anion sublattice. However, interactions via fluoride ions are known to be weaker than via oxide ions. [56] A reduced strength of the exchange along the long crystallographic axis between the perovskite-type building blocks via the rock salt-type layer can be, furthermore, expected, since the interactions between the transition metal cations take place via two anions. In addition, the intercalation of additional anions results in an increase of the distance between the building blocks and the interactions have to be mediated via longer distances, leading also to a reduced strength of the interactions. These factors have a significant influence on the magnitude of the magnetic moments and the ordering temperatures of the topochemically formed phases.

The La_2NiO_{4+d} system could be used to demonstrate these effects. The oxyfluoride $La_2NiO_3F_2$, obtained after the non-oxidative fluorination showed an antiferromagnetic ordering of the magnetic moments of the Ni cations. However, in comparison to the precursor oxide [43], decreased magnetic moments and a lower ordering temperature was found. Interestingly, for the subsequently chemically reduced phase with a composition of $La_2NiO_3F_{1.93}$, much higher magnetic moments, which are even comparable to the moments found in stoichiometric La_2NiO_4 [44], and a higher transition temperature were observed. This is related to the structural distortion within this phase, induced due to the extraction of fluoride and the effect of the resulting Jahn-Teller active d^9 Ni cations. In addition, a partial replacement of Ni-F-F-Ni super-superexchange by Ni-F-Ni superexchange interactions, which seems to strengthen the exchange between neighbouring perovskite building blocks, can be expected. This indicates that the strength of the magnetic interaction and the ordering temperature of a paramagnetic to antiferromagnetic transition can be significantly influenced by topochemical modifications.

This reduced phase was also accessible via electrochemical reactions in fluoride-ion batteries. Moreover, a highly fluorinated phase could be synthesised upon the electrochemical fluorination of $La_2NiO_3F_2$. It can be assumed that the reversible electrochemical reactions resulted in similar changes of magnetic properties and a switching between distinctive magnetic states of the obtained phases should be possible, even though they seem not to be adequately determinable based on SQUID measurements only. The changes in magnetisation are comparably small, since only paramagnetic and antiferromagnetic transitions were observed. Higher absolute changes of the magnetisation are required for technological applications based on the tuning of magnetic properties. This shows that the choice of the investigated material system is decisive for an application-relevant magnetoelectric switching between magnetic states. Especially, the switching between a ferromagnetically ordered phase, in which the interactions are mediated by strong double-exchange, and an antiferromagnetically ordered or paramagnetic phase with significantly reduced magnetisations is interesting.

To substantiate this important concept, the reversible magnetoelectric tuning based on ferromagnetic $La_{1.3}Sr_{1.7}Mn_2O_7$ was studied in detail. Upon fluorination, a considerably reduced magnetisation due to the formation of antiferromagnetic or paramagnetic fluorinated phases, which could be also partly defluorinated, was observed. The intercalation of fluoride ions into the fluorinated phases led to a considerable decrease of the strengths of the magnetic interactions due to the increased distances between the perovskite-type building blocks, hampering a ferromagnetic ordering. The cycling of cells showed that a switching between a strong and a weak ferromagnetic state was possible. Additionally, high Coulombic efficiencies during cycling and high relative magnetisation changes between the charged and the discharged states could be observed. Moreover, one of the highest reported magnetoelectric coupling coefficients for tuneable magnetic systems was found, which illustrates the potential of reversible magnetic property tuning within fluoride-ion batteries.

It could be also shown that the choice of suitable charging and discharging cut-off potentials has a severe impact on the observed absolute magnetisation changes. A higher charging cut-off potential was found to result in lower absolute changes of the magnetisation due to a higher content of residual fluoride ions present in the Ruddlesden-Popper-type phases of the discharged cathode material. These ions suppressed the ferromagnetic ordering in the discharged phases. Therefore, the elaboration of compound-specific charging and discharging conditions is of great importance for the designing of experiments for future investigations of other Ruddlesden-Popper-type compounds.

For potential future technological applications, the temperature required for the reversible electrochemical fluorination within fluoride-ion batteries and the magnetic ordering transition temperatures of the investigated materials have to be brought closer together. A crucial step is the development of room-temperature electrolytes for fluoride-ion batteries. In this research area, considerable efforts have been made in the recent years. [136-142] In addition, the strength of the magnetic interactions of the investigated materials, resulting also in an increase of the ferromagnetic ordering temperature, has to be sufficiently high. Concerning this, Ruddlesden-Popper-type compounds with a higher order n and/or different doping approaches could be suitable, despite the difficulties correlated to the synthesis of such high-order phases. In such compounds, the relative influence of the reduced strength of the exchange interactions between the perovskite-type building blocks via the rock salt-type layer might be less significant. However, so far no room-temperature ferromagnetic Ruddlesden-Popper-type compounds have been reported, which requires an extension of these investigations to ferromagnetic anion-deficient perovskite-type compounds. [285]

6 Appendix

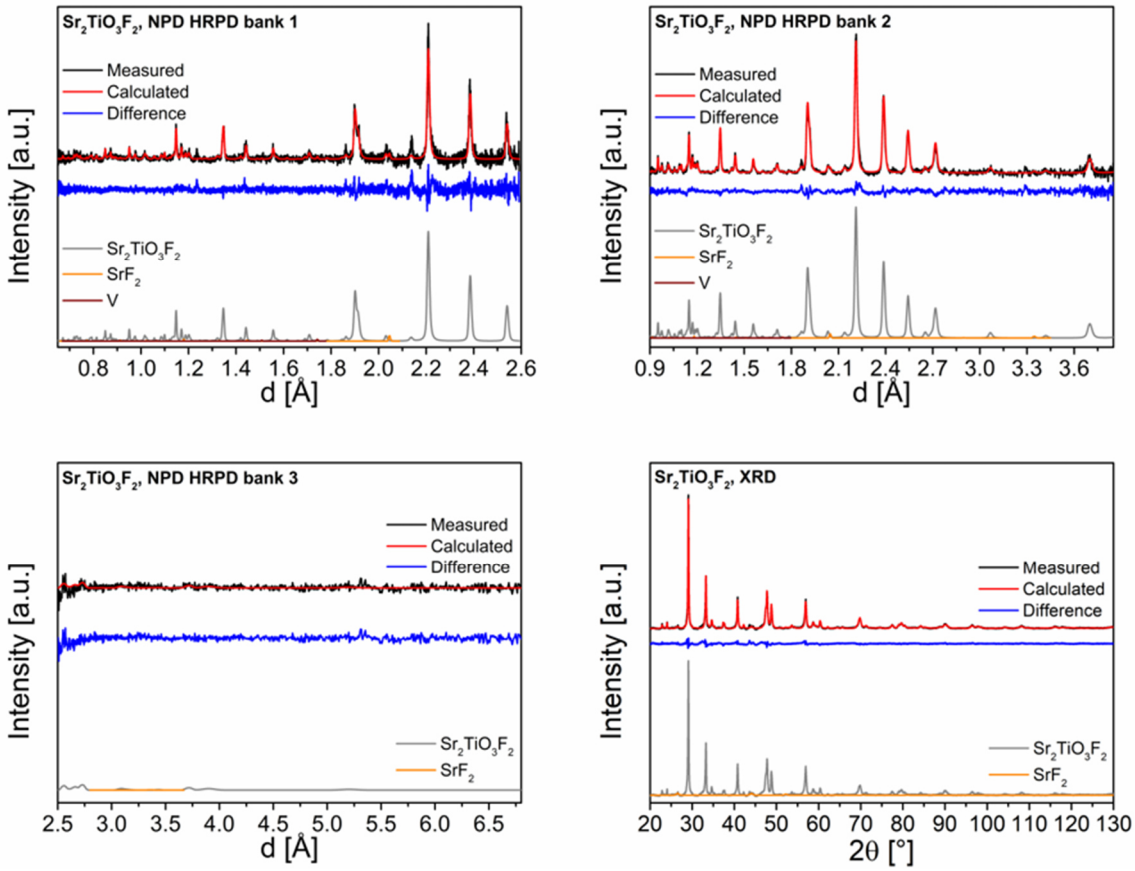

Figure 6-1: Coupled Rietveld refinements of $Sr_2TiO_3F_2$ of HRPD banks 1-3 and XRD data.

Table 6-1: Structural parameters of $Sr_2TiO_3F_2$ (space group: *P4/nmm*) derived from coupled Rietveld analysis of XRD and NPD data. The obtained parameters correspond to the structure reported in reference 72. The anion sites $X1^{eq}$, $X2^{ap}$ and $X3^{int}$ refer to the equatorial, apical and interstitial sites, respectively.

Atom	**Wyckoff position**	**x**	**y**	**z**	**Occupancy**	**B [Å²]**
Sr1	2c	**3/4**	**3/4**	0.0976(1)	**1**	0.84(6)
Sr2	2c	**3/4**	**3/4**	0.3949(1)	**1**	0.84(6)
Ti1	2c	**1/4**	**1/4**	0.2584(2)	**1**	0.84(6)
O1 at $X1^{eq}$	4*f*	**1/4**	**3/4**	0.2861(2)	**1**	0.84(6)
O2 at $X2a^{ap}$	2c	**1/4**	**1/4**	0.1579(3)	**1**	0.84(6)
F1 at $X2b^{ap}$	2c	**1/4**	**1/4**	0.4444(1)	**1**	0.84(6)
F2a at $X3a^{int}$	2a	**1/4**	**3/4**	**0**	1.03(1)	0.84(6)
F2b at $X3b^{int}$	2b	**1/4**	**3/4**	**1/2**	0	0.84(6)
***a* [Å]**	3.7929(1)		*c* [Å]	15.463(2)		
R_{wp}(XRD+NPD) [%]	2.50	**GOF(XRD+NPD)**	2.43	**R_{Bragg} [%]**	0.94 (XRD) 1.50 (NPD, bank 2)	

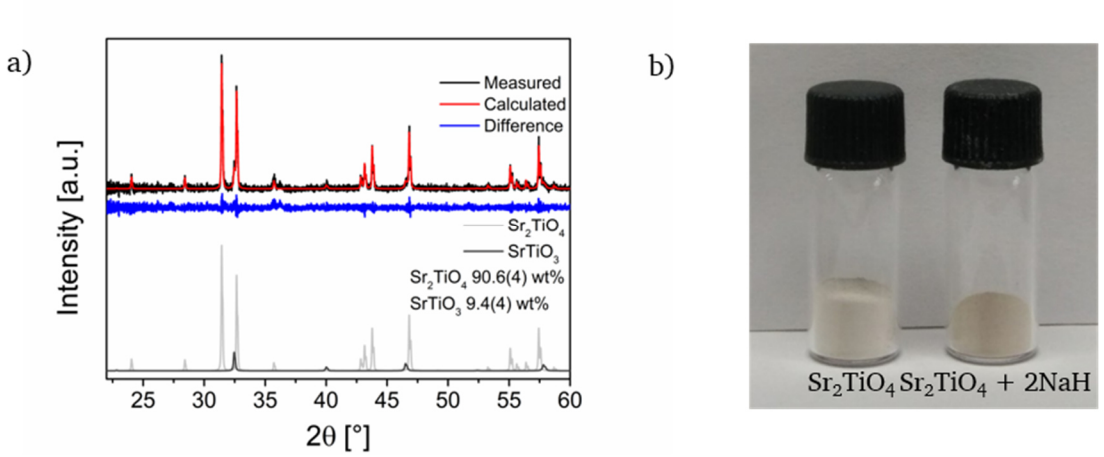

Figure 6-2: a) Rietveld refinement and quantitative phase analysis of the XRD pattern of the reduction product Sr_2TiO_4 + x NaH with x = 2; b) Photograph of Sr_2TiO_4 and the reaction product Sr_2TiO_4 + x NaH with x = 2.

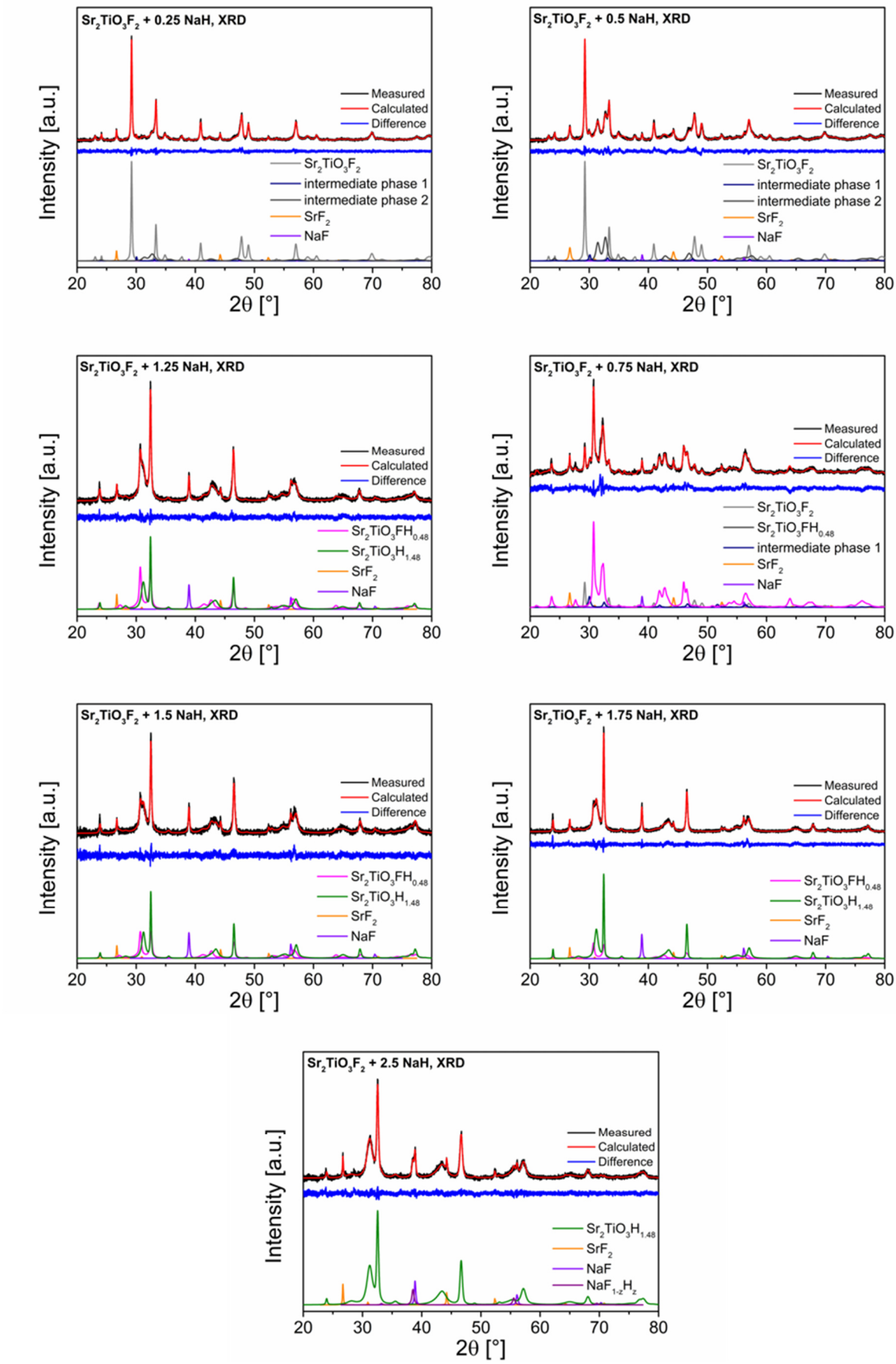

Figure 6-3: Rietveld refinements of XRD patterns of the reduction products of $Sr_2TiO_3F_2$ + x NaH with x = 0.25, 0.5, 0.75, 1.25, 1.5, 1.75 and 2.5. The refinements of the reduction products of $Sr_2TiO_3F_2$ + x NaH with x = 1 and 2 are given in Figure 4-6.

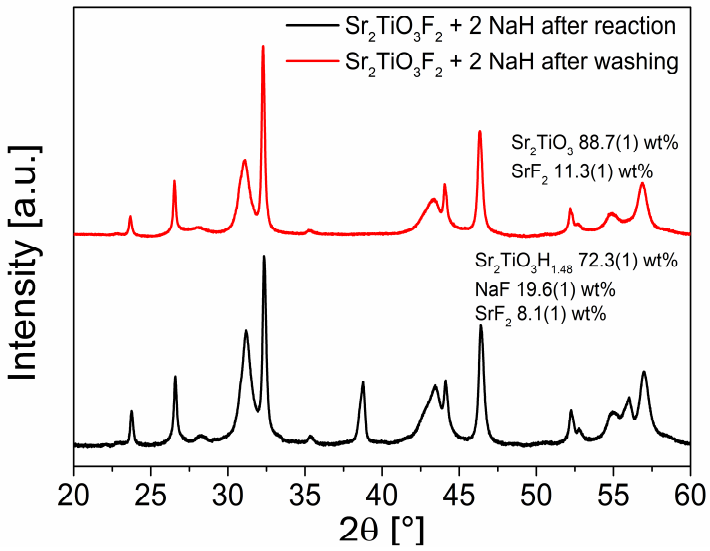

Figure 6-4: X-ray diffraction patterns and quantitative phase analysis of XRD patterns of reduction product $Sr_2TiO_3F_2$ + x NaH with x = 2 before and after removal of NaF by washing with 0.25 M NH_4Cl in dry methanol.

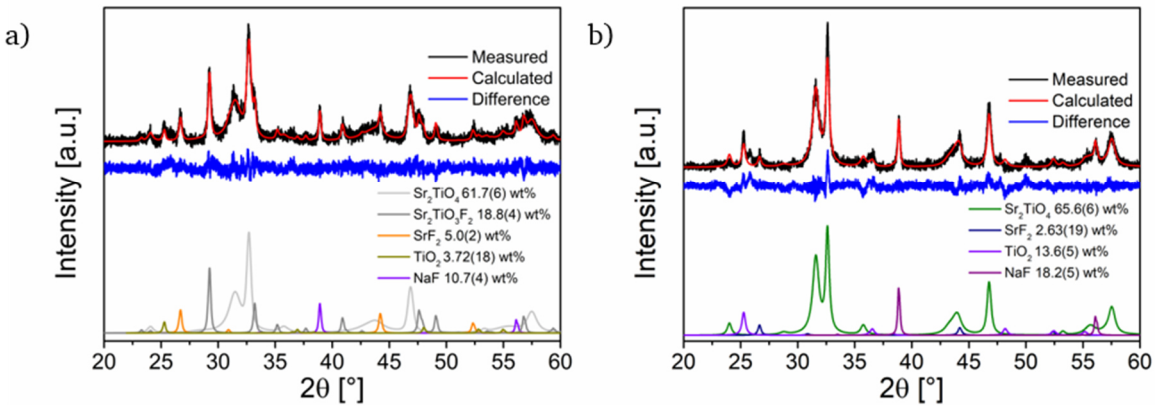

Figure 6-5: Rietveld refinements and quantitative phase analysis of XRD patterns of re-oxidized reduction products $Sr_2TiO_3F_2$ + x NaH with x = 1 (a) and x = 2 (b).

Figure 6-6: Symmetry tree for the symmetry lowering from *I*4/*mmm* to *P*-1. The different anion sites X1, X2 and X3 refer to the equatorial, apical and interstitial sites, respectively.

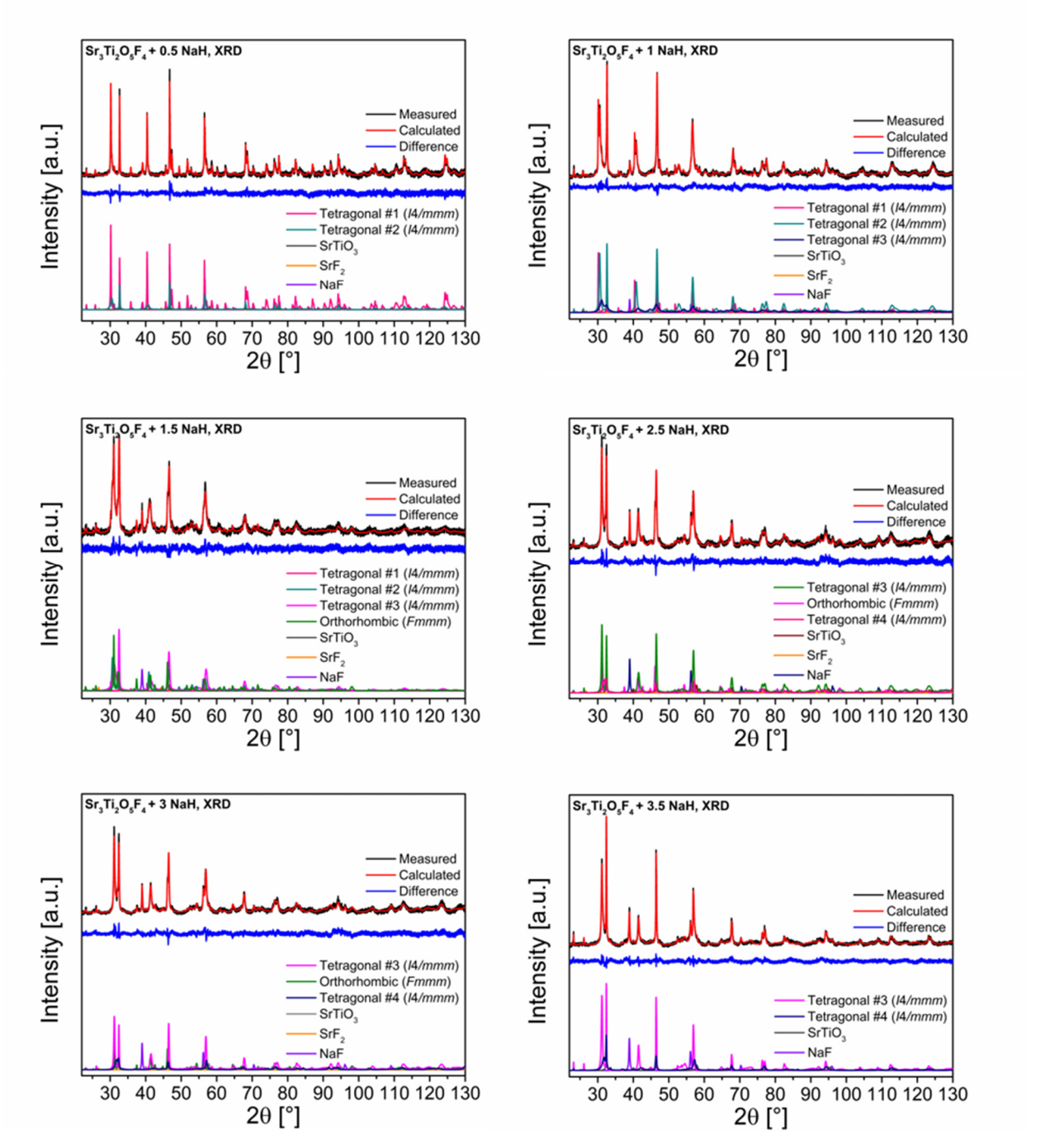

Figure 6-7: Rietveld refinements of XRD patterns of the reduction products of $Sr_3Ti_2O_5F_4$ + x NaH with x = 0.5, 1, 1.5, 2.5, 3 and 3.5. The refinements of the reduction products of $Sr_2TiO_3F_2$ + x NaH with x = 2 and 4 are given in Figure 4-19 and Figure 6-9, respectively.

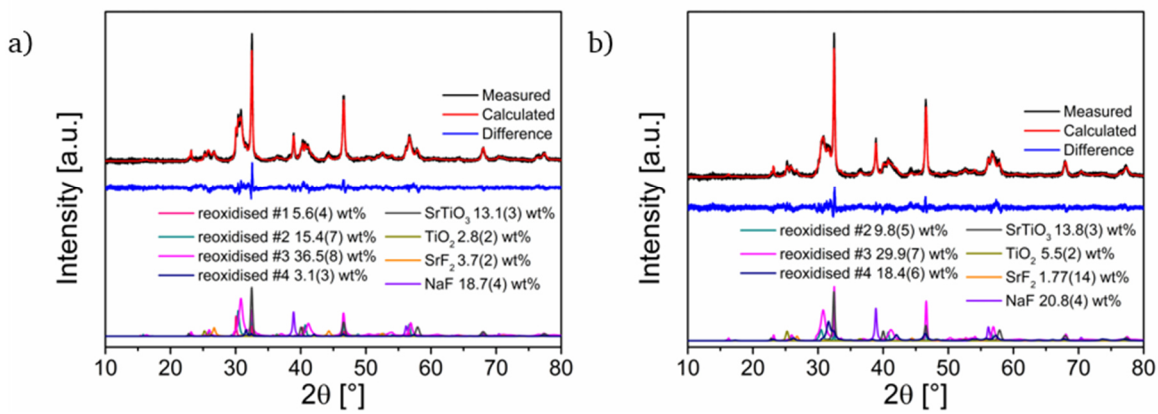

Figure 6-8: Rietveld refinements and quantitative phase analysis of XRD patterns of re-oxidised reduction products $Sr_2TiO_3F_2$ + x NaH with x = 2 (a) and x = 4 (b).

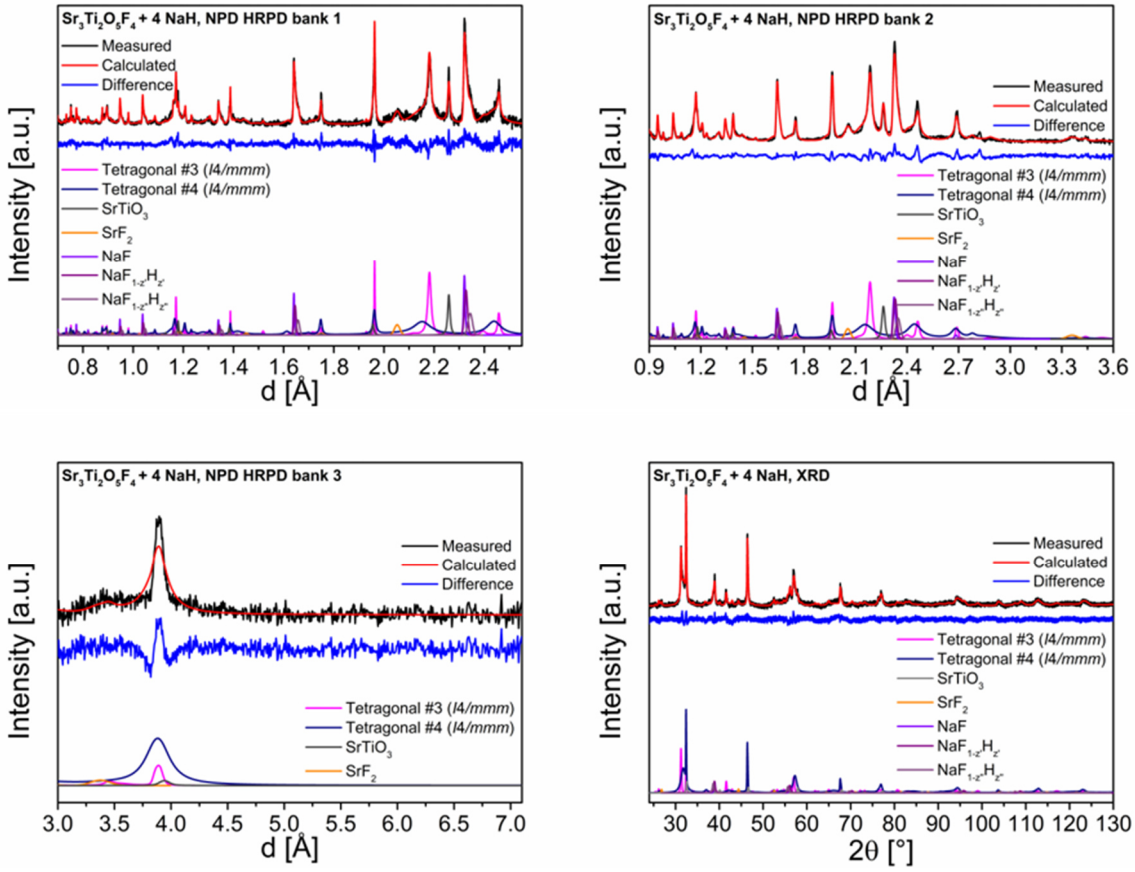

Figure 6-9: Coupled Rietveld refinements of the reduction products of $Sr_3Ti_2O_5F_4$ + x NaH with x = 4 of HRPD banks 1-3 and XRD data.

Table 6-2: Structural parameters of tetragonal #3 phase (space group: *I*4/*mmm*) derived from coupled Rietveld analysis of XRD and NPD data of the reduction product of $Sr_3Ti_2O_5F_4$ + x NaH with x = 4. The anion sites $X1^{eq}$, $X2^{ap,central}$, $X3^{ap,terminal}$ and $X4^{int}$ refer to the equatorial, central apical, terminal apical and interstitial sites, respectively.

Atom	**Wyckoff position**	**x**	**y**	**z**	**Occupancy**	**B [Å²]**
Sr1	2*b*	**0**	**0**	½	**1**	0.473(3)
Sr2	4*e*	**0**	**0**	0.3155(3)	**1**	0.473(3)
Ti	4*e*	**0**	**0**	0.0965(6)	**1**	0.473(3)
O1 at $X1^{eq}$	8*g*	**0**	½	0.1009(3)	**1**	0.473(3)
O2 at $X2^{ap,central}$	2*a*	**0**	**0**	**0**	**1**	0.473(3)
F1 at $X3^{ap,terminal}$	4*e*	**0**	**0**	0.83122(5)	1.00(2)	0.473(3)
F2 at $X4^{int}$	4*d*	½	**0**	¼	0.30(1)	0.473(3)
a [Å]	3.9169(1)		***c*** [Å]	21.135(2)		
R_{wp}(XRD+NPD) [%]	3.42	**GOF(XRD+NPD)**	1.86	**R_{Bragg} [%]**	1.30 (XRD) 1.80 (NPD, bank 1)	

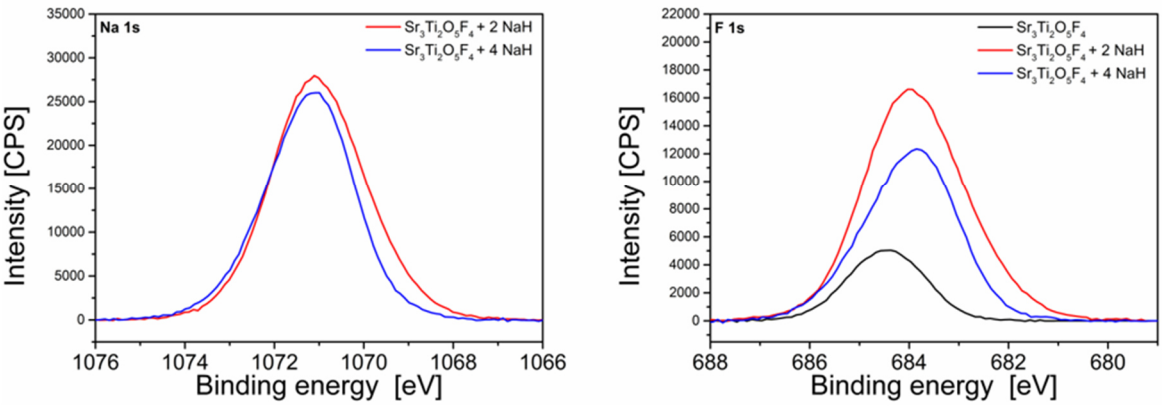

Figure 6-10: Na 1*s* and F1*s* spectra of $Sr_3Ti_2O_5F_4$ and reduction products $Sr_3Ti_2O_5F_4$ + x NaH with x = 2 and 4.

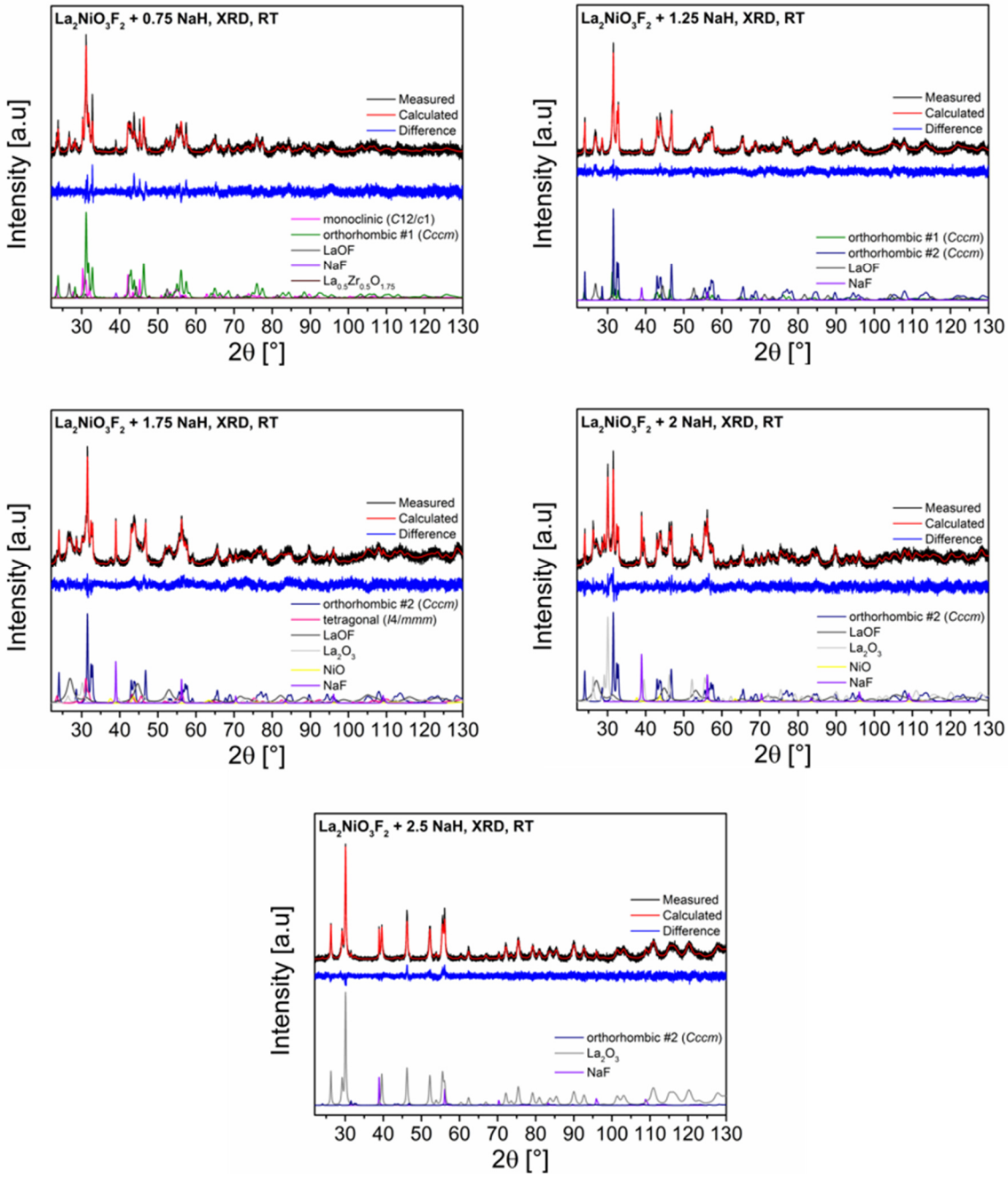

Figure 6-11: Rietveld refinements of XRD patterns of the reduction products of $La_2NiO_3F_2$ + x NaH with x = 0.75, 1.25, 1.75, 2 and 2.5. The refinements of the reduction products of $La_2NiO_3F_2$ + x NaH with x = 0.25, 0.5, 1 and 1.5 are given in Figure 4-37, Figure 4-38, Figure 6-14 and Figure 4-39, respectively.

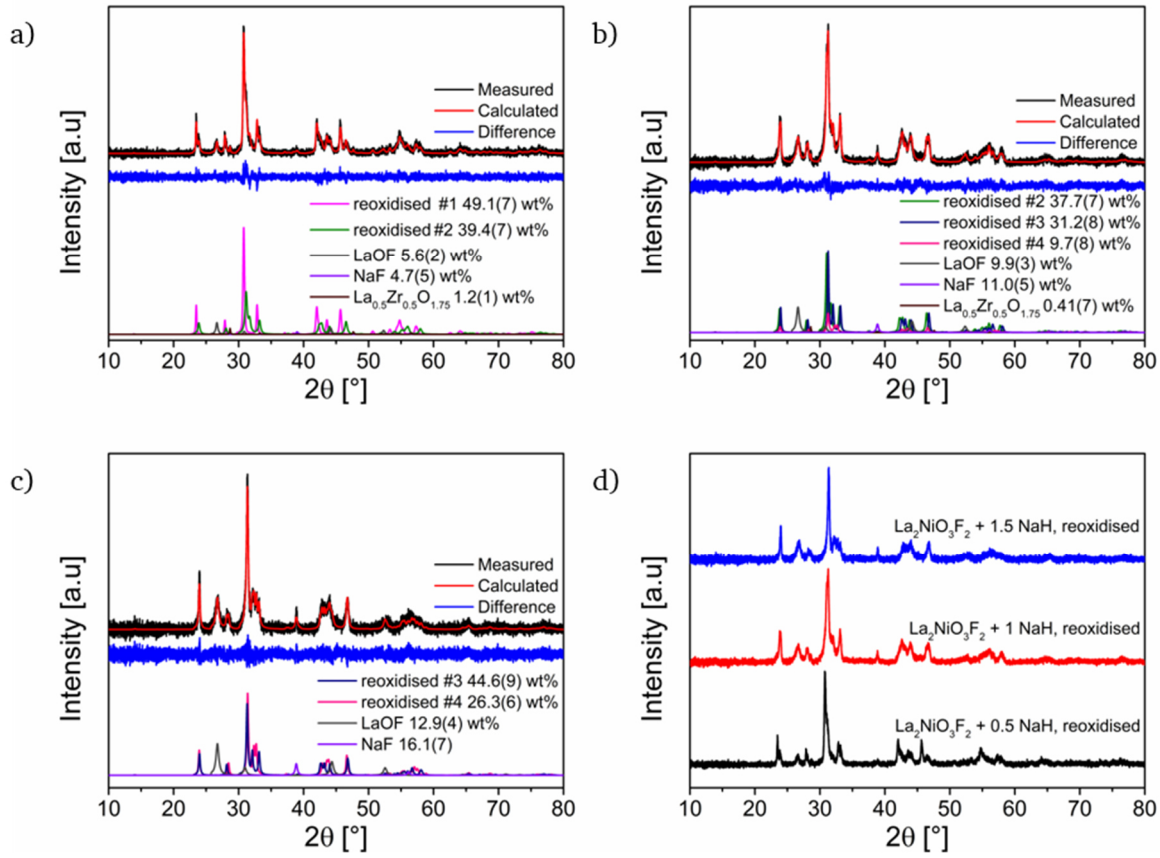

Figure 6-12 Rietveld refinements and quantitative phase analysis of XRD patterns of re-oxidised reduction products $La_2NiO_3F_2$ + x NaH with x = 0.5 (a), x = 1 (b) and x = 1.5 (b). A comparison of the re-oxidised reduction products (d) is additionally given.

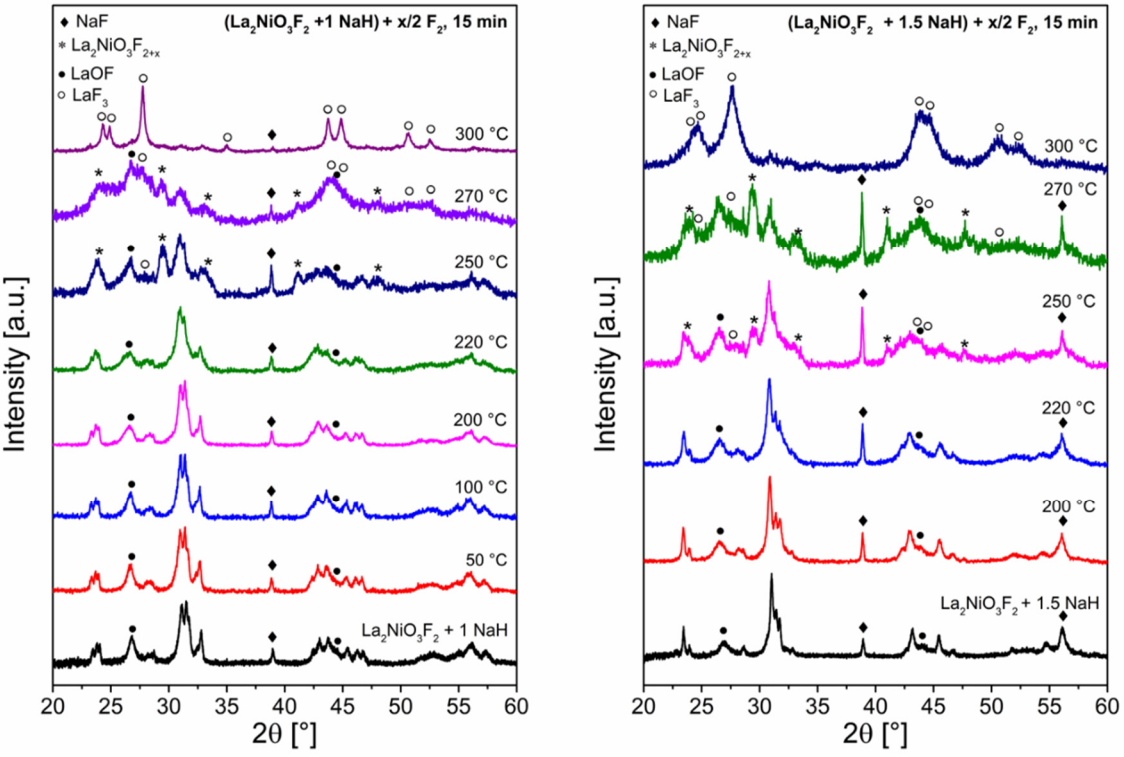

Figure 6-13: XRD patterns of re-fluorinated reduction products $La_2NiO_3F_2$ + x NaH with x = 1 and 1.5. The fluorination was performed using F_2 gas at various temperatures for 15 min.

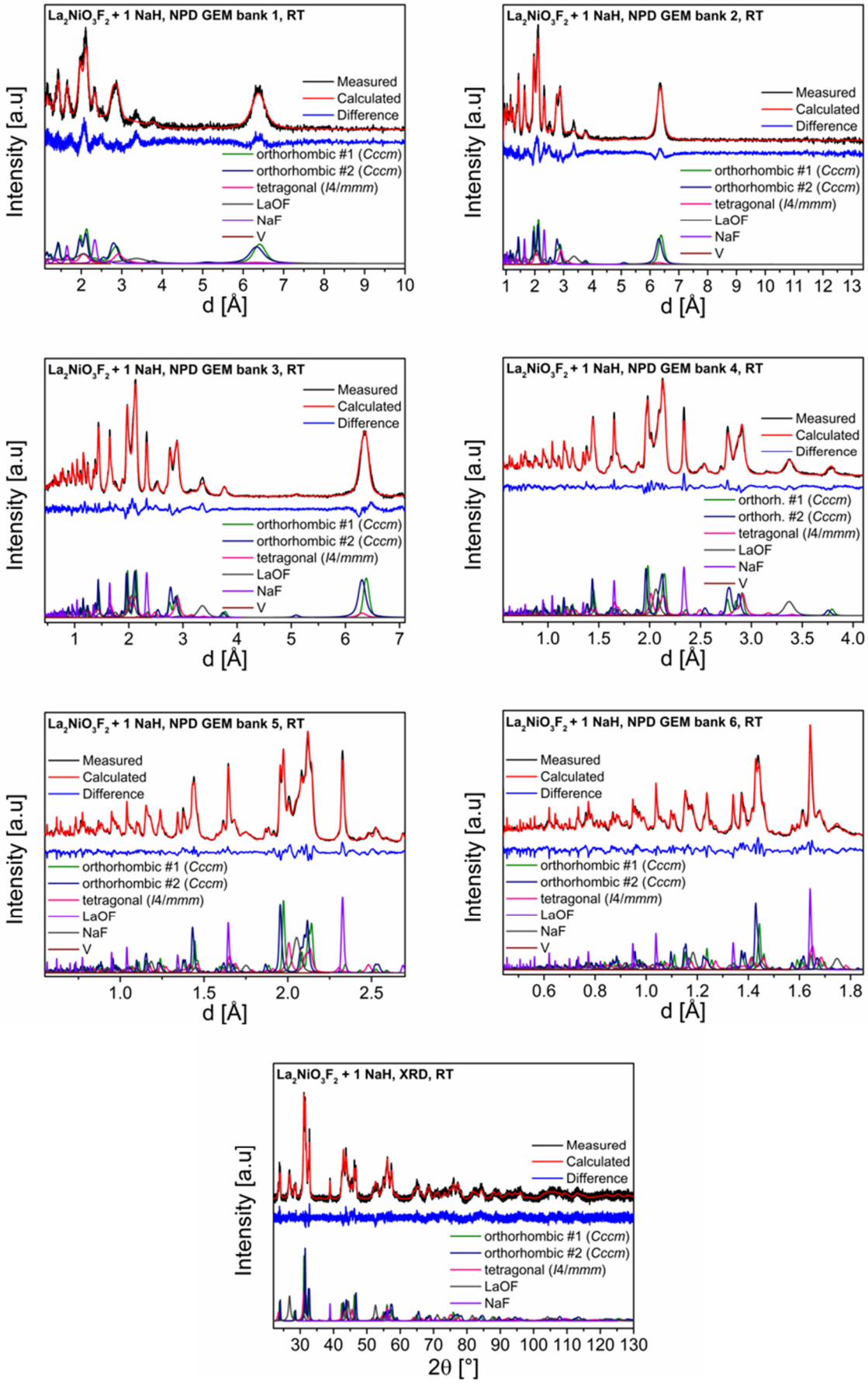

Figure 6-14: Coupled Rietveld refinements of the reduction product of $La_2NiO_3F_2$ + x NaH with x = 1 of GEM banks 1-6 and XRD data measured at room-temperature (RT).

Table 6-3: Data acquisition, structure solution and dynamical refinement parameters of the crystals used for structure determination from Fast-ADT measurements. The crystal structures of $La_2NiO_3F_2$ and the reduced monoclinic phase in the reduction product of $La_2NiO_3F_2$ + 0.25 NaH were determined.

	$La_2NiO_3F_2$	**Monoclinic phase**
Space group	*Cccm*	*C*12/*c*1
Structure solution		
Tilt range [°]	-35/40	-40/40
Acquired diffraction patterns	76	81
Num. of sampled reflections	3630	3948
Num. of ind. reflections	132	521
Used resolution [Å]	0.8	0.7
Ind. reflection coverage [%]	56.9	82.1
Overall B [Å^2]	0.721	0.898
R_{sym}	0.276	0.077
Residual R(F) (Sir2014)	0.133	0.207
Dynamical refinement		
Num. of used reflections (obs/all)	1070/500	1320/811
R1 (obs/all)	0.146/0.247	0.086/0.127

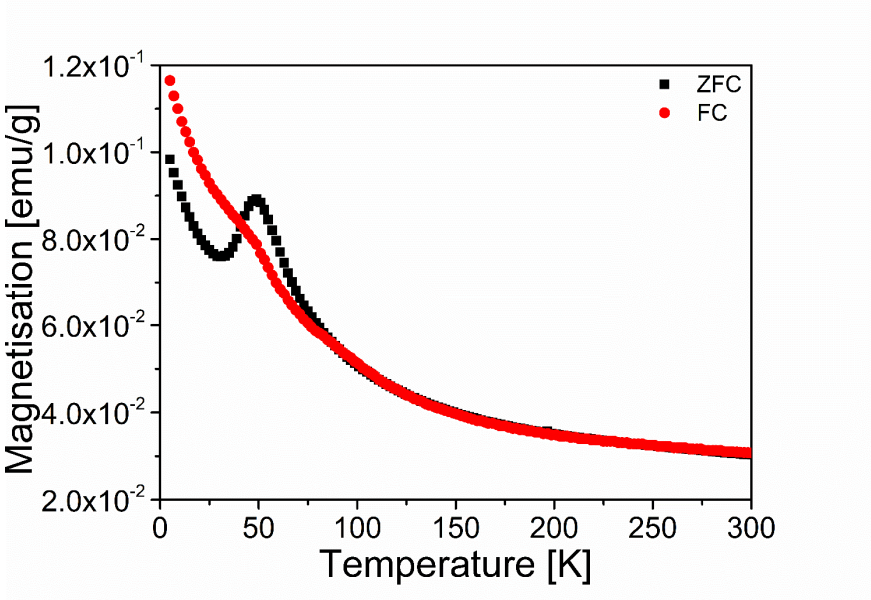

Figure 6-15: ZFC and FC M(T) curves of $La_2NiO_3F_2$ measured at μ_0 = 1 T.

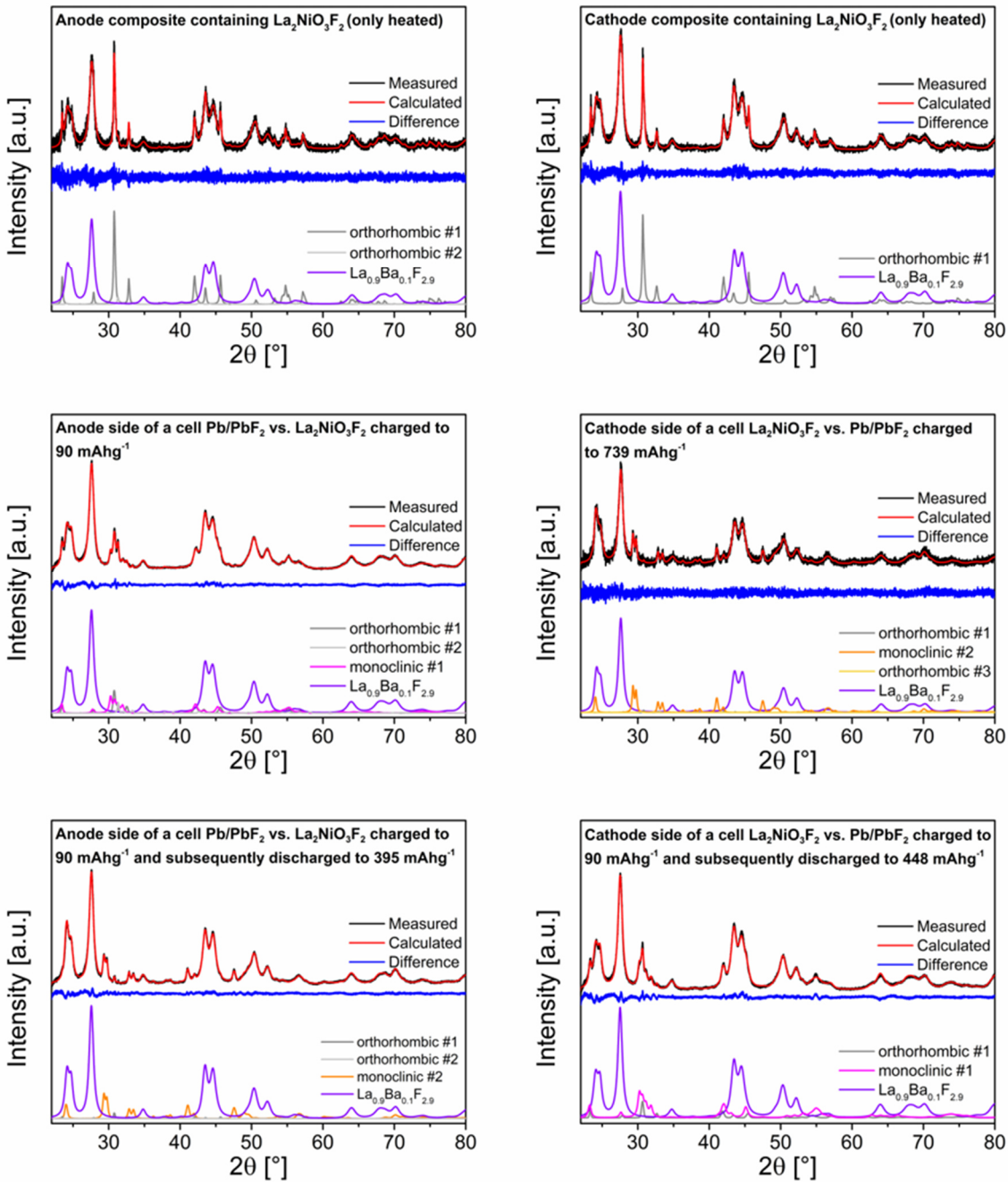

Figure 6-16: Rietveld refinements of XRD patterns of anode sides of cells Pb/PbF_2 against $La_2NiO_3F_2$ heated to 170 °C for 72 h, charged to 90 $mAhg^{-1}$ and charged to 90 $mAhg^{-1}$ and subsequently discharged to 395 $mAhg^{-1}$ and of cathode sides of cells $La_2NiO_3F_2$ against Pb/PbF_2 heated to 170 °C for 72 h, charged to 739 $mAhg^{-1}$ and charged to 90 $mAhg^{-1}$ and subsequently discharged to 448 $mAhg^{-1}$

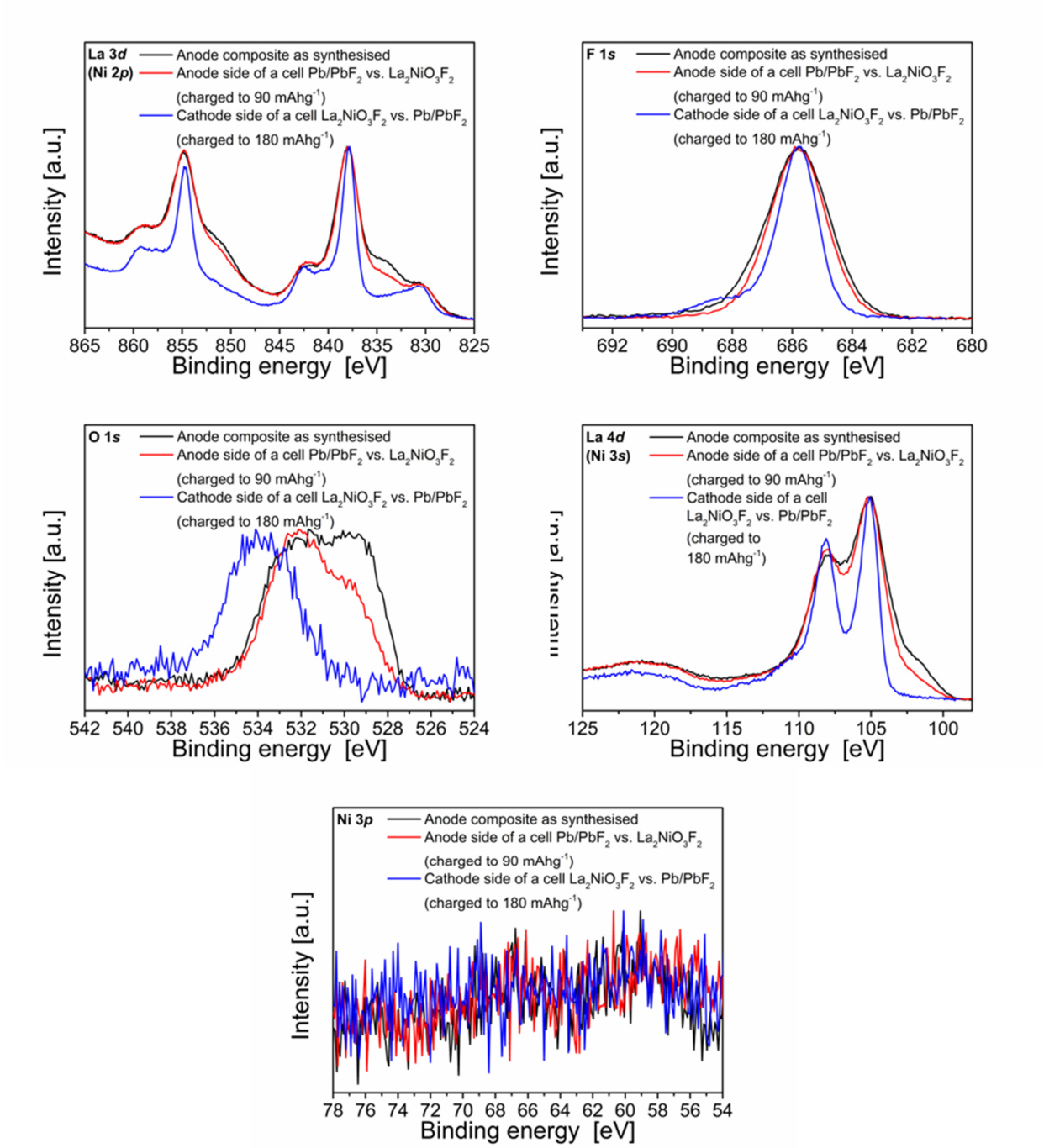

Figure 6-17: La 3*d* (Ni 2*p*), F 1*s*, O 1*s*, La 4*d* (Ni 3*s*) and Ni 3*p* XPS spectra of the anode composite containing $La_2NiO_3F_2$ after milling, of the anode side of a cell Pb/PbF_2 against $La_2NiO_3F_2$ charged to 90 $mAhg^{-1}$ and of the cathode side of a cell $La_2NiO_3F_2$ against Pb/PbF_2 charged to 180 $mAhg^{-1}$. Due to expected shifts of the carbon signals of the reduced and oxidized samples, the C *1s* line could not be used to calibrate the samples. Since shifts in the F *1s* signal should be small, the F *1s* emission line was used for the calibration of the reduced and oxidized samples. When doing so, the La and Ni lines, which are dominated by the La signal from the stable (and, therefore, unaffected by chemical shifts) electrolyte $La_{0.9}Ba_{0.1}F_{2.9}$, also aligned. Due to the strong signal of La, a deconvolution of the La and Ni signals was not possible. The found binding energies of La $3d_{5/2}$, La $3d_{3/2}$ and F *1s* signals agree well with reference values of signals of LaF_3, which is close to that of the dominating phase $La_{0.9}Ba_{0.1}F_{2.9}$. [286-289] The Ni 3*p* lines could not be used for the determination of the oxidation state due to their very low intensities.

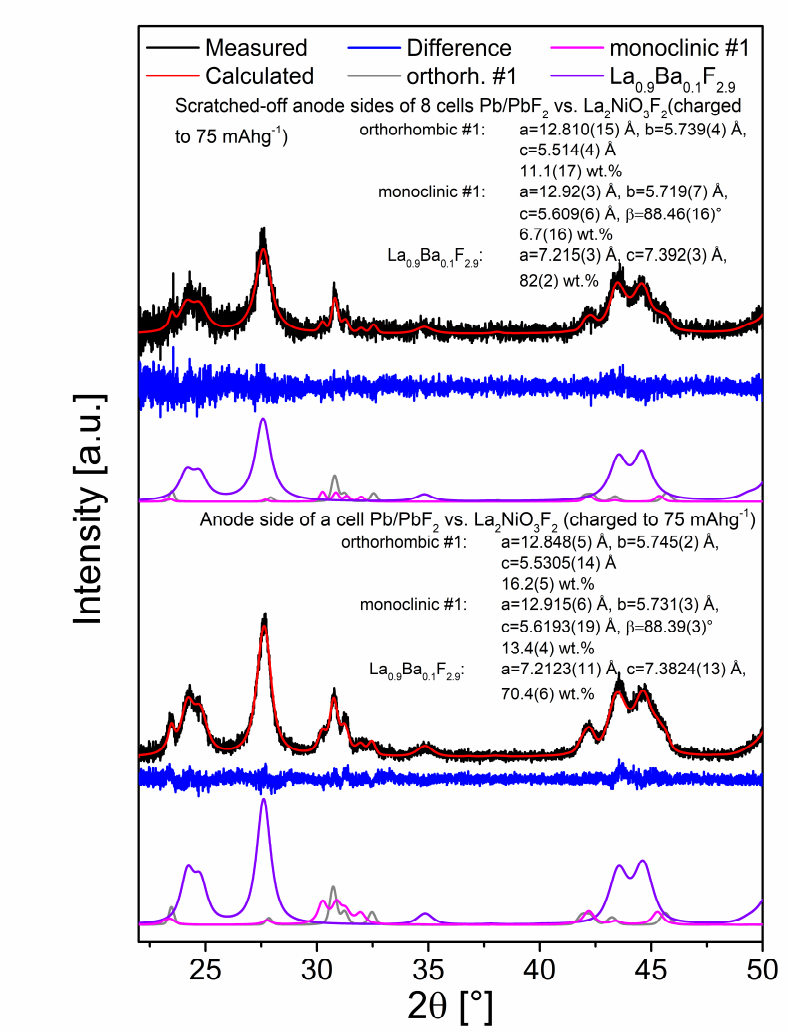

Figure 6-18: Rietveld refinements of XRD data of the anode side of a cell Pb/PbF_2 vs. $La_2NiO_3F_2$ charged to 75 $mAhg^{-1}$ and of scratched-off anode sites of 8 cells Pb/PbF_2 vs. $La_2NiO_3F_2$ charged to 75 $mAhg^{-1}$.

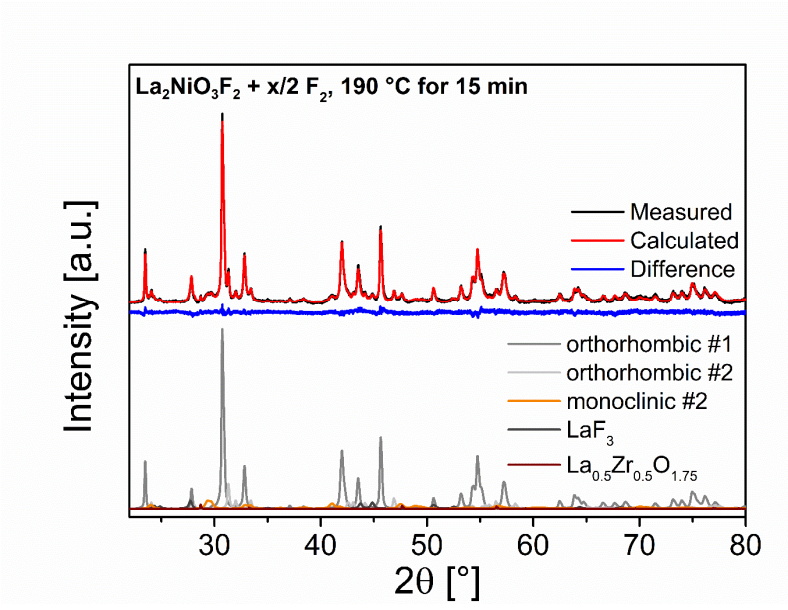

Figure 6-19: Rietveld refinement of the XRD data of the fluorination product containing additionally fluorinated $La_2NiO_3F_{2+x}$. The product was obtained using F_2 gas for the optimised reaction conditions of 190 °C for 15 min.

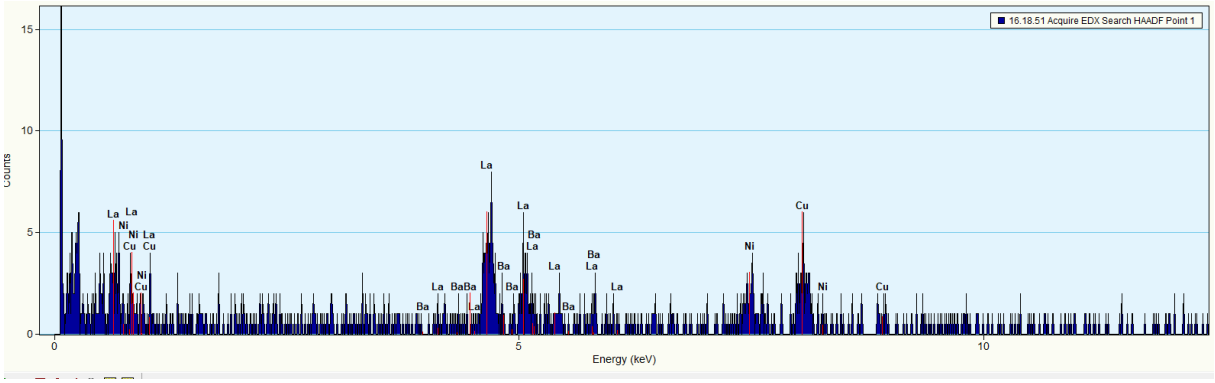

Figure 6-20: EDX spectrum of the RP-type crystal measured in μ-STEM-NED mode confirming the presence of Ni within the crystal. The phase was obtained using galvanostatic charging of a cell $La_2NiO_3F_2$ vs. Pb/PbF_2.

Table 6-4: Data acquisition, structure solution and refinement parameters of the crystal used for structure determination of the oxidised monoclinic #2 RP-type phase obtained using galvanostatic charging of a cell $La_2NiO_3F_2$ vs. Pb/PbF_2 from Fast-ADT measurements.

Space group	***C*12/*c*1**
Structure solution	
Tilt range [°]	-20/25
Acquired diffraction patterns	46
Num. of sampled reflections	1157
Num. of ind. reflections	100
Used resolution [Å]	0.8
Ind. reflection coverage [%]	55
R_{sym}	0.1051
Overall U [$Å^2$]	0.3607
Residual R(F) (Sir2014)	21.89
Reflections/parameter ratio	2.96
Structure refinement all data	
No. of independent reflections (Fo > 3σ)	306
Used resolution [Å]	0.59
Reflections/parameter ratio	23.54
R(F) (Fo > 4σ)/all	0.3872/0.4114
Goodness of fit	9.27

Table 6-5: Atomic positions for $La_2NiO_3F_{2+x}$ in space group *C*12/*c*1 refined using SIR 2014. However, due to the low completeness of the reciprocal space sampling displacement factors have been found to be not reliable. Therefore, only a positional refinement of the weak scattering anions has been undertaken using a fixed U_{iso}. Furthermore, an assignment of oxide or fluoride ions to the anion sites was not possible. Assuming a full occupation of all anion sites, a composition of La_2NiX_6 (respectively $La_2NiO_3F_3$) can be followed.

Monoclinic #2 (space group: *C*12/*c*1)

Atom	**Wyckoff position**	**x**	**y**	**z**	**U_{iso} [$Å^2$]**	**Site symmetry**	**Occupancy**
La1	8*f*	0.88613	0.23878	0.98903	0.042	1	1
Ni1	4*c*	¾	¼	½	0.041	-1	1
X1 at X1^{eq}	8*f*	0.79179	0.05547	0.12430	0.021	1	1
X2 at X2^{ap}	8*f*	0.86643	0.67644	0.96068	0.021	1	1
X3a at X3a^{int}	4*e*	**0**	-0.00376	¼	0.021	2	1
X3b at X3b^{int}	4*e*	**0**	0.4875	¼	0.022	2	1

Table 6-6: Atomic positions for La_2NiX_6 in space group *C*12/*m*1.

Atom	Wyckoff position	x	y	z	Site symmetry	Occupancy
La1	4*i*	0.637	**0**	-0.016	m	1
La2	4*i*	0.12	**0**	0.481	m	1
Ni1	2*a*	**0**	**0**	**0**	2/m	1
Ni2	2*b*	**0**	½	½	2/m	1
X1 at X1^{eq}	8*j*	-0.015	0.763	0.235	1	1
X2a at X2a^{ap}	4*i*	0.145	**0**	0.06	m	1
X2bat X2b^{ap}	4*i*	0.629	**0**	0.46	m	1
X3b at X3b^{int}	8*j*	0.258	0.258	0.23	1	1

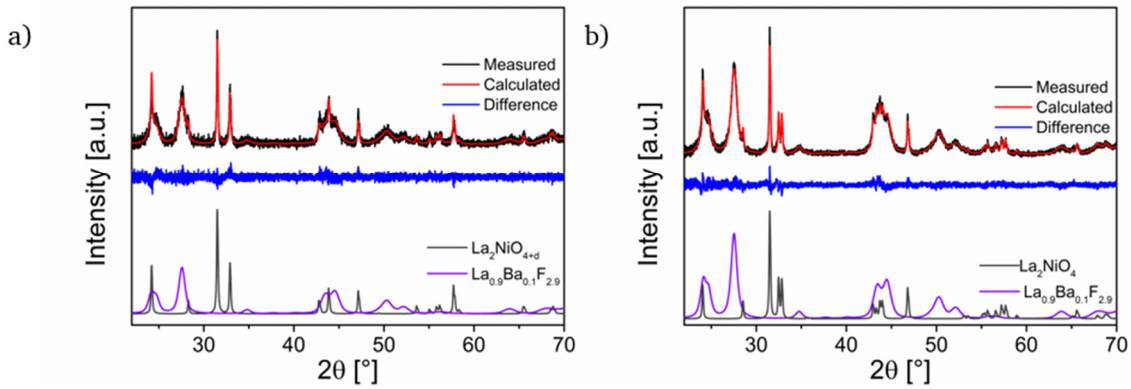

Figure 6-21: Rietveld refinement of XRD data of anode sides of cells Pb/PbF_2 against $La_2NiO_{4.13}$ heated to 170 °C for 72 h (a) and charged to 350 $mAhg^{-1}$ (b).

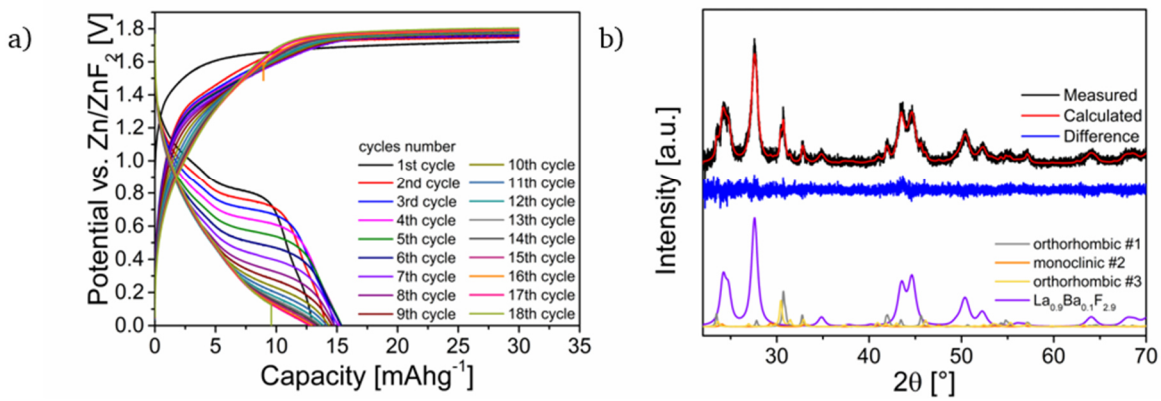

Figure 6-22: a) Cycling curve of a cell $La_2NiO_3F_2$ against Zn/ZnF_2 cycled between the charging cut-off capacity 30 $mAhg^{-1}$ and the discharging cut-off voltage 0 V; b) Rietveld refinement of XRD data of a cell $La_2NiO_3F_2$ against Zn/ZnF_2 cycled between the charging cut-off capacity 30 $mAhg^{-1}$ and the discharging cut-off voltage 0 V for 18 cycles.

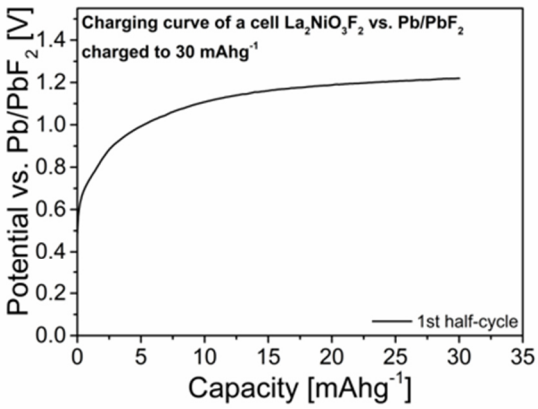
Charging curve of a cell $La_2NiO_3F_2$ vs. Pb/PbF_2 charged to 30 $mAhg^{-1}$
Potential vs. Pb/PbF_2 [V]
Capacity [$mAhg^{-1}$]
1st half-cycle

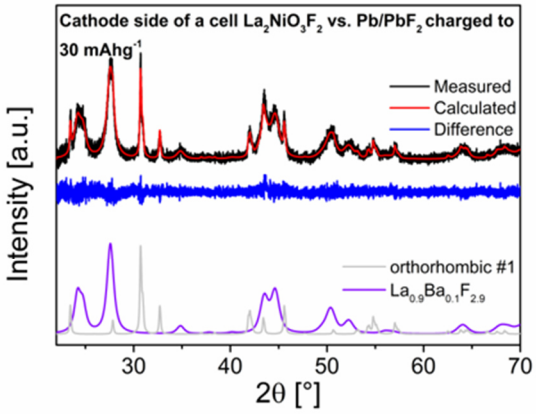
Cathode side of a cell $La_2NiO_3F_2$ vs. Pb/PbF_2 charged to 30 $mAhg^{-1}$
Intensity [a.u.]
2θ [°]
Measured
Calculated
Difference
orthorhombic #1
$La_{0.9}Ba_{0.1}F_{2.9}$

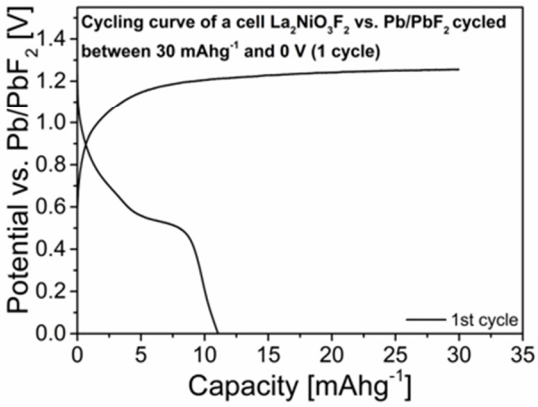
Cycling curve of a cell $La_2NiO_3F_2$ vs. Pb/PbF_2 cycled between 30 $mAhg^{-1}$ and 0 V (1 cycle)
Potential vs. Pb/PbF_2 [V]
Capacity [$mAhg^{-1}$]
1st cycle

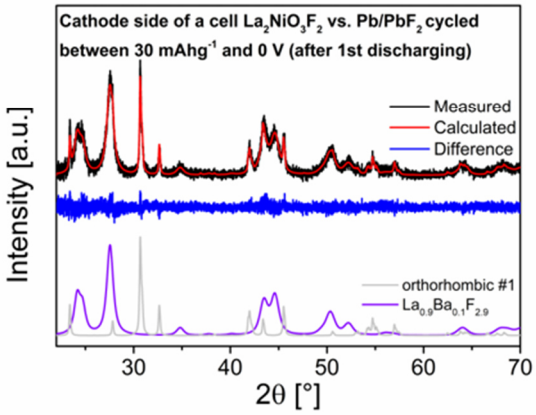
Cathode side of a cell $La_2NiO_3F_2$ vs. Pb/PbF_2 cycled between 30 $mAhg^{-1}$ and 0 V (after 1st discharging)
Intensity [a.u.]
2θ [°]
Measured
Calculated
Difference
orthorhombic #1
$La_{0.9}Ba_{0.1}F_{2.9}$

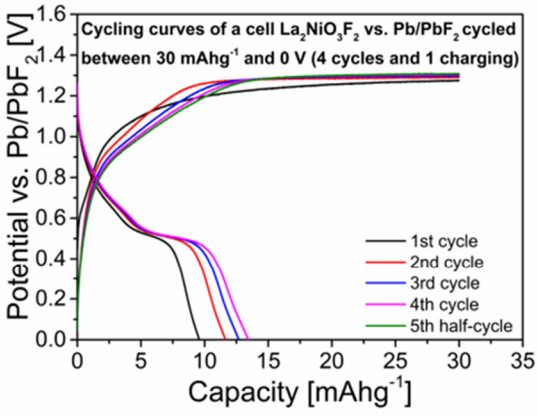
Cycling curves of a cell $La_2NiO_3F_2$ vs. Pb/PbF_2 cycled between 30 $mAhg^{-1}$ and 0 V (4 cycles and 1 charging)
Potential vs. Pb/PbF_2 [V]
Capacity [$mAhg^{-1}$]
1st cycle
2nd cycle
3rd cycle
4th cycle
5th half-cycle

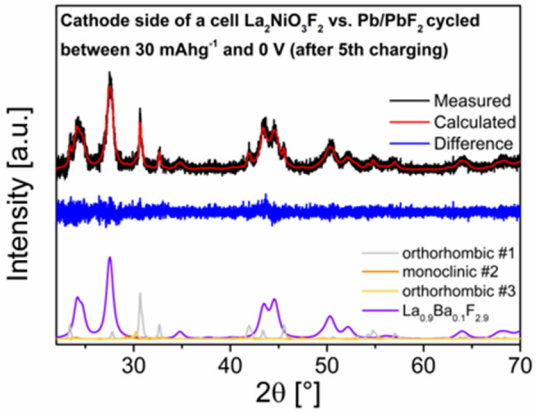
Cathode side of a cell $La_2NiO_3F_2$ vs. Pb/PbF_2 cycled between 30 $mAhg^{-1}$ and 0 V (after 5th charging)
Intensity [a.u.]
2θ [°]
Measured
Calculated
Difference
orthorhombic #1
monoclinic #2
orthorhombic #3
$La_{0.9}Ba_{0.1}F_{2.9}$

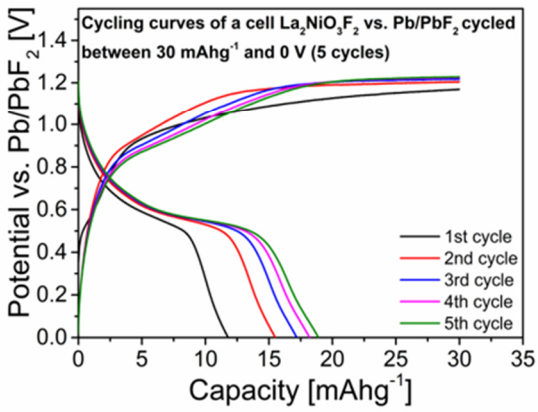
Cycling curves of a cell $La_2NiO_3F_2$ vs. Pb/PbF_2 cycled between 30 $mAhg^{-1}$ and 0 V (5 cycles)
Potential vs. Pb/PbF_2 [V]
Capacity [$mAhg^{-1}$]
1st cycle
2nd cycle
3rd cycle
4th cycle
5th cycle

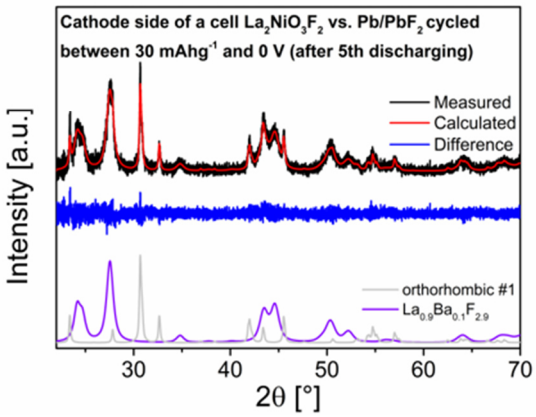
Cathode side of a cell $La_2NiO_3F_2$ vs. Pb/PbF_2 cycled between 30 $mAhg^{-1}$ and 0 V (after 5th discharging)
Intensity [a.u.]
2θ [°]
Measured
Calculated
Difference
orthorhombic #1
$La_{0.9}Ba_{0.1}F_{2.9}$

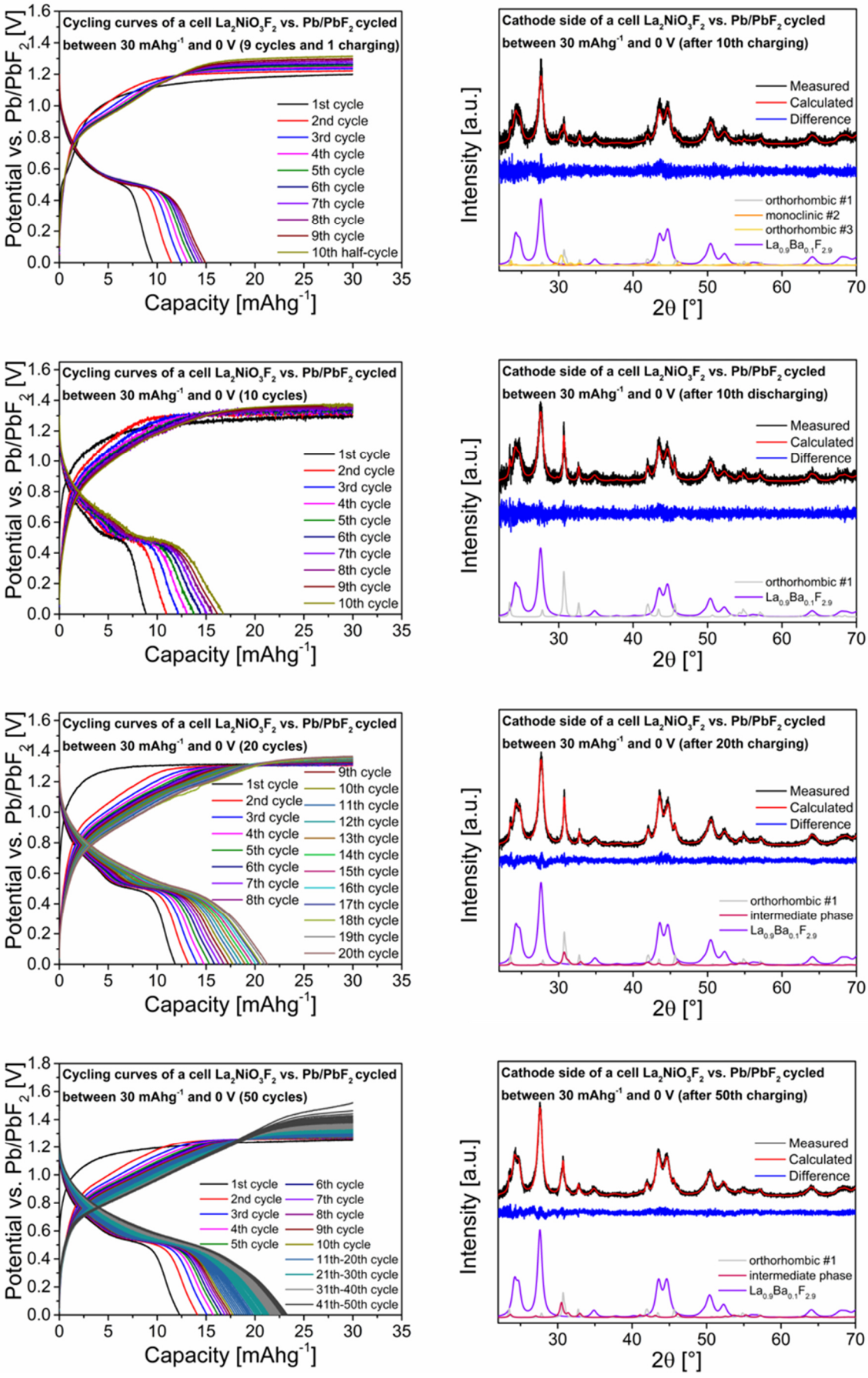

Figure 6-23: Cycling curves and Rietveld refinements of XRD data of cells $La_2NiO_3F_2$ against Pb/PbF_2 cycled between the charging cut-off capacity 30 $mAhg^{-1}$ and the discharging cut-off voltage 0 V over various cycle numbers.

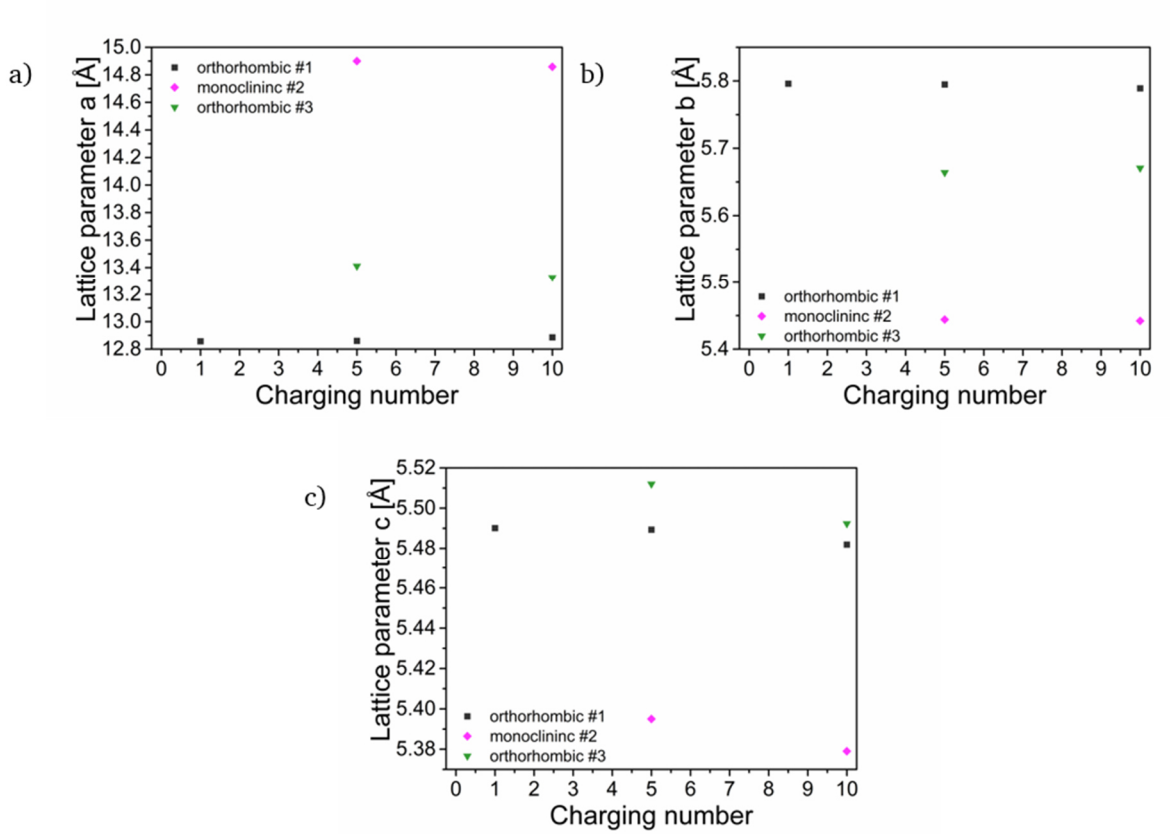

Figure 6-24: Lattice parameters *a* (a), *b* (b) and *c* (c) of RP-type orthorhombic #1, monoclinic #2 and orthorhombic #3 phases in the cathode sides of cells $La_2NiO_3F_2$ against Pb/PbF_2 cycled for various cycle numbers between the charging cut-off capacity 90 $mAhg^{-1}$ and the discharging cut-off potential 0 V. The fractions of cathode sides of cells within the charged state are shown.

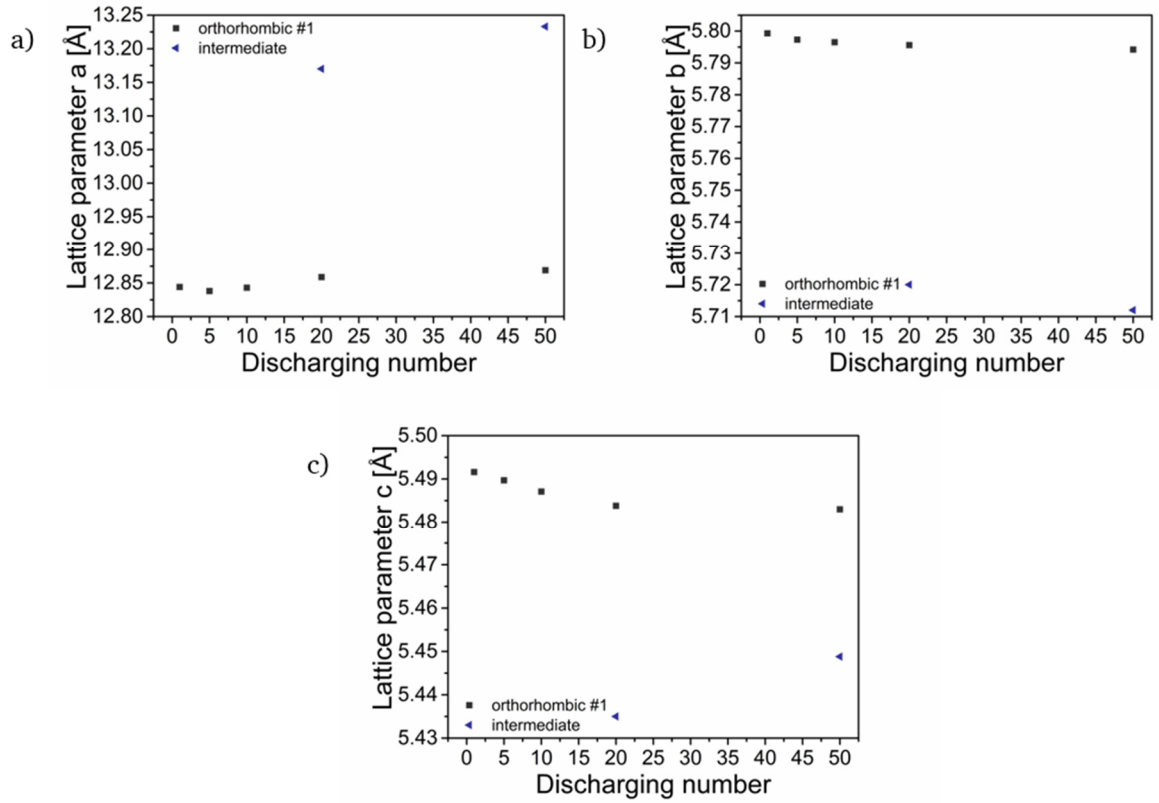

Figure 6-25: Lattice parameters *a* (a), *b* (b) and *c* (c) of RP-type orthorhombic #1 phase and an intermediate phase in the cathode sides of cells $La_2NiO_3F_2$ against Pb/PbF_2 cycled for various cycle numbers between the charging cut-off capacity 90 $mAhg^{-1}$ and the discharging cut-off potential 0 V. The fractions of cathode sides of cells within the discharged state are shown.

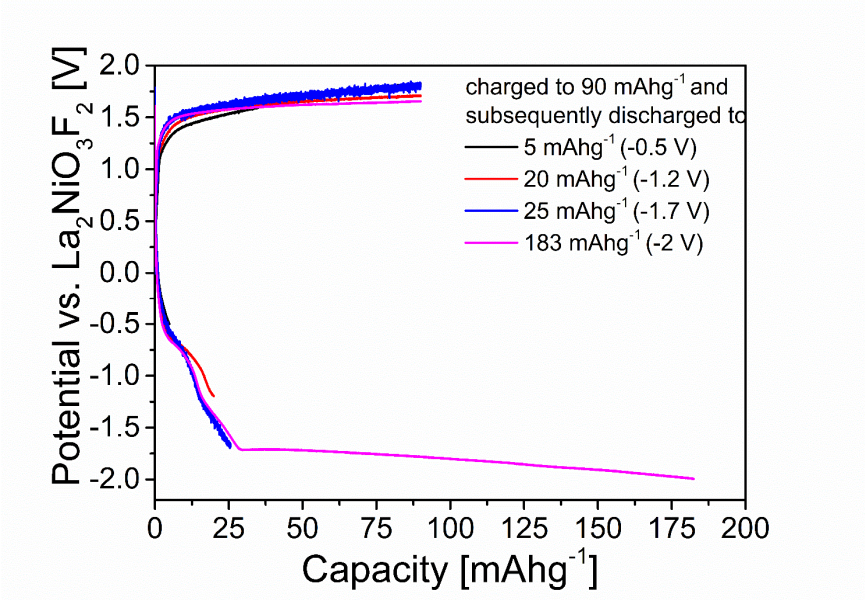

Figure 6-26: Charging and discharging curves of cells La_2NiO_{4+d} against $La_2NiO_3F_2$ charged to 90 $mAhg^{-1}$ and subsequently discharged to various cut-off potentials.

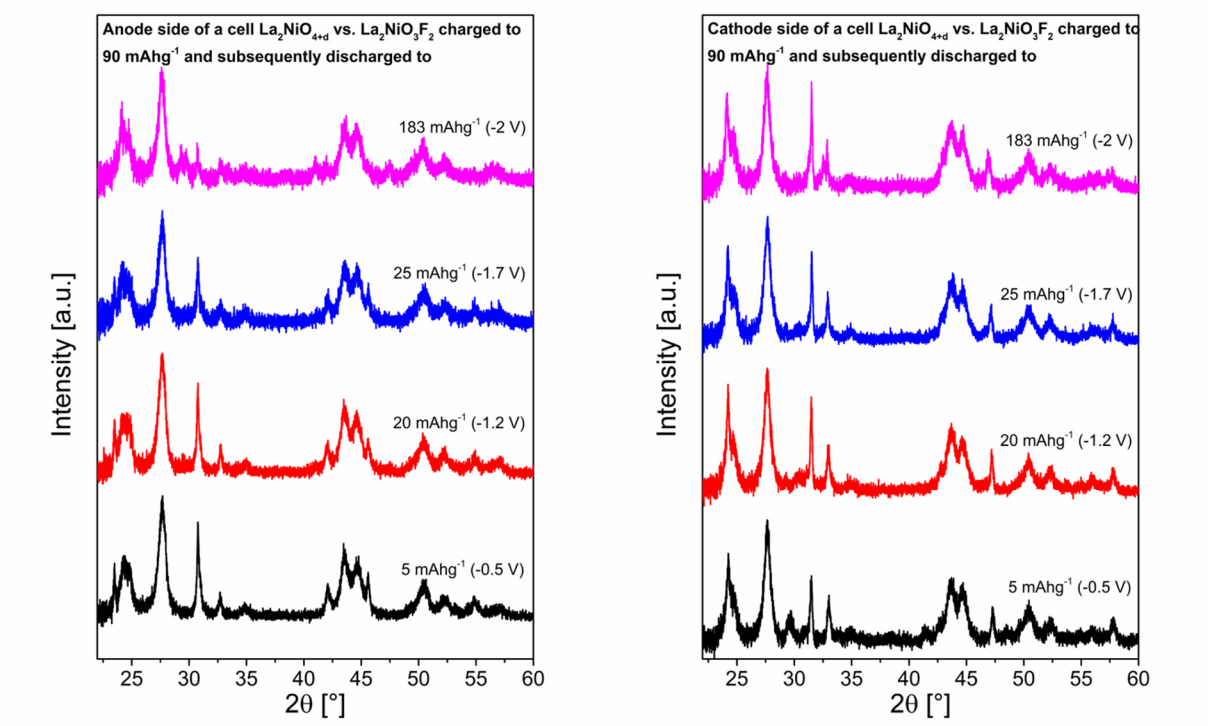

Figure 6-27: XRD patterns of anode and cathode sides of cells La_2NiO_{4+d} against $La_2NiO_3F_2$ charged to 90 $mAhg^{-1}$ and subsequently discharged to various cut-off potentials.

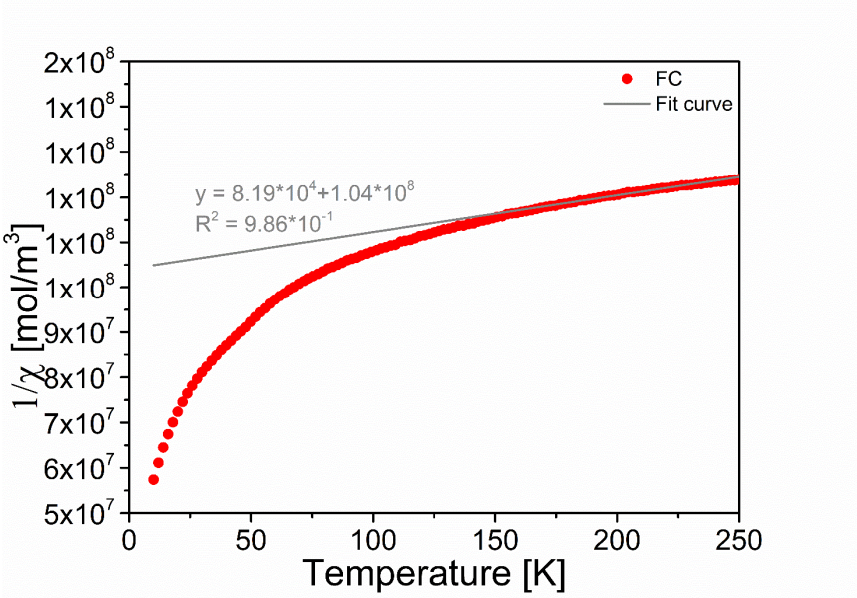

Figure 6-28: $\chi^{-1}(T)$ curve of a scratched-off cathode side of a cell $La_2NiO_3F_2$ vs. Pb/PbF_2 containing a large relative phase fraction of the monoclinic #2 phase measured at $\mu_0 = 1$ T. The fitting curve of the Curie-Weiss fit, the corresponding linear function and the coefficient of determination are also given. The curve is corrected from the diamagnetic contributions of the present phases and the gelatine capsules and straws used for the measurements

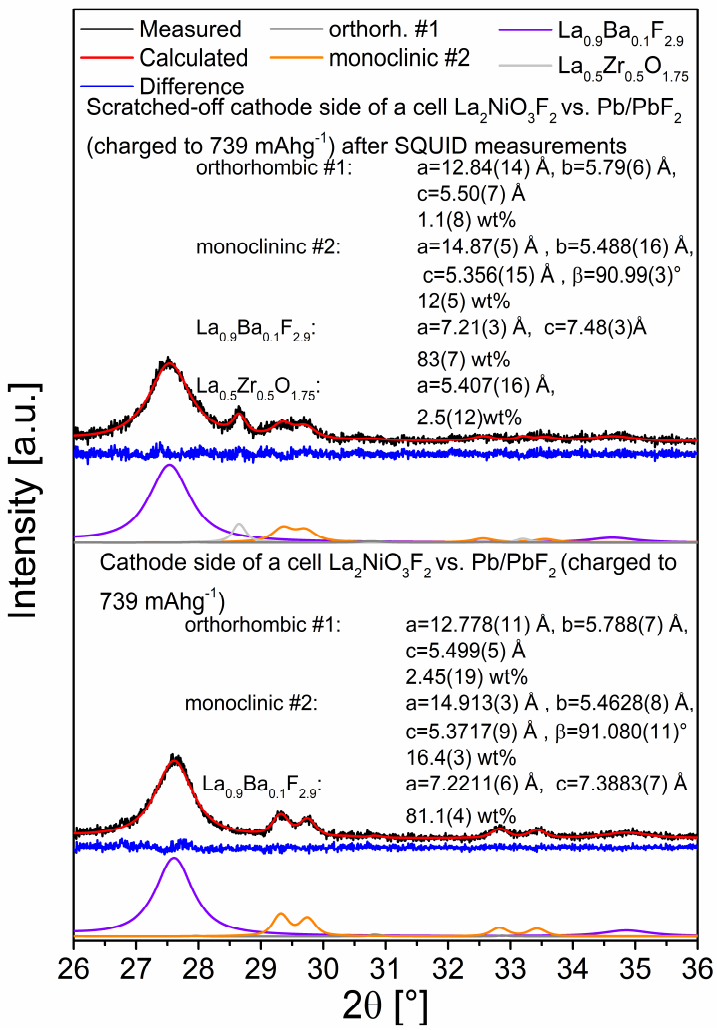

Figure 6-29: Rietveld refinements of XRD data of the cathode side of a cell $La_2NiO_3F_2$ vs. Pb/PbF_2 charged to 739 $mAhg^{-1}$ and of scratched-off cathode site of a cell $La_2NiO_3F_2$ vs. Pb/PbF_2 charged to 739 $mAhg^{-1}$ after SQUID measurements.

Table 6-7: Structural parameters of $La_{1.3}Sr_{1.7}Mn_2O_7$ (space group: *I*4/*mmm*) derived from Rietveld analysis of XRD data. The obtained parameters correspond well with the structure reported in reference 226. The occupation factors of La1/Sr1 and La2/Sr2 were adjusted to the nominal composition assuming a random La/Sr distribution. The anion sites $X1^{eq}$, $X2^{ap,central}$, $X3^{ap,terminal}$ and $X4^{int}$ refer to the equatorial, central apical, terminal apical and interstitial sites, respectively.

Atom	Wyckoff position	x	y	z	Occupancy	B [Å²]
La1/Sr1	2*b*	**0**	**0**	½	**0.481/0.519**	1.81(6)
La2/Sr2	4*e*	**0**	**0**	0.31599(9)	**0.410/0.590**	1.81(6)
Mn1	4*e*	**0**	**0**	0.0976(2)	**1**	1.81(6)
O1 at $X1^{eq}$	8*g*	**0**	½	0.0923(6)	**1**	1.81(6)
O2 at $X2^{ap,central}$	2*a*	**0**	**0**	**0**	**1**	1.81(6)
O3 at $X3^{ap,terminal}$	4*e*	**0**	**0**	0.7948(7)	**1**	1.81(6)
$X4^{int}$	4*d*	½	**0**	¼	**0**	1.81(6)
a [Å]	3.8745(1)			***c*** [Å]	20.1673(5)	
R_{wp}(XRD) [%] 8.08		**GOF(XRD)** 1.25			**R_{Bragg} [%]** 2.84 (XRD)	

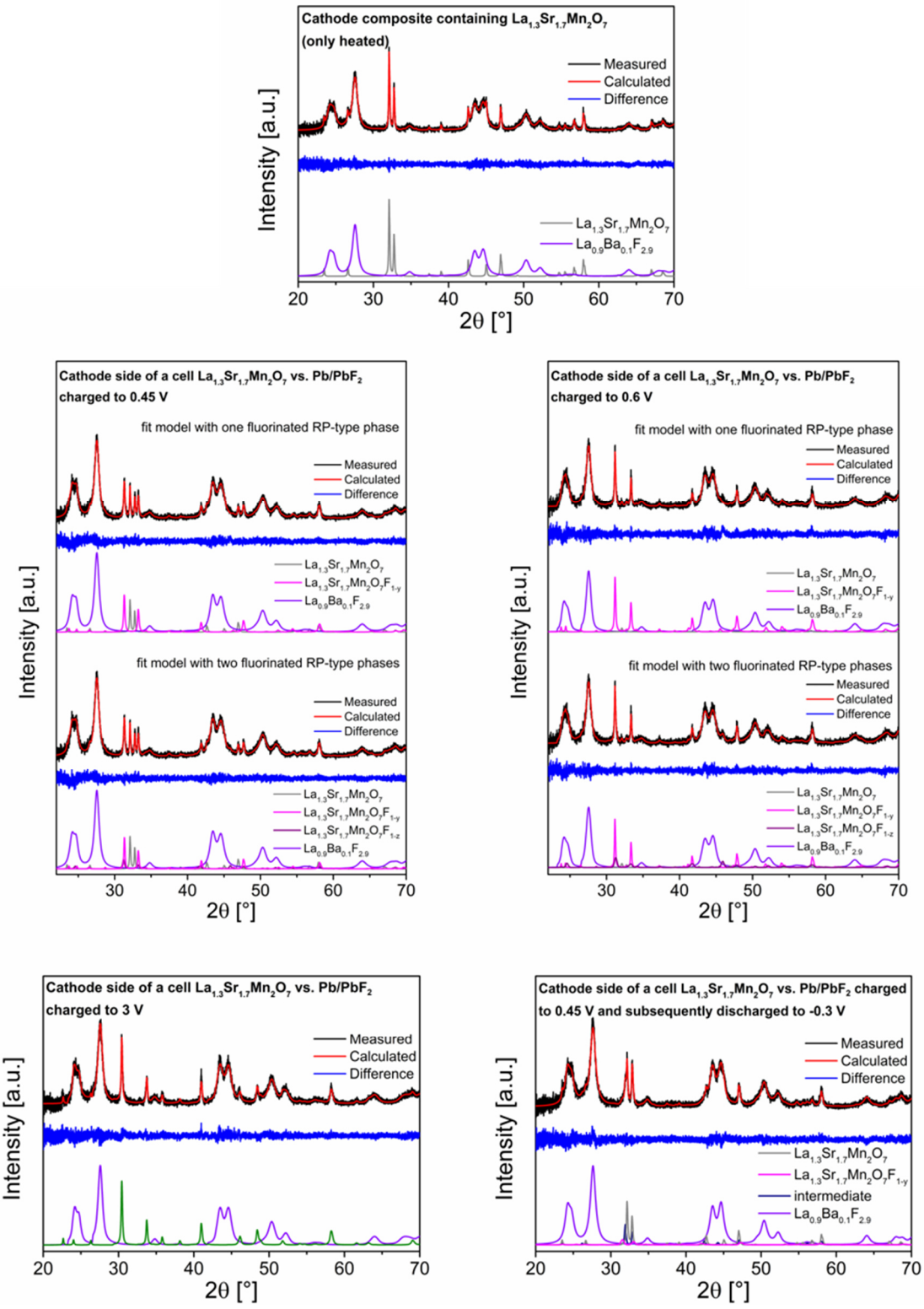

Figure 6-30: Rietveld refinements of XRD patterns of cathode sides of cells $La_{1.3}Sr_{1.7}Mn_2O_7$ against Pb/PbF_2 heated to 170 °C for 240 h, charged to 0.45, 0.6 and 3 V and charged to 0.45 V and subsequently discharged -0.3 V. Improved fits for the patterns of the charged cells could be obtained when using a fit model with two RP-type phases with slightly varying lattice parameters. For some these samples, a texturing of one of these fluorinated phases was found in addition. The discussed phase fractions, unit cell volumes and lattice parameters were, however, derived using a fit model with only one fluorinated RP-type phase. The correlated errors should be in the same order of magnitude for all samples.

Table 6-8: Structural parameters of $La_{1.3}Sr_{1.7}Mn_2O_7F_{1-y}$ (space group: *P*4/*nmm*) derived from Rietveld analysis of XRD data. The parameters were determined on the XRD pattern of the cathode side of the cell $La_{1.3}Sr_{1.7}Mn_2O_7$ against Pb/PbF_2 charged to 0.7 V, containing the highest phase fraction of this phase. The obtained parameters correspond well with the structure reported in reference 22, even though the atomic positions of the anions were not refined. The occupation factors of La1/Sr1 and La2/Sr2 were adjusted to the nominal composition assuming a random La/Sr distribution. The anion sites $X1^{eq}$, $X2^{ap,central}$, $X3^{ap,terminal}$ and $X4^{int}$ refer to the equatorial, central apical, terminal apical and interstitial sites, respectively.

Atom	**Wyckoff position**	**x**	**y**	**z**	**Occupancy**	**B [Å²]**
La1/Sr1	2*c*	¼	¼	0.2378(8)	**0.433/0.566**	-1.7(2)
La2a/Sr2b	2*c*	¼	¼	0.4316(8)	**0.433/0.566**	-1.7(2)
La2b/Sr2b	2*c*	¼	¼	0.0681(7)	**0.433/0.566**	-1.7(2)
Mn1	2*c*	¾	¾	0.1481(15)	**1**	-1.7(2)
Mn2	2*c*	¾	¾	0.3306(19)	**1**	-1.7(2)
O1a at $X1^{eq}$a	4*f*	¾	¼	**0.1430**	**1**	-1.7(2)
O1b at $X1^{eq}$b	4*f*	¾	¼	**0.3193**	**1**	-1.7(2)
O2 at $X2^{ap,central}$	2*c*	¾	¾	**0.2298**	**1**	-1.7(2)
O3a at $X3^{ap,terminal}$a	2*c*	¾	¾	**0.0519**	**1**	-1.7(2)
O3b at $X3^{ap,terminal}$b	2*c*	¾	¾	**0.407**	**1**	-1.7(2)
F1 at $X4^{int}$	2*b*	¾	¼	½	**1**	-1.7(2)
a [Å]	3.8019(5)		***c*** [Å]	21.974(5)		
R_{wp}(XRD) [%] 7.74	**GOF(XRD)** 1.07			**R_{Bragg} [%]** 1.92 (XRD)		

Table 6-9: Structural parameters of $La_{1.3}Sr_{1.7}Mn_2O_7F_{2-x}$ (space group: *I*4/*mmm*) derived from Rietveld analysis of XRD data. The parameters were determined on the XRD pattern of the cathode side of the cell $La_{1.3}Sr_{1.7}Mn_2O_7$ against Pb/PbF_2 chatged to 3 V, containing the highest phase fraction of this phase. The obtained parameters correspond well with the structure reported in reference 23. The occupation factors of La1/Sr1 and La2/Sr2 were adjusted to the nominal composition assuming a random La/Sr distribution. The anion sites $X1^{eq}$, $X2^{ap,central}$, $X3^{ap,terminal}$ and $X4^{int}$ refer to the equatorial, central apical, terminal apical and interstitial sites, respectively.

Atom	**Wyckoff position**	**x**	**y**	**z**	**Occupancy**	**B [Å²]**
La1/Sr1	2*b*	**0**	**0**	½	**0.481/0.519**	-0.7(1)
La2/Sr2	4*e*	**0**	**0**	0.3205(3)	**0.410/0.590**	-0.7(1)
Mn1	4*e*	**0**	**0**	0.0824(7)	**1**	-0.7(1)
O1 at $X1^{eq}$	8*g*	**0**	½	0.8303(16)	**1**	-0.7(1)
O2 at $X2^{ap,central}$	2*a*	**0**	**0**	**0**	**1**	-0.7(1)
O3 at $X3^{ap,terminal}$	4*e*	**0**	**0**	0.0825(16)	**1**	-0.7(1)
F1 $X4^{int}$	4*d*	½	**0**	¼	**0**	-0.7(1)
a [Å]	3.7649(3)		***c*** [Å]	23.639(3)		
R_{wp}(XRD) [%] 7.39	**GOF(XRD+NPD)** 1.09			**R_{Bragg} [%]** 2.84 (XRD)		

Table 6-10: Estimation of fluoride content in $La_{1.3}Sr_{1.7}Mn_2O_7F_{1-y}$ based on the reached capacity and the relative phase fraction of $La_{1.3}Sr_{1.7}Mn_2O_7F_{1-y}$ found in the cathode side of a cell after charging to a specific cut-off potential.

Charging cut-off potential [V]	**Reached charging capacity [mAhg^{-1}]**	**Average fluoride content**	**Relative phase fraction of $La_{1.3}Sr_{1.7}Mn_2O_7F_{1-y}$ [%]**	**Fluoride content in $La_{1.3}Sr_{1.7}Mn_2O_7F_{1-y}$**
0.45	~ 18	~ 0.37	~ 61	~ 0.61
0.5	~ 27	~ 0.54	~ 88	~ 0.62
0.55	~ 29	~ 0.59	~ 89	~ 0.66
0.6	~ 30	~ 0.62	~ 94	~ 0.66
0.7	~ 32	~ 0.65	~ 100	~ 0.65

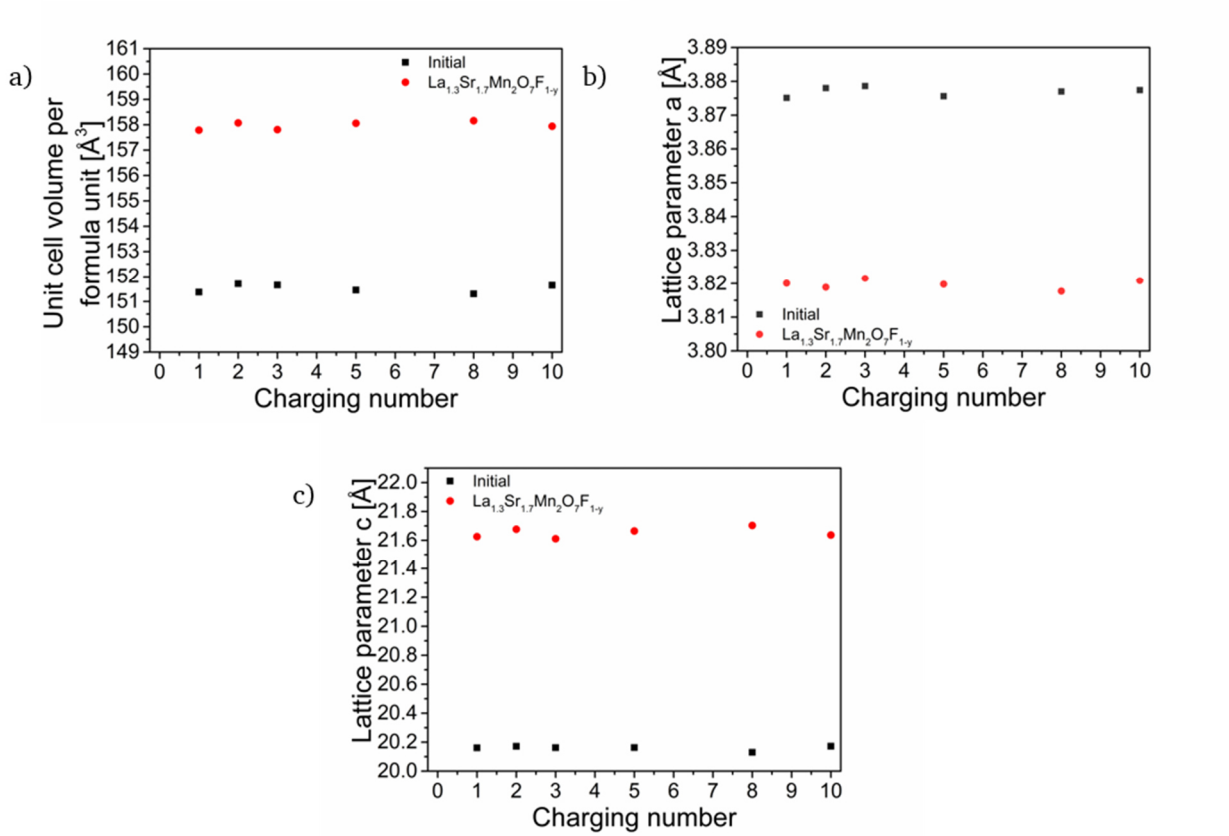

Figure 6-31: Unit cell volumes per formula unit (a) and lattice parameters *a* (b) and *c* (c) of $La_{1.3}Sr_{1.7}Mn_2O_7$, $La_{1.3}Sr_{1.7}Mn_2O_7F_{1-y}$ and an intermediate phase in the cathode sides of cells $La_{1.3}Sr_{1.7}Mn_2O_7$ against Pb/PbF_2 cycled for various cycle numbers between the charging cut-off potential 0.45 V and the discharging cut-off potential -0.3 V. The volumes and lattice parameters of cathode sides of cells within the charged state are shown.

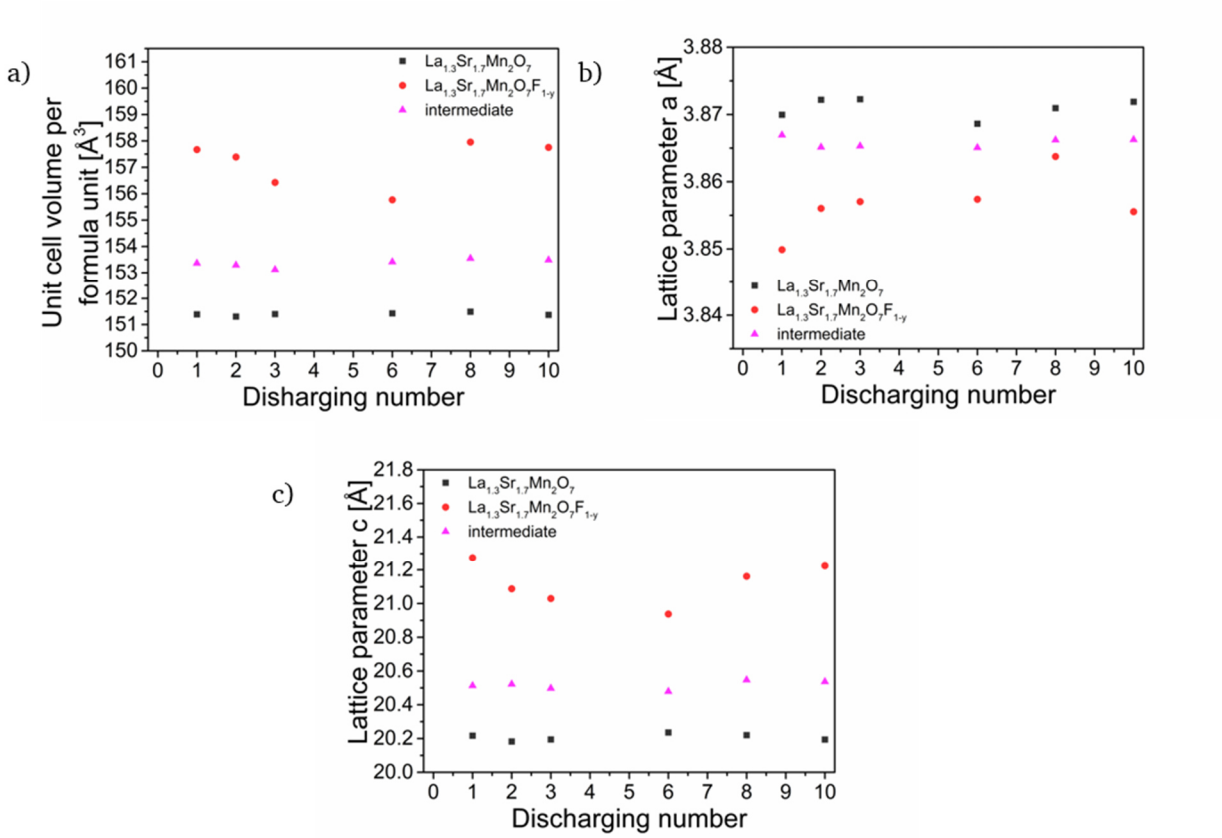

Figure 6-32: Unit cell volumes per formula unit (a) and lattice parameters *a* (b) and *c* (c) of $La_{1.3}Sr_{1.7}Mn_2O_7$, $La_{1.3}Sr_{1.7}Mn_2O_7F_{1-y}$ and an intermediate phase in the cathode sides of cells $La_{1.3}Sr_{1.7}Mn_2O_7$ against Pb/PbF_2 cycled for various cycle numbers between the charging cut-off potential 0.45 V and the discharging cut-off potential -0.3 V. The volumes and lattice parameters of cathode sides of cells within the discharged state are shown.

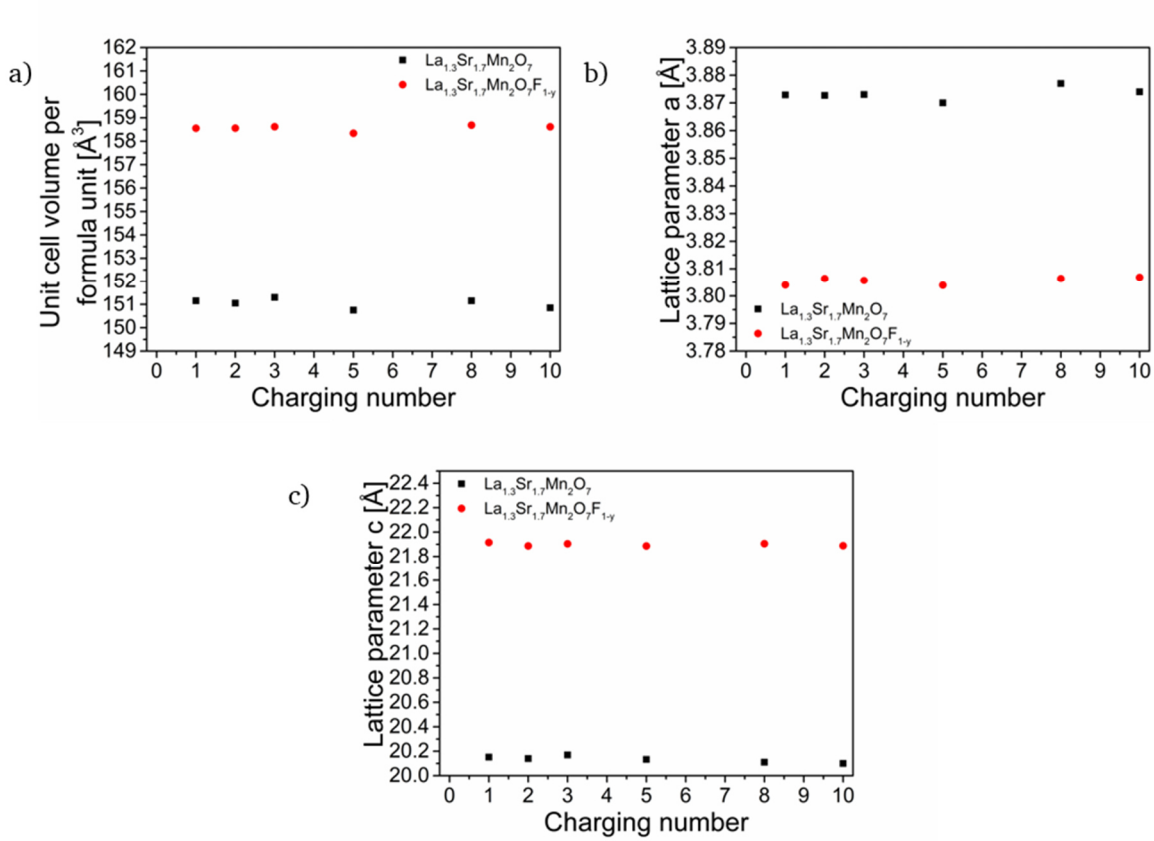

Figure 6-33: Unit cell volumes per formula unit (a) and lattice parameters *a* (b) and *c* (c) of $La_{1.3}Sr_{1.7}Mn_2O_7$, $La_{1.3}Sr_{1.7}Mn_2O_7F_{1-y}$ and an intermediate phase in the cathode sides of cells $La_{1.3}Sr_{1.7}Mn_2O_7$ against Pb/PbF_2 cycled for various cycle numbers between the charging cut-off potential 0.6 V and the discharging cut-off potential -0.3 V. The volumes and lattice parameters of cathode sides of cells within in charged state are shown.

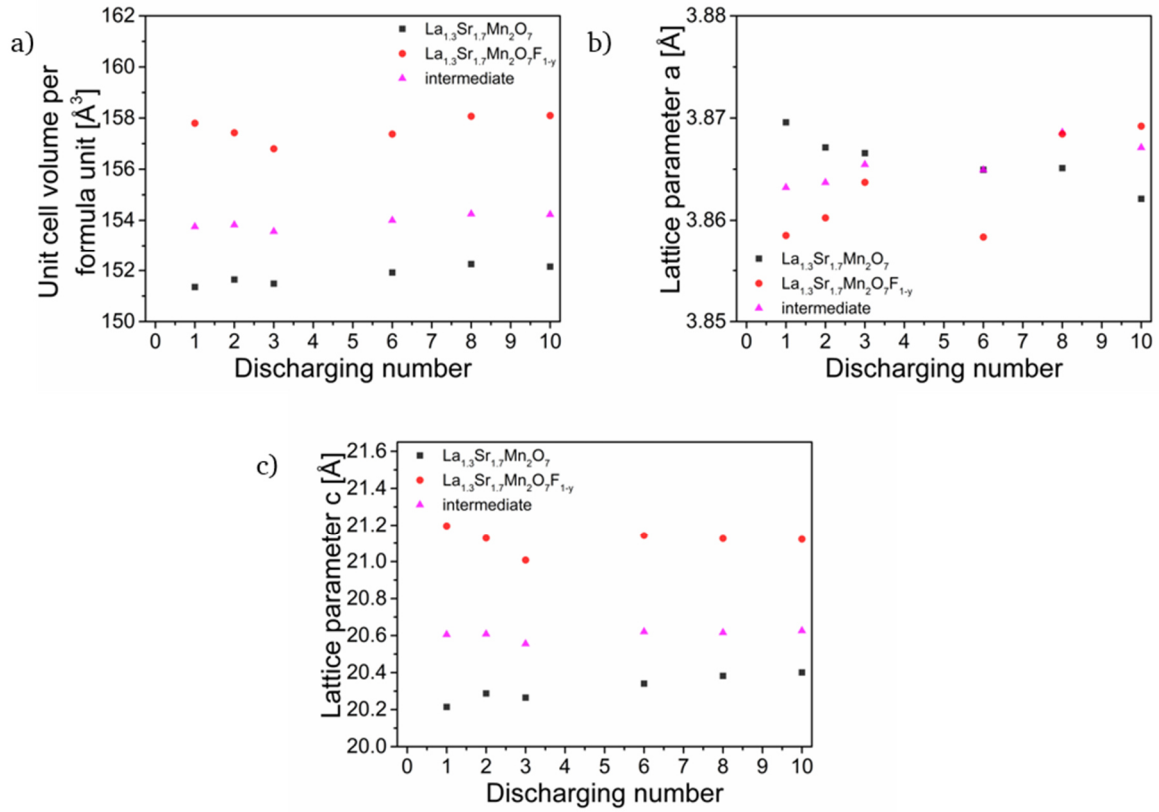

Figure 6-34: Unit cell volumes per formula unit (a) and lattice parameters *a* (b) and *c* (c) of $La_{1.3}Sr_{1.7}Mn_2O_7$, $La_{1.3}Sr_{1.7}Mn_2O_7F_{1-y}$ and an intermediate phase in the cathode sides of cells $La_{1.3}Sr_{1.7}Mn_2O_7$ against Pb/PbF_2 cycled for various cycle numbers between the charging cut-off potential 0.6 V and the discharging cut-off potential -0.3 V. The volumes and lattice parameters of cathode sides of cells within in discharged state are shown.

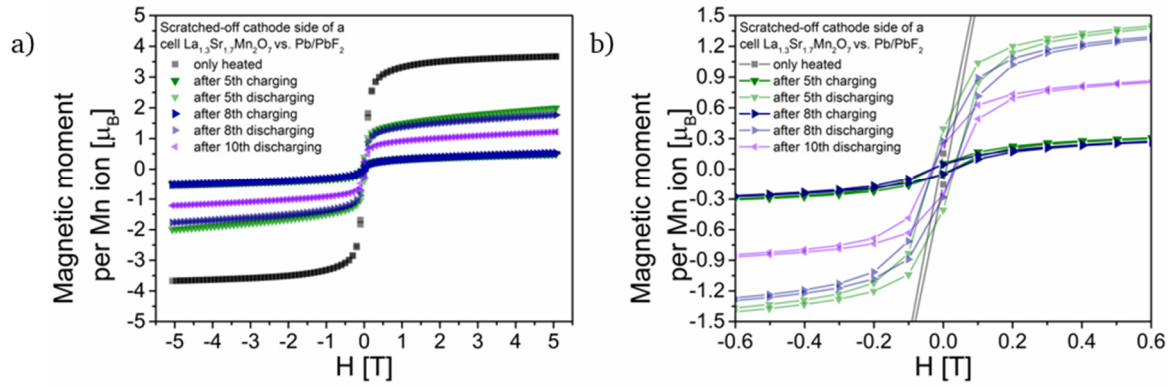

Figure 6-35: Comparison of M(H) curves of scratched-off cathode side of cells $La_{1.3}Sr_{1.7}Mn_2O_7$ against Pb/PbF_2 cycled for various cycle numbers between the charging cut-off potential 0.45 V and the discharging cut-off potential -0.3 V measured at 10 K (a) and a magnification of the M(H) curves in the T_c temperature region (b). Measurements of scratched-off cathode sides of cells within the charged and discharged states are shown. For reference, a cell, which was only heated (discharged state), is given.

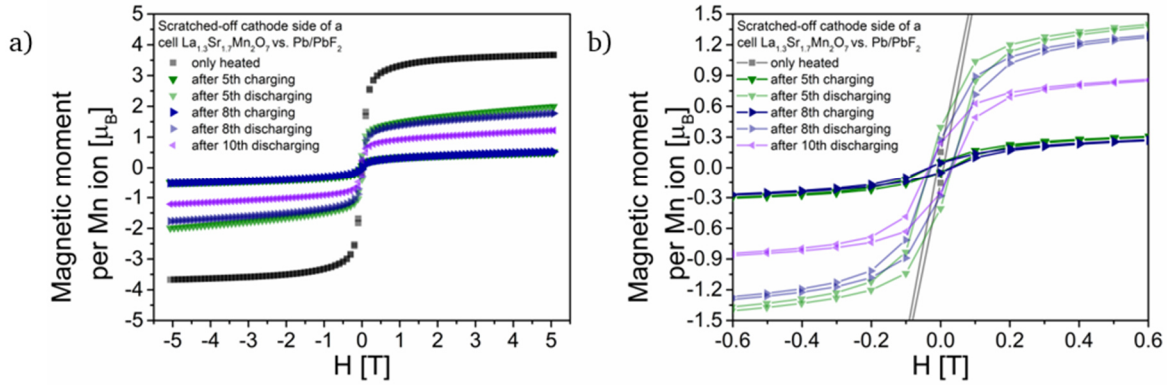

Figure 6-36: Comparison of M(H) curves of scratched-off cathode side of cells $La_{1.3}Sr_{1.7}Mn_2O_7$ against Pb/PbF_2 cycled for various cycle numbers between the charging cut-off potential 0.45 V and the discharging cut-off potential -0.3 V measured at 10 K (a) and a magnification of the M(H) curves in the T_c temperature region (b). Measurements of scratched-off cathode sides of cells within the charged and discharged states are shown. For reference, a cell, which was only heated (discharged state), is given.

7 References

1. Wissel, K.; Dasgupta, S.; Benes, A.; Schoch, R.; Bauer, M.; Witte, R.; Fortes, A. D.; Erdem, E.; Rohrer, J.; Clemens, O., Developing intercalation based anode materials for fluoride-ion batteries: topochemical reduction of $Sr_2TiO_3F_2$ via a hydride based defluorination process. *Journal of Materials Chemistry A* **2018,** *6* (44), 22013-22026.

2. Wissel, K.; Vogel, T.; Dasgupta, S.; Fortes, A. D.; Slater, P. R.; Clemens, O., Topochemical Fluorination of n = 2 Ruddlesden-Popper Type $Sr_3Ti_2O_7$ to $Sr_3Ti_2O_5F_4$ and Its Reductive Defluorination. *Inorg. Chem.* **2020,** *59* (2), 1153-1163.

3. Wissel, K.; Heldt, J.; Groszewicz, P. B.; Dasgupta, S.; Breitzke, H.; Donzelli, M.; Waidha, A. I.; Fortes, A. D.; Rohrer, J.; Slater, P. R.; Buntkowsky, G.; Clemens, O., Topochemical Fluorination of La_2NiO_{4+d}: Unprecedented Ordering of Oxide and Fluoride Ions in $La_2NiO_3F_2$. *Inorg. Chem.* **2018,** *57* (11), 6549-6560.

4. Wissel, K.; Malik, A. M.; Vasala, S.; Plana-Ruiz, S.; Kolb, U.; Slater, P. R.; da Silva, I.; Alff, L.; Rohrer, J.; Clemens, O., Topochemical Reduction of $La_2NiO_3F_2$: The First Ni-Based Ruddlesden–Popper n = 1 T′-Type Structure and the Impact of Reduction on Magnetic Ordering. *Chem. Mater.* **2020,** *32* (7), 3160-3179.

5. Vasala, S.; Jakob, A.; Wissel, K.; Waidha, A. I.; Alff, L.; Clemens, O., Reversible Tuning of Magnetization in a Ferromagnetic Ruddlesden–Popper-Type Manganite by Electrochemical Fluoride-Ion Intercalation. *Advanced Electronic Materials* **2019,** *6* (2), 1900974.

6. Greaves, C.; Francesconi, M. G., Fluorine insertion in inorganic materials. *Curr. Opin. Solid State Mater. Sci.* **1998,** *3* (2), 132-136.

7. Clemens, O.; Slater, P. R., Topochemical modifications of mixed metal oxide compounds by low-temperature fluorination routes. *Rev. Inorg. Chem.* **2013,** *33* (2-3).

8. Slater, P.; Driscoll, L., Modification of Magnetic and Electronic Properties, in Particular Superconductivity, by Low Temperature Insertion of Fluorine into Oxides. In *Progr Fluor Sci Ser*, Tressaud, A.; Poeppelmeier, K., Eds. Elsevier: Boston, 2016, DOI: https://doi.org/10.1016/B978-0-12-801639-8.00018-0 pp 401-421.

9. McCabe, E. E.; Greaves, C., Review: Fluorine insertion reactions into pre-formed metal oxides. *J. Fluorine Chem.* **2007,** *128*, 448-458.

10. Sanjaya Ranmohotti, K. G.; Josepha, E.; Choi, J.; Zhang, J.; Wiley, J. B., Topochemical Manipulation of Perovskites: Low-Temperature Reaction Strategies for Directing Structure and Properties. *Adv. Mater.* **2011,** *23* (4), 442-460.

11. Hayward, M. A., Topochemical reactions of layered transition-metal oxides. *Semicond. Sci. Technol.* **2014,** *29* (6), 064010.

12. Yamamoto, T.; Kageyama, H., Hydride Reductions of Transition Metal Oxides. *Chem. Lett.* **2013,** *42* (9), 946-953.

13. Kageyama, H.; Hayashi, K.; Maeda, K.; Attfield, J. P.; Hiroi, Z.; Rondinelli, J. M.; Poeppelmeier, K. R., Expanding frontiers in materials chemistry and physics with multiple anions. *Nature Communications* **2018,** *9* (1), 772.

14. Ruddlesden, S. N.; Popper, P., New compounds of the K_2NiF_4 type. *Acta Crystallographica* **1957,** *10* (8), 538-539.

15. Ruddlesden, S. N., Popper P. , The compund $Sr_3Ti_2O_7$ and its structure. *Acta Cryst.* **1958,** *11*, 54-55.

16. Beznosikov, B. V.; Aleksandrov, K. S., Perovskite-like crystals of the Ruddlesden-Popper series. *Crystallography Reports* **2000,** *45* (5), 792-798.

17. West, A. R., *Solid State Chemistry and its Applications*. 2. illustrated ed.; John Wiley & Sons: 2014, DOI.

18. Nowroozi, M. A.; Ivlev, S.; Rohrer, J.; Clemens, O., La_2CoO_4: a new intercalation based cathode material for fluoride ion batteries with improved cycling stability. *Journal of Materials Chemistry A* **2018,** *6* (11), 4658-4669.

19. Nowroozi, M. A.; Wissel, K.; Donzelli, M.; Hosseinpourkahvaz, N.; Plana-Ruiz, S.; Kolb, U.; Schoch, R.; Bauer, M.; Malik, A. M.; Rohrer, J.; Ivlev, S.; Kraus, F.; Clemens, O., High cycle life all-solid-state fluoride ion battery with La_2NiO_{4+d} high voltage cathode. *Communications Materials* **2020,** *1* (1), 27.

20. Nowroozi, M. A.; Wissel, K.; Rohrer, J.; Munnangi, A. R.; Clemens, O., $LaSrMnO_4$: Reversible Electrochemical Intercalation of Fluoride Ions in the Context of Fluoride Ion Batteries. *Chem. Mater.* **2017,** *29* (8), 3441-3453.

21. Aikens, L. D.; Gillie, L. J.; Li, R. K.; Greaves, C., Staged fluorine insertion into manganese oxides with Ruddlesden–Popper structures: $LaSrMnO_4F$ and $La_{1.2}Sr_{1.8}Mn_2O_7F$. *J. Mater. Chem.* **2002,** *12* (2), 264-267.

22. Greaves C., K. J. L., Francesconi M.G., Aikens L.D. and Gillie J.L., Synthetic strategies for new inorganic oxide fluorides and oxidesulfates. *J. Mater. Chem.* **1998,** *9*, 111-116.

23. Asano, H.; Hayakawa, J.; Matsui, M., Giant magnetoresistance of a two-dimensional ferromagnet $La_{2-2x}Ca_{1+2x}Mn_2O_7$. *Appl. Phys. Lett.* **1996,** *68* (25), 3638-3640.

24. Wang, A.; Cao, G., Electron-transport and magnetic properties of the layered perovskite $La_{2-2x}Sr_{1+2x}Mn_2O_7$. *J. Magn. Magn. Mater.* **2006,** *305* (2), 520-523.

25. Vaknin, D.; Sinha, S. K.; Moncton, D. E.; Johnston, D. C.; Newsam, J. M.; Safinya, C. R.; King, H. E., Antiferromagnetism in La_2CuO_{4-y}. *Phys. Rev. Lett.* **1987,** *58* (26), 2802-2805.

26. Grenier, A.; Porras-Gutierrez, A. G.; Body, M.; Legein, C.; Chrétien, F.; Raymundo-Piñero, E.; Dollé, M.; Groult, H.; Dambournet, D., Solid Fluoride Electrolytes and Their Composite with Carbon: Issues and Challenges for Rechargeable Solid State Fluoride-Ion Batteries. *The Journal of Physical Chemistry C* **2017,** *121* (45), 24962-24970.

27. Anji Reddy, M.; Fichtner, M., Batteries based on fluoride shuttle. *J. Mater. Chem.* **2011,** *21* (43), 17059-17062.

28. Rongeat, C.; Anji Reddy, M.; Diemant, T.; Behm, R. J.; Fichtner, M., Development of new anode composite materials for fluoride ion batteries. *J. Mater. Chem. A* **2014,** *2* (48), 20861-20872.

29. Nowroozi, M. A.; Clemens, O., Insights on the Behavior of Conversion-Based Anode Materials for Fluoride Ion Batteries by Testing against an Intercalation-Based Reference Cathode. *ACS Applied Energy Materials* **2018,** *1* (11), 6626-6637.

30. Dasgupta, S.; Das, B.; Knapp, M.; Brand, R. A.; Ehrenberg, H.; Kruk, R.; Hahn, H., Intercalation-Driven Reversible Control of Magnetism in Bulk Ferromagnets. **2014,** *26* (27), 4639-4644.

31. Dasgupta, S.; Das, B.; Li, Q.; Wang, D.; Baby, T. T.; Indris, S.; Knapp, M.; Ehrenberg, H.; Fink, K.; Kruk, R.; Hahn, H., Toward On-and-Off Magnetism: Reversible Electrochemistry to Control Magnetic Phase Transitions in Spinel Ferrites. **2016,** *26* (41), 7507-7515.

32. Zhang, Q.; Luo, X.; Wang, L.; Zhang, L.; Khalid, B.; Gong, J.; Wu, H., Lithium-Ion Battery Cycling for Magnetism Control. *Nano Lett.* **2016,** *16* (1), 583-587.

33. Wei, G.; Wei, L.; Wang, D.; Chen, Y.; Tian, Y.; Yan, S.; Mei, L.; Jiao, J., Reversible control of the magnetization of spinel ferrites based electrodes by lithium-ion migration. *Scientific Reports* **2017,** *7* (1), 12554.

34. Molinari, A.; Hahn, H.; Kruk, R., Voltage-Control of Magnetism in All-Solid-State and Solid/Liquid Magnetoelectric Composites. **2019,** *31* (26), 1806662.

35. Navarro-Senent, C.; Quintana, A.; Menéndez, E.; Pellicer, E.; Sort, J., Electrolyte-gated magnetoelectric actuation: Phenomenology, materials, mechanisms, and prospective applications. **2019,** *7* (3), 030701.

36. Bednorz, J. G.; Müller, K. A., Possible highT c superconductivity in the Ba-La-Cu-O system. *Zeitschrift für Physik B Condensed Matter* **1986,** *64* (2), 189-193.

37. Cava, R. J.; Batlogg, B.; Chen, C. H.; Rietman, E. A.; Zahurak, S. M.; Werder, D., Oxygen stoichiometry, superconductivity and normal-state properties of $YBa_2Cu_3O_{7-\delta}$. *Nature* **1987,** *329* (6138), 423-425.

38. Chevalier, B.; Tressaud, A.; Lepine, B.; Amine, K.; Dance, J. M.; Lozano, L.; Hickey, E.; Etourneau, J., Stabilization of a New Superconducting Phase by Low-Temperature Fluorination of La_2CuO_4. *Physica C* **1990,** *167* (1-2), 97-101.

39. Chu, C. W.; Hor, P. H.; Meng, R. L.; Gao, L.; Huang, Z. J.; Wang a, Y., Evidence for superconductivity above 40 K in the La-Ba-Cu-O compound system. *Phys. Rev. Lett.* **1987,** *58* (4), 405-407.

40. Demazeau, G.; Tresse, F.; Plante, T.; Chevalier, B.; Etourneau, J.; Michel, C.; Hervieu, M.; Raveau, B.; Lejay, P.; Sulpice, A.; Tournier, R., Evolution of the Superconducting Properties in the La_2CuO_4 Lattice Versus Oxygen-Pressure. *Physica C* **1988,** *153*, 824-825.

41. MacManus, J. L.; Fray, D. J.; Evetts, J. E., Fluorination of $Y_1Ba_2Cu_3O_{7-x}$ by a solid state electrochemical method. *Physica C: Superconductivity and its Applications* **1991,** *184* (1-3), 172-184.

42. Chen, J. M.; Nachimuthu, P.; Liu, R. S.; Lees, S. T.; Gibbons, K. E.; Gameson, I.; Jones, M. O.; Edwards, P. P., Hole states in fluorine-doped La_2CuO_4 thin films probed by polarized x-ray-absorption spectroscopy. *Physical Review B* **1999,** *60* (9), 6888-6892.

43. Freltoft, T.; Buttrey, D. J.; Aeppli, G.; Vaknin, D.; Shirane, G., Magnetic correlations and their dependence on excess oxygen in $La_2NiO_{4+\delta}$. *Physical Review B* **1991,** *44* (10), 5046-5056.

44. Rodriguez-Carvajal, J.; Fernandez-Diaz, M. T.; Martinez, J. L., Neutron diffraction study on structural and magnetic properties of La_2NiO_4. *J. Phys.: Condens. Matter* **1991,** *3*, 3215-3234.

45. Hayward, M. A., Structural and Magnetic Properties of Topotactically Reduced $YSr_2Mn_2O_{7-x}$ ($0 < x < 1.5$). *Chem. Mater.* **2006,** *18*, 321-327.

46. Gurusinghe, N. N.; Fones, J. C.; Marco, J. F.; Berry, F. J.; Greaves, C., Fluorine insertion into the Ruddlesden-Popper phase $La_2BaFe_2O_7$: the structure and magnetic properties of $La_2BaFe_2O_5F_4$. *Dalton Trans* **2014,** *43* (5), 2038-43.

47. Battle, P. D.; Rosseinsky, M. J., Synthesis, structure, and magnetic properties of n=2 Ruddlesden–Popper manganates. *Curr. Opin. Solid State Mater. Sci.* **1999,** *4* (2), 163-170.

48. McCabe, E. E.; Greaves, C., Synthesis and Structural and Magnetic Characterization of Mixed Manganese−Copper n = 1 Ruddlesden−Popper Phases. *Chem. Mater.* **2006,** *18* (24), 5774-5781.

49. Sánchez-Andújar, M.; Señarís-Rodríguez, M. A., Cation Ordering and Electrical Properties of the Ruddlesden-Popper $Gd_{2-2x}Sr_{1+2x}Co_2O_7$ Compounds (x = 0 and 0.10). **2007,** *633* (11-12), 1890-1896.

50. Müller-Buschbaum, H.; Wollschläger, M. W., Über ternäre Oxocuprate. VII. Zur Kristallstruktur von Nd_2CuO_4. *Z. Anorg. Allg. Chem.* **1975,** *414* (1), 76-80.

51. Chen, B.-H., Introduction of a Tolerance Factor for the Nd_2CuO_4 (T′)-Type Structure. *J. Solid State Chem.* **1996,** *125* (1), 63-66.

52. Chaillout, C.; Cheong, S. W.; Fisk, Z.; Lehmann, M. S.; Marezio, M.; Morosin, B.; Schirber, J. E., The crystal structure of superconducting $La_2CuO_{4.032}$ by neutron diffraction. *Physica C: Superconductivity* **1989,** *158* (1), 183-191.

53. Longo, J. M.; Raccah, P. M., The structure of La_2CuO_4 and $LaSrVO_4$. *J. Solid State Chem.* **1973,** *6* (4), 526-531.

54. Shannon, R. D., Revised Effective Ionic Radii and Systematic Studies of Interatomie Distances in Halides and Chaleogenides. *Acta. Cryst. A* **1976,** *32*, 751.

55. Ishii, T.; Tsuboi, S.; Sakane, G.; Yamashita, M.; Breedlove, B. K., Universal spectrochemical series of six-coordinate octahedral metal complexes for modifying the ligand field splitting. *Dalton Transactions* **2009**, DOI: 10.1039/B810590A (4), 680-687.

56. Takeiri, F.; Yamamoto, T.; Hayashi, N.; Hosokawa, S.; Arai, K.; Kikkawa, J.; Ikeda, K.; Honda, T.; Otomo, T.; Tassel, C.; Kimoto, K.; Kageyama, H., $AgFeOF_2$: A Fluorine-Rich Perovskite Oxyfluoride. *Inorg. Chem.* **2018,** *57* (11), 6686-6691.

57. Clemens, O.; Slater, P. R., Topochemical modifications of mixed metal oxide compounds by low-temperature fluorination routes. *Reviews in Inorganic Chemistry* **2013,** *33* (2-3), 105-117.

58. Pauling, L., The Principles Determining the Structure of Complex Ionic Crystals. *J. Am. Chem. Soc.* **1929,** *51* (4), 1010-1026.

59. Tsujimoto, Y.; Yamaura, K.; Hayashi, N.; Kodama, K.; Igawa, N.; Matsushita, Y.; Katsuya, Y.; Shirako, Y.; Akaogi, M.; Takayama-Muromachi, E., Topotactic Synthesis and Crystal Structure of a Highly Fluorinated Ruddlesden–Popper-Type Iron Oxide, $Sr_3Fe_2O_{5+x}F_{2-x}$ ($x \approx 0.44$). *Chem. Mater.* **2011,** *23* (16), 3652-3658.

60. Aikens, L. D.; Li, R. K.; Greaves, C., The synthesis and structure of a new oxide fluoride, $LaSrMnO_4F$, with staged fluorine insertion. *Chem. Commun.* **2000**, DOI: 10.1039/b007045i (21), 2129-2130.

61. Senff, D.; Reutler, P.; Braden, M.; Friedt, O.; Bruns, D.; Cousson, A.; Bouree, F.; Merz, M.; Buchner, B.; Revcolevschi, A., Crystal and magnetic structure of $La_{1-x}Sr_{1+x}MnO_4$: Role of the orbital degree of freedom. *Physical Review B* **2005,** *71* (2), 024425.

62. Sivakumar, T.; Wiley, J. B., Topotactic route for new layered perovskite oxides containing fluorine: $Ln_{1.2}Sr_{1.8}Mn_2O_7F_2$ (Ln=Pr, Nd, Sm, Eu, and Gd). *Mater. Res. Bull.* **2009,** *44* (1), 74-77.

63. Slater, P. R., Poly(vinylidene fluoride) as a reagent for the synthesis of K_2NiF_4-related inorganic oxide fluorides. *J. Fluorine Chem.* **2002,** *117* (1), 43-45.

64. Heap, R. S., P.R., Synthesis of $Ca_{2-x}Sr_xCuO_2F_2$ ($0 \leq x \leq 2$) with the T'-structure through fluorination of $Ca_{2-x}Sr_xCuO_3$with poly(vinylidenefluoride)/poly(tetrafluoroethylene). University of Birmingham, Birmingham. Unpublished work (Avialable at: http://epapers.bham.ac.uk/1667/ (accessed 18th of March 2020)), 2009.

65. Al-Mamouri, M.; Edwards, P. P.; Greaves, C.; Slaski, M., Synthesis and superconducting properties of the strontium copper oxy-fluoride $Sr_2CuO_2F_{2+d}$. *Nature* **1994,** *369* (6479), 382-384.

66. Al-Mamouri, M.; Edwards, P. P.; Greaves, C.; Slater, P. R.; Slaski, M., Synthesis and structure of the calcium copper oxyfluoride, $Ca_2CuO_2F_{2+d}$. *J. Mater. Chem.* **1995,** *5* (6), 913-916.

67. Slater P.R., H. J. P., Francesconi M.G., Edwards P.P., Greaves C., Gameson I., Slaski M., An improved route to the synthesis of superconducting copper oxyfluorides $Sr_{2-x}A_xCUO_2F_{2+delta}$ (A = Ca, Ba) using transition metal difluorides as fluorinating reagents. *Physica C* **1995,** *1999* (253), 16-22.

68. Ardashnikova, E. I.; Lubarsky, S. V.; Denisenko, D. I.; Shpanchenko, R. V.; Antipov, E. V.; Van Tendeloo, G., A new way of synthesis and characterization of superconducting oxyfluoride $Sr_2Cu(O, F)_{4+\delta}$. *Phys. C* **1995,** *253* (3–4), 259-265.

69. Kissick, J. L.; Greaves, C.; Edwards, P. P.; Cherkashenko, V. M.; Kurmaev, E. Z.; Bartkowski, S.; Neumann, M., Synthesis, structure, and XPS characterization of the stoichiometric phase $Sr_2CuO_2F_2$. *Phys. Rev. B.* **1997,** *56* (5), 2831-2835.

70. Hyatt, N. C.; Gray, L.; Gameson, I.; Edwards, P. P.; Hull, S., High-pressure neutron diffraction study of the quasi-one-dimensional cuprate Sr_2CuO_3. *Physical Review B* **2004,** *70* (21), 214101.

71. Slater, P. R.; Gover, R. K. B., Synthesis and structure of the new oxide fluoride $Sr_2TiO_3F_2$ from the low temperature fluorination of Sr_2TiO_4: an example of a staged fluorine substitution/insertion reaction. *J. Mater. Chem.* **2002,** *12* (2), 291-294.

72. Berry, F. J.; Moore, E.; Mortimer, M.; Ren, X.; Heap, R.; Slater, P.; Thomas, M. F., Synthesis and structural investigation of a new oxide fluoride of composition $Ba_2SnO_{2.5}F_3{\cdot}xH_2O$ (x≈0.5). *J. Solid State Chem.* **2008,** *181* (9), 2185-2190.

73. Lines, D. R.; Weller, M. T.; Currie, D. B.; Ogbome, D. M., Alkaline earth copper oxides. *Mater. Res. Bull.* **1991,** *26* (4), 323-331.

74. Hancock, C. A.; Herranz, T.; Marco, J. F.; Berry, F. J.; Slater, P. R., Low temperature fluorination of $Sr_3Fe_2O_{7-x}$ with polyvinylidine fluoride: An X-ray powder diffraction and Mössbauer spectroscopy study. *J. Solid State Chem.* **2012,** *186*, 195-203.

75. Hernden, B. C.; Lussier, J. A.; Bieringer, M., Topotactic Solid-State Metal Hydride Reductions of Sr_2MnO_4. *Inorg. Chem.* **2015,** *54* (9), 4249-56.

76. Kobayashi, Y.; Hernandez, O.; Tassel, C.; Kageyama, H., New chemistry of transition metal oxyhydrides. *Science and Technology of Advanced Materials* **2017,** *18* (1), 905-918.

77. Kobayashi, Y.; Li, Z.; Hirai, K.; Tassel, C.; Loyer, F.; Ichikawa, N.; Abe, N.; Yamamoto, T.; Shimakawa, Y.; Yoshimura, K.; Takano, M.; Hernandez, O. J.; Kageyama, H., Gas phase contributions to topochemical hydride reduction reactions. *J. Solid State Chem.* **2013,** *207*, 190-193.

78. Bridges Craig A., D. G. R., Hayward Michael A., Rosseinsky Matthew J. , Electronic Structure, Magnetic Ordering, and Formation Pathway of the Transition Metal Oxide Hydride $LaSrCoO_3H_{0.7}$. *J. Am. Chem. Soc.* **2005,** *127*, 5996-6011.

79. Pussacq, T.; Kabbour, H.; Colis, S.; Vezin, H.; Saitzek, S.; Gardoll, O.; Tassel, C.; Kageyama, H.; Laberty Robert, C.; Mentré, O., Reduction of $Ln_2Ti_2O_7$ Layered Perovskites: A Survey of the Anionic Lattice, Electronic Features, and Potentials. *Chem. Mater.* **2017,** *29* (3), 1047-1057.

80. Blundred, G. D.; Bridges, C. A.; Rosseinsky, M. J., New oxidation states and defect chemistry in the pyrochlore structure. *Angew. Chem. Int. Ed. Engl.* **2004,** *43* (27), 3562-3565.

81. Hayward, M. A., Phase Separation during the Topotactic Reduction of the Pyrochlore $Y_2Ti_2O_7$. *Chem. Mater.* **2005,** *17* (3), 670-675.

82. Gasperin, M., Dititanate de lanthane. *Acta Crystallographica Section B* **1975,** *31* (8), 2129-2130.

83. Masuda, N.; Kobayashi, Y.; Hernandez, O.; Bataille, T.; Paofai, S.; Suzuki, H.; Ritter, C.; Ichijo, N.; Noda, Y.; Takegoshi, K.; Tassel, C.; Yamamoto, T.; Kageyama, H., Hydride in $BaTiO_{2.5}H_{0.5}$: A Labile Ligand in Solid State Chemistry. *J. Am. Chem. Soc.* **2015,** *137* (48), 15315-15321.

84. Kobayashi, Y.; Hernandez, O. J.; Sakaguchi, T.; Yajima, T.; Roisnel, T.; Tsujimoto, Y.; Morita, M.; Noda, Y.; Mogami, Y.; Kitada, A.; Ohkura, M.; Hosokawa, S.; Li, Z.; Hayashi, K.; Kusano, Y.; Kim, J. e.; Tsuji, N.; Fujiwara, A.; Matsushita, Y.; Yoshimura, K.; Takegoshi, K.; Inoue, M.; Takano, M.; Kageyama, H., An oxyhydride of $BaTiO_3$ exhibiting hydride exchange and electronic conductivity. *Nature Materials* **2012,** *11* (6), 507-511.

85. Yajima, T.; Kitada, A.; Kobayashi, Y.; Sakaguchi, T.; Bouilly, G.; Kasahara, S.; Terashima, T.; Takano, M.; Kageyama, H., Epitaxial Thin Films of $ATiO_{3-x}H_x$ (A = Ba, Sr, Ca) with Metallic Conductivity. *J. Am. Chem. Soc.* **2012,** *134* (21), 8782-8785.

86. Bouilly, G.; Yajima, T.; Terashima, T.; Yoshimune, W.; Nakano, K.; Tassel, C.; Kususe, Y.; Fujita, K.; Tanaka, K.; Yamamoto, T.; Kobayashi, Y.; Kageyama, H., Electrical Properties of Epitaxial Thin Films of Oxyhydrides $ATiO_{3-x}H_x$ (A = Ba and Sr). *Chem. Mater.* **2015,** *27* (18), 6354-6359.

87. Sakaguchi, T.; Kobayashi, Y.; Yajima, T.; Ohkura, M.; Tassel, C.; Takeiri, F.; Mitsuoka, S.; Ohkubo, H.; Yamamoto, T.; Kim, J.; Tsuji, N.; Fujihara, A.; Matsushita, Y.; Hester, J.; Avdeev, M.; Ohoyama, K.; Kageyama, H., Oxyhydrides of (Ca,Sr,Ba)TiO_3 perovskite solid solutions. *Inorg. Chem.* **2012,** *51* (21), 11371-6.

88. Kim, I.-S.; Itoh, M.; Nakamura, T., Electrical Conductivity and Metal-Nonmetal Transition in the Perovskite-Related Layered System $Ca_{n+1}Ti_nO_{3n+1-\delta}$ (n = 2, 3, and infinity). *J. Solid State Chem.* **1992,** *101*, 77-86.

89. Rey, M. J.; Dehaudt, P.; Joubert, J. C.; Lambert-Andron, B.; Cyrot, M.; Cyrot-Lackmann, F., Preparation and structure of the compounds $SrVO_3$ and Sr_2VO_4. *J. Solid State Chem.* **1990,** *86* (1), 101-108.

90. Denis Romero, F.; Leach, A.; Moller, J. S.; Foronda, F.; Blundell, S. J.; Hayward, M. A., Strontium vanadium oxide-hydrides: "square-planar" two-electron phases. *Angew. Chem. Int. Ed. Engl.* **2014,** *53* (29), 7556-9.

91. Amano Patino, M.; Zeng, D.; Blundell, S. J.; McGrady, J. E.; Hayward, M. A., Extreme Sensitivity of a Topochemical Reaction to Cation Substitution: $SrVO_2H$ versus $SrV_{1-x}Ti_xO_{1.5}H_{1.5}$. *Inorg. Chem.* **2018,** *57* (5), 2890-2898.

92. Hayward, M. A., Selective deintercalation of apex over face-shared oxide ions in the topotactic reduction of $Sr_7Mn_4O_{15}$ to $Sr_7Mn_4O_{12}$. *Chem. Commun.* **2004**, DOI: 10.1039/b312792c (2), 170-1.

93. Hayward, M. A.; Rosseinsky, M. J., Cool conditions for mobile ions. *Nature* **2007,** *450*, 960-961.

94. Kageyama, H.; Watanabe, T.; Tsujimoto, Y.; Kitada, A.; Sumida, Y.; Kanamori, K.; Yoshimura, K.; Hayashi, N.; Muranaka, S.; Takano, M.; Ceretti, M.; Paulus, W.; Ritter, C.; André, G., Spin-Ladder Iron Oxide: $Sr_3Fe_2O_5$. *Angew. Chem. Int. Ed.* **2008,** *47* (31), 5740-5745.

95. Tsujimoto, Y.; Tassel, C.; Hayashi, N.; Watanabe, T.; Kageyama, H.; Yoshimura, K.; Takano, M.; Ceretti, M.; Ritter, C.; Paulus, W., Infinite-layer iron oxide with a square-planar coordination. *Nature* **2007,** *450* (7172), 1062-1065.

96. Crespin, M.; Levitz, P.; Gatinea, L., Reduced Forms of $LaNi0_3$ Perovskite Part 1.-Evidence for New Phases: $La_2Ni_20_5$ and $LaNiO_2$. *J. Chem. SOC., Faraday Trans. 2* **1983,** *79*, 1181-1194.

97. Hayward, M. A.; Green, M. A.; Rosseinsky, M. J.; Sloan, J., Sodium hydride as a powerful reducing agent for topotactic oxide deintercalation: Synthesis and characterization of the nickel(I) oxide $LaNiO_2$. *J. Am. Chem. Soc.* **1999,** *121* (38), 8843-8854.

98. Crespin, M.; Isnard, O.; Dubois, F.; Choisnet, J.; Odier, P., $LaNiO_2$: Synthesis and structural characterization. *J. Solid State Chem.* **2005,** *178* (4), 1326-1334.

99. Poltavets, V. V.; Lokshin, K. A.; Croft, M.; Mandal, T. K.; Egami, T.; Greenblatt, M., Crystal structures of $Ln_4Ni_3O_8$ (Ln = La, Nd) triple layer T'-type nickelates. *Inorg. Chem.* **2007,** *46* (25), 10887-10891.

100. Poltavets, V. V.; Lokshin, K. A.; Dikmen, S.; Croft, M.; Egami, T.; Greenblatt, M., $La_3Ni_2O_6$: a new double T'-type nickelate with infinite $Ni^{1+/2+}O_2$ layers. *J. Am. Chem. Soc.* **2006,** *128* (28), 9050-9051.

101. Lacorre, P., Passage from T-Type to T'-Type Arrangement to by Reducing $R_4Ni_3O_{10}$ to $R_4Ni_3O_8$ (R = La, Pr, Nd). *J. Solid State Chem.* **1992,** *97*, 495-500

102. Retoux, R.; Rodriguez-Carvajal, J.; Lacorre, P., Neutron diffraction and TEM studies of the crystal structure and defects of $Nd_4Ni_3O_8$. *J. Solid State Chem.* **1998,** *140* (2), 307-315.

103. Takamatsu, T.; Kato, M.; Noji, T.; Koike, Y., Low-temperature synthesis of the infinite-layer compound $LaNiO_2$ using CaH_2 as reductant. *Physica C: Superconductivity and its Applications* **2010,** *470*, S764-S765.

104. Takamatsu, T.; Kato, M.; Noji, T.; Koike, Y., Low-Temperature Synthesis of the Infinite-Layer Compound $LaNiO_2$ by Soft-Chemical Techniques. *Japanese Journal of Applied Physics* **2010,** *49* (9).

105. Hayward, M. A., Synthesis and Magnetism of Extended Solids Containing Transition-Metal Cations in Square-Planar, MO_4 Coordination Sites. *Inorg. Chem.* **2019,** *58* (18), 11961-11970.

106. Ling, C. D.; Argyriou, D. N.; Wu, G.; Neumeier, J. J., Neutron Diffraction Study of $La_3Ni_2O_7$: Structural Relationships Among n=1, 2, and 3 Phases $La_{n+1}Ni_nO_{3n+1}$. *J. Solid State Chem.* **2000,** *152* (2), 517-525.

107. García-Muñoz, J. L.; Rodríguez-Carvajal, J.; Lacorre, P.; Torrance, J. B., Neutron-diffraction study of $RNiO_3$ (R=La,Pr,Nd,Sm): Electronically induced structural changes across the metal-insulator transition. *Physical Review B* **1992,** *46* (8), 4414-4425.

108. Delville, M. H.; Barbut, D.; Wattiaux, A.; Bassat, J. M.; Menetrier, M.; Labrugere, C.; Grenier, J. C.; Etourneau, J., Electrochemical fluorination of La_2CuO_4: a mild "chimie douce" route to superconducting oxyfluoride materials. *Inorg. Chem.* **2009,** *48* (16), 7962-7969.

109. Anisimov, V. I.; Bukhvalov, D.; Rice, T. M., Electronic structure of possible nickelate analogs to the cuprates. *Physical Review B* **1999,** *59* (12), 7901-7906.

110. Poltavets, V. V.; Lokshin, K. A.; Nevidomskyy, A. H.; Croft, M.; Tyson, T. A.; Hadermann, J.; Van Tendeloo, G.; Egami, T.; Kotliar, G.; ApRoberts-Warren, N.; Dioguardi, A. P.; Curro, N. J.; Greenblatt, M., Bulk magnetic order in a two-dimensional Ni^{1+}/Ni^{2+} (d^9/d^8) nickelate, isoelectronic with superconducting cuprates. *Phys. Rev. Lett.* **2010,** *104* (20), 206403.

111. Poltavets, V. V.; Greenblatt, M.; Fecher, G. H.; Felser, C., Electronic properties, band structure, and fermi surface instabilities of Ni^{1+}/Ni^{2+} nickelate $La_3Ni_2O_6$, isoelectronic with superconducting cuprates. *Phys. Rev. Lett.* **2009,** *102* (4), 046405.

112. Li, D.; Lee, K.; Wang, B. Y.; Osada, M.; Crossley, S.; Lee, H. R.; Cui, Y.; Hikita, Y.; Hwang, H. Y., Superconductivity in an infinite-layer nickelate. *Nature* **2019,** *572* (7771), 624-627.

113. Jin, L.; Lane, M.; Zeng, D.; Kirschner, F. K. K.; Lang, F.; Manuel, P.; Blundell, S. J.; McGrady, J. E.; Hayward, M. A., $LaSr_3NiRuO_4H_4$: A 4d Transition-Metal Oxide-Hydride Containing Metal Hydride Sheets. *Angew. Chem. Int. Ed. Engl.* **2018,** *57* (18), 5025-5028.

114. Kobayashi, Y.; Tsujimoto, Y.; Kageyama, H., Property Engineering in Perovskites via Modification of Anion Chemistry. *Annual Review of Materials Research* **2018,** *48* (1), 303-326.

115. Grenier, J. C.; Wattiaux, A.; Monroux, C.; Pouchard, M.; Locquet, J. P., Electrochemical oxygen insertion into La2CuO4-related compounds. *Physica C: Superconductivity* **1994,** *235-240*, 79-82.

116. Demourgues, A.; Weill, F.; Grenier, J. C.; Wattiaux, A.; Pouchard, M., Electron microscopy study of electrochemically prepared $La_2NiO_{4+\delta}$ ($0.17\leq\delta\leq0.26$). *Physica C: Superconductivity* **1992,** *192* (3), 425-434.

117. Grenier, J. C.; Wattiaux, A.; Demourgues, A.; Pouchard, M.; Hagenmuller, P., Electrochemical oxidation: a new way for preparing high oxidation states of transition metals. *Solid State Ionics* **1993,** *63-65*, 825-832.

118. Grenier, J.-C.; Pouchard, M.; Wattiaux, A., Electrochemical synthesis: oxygen intercalation. *Curr. Opin. Solid State Mater. Sci.* **1996,** *1* (2), 233-240.

119. Grenier, J. C.; Bassat, J. M.; Doumerc, J. P.; Etourneau, J.; Fang, Z.; Fournes, L.; Petit, S.; Pouchard, M.; Wattiaux, A., Relevant examples of intercalation-deintercalation processes in solid state chemistry: application to oxides. *J. Mater. Chem.* **1999,** *9* (1), 25-33.

120. Delville, M.-H. l. n.; Barbut, D.; Wattiaux, A.; Grenier, J.-C.; Etourneau, J., Room-Temperature Electrochemical Intercalation of Oxygen or Fluorine into La_2CuO_4 Using Organic Electrolytic Media: Mechanistic Approach. *J. Electrochem. Soc.* **2004,** *151* (10), J69.

121. Kennedy, J. H.; Hunter, J. C., Thin-Film Galvanic Cell $Pb / PbF_2 / PbF_2 , CuF_2 / Cu$. **1976,** *123* (1), 10-14.

122. Schoonman, J., A Solid-State Galvanic Cell with Fluoride-Conducting Electrolytes. **1976,** *123* (12), 1772-1775.

123. Schoonman, J.; Wolfert, A., Solid-state galvanic cells with fast fluoride conducting electrolytes. *Solid State Ionics* **1981,** *3-4*, 373-379.

124. Danto, Y.; Poujade, G.; Pistré, J. D.; Lucat, C.; Salardenne, J., A Pb|PbF_2|BiF_3|Bi thin solid film reversible galvanic cell. *Thin Solid Films* **1978,** *55* (3), 347-354.

125. Schoonman, J.; Wapenaar, K. E. D.; Oversluizen, G.; Dirksen, G. J., Fluoride-Conducting Solid Electrolytes in Galvanic Cells. **1979,** *126* (5), 709-713.

126. Kosacki, I., Physical properties and applications of $Cd_{1-x}Pb_xF_2$ superionic crystals. *Appl. Phys. A* **1989,** *49* (4), 413-424.

127. Sher, A.; Solomon, R.; Lee, K.; Muller, M. W., Transport Properties of LaF_3. *Physical Review* **1966,** *144* (2), 593-604.

128. Schoonman, J.; Oversluizen, G.; Wapenaar, K. E. D., Solid electrolyte properties of LaF_3. *Solid State Ionics* **1980,** *1* (3), 211-221.

129. Bollmann, W., Ionic conductivity of pure and doped BaF_2 crystals. **1973,** *18* (1), 313-321.

130. Hagenmuller, P.; Réau, J.-M.; Lucat, C.; Matar, S.; Villeneuve, G., Ionic conductivity of fluorite-type fluorides. *Solid State Ionics* **1981,** *3-4*, 341-345.

131. Roos, A.; van de Pol, F. C. M.; Keim, R.; Schoonman, J., Ionic conductivity in tysonite-type solid solutions $La_{1-x}Ba_xF_{3-x}$. *Solid State Ionics* **1984,** *13* (3), 191-203.

132. Sobolev, B. P.; Sviridov, I. A.; Fadeeva, V. I.; Sul'yanov, S. N.; Sorokin, N. I.; Zhmurova, Z. I.; Herrero, P.; Landa-Canovas, A.; Rojas, R. M., Mechanochemical synthesis of nonstoichiometric fluorite $Ca_{1-x}La_xF_{2+x}$ nanocrystals from CaF_2 and LaF_3 single crystals. *Crystallography Reports* **2005,** *50* (3), 478-485.

133. Rongeat, C.; Reddy, M. A.; Witter, R.; Fichtner, M., Nanostructured Fluorite-Type Fluorides As Electrolytes for Fluoride Ion Batteries. *The Journal of Physical Chemistry C* **2013,** *117* (10), 4943-4950.

134. Rongeat, C.; Reddy, M. A.; Witter, R.; Fichtner, M., Solid electrolytes for fluoride ion batteries: ionic conductivity in polycrystalline tysonite-type fluorides. *ACS Appl Mater Interfaces* **2014,** *6* (3), 2103-10.

135. Chable, J.; Martin, A. G.; Bourdin, A.; Body, M.; Legein, C.; Jouanneaux, A.; Crosnier-Lopez, M. P.; Galven, C.; Dieudonné, B.; Leblanc, M.; Demourgues, A.; Maisonneuve, V., Fluoride solid electrolytes: From microcrystalline to nanostructured tysonite-type $La_{0.95}Ba_{0.05}F_{2.95}$. *J. Alloys Compd.* **2017,** *692*, 980-988.

136. Dieudonné, B.; Chable, J.; Body, M.; Legein, C.; Durand, E.; Mauvy, F.; Fourcade, S.; Leblanc, M.; Maisonneuve, V.; Demourgues, A., The key role of the composition and structural features in fluoride ion conductivity in tysonite $Ce_{1-x}Sr_xF_{3-x}$ solid solutions. *Dalton Transactions* **2017,** *46* (11), 3761-3769.

137. Dieudonné, B.; Chable, J.; Mauvy, F.; Fourcade, S.; Durand, E.; Lebraud, E.; Leblanc, M.; Legein, C.; Body, M.; Maisonneuve, V.; Demourgues, A., Exploring the $Sm_{1-x}Ca_xF_{3-x}$ Tysonite Solid Solution as a Solid-State Electrolyte: Relationships between Structural Features and F^- Ionic Conductivity. *The Journal of Physical Chemistry C* **2015,** *119* (45), 25170-25179.

138. Mohammad, I.; Witter, R.; Fichtner, M.; Anji Reddy, M., Room-Temperature, Rechargeable Solid-State Fluoride-Ion Batteries. *ACS Applied Energy Materials* **2018,** *1* (9), 4766-4775.

139. Mohammad, I.; Witter, R.; Fichtner, M.; Reddy, M. A., Introducing Interlayer Electrolytes: Toward Room-Temperature High-Potential Solid-State Rechargeable Fluoride Ion Batteries. *ACS Applied Energy Materials* **2019,** *2* (2), 1553-1562.

140. Liu, L.; Yang, L.; Liu, M.; Li, X.; Shao, D.; Luo, K.; Wang, X.; Luo, Z., SnF_2-based fluoride ion electrolytes $MSnF_4$ (M = Ba, Pb) for the application of room-temperature solid-state fluoride ion batteries. *J. Alloys Compd.* **2020,** *819*, 152983.

141. Liu, L.; Yang, L.; Shao, D.; Luo, K.; Zou, C.; Luo, Z.; Wang, X., Nd^{3+} doped $BaSnF_4$ solid electrolyte for advanced room-temperature solid-state fluoride ion batteries. *Ceram. Int.* **2020**, DOI: https://doi.org/10.1016/j.ceramint.2020.05.161.

142. Davis, V. K.; Bates, C. M.; Omichi, K.; Savoie, B. M.; Momčilović, N.; Xu, Q.; Wolf, W. J.; Webb, M. A.; Billings, K. J.; Chou, N. H.; Alayoglu, S.; McKenney, R. K.; Darolles, I. M.; Nair, N. G.; Hightower, A.; Rosenberg, D.; Ahmed, M.; Brooks, C. J.; Miller, T. F.; Grubbs, R. H.; Jones, S. C., Room-temperature cycling of metal fluoride electrodes: Liquid electrolytes for high-energy fluoride ion cells. *Science* **2018,** *362* (6419), 1144-1148.

143. Nitta, N.; Wu, F.; Lee, J. T.; Yushin, G., Li-ion battery materials: present and future. *Mater. Today* **2015,** *18* (5), 252-264.

144. Clemens, O.; Rongeat, C.; Reddy, M. A.; Giehr, A.; Fichtner, M.; Hahn, H., Electrochemical fluorination of perovskite type $BaFeO_{2.5}$. *Dalton Trans* **2014,** *43* (42), 15771-15778.

145. Crespin, M.; Landron, C.; Odier, P.; Bassat, J. M.; Mouron, P.; Choisnet, J., Evidence for nickel-(I)-rich mixed oxide with a defect K_2NiF_4-type structure. *J. Solid State Chem.* **1992,** *100* (2), 281-291.

146. Coey, J. M. D., *Magnetism and Magnetic Materials*. Cambridge University Press: Cambridge, 2010, DOI: 10.1017/CBO9780511845000.

147. Spaldin, N. A., *Magnetic Materials: Fundamentals and Applications*. 2., ed.; Cambridge University Press: Cambridge, 2010, DOI: 10.1017/CBO9780511781599.

148. Kittel, C., *Einführung in die Festkörperphysik*. 14., überarb. und erw. Aufl.; Oldenbourg Verlag: München, 2006.

149. Opel, M., Spintronic oxides grown by laser-MBE. *J. Phys. D: Appl. Phys.* **2011,** *45* (3), 033001.

150. Goodenough, J. B., Theory of the Role of Covalence in the Perovskite-Type Manganites [La,M(II)]MnO_3. *Physical Review* **1955,** *100* (2), 564-573.

151. Goodenough, J. B., An interpretation of the magnetic properties of the perovskite-type mixed crystals $La_{1-x}Sr_xCoO_{3-\lambda}$. *J. Phys. Chem. Solids* **1958,** *6* (2), 287-297.

152. Kanamori, J., Superexchange interaction and symmetry properties of electron orbitals. *J. Phys. Chem. Solids* **1959,** *10* (2), 87-98.

153. Anderson, P. W., Antiferromagnetism. Theory of Superexchange Interaction. *Physical Review* **1950,** *79* (2), 350-356.

154. Spieß, L.; Teichert, G.; Schwarzer, R.; Behnken, H.; Genzel, C., *Moderne Röntgenbeugung: Röntgendiffraktometrie für Materialwissenschaftler, Physiker und Chemiker*. 2., Aufl.; Vieweg+Teubner Verlag: Wiesbaden, 2009, DOI: 10.1007/978-3-8349-9434-9.

155. Pecharsky, V. K.; Zavalij, P. Y., *Fundamentals of Powder Diffraction and Structural Characterization of Materials*. Springer US: Boston, MA, 2009, DOI: 10.1007/978-0-387-09579-0.

156. Dinnebier, R. E.; Billinge, S. J. L.; Le Bail, A.; Madsen, I.; Cranswick, L. M. D.; Cockcroft, J. K.; Norby, P.; Zuev, A. D.; Fitch, A.; Rodriguez-Carvajal, J.; Giacovazzo, C.; Von Dreele, R. B.; Scardi, P.; Popa, N. C.; Allmann, R., *Powder Diffraction: Theory and Practice*. Royal Society of Chemistry: Cambridge, 2008, DOI: 10.1039/9781847558237.

157. Borchardt-Ott, W., *Kristallographie: Eine Einführung für Naturwissenschaftler*. 7., überarb. und erw. Aufl.; Springer-Verlag Berlin Heidelberg: Berlin, 2009, DOI: 10.1007/978-3-540-78271-1.

158. Kleber, W.; Bautsch, H.-J.; Bohm, J., *Einführung in die Kristallographie*. 19., überarb. Aufl.; Oldenbourg Verlag: München, 2010.

159. Hammond, C., *The basics of crystallography and diffraction*. 4., ed.; Oxford University Press: Oxford, 2015; Vol. 21.

160. Young, R. A., *The Rietveld method*. Oxford University Press: Oxford, 1993; Vol. 5.

161. Will, G., *Powder diffraction. The Rietveld method and the two-stage method to determine and refine crystal structures for powder diffraction data*. Springer-Verlag Berlin Heidelberg: Germany, 2006, DOI: 10.1007/3-540-27986-5.

162. *Diffrac.suite - User Manual TOPAS 5*. Bruker AXS: Karlsruhe, Germany, 2014.

163. Coelho, A. A. TOPAS-Academic. http://www.topas-academic.net (accessed 20th of October 2014).

164. Cromer, D. T.; Mann, J. B., X-ray scattering factors computed from numerical Hartree-Fock wave functions. *Acta Crystallographica Section A* **1968,** *24* (2), 321-324.

165. Sears, V. F., Neutron scattering lengths and cross sections. *Neutron News* **1992,** *3* (3), 26-37.

166. Kisi, E. H., *Applications of neutron powder diffraction*. Oxford University Press: Oxford, 2008, DOI: 10.1093/acprof:oso/9780198515944.001.0001.

167. Brown, I. D., The Bond-Valence Method: An Empirical Approach to Chemical Structure and Bonding. In *Structure and Bonding in Crystals*, O'Keeffe, M.; Navrotsky, A., Eds. Elsevier: 1981; Vol. 2, pp 1-30.

168. Brown, I. D., *The Chemical Bond in Inorganic Chemistry: The Bond Valence Model*. Oxford University Press: Oxford, 2016, DOI: 10.1093/acprof:oso/9780199298815.001.0001.

169. Weirich, T. E.; Lábár, J. L.; Zou, X., *Electron Crystallography : Novel Approaches for Structure Determination of Nanosized Materials*. 1., ed.; Springer Netherlands: Dordrecht, 2006; Vol. 211.

170. Asadi Asadabad, M.; Eskandari, M., Electron Diffraction. In *Modern Electron Microscopy in Physical and Life Sciences*, Janecek, M.; Kral, R., Eds. InTech: 2016, DOI: 10.5772/61781 pp 3-25.

171. Popa, N., The (hkl) Dependence of Diffraction-Line Broadening Caused by Strain and Size for all Laue Groups in Rietveld Refinement. *J. Appl. Crystallogr.* **1998,** *31* (2), 176-180.

172. Järvinen, M., Application of symmetrized harmonics expansion to correction of the preferred orientation effect. *J. Appl. Crystallogr.* **1993,** *26* (4), 525-531.

173. Stephens, P., Phenomenological model of anisotropic peak broadening in powder diffraction. *J. Appl. Crystallogr.* **1999,** *32* (2), 281-289.

174. Leineweber, A., Understanding anisotropic microstrain broadening in Rietveld refinement. *Zeitschrift für Kristallographie Crystalline Materials* **2011,** *226* (12), 905-923.

175. Cheary, R. W.; Coelho, A., A fundamental parameters approach to X-ray line-profile fitting. *J. Appl. Crystallogr.* **1992,** *25* (2), 109-121.

176. Cheary, R. W.; Coelho, A. A.; Cline, J. P., Fundamental Parameters Line Profile Fitting in Laboratory Diffractometers. *Journal of Research of the National Institute of Standards and Technology* **2004,** *109* (1), 1-25.

177. Bergmann, J.; Kleeberg, R.; Haase, A.; Breidenstein, B., Advanced Fundamental Parameters Model for Improved Profile Analysis. *Mater. Sci. Forum* **2000,** *347-349*, 303-308.

178. Rietveld, H. M., Line profiles of neutron powder-diffraction peaks for structure refinement. *Acta Cryst.* **1966,** *22*, 151-152.

179. Rietveld, H. M., A Profile Refinement Method for Nuclear and Magnetic Structures. *J. Appl. Cryst.* **1969,** *2*, 65-71.

180. Rietveld, H. M., The Rietveld method. *Phys. Scr.* **2014,** *89* (9), 098002.

181. Ibberson, R. M. D., W.I.F.; Knight, K.S., The high resolution powder diffractometer (HRPD) at ISIS - a user guide. **1992**.

182. Williams, W. G.; Ibberson, R. M.; Day, P.; Enderby, J. E., GEM — General materials diffractometer at ISIS. *Physica B: Condensed Matter* **1997,** *241-243*, 234-236.

183. Day, P.; Enderby, J.; Williams, W.; Chapon, L.; Hannon, A.; Radaelli, P.; Soper, A., Scientific Reviews: GEM: The General Materials Diffractometer at ISIS-Multibank Capabilities for Studying Crystalline and Disordered Materials. *Neutron News* **2004,** *15* (1), 19-23.

184. Kolb, U.; Mugnaioli, E.; Gorelik, T. E., Automated electron diffraction tomography – a new tool for nano crystal structure analysis. **2011,** *46* (6), 542-554.

185. Vincent, R.; Midgley, P. A., Double conical beam-rocking system for measurement of integrated electron diffraction intensities. *Ultramicroscopy* **1994,** *53* (3), 271-282.

186. Kolb, U.; Gorelik, T.; Otten, M. T., Towards automated diffraction tomography. Part II—Cell parameter determination. *Ultramicroscopy* **2008,** *108* (8), 763-772.

187. Plana-Ruiz, S.; Krysiak, Y.; Portillo, J.; Alig, E.; Estradé, S.; Peiró, F.; Kolb, U., Fast-ADT: A fast and automated electron diffraction tomography setup for structure determination and refinement. *Ultramicroscopy* **2020,** *211*, 112951.

188. Kolb, U.; Krysiak, Y.; Plana-Ruiz, S., Automated electron diffraction tomography - development and applications. *Acta Crystallographica Section B* **2019,** *75* (4), 463-474.

189. Kolb, U.; Gorelik, T.; Kübel, C.; Otten, M. T.; Hubert, D., Towards automated diffraction tomography: Part I—Data acquisition. *Ultramicroscopy* **2007,** *107* (6), 507-513.

190. Mugnaioli, E.; Kolb, U., Applications of automated diffraction tomography (ADT) on nanocrystalline porous materials. *Microporous Mesoporous Mater.* **2013,** *166*, 93-101.

191. Fagaly, R. L., Superconducting quantum interference device instruments and applications. *Rev. Sci. Instrum.* **2006,** *77* (10), 101101.

192. Buchner, M.; Höfler, K.; Henne, B.; Ney, V.; Ney, A., Tutorial: Basic principles, limits of detection, and pitfalls of highly sensitive SQUID magnetometry for nanomagnetism and spintronics. *J. Appl. Phys.* **2018,** *124* (16), 161101.

193. Caliebe, W. A.; Murzin, V.; Kalinko, A.; Görlitz, M., High-flux XAFS-beamline P64 at PETRA III. *AIP Conference Proceedings* **2019,** *2054* (1), 060031.

194. Welter, E.; Chernikov, R.; Herrmann, M.; Nemausat, R., A beamline for bulk sample X-ray absorption spectroscopy at the high brilliance storage ring PETRA III. **2019,** *2054* (1), 040002.

195. Newville, M., Fundamentals of XAFS. *Reviews in Mineralogy and Geochemistry* **2014,** *78* (1), 33-74.

196. Bauer, M.; Bertagnolli, H., X-Ray Absorption Spectroscopy – the Method and Its Applications. In *Methods in Physical Chemistry*, Schäfer, R.; Schmidt, P. C., Eds. Wiley-VCH Weinheim, 2012, DOI: 10.1002/9783527636839.ch7pp 231-269.

197. Schoch, R. Active species identification of iron-based homogeneously and heterogeneously catalyzed reactions Universität Paderborn, Paderborn, 2017.

198. Watts, J. F.; Wolstenhome, J., *An introduction to surface analysis by XPS and AES*. Wiley-VCH: Weinheim, 2003, DOI: 10.1002/0470867930.

199. Goldstein, J.; Newbury, D. E.; Michael, J. R.; Ritchie, N. W. M.; Scott, J. H. J.; Joy, D. C., *Scanning electron microscopy and x-ray microanalysis*. 4., ed.; Springer US: New York, 2018.

200. Clemens, O.; Vasala, S.; da Silva, I.; Wissel, K.; Slater, P., Investigation of $La_2NiO_3F_2$ and defluorinated phases with Ruddlesden-Popper type structure. STFC ISIS Neutron and Muon Source 2018, DOI: 10.5286/ISIS.E.RB1820423.

201. Arnold, O.; Bilheux, J. C.; Borreguero, J. M.; Buts, A.; Campbell, S. I.; Chapon, L.; Doucet, M.; Draper, N.; Ferraz Leal, R.; Gigg, M. A.; Lynch, V. E.; Markvardsen, A.; Mikkelson, D. J.; Mikkelson, R. L.; Miller, R.; Palmen, K.; Parker, P.; Passos, G.; Perring, T.

G.; Peterson, P. F.; Ren, S.; Reuter, M. A.; Savici, A. T.; Taylor, J. W.; Taylor, R. J.; Tolchenov, R.; Zhou, W.; Zikovsky, J., Mantid—Data analysis and visualization package for neutron scattering and μ SR experiments. *Nuclear Instruments and Methods in Physics Research Section A: Accelerators, Spectrometers, Detectors and Associated Equipment* **2014,** *764* (Supplement C), 156-166.

202. Mugnaioli, E.; Gorelik, T.; Kolb, U., "Ab initio" structure solution from electron diffraction data obtained by a combination of automated diffraction tomography and precession technique. *Ultramicroscopy* **2009,** *109* (6), 758-65.

203. Burla, M. C.; Caliandro, R.; Carrozzini, B.; Cascarano, G. L.; Cuocci, C.; Giacovazzo, C.; Mallamo, M.; Mazzone, A.; Polidori, G., Crystal structure determination and refinement via SIR2014. *J. Appl. Crystallogr.* **2015,** *48*, 306-309.

204. Petříček, V.; Dušek, M.; Palatinus, L., Crystallographic Computing System JANA2006: General features. *Zeitschrift für Kristallographie - Crystalline Materials* **2014,** *229* (5), 345–352.

205. Palatinus, L.; Brazda, P.; Jelinek, M.; Hrda, J.; Steciuk, G.; Klementova, M., Specifics of the data processing of precession electron diffraction tomography data and their implementation in the program PETS2.0. *Acta Crystallographica Section B* **2019,** *75* (4), 512-522.

206. Bain, G. A.; Berry, J. F., Diamagnetic Corrections and Pascal's Constants. *J. Chem. Educ.* **2008,** *85* (4).

207. Moulder, J. F.; Chastain, J., *Handbook of X-ray Photoelectron Spectroscopy: A Reference Book of Standard Spectra for Identification and Interpretation of XPS Data*. Physical Electronics Division, Perkin-Elmer Corporation: 1992.

208. Shirley, D. A., High-Resolution X-Ray Photoemission Spectrum of the Valence Bands of Gold. *Phys. Rev. B.* **1972,** *5* (12), 4709-4714.

209. Kresse, G.; Joubert, D., From ultrasoft pseudopotentials to the projector augmented-wave method. *Physical Review B* **1999,** *59* (3), 1758-1775.

210. Blöchl, P. E., Projector augmented-wave method. *Phys. Rev. B.* **1994,** *50* (24), 17953-17979.

211. Kresse, G.; Hafner, J., Ab initio molecular-dynamics simulation of the liquid-metal--amorphous-semiconductor transition in germanium. *Physical Review B* **1994,** *49* (20), 14251-14269.

212. Kresse, G.; Furthmüller, J., Efficiency of ab-initio total energy calculations for metals and semiconductors using a plane-wave basis set. *Computational Materials Science* **1996,** *6* (1), 15-50.

213. Perdew, J. P.; Burke, K.; Ernzerhof, M., Generalized Gradient Approximation Made Simple. *Phys. Rev. Lett.* **1996,** *77*, 3865.

214. Perdew, J. P.; Burke, K.; Ernzerhof, M., Erratum: Generalized Gradient Approximation Made Simple. *Phys. Rev. Lett.* **1997,** *78*, 1396.

215. Shick, A. B.; Liechtenstein, A. I.; Pickett, W. E., Implementation of the LDA+U method using the full-potential linearized augmented plane-wave basis. *Phys. Rev. B.* **1999,** *60* (15), 10763.

216. Liechtenstein, A. I.; Anisimov, V. I.; Zaanen, J., Density-functional theory and strong interactions: Orbital ordering in Mott-Hubbard insulators. *Phys. Rev. B.* **1995,** *52* (8), R5467.

217. Dudarev, S. L.; Botton, G. A.; Savrasov, S. Y.; Humphreys, C. J.; Sutton, A. P., Electron-energy-loss spectra and the structural stability of nickel oxide: An LSDA+U study. *Physical Review B* **1998,** *57* (3), 1505-1509.

218. Hu, Z.; Metiu, H., Choice of U for DFT+U Calculations for Titanium Oxides. *The Journal of Physical Chemistry C* **2011,** *115* (13), 5841-5845.

219. Zhou, F.; Cococcioni, M.; Marianetti, C. A.; Morgan, D.; Ceder, G., First-principles prediction of redox potentials in transition-metal compounds with LDA+U. *Phys. Rev. B.* **2004,** *70* (23), 235121.

220. Wang, L.; Maxisch, T.; Ceder, G., Oxidation energies of transition metal oxides within the GGA+U framework. *Phys. Rev. B.* **2006,** *73*, 195107.

221. Pardo, V.; Pickett, W. E., Metal-insulator transition in layered nickelates $La_3Ni_2O_{7-\delta}$ (δ=0.0, 0.5, 1). *Physical Review B* **2011,** *83* (24).

222. Monkhorst, H. J.; Pack, J. D., Special points for Brillouin-zone integrations. *Physical Review B* **1976,** *13* (12), 5188-5192.

223. Kubota, M.; Fujioka, H.; Hirota, K.; Ohoyama, K.; Moritomo, Y.; Yoshizawa, H.; Endoh, Y., Relation between Crystal and Magnetic Structures of Layered Manganite $La_{2-2x}Sr_{1+2x}Mn_2O_7$ ($0.30 \leq x \leq 0.50$). *J. Phys. Soc. Jpn.* **2000,** *69* (6), 1606-1609.

224. Kubota, M.; Fujioka, H.; Ohoyama, K.; Hirota, K.; Moritomo, Y.; Yoshizawa, H.; Endoh, Y., Neutron scattering studies on magnetic structure of the double-layered manganite $La_{2-2x}Sr_{1+2x}Mn_2O_7$ ($0.30 \leq x \leq 0.50$). *J. Phys. Chem. Solids* **1999,** *60* (8), 1161-1164.

225. Dilts, J. A.; Ashby, E. C., Thermal decomposition of complex metal hydrides. *Inorg. Chem.* **1972,** *11* (6), 1230-1236.

226. Deshpande, V., Thermal expansion of sodium fluoride and sodium bromide. *Acta Crystallographica* **1961,** *14* (7), 794.

227. Shull, C. G.; Wollan, E. O.; Morton, G. A.; Davidson, W. L., Neutron Diffraction Studies of NaH and NaD. *Physical Review* **1948,** *73* (8), 842-847.

228. Luca, V.; Djajanti, S.; Howe, R. F., Structural and Electronic Properties of Sol−Gel Titanium Oxides Studied by X-ray Absorption Spectroscopy. *The Journal of Physical Chemistry B* **1998,** *102* (52), 10650-10657.

229. Uozumi, T.; Okada, K.; Kotani, A.; Durmeyer, O.; Kappler, J. P.; Beaurepaire, E.; Parlebas, J. C., Experimental and Theoretical Investigation of the Pre-Peaks at the Ti K -Edge Absorption Spectra in TiO_2. *EPL* **1992,** *18* (1), 85.

230. Chaboy, J.; Nakajima, N.; Tezuka, Y., Ab initio x-ray absorption near-edge structure study of Ti K-edge in rutile. *J. Phys.: Condens. Matter* **2007,** *19* (26), 266206.

231. Yoon, S.; Maegli, A. E.; Karvonen, L.; Matam, S. K.; Shkabko, A.; Riegg, S.; Großmann, T.; Ebbinghaus, S. G.; Pokrant, S.; Weidenkaff, A., Bandgap tuning in $SrTi(N,O,F)_3$ by anionic-lattice variation. *J. Solid State Chem.* **2013,** *206* (Supplement C), 226-232.

232. Yamamoto, T., Assignment of pre-edge peaks in K-edge x-ray absorption spectra of 3d transition metal compounds: electric dipole or quadrupole? *X-Ray Spectrom.* **2008,** *37* (6), 572-584.

233. Khan, M. A.; Kotani, A.; Parlebas, J. C., Electronic structure and core level photoemission spectra in TiO_2 compounds. *J. Phys.: Condens. Matter* **1991,** *3* (12), 1763.

234. Waychunas, G. A., Synchrotron radiation xANES spectroscopy of Ti in minerals: Effects of Ti bonding distances, Ti valence, and site geometry on absorption edge structure. *Am. Mineral.* **1987,** *72*, 89-101.

235. Atuchin, V. V.; Kesler, V. G.; Pervukhina, N. V.; Zhang, Z., Ti 2p and O 1s core levels and chemical bonding in titanium-bearing oxides. *J. Electron. Spectrosc. Relat. Phenom.* **2006,** *152* (1-2), 18-24.

236. Ge, W.; Zhu, C.; An, H.; Li, Z.; Tang, G.; Hou, D., Sol–gel synthesis and dielectric properties of Ruddlesden–Popper phase $Sr_{n+1}Ti_nO_{3n+1}$ (n=1, 2, 3, ∞). *Ceram. Int.* **2014,** *40* (1), 1569-1574.

237. Lee, S.-J.; Thiyagarajan, P.; Lee, M.-J., Synthesis and characterization of strontium titanate powder via a simple polymer solution route. *Journal of Ceramic Processing Research* **2008,** *9* (4), 385-388.

238. Shih, S.-J.; Tzeng, W.-L., Manipulation of morphology of strontium titanate particles by spray pyrolysis. *Powder Technol.* **2014,** *264*, 291-297.

239. Chase Jr., M. W., NIST-JANAF Thermochemical Tables, Fourth Edition, Monograph 9 (Part I and Part II). *J. Phys. Chem. Ref. Data* **1998**.

240. Kharton, V. V., *Solid State Electrochemistry I & II*. WILEY-VCH: Weinheim, Germany, 2009.

241. Clemens, O.; Haberkorn, R.; Slater, P. R.; Beck, H. P., Synthesis and characterisation of the $Sr_xBa_{1-x}FeO_{3-y}$-system and the fluorinated phases $Sr_xBa_{1-x}FeO_2F$. *Solid State Sciences* **2010,** *12* (8), 1455-1463.

242. Clemens, O.; Berry, F. J.; Wright, A. J.; Knight, K. S.; Perez-Mato, J. M.; Igartua, J. M.; Slater, P. R., A neutron diffraction study and mode analysis of compounds of the system $La_{1-x}Sr_xFeO_{3-x}F_x$ (x=1, 0.8, 0.5, 0.2) and an investigation of their magnetic properties. *J. Solid State Chem.* **2013,** *206*, 158-169.

243. Clemens, O.; Kruk, R.; Patterson, E. A.; Loho, C.; Reitz, C.; Wright, A. J.; Knight, K. S.; Hahn, H.; Slater, P. R., Introducing a large polar tetragonal distortion into Ba-doped $BiFeO_3$ by low-temperature fluorination. *Inorg. Chem.* **2014,** *53* (23), 12572-83.

244. Clemens, O., Structural characterization of a new vacancy ordered perovskite modification found for $Ba_3Fe_3O_7F$ ($BaFeO_{2.333}F_{0.333}$): Towards understanding of vacancy ordering for different perovskite-type ferrites. *J. Solid State Chem.* **2015,** *225*, 261-270.

245. Atuchin, V. V.; Gavrilova, T. A.; Grivel, J. C.; Kesler, V. G., Electronic structure of layered ferroelectric high-k titanate $La_2Ti_2O_7$. *J. Phys. D: Appl. Phys.* **2008,** *42* (3), 035305.

246. Hancock, C. A. Anion substitution in Perovskite related materials for fuel cell applications. Ph.D. thesis, University of Birmingham, Birmingham, 2012.

247. Berry, F. J.; Heap, R.; Helgason, Ö.; Moore, E. A.; Shim, S.; Slater, P. R.; Thomas, M. F., Magnetic order in perovskite-related $SrFeO_2F$. *J. Phys.: Condens. Matter* **2008,** *20* (21), 215207.

248. Berry, F. J.; Ren, X.; Heap, R.; Slater, P.; Thomas, M. F., Fluorination of perovskite-related $SrFeO_{3-\delta}$. *Solid State Commun.* **2005,** *134* (9), 621-624.

249. Clauberg, R.; Gudat, W.; Kisker, E.; Kuhlmann, E.; Rothberg, G. M., Nature of the Resonant 6-eV Satellite in Ni: Photoelectron Spin-Polarization Analysis. *Phys. Rev. Lett.* **1981,** *47* (18), 1314-1317.

250. Ning, X.; Wang, Z.; Zhang, Z., Fermi level shifting, charge transfer and induced magnetic coupling at $La_{0.7}Ca_{0.3}MnO_3/LaNiO_3$ interface. *Sci Rep* **2015,** *5*, 8460.

251. Qiao, L.; Bi, X., Direct observation of Ni^{3+} and Ni^{2+} in correlated $LaNiO_{3-\delta}$ films. *EPL* **2011,** *93* (5), 57002.

252. Marco, J. F.; Gancedo, J. R.; Ortiz, J.; Gautier, J. L., Characterization of the spinel-related oxides $Ni_xCo_{3-x}O_4$ (x=0.3,1.3,1.8) prepared by spray pyrolysis at 350 °C. *Appl. Surf. Sci.* **2004,** *227* (1), 175-186.

253. Tranquada, J. M.; Kong, Y.; Lorenzo, J. E.; Buttrey, D. J.; Rice, D. E.; Sachan, V., Oxygen intercalation, stage ordering, and phase separation in $La_2NiO_{4+\delta}$ with $0.05\lesssim\delta\lesssim0.11$. *Phys. Rev. B.* **1994,** *50* (9), 6340-6351.

254. Rice, D. E.; Buttrey, D. J., An X-Ray Diffraction Study of the Oxygen Content Phase Diagram of $La_2NiO_{4+\delta}$. *J. Solid State Chem.* **1993,** *105*, 197-210.

255. Jorgensen, J. D.; Dabrowski, B.; Pei, S.; Richards, D. R.; Hinks, D. G., Structure of the interstitial oxygen defect in $La_2NiO_{4+\delta}$. *Physical Review B* **1989,** *40* (4), 2187-2199.

256. Demourgues, A.; Weill, F.; Darriet, B.; Wattiaux, A.; Grenier, J. C.; Gravereau, P.; Pouchard, M., Additional Oxygen Ordering in "$La_2NiO_{4.25}$" ($La_8Ni_4O_{17}$): I. Electron and Neutron Diffraction Study. *J. Solid State Chem.* **1993,** *106* (2), 317-329.

257. Demourgues, A.; Weill, F.; Darriet, B.; Wattiaux, A.; Grenier, J. C.; Gravereau, P.; Pouchard, M., Additional Oxygen Ordering in "$La_2NiO_{4.25}$" ($La_8Ni_4O_{17}$): II. Structural Features. *J. Solid State Chem.* **1993,** *106* (2), 330-338.

258. Clemens, O.; Kuhn, M.; Haberkorn, R., Synthesis and characterization of the $La_{1-x}Sr_xFeO_{3-\delta}$ system and the fluorinated phases $La_{1-x}Sr_xFeO_{3-x}F_x$. *J. Solid State Chem.* **2011,** *184* (11), 2870-2876.

259. Dervos, C. T.; Vassiliou, P.; Novacovich, J.; Kollia, C., Vacuum heated electroless nickel plated contacts. *IEEE Transactions on Components and Packaging Technologies* **2004,** *27* (1), 131-137.

260. Jović, V. D.; Maksimović, V.; Pavlović, M. G.; Popov, K. I., Morphology, internal structure and growth mechanism of electrodeposited Ni and Co powders. *J. Solid State Electrochem.* **2006,** *10* (6), 373-379.

261. Vanysek, P., Electrochemical Series. In *CRC Handbook of Chemistry and Physics*, 94., ed.; Haynes, W. M., Ed. CRC Press: Boca Rato, FL, 2016.

262. Perez-Mato, J. M.; Gallego, S. V.; Tasci, E. S.; Elcoro, L.; de la Flor, G.; Aroyo, M. I., Symmetry-Based Computational Tools for Magnetic Crystallography. *Annu Rev Mater Res* **2015,** *45*, 217-248.

263. Patra, L.; Kishore, M. R. A.; Vidya, R.; Sjåstad, A. O.; Fjellvåg, H.; Ravindran, P., Electronic and Magnetic Structures of Hole Doped Trilayer $La_{4-x}Sr_xNi_3O_8$ from First-Principles Calculations. *Inorg. Chem.* **2016,** *55* (22), 11898-11907.

264. Nowroozi, M. A.; de Laune, B.; Clemens, O., Reversible Electrochemical Intercalation and Deintercalation of Fluoride Ions into Host Lattices with Schafarzikite-Type Structure. *ChemistryOpen* **2018,** *7* (8), 617-623.

265. Guo, Y.; Wei, Y.; Li, H.; Zhai, T., Layer Structured Materials for Advanced Energy Storage and Conversion. **2017,** *13* (45), 1701649.

266. Xu, J.; Dou, Y.; Wei, Z.; Ma, J.; Deng, Y.; Li, Y.; Liu, H.; Dou, S., Recent Progress in Graphite Intercalation Compounds for Rechargeable Metal (Li, Na, K, Al)-Ion Batteries. **2017,** *4* (10), 1700146.

267. Li, Y.; Lu, Y.; Adelhelm, P.; Titirici, M.-M.; Hu, Y.-S., Intercalation chemistry of graphite: alkali metal ions and beyond. *Chem. Soc. Rev.* **2019,** *48* (17), 4655-4687.

268. Aronson, S.; Salzano, F. J.; Bellafiore, D., Thermodynamic Properties of the Potassium–Graphite Lamellar Compounds from Solid-State emf Measurements. **1968,** *49* (1), 434-439.

269. Asher, R. C., A lamellar compound of sodium and graphite. *J. Inorg. Nucl. Chem.* **1959,** *10* (3), 238-249.

270. Nobuhara, K.; Nakayama, H.; Nose, M.; Nakanishi, S.; Iba, H., First-principles study of alkali metal-graphite intercalation compounds. *J. Power Sources* **2013,** *243*, 585-587.

271. Wang, Z.; Selbach, S. M.; Grande, T., Van der Waals density functional study of the energetics of alkali metal intercalation in graphite. *RSC Advances* **2014,** *4* (8), 4069-4079.

272. Zhang, Y.; Liu, S.; Ji, Y.; Ma, J.; Yu, H., Emerging Nonaqueous Aluminum-Ion Batteries: Challenges, Status, and Perspectives. **2018,** *30* (38), 1706310.

273. Xiao, B.; Rojo, T.; Li, X., Hard Carbon as Sodium-Ion Battery Anodes: Progress and Challenges. *ChemSusChem* **2019,** *12* (1), 133-144.

274. Imaduddin, A.; Nakanishi, Y.; Shimomura, K.; Kanazawa, H.; Nakamura, M.; Yoshimoto, N.; Yoshizawa, M., Elastic and Magnetic Properties of Bilayer Manganites: $La_{2-2x}Sr_{1+2x}Mn_2O_7$ for x=0.35 and 0.40. *J. Phys. Soc. Jpn.* **2002,** *71* (8), 1965-1973.

275. Li, R. K.; Greaves, C., Synthesis and Characterization of the Electron-Doped Single-Layer Manganite $La_{1.2}Sr_{0.8}MnO_{4-\delta}$ and Its Oxidized Phase $La_{1.2}Sr_{0.8}MnO_{4+\delta}$. *J. Solid State Chem.* **2000,** *153* (1), 34-40.

276. Yu, G. Q.; Wang, Y. Q.; Liu, L.; Yin, S. Y.; Ren, G. M.; Miao, J. H.; Xiao, X.; Yuan, S. L., The effect of transition element doping on the electronic and magnetic properties of $La_{1.4}Sr_{1.6}Mn_2O_7$. *Solid State Commun.* **2007,** *141* (3), 136-140.

277. Zheng, L.; Lu, Y.; Zhao, J.-J.; Zhang, X.-Q.; Xing, R.; Wu, H.-Y.; Jin, X.; Zhou, M.; Cheng, Z.-H., Magnetic and transport properties of Dy substituted layered perovskite $La_{1.3}Sr_{1.7}Mn_2O_7$. *Chinese Physics B* **2010,** *19* (12), 127501.

278. Velázquez, M.; Revcolevschi, A.; Renard, J. P.; Dupas, C., The magnetism of $La_{1.2}Sr_{1.8}Mn_2O_7$. **2001,** *23* (3), 307-317.

279. Asano, H.; Hayakawa, J.; Matsui, M., Two-dimensional ferromagnetic ordering and magnetoresistance in the layered perovskite $La_{2-2x}Ca_{1+2x}Mn_2O_7$. *Physical Review B* **1997,** *56* (9), 5395-5403.

280. Gupta, A. K.; Bhalla, G. L.; Khare, N., Magnetic phase diagram of double-layered $La_{2-2x}Ca_{1+2x}Mn_2O_7$ manganite. *J. Phys. Chem. Solids* **2006,** *67* (11), 2358-2364.

281. Asano, H.; Hayakawa, J.; Matsui, M., Magnetotransport in perovskite series $La_{n-nx}Ca_{1+nx}Mn_nO3_{n+1}$ ferromagnets. *Physical Review B* **1998,** *57* (2), 1052-1056.

282. Martin, W., The Solid Electrolyte Interphase – The Most Important and the Least Understood Solid Electrolyte in Rechargeable Li Batteries. *Z. Phys. Chem.* **2009,** *223* (10-11), 1395-1406.

283. Verma, P.; Maire, P.; Novák, P., A review of the features and analyses of the solid electrolyte interphase in Li-ion batteries. *Electrochim. Acta* **2010,** *55* (22), 6332-6341.

284. Standard Thermodynamic Properties of Chemical Substances. In *CRC Handbook of Chemistry and Physics*, 94., ed.; Haynes, W. M., Ed. CRC Press: Boca Rato, FL, 2016.

285. Anitha Sukkurji, P.; Molinari, A.; Reitz, C.; Witte, R.; Kübel, C.; Chakravadhanula, V. S. K.; Kruk, R.; Clemens, O., Anion Doping of Ferromagnetic Thin Films of $La_{0.74}Sr_{0.26}MnO_{3-\delta}$ via Topochemical Fluorination. *Materials* **2018,** *11* (7), 1204.

286. De Marco, R.; Cattrall, R. W.; Liesegang, J.; Nyberg, G. L.; Hamilton, I. C., XPS studies of the fluoride ion-selective electrode membrane LaF_3: Ion interferences. *Surf. Interface Anal.* **1989,** *14* (8), 457-462.

287. Shen, W.; Wang, X. D.; Cattrall, R. W.; Nyberg, G. L.; Liesegang, J., XPS analysis of hydroxide ion surface reactions on reactions on CeF_3 and LaF_3 fluoride ion-selective electrodes. **1997,** *9* (12), 917-921.

288. Li, C.; Liu, X.; Yang, P.; Zhang, C.; Lian, H.; Lin, J., LaF_3, CeF_3, CeF_3:Tb^{3+}, and CeF_3:Tb^{3+}@LaF_3 (Core−Shell) Nanoplates: Hydrothermal Synthesis and Luminescence Properties. *The Journal of Physical Chemistry C* **2008,** *112* (8), 2904-2910.

289. Selvasekarapandian, S.; Vijayakumar, M.; Gnanasekaran, T.; Fujihara, S.; Koji, S., Ion conduction studies on LaF_3 thin film by impedance spectroscopy. *Physica B: Condensed Matter* **2003,** *337* (1), 52-57.

8 List of Abbreviations

ADT	automated diffraction tomography
CB	carbon black
CCD	charged-coupled device
CHA	concentric hemispherical analysers
DESY	Deutsches Elektronen-Synchrotron
EDX	energy dispersive X-ray spectroscopy
EXAFS	extended X-ray absorption spectroscopy
FC	field-cooled
FIB	fluoride-ion battery
GEM	general materials diffractometer
GII	global instability index
GGA	generalised gradient approximation
GOF	goodness-of-fit
HAADF	high-angle annular dark field
HRPD	high-resolution powder diffractometer
HRTEM	high-resolution transmission electron microscopy
NPD	neutron powder diffraction
OCV	open cell voltage
PAW	projector-augmented wave
PBE	Perdew-Burke-Ernzerhof
PED	precession electron diffraction
PTFE	polytetrafluoroethylene
PVDF	polyvinylidene difluoride
RP	Ruddlesden-Popper
RT	room-temperature
SEM	scanning electron microscopy

SQUID	superconducting quantum interference device
TEM	transmission electron microscopy
TOF	time-of-flight
VASP	Vienna ab-initio simulation package
XANES	X-ray absorption near-edge spectroscopy
XAS	X-ray absorption spectroscopy
XPS	X-ray photoelectron spectroscopy
XRD	X-ray diffraction
ZFC	zero-field-cooled

Acknowledgements

At this point, I would like to thank everyone who directly or indirectly contributed to this work.

First and foremost, I would like to express my gratitude to Prof. Dr Oliver Clemens for giving me the opportunity to work in his research group. I thank him for his endless support and trust during the entire time. Without his constant availability for discussions and his impulses, this work would not have been possible in its current form. Sincere thanks for pushing me out of my comfort zone for so many times!

Prof. Dr. Peter R. Slater is acknowledged for being the co-examiner of this work. Additionally, I would like to thank him for allowing me to work in his group during my stay at the University of Birmingham and his valuable input over the last years. I would also like to thank the other members of the examination committee, Prof. Dr. Wolfgang Donner and Prof. Dr. Wolfgang Ensinger.

I would like to thank my current research group Materialdesign durch Synthese for the company and the permanent support. I also thank Fouad Alassani, Ivan Genov, Jonas Heldt, Anna Jakob and Johanna Steinmann for their excellent work during their advance research lab and Master thesis projects and/or as student research assistants. Special thanks to Maria Walker for her support in her role as secretary of the research group.

I would also like to extend my gratitude towards all other collaborators, who made important contributions to this work: Supratik Dasgupta, Dr. Sami Vasala and Dr. Ralf Witte (SQUID measurements), Dr. Alexander Benes, Manuel Donzelli and Tobias Vogel (XPS measurements), Prof. Dr. Matthias Bauer and Dr. Roland Schoch (XAS measurements and analysis), Dr. Ivan da Silva and Dr. Andrew Dominic Fortes (beamline scientists at HRPD and GEM at ISIS), Dr. Emre Erdem (EPR measurements and analysis), Ali Muhammad Malik and Dr. Jochen Rohrer (DFT calculations), Dr. Hergen Breitzke, Prof Dr. Gerd Buntkowsky and Dr. Pedro. B. Groszewicz (NMR measurements and analysis), Aamir Waidha (titration experiments), Prof. Dr. Ute Kolb Dr. Galina Matveeva and Sergi Plana-Ruiz (ADT measurements and analysis).

I gratefully acknowledge the financial support of the Deutsche Forschungsgemeinschaft within the Emmy Noether program (Grant No. CL551/2-1) and of the JUICED Hub (EPSRC Grant No. EP/R023662/1). Neutron diffraction beam time at ISIS was thankfully provided by the Science and Technology Facilities Council (Grant No. 1720040 and RB1820423).

Last but not least, my deepest thanks to my family!